Development of perovskite-like structures for hydrogen production via two-step thermochemical water splitting

George E. Wilson

PhD Thesis

Department of Materials,
Imperial College London

2022

Declaration

I, George E. Wilson, declare the work included within this thesis is wholly my own except where reference is made to that of others. The contents of this work form solely as part fulfilment of doctoral requirements of Imperial College London, and do not contribute towards any other degree course at another institution.

This thesis contains fewer than 36,434 words excluding captions, contents table and references.

George E. Wilson
2022

Copyright

The copyright of this thesis rests with the author. Unless otherwise indicated, its contents are licensed under a Creative Commons Attribution-Non Commercial 4.0 International Licence (CC BY-NC).

Under this licence, you may copy and redistribute the material in any medium or format. You may also create and distribute modified versions of the work. This is on the condition that: you credit the author and do not use it, or any derivative works, for a commercial purpose.

When reusing or sharing this work, ensure you make the licence terms clear to others by naming the licence and linking to the licence text. Where a work has been adapted, you should indicate that the work has been changed and describe those changes.

Please seek permission from the copyright holder for uses of this work that are not included in this licence or permitted under UK Copyright Law.

Acknowledgements

First and foremost, I would like to thank Dr Ainara Aguadero for allowing me the chance to carry out this research project. Her mentorship over the past 5 years has allowed this project to progress and investigate a wide range of materials. Ainara's knowledge of solid-state chemistry is astounding and been able to guide me through the trickiest of problems.

Secondly, Dr Andrea Cavallaro, who inspired me with his practical prowess for experiments and deep knowledge of surface chemistry. From first showing me initial synthesis methods as a MEng student to being able to discuss complex scientific problems, his curiosity for the work covered in this project encouraged me to persist during the toughest times.

Next, Professor Stephen Skinner, has been able to not only provide fruitful scientific discussion but also willing to help with experienced and realistic suggestions for issues regarding experiments and beyond.

Over the course of this work, I have been fortunate enough to work with several talented postdoctoral researchers within the Electroceramics Group. Dr Ieuan Seymour truly reinvigorated my project, and I would like to thank him for the endless effort and patience when teaching the computational side of this work. Dr Paul Boldrin who first helped develop the thermochemical water splitting rig from scratch. Dr Özden Celikbilek, Dr Zonghao Shen, Dr Rowena Brugge, Dr Celeste van den Bosch and Dr Shrikant Kawale for sharing their scientific wisdom and welcoming me to the group. Dr Federico Pesci and Dr Mathew Niania for always leading the charge to the pub on Friday afternoons.

The experimental work in this thesis could not have been completed without the traning and guidance of the departmental research facility managers; Dr Gwilherm Kerheve, Dr Sarah Fearn, Dr Andrey Berenov, Dr Mahmoud Ardakani. Mr Richard Sweeney who I worried too much with my experimental requirements and wish to thank him for his trust and opportunities to develop my teaching skills.

I am thankful to the centre of doctoral training for fuel cells and their fuels for providing funding for this project. This program has provided opportunities to travel the world to share my research. The training modules allowed me to gain a comprehensive understanding of

hydrogen technologies alongside meeting some amazing like-minded researchers who have become great friends.

My friends who have undertaken the PhD journey with me and provided fruitful conversation. The brilliant surface scientists Dr Zijie (Jerry) Sha and Mr Edouard Querel for taking their time to discuss XPS fittings. Mr Nicholas Williams for computational and theoretical discussions, and endless enthusiasm for exercise and life. Mr Nomaan Nabi, Miss Jia Guo and Miss Ritika Vastani for their assistance and happy nature in the laboratory. Miss Fiona Sandler, Miss Daisy Thornton, Miss Caoimhe Joyce, Mr Debesh Mandal, Mr Sam Rogers and Mr Tristan Dell for providing a social escape with lunchtime chats, coffees and pints.

Further thanks are given to those who supported me from beyond Imperial College who have had to listen to me talk about my PhD to no personal avail - Mr Alexander Powel, Mr Michael Howlett, Miss Chantal Whitfield, Mr Andrew Rolland, Mr Spike Ibeji and Mr Robert Williams.

Thank you to my wonderful family who have provided endless support throughout this journey and always shown interest into the topic of my project. They have seen me overcome some of the largest hurdles in my life so far and were always there for me, for which I am forever grateful.

Finally, Miss Rose Oates, for her endless love and encouragement throughout the ups and downs in this project. Without Rose's support none of the achievements from this project would be possible.

Abstract

Hydrogen powered technologies are proposed to help mitigate climate change as low carbon-emitting technologies. Devices such as fuel cells convert the chemical energy stored within hydrogen molecules via electrochemical redox processes to electrical energy for work. These technologies have the primary benefit of not emitting carbon dioxide – one of the main contributing pollutants towards the greenhouse effect. However, current commercial hydrogen production technologies require fossil fuel reactants and emit carbon dioxide as a product. Therefore, research into ways of producing hydrogen from sustainable non-polluting sources has been of keen interest within the scientific community. One such technique is high temperature thermochemical water splitting. This process uses renewable concentrated solar power to heat up and thermally reduce metal oxide compounds and induce an oxygen non-stoichiometry within the lattice. The oxygen deficiency is then removed upon reoxidising with steam and producing hydrogen gas.

Numerous thermochemical redox cycles have been proposed within the literature with the main aim to lower the reduction temperatures and increase the hydrogen production volumes. This has turned the attention of the field to investigate the ABO_3 perovskite structures due to their ability to support a larger oxygen deficiency at lower temperatures compared to the benchmark material, cerium oxide, CeO_2. This thesis combines theoretical first principle approaches and a wide range of experimental techniques to understand and discuss three different families of perovskite and perovskite-like metal oxide structures.

The main findings of this thesis can be summarised as the following:

Effect of antimony incorporation on the redox kinetics of $SrCoO_{3-\delta}$

- Thermal analysis techniques observe large oxygen production volumes onset between 300 and 400 °C under an inert gas flow with increased antimony content lowering total production.
- Density Functional Theory (DFT) confirms the low reduction enthalpy in the region of 0.5 eV/O atom. Increased Sb concentration and proximity to the dopant increases vacancy formation energy.

- Low reduction enthalpy of the material was not favourable to drive thermochemical water splitting, however isothermal redox cycling demonstrated good performance for the alternative application of thermochemical oxygen separation compared to literature materials.
- Antimony donor ions are postulated to lower the cobalt crystal field splitting to support an intermediate spin electron configuration with more favourable orbital filling for fast redox kinetics (e_g=1).

Effect of iron incorporation in $(La_{0.8}Sr_{0.2})_{0.95}Cr_{1-x}Fe_xO_{3-\delta}$ perovskites for thermochemical water splitting

- Thermal analysis used to observed increasing Fe content coincides with an increase the oxygen production volumes and rates
- DFT used to confirm lower vacancy formation energy in positions neighbouring Fe cations. Further predicted to have favourable thermodynamic properties for thermochemical water splitting.
- Thermochemical water splitting observed hydrogen production rates similar to literature materials, $Ce_{0.75}Zr_{0.25}O_{2-\delta}$.
- Surface analysis techniques novel to this research field revealed increased strontium segregation towards the surface that prevented cyclability of the compounds.
- Strontium-enriched perovskite surfaces can undergo reconstruction to form derivative phases such as Ruddlesden-Popper oxides, $A_{n+1}B_nO_{3n+1}$.

Computational screening of n=1 Ruddlesden-Popper oxides for thermochemical water splitting

- Screening study uses a combination of well-known crystallographic principles and DFT simulations to narrow down the field of this underexplored metal oxide family for use in thermochemical water splitting.
- From an initial 27,899 structures, this study outlines a potential 30 A_2BO_4 Ruddlesden-Popper structures that have favourable reduction thermodynamics and "synthesisable" under laboratory conditions.
- A new simpler and better fitting descriptor based on the lattice enthalpy is proposed to assist future screening work of Ruddlesden-Popper oxides at significantly reduced computational expense.

Investigating Ca_2MnO_4 Ruddlesden-Popper oxide for thermochemical water splitting

- Outputted compound from the prior screening study is explored further due its abundant constituent elements and favourable reduction thermodynamics.
- Thermal analysis techniques observe similar oxygen production behaviour to the $(La_{0.8}Sr_{0.2})_{0.95}Cr_{1-x}Fe_xO_{3-\delta}$ perovskites investigated in a previous chapter.
- Hydrogen was successfully produced via thermochemical redox reactions cycling between 1000 and 800 °C, thus experimentally verifying the screening study.
- Further improvements are suggested by including doping ions to alter the thermodynamics or investigating the effect of perovskite/Ruddlesden-Popper heterostructures that have previously been observed to accelerate oxidation reactions.

List of Publications

Chapter 4 contains information from:

Wilson, G. E., Seymour, I. D., Cavallaro, A., Skinner, S. J., Aguadero, A.. Fast redox kinetics in $SrCo_{1-x}Sb_xO_{3-\delta}$ perovskites for thermochemical energy storage and oxygen separation, *J. Electrochem. Soc.* 2022, **169**, 044509

Other publications not included within this thesis:

Cavallaro, A., **Wilson, G. E.,** Kerheve, G., Cali, E., van den Bosch, C. A. M., Boldrin, P., Payne, D., Skinner, S. J., Aguadero, A.. Analysis of H_2O-induced surface degradation in $SrCoO_3$-derivatives and its impact on redox kinetics. *J. Mater. Chem. A,* 2021, 9, 24528-24538

Guo, J., Cai, R., Cali, E., **Wilson, G.E.,** Kerheve, G., Haigh, S. J., Skinner, S. J.. Low-Temperature Exsolution of Ni–Ru Bimetallic Nanoparticles from A-Site Deficient Double Perovskites. *Small*, 2022, 2107020.

High. M., Patzschke, C.F., Zheng, L., Zeng, D., Gavaldà Diaz, O., Ding, N., Chien, K. H. H., Zhang, Z., **Wilson, G.E.,** Berenov, A. V., Skinner, S. J., Sedransk-Campbell, K. L., Scott, S., Xiao, R., Fennell, P. S., Song Q.. Precursor engineering of hydrotalcite-derived copper-based redox sorbents for reversible and stable oxygen storage in chemical looping processes. (Submitted)

Table of Contents

Declaration **2**

Acknowledgements **3**

Abstract **5**

List of Publications **8**

Table of Contents **9**

List of Figures **11**

List of Tables **18**

Nomenclature and Abbreviations **19**

1. Introduction **20**

1.1. Motivation 20
1.2. Water Splitting Technologies 24

2. Fundamentals of Thermochemical Water Splitting **31**

2.1. Defect chemistry in oxides 31
2.2. Extrinsic Defects 33
2.3. Transition metal-Oxygen bonding in perovskites 34
2.4. Thermodynamics 37
2.5. Reaction Kinetics 42
2.6. Efficiency 48
2.7. Material Design for Optimal performance 50

3. Literature Review of thermochemical redox materials **51**

3.1. Stoichiometric Systems 53
3.2. Non-stoichiometric Systems 55
3.3. Beyond Perovskite materials 63
3.4. Summary 63

4. Thesis outline **65**

5. Materials and Methods **67**

5.1. Powder Synthesis by Modified Sol-Gel Method 67
5.2. Powder characterisation 68
5.3. Surface Chemistry Analysis 73
5.4. Thermal Analysis techniques 78
5.5. Measuring Thermochemical Water Splitting Performance 81

5.6. First Principles modelling through Density Functional Theory 84

6. Investigating the effect of antimony concentration on the fast redox kinetics of $SrCo_{1-x}Sb_xO_{3-\delta}$ for thermochemical energy storage, oxygen separation and water splitting 97

6.1. Introduction to $SrCo_{1-x}Sb_xO_{3-\delta}$ 97

6.2. Results and Discussion 100

6.3. Conclusions 128

7. Investigating the effect of iron concentration in $(La_{0.8}Sr_{0.2})_{0.95}Cr_{1-x}Fe_xO_{3-\delta}$ for thermochemical water splitting 129

7.1. Introduction to $(La_{0.8}Sr_{0.2})_{0.95}Cr_{1-x}Fe_xO_{3-\delta}$ 129

7.2. Results and Discussion 131

7.3. Conclusion 174

8. Screening of new n=1 Ruddlesden-Popper materials for thermochemical water splitting by reduction thermodynamics 175

8.1. Introduction to Ruddlesden-Popper Oxides 175

8.2. Screening criteria 177

8.3. Computational Results and Discussion 179

8.4. Conclusions 200

9. Investigating Ca_2MnO_4 for thermochemical water splitting 201

9.1. Previous investigations into Ca2MnO4 201

9.2. Results and Discussion 202

9.3. Conclusions 222

10. Conclusions 224

11. Future Work 226

References 228

Appendix A – Supplementary information for Chapter 4 277

Appendix B – Supplementary information for Chapter 6 279

Appendix C – Supplementary information for Chapter 7 288

Appendix D – Supplementary information for Chapter 8 289

Appendix E – Supplementary information for Chapter 9 300

List of Figures

Figure 1-1. Demonstration of how the peak electricity load of the grid progresses over the duration of a week. [4] 21
Figure 1-2. Schematics of a) low temperature polymer electrolyte membrane fuel cell, and b) high temperature solid oxide fuel cell. 22
Figure 1-3. Hydrogen fuel cell bus operating in London September 2021 23
Figure 1-4. Schematic diagrams of a) alkaline electrolysers, b) polymer electrolyte membrane electrolysers, and c) solid oxide electrolysers. 26
Figure 1-5. Schematic of a photoelectrochemical water splitting device based on a photoanode and metal cathode. 27

Figure 2-1. Schematic representation of interstitial and vacancy point defects in a lattice structure. .. 31
Figure 2-2. a) Evolution of electron energy as metal cations and oxygen anions are moved from free ions to octahedral coordination within the perovskite lattice. The crystal field splitting of the d-orbitals is observed alongside the formation of bonding states. Translational symmetry within the solid causes these states to appear as bands in real systems. Adapted from [55], [56], [60] b) Metal d and oxygen-orbital spacing in octahedral configurations giving rise to the crystal field splitting effect. 36
Figure 2-3. Schematic showing the evolution of density of states during metal oxide lattice reduction. Adapted from [56]. 37
Figure 2-4. Gibbs free energy curve for the thermochemical redox of a metal oxide. The dashed blue line demonstrates how lowering the oxygen partial pressure can lower the required reduction temperature. The dashed orange line represents how increasing the moles of H_2O can drive the oxidation reaction at higher temperatures. 39
Figure 2-5. Schematic representation of a) typical oxygen non-stoichiometry data plotted as function of oxygen partial pressure, b) van't Hoff representation of the data to calculate the thermodynamic quantities. 42
Figure 2-6. Relationship between energy and ion migration within solid lattices. 44
Figure 2-7. Summary of steps in the reaction between steam and reduced metal oxide surface. 47
Figure 2-8. Schematic of a Heliostat concentrated solar power reactor commonly used for thermochemical water splitting. 49
Figure 3-1. Comparison between the evolution of oxygen content as temperature increases between stoichiometric and non-stoichiometric metal oxides. 52
Figure 3-2. Categorising the different classes of thermochemical water splitting metal oxides. 52

Figure 3-3. Crystal structure of a) Fe_3O_4 inverse spinel magnetite phase and b) FeO rock salt phase. Blue polyhedra represent the Fe^{3+} tetrahedra and the brown polyhedra demonstrates the Fe^{2+} or Fe^{3+} octahedra. 54
Figure 3-4. Crystal structure of face centred cubic CeO_2. 56
Figure 3-5. Dopant elements in ceria investigated for thermochemical water splitting reviewed in [132]. 57
Figure 3-6. Perovskite with $Pm3m$ crystal structure. 60

Figure 5-1. Schematic demonstrating Bragg's Law for X-ray diffraction between two atomic planes. Adapted from [7]. 69
Figure 5-2. Schematic representation of a scanning electron microscope column. 72
Figure 5-3. Schematics showing the formation of a) secondary electrons, b) backscattered electrons, and c) characteristic X-rays, in scanning electron microscopy. 72
Figure 5-4. Schematic showing the interaction volume of an electron beam and sample surface. 73
Figure 5-5. Schematic demonstration of the photoelectron emission of electrons in XPS. Adapted from [189]. 74
Figure 5-6. Schematic of X-Ray photoelectron spectrometer. 76
Figure 5-7. Schematic showing the scattering of primary ion used within LEIS. Adapted from [196]. 77
Figure 5-8. Schematic of Simultaneous Thermal Analyser (TGA/DSC). 79
Figure 5-9. Schematic of the home-built thermochemical water splitting setup. 81
Figure 5-10. Schematic representation of a quadrupole mass spectrometer. 84
Figure 5-11. Schematic demonstrating the allowed values of k as points. The number of states located within the shell defined by radius, k, and thickness, dk, can be represented as a function of energy using the electron dispersion relationship. 91
Figure 5-12. Schematic demonstrating the Bader charge analysis principle. 93
Figure 5-13. Schematic representation of a convex hull to determine thermodynamic stability of a binary compound. 94
Figure 5-14. Typical DFT calculation workflow used for the simulations in this thesis. 96
Figure 6-1. Strontium cobalt oxide polymorphs. a) 2H face-sharing octahedra polymorph, b) P4mmm tetragonal structure, c) 3C cubic polymorph. 99
Figure 6-2. a) Stirring solution of Sr, Co and Sb nitrate salts in citric acid, b) Subsequent gel formed upon polymerisation. 100
Figure 6-3. XRD diffractograms of the different Sb-doped SrCoO3 compounds, a) $SrCo_{0.95}Sb_{0.05}O_{3-\delta}$, b) $SrCo_{0.90}Sb_{0.10}O_{3-\delta}$ and c) $SrCo_{0.80}Sb_{0.20}O_{3-\delta}$. 103

Figure 6-4. Scanning electron micrographs of synthesis $SrCo_{0.95}Sb_{0.05}O_3$ powder showing a) the size distribution and b) increased magnification of the particle. 104
Figure 6-5. Thermal analysis of $SrCo_{1-x}Sb_xO_{3-\delta}$ showing a) thermogravimetric signal converted to oxygen stoichiometry, b) DSC signal, c) O_2 production detected in the exhaust stream. d) peak rate and total volume of O_2 production as a function of Sb concentration. 106
Figure 6-6. HT-XRD patterns collected at 50 °C intervals up to 800 °C for a) 5% Sb, b) 10% Sb and c) 20% Sb compounds. The splitting of the (101) peak is observed above 400 °C in a). References for the P4mmm and $Pm3m$ space groups' Bragg reflections are displayed beneath the 25 °C diffractograms. Symbols denote the following: ♥ - Sb_2O_3, ♦ - Sb_2O_5, ♣ - Co_3O_4. 109
Figure 6-7. Geometrically relaxed structures for the a) 0%, b) 3.125%, c) 6.25% and d) 25% Sb-doped $SrCoO_3$ compounds. 112
Figure 6-8. Density of states plots for the a) 0%, b) 3.125%, c) 6.25% and d) 25% Sb-doped $SrCoO_3$ compounds. The vertical lines display the position of the Fermi energy (solid) and oxygen p band centre (dashed). 113
Figure 6-9. a) Computed oxygen vacancy formation enthalpy as a function of Sb concentration and coordination sphere with dopant cation. b) Relationship between O p band centre and Sb concentration within the structure. 115
Figure 6-10. $SrCo_{0.9}Sb_{0.1}O_{3-\delta}$ isothermal redox cycling experiment at 600 °C. 116
Figure 6-11. Comparison between reduction reaction conversions for different Sb concentrations at increasing temperatures. 117
Figure 6-12. Comparison between oxidation reaction conversions for different Sb concentrations at increasing temperatures. 118
Figure 6-13. a) Predicted number of e_g^* electrons and as a function of temperature for each of the $SrCo_{1-x}Sb_xO_{3-\delta}$ compounds, b) comparison between oxidation reaction conversion at 600 °C of the $SrCo_{1-x}Sb_xO_{3-\delta}$ against oxygen separation materials reported within the literature. [260] 119
Figure 6-14. Theoretical oxygen exchange volumes for $SrCo_{1-x}Sb_xO_{3-\delta}$ compounds under a) temperature-swing conditions T_{red} = 800 °C, and b) isothermal conditions T_{red}=T_{ox}. 120
Figure 6-15. Comparisons generated from the DSC signal to show temperature and Sb effects on a) energy released, b) energy stored, and cyclability of c) energy storage and d) oxygen incorporation kinetics. 121
Figure 6-16. Scanning electron micrographs of the a) and b) 5% Sb compound and the c) and d) 20% Sb sample after isothermal redox cycling at 800 ºC. 122
Figure 6-17. Post-cycling XRD patterns for a) 5%, b) 10% and c) 20% Sb compounds. Reference peaks for the $SrCo_6O_{11}$, $Sr_6Co_5O_{15}$ and $Sr_2Sb_2O_7$ peaks are shown below the diffractograms of the powder cycles at 500 °C. Symbols denote the following: ♥ - Sb_2O_3, ♦ - Sb_2O_5, ♣ - Co_3O_4. 124

Figure 6-18. Hydrogen and oxygen production detected throughout a thermochemical water splitting cycle run between 800 and 400 °C. 125
Figure 6-19. XRD pattern of Sb 20% compound post thermochemical water splitting. 126
Figure 6-20. Scanning electron micrographs of the Sb 20% compound after thermochemical water splitting experiment cycling between 800 and 400 °C. 127

Figure 7-1. Schematic demonstrating the principles of an oxygen transport membrane. 130
Figure 7-2. Le Bail refinement of LSCrF-8273 pristine powder with a $R3c$ space group. 133
Figure 7-3. Le Bail refinement of LSCrF-8282 pristine powder with a $R3c$ space group. 133
Figure 7-4. Le Bail refinement of LSCrF-8291 pristine powder with a $R3c$ space group. 134
Figure 7-5. XPS Spectra for the Sr 3d level for a) LSCrF-8273, b) LSCrF-8282 and c) LSCrF-8291. 135
Figure 7-6. XPS Spectra for the Cr 2p level for a) LSCrF-8273, b) LSCrF-8282 and c) LSCrF-8291. 136
Figure 7-7. XPS Spectra for the Fe 2p level for a) LSCrF-8273, b) LSCrF-8282 and c) LSCrF-8291. 137
Figure 7-8. Secondary electron micrographs of the LSCrF-8282 powder. 138
Figure 7-9. Oxygen evolution from the LSCrF powders heating at 20 °C/min. 140
Figure 7-10. Comparisons between the total oxygen production and peak oxygen production of the LSCrF powders up to 1200 °C. 140
Figure 7-11. Geometrically relaxed structures of the $LaCrO_3$ structures with a) 0%, b) 6.25%, c) 12.5% and d) 25% Fe substituted onto the B-site. 142
Figure 7-12. Oxygen vacancy formation energy for $LaCr_{1-x}Fe_xO_3$ as function of Fe content a spatial coordination to the Fe cation within the structure. 143
Figure 7-13. DOS plots for a) 0%, b) 6.25%, c) 12.5% and d) 25% Fe content on $LaCr_{1-x}Fe_xO_3$. 144
Figure 7-14. Partial molar enthalpy and entropy for lanthanum chromium-based perovskites and other thermochemical water splitting materials reported within literature. [126], [345] 147
Figure 7-15. High temperature X-ray diffraction under nitrogen up to 1200 °C in 100 °C intervals for a) LSCrF-8273, b) LSCrF-8282 and c) LSCrF-8291. 151
Figure 7-16. Lattice parameters and cell volume as a function of temperature for the LSCrF powders. 153
Figure 7-17. Secondary electron image showing the macrosphere structure of the a) LSCrF-8273 and b) LSCrF-8282 powders after heating to 1200 °C for 2 hours under flowing argon. 154
Figure 7-18. Secondary electron micrographs of the LSCrF-8282 powder surface a) as-received and heating under flowing argon for two hours at b) 800 °C, c) 1000 °C and d) 1200 °C. 156

Figure 7-19. Gas evolution from LSCrF-8273 throughout the 1200-800 °C thermochemical water splitting cycle. 159
Figure 7-20. Gas evolution from LSCrF-8282 throughout the 1200-800 °C thermochemical water splitting cycle. 160
Figure 7-21. Gas evolution from LSCrF-8291 throughout the 1200-800 °C thermochemical water splitting cycle. 160
Figure 7-22. Comparison between H_2 evolution of the LSCrF powders (T_{red} = 1200 °C; T_{ox} = 800 °C) and $Ce_{0.75}Zr_{0.25}O_2$ (T_{red} = 1400 °C; T_{ox} = 1000 °C). The signals have been smoothed using an adjacent-average method for enhanced clarity. 161
Figure 7-23. Secondary electron micrographs of a,b) LSCrF-8273, c,d) LSCrF-8282, and e,f) LSCrF-8291 powders after thermochemical water splitting cycles at 1200/800 °C. 162
Figure 7-24. XRD diffractograms for a) LSCrF-8273, b) LSCrF-8282 and c) LSCrF-8291 compounds after 1200/800 °C thermochemical water splitting cycles. 165
Figure 7-25. XPS spectra of the Sr 3d core level at RT (first row), 800 (second row) and 1200 (third row), for the LSCrF compounds 8273 (first column a, d, g), 8282 (second column b, e, h) and 8291 (third column c, f, i). 167
Figure 7-26. Ratio of Sr 3d5 to La 3d5 core level peaks in the LSCrF powders as a function of thermal history. 168
Figure 7-27. LEIS depth profiles of A-site cations at RT (first row), 800 (second row), 1000 (third row) and 1200 °C (fourth row), for the LSCrF compounds 8273 (first column a, d, g, j), 8282 (second column b, e, h, k) and 8291 (third column c, f, i, l). 172
Figure 7-28. LEIS depth profiles of B-site cations at RT (first row), 800 (second row), 1000 (third row) and 1200 °C (fourth row), for the LSCrF compounds 8273 (first column a, d, g, j), 8282 (second column b, e, h, k) and 8291 (third column c, f, i, l). 173

Figure 8-1. Possible Ruddlesden-Popper structures as a function of n. 176
Figure 8-2. Reduction in number of potential vacancy-supporting compounds after initial screening parameters were applied. 179
Figure 8-3. Comparisons of prospective vacancy supporting compounds properties prior after initial screening parameters. 180
Figure 8-4. Reduction in number of potential interstitial candidates after initial screening parameters were applied. 181
Figure 8-5. Comparisons of prospective interstitial supporting compounds properties prior after initial screening parameters. 182
Figure 8-6. Comparisons of a) A-site elements and b) Cation oxidation states of stable RP-214 structures that are able to support the formation of oxygen vacancies. 184

Figure 8-7. Comparisons of a) A-site elements and b) Cation oxidation states of stable RP-214 structures that are able to support the formation of oxygen interstitials. 184
Figure 8-8. Locations of the different defects introduced in the RP-214 structure. 185
Figure 8-9. Reduction enthalpy of oxygen vacancy supporting thermodynamically stable RP-214 compounds. The compounds are grouped with common A-site cations and arrange B-sites with increasing atomic number. The colours are unique to B-site elements. 188
Figure 8-10. Electron configurations of a B-O-B bond in Sr_2MO_4 (M=Cr to Fe) in the a) oxidised state (δ=0) and b) reduced state. (δ = -0.25) after the vacancy has been formed. 189
Figure 8-11. Reduction enthalpy of oxygen interstitial supporting thermodynamically stable RP-214 compounds. The compounds are grouped with common A-site cations and arrange B-sites with increasing atomic number. The colours are unique to B-site elements. 191
Figure 8-12. B-site element electron configurations of a) oxidised $La_2MO_{4.25}$ and b) reduced La_2MO_4 (M=Co, Ni or Cu) after the oxygen interstitial has been removed. Both spin configurations are shown here as a short comparison. 192
Figure 8-13. Comparison between reduction enthalpy and oxygen p band centre for the n=1 Ruddlesden-Popper phases. 195
Figure 8-14. Comparison between reduction enthalpy and charge delocalisation for the n=1 Ruddlesden-Popper phases. 197
Figure 8-15. Comparison between reduction enthalpy and ionic electrostatic potential for the n=1 Ruddlesden-Popper phases. 199

Figure 9-1. Ca_2MnO_4 structures with an oxygen vacancy introduced on the a) equatorial and b) apical lattice sites. The orange octahedra indicate the manganese ions with increased magnetic moment indicating a decrease in oxidation state. 204
Figure 9-2. Images of the Ca_2MnO_4 synthesis process showing a) formed gel of metal nitrate solutions and b) final powder state. 205
Figure 9-3. XRD diffractogram of the synthesised Ca_2MnO_4 powder. 206
Figure 9-4. XPS spectra obtained for the Ca_2MnO_4. a) Ca 2p, b) O 1s, c) Mn 2p and d) Mn 3s core level spectra. 208
Figure 9-5. Secondary electron images of the synthesised Ca_2MnO_4 powder. 209
Figure 9-6. Thermal analysis results from heating Ca_2MnO_4 under an argon environment. a) Mass % and DSC signal as a function of temperature, b) O_2 detected in the exhaust stream and oxygen stoichiometry converted from the mass loss. 211
Figure 9-7. High temperature X-ray diffractograms between 600 and 1200 °C of Ca_2MnO_4 under a nitrogen flow. Asterisks indicate the presence of $CaMn_2O_4$ spinel phase forming at high temperatures. 213

Figure 9-8. Contrast enhanced images of the $Ca2MnO_4$ powders heated under inert gas flow to a) 1000 °C and b) 1200°C. Presence of the $CaMn_2O_4$ spinel phase is observed by the reddish-brown spots in b). 214
Figure 9-9. Comparison between the oxygen evolution for Ca_2MnO_4 measured directly from the exhaust gas and calculated production from the TG mass signal. 214
Figure 9-10. Lattice parameters outputted from the high-temperature X-ray diffraction of Ca_2MnO_4 under nitrogen gas. 215
Figure 9-11. Gas production of the 1000/800 °C thermochemical water splitting cycle for Ca_2MnO_4. 217
Figure 9-12. X-ray diffractogram of Ca_2MnO_4 after thermochemical water splitting cycle at 1000 and 800 °C. 218
Figure 9-13. Secondary electron micrographs of the Ca_2MnO_4 powder after a) synthesis, b) heating to 1000 °C under Argon and c) after thermochemical water splitting at 1000/800 °C. 219
Figure 9-14. XPS spectra of the Mn core levels for Ca_2MnO_4 powder after a,b) heating to 1000 °C under argon and c,d) thermochemical water splitting at 1000/800 °C. 221
Figure 9-15. XPS spectra of the Ca 2p and O 1s core levels for Ca_2MnO_4 powder after a,b) heating to 1000 °C under argon and c,d) thermochemical water splitting at 1000/800 °C. 222

List of Tables

Table 5-1. Possible photoelectron peaks arising due to spin orbital coupling. 75
Table 5-2. List of U corrections used within this thesis..... 88
Table 6-1. Commonly investigated non-redox-active B-site dopants for strontium cobalt oxide compounds. 98

Table 6-2. Refined lattice parameters for the $SrCo_{1-x}Sb_xO_{3-\delta}$. 103

Table 7-1. Outputted lattice parameters from Le Bail refinement of LSCrF powders. 134
Table 7-2. Interpolated partial molar enthalpy and entropy values for the LSCrF powders used in this study. 148
Table 7-3. Gas evolution volumes for the LSCrF compounds over two cycles at 1200 and 800 °C. 158
Table 7-4. Lattice parameters and fitting results for the Le Bail refinement of the LSCrF compounds after thermochemical water splitting cycles..... 165

Table 8-1. List of Ruddlesden-Popper metal oxides favourable for thermochemical water splitting using vacancy point defects. 193
Table 8-2. List of Ruddlesden-Popper metal oxides favourable for thermochemical water splitting using institial point defects. 194

Table 9-1. Comparison of reduction enthalpy, oxygen band centre and oxygen charge for the perovskite and n=1 Ruddlesden-Popper calcium manganate phases. 203
Table 9-2. Lattice parameters for the synthesised Ca_2MnO_4 compared to reference literature data. . 207
Table 9-3. Gas production volumes for Ca_2MnO_4 thermochemical water splitting cycle between 1000 and 800 °C and 50% humidity. 217
Table 9-4. Comparison of lattice parameters of the synthesised Ca_2MnO_4 and post thermochemical water splitting cycle powder. 218

Nomenclature and Abbreviations

TWS	Thermochemical Water Splitting
δ	Oxygen non-stoichiometry
DFT	Density Functional Theory
SCO	$SrCoO_{3-\delta}$
LSCrF	$La_{1-x}Sr_xCr_{1-y}Fe_yO_{3-\delta}$
RP-214	Ruddlesden Popper A_2BO_4
HS	High Spin
LS	Low Spin
IS	Intermediate Spin
TGA	Thermogravimetric Analysis
DSC	Differential Scanning Calorimetry
XRD	X-Ray Diffraction
SEM	Scanning Electron Microscopy
LEIS	Low Energy Ion Scattering
XPS	X-Ray Photoelectron Spectroscopy

1. Introduction

1.1. Motivation

Within modern society there is a requirement for technologies to do more. Transport needs to go further and faster, devices need to respond faster and have a longer lifetime. With these developments in technology there is a consequently increase in demand for energy. Traditionally, these demands have been met by the combustion of fossil fuels, however these produce greenhouse gases that are detrimental to the environmental due to their contribution towards climate change, air pollution and acid rain. [1], [2] These resulting environmental issues have instigated the innovation of cleaner technologies that convert abundant renewable sources such as wind and solar power into more useful forms of energy. Renewable technologies have boomed in recent years and are providing a larger share of global energy generation. In 2019, nearly 8000 TWh was produced by renewable sources equating to a share of 23.2%.[3] Comparing to a 17% share in 2009, renewable electricity generation has shown year-on-year increase despite the global COVID-19 pandemic. [3]

However, there are times when the demand for energy is not in-line with the peak production of renewables. For example, the peak demand in energy is usually towards the late afternoon/evening on weekdays when people return home from work. In combination with unpredictable renewable energy supplies, it makes it difficult for energy companies to manage the electricity grid leading to volatile prices for the consumer. To overcome this, ideally renewable energy can be stored and used during these times of high demand.[4] Previously, the scaling up of technologies such as secondary batteries, has been used to store renewable energy in forms of chemical energy. Even though batteries are a well-established technology and have promising potential for transportation and personal devices, there have been concerns of their use for long-term grid scale storage due to limited energy densities and degradation of the electrodes. [5]

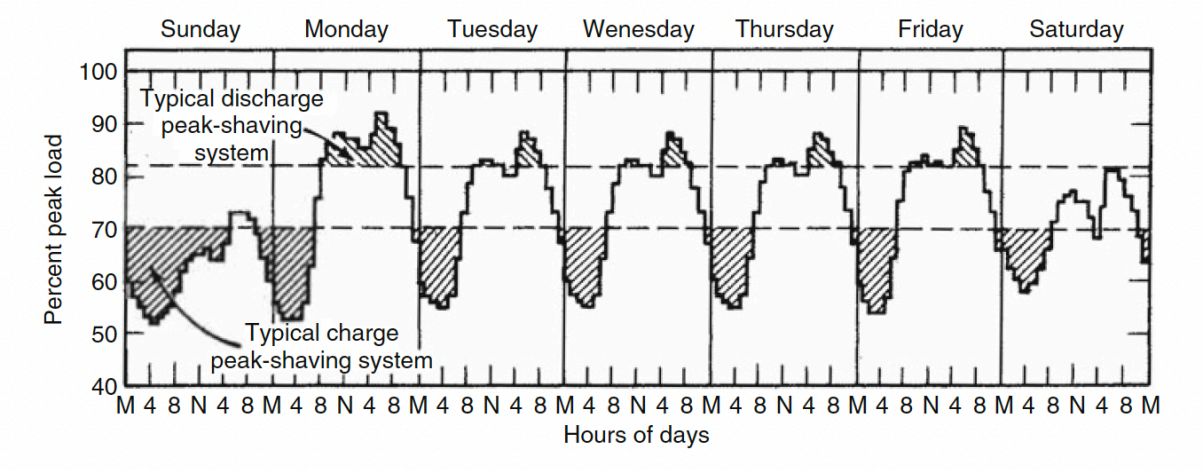

Figure 1-1. Demonstration of how the peak electricity load of the grid progresses over the duration of a week. [4]

Hydrogen has been actively researched as an alternative energy storage technology. Hydrogen gas has the highest energy content of any carbon free fuel. (120 MJ/kg). In particular it is at least double the value compared to conventional hydrocarbon fuels (Methane = 50 MJ/kg and Diesel = 42.5 MJ/kg). [6] This chemical energy can be converted through electrochemical devices such as fuel cells. Hydrogen and oxygen are fed to opposite electrodes of the device where they undergo respective redox reactions depending on the fuel cell chemistry. Electrons produced by the anodic reaction are transported via an external circuit to do work at other electrical devices. Ions are chemically driven across the electronically insulating electrolyte to participate in the redox reaction at the opposite electrode. The resulting overall reaction for hydrogen-based fuel cells is given by Equation 1.1. Importantly the only product is water, therefore these devices are carbon neutral. Figure 1-2 show the schematic workings of the two common type of hydrogen-based fuel cells - low temperature polymer electrolyte membrane fuel cells and high temperature solid oxide fuel cells.

$$H_2 + \frac{1}{2}O_2 \rightarrow H_2O \tag{1.1}$$

a)

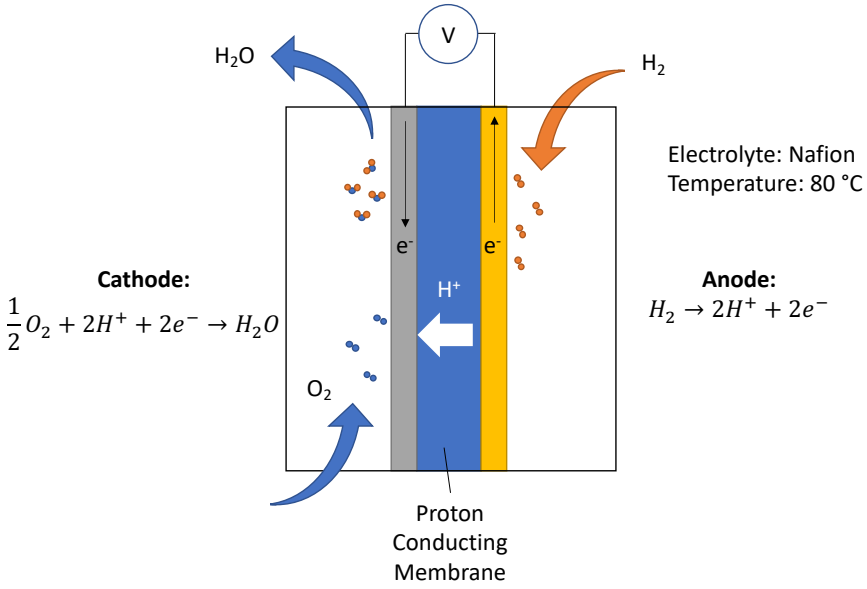

b)

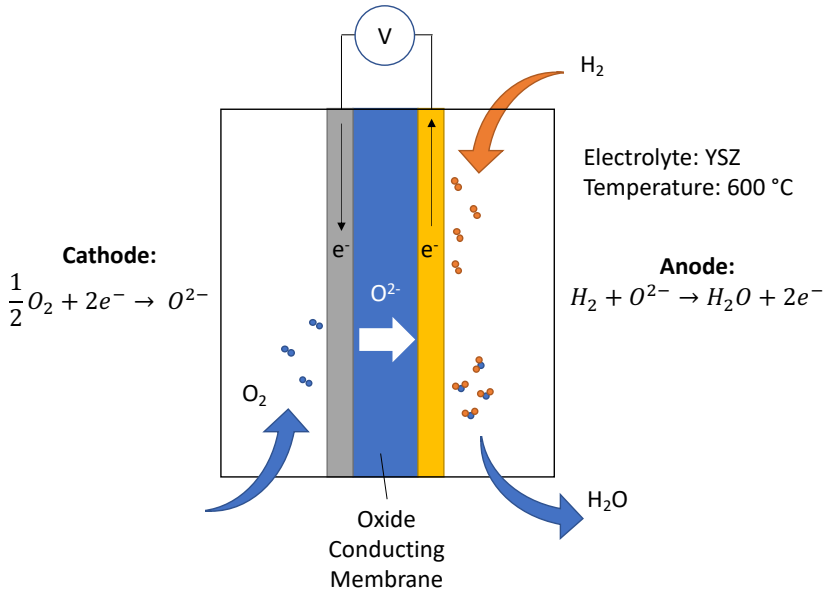

Figure 1-2. Schematics of a) low temperature polymer electrolyte membrane fuel cell, and b) high temperature solid oxide fuel cell.

The absence of polluting gases mitigates the greenhouse effect and the other adverse effects from burning fossil fuels. The public awareness of the climate crisis has increased in recent years with large global events such as COP-26. [7] Fuel cell technologies are in the infancy of commercialisation with vehicles such as cars and buses starting to be rolled out (Figure 1-3).

Furthermore, the demand for hydrogen is projected to only increase as greater market shares are carved out.[8], [9]

Figure 1-3. Hydrogen fuel cell bus operating in London September 2021.

The main drawback of hydrogen-based technologies is the hydrogen production methods. Despite being one of the most abundant elements in the universe, hydrogen gas is not available for use under standard conditions and therefore needs to be produced using efficient, sustainable, and reliable methods. Currently, most hydrogen gas is generated through the steam-methane reforming and water gas shift process. (Equation 1.2) [10] Despite having a high conversion rate for hydrogen production, this process not only requires a fossil fuel reactant but also still produces CO_2 gas. Furthermore, trace impurities can be detrimental in the performance of fuel cells. The methods by which hydrogen is produced are classified by colour depending on their level of carbon dioxide emission. The steam methane reformed

hydrogen is termed “grey hydrogen”, whereas if the technology is coupled with carbon capture solutions it is improved to “blue hydrogen”. [9]

$$\begin{aligned} Steam\ Methane\ Reforming: &\quad CH_4 + H_2O \rightarrow 3\,H_2 + CO \\ Water\ Gas\ Shift: &\quad H_2O + CO \rightarrow H_2 + CO_2 \end{aligned} \tag{1.2}$$

Fortunately, there are technologies that can produce high purity hydrogen directly from water using renewable energy resources named water splitting technologies without carbon produced. This is termed “green hydrogen” and provides the basis of a sustainable, circular hydrogen economy. [11] With the hydrogen market potentially being worth a $1 trillion industry [12], it is important to understand the different types of production techniques and all hues of hydrogen. The next section will briefly introduce and compare some green hydrogen technologies based on producing hydrogen directly from water.

1.2. Water Splitting Technologies

1.2.1. Electrochemical methods

The most thought of alternative hydrogen production technique is through electrochemical methods. Electrical energy can be used to split the water molecule into its constituent elements (Equation 1.3). This technology composes of two electrodes separated by an ion conducting electrolyte. Although this is not a new technology (Troostwijk and Diemann supposedly proposed electrolysis in 1799)[13], [14], it is still heavily researched. The electrolyser technologies can be broadly categorised, by the ion conducting species in the electrolyte, such as alkaline, proton exchange or solid oxide.

$$2H_2O \xrightarrow{+\,electricity} 2H_2 + O_2 \quad \Delta H = 285\ kJ/mol \tag{1.3}$$

Alkaline electrolysers are based on the transport of OH^- ions within a KOH electrolyte. The cathode reduces water molecules into hydrogen gas and OH^- ions. The ions are transported across a membrane to the anode where they undergo the oxidation reaction and form oxygen gas and a water molecule (Figure 1-4a). These reactors are the most commercialised, however, they are limited by the current density per electrode area and inability to operate at high

pressures. [15], [16] Furthermore, the requirement of the diaphragm to prevent gas mixing and ensure safety introduces additional system complexities.[16]

Replacing the KOH electrolyte with a hydrated polymer membrane provides a compact device with a larger electrode area. Water molecules are introduced and split at the anode to produce oxygen gas and protons. The latter are transported across a hydrated polysulfonated Nafion membrane towards the cathode where they are reduced to form hydrogen gas (Figure 1-1b). [17] The introduction of the membrane provides inherent separation for the evolved gases and can increase the current density of the device. [18] However, there is concern since the electrodes require expensive precious metal catalysts such as Pt, Ir or Ru. [18], [19] This together with the high demand for electricity to drive the splitting reaction lowers the commercial viability of the PEM technologies to provide a hydrogen production on a grid-scale. It is currently being widely researched to find alternative cheaper electrocatalysts or new techniques to optimise loading without compromising current density. [20]–[22] Recently, there have been developments into alkaline conducting membranes that combine the compactness of PEM electrolysers and the low-cost electrodes of alkaline technologies. [17]

Solid oxide electrolysers (SOECs) are another electrolysis technique operating at significantly higher temperatures (>400 °C). The cells operate by the transport of an oxide-ion across a ceramic electrolyte membrane. The enthalpy of water splitting reaction in equation 1.3, does not vary significantly with temperature. If the Gibbs free energy equation is rewritten as equation 1.4, the first term, ΔG, is the electricity needed to be supplied to drive the electrolysis reaction.[23] Since the entropy is positive for the splitting reaction, due to an increase in gas molecules produced, increases in temperature lowers the electrical demand for the reaction to proceed. As a result, lowers the hydrogen production costs. [24]

$$\Delta H = \Delta G + T\Delta S \tag{1.4}$$

Furthermore, additional cost is saved by the removal of expensive noble metal catalysts for the electrodes, thus providing a lower price per unit of hydrogen produced. [17] However, compared to the lower temperature electrolysis processes, SOECs are only on the cusp of commercialisation and still have issues with degradation due to the harsh operating conditions applied to the cells e.g. high humidity and temperatures. [24]

a)

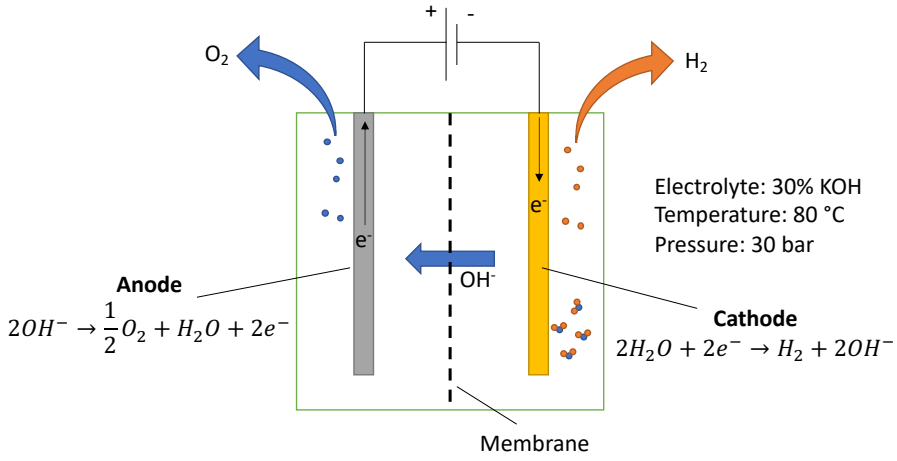

b)

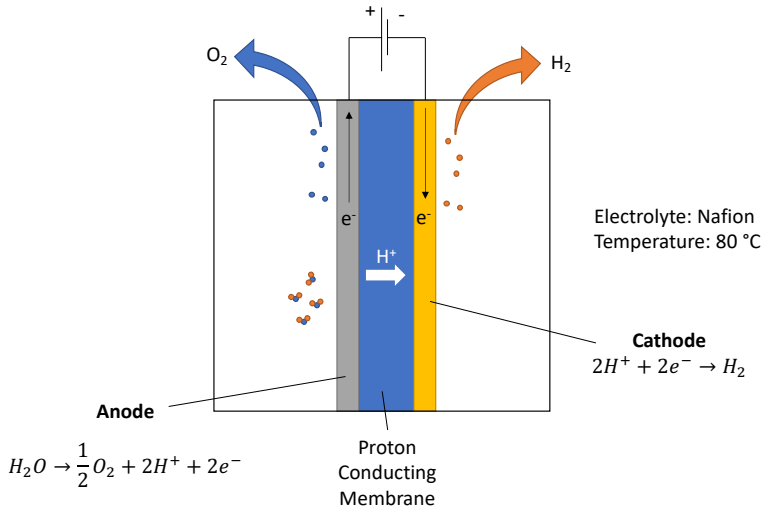

c)

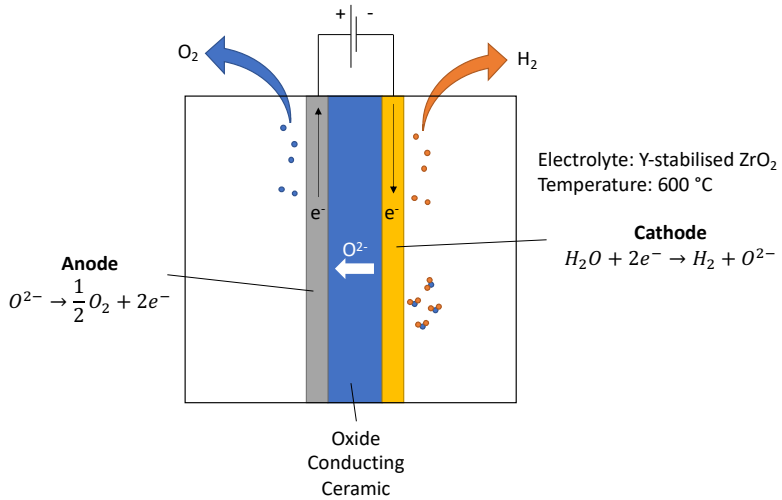

Figure 1-4. Schematic diagrams of a) alkaline electrolysers, b) polymer electrolyte membrane electrolysers, and c) solid oxide electrolysers.

1.2.2. Photoelectrochemical methods

It is reported that there is surplus solar energy supplied to the Earth's surface every minute of the day however this is far from being harnessed to meet the annual global energy demands. [25] Photoelectrochemical water splitting avoids the initial solar to electricity conversion by photovoltaic devices and directly uses solar energy to drive the splitting reaction. In semiconductor devices, the energy difference between the valence and conduction band is known as the band gap. Upon illumination with photons exceeding the band gap energy, electrons can hop from the valence and conduction bands forming an electron hole pair within the material. The hole formed within the material oxidises the water molecule to form oxygen gas and protons. The electron travels around an external circuit towards the metal cathode where it reduces the protons in the electrolyte to form hydrogen gas (Figure 1-5). [26], [27] Similar to the alkaline electrolyser a membrane is used to prevent mixing of the evolved gases.

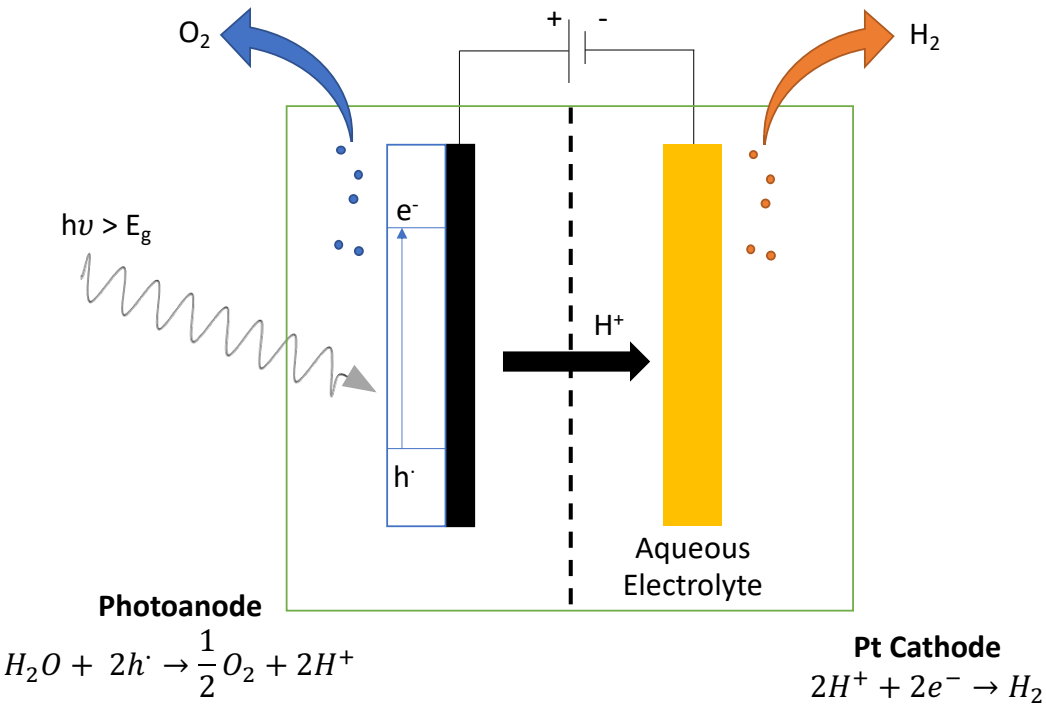

Figure 1-5. Schematic of a photoelectrochemical water splitting device based on a photoanode and metal cathode.

The materials chosen for the photoelectrodes must meet several requirements to ensure sufficient operation. This is mainly focussed on the band gap size and its positioning with respect to the redox couples of hydrogen and oxygen. Photoelectrodes require a band gap of greater than 1.23 eV to overcome the enthalpy for water splitting.[28] Materials with band gaps

in the range of 1.6 to 2 eV are desirable since they will be able to absorb most of the sunlight composing of visible and ultraviolet light and overcome any photoelectrode losses. [29] Some previously investigated materials have been TiO_2, WO_3 and GaN.[30] However, the surface of photoelectrodes in aqueous electrolytes can oxidise and form blocking layers, thus significantly reducing the reaction efficiency. [31] This technology is still being researched to find better performing and more robust photoelectrodes.

1.2.3. Thermochemical methods

The hydrogen production methods described in the previous sections were all driven by electrons. Alternatively, thermal energy can be used to split water molecules into their constituent elements. Concentrated solar power reactors use a series of large mirrors focus sunlight and achieve high temperatures to drive chemical reactions.[32] Concentrating the solar power makes use of the whole solar spectrum instead of the small fraction that is used for photovoltaic technologies.[33]

Direct thermolysis of water can occur at temperatures exceeding 2000 °C. [34] However, at these temperatures there is a requirement to prevent recombination of the hydrogen and oxygen. This can be achieved by using electrochemical zirconia pumps to remove oxygen from the gas mixture, however this presents an issue regarding the stability of the electroceramics for this purpose at the thermolysis temperature. Instead, thermally driven water splitting can be accommodated by separating the process into smaller reactions, as long one reaction has an entropy change exceeding that of the net water splitting reaction. [35] The reaction can be split into any number of redox processes such as the case of the iodine-sulfur cycle.[36]–[39] However, additional reaction steps introduces additional system complexity.

Two-step thermochemical redox reactions use high temperatures from sustainable sources to drive the thermal reduction of metal oxides and create an oxygen deficiency within the lattice (Equation 1.3). This reduction reaction stores the solar energy within the chemical bonds of the metal oxide. The entropy change of this reaction is intuitively larger than the overall water splitting reaction due to the formation of gas molecules from a solid. The oxygen deficiency can then be subsequently exploited by reoxidising with steam to produce hydrogen (Equation 1.4a). [40], [41] Other oxidants can be used such as carbon dioxide or oxygen to produce carbon

monoxide or the release of heat (Equation 1.4b and c). [42], [43] Syngas mixtures (CO and H_2) can be obtained through the co-splitting of steam and carbon dioxide, and further upgraded to higher value liquid fuels through Fischer-Tropsch processing. [44] The oxygen and hydrogen gases produced using this technique are inherently separated and removes the need for membranes thus simplifying design. Although the temperatures are lower than those required for direct thermolysis, the temperatures required to drive the initial thermal reduction are exceeding 1200 °C and require not only complex engineering solutions but also a large area for mirrors to concentrate enough solar power. This would incur a large initial capital cost, however in recent years the technology has started to become commercialised by companies such as Synhelion and Heliogen. [45], [46]

$$MO_x \xrightarrow{+\Delta H} MO_{x-\delta} + \frac{\delta}{2} O_2 \tag{1.3}$$

$$MO_{x-\delta} + \delta H_2O \rightarrow MO_x + \delta H_2 \tag{1.4a}$$

$$MO_{x-\delta} + \frac{\delta}{2} O_2 \rightarrow MO_x + Heat \tag{1.4b}$$

$$MO_{x-\delta} + \delta CO_2 \rightarrow MO_x + \delta CO \tag{1.4c}$$

Table 1.1 provides a short comparison between the previously discussed technologies. The cost of hydrogen production is displayed in the table as previously calculated by El-Emam and Özcan, and Nikolaidis and Poullikkas. [6], [47] It is no surprise the current commercial steam methane reforming has the lowest cost of 2.25 $/kg. The technology is mature and well-integrated within current infrastructure. The other technologies have much higher costs and will need to be lowered to commercially rival steam methane reforming.

This thesis investigates new materials for thermochemical water splitting with the aim to contribute towards this effort. The following chapter will outline the fundamentals required to be considered when designing a new material for this process.

Table 1.1 shows the advantages and disadvantages between the different hydrogen production technologies. Hydrogen cost data is taken from ref. [6], [47]

	Hydrogen Cost ($/kg)	Advantages	Disadvantages
Steam Methane Reforming	2.25	- Cheap - Commercialised	- Requires fossil fuels - Produces CO_2
Alkaline Electrolysers	7.5	- Commercialised - No CO_2	- Low current density
PEM Electrolysers	5 - 12	- Compact - High purity H_2 - High current density	- Expensive catalysts
Solid Oxide Electrolysers	3 - 11	- High energy efficiency - No precious metal catalysts	- Electrode degradation - High temperature sealants
Photoelectrochemical	11.4	- Direct solar energy	- Photoelectrode degradation - Low efficiencies
Thermochemical Redox Reactors	4.5 - 10	- Direct solar energy - Inherent gas separation	- High temperatures - High capital cost

2. Fundamentals of Thermochemical Water Splitting

In this chapter we will explore the fundamental principles that are needed to understand two step thermochemical water splitting using metal oxides. Starting from basics of defect chemistry within oxides, and transition metal oxide bonding; further ideas on the reaction thermodynamics, kinetics and efficiency will be explored and relationship to each other discussed.

2.1. Defect chemistry in oxides

2.1.1. Point Defects

Solid phases are those where the atoms are regularly positioned in a repeating unit, they come together to form a crystal lattice structure with perfect order (Figure 2-1). Although above 0 K there is rarely perfect regularity within structures, due to the presence of defects.[48] These defects can have different dimensionality ranging from 0D point defects to 3D voids or precipitates.[49] Herein we will discuss the nature of 0D point defects due to their relation to this work and how they affect the chemistry of metal oxide materials.

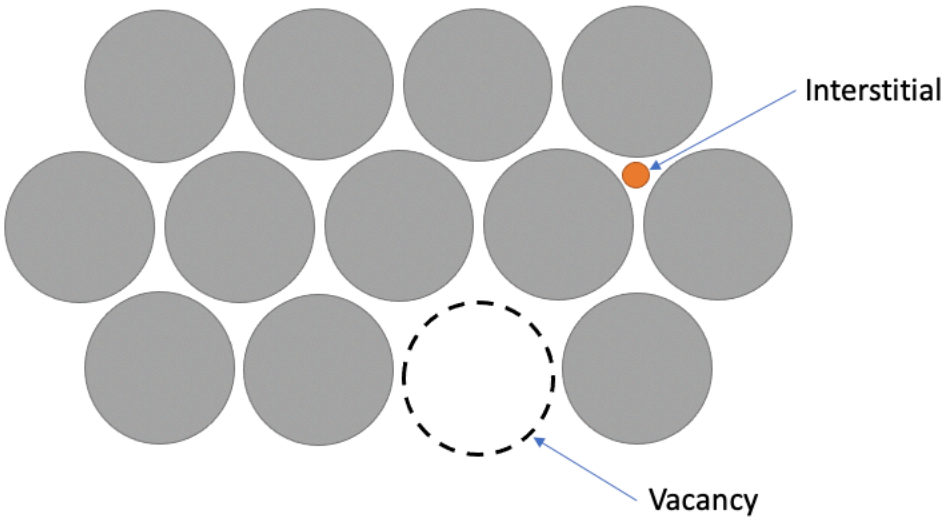

Figure 2-1. Schematic representation of interstitial and vacancy point defects in a lattice structure.

The two main categories of point defects are ionic-based or electronic-based. Ionic based defects are further split into vacancies and interstitials. [49], [50] As its name suggests the

vacancy is an absence of an ion on its nominal lattice site, whereas an interstitial is an ion present in between two lattice sites (Figure 2-1). The inclusion of defects causes an effective charge associated within them due to the removal or addition of ions within the lattice. Kroger-Vink notation is used to describe the species' type, location, and effective charge.[51] Superscripted • or ′ or x are used to denote positive, negative, and neutral charges respectively. Equation 2.1 displays the Kroger-Vink notation for a neutral La on a La site, an oxygen anion on an interstitial site with a 2- charge and a vacancy on an oxygen site with a 2+ charge.

$$La_{La}^{X} \; or \; O_i'' \; or \; V_O^{\cdot\cdot} \; \rightarrow \; Species_{Site}^{Charge} \tag{2.1}$$

Two common types of ionic defect are Schottky and Frenkel defects. [52] A Schottky defect is the combination of a cation and anion vacancy pair. The involved atoms move towards the surface, but equal and opposite charges cancel to maintain a neutral defect. Frenkel defect are cation vacancy-interstitial pairs introduced by the movement of a cation from a distinguished lattice site to an interstitial. This type of defect pair involving anions is known as Anti-Frenkel disorder. Electronic defects can occur from the intrinsic ionisation of electrons within the structure (Equation 2.4).[52] Electrons promoted to the conduction band can form hole states in the valence band to maintain charge neutrality. These differ from the excited states that may occur due to the energetic promotion of an electron from low energy states to higher energy in terms due to their longer lifetime.

Schottky: $$\text{null} \rightarrow \; V_M'' + \; V_O^{\cdot\cdot} + M_{surf.}^{\cdot\cdot} + O_{surf.}'' \tag{2.2}$$

Frenkel: $$M_M^X \rightarrow \; M_i^{\cdot\cdot} + V_M'' \tag{2.3a}$$

Anti-Frenkel: $$O_O^X \rightarrow \; O_i'' + \; V_O^{\cdot\cdot} \tag{2.3b}$$

Electronic: $$null \; \rightarrow e + h \tag{2.4}$$

The concentration of intrinsic defects demonstrates a temperature dependence in accordance with equation 2.5. The concentration is very small at low temperatures, however quickly rises as thermal energy is introduced to the system. This can contribute to changes in material

properties such as conductivity. However, the concentration of point defects can be altered more drastically by the inclusion of extrinsic defects in the form of substitutional ions.

$$n_i = N \cdot exp\left(\frac{-\Delta H_i}{2kT}\right) \tag{2.5}$$

Where n_i is the concentration of defect i, N is the number of possible defect sites, $-\Delta H_i$ is the formation enthalpy of defect i, k is the Boltzmann constant and T is temperature.

2.2. Extrinsic Defects

The concentration of point defect species can be manipulated by changing extrinsic factors such as temperature, oxygen partial pressure, or the inclusion of aliovalent solutes to introduce a charge imbalance within the structure.[50] The concentrations of point defects then change as a response to rectify the imbalance. The effect of temperature and oxygen partial pressure on the concentration of oxide defects will be discussed later in section 2.4. Here effect of aliovalent solutes will be briefly introduced.

Broadly the aliovalent solutes can be separated into two categories known as acceptors and donors. Acceptor solutes have a lower oxidation state compared to their host lattice site, thus introducing an effective negative charge. Consequently, the concentration increases of positively charged defects such as oxygen vacancies, holes or cation interstitials. One common practice used in solid oxide fuel cell technologies is the introduction of Y^{3+} into ZrO_2 to improve the ionic conductivity through the increase in oxygen vacancies (Equation 2.6). [53]

$$Y_2O_3 \underset{ZrO_2}{\Longrightarrow} 2Y'_{Zr} + V_O^{\cdot\cdot} + \frac{3}{2}O_2 \tag{2.6}$$

On the other hand, introducing a solute species with a higher oxidation induces a positive charge that must be compensated by negative species e.g. oxygen interstitials, cation vacancies or electrons. These solutes are known as donors. In silicon technologies P^{5+} is added to increase the electron concentration and thus the room temperature conductivity (Equation 2.7). [54]

$$P_4O_{10} \underset{SiO_2}{\Longrightarrow} 4P_{Si}^{\cdot} + 4e' + 5\ O_2 \quad (2.7)$$

The manipulation of defect concentrations by the introduction aliovalent solutes is common practise in thermochemical water splitting materials to alter the oxygen non-stoichiometry and therefore the fuel production volumes.

2.3. Transition metal-Oxygen bonding in perovskites

This section will provide a brief introduction to the metal-oxygen bonding within perovskite structures. Thermochemical redox reactions are based on the breaking and reforming of oxygen-bonds. The nature of these bonds in perovskite materials have been heavily studied to optimise electronic, structural and catalytic properties for different applications.

Perovskite oxides with the structure ABO_3, where A is a XII coordinated body centred cation with BO_6 octahedra on the unit cell corners. The A and B site cation are consequently surrounded by negatively charged anions. When these individual free ions are brought together from a theoretical vacuum, the cation electrons are destabilised due to the repulsion from the oxygen anions. Conversely, the oxygen anions are stabilised by the attracted to the positive cations. These repulsive and attractive forces are due to the Madelung potential.[55] This potential can determine the stability of the perovskite lattice and is tested later as a descriptor for predicting redox performance. Figure *2-2*a schematically shows the effect of the Madelung potential on the ion energies from free space to the perovskite.[55], [56] In the perovskite structure the A-site s-states are usually much higher in energy than the occupied oxygen 2p and d-states and therefore remains unoccupied and does not play a part in the electron transfer redox processes. However, through the Madelung potential the A-site still plays a part with electrostatic interactions and has strong steric effects on the perovskite structure that in turn effects the redox behaviour. The B-site cations are coordinated in an octahedral arrangement surrounded by 6 oxygen anions. The lobes of the metal d_{z^2} and $d_{x^2-y^2}$ orbitals spatially overlap with the oxygen 2p orbital lobes (Figure *2-2*b). These orbitals hybridise to form metal-oxide σ bonding and σ* anti-bonding states. The coulombic repulsion slightly destabilizes these orbitals to higher energies known as e_g states. The remaining d-orbitals (d_{xy}, d_{yz}, d_{xz}) have lower spatial overlap with oxygen orbitals and form π and π* bonding states and stabilise

to slightly lower energies known as t_{2g} states. [56] The energy difference between the t_{2g} and e_g states in known as the crystal field splitting, Δ_c, and can influence the perovskite electronic properties. According to the Hund's rules, every degenerate orbital is singly occupied before pairing occurs in the same sub-orbital. This is due to the Aufbau principle to keep electrons at their lowest possible energy state, and the pairing energy penalty due to electron-electron repulsion. For transition metals with between d^4 and d^8 electrons, a low-spin configuration (fourth electron fills a t_{2g} state) will be adopted if the electron pairing energy exceeds Δ_c.[57] Conversely, if Δ_c is lower than the pairing energy, the fourth electron will occupy the e_g state and form a high-spin configuration. Those 2p states that do not overlap with any d-states undergo 2sp self-hybridisation with neighbouring O^{2-} groups to form non-bonding σ_0 states. [55] In a real system with large number of atoms and the translational symmetry of the metal oxides, these orbitals appear as bands. Importantly, the bonds formed in the octahedral coordinations are of polar covalent nature with both metallic and oxygen behaviour. The extent of covalency can be calculated from the difference in electronegativity between the metal cation and oxygen.[55]

Thermal energy provided by heating the metal oxides can lead to the breaking of transition metal oxygen bonds and the consequent removal of oxygen anions. (Figure 2-3).[56] This lowers the density of states of oxygen and the additional electron density increases the Fermi energy. [56] The greater electronegativity of the transition metal cation lowers the energy of metal d state closer towards the oxygen p-band centre thereby lowering the energy required to activate thermal reduction and form oxygen vacancies.[58], [59]

a)

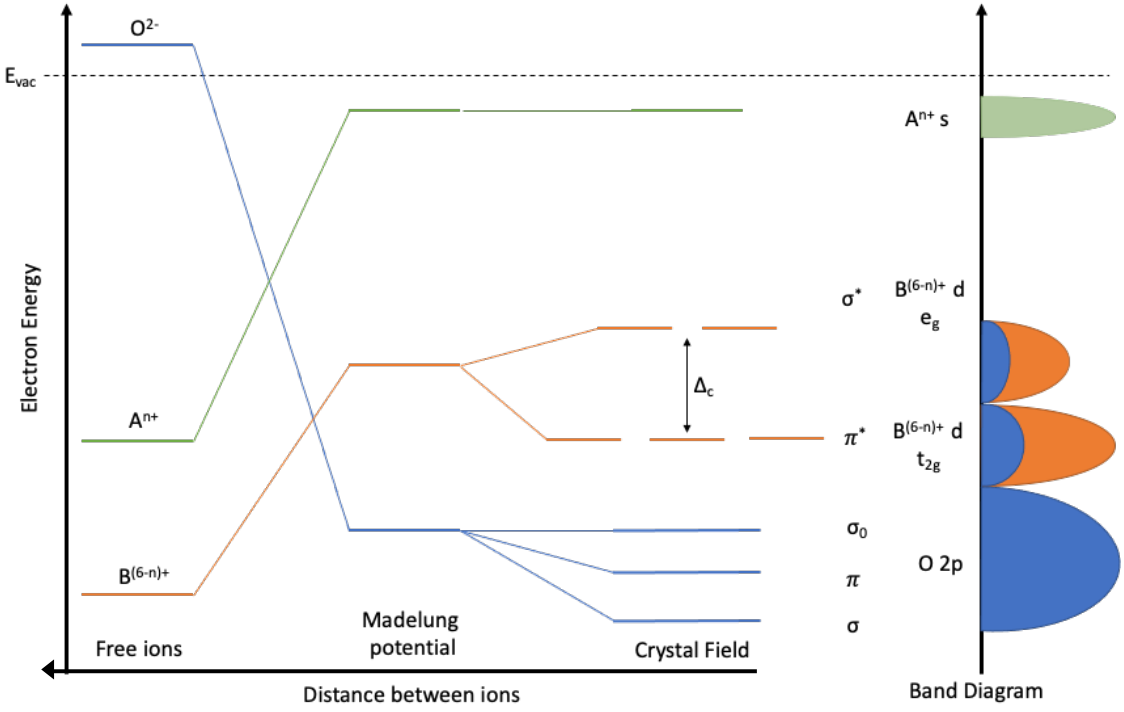

b)

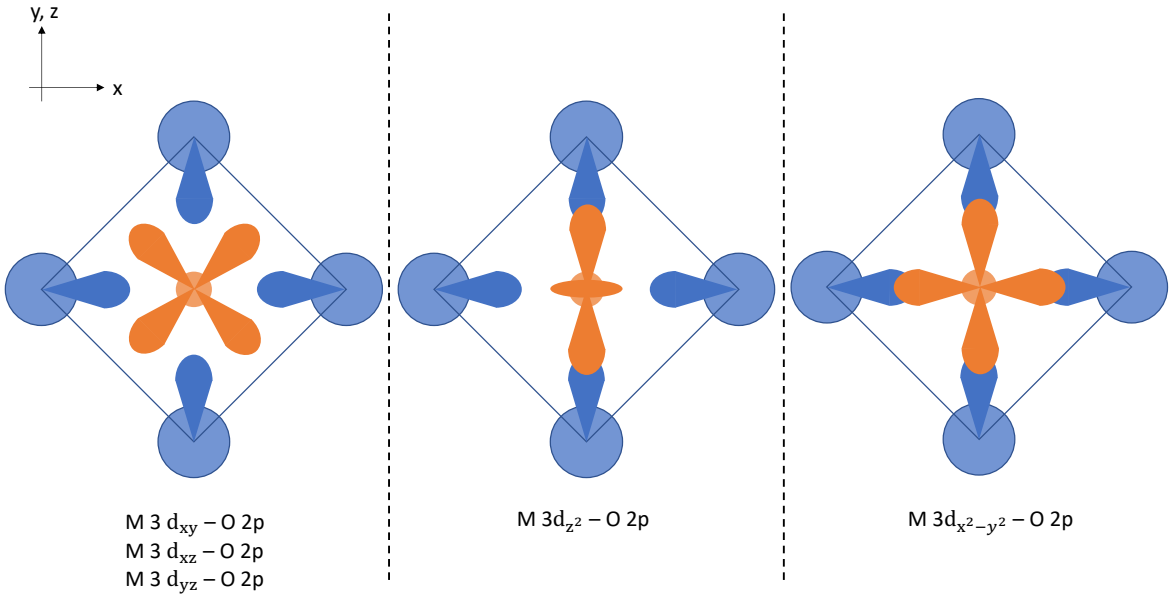

Figure 2-2. a) Evolution of electron energy as metal cations and oxygen anions are moved from free ions to octahedral coordination within the perovskite lattice. The crystal field splitting of the d-orbitals is observed alongside the formation of bonding states. Translational symmetry within the solid causes these states to appear as bands in real systems. Adapted from [55], [56], [60] b) Metal d and oxygen-orbital spacing in octahedral configurations giving rise to the crystal field splitting effect.

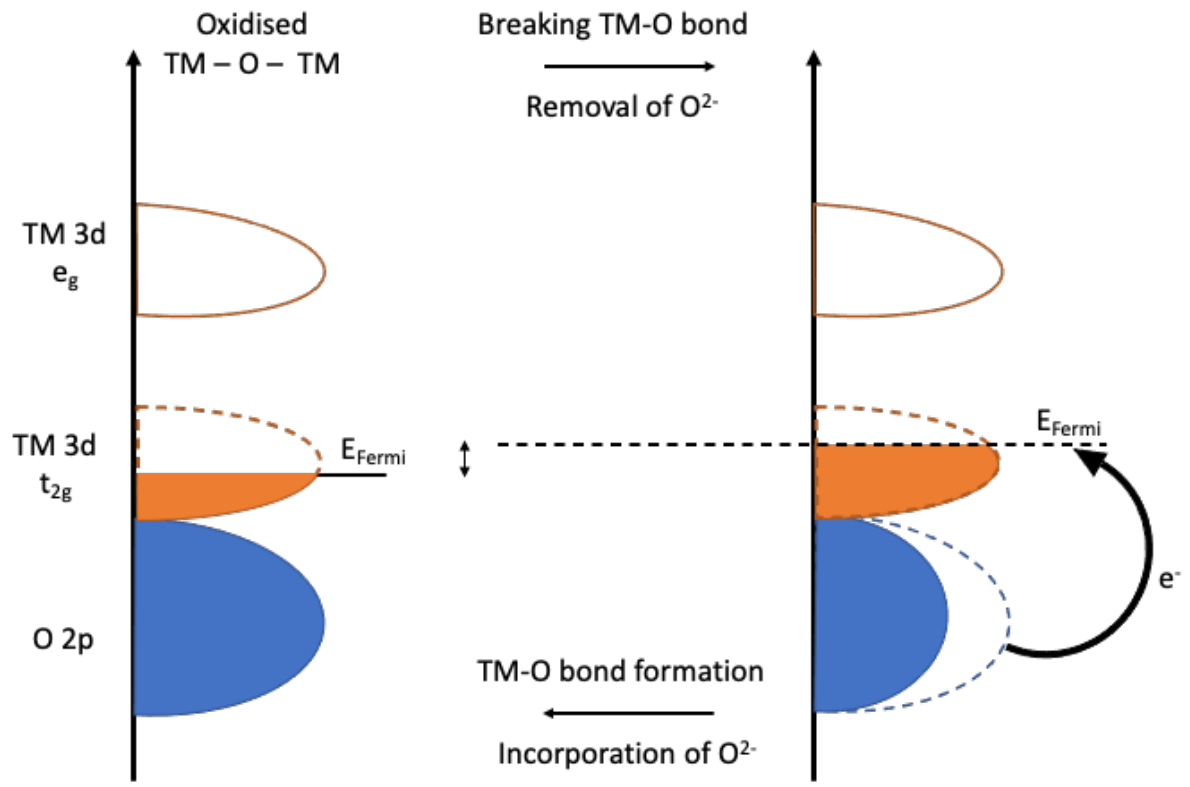

Figure 2-3. Schematic showing the evolution of density of states during metal oxide lattice reduction. Adapted from [56].

2.4. Thermodynamics

The understanding of the thermodynamic principles of two-step thermochemical water splitting are crucial for designing better metal oxide materials and underpins a lot of the work covered in this thesis. This section will provide a brief introduction into the ideas of equilibrium and thermodynamic driving forces in terms of stoichiometric and non-stoichiometric oxides (explained further in Chapter 3). A comprehensive and detailed description is provided by Scheffe *et al.* in reference [35].

Equation 2.8 represents a theoretical reaction whereby species A and B react to give products C and D with stoichiometric ratios a, b, c and d. The equilibrium constant, K, of this reaction is calculated by equation 2.9. and determines whether the reaction favours the products (K>1) or reactants (K<0).

$$xX + yY \leftrightarrow cC + dD \tag{2.8}$$

$$K = \frac{{a_C}^c \cdot {a_D}^d}{{a_X}^x \cdot {a_Y}^y} \quad (2.9)$$

Where a_I^i is activity of species I and i is the stoichiometry.

The Gibbs free energy, ΔG°, of this reaction determines whether the reaction is spontaneous and is related to the equilibrium constant through equation 2.10.

$$\Delta G^o = -RTlnK \quad (2.10)$$

Where R is the ideal gas constant 8.3145 J mol^{-1} $K^{=1}$, and T is temperature (K).

Furthermore the Gibbs free energy is related to the reaction enthalpy, ΔH°, and entropy, ΔS°, by the well-known Gibbs equation (Eq. 2.11) to give a temperature dependence of the reaction.

$$\Delta G^o = \Delta \mathrm{H}^o - T\Delta \mathrm{S}^o \quad (2.11)$$

The fundamental chemical equations outlining the two-step water splitting for stoichiometric spinel oxides are summarised below. (Eq. 2.12-2.13) Iron oxide spinels were some of the originally reported metal oxides for thermochemical water splitting and provided a base for a lot of the theoretical groundwork. Combining the reduction and oxidation reactions results in the overall water splitting equation (Eq. 2.14).

Reduction: $$M_3O_4 \rightarrow 3MO + \frac{1}{2}O_2 \quad (2.12)$$

Oxidation: $$3MO + H_2O \rightarrow M_3O_4 + H_2 \quad (2.13)$$

Overall: $$H_2O \rightarrow H_2 + \frac{1}{2}O_2 \quad (2.14)$$

First, the thermal reduction reaction is considered at equilibrium (ΔG°=0), under the assumption of ideal gas behaviour and unity activity for solids. Combining equations 2.9, 2.10

and 2.11, a relationship between the temperature and oxygen partial pressure, P_{O_2} is determined (Equation 2.15.) The Gibbs free energy can be plotted to find the temperature at which the reduction reaction is spontaneous (Figure 2-4). Lowering the oxygen partial pressure, P_{O_2}, is seen to lower the temperature for the onset of reduction. In thermochemical reactor systems this is achieved by using an inert sweep gas such as argon or nitrogen to dilute the oxygen in the system, or using vacuum pumps. [61] Alternatively designing materials with lower reduction enthalpy or larger reduction entropy by methods such as aliovalent doping can further lower the reduction temperature.

$$\Delta G_{red} = \Delta H^{\circ}_{red} - T\Delta S^{\circ}_{red} + \frac{1}{2}RTln\left(\frac{p_{O_2}}{p^{\circ}}\right) \tag{2.15}$$

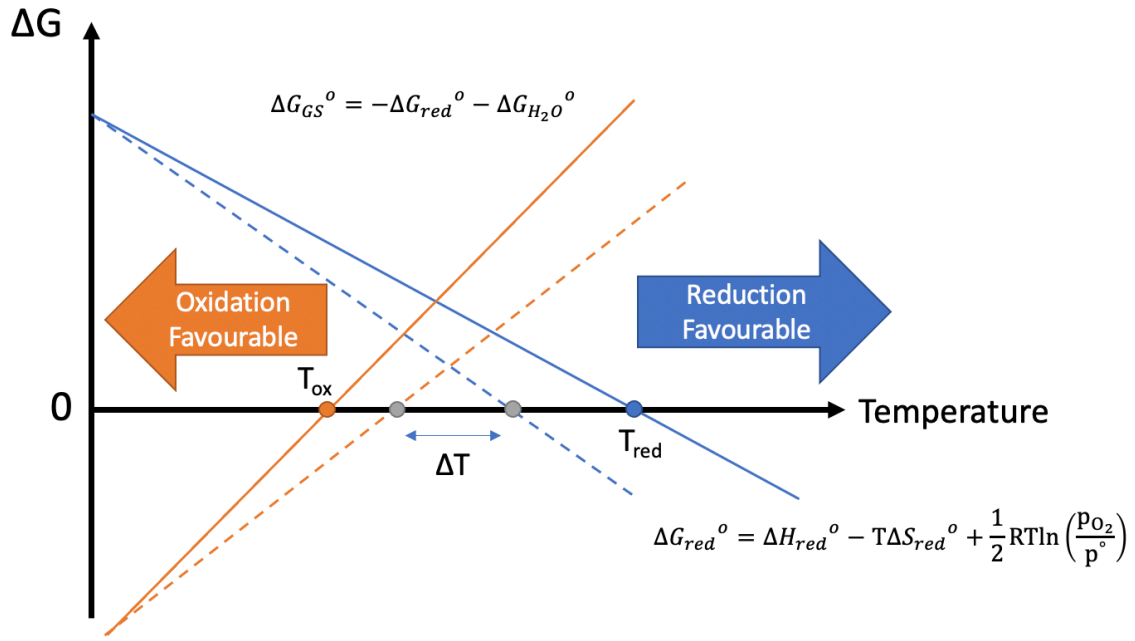

Figure 2-4. Gibbs free energy curve for the thermochemical redox of a metal oxide. The dashed blue line demonstrates how lowering the oxygen partial pressure can lower the required reduction temperature. The dashed orange line represents how increasing the moles of H_2O can drive the oxidation reaction at higher temperatures.

The Gibbs free energy of the gas splitting reaction, ΔG_{GS}, can be thought as the opposite of the reduction reaction summed with the thermolysis of water, ΔG_{H_2O}. (Equation 2.16)

$$\Delta G_{GS} = -\Delta G_{red} + \Delta G_{H_2O} \tag{2.16}$$

At the gas splitting temperature T_{GS}, equation 2.16 is expanded to further understand material requirements (equation 2.17). [62] The final simplified form of the Gibbs equation can provide some material design limits to abide. In most cases, the reduction entropy of the metal oxide, S°_{red} is larger than the thermolysis entropy, $\Delta S^{\circ}_{H_2O}$ causing the second term to be positive.[35] Therefore to ensure the reaction is spontaneous the first term should be negative. To allow this, the reduction enthalpy of the metal oxide, ΔH°_{red}, must be larger than the enthalpy for water splitting, $\Delta H^{\circ}_{H_2O}$. This is a common selection criterion for computational exploration of new thermochemical materials due to the simplicity and low expense of the reduction enthalpy calculation. [63]

$$\begin{aligned}\Delta G_{GS} &= -\left(\Delta H^{\circ}_{red} - T_{GS}\Delta S^{\circ}_{red}\right) + \left(\Delta H^{\circ}_{H_2O} - T_{GS}\Delta S^{\circ}_{H_2O}\right) \\ &= -\Delta H^{\circ}_{red} + T_{GS}\Delta S^{\circ}_{red} + \Delta H^{\circ}_{H_2O} - T_{GS}\Delta S^{\circ}_{H_2O} \\ &= (\Delta H^{\circ}_{H_2O} - \Delta H^{\circ}_{red}) - T_{GS}(\Delta S^{\circ}_{H_2O} - \Delta S^{\circ}_{red})\end{aligned} \tag{2.17}$$

$$\Rightarrow \Delta G_{GS} < 0, \quad \Delta H^{\circ}_{red} > \Delta H^{\circ}_{H_2O} = 285\frac{kJ}{mol} or\ 2.9\ eV\ @\ RT$$

When placing this in context of a Gibbs free energy curve (Figure 2-4), the effect of the entropy shows the Gibbs free energy increases with temperature therefore suggesting the reaction becomes more unfavourable. This usually results in the thermochemical cycles operating in a temperature swing condition where the oxidation reaction is at lower temperatures. This can cause issues with system efficiencies since increased energy is required to reheat the material to the reduction temperature, and the cooler temperature may have slower kinetics and solid oxide diffusion.[35] This has led to some researchers proposing isothermal cycles, whereby the reaction is driven by excessive steam content in the oxidising gas flow. [64]–[66] Although this reaction design is also simpler with potentially faster kinetics, the efficiency is not always improved since additional energy is required to heat more steam to higher temperatures. Usually a common ground is found between the two operating conditions, whereby the difference in temperature is <300 °C. [67] Some authors have shown altering the reduction entropy has an effect on the operating conditions due to this affecting the slope of the Gibbs curves. A larger reduction entropy leads to lower reduction temperatures, but also requires a smaller change in temperature between the reduction and oxidation steps. [68] However,

sensitivity studies on each of the parameters by Carrillo and Scheffe demonstrated changing the reduction enthalpy has s significantly larger effect on the reduction thermodynamics. [68]

In terms of non-stoichiometric splitting materials (to be discussed in section 3), continuous levels of oxygen are removed from the lattice without the compound changing phase. In this case partial molar quantities per mole of monoatomic oxygen are used for the thermodynamic properties due to the consideration of an infinitesimal change in oxidation state.

Reduction: $$\lim_{\delta_f-\delta_i=0} MO_{2-\delta_i} \rightarrow MO_{2-\delta_f} + \frac{1}{2}O_2 \quad (2.18)$$

Oxidation: $$\lim_{\delta_f-\delta_i=0} MO_{2-\delta_f} + H_2O \rightarrow MO_{2-\delta_i} + H_2 \quad (2.19)$$

Overall: $$H_2O \rightarrow H_2 + \frac{1}{2}O_2 \quad (2.20)$$

The reaction thermodynamics behave in near identical fashion except with the partial molar thermodynamic quantities have an additional dependence on the oxygen non-stoichiometry. This transforms the Gibbs relation for the reduction reaction to the expression in equation 2.21, and the oxidation reaction to 2.22.

$$\Delta g_O(\delta, T) = \Delta h_O(\delta) - T\Delta s_O(\delta) + \frac{1}{2}RTln\left(\frac{p_{O_2}}{p^\circ}\right) \quad (2.21)$$

$$\Delta G_{GS} = -\Delta g_O(\delta_i, T) + \Delta G_{H_2O} \quad (2.22)$$

At equilibrium the difference in chemical potential of oxygen in the lattice and the gas phase is zero thus maintaining a fixed non-stoichiometry within the structure. Experimental techniques such as thermogravimetry and coulometric titration can be used to determine oxide non-stoichiometry at a given oxygen partial pressure and temperature (Figure 2-5a). [69], [70] The outputted data is usually plotted as isotherms on a non-stoichiometry vs partial pressure graph. Equation 2.21 can be rearranged to give the van't Hoff style relationship to determine the thermodynamic quantities from the intercept and gradients for constant non-stoichiometry values (Eq. 2.23) (Figure 2-5b).

$$ln\left(\frac{p_{O_2}}{p^\circ}\right) = \frac{2\Delta S_O}{R} - \frac{2\Delta H_O}{R} \cdot \frac{1}{T} \Big|_{\delta=constant} \tag{2.23}$$

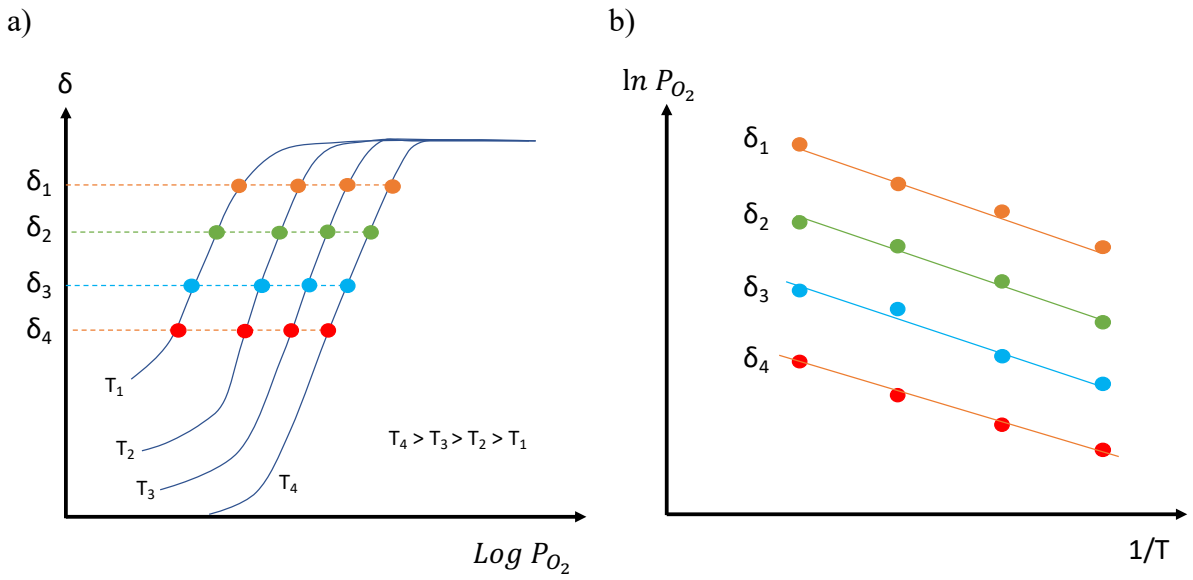

Figure 2-5. Schematic representation of a) typical oxygen non-stoichiometry data plotted as function of oxygen partial pressure, b) van't Hoff representation of the data to calculate the thermodynamic quantities.

2.5. Reaction Kinetics

Designing the perfect material for thermochemical water splitting from the thermodynamic principles would not be worthwhile if the reactions were not to happen under a reasonable timescale. Therefore, there is a significant motivation to understand the reaction kinetics. The global thermochemical redox reaction can be broken down to determine reaction mechanisms. These reactions are driven by the movement of oxide defect species along chemical potential gradients from regions of high to low. A lot of work has been focussed on general kinetic models for the whole reduction or oxidation steps. [71]–[73] A typical kinetic equation is displayed by Equation 2.24.

$$\frac{d\alpha}{dt} = A \cdot \exp\left(\frac{-E_a}{RT}\right) \cdot f(\alpha) \tag{2.24}$$

where α is reaction conversion, A is the pre-exponential term, E_a is the activation energy, and f(α) is the mathematical representation of the reaction mechanism.

A contracting sphere model for the reaction mechanisms was previously fitted to experimental data and determined activation energies in the region of 150 kJ mol^{-1} for accepter doped lanthanum manganates.[74] However there is debate since other reaction models also provided a good fit. McDaniel *et al.* analysed the oxidation reaction kinetics through the compounding of several reaction models together that each focussed on smaller parts of the reaction e.g. steam introduction, H_2 production and gas mixing.[74] Davenport *et al.* introduced a thermokinetic models for oxidation and reduction reactions based on thermodynamic parameters, gas flow rates and mass balance. This reaction model style allows not only the tailoring of the material properties but also the understanding of reactor design to determine optimum gas production. [75], [76]

Broadly, these global reactions can be split further into a surface reaction and bulk chemical diffusion whose values are commonly denoted, k_{chem} and D_{chem} respectively. Fortunately, the movement of oxide species is heavily studied in solid state ionics technologies. Numerous experimental techniques can obtain these parameters, such as isotopically labelled ^{18}O followed by secondary ion mass spectrometry [77], [78] or electronic conductivity relaxation [79], [80], or atom probe tomography [81] although they are not commonly reported within thermochemical redox literature. The effect of different chemistries on these parameters can allow further understanding of the thermochemical water and better the design of new materials.

2.5.2. Bulk Diffusion

Throughout a crystal lattice, ion species can move away from their equilibrium positions in response to changes in different stimuli such as electrical or chemical potential. The latter drives ion migration from regions of high to low potential. Ions can jump between lattice sites by different mechanisms depending on the point defect present within the structure. For example, for oxide materials – like those in this thesis – the oxide species can diffuse by a vacancy mechanism due to the presence of oxygen vacancies such as in perovskite materials. Alternatively, interstitial and interstitialcy diffusion mechanisms can transport oxide ions in Ruddlesden-Popper structures (discussed in chapter 8).[82] Regardless of which mechanism, there is an energy penalty for each lattice site hop, known as the migration barrier, E_m, (Figure

2-6). This barrier controls the frequency of site hops through equation 2.25 and is further related to the diffusivity D_i (equation 2.26).

$$\upsilon = \upsilon_0 \, exp\left(\frac{-E_m}{k_B T}\right) \tag{2.25}$$

Where υ is hop frequency, υ_0 is a constant related to the harmonic vibrational frequencies between the energy minima and transition point, [83], k_B is the Boltzmann constant, T is temperature.

$$D_i = c_i \, f \, \lambda^2 \, \upsilon_0 \, exp\left(\frac{-E_m}{k_B T}\right) \tag{2.26}$$

Where c_i is concentration of species i, f is s geometry factor, λ is the hop distance.

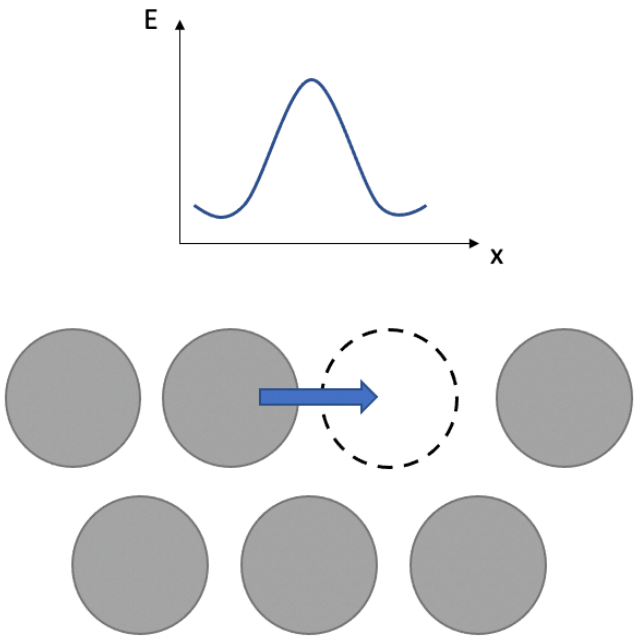

Figure 2-6. Relationship between energy and ion migration within solid lattices.

In thermochemical redox materials, oxide defect diffusion is important since oxide species move to and from the surface to take part in the different redox reactions. It is thought that the main diffusion process within this process is ambipolar diffusion. This is the movement of vacancies and electrons throughout the lattice in tandem to maintain charge neutrality. [84] The ambipolar diffusivity, $\widetilde{D}$, within a structure is calculated using equation 2.27. [84]

$$\widetilde{D} = \frac{(C_O + C_e) \cdot D_O \cdot D_e}{C_O D_O + C_e D_e} \quad (2.27)$$

Where D_O and D_e are self-diffusion coefficients of oxide defect and electrons respectively, C_O and C_e are the concentration of oxide defect and electrons respectively.

Under the assumption that the diffusing species' mobility is constant, the diffusivity is given by equation 2.28. However, early studies by Blumethal and co-workers reported the dependence of oxygen non-stoichiometry on the electron mobility.[85], [86] This was discussed to be related to the increase in hopping distance due to the chemical expansion of the lattice.

$$D_i = D_O \cdot exp\left(\frac{-E_A}{RT}\right) \quad (2.28)$$

Consequently, Ackermann *et al.* postulated and proved using isothermal gas switching in thermogravimetry, the ambipolar diffusion within ceria was temperature dependent but also had an inverse proportionality to the oxygen non-stoichiometry.[84] Ackermann expanded their work to understand the diffusion during the oxidation reaction with CO_2. [72] The authors further suggested the increased oxygen non-stoichiometry (δ>0.2) decreased the ambipolar diffusivity due to the presence of defect clusters within the lattice, however intermediate values ($\delta \approx 0.06$) demonstrated the opposite with diffusion increasing with non-stoichiometry.

Yang *et al.* investigated the diffusion kinetics of $La_{1-x}Sr_xMnO_3$ during thermochemical water splitting cycles. [87] The authors concluded the inclusion of Sr affected the oxide diffusion during the hydrogen reaction step, although the surface reaction was found to be rate-limiting step. The improvement of oxide diffusion has been of intense research within the solid state ionics community and can be easily transferred over to thermochemical water splitting. One interesting strategy alongside doping strategies can be morphologically engineering grain boundary density since these have been observed facilitate faster oxide diffusion. [88]

2.5.3. Water Splitting Surface Reaction Mechanism

The surface mechanism of the water splitting reaction between steam and the reduced metal oxide has been researched beyond the thermochemical water splitting field. The reaction of steam on the surface is also relevant in electrolyser and chemical looping technologies. Hansen and Wolverton outline a reaction mechanism on a Ceria (111) surface using a nudged elastic band method. [89] The authors outlined the splitting reaction occurs through a series of steps (Figure 2-7). Initially the steam is adsorbed onto the material surface near to a vacant oxygen site. The steam dissociates to form two hydroxyl groups on the surface. (Eq. 2.29 and Figure 2-7a). This step was found to be incredibly exothermic due to the stable nature of hydroxyls on metal oxide surfaces.

$$H_2O\ (g)\ +\ O_O^X\ +\ V_O^{\cdot\cdot}\ \rightarrow 2OH_O' \tag{2.29}$$

The hydroxyls were calculated to be unstable at temperatures above 600 K as charge transfers from a reduced cerium site associated with the surface oxygen to one of the surface hydroxyl groups (Figure 2-7c). This oxidises the cerium and weakens the bonding of the hydrogen allowing it to diffuse over the surface until it reacts with another OH_O' group to form hydrogen. The reaction oxidises the second cerium cation associated with the vacancy (Eq. 2.30 and Figure 2-7d). The breaking of the initial O-H bond is highly endothermic and is considered the rate limiting step of this mechanism. [89]

$$2OH_O'\ +2Ce_{Ce}'\ \rightarrow\ 2O_O^X\ +2Ce_{Ce}^X\ +H_2(g) \tag{2.30}$$

Fu *et al.* developed a hydrogen production mechanism with similar steps for the $LaMnO_3$ (010) surface outlining the breaking of the initial OH bond as the limiting step. [90] Fu expanded on their work by investigating the effect of A-site and B-site dopants on within the $LaMnO_3$ structure. Substituting more Sr onto the A-site was observed to lengthen the time to complete oxidation, whereas small concentrations of B-site inclusions (Ti, Ga, Al and Mo) were found to improve the reaction kinetics. The authors did not provide much explanation for their results but showed good agreement with previous reports in literature.[91], [92]

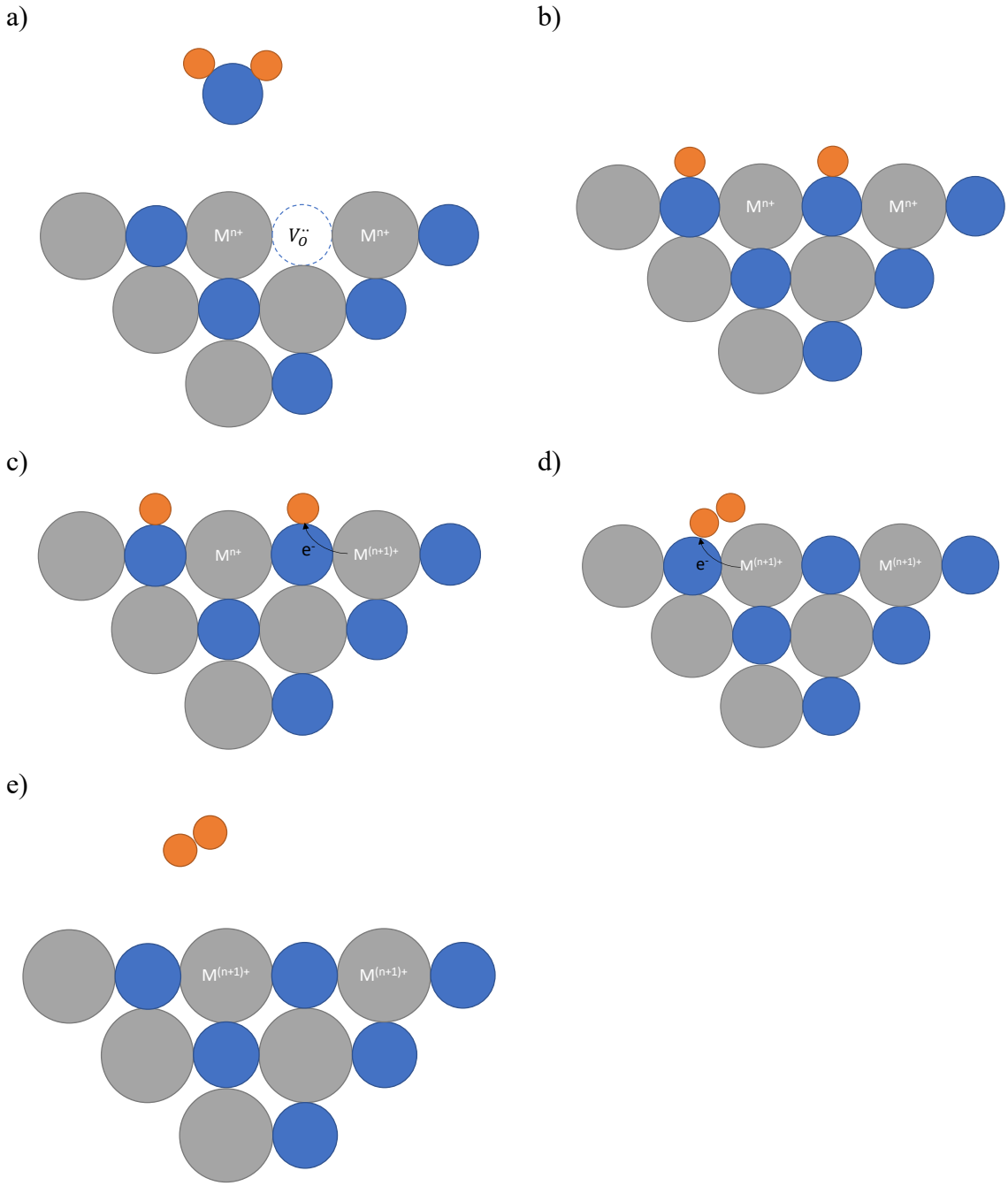

Figure 2-7. Summary of steps in the reaction between steam and reduced metal oxide surface.

Both the ceria and perovskite reaction mechanism are in good agreement with the rate determining step being the electron transfer to breaking the initial M-OH bond. As suggested by Hansen and Wolverton, the destabilisation of this hydroxyl bond can be beneficial in improving the kinetics. [89] Ultimately, the fast reaction kinetics for thermochemical water splitting requires a combination of surface vacancy concentration, facile charge transfer and fast bulk oxide diffusion. Although there are not a lot of literature sources directly related to the reaction kinetics of thermochemical water splitting materials, different aspects can be

transferred from other research fields, such as SOFCs, to help optimise the material performance.

2.6. Efficiency

The overall efficiency of thermochemical water splitting is denoted as solar to hydrogen efficiency and calculated by Equation 2.31. Similar to most efficiency equations, it is a ratio of the energy out (chemical energy in the hydrogen produced) to the energy supplied (concentrated solar power).

$$\eta_{solar-to-hydrogen} = \frac{HHV_{H_2} \cdot n_{H_2}}{Q_{solar}} \tag{2.31}$$

where HHV_{H_2} is the higher heating value for hydrogen, n_{H_2} is the number of moles of hydrogen, and Q_{solar} is the concentrated solar power input.

A variety of different efficiency models have been published based on different operating conditions i.e. temperature swing or isothermal and reactor designs.[93]–[97] All have a same overall master equation (Eq. 2.31) but with varying levels of complexity related to heat recoveries from either the solids or gases cooling between reaction temperatures, and forming a low oxygen partial pressure environment (sweep gas/vacuum pump efficiencies). Here, a basic efficiency calculation will be introduced, relating to the material design.

Most thermochemical water splitting reactors utilise a heliostat reactor setup. As mentioned in the thesis introduction this is to utilise concentrated solar power to drive the chemical reactions at high temperatures. A heliostat reactor is simply a field of mirrors that reflect and focus the sunlight onto a central receiver (Figure 2-8).[32] Commercialised thermochemical water splitting companies, such as Heliogen and Synhelion, as well as small scale experimental reactors use similar heliostat setups.[98], [99] Some researchers have estimated current system efficiencies of approximately 20% are feasible, surpassing photovoltaic systems.[100]

The total solar input, Q_{solar}, is equal to the product of solar flux and the area of mirrors that focus on the aperture. However, the amount of heat that is supplied to the aperture, Q_A, is

dependent on the mirror efficiency that is related to cleanliness, shading and alignment. Q_{TC} is the heat available to drive the thermochemical reactions. Its value is related to the apertures ability to absorb heat (α = absorptivity) and minimise reradiation (Q_{rered}) and convection (Q_{con}).

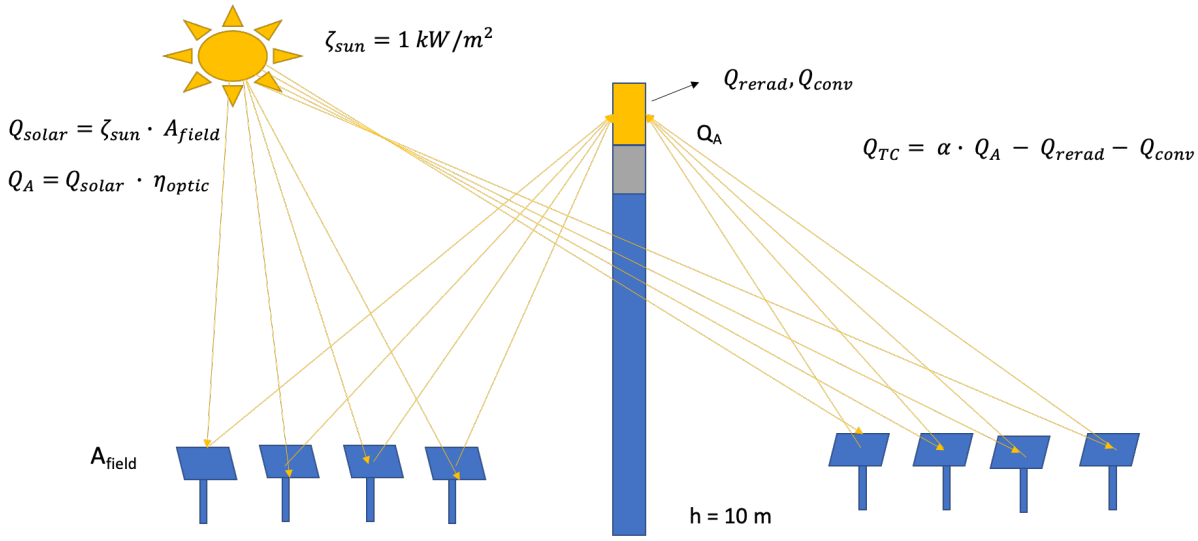

Figure 2-8. Schematic of a Heliostat concentrated solar power reactor commonly used for thermochemical water splitting.

The amount of hydrogen produced is determined by the ratio of Q_{TC} and the heat required to produce 1 mole of hydrogen, Q_{mol} (Equation 2.32).

$$n_{H_2} = \frac{Q_{TC}}{Q_{mol}} \tag{2.32}$$

Q_{mol} is a sum of the reduction enthalpy, sensible heat of the metal oxide, Q_{SH}, and the sweep gas, Q_{IH}, the heating requirement for water to T_{ox}, Q_{H_2O}, and auxiliary terms, Q_{aux}, (Eq. 2.33). This auxiliary term includes most factors that distinguish different efficiency models such as heat recovery, pumping efficiency, gas separation and mechanical movement of samples.

$$Q_{mol} = \Delta H_{red} + Q_{SH} + Q_{IH} + Q_{H_2O} + Q_{aux} \tag{2.33}$$

Equation 2.33 suggests smaller reduction enthalpy will be preferential for a higher overall efficiency, however caution is advised since this may lower the overall efficiency. As mentioned earlier when discussing thermodynamic requirements, lower reduction enthalpies

require greater volumes of steam or lower temperatures to drive the oxidation reaction. Therefore, increased heating requirements for additional steam or additional sensible heat for reheating of the oxide material to the reduction temperature can quickly dwarf the benefit of lower reduction temperatures. Overall, it is a tricky optimisation problem to find a thermodynamically favourable material that is also efficient. There is still plenty of scope for research not only with the design of new metal oxides but also more systems engineering to optimise reactor designs.

2.7. Material Design for Optimal performance

From understanding the fundamental requirements for a good thermochemical water splitting material, it allows the design of new materials. It is possible to summarise the basic requirements outlined by the principles outlined in this chapter plus a few more considerations needed for translation to real-world applications.

Requirements for thermochemical water splitting materials

- Thermal reduction enthalpy, $\Delta H_{red} > \Delta H_{WS} = 285$ kJ mol^{-1}
- Large reduction entropy to minimise ΔT required to drive the splitting reaction
- Large fuel production potential (δ>0.1)
- Stability under reduction and humid conditions at the reaction temperatures
- Morphologically stable and sintering resistant to allow stable performance over many cycles
- Compatible with current TWS reactor materials e.g. Al_2O_3 for easy implementation
- Fast oxygen bulk diffusion and electron transfer to surface hydroxyls
- Cheap and abundant elements

The next chapter will provide a brief literature review into the main groups of materials currently being researched for thermochemical water splitting.

3. Literature Review of thermochemical redox materials

There have been numerous materials reported for thermochemical redox reactions used for either energy storage, CO_2 splitting or for H_2O splitting. The materials are usually categorised into either volatile or non-volatile. As the name suggests volatile metal oxides tend to sublime during the reduction reaction to a gaseous state. The common volatile systems are the ZnO or SnO_2. [101]–[103] Although the oxygen gas production is large and the volatility is entropically favourable, these systems have issues with losing the redox active material.[104] Additional components are needed to rapidly quench the Zn and Sn and further consideration is needed to prevent the parasitic re-oxidation reaction by oxygen.[105]

Non-volatile systems retain their solid phase throughout the reduction reaction. These are further split into stoichiometric and non-stoichiometric systems. Stoichiometric systems undergo a step change reduction to form solid solutions of a reduced phase and the starting oxidised phase (Figure 3-1). These systems have larger production volumes compared to the non-stoichiometric systems, however the high reduction temperatures near the material melting point can cause deactivation by sintering. Consequently, these materials can have slow kinetics due the lowering of active surface area. The non-stoichiometric systems undergo continuous oxygen removal from the lattice during the reduction reaction whilst maintaining the original parent phase. In contrast to stoichiometric systems, reactions operate at lower temperatures and much lower compared to their melting point. This ensures better cyclability and long-term stability alongside good kinetics although at the cost of fuel production.

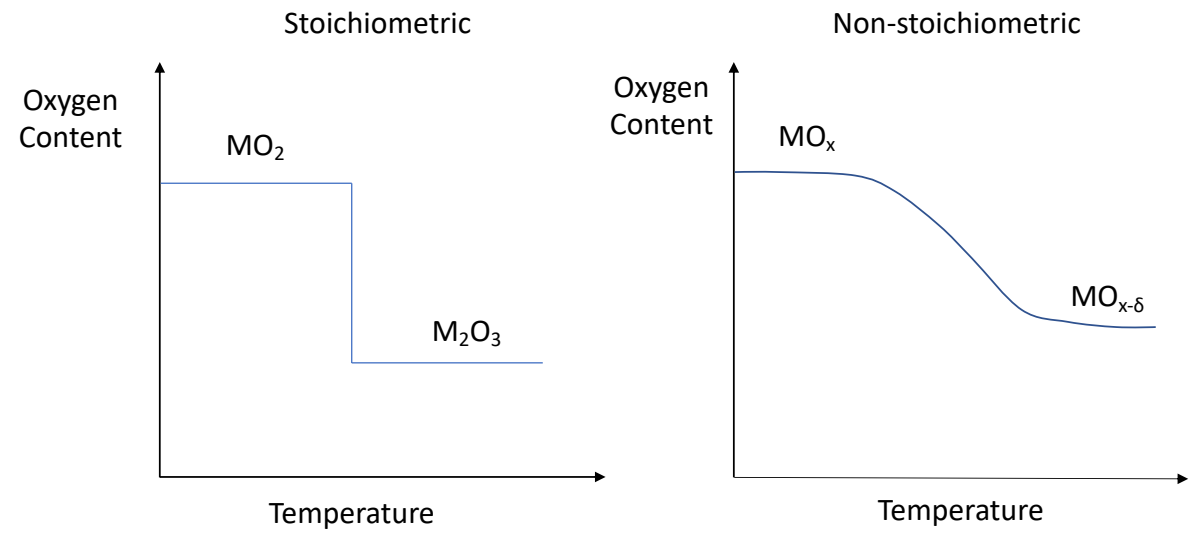

Figure 3-1. Comparison between the evolution of oxygen content as temperature increases between stoichiometric and non-stoichiometric metal oxides.

There have been numerous reviews published in recent years comparing the different types of redox active materials, and direction to reviews by Lu *et al.* and Abanades is recommended for further reading.[106], [107] This chapter will provide a brief overview of those non-volatile metal oxides investigated for thermochemical water splitting or carbon dioxide reduction.

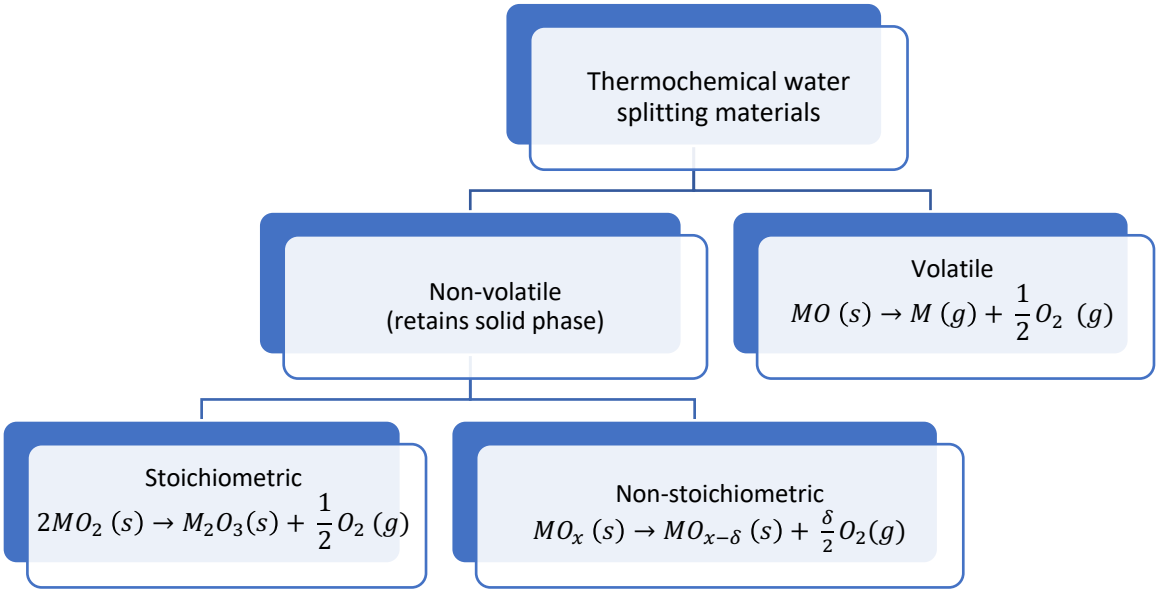

Figure 3-2. Categorising the different classes of thermochemical water splitting metal oxides.

3.1. Stoichiometric Systems

3.1.1. Iron Oxide

The original thermochemical water splitting cycle was proposed by Nakamura in the 1970s. [108] The author investigated the abundant metal oxide Fe_3O_4 inverse spinel system. Reduction of iron oxide to FeO starts at 2500 K. However, this temperature is above the melting point of FeO, and therefore there is a loss of microstructural integrity that results in particle coarsening and loss of active area. Despite this issue, some authors have reported good cyclability of iron oxide systems using aerosol reactors to keep the particles separated or crushing the powder between reduction and reoxidation. Oxygen partial pressures required to bring the reduction temperature below the melting point are far below that of sweep gases and ultra-high vacuum pumps.[109]

$$Fe_3O_4 \rightarrow 3FeO + \frac{1}{2}O_2 \tag{3.1}$$

Furthermore, some studies with isotopically labelled CO_2 demonstrated the slow reoxidation kinetics of the FeO phase.[90] Smaller grains would be preferential to overcome the kinetics, however, may further enhance the post-sintering at the high reduction temperatures.

a)

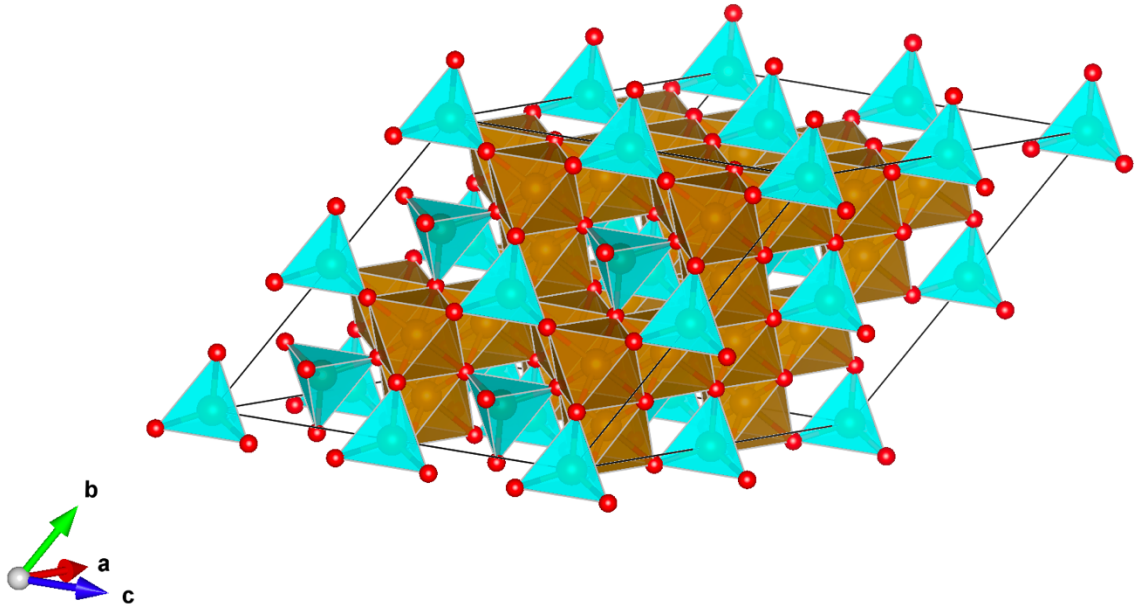

b)

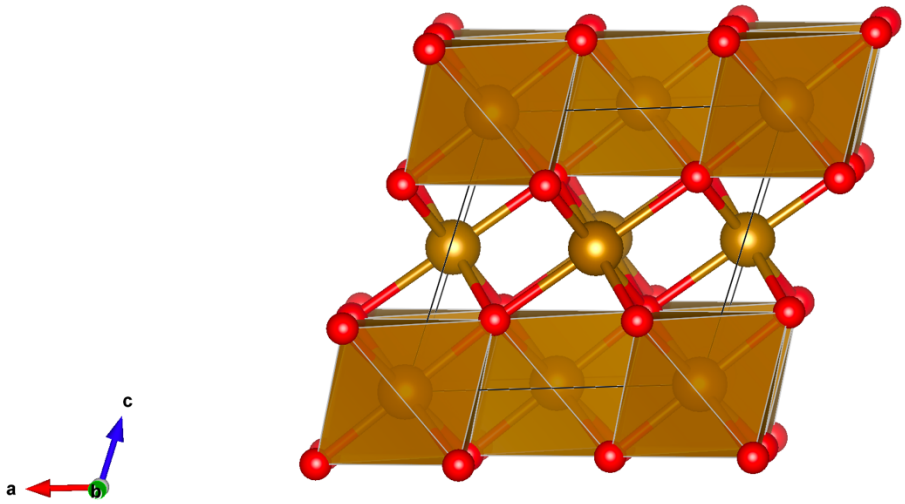

Figure 3-3. Crystal structure of a) Fe_3O_4 inverse spinel magnetite phase and b) FeO rock salt phase. Blue polyhedra represent the Fe^{3+} tetrahedra and the brown polyhedra demonstrates the Fe^{2+} or Fe^{3+} octahedra.

To improve the stability, Fe_3O_4 was deposited on scaffold materials such as YSZ. [111], [112] The reduced Fe^{2+} becomes incorporated within the YSZ structure, thus preventing the formation of the liquid FeO phase.[92] The scaffold was further observed to have a secondary effect of improving the redox kinetics due to the fast oxygen within YSZ. [111] Although despite its benefits, the addition of the scaffold can lower the overall efficiency due to the additional sensible heat required to heat the scaffold instead to powering the reduction reaction.

3.1.2. Developments of Iron Oxide

Iron oxide systems were further investigated by the substitution of more reducible cations (Ni,Co) into the structure. [113] These additions lowered the reduction temperature and increased the oxygen evolution. Kodama *et al.* investigated the complete substitution to Co_3O_4 however no hydrogen production was observed upon introduction of steam.[114] This was likely due to the lowering of the reduction thermodynamics by too much, therefore not supporting sufficient thermal energy to facilitate the water splitting reaction. However, Co_3O_4 spinels have been found to be ideal candidates for thermochemical energy storage due to its exceptionally large oxygen storage capability, [115] but suffers from sintering and slow

oxidation kinetics. [116], [117] Similarly, substituting more stable cations onto Co_3O_4 are investigated to improve the stability and ultimately cyclability for thermochemical energy storage. [118]

The mixing of Co-substituted Fe_3O_4 with Al_2O_3 was observed to lower the reduction enthalpy by favouring the formation of iron aluminate structures.[119] Originally thought to be undesirable due to potential deactivation of the surface, this approach significantly increased the oxygen production at lower temperatures.[119] Furthermore, hydrogen production was observed at lower temperatures compared with non-Al_2O_3 supported samples.

3.2. Non-stoichiometric Systems

3.2.3. Cerium Oxide

Cerium oxide is widely considered the benchmark material for thermochemical water splitting. This metal oxide has face centred cubic $Fm\bar{3}m$ fluorite structure with eight coordinated Ce^{4+} cations present within the structure (Figure 3-4). This material has been heavily studied in a wide range of catalytic and energy conversion devices from CO oxidation to solid oxide cells and has demonstrated an ability to topotactically exchange oxygen with its environment. [120]–[122]

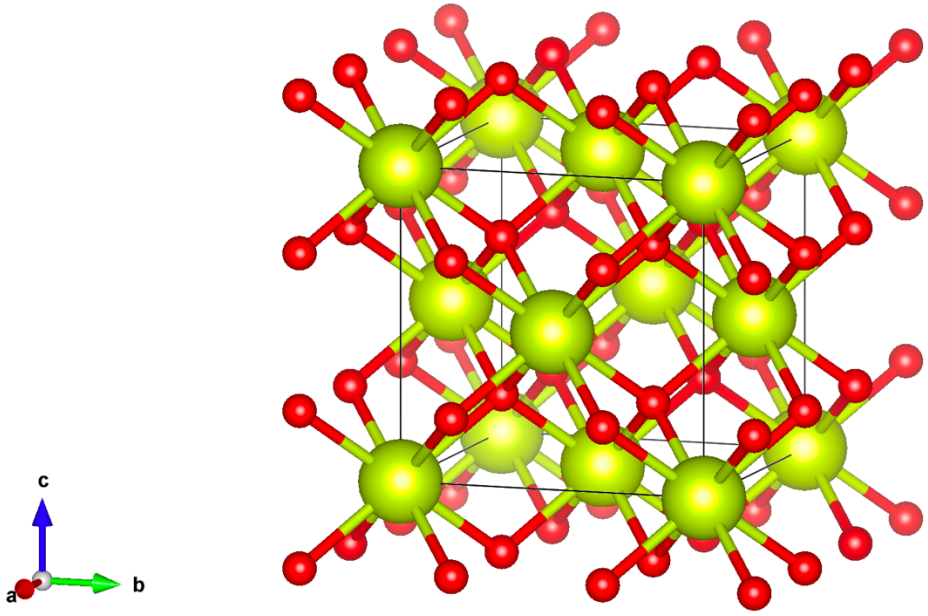

Figure 3-4. Crystal structure of face centred cubic CeO_2.

Originally investigated by Abanades and Flamant as the stoichiometric CeO_2/Ce_2O_3 system, and despite the fast reoxidation of Ce^{3+} ions by steam, it was re-studied as a non-stoichiometric system due to issues with sublimation at the high reduction temperatures (>2000 °C). [123] The partial reduction of cerium cations at 1400 °C under inert gas flow observes a continuous change in the oxygen non-stoichiometry over the redox cycle steps thus mitigating a phase change (Equation 3.2).[124] Chueh *et al.* demonstrated impressive cyclability of CeO_2 between 1500 and 800 °C for over 500 cycles – although an initial decrease in gas production is observed over the first 100 cycles that have been attributed to the sintering.[125] Fortunately, the redox thermodynamics of CeO_2 has been heavily studied due to its interest in wide variety of technologies. [126]–[128] Cerium oxide was observed to have a partial molar enthalpy in the region of 400 to 480 kJ/mol and a partial molar entropy of 175 to 300 J/K/mol. These values are sufficiently above the thermodynamic criteria required (ΔH>250 kJ/mol) as discussed in chapter 2.4, and the large entropy values ensures that a lower difference in temperature is required to promote the oxidation reaction.[129] In this case numerous isothermal cycling of ceria has also been reported. [66] Furthermore, the bulk diffusion of oxygen within ceria has been observed to be significantly faster compared to stoichiometric oxides. This has allowed structures to be formed of the material with longer diffusion lengths compared to iron oxides.[130], [131]

$$CeO_2 \rightarrow CeO_{2-\delta} + \frac{\delta}{2} O_2 \tag{3.2}$$

However, motivation to increase the fuel production and lower the reduction temperature has led to investigations of doping these fluorite structures with a range of different elements.

3.2.4. Doped Cerium Oxide

The field of doped ceria is vast for thermochemical water splitting. Figure 3-5 shows the number of different elements incorporated within the ceria lattice to try improving the thermochemical redox performance. The field can be split into acceptor, donor and isovalent elements, each with different effects on the thermochemical redox performance.

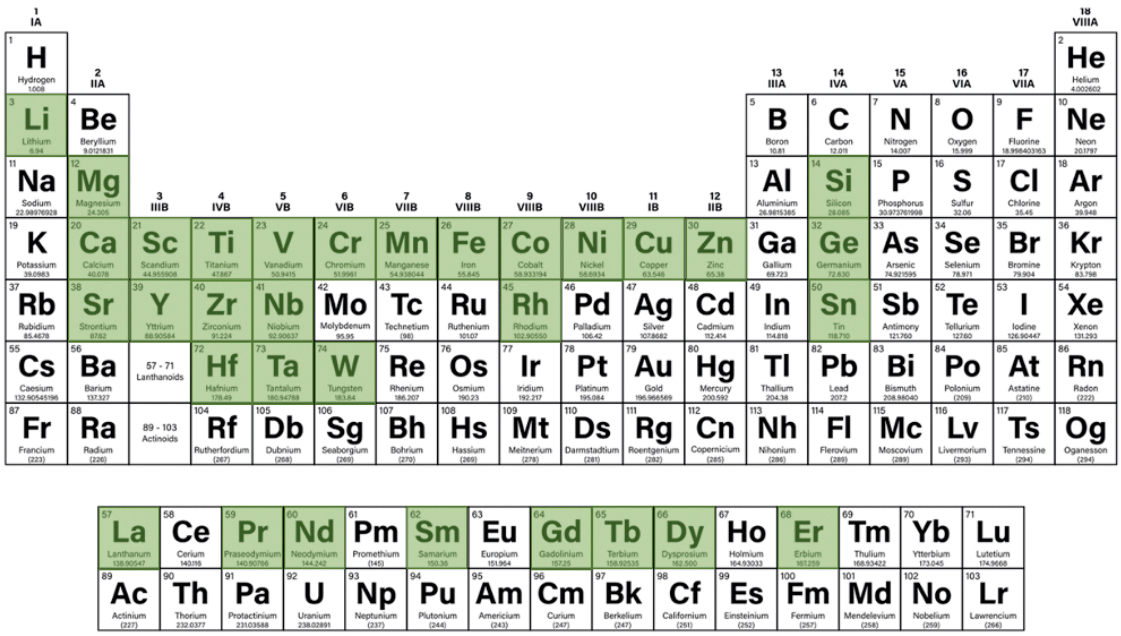

Figure 3-5. Dopant elements in ceria investigated for thermochemical water splitting reviewed in [132].

Acceptor dopants with a lower oxidation state compared to Ce^{4+} would observe an increased inherent oxygen vacancy concentration within the lattice to compensate the negative charge. Several authors have reported improved oxygen production volumes at lower temperatures upon introduction of elements such as Er^{3+}, Y^{3+}, or Tb^{3+}.[133], [134] Kaneko *et al.* reported the improvement in the oxygen evolution by incorporation elements from the first row of transition metals due to their ability to accommodate different oxidation states within the

lattice. [135] Mn- and Co-doped compounds increase the oxygen evolution significantly for the first cycle but shows depreciation beyond as the material is further cycled. Co- and Mn-oxides were detected by XRD after the first reduction cycle suggesting low instability of these compounds. [135] Further instability was observed with pentavalent donor doped compounds upon reduction. Nb^{5+}, V^{5+} and Ta^{5+} inclusions above 10% would form $CeNbO_4$, $CeVO_4$ and $CeTaO_4$ secondary phases respectively. [136], [137]

Isovalent Zr^{4+} and Hf^{4+} are other elements proven to improve the reduction reaction. [133], [138]–[140] These tetravalent cations have no electronic effect on the ceria lattice however have a slightly smaller ionic radii and strain the metal oxide bonds within the lattice. Vacancies a preferentially formed adjacent to the Zr^{4+} or Hf^{4+} cations to relieve the tensile strain within this lattice. However, this comes at a cost of reoxidation kinetics, whereby increased dopant concentration significantly slows the reoxidation.[141] Muhich and Steinfeld computationally investigated the doping principles in ceria for thermochemical water splitting.[142] Charge compensating vacancies are spontaneous within the lattice due to acceptor dopants, and although they increase the charge carrier concentration within the lattice, consequently increasing oxygen mobility, they do not store chemical energy that can be used to split water molecules. Further creation of vacancies within the structure thermally reduces the cerium cations within the structure with the similar energy requirements as undoped ceria. Therefore, the inclusion of straining cations such as Zr^{4+} and Hf^{4+} are seen as an improvement. Jacot *et al.* suggested an ionic radius of 0.8 Å is optimal. [136] Mg^{2+} and Sc^{3+} have been observed to successfully improve both reduction and oxidation performance of ceria. [143], [144] These ions strain the bonds within the lattice and demonstrate improved oxygen diffusion due to charge compensating vacancies within the structure. Furthermore, these elements were observed to improve the thermal stability of the metal oxide by limiting sintering effects. [143] Mg^{2+} was further observed to improve the stability and kinetics of Zr^{4+} doped compounds.[145] However, the introduction of dopants into the lattice reduces the numbers of redox active cations within the structure and limits the production volumes. [144] Moreover, the elements that are introduced to improve the reduction performance often limit the reoxidation kinetics, therefore increased consideration and understanding is required.

3.2.5. Perovskites

Perovskites are inorganic compounds with the formula ABX_3. A and B are metal cations and X is an anion – oxygen in this case. A is a larger cation compared of B, situated in a twelve coordinated body centred position surrounded by BO_6 octahedra positioned on the unit cell corners. The Goldschmidt tolerance factor, t, is used to determine the crystal stability of perovskite materials (Equation 3.3). The "ideal" perovskite has the cubic $Pm\bar{3}m$ crystal structure and a Goldschmidt tolerance factor equal to 1 (Figure 3-6). Changes in the ionic radii ratio cause deviations from this structure. If the A-site size is decreased, the Goldschmidt tolerance factor decreases. The A-O metal oxide bonds are under tensile strain and the octahedra within the lattice undergo a tilt transformation to lower the A-O distance and relieve the stress within the structure. This gives rise to rhombohedral and orthorhombic crystal structures dependent on the axis of rotation. This change in structure is observed by additional Bragg reflections formed in XRD patterns that will not be present in the ideal structure.[146] In contrast, increasing the A-site ionic radii compresses the A-O bonds and the BO_6 octahedra transform to a face-sharing arrangement to alleviate the stress. The structure transforms to a hexagonal polymorph whereby the strong electrostatic repulsion across octahedral faces induces columns of BO_6 octahedra. [147]

$$t = \frac{r_A + r_O}{\sqrt{2}(r_B + r_O)} \tag{3.3}$$

Much like ceria, perovskites have been heavily investigated for oxygen conducting technologies.[148] Their ability to accommodate large oxygen non-stoichiometries within the structure at lower temperatures compared to ceria have seen their interest grown for thermochemical redox reactions. Furthermore, properties can be tweaked by the introduction of dopants on either A- or B-site allows a large compositional space to be explored. [149]

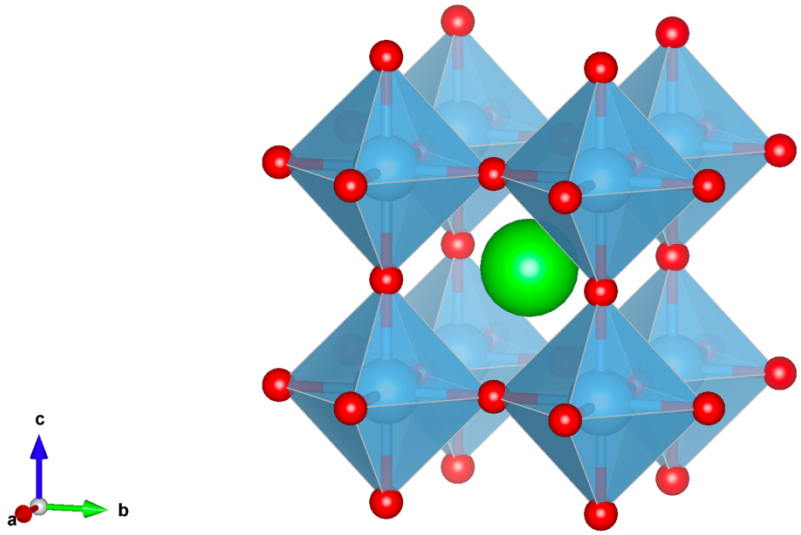

Figure 3-6. Perovskite with $Pm\bar{3}m$ crystal structure.

Lanthanum manganates ($LaMnO_3$) are the widest perovskite family to be explored for thermochemical redox splitting reactions. Scheffe *et al.* first reported thermochemical splitting performance of $La_{1-x}Sr_xMnO_{3-\delta}$ at reduction temperatures lower than ceria (1600 K versus 1800 K). [150] The addition of strontium into the $LaMnO_3$ structure introduces electronic charge compensating defect that is situated on the manganese cation, promoting the oxidation state of the manganese to 4+. This not only improves the electronic conductivity – a common tactic used in SOC air electrodes – but also promotes reduction extent of these perovskites as at high temperatures the charge is compensated by the formation of oxygen vacancies within the structure. Increasing the strontium content was observed to improve the reduction extent due to the lowering of the partial molar entropy and enthalpy. [87] Yang *et al.* demonstrated that kinetically a 20% Sr incorporation onto the A-site was favourable for hydrogen production. Increased concentrations decreased the hydrogen productions but increased the volumes due to the increased number of vacancies within the structure. [87] Ignatowich *et al.* later suggested a decrease in the chemical driving force was the cause for slowing splitting kinetics. [151] Dey *et al.* demonstrated that the lowering of the reduction thermodynamics has a larger effect when using Ca^{2+} instead of Sr^{2+} due to higher lattice distortions. [152] However, Wang *et al.* further showed a Ca^{2+} concentration of 40% had the best kinetic performance, although there are differences in materials testing methods. [153] First principles calculations by Deml *et al.*

suggested the inclusion of Sr^{2+} induces unoccupied electronic states near the Fermi energy that are readily filled upon vacancy formation. [154]

B-site cations have also demonstrated effects on the thermochemical performance. McDaniel *et al.* increased the reduction extent at lower temperature by introducing Al^{3+} onto the B-site of the $La_{1-x}Sr_xMnO_3$, leading to increased H_2 and CO production. [155] Dey *et al.* expanded on this work to show increased CO production up to concentrations of 50% Al^{3+}. [156] The authors expanded their study to Ga^{3+} and Sc^{3+} dopants who improved the production volumes due to their increased ionic radii distorting the crystal structure. However, vacancy clustering around the dopant cation limits oxygen diffusion within the structure and consequently lowers the kinetic performance. [156] Wang *et al.* investigated the effect of the first row of transition metals on the thermochemical performance of $La_{0.6}Sr_{0.4}BO_3$ perovskites. [157] The oxygen evolved from the structures increased as B was changed to later transition metals in agreement with the first principle calculations conducted by Deml *et al.*. [154] Demont et al. experimentally screened known solid oxide fuel cathode materials for thermochemical water splitting.[158] Although materials such as $La_{1-x}Sr_xCo_yFe_{1-y}O_{3-\delta}$ and $Ba_{1-x}Sr_xCo_yFe_{1-y}O_{3-\delta}$ with lower vacancy formation energies demonstrated redox cycling at lower temperatures (1000 °C for $Ba_{1-x}Sr_xCo_yFe_{1-y}O_{3-\delta}$), the H_2 production worsened. Ultimately, it is a similar case for the doped ceria materials in which improvements in the reduction performance leads to more unfavourable reoxidation. [159] Authors have moved in the direction of introducing "less reducible" cations to the B-site. Carrillo *et al.* demonstrated improvements of fuel production kinetics by inclusions of up to 85% Cr onto the B-site. However, this came at a cost of total fuel production which was said to be optimised at 30% Cr. [160]

There have been several perovskite compositions reported for thermochemical redox reactions that are not based upon lanthanum manganate. Dey *et al.* investigated the effect of exchange the lanthanum A-site for different rare earth elements. [161] They reported the lower ionic radii elements e.g. Y^{3+} increased oxygen evolution volumes due to increased lattice distortion, although the reoxidation kinetics and $CO:O_2$ ratio decreased. Carrillo *et al.* reported the improvement of kinetics with inclusion of Al^{3+} onto the B-site of YSM perovskites using the similar rational to that of McDaniel *et al.* Although the authors admitted the these materials do not demonstrate optimal thermodynamics for thermochemical water splitting. [162] Barcellos *et al*. tried to find a thermodynamic compromise between the reducible $BaMnO_3$ and

irreducible $BaCeO_3$ phases. [163] The compound of $BaCe_{0.25}Mn_{0.75}O_3$ reported greater gas production over the Al-doped LSM compounds at lower temperatures. Importantly this compound required less excess humidity to drive the oxidation reaction. If lower steam is required, there are significant energy savings in the system efficiency since the heating of the water requires a lot of heat. [164]

Other perovskite compounds have been reported through computational exploration. Ong *et al.* proposed the $BiVO_3$ structure to have similar properties to ceria from DFT entropy and enthalpy calculations.[165] However this is yet to be reported experimentally. Chen *et al.* combined computational and experimental techniques to report H_2 production in $LaGaO_3$ was improved upon substituting Co into the structure with increase in oxygen vacancy concentration.[166] Due to the large compositional space of perovskites, Emery *et al.* conducted a vast DFT screening study of all possible A and B site combinations. [167] This study outlined 383 potential candidates based on partial molar enthalpy and perovskite crystallographic descriptors. Many of these compounds remain untested experimentally, and the study did not delve into dopants. However, it is a good starting point for future perovskite structures.

Recently, some authors have sought to include redox active elements such as Ce onto the A-site of the perovskites. As described by Gautam *et al.* the purpose is to activate the configurational entropy of the perovskite lattice so that the partial molar change increases to be in line with ceria.[168] This computational study proposed $Ca_{0.5}Ce_{0.5}MnO_3$ as a potential dual-site reduction perovskite with favourable thermodynamics, but the compound was not experimentally verified. Carrillo *et al.* discuss the benefits of increasing the partial molar enthalpy to improve thermochemical performance. The entropy controls the gradient of the Gibbs free energy curve and thus a higher energy can lead to lower reduction temperatures and smaller required temperature differences between T_{red} and $T_{ox.}$ [129]

Recently there have been a small handful of publications that have related to altering the surface for the improvement of thermochemical redox reactions. Carrillo *et al.* modified the surface of $La_{0.6}Sr_{0.4}Cr_{0.8}Co_{0.2}O_3$ by exsolving Co nanoparticles from the B-site sublattice to the surface.[169] The presence of Co on the surface was observed to rapidly improve the CO_2 reduction kinetics and exceed those observed by ceria with greater production volumes. The same author also investigated composite structures with varying ratios of LSM/CeO_2. [170]

The combination of phases favourable for each half of the redox cycle did improve the oxygen evolution of the reduction reaction. However, the CO evolution never exceeded undoped ceria. Although this remains an interesting avenue of research that can be explored further with different material combinations.

3.3. Beyond Perovskite materials

The have been a handful of other materials investigated for thermochemical water splitting or CO_2 reduction. Firstly, Mulmi *et al.* proposed the $Ba_2Ca_{0.66}Nb_{1.34-x}Fe_xO_{3-\delta}$ double perovskite structure.[171] The authors indirectly showed improved CO_2 reduction behaviour with increased Fe concentrations due to increased presence of lattice vacancies. Ruan *et al.* reported utilised the $Ce^{3/4+}$ redox couple for thermochemical water splitting using the $Ce_2Sn_2O_7$ pyrochlore structure. [172] This material underwent the stoichiometric phase transformation to form a CeO_2/SnO_2 solid solution with increased O_2 production volumes, but slower H_2 production compared to the benchmark CeO_2.

Ruddlesden-Popper oxides with the structure A_2BO_4 are another group of metal oxides that have shown thermochemical splitting properties. Demont *et al.* investigated $LaSrCoO_4$ and $LaSrFeO_4$ as part of an experimental screening of solid oxide fuel cell cathodes.[158] $LaSrCoO_4$ demonstrated cyclable thermochemical water splitting behaviour on par with $La_{1-x}Sr_xMnO_3$ at lower reduction temperatures. Nair *et al.* demonstrated the redox performance of $Sr_{1.5}La_{0.5}MnO_4$ and $Sr_2LaMn_2O_7$ structures between 1400 and 1050 °C with no observations of microstructural degradation. [173] Recently, Bergeson-Keller *et al.* reported the hydrogen production using the $Sr_{2-x}Ce_xMnO_4$ structure, and despite favourable thermodynamic behaviour, kinetics limited the material from exceeding the performance of its comparative perovskite structure. Ruddlesden-Popper oxides remain of interest in the thermochemical water splitting field. The thesis explores the Ruddlesdenn-Popper family further using a combination of computational screening studies and experimental investigations.

3.4. Summary

To summarise, there have been a lot of different metal oxide compounds investigated for thermochemical water splitting. The overall trend to lower the reduction temperature without

compromising fuel production volumes has driven material development away from simple binary metal oxides. Here we have summarised one class of thermochemical redox materials that have been investigated for water splitting or CO_2 reduction. Firstly, understanding Fe_3O_4/FeO stoichiometric system and how the high reduction temperatures, instability and oxygen diffusion kinetics caused the field to pivot towards non-stoichiometric systems such as ceria. This compound demonstrated faster kinetics at lower temperatures and is still considered to be the benchmark material. Thermal reduction of ceria only induces a small oxygen deficiency; therefore, dopants have been introduced to improve the reduction extents and lower the operating temperatures. However, there has not been an overly successful dopant candidate reported since the related thermodynamic properties of the reduction and oxidation reactions usually do not allow both halves of the redox cycle to be improved. This motivated the field to turn to other metal oxide family such as perovskite materials due to their ability to accommodate large oxygen non-stoichiometries and vast compositional space. Lanthanum manganate has been heavily studied with various different elements incorporated into this compound to improve the fuel production, or rates, or lower the reduction temperature. However, a similar trend is observed in the perovskite field to doped ceria, in which improving one half of the redox cycle does not correspond to the other. Recent advances in computational modelling have allowed this field to be further narrowed down the field to find compositions beyond perovskite structures that can be further modified by doping strategies or surface modification to improve the performance to comparable levels with ceria.

4. Thesis outline

Although the literature review has highlighted some concerns with the perovskite materials for thermochemical water splitting, the compositional space is still vast and underexplored. Furthermore, considering other derivatives such as layered perovskite structures, double perovskites and composite structures this area significantly increases. In this thesis we aim to continue the work focussing on perovskite and perovskite-like materials for thermochemical water splitting by using a combinatorial experimental and computational approach to understand material performance from first principles.

In chapter 6, the effect of antimony incorporation in $SrCoO_3$ on the redox kinetics is observed using thermogravimetric analysis and density functional theory. The incorporation of fixed valence B-site donor dopants is widely reported to improve the oxygen exchange performance. This chapter aims to understand this effect through density functional theory simulations and to validate experimental observations with the hope of tuning this material for thermochemical water splitting.

Chapter 7 aims to expand on the previous work of lanthanum chromate perovskites for thermochemical water splitting by investigating the effect of Fe concentration within $(La_{0.8}Sr_{0.2})_{0.95}Cr_{1-x}Fe_xO_{3-\delta}$. Using a similar combination of computational and experimental methods, this chapter aims to understand the trends observed by characterisation techniques. Furthermore, this chapter uses novel surface characterisation techniques in the thermochemical water splitting field to develop understanding on the materials performance and degradation under redox cycling conditions.

Following on from the previous section on a slight tangent, chapter 8 computationally investigates the potential of the Ruddlesden-Popper family of metal oxides for thermochemical water splitting. This chapter expands on the efforts of previous high throughput screening studies for accelerated material discovery to narrow down the number of potential candidates for experimental testing. Using the A_2BO_4 structure as the target family, several screens based on crystallographic principles and thermodynamic properties calculated from DFT simulations are used to predict new compounds.

The final results chapter experimentally investigates one of the screened Ruddlesden-Popper compounds, Ca_2MnO_4. This compound comprised of abundant elements is synthesised using a nitrate-citrate method and characterised to understand the crystal structure and chemical nature. Subsequent thermochemical water splitting experiments are carried out to propose a new candidate material and provide validation to the screening investigation.

5. Materials and Methods

This chapter will provide an overview of the experimental and computational techniques used within this thesis. These techniques have been used extensively throughout the work covered within this thesis. Dr Ieuan Seymour taught the principles of density functional theory and guided calculations throughout the project.

5.1. Powder Synthesis by Modified Sol-Gel Method

For all non-commercial powder used within this study, they were synthesised using wet-chemistry methods, specifically a modified sol-gel method.[174], [175] This method is composed of several steps to ensure a pure, crystalline product.

Metal nitrate precursors are dissolved under a stirring solution of citric acid heated to 80 °C to ensure a well dispersed solution of metal cation ions. Upon further heating and stirring, the solution starts to form a gel network that is then dried at 300 °C. Further decomposition at 600 °C for 12 hours removes all trace organics from the gel and leave behind a well-dispersed mixture of metal oxides. Further heating treatments were carried out in an alumina crucible at 900 °C, 1000 °C for 12 and 24 hours respectively. It is noted that at these temperatures the cobalt reacts with the alumina crucible and causes a blue stain. To avoid this side reaction affecting the purity of the sample, the powder was lightly uniaxially pressed to a pressure of 0.2 tonne in a 13 mm diameter die. This pellet was placed on a bed of sacrificial powder bed. The pellet underwent intermittent grinding steps using a pestle and mortar are important to improve the phase purity and crystallinity.

The modified sol-gel method has advantages over the more traditional solid-state method, by achieving small grains with high surface area to volume ratios primarily due to the lower temperatures required, thus providing a greater area for reactions. This has been shown with previously reported Zr-doped Ceria compounds, whereby an (2x) improvement was seen in oxygen and hydrogen production volumes.[176]

5.2. Powder characterisation

5.2.1. Crystallographic structure by X-Ray Diffraction

X-Ray Diffraction (XRD) is a technique used to understand the crystallographic nature of samples. X-rays have a wavelength in a similar length scale to the atomic spacing within solid crystals. This relationship causes diffraction behaviour when X-rays illuminate the crystal surfaces of the sample and are consequently scattered in all directions by atoms in the lattice. The majority of scattered X-rays deconstructivity interfere and contribute to the background level. Figure 5-1 demonstrates X-rays scattering between atoms arranged in a periodic solid. X-rays scattered in certain directions will satisfy Bragg's law (Equation 5.1) and undergo constructive interference to produce a maximum in the diffraction pattern. These coherent X-rays will be scattered by atoms in planes separated by a distance, d, and have a path difference of AB+BC.

$$n\lambda = 2d_{hkl} \cdot sin\theta \tag{5.1}$$

Where n is the order of diffraction (n=1), λ is the X-ray wavelength, d_{hkl} is lattice spacing of plane (hkl) and θ is the diffraction angle.

The ideal diffraction pattern will appear as a series of sharp lines above a background level. Although Bragg's law determines the angle at which diffraction will occur. The intensity of diffraction is determined by the structure factor equation (Equation 5.2). [177] The diffraction intensity occurring from atom, j, from plane, hkl, is calculated by the product of atomic scattering factor ,f_j, and the fractional atomic position in the unit cell (x, y , z). The atomic scattering factor is proportional to the atomic number of the atom, therefore lighter elements (e.g. oxygen) do not diffract as well. Furthermore, the structure factor is used to determine systematic absences within the pattern that are omitted due to the crystal structure symmetry causing additional destructive interference. In reality, the diffraction pattern appears as a series of broader peaks rather than fine line due to features present within the sample e.g. atomic concentration, strain, or instrumental effects.[178]

$$F_{hkl} = \sum_{j=1}^{N} f_j \cdot exp\left[2\pi i\left(hx_j + hk + lz_j\right)\right] \tag{5.2}$$

Where F_{hkl} is the structure factor, f_j is the atomic scattering factor of atom j, x_j, y_j, z_j are atomic positions of atom, j.

By measuring the intensity of diffracted X-rays across a wide range of θ values it is possible to obtain a full pattern that is used to match against known phases reported in databases such as the Inorganic Crystal Structure Database (ICSD). [179] A simple comparison to known phases can be sufficient in understanding the chemistry of the sample with useful information such as crystal phase and lattice parameters. However, more advanced techniques such as "Le Bail" or "Rietveld" refinements compare the measured pattern to calculated patterns to theoretical pattern through least squares fit.[180], [181] Quantitative structural information can be obtained to further understand element concentration, positions and weight fraction of phases. However, under laboratory XRD conditions this can prove troublesome when refining the oxygen position in metal oxides due to its low scattering contribution. Alternative techniques such as neutron diffraction are more useful for providing structural information in this case. Within this study, Le Bail refinement is used to avoid this concern. This technique differs by not considering structural information and matching to pattern to known crystal structure. This refinement process can still output information regarding the lattice parameters and phases present, thus sufficient information for this study.

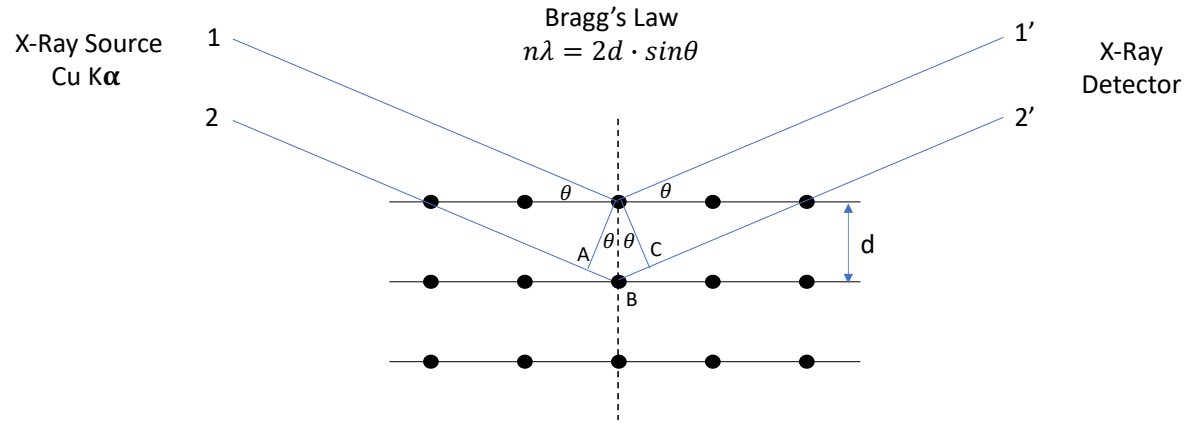

Figure 5-1. Schematic demonstrating Bragg's Law for X-ray diffraction between two atomic planes. Adapted from [7].

Laboratory instrument X-rays are typically produced by accelerating electrons from a tungsten filament towards a Cu target. These high energy electrons cause the emission of an electron from the inner electron shell of the Cu. As a result an electron from a higher shell relaxes down to fill this hole in the lower level and consequently through the conservation of energy an X-

ray photon is emitted. These X-ray photons are channelled through a series of optics and slits to be directed onto the sample surface. Importantly, these X-rays are filtered through a Nickel filter to minimise the contributions of K_β, $K_{\alpha 2}$, and Bremsstrahlung radiation to the X-ray beam, thus leaving as narrow spectrum as possible for the value of λ in the Bragg's Law.

This study uses two types of diffractometers to understand the crystallographic behaviour of powder samples. A Panalytical X'Pert Pro MPD was used for room temperature analyses to observe the phases present after synthesis, redox cycling and thermochemical water splitting experiments. The diffractometer was set-up in a Bragg-Brentano geometry whereby the sample remains stationary and the X-ray source and detector move concentrically at the same angular rate. Powder samples loaded onto a "zero background" single crystal silicon wafer sample holder and scanned over a 2θ range of 10 to 90 ° at a step size of 0.034 °.

High temperature XRD was used a Panalytical Empyrean diffractometer to understand the phase stability as a function of temperature under low P_{O_2} atmospheres (approx. 10^{-5} atm). Powder samples were loaded onto an alumina plate and placed within an Anton-Paar HTK1200N chamber. High purity dry nitrogen gas was flowed through the chamber at a rate of 50 ml/min to achieve a low P_{O_2} environment. The samples were heated using a pre-defined program between temperatures of interest relating to prior thermal analyses. Powder samples were heated at a rate of 10 °C/min and held at the target temperature for 20 min before scanning to ensure there was an equilibrium (or close to) oxygen stoichiometry within the lattice. The X-ray beam was focussed onto the centre of the sample prior to scanning and automatic incident slits were in operation to ensure the same area was illuminated throughout the scan. This minimised the effect of contributions to the diffraction pattern from the alumina holder, although it does produce an increase in the background level due to increased volume of powder being illuminated at higher angles. The simplicity of Le Bail refinement is less affected by this effect and the lattice parameters were refined using FULLPROF software. [183]

5.2.2. Powder Morphology by Scanning Electron Microscopy

Scanning electron microscopy is an imaging technique used to understand the morphology and

surface appearance of samples. Unlike optical microscopes this technique is not limited by the wavelength of white light and has much higher resolving power. Electrons have a smaller wavelength and can observe features less than 200 nm. Electrons are emitted from a filament and accelerated towards a positively charged sample. A series of electromagnetic lenses are used to focus the beam onto the sample surface whereby the electrons interact with sample surface. Figure 5-2 shows schematically the electron path within the scanning electron microscopy.[184]

The incoming electron beam interacts with the electron cloud of atoms near the surface in different ways. Firstly, the electron beam can cause the inelastic emission of a secondary electron from the highest occupied orbital (Figure 5-3a). They are attracted towards the positively charged Everhart-Thornley detector and converted a voltage signal to be read by the PC. Secondary electrons have low energies and small mean free interaction path, therefore only have the lifetime to provide information from the outermost of the interaction volume. However, they do provide highly accurate information regarding the surface morphology.[185]

Further to secondary electrons, backscattered electrons are produced through the elastic scattering of the primary electron beam. These electrons have a higher energy providing information from deeper in the interaction volume (Figure 5-3b). The backscattering of electrons has a higher probability with greater atomic number, and therefore these electrons can provide compositional information of the surface. [186]

The third type of interaction causes the emission of characteristic X-rays to provide elemental analysis (Figure 5-3c). Similar to X-ray production described in the previous section, an emission of an electron from a lower energy shell can cause the relaxation from higher energy shells. The difference in energy is conserved through the emission of an X-ray photon. This can be used for chemical analysis in a technique known as Energy-Dispersive X-ray Spectroscopy (EDS). However, accuracies can be limited by the presence of overlapping peaks, it is possible to provide an indication of elements present. [187]

The work presented in this thesis used scanning electron microscopy in the secondary electron mode to understand the changes in surface morphology. The powder samples were mounted on conducting carbon tape and imaged using a JEOL 6010LA scanning electron microscope. A beam voltage of 20 kV was used with a working distance close to 25 mm and spot size close

to 50 nm. Powder samples were loaded on to a conducting carbon tape stuck by lightly sprinkling powder from a spatula.

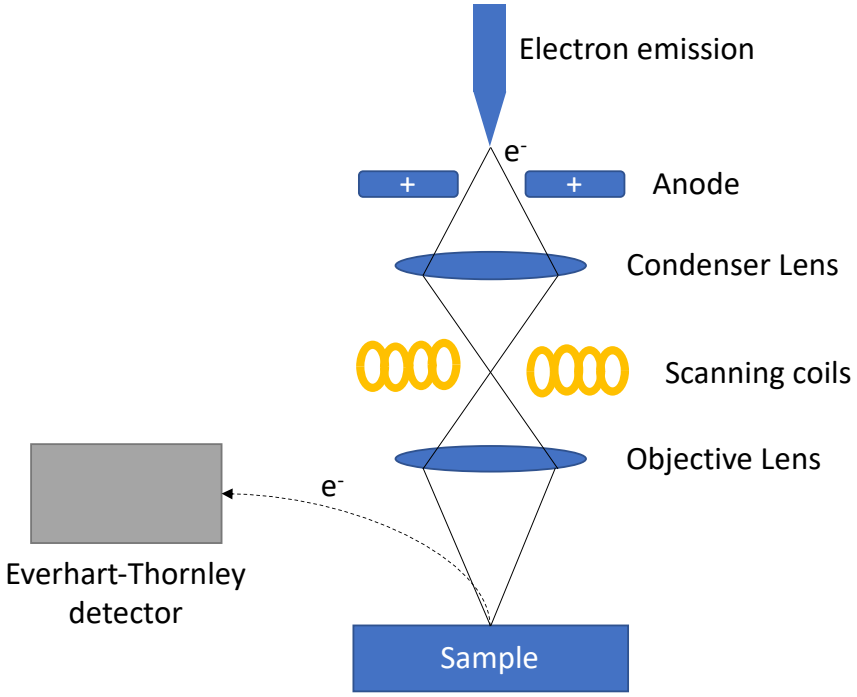

Figure 5-2. Schematic representation of a scanning electron microscope column.

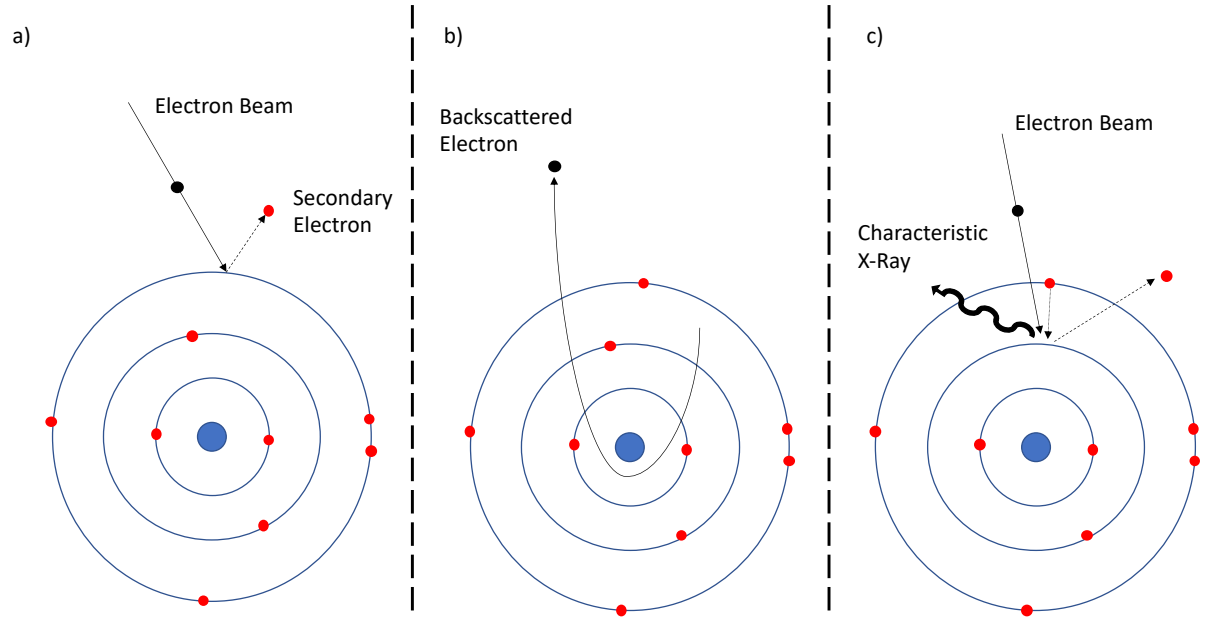

Figure 5-3. Schematics showing the formation of a) secondary electrons, b) backscattered electrons, and c) characteristic X-rays, in scanning electron microscopy.

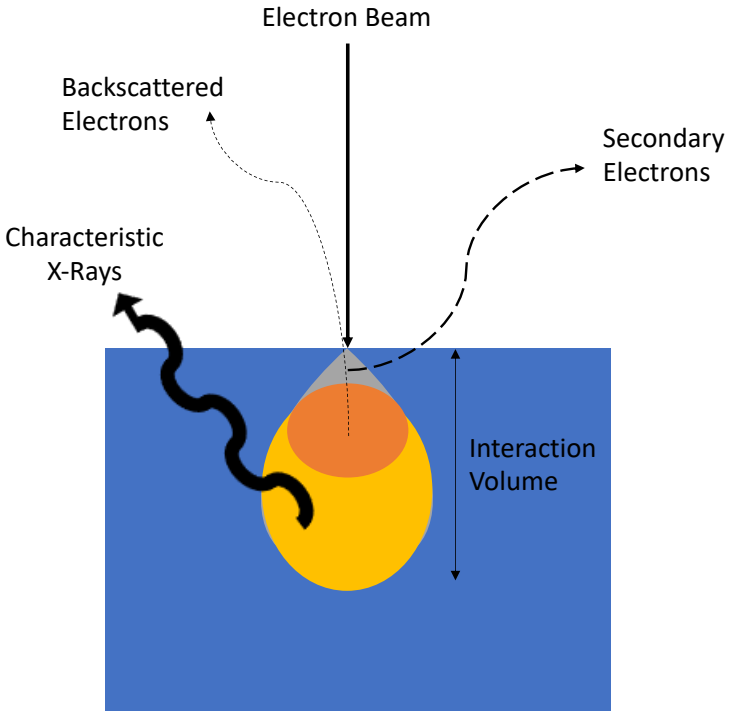

Figure 5-4. Schematic showing the interaction volume of an electron beam and sample surface.

5.3. Surface Chemistry Analysis

5.3.1. X-Ray Photoelectron Spectroscopy

The understanding of metal oxides' surface chemistry has been of keen interest in the solid-state ionic community. X-ray photoelectron spectroscopy (XPS) provides information regarding the surface species and bonding environment down to depths of approximately 10 nm. [188] Illuminating the sample surface with low energy X-rays (1.5 keV) utilises the photoelectric effect to emit photoelectrons from the core-electron levels of surface species (Figure 5-5). The kinetic energy (E_k) of the emitted photoelectron is detected and related to the binding energy (E_B) through Equation 5.3. The binding energy indicates the electron shell and element from which the photoelectron originates.

$$E_B = h\upsilon - E_k - \phi \tag{5.3}$$

Where $h\upsilon$ is X-ray photon energy and ϕ is the work function of the spectrometer.

Photoelectrons originating from p, d or f shells undergo spin orbital splitting due to the interaction between the electron and orbital angular momenta. [189] The orbital angular momentum number, l, is equal to the integer value in Table 5.1. These momentum vectors are added to the spin angular momentum, (s = ±1/2) using equation 5.4 to give a better description of the electron position. The couplet peaks are always present together and with characteristic relative intensities based on electron degeneracy (Equation 5.5). [190] Peaks caused by photoelectrons from these positions are important to recognise when interpreting the XPS spectra to deconvolute possible peaks from other elements. Furthermore, this effect is greater with higher atomic number or larger principal quantum number.

$$j = |l + s| \tag{5.4}$$

$$Intensity = (2j + 1) \tag{5.5}$$

Elements with multiple oxidation states e.g. transition metals go undergo even further splitting if there are unpaired electrons in the valence band. Doublets of the core levels appear from the spin distributions in the band structure and most prominent in Mn, Cr, Co and Ni. [191]

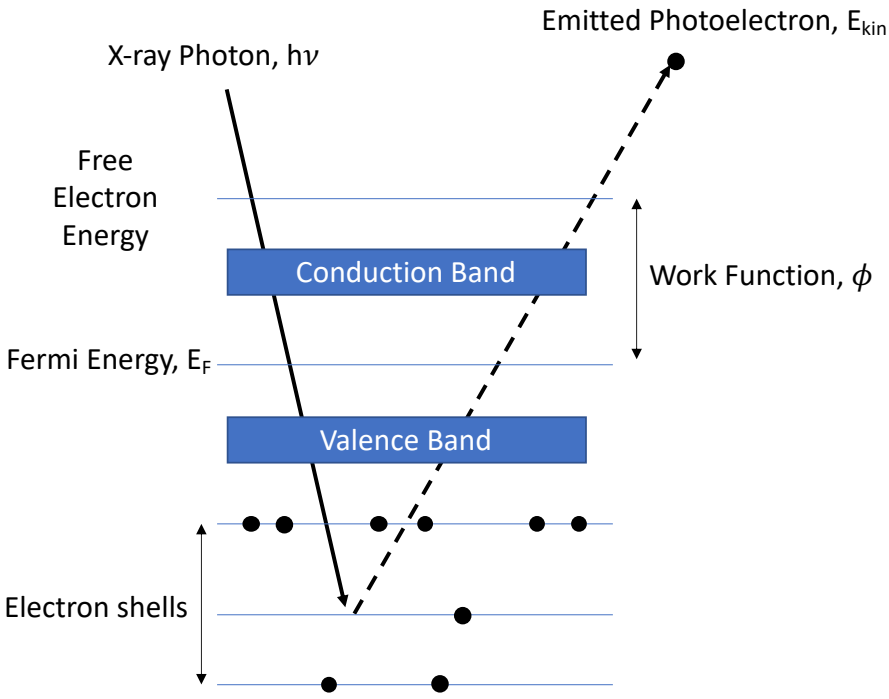

Figure 5-5. Schematic demonstration of the photoelectron emission of electrons in XPS. Adapted from [189].

Table 5-1. Possible photoelectron peaks arising due to spin orbital coupling.

Orbital Angular Momentum Number, l		**Possible Photoelectron Peaks**	**Peak ratios**
s	0	s	-
p	1	$p_{3/2}$ $p_{1/2}$	0.5
d	2	$d_{5/2}$ $d_{3/2}$	0.67
f	3	$f_{7/2}$ $f_{5/2}$	0.75

XPS can be used to measure these orbitals individually to understand changes in chemistry of certain elements e.g. bonding environment, oxidation state etc. This is done by eye comparing to features to well-known references or through fitting Gaussian-Lorentzian peaks for each photoelectron core level through a least squares' method.[192] The Gaussian contribution is related to effects from the spectrometer, whereas the natural emission from the core level is more Lorentzian.[193] The background intensity is mainly contributed from lower kinetic energy photoelectrons that have undergone several scattering events before detection. Multiple scattering events can also be the cause of shoulders on core level peaks or shake-up peaks at higher binding energies. [188]

In this thesis, the XPS results were obtained using a Thermo Scientific K-Alpha+ spectrometer (Schematically shown in Figure 5-6). The primary X-ray beam was from a monochromated Al K_α source and a spot size of 400 μm^2. Survey spectra were obtained to understand the presence of all surface species before the core levels of interest were scanned in greater detail for improved accuracy. A pass energy of 20 eV was used to analyse the core energy levels, and the binding energy as corrected by shifting the C 1s peak to 284.8 eV. An electron flood gun was used to minimise any surface charging effects occurring with the samples. Thermo Scientific Avantage software was used to analyse the spectra and fit the core level peaks using a smart-Shirley background. Information regarding peak fitting of elements was taken from Biesinger *et al.* [191] and assistance from Dr. Zijie Sha and their publication. [194]

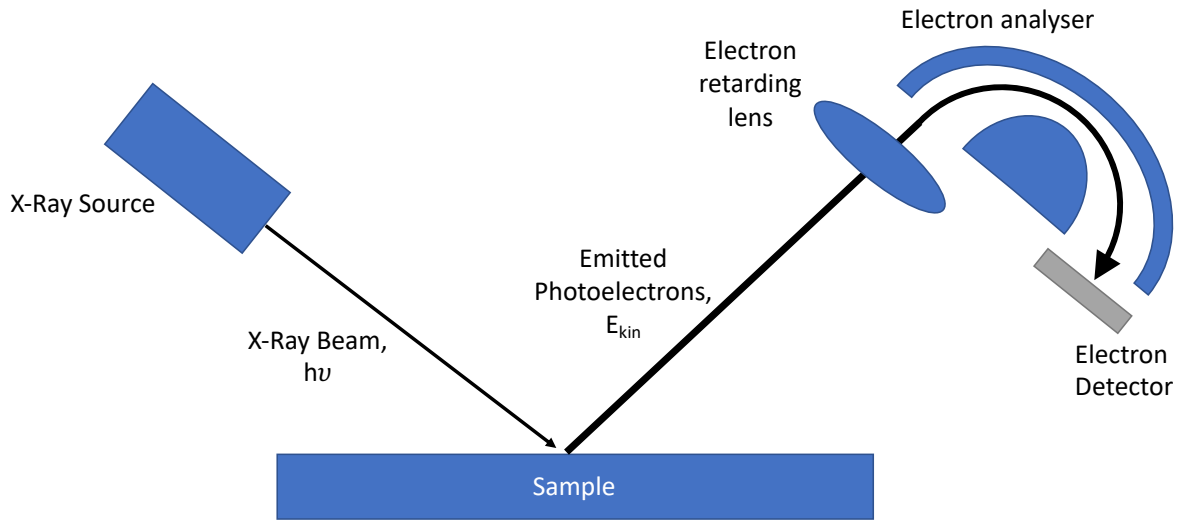

Figure 5-6. Schematic of X-Ray photoelectron spectrometer.

5.3.2. Low Energy Ion Scattering

Further understanding of the surface chemical composition can be achieved using low energy ion scattering (LEIS). This technique is used to observe the species present on the outermost atomic layer of the surface. A primary ion beam (usually either He^+, Ne^+, Kr^+) is accelerated towards the sample surface at energies of 1 to 5 keV before being scattered (Figure 5-7). This scattering effect causes the primary ion to lose kinetic energy, but importantly only occurs if lighter than the surface ions otherwise the primary ions bombard the surface.[195] Using principles based on conservation of energy, the kinetic energy of the scattered ion, E_s, can be related to the mass of the surface species, M_s, through equation 5.6 by fixing the angle of the detector, θ.

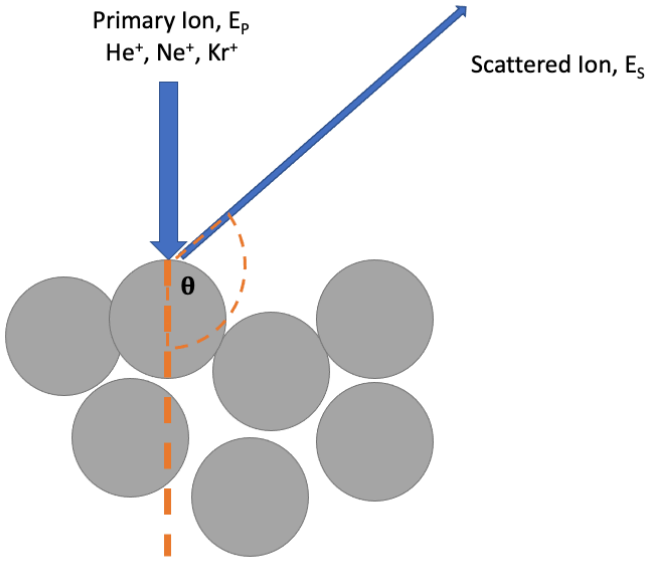

Figure 5-7. Schematic showing the scattering of primary ion used within LEIS. Adapted from [196].

$$E_S = \left(\frac{\cos(\theta) + \sqrt{\left(\frac{M_s}{M_p}\right)^2 - sin^2(\theta)}}{1 + \frac{M_s}{M_p}} \right) \cdot E_p \tag{5.6}$$

Where E_s is the energy of the scattered ion, θ is the scattering angle, M_p and M_s are the masses of the primary ion and surface species, and E_p is the energy of the primary ion.

The detection of ions has a similar process to XPS. The use of an electrostatic analyser controls the voltage to only allow ions of specific kinetic energies to pass to the detector. Ions with too large energies will not curve with the hemisphere, whereas too low energy will curve too much, with both cases ending with the ion hitting the walls.

An Ar^+ sputter gun can be employed for use in tandem with LEIS instruments to provide a depth profile into the sample. An ion dose in excess of the static limit (10^{12} ions/cm^2) is applied thus causing the disruption of the lattice and the receding of the sample surface. [197] Intermittent LEIS and sputtering can provide a quantification of the surface composition and help understand processes such as cation segregations. [15]

Herein, an IONTOF Qtac^{100} LEIS instrument was used to understand the surface compositions of water splitting materials. Powder samples, pressed flat onto sample holders, were analysed with a 6 keV Ne^+ beam on a 1000 μm^2 area. A 1 keV Ar^+ beam was used to sputter the surface over an intentionally larger 1500 μm^2 area concentric to the analysis area in order to avoid any edge effects.

5.4. Thermal Analysis techniques

Thermochemical redox reactions are driven by high temperatures therefore it is logical to use thermal analysis techniques to understand the properties as a function of temperature. The instrument used in this study, (Netzsch 449c F5), simultaneously measures two thermal analysis techniques. The first is thermogravimetric analysis (TGA) and the second is differential scanning calorimetry (DSC). TGA simply measures the change is mass as function of temperature. It can either be dynamic, i.e. constantly heating, or isothermal, i.e. observing a change in mass at a constant temperature. TGAs have a very precise balance ($\pm 1x10^{-7}$ g) and can provide information on chemical processes such as decomposition. [199] DSC is a technique used to understand reactions or processes that may occur as a function of temperature, e.g. oxidation/reduction, crystallisation etc. It is a comparison between the heat flow supplied to the sample and a separate reference material to maintain the same temperature.[199], [200] It can be a direct measurement of exo/endothermic reactions, if less or more heat is required to be supplied respectively. The combination of DSC with TGA is useful if some of the processes do not involve a change in mass e.g. melting. Typically, Al_2O_3 is used as an inorganic reference due to its chemical inertness and lack of chemical processes within the instrumental temperatures (<1500 °C). Figure 5-8 shows a typical TGA/DSC experimental setup.

There are numerous possible experimental configurations available for thermal analysis. Users have control of target temperature, heating rate, isothermal times, gas atmospheres and gas flow rates. A new correction file with an empty sample must be created for each experimental configuration. This is correction file records the effects of the heating program on the instrument and when subtracted from experimental runs it leaves information only relating to the sample.

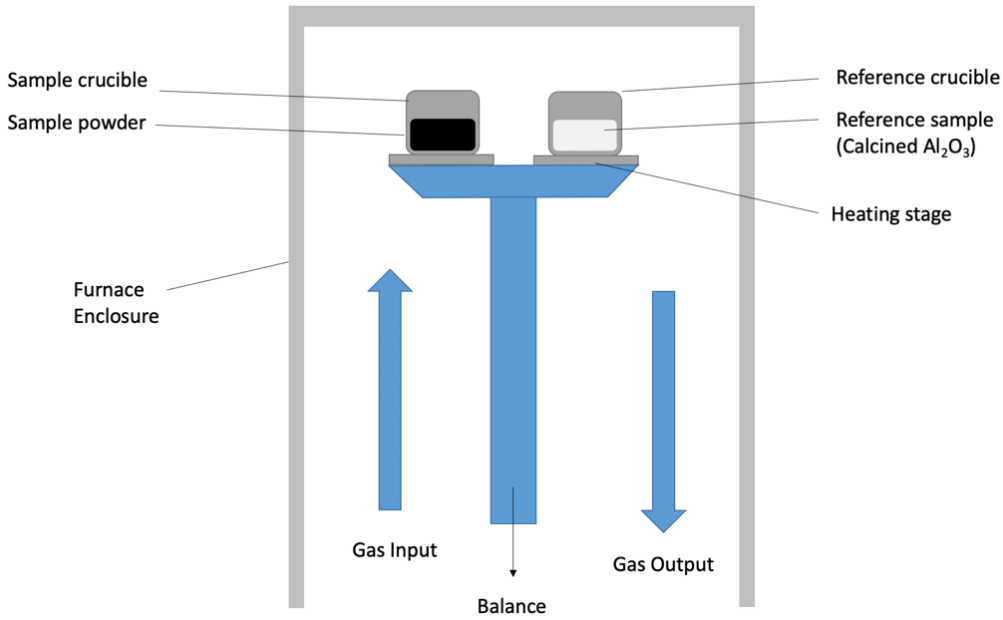

Figure 5-8. Schematic of Simultaneous Thermal Analyser (TGA/DSC).

In tandem to the thermal analysis techniques, evolved oxygen gas is measured to record changes in oxygen partial pressure levels to further understand thermally driven oxidation and reduction processes in metal oxides.[201] The sensor is based on a zirconia Nernst cell and able to measure from ppm to % concentrations. A dense membrane with platinum electrodes separates the test side from a known reference oxygen partial pressure. The difference in oxygen partial pressure generates a potential difference using the principles of the Nernst equation (Eq. 5.7). This potential difference can be measured and read by the computer.

$$E = \frac{RT}{4F} \ln\left(\frac{P_{O_2}}{P^0_{O_2}}\right) \tag{5.7}$$

where R is the universal gas constant, T is temperature, F is Faraday's constant, $p^0_{O_2}$ is oxygen partial pressure of the reference. [202]

Quantification of oxygen gas in the exhaust stream is conducted by calibrating the oxygen sensor to known flow rates of oxygen using 2% oxygen:argon gas. The oxygen flow rate is further converted to molar flow rates normalised by the mass of initial powder using equation 5.8.

$$\nu_{mol}\left[\frac{\frac{mol}{min}}{g}\right] = \nu_V\left[\frac{ml}{min}\right] \cdot \frac{1}{V_M} \cdot \frac{1}{m_s} \tag{5.8}$$

Where ν_{mol} is the molar flow rate, ν_V is the volumetric flow rate, V_M is the ideal gas volume at STP (1 mol = 22400 ml), m_s is initial powder mass.

This work uses thermal analysis in the following steps:

1. Thermal Behaviour under inert atmospheres to observe metal oxide decomposition

   A simple heat up under flowing argon (100 ml/min) to measure oxygen evolution and observe mass loss and phase transformations. For clear oxygen evolution observations, the TGA chamber was twice evacuated using a scroll pump and backfilled with argon to achieve an approximate 20 ppm oxygen environment. The mass loss was converted to changes in oxygen stoichiometry using equation 5.9.

$$\Delta\delta = \frac{\Delta m \cdot M_s}{m_0 \cdot M_O} \tag{5.9}$$

where $\Delta\delta$ is change in stoichiometry, Δm is change in mass, m_0 is the initial mass, M_s and M_O are the molecular weight of sample and oxygen respectively.

2. Isothermal Redox Cycling

   Switching gases between inert and compressed air to observe the redox kinetics at different set temperatures. DSC was used in tandem to reveal the clear endo/exothermic peaks associated with the reduction and oxidation reactions respectively.

5.5. Measuring Thermochemical Water Splitting Performance

5.5.1. Fixed Bed Reactor Design

The thermal analysis equipment is limited by which gas environment can be used within the furnace, and as such was not possible to run thermochemical water splitting experiments. Consequently, a fixed bed reactor was designed and built, with assistance from Dr. Andrea Cavallaro and Dr. Paul Boldrin (Electrochemical Science and Engineering Group – Imperial College London). Figure 5-9 shows a schematic of the reactor design of the reactor in laboratory RSM 1.14a.

Fixed bed reactors are a common reactor design reported in the literature for testing new materials for thermochemical redox reactions before they are scaled up to industrial reactors. [203]–[206] A simplistic view of a fixed bed reactor is the positioning of a reactant material bed in a stationary position with respect to the other reactants flowing through the bed. The rate of gas flow is controlled by calibrated mass flow controllers and the outputted gas stream is measured using an analyser, either electrochemical sensor, gas chromatographer, or, as in the case for this work, a mass spectrometer.

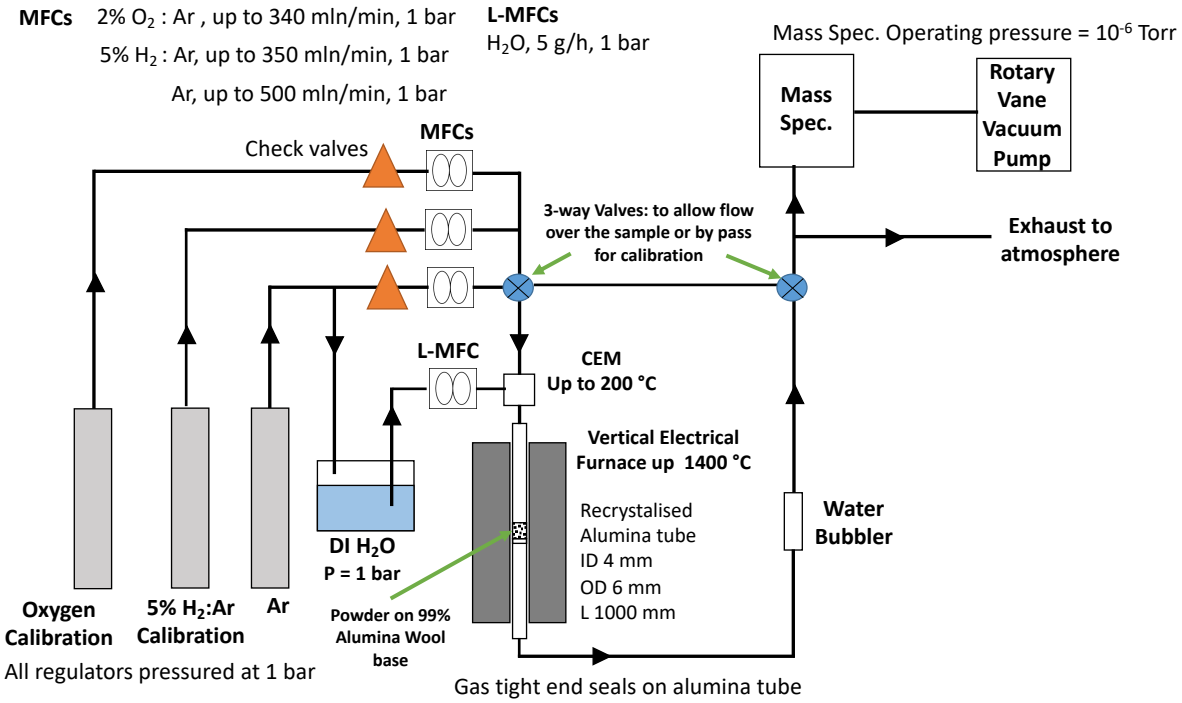

Figure 5-9. Schematic of the home-built thermochemical water splitting setup.

There are numerous chemical engineering principles to fixed bed reactor design that will not be covered in this section, however most important is to maintain a consistent flow for accurate reading of exhaust gases. This is achieved by minimising the pressure drop over the reaction bed. For better understanding readers are directed to the following paper that thoroughly discusses design principles in depth. [203], [207], [208] Minimising the pressure drop allows for optimum operation of the mass flow controllers and allows uninterrupted monitoring of the redox reactions. The pressure drop, Δp, is determined through the Ergun equation (Equation 5.9).

$$\Delta p = \frac{150 \cdot \mu \cdot L}{{D_p}^2} \cdot \frac{(1-\varepsilon)^2}{\varepsilon^3} \cdot \nu_s + \frac{1.75 \cdot L \cdot \rho}{D_p} \cdot \frac{(1-\varepsilon)}{\varepsilon^3} \cdot {\nu_s}^2 \tag{5.9}$$

where μ is gas viscosity, L is bed length, D_p is particle diameter, ε is void fraction of bed, ν_s is superficial gas flow rate (gas flow rate with no bed), and ρ is gas density.

From inspection of equation 5.9, it can be seen the parameters related to the bed morphology, L, D_p and ε have inverse relationships and direct relationships respectively. Minimal pressure drop can be achieved by minimising L and D_p and maximising ε with a porous, flat bed of large particles. However, it is an optimisation problem since fast reaction kinetics would desire small particle size for large active surface areas. Furthermore, the reactor bed needs to have enough mass/length for a detectable volumes of gas production. Unfortunately, due to the reactor being operational so late on into the experimental timeframe, the particle morphology has not been optimised fully, however from the tests conducted on powder samples in this thesis, a mass of approximately 0.1 g or bed length of approximately 3 mm, provides stable flow rates.

The fixed bed reactor in this thesis used El-Flow and Liqui-Flow mass flow controllers (Bronkhorst plc.), a STF 15/180 electrical furnace (Carbolite), and CatalySys mass spectrometer (ESS ltd.). All gases were supplied from BOC. The main carrier gas was chosen argon. Oxygen and hydrogen production calibrations were carried out using 2% oxygen:argon and 5% hydrogen:argon mixtures respectively. All gas connections were made using Swagelok fittings to ensure tightness and minimal leaks from atmospheric gases. The reactor was purged overnight prior to each experiment to ensure a low hydrogen and oxygen environments. The

liquid flow rates required to achieve desired humidity were calculated using Bronkhorst Fluidat software. Correction runs were carried out similar to thermal analysis experiments by running identical thermochemical cycles with empty reaction tubes. The results were subsequently subtracted from the experimental runs to leave only data regarding the metal oxide. The furnace was calibrated using a thermocouple on the outside of the reactor tube. Due to the thin reactor walls and the difficulty of placing the thermocouple to read inside the reactor tube, it was assumed the thermocouple reading was equal to the temperature experience by the sample within the tube. Production gases were calibrated to a linear fit of five known flow rates equal to at least double that observed by the thermal analysis.

5.5.2. Gas Analysis by Quadrupole Mass Spectroscopy

Mass spectrometry is a technique that aims to identify the presence of species by measuring the abundance of different mass to charge ratios (m/z). Quadrupole mass spectrometers are a versatile instrument for measuring evolved gases throughout an experiment. [209], [210] Molecules enter a leak valve and are electronically ionised from electrons produced by a heated filament. The ionised species enter a quadrupole mass filter with approximately equal energies and velocities. The electronic bias applied by the two opposite poles is equal to $\pm(U + Vcos(\omega t)$, where U is the DC voltage, $Vcos(\omega t)$ is AC voltage of frequency ω, t is time-period and V is RF voltage. Each pair of poles exerts a force on the ions to cause oscillations between the two poles. The force from the oppositely biased poles is superimposed causing the ion to travel in a helical path. Tuning the voltage ratios (U:V) can control the amplitude of deflection of the helical path, r, by preferentially damping the oscillation towards one of the poles. If the amplitude of deflection is less than the spacing between the poles, r_0, the ions path will continue to reach the detector. If the deflection exceeds this value, the ion bombards, and discharges on the surfaces. The set voltages will only allow a certain mass through the filter. Those ions with masses greater or less than the chosen mass is will not experience sufficient damping from both sets of the quadrupole and will not pass through the filter.

The detectors commonly used are either Faraday cups or secondary electron multipliers and measures the ion impacts as a current. Measurements can be programmed to follow specific masses or to attain a full mass spectrum by incrementally increasing the RF voltage.[209], [210] Caution is advised since the ionisation process can cause double charge or fragmentation

of molecules. This can split the expected intensities of some molecules so that 100% intensity is not at the nominal mass. The total gas production can be quantified by dividing the intensity by the fragmentation factor of the molecule from databases. Alternatively, if following a specific mass, the current of a single mass peak can be calibrated against the same mass peak of known flow rates of calibration gas. Prior to thermochemical water splitting measurements, the system was purged overnight to remove any residual gases present from the atmosphere and improve the signal to noise ratio of produced gases.

Since this instrument arrived with one month remaining of the experimental period of the PhD programme, in this thesis the results are used as proof of concept and to observe gas production. Further work will be conducted during a subsequent postdoctoral position to tune the sensitivity of the instrument and improve accuracy for total productions and kinetics experiments.

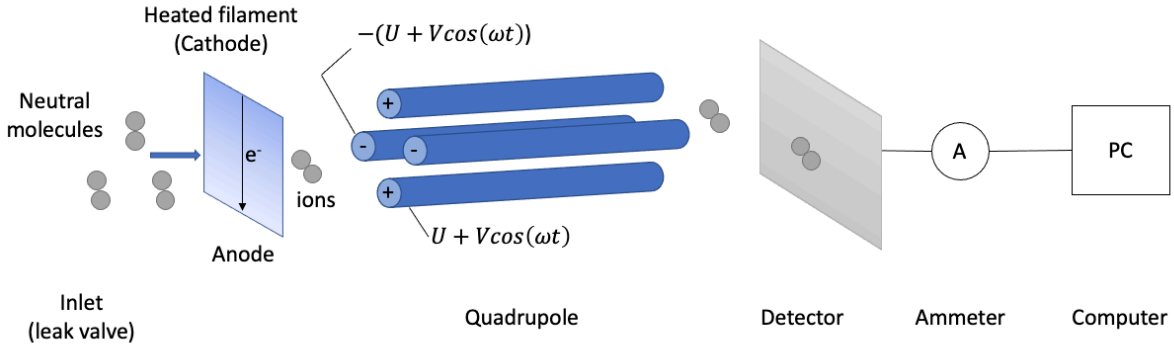

Figure 5-10. Schematic representation of a quadrupole mass spectrometer.

5.6. First Principles modelling through Density Functional Theory

The combination of experimental and computational techniques can provide further information on the fundamental properties of metal oxides thus allowing for better design of new materials. First principles modelling by density functional theory has previously been used extensively within the thermochemical water splitting field to understand the defect formation thermodynamics and explore new material compositions.[154], [167], [168], [211]–[213] Here, they are used as a tool to primarily assist in understanding trends within material classes for point defect formation energies and electronic band structures. This is then extended to

form part of a screening study for a new family of metal oxides for thermochemical water splitting. Different computed values will then be tested as descriptors for the computed reduction enthalpy of these new metal oxides. A brief description into the DFT fundamentals will be provided herein, although direction towards the book "Density Functional Theory: A practical introduction" by Scholl and Steckel can provide a more comprehensive explanation.[214]

Initially first principles modelling is based on the determining solutions to the time-independent Schrödinger equation (Equation 5.10). The understanding of this equation allows the prediction of material properties by predicting atomic positions and the consequences of moving these atoms on the energy of the structures.

$$H\psi = E\psi \tag{5.10}$$

Where ψ is the many-body wave function, H is the Hamiltonian operator and E is energy.

Applying the Born-Oppenheimer approximation to this equation – instantaneous movement of electrons with change in nuclei position due to large difference in mass – allows the equation to be simplified by considering the atoms "static" and determine the lowest energy configuration of fast-moving electrons. For a single electron moving in a potential, the Hamiltonian operator is expanded to convert the Schrödinger equation to Equation 5.11.

$$[T + V(r)]\psi(r) = E\psi(r) \tag{5.11}$$

Where the T is the kinetic energy of the electron and V is the potential.

For many electron problems like those used in this thesis, and additional term in introduced to the Hamiltonian to account for the electron-electron interaction (Equation 5.12) leading to the many-body Schrödinger equation for N electrons (Equation 5.13).

$$H = T + V + U \; = -\frac{\hbar^2}{2m}\sum_{i}^{N} {\nabla_i}^2 + \sum_{i}^{N} V(r_i) + \sum_{i<j}^{N} \frac{{q_e}^2}{|r_i - r_j|} \tag{5.12}$$

$$\left[-\frac{\hbar^2}{2m}\sum_{i}^{N}{\nabla_i}^2+\sum_{i}^{N}V(r_i)+\sum_{i<j}^{N}\frac{e^2}{|r_i-r_j|}\right]\psi_i(r)=E\psi_i(r) \tag{5.13}$$

where r_i is position of electron, $\hbar$ is reduced Planck's constant, m is the mass of an electron and e is the elementary charge of an electron.

Exact solutions to the Schrödinger equation cannot be determined explicitly for the many-electron cases used in this work, however several computational methods can estimate solutions to a good level of accuracy. One such example is density functional theory, and the following sections will discuss the general principles and how it has been used in this thesis.

5.6.1. Fundamental Principles of DFT

Density Functional Theorem (DFT) is a computational technique used to approximate solutions the Schrödinger equation to obtain information regarding the crystal structure, electronic behaviour, and thermodynamics. Theories originally proposed Hohenberg and Kohn simplified the problem of calculating the multi-dimensional, 3N, wave-function for N electrons, to one based on the electron density, $\rho(r)$. [215] Individual electrons are indistinguishable and their spatial locations are commonly provided as probabilities. Electron density is instead described by three spatial variables and contains all the information of the wave-function (equation 5.14) whilst being physically observable with experimental techniques.

$$\rho(r)=2\sum_{i}\psi_i^*(r)\cdot\psi_i(r) \tag{5.14}$$

Where $\psi_i(r)$ is the wave-function of electron i at position r and $\psi_i^*(r)$ is the complex conjugate.

The first theory proposed the ground state energy of a structure is a unique functional of electron density not dependent on external potential. The second theory delved further to state the electron density that minimises the ground state energy is the true ground state electron

density that relates to the solution of the Schrödinger equation. By minimising the functional value with respect to electron density, one can find the true electron ground state, however the nature of functional is unknown.

Kohn and Sham later expanded on the original work by comparing interacting electrons with a reference set of non-interacting electrons with the same density. [216] This is shown in the first bracket of Equation 5.15 as the sum of three terms.

$$\left[-\frac{\hbar^2}{2m}\nabla^2 + V(r) + e^2\int\frac{\rho(r')}{|r-r'|}d^3r' + V_{XC}(r)\right]\psi_i(r) = \varepsilon_i\psi_i(r) \tag{5.15}$$

The first term being the contribution from kinetic energy of non-interacting electrons. The second is known as the Hartree term – essentially the classical part of electron-electron interactions. Third and finally is the exchange correlation functional.

An iterative approach is used to minimise the ground state energy. An initial trial electron density is used to construct the new potential and Hamiltonian operator (Equation 5.15). The Hamiltonian is then diagonalised to form the new eigenvalues and eigenstates. From these values a new charge density can be calculated using equation 5.14. If this new electron density is within a specified tolerance of the initial electron density, then it can be agreed that the ground state has been found within some confidence. If not the cycle is repeated self-consistently until the ground state is found.

This exchange correlation term, $V_{XC}(r)$, remains a hot topic of research that affects the accuracy of the calculations. It encompasses the difference in kinetic energies between the reference and real systems electrons, but also non-classical electron-electron interaction parts. Most commonly it is approximated using methods such as localised density (LDA) [217] or generalised gradient approximations (GGA).[218] The localised density approximation provides the simplest solution by assuming the exchange correlation functional of the density of the test system is equal to that of a homogenous electron gas. Although this is good for simple metal systems, for more complex systems like those within this thesis, it is more common to use the GGA. This approximation models the non-uniform distribution of electrons by including a spatial dependency on the electron density. Although even when using GGA functional with metal oxides a correction is needed to be applied to the final computed energies

to account for the overbinding of oxygen within the structure. [219] This is due to the covalency within the lattice structure being overpredicted. Wang *et al.* compared the calculated values of binary metal oxides to their experimental formation energies and introduced a correction equal to the enthalpy of an oxygen molecule to overcome this systematic error. [219]

Furthermore, improvements are made when trying to calculate systems with highly localised electrons e.g. elements with d or f orbitals. The GGA begins to struggle with these electrons due to the inherent self-interaction error present within the DFT calculations. This is included within the Hartree functional and is due to the evaluated electron interacting with the local electron density whilst being part of that density itself. Anisimov [220] and later Liechtenstein, [221] and Anisimov and Dudarev, [222] developed a Hubbard potential term to be applied to improve the accuracy of systems with highly correlated electron states. This correction, known as DFT+U, is widely used in metal oxide simulations with d or f states to capture the effects of extra charge localisation with improved accuracy. A list of the U parameters within this thesis is presented in Table 5-2.

Table 5-2. List of U corrections used within this thesis.

Element	**U correction (eV)**
V	3.25
Cr	3.70
Mn	3.90
Fe	5.30
Co	3.32
Ni	6.20
Mo	4.38
W	6.20

Although still not perfect – there are issues with predicting overly localised charge – DFT+U allows the creation and understanding of material property trends within structures, for only slight increased computational expense. Additional complexity can be added to DFT calculations in an attempt to provide more accurate results. For example, the use of meta-GGA

functionals further consider the curvature of the electron density, or the use of hybrid functionals that combine exact exchange energy from the Hartree-Fock non-local exchange energy with localised density of either LDA or GGA.[223] Hybrid functionals aim to cancel the detriments of both Hartree-Fock exchange (overly localised ionic states) and DFT (overly localised metallic states) to provide a blend of the two that accurately predicts electron density of metals and oxygens. However, this is at the cost of significantly increased computational expense. [214]

5.6.2. Basis Functions and Pseudopotentials

In this work, density functional theory is used in the modelling of periodic solids. With the use of Bloch's theorem and the periodic nature of potential energy within solids, it allows the wavefunction to be evaluated in the boundaries of the reciprocal space unit cell vector – the first Brillouin zone. Solutions of the wave function can be found through the sum of plane wave terms, exp (ikr), multiplied by a function with the same periodicity as the lattice, $u_n(r)$ (equation 5.14). [224] This wave-function can be squared to give electron density (in the case of eq. 5.12).

$$\psi_{n,k}(r) = \exp(ikr) \cdot u_n(r) \tag{5.14}$$

Commonly in DFT, solutions using reciprocal space vectors, k, are more convenient to solve. However, k is a continuous variable with limitless solutions. This is overcome by choosing a discrete number of k-points to evaluate the plane wave solutions. This is 3D reciprocal space this is usually considered a "mesh" with the dimensions n×n×n. The number of k-points used to accurately integrate the wave-function is subject to energy-convergence testing, since the computational time scales with the number of k-points but above a certain value no greater accuracy is achieved.

The periodic nature of solids means the periodicity term can be expanded to consider a special set of plane wave vectors, G, (Equation 5.15). This is incorporated in equation 5.14 to give the solution for the wave function (Equation 5.16).

$$u_k(r) = \sum_G c_G \cdot \exp\,(iGr) \tag{5.15}$$

$$\psi_{n,k}(r) = \sum_G c_G \cdot \exp(iGr)\exp(ikr) = \sum_G c_{G+k} \cdot \exp(i(G+k)r) \tag{5.16}$$

$$E_{cut} = \frac{\hbar^2 {G_{max}}^2}{2m_e} \tag{5.17}$$

For each value of k there are infinite solutions to G, however this accommodated by truncating the series up to a maximum value, G_{max}. This value relates to an energy cut off, E_{cut}, value (Equation 5.17) under which the energies are physically important. However, the value of the cut off energy is also subject to convergence testing to assure that the system is being accurately modelled. The main issue with this plane wave basis set approach is the modelling of tightly bound and rapidly oscillating core electrons would require large energy cut off values and extended plane wave descriptions, both of which increase the computational expense. However, the core electrons contribute very little to the properties of interest within this thesis, such as chemical bonding. Therefore, the solution to replace the electron density from core electrons with a smoother homogenous density that is frozen in space. This replacement is known as a pseudopotential. [225] The number of electrons included within the "core" determines the hardness of the pseudopotential. Cores with larger number of frozen valence electrons are considered soft and reduce computational cost by lowering the cut-off energy. Conversely, harder pseudopotentials consider a larger number of valence electrons, but require higher cut-off energies for more accurate results. An alternative approach used in this thesis is the Project Augmented wave method, that applies a linear transformation to the pseudeopotential smoothed wave function to provide information on the all-electron wavefunction within the frozen core.[226] Commercial DFT codes have developed different pseudopotentials and, in this thesis, those used are identical to the of structures reported in the materialsproject in order for direct comparison with that database. [227] A list of the pseudopotentials used in this work is given in appendix A.

5.6.3. Electronic Band Structures

The following few sections will describe in more depth how DFT was used for the work in this thesis. Firstly, the use of DFT in the understanding the electronic properties and charges present

within the structures. Electron states that satisfy the plane wave expression in Equation 5.16 are represented by a point in *Figure 5-11*. These states can be described by a vector, k. The density of states (DOS) is the number of states per unit volume per energy and can yield information regarding the electronic behaviour of materials. The number of states in a spherical shell volume in k-space is given by Equation 5.18.

$$Number\ of\ states = \frac{1}{2\pi^2} \cdot 4\pi k^2 \cdot dk \tag{5.18}$$

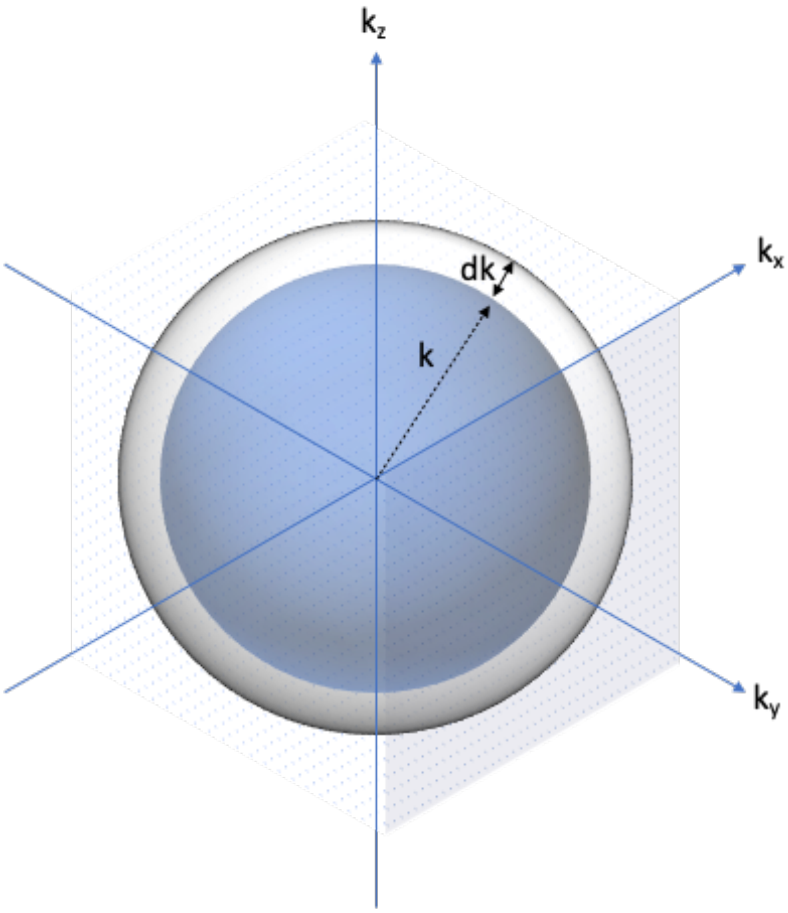

Figure 5-11. Schematic demonstrating the allowed values of k as points. The number of states located within the shell defined by radius, k, and thickness, dk, can be represented as a function of energy using the electron dispersion relationship.

Using the electron dispersion relationship given by Equation 5.19, the density of states, g(E), can be transformed per unit volume in the energy range E to E+dE, given by Equation 5.20. [214]

$$E = \frac{(\hbar k)^2}{2m} \tag{5.19}$$

$$g(E) = \frac{1}{2\pi^2}\left(\frac{2m}{\hbar^2}\right)^{\frac{3}{2}} E^{\frac{1}{2}} \tag{5.20}$$

The quality of density of states information is dependent on the k-point mesh density, since a higher density can provide a better description of the plane wave landscape. Usually, for a smooth DOS plot the number of k-points is at least doubled to provide a more accurate understanding. These plots of DOS against energy are used to provide insight into the band structure and electronic properties such as band gap (region where g(E) = 0) and conductive behaviour. Furthermore, the DOS plots can be partitioned into elemental contributions and more specifically the type of orbital to provide further insight into bonding behaviour. In particular researchers have related the energy separation between the oxygen p-band and Fermi energy to provide insight into vacancy formation energy [228], surface bonding [229], and oxygen migration [230], [231] behaviour in metal oxide structures.

Furthermore, DFT can provide insights into the localised charge on each atom within the structure. This work uses the Bader approach to understand the charge density. [232], [233] The Bader approach partitions the total charge density of a molecule into individual atomic contributions based on the charge density reaching a minimum between two atoms (Figure 5-12). The surface at which this minimum is achieved provides the outermost edge of the atom, and the charge within provides an approximation of the total electronic charge of the atom. Henkelman developed an efficient way of partitioning the outputted charge density from DFT into Bader volumes based on a grid method. [234], [235] This method inspects the gradient of the charge density and places grid points as it walks uphill against the steepest path until it reaches a maxima or previously found grid point. This algorithm is crucially linearly scalable with atoms and has been shown to correlate well with metal oxides compounds.

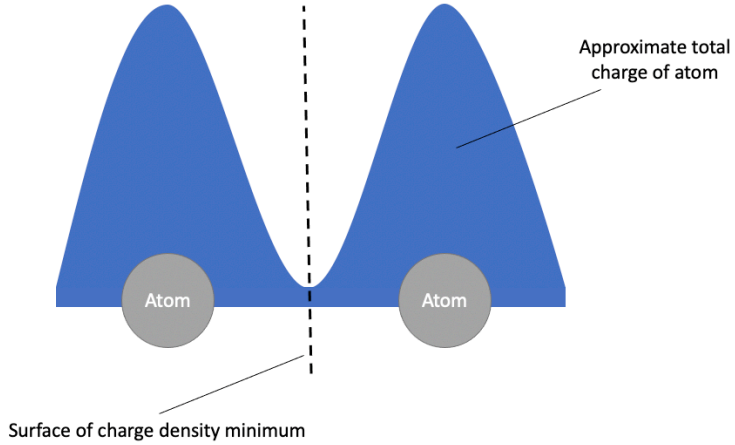

Figure 5-12. Schematic demonstrating the Bader charge analysis principle.

Understanding the charge density situated on an atom within the lattice can help understand the lattice enthalpy of a material. The lattice enthalpy is the energy required to break a lattice into its gaseous constituent elements. Born and Landé and later proposed lattice enthalpy has a coulombic relationship proportional to the charge attraction and distance between two oppositely charged ions (Equation 5.21). The computation of charges through the Bader method can be a useful descriptor in the search of new thermochemical redox materials. Furthermore, this property can be experimentally verified through X-ray charge density analysis.[236]

$$\Delta H_{lat} \propto \frac{q_1 q_2}{r} \tag{5.21}$$

5.6.4. Convex Hull Analysis

As part of the computational screening study covered in chapter 8, the thermodynamic stability of compound was determined using convex hull analysis. The energy of known compounds are plotted as a function of elemental concentration. Linear interpolation between these point forms a hull defining the thermodynamic stability (Figure 5-13). If the energy of a compound sits above this hull (compound 1 in Figure 5-13), it is considered unstable and the distance from the convex hull is known as the energy above hull, E_{hull}. If the compound energy is lower

than the current hull (compound 1 in Figure 5-13), a new hull forms that including the new low-energy compound.

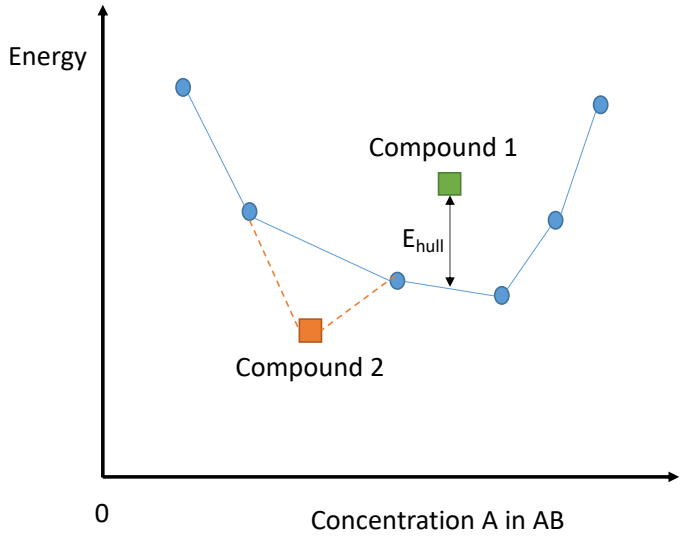

Figure 5-13. Schematic representation of a convex hull to determine thermodynamic stability of a binary compound.

Previously authors have used this as a guide for "synthesisability" of new compounds. [167], [237] Convex hulls can be constructed using compounds present in large DFT databases such as A-Flow [238], OQMD [239], or in the case for this thesis the materialsproject [240]. number of components in the compound changes the dimensionality of the hull to become a surface for 3D.

5.6.5. Defect Formation Energy

The main way DFT has been used in the thermochemical water splitting field is the understanding of defect formation energies. This property has been used in identifying new materials through screening studies and understanding thermodynamic behaviour. [241], [242] The simulation of defected structures is common in other solid-state fields such as photovoltaics and fuel cells. The primary method is to generate a supercell of the interested structure and introduce point defect with sufficient dilution to not feel effects arising from the periodic nature of the lattice.[243] For the work covered in this thesis, the lattice structures have been increased to try to balance the dilute nature defect calculations without significantly

increasing the computational expense. This was achieved by aiming for a unit cell with close to equidistant lattice parameters greater than 10 Å.

Metal oxide reduction enthalpy per O atom was calculated using equation 5.22. The oxidised and reduced metal oxide phases are differing by a single oxygen atom and have undergone full simulation workflows (described in the next section). The oxygen molecule energy was calculated by simulating an O_2 molecule in a 12x12x12 Å rhombohedral box. It is important to note the oxygen defect in these calculations was calculated to be uncharged for consistency with previous screening studies. Further understanding on the defect nature can be achieved by introducing charge onto the defect although at higher computational expense. For further information on modelling charged defects, readers are directed to the following references [244]–[246].

$$\Delta H = \left(\mathrm{E}(MO_{reduced}) + \frac{1}{2}E(O_2)\right) - (MO_{oxidised}) \tag{5.22}$$

5.6.6. DFT+U modelling workflow

This section will describe the workflow used for the first principal calculations within this thesis (Figure 5-14). Initial spin-polarized density functional theory calculations were performed using the Vienna Ab Initio Simulation Package (VASP) version 5.4.4 [247] using the Perdew–Burke–Ernzerhof (PBE) exchange–correlation functional.[218] Undoped metal oxide structures obtained from the Materials Project online database. [227] Projector-augmented wave (PAW) pseudopotentials [248] were used for all species and +U corrections applied to be consistent with simulations included within the materials project. A typical plane wave cut off of 520 eV – in agreement with convergence testing on the undoped structures. The lattice parameters and atoms within the structure was geometrically relaxed until it found a local energy minimum. Subsequent single-point calculations to determine electronic structure were carried out with a denser gamma-centered k-point mesh and a Blöchl-tetrahedron smearing algorithm. An anion correction 0.70 eV per O atom was applied to correct for the overbinding of the O_2 molecule, as previously discussed by Wang et al. [219] and implemented within the pymatgen analysis code.[249]

Post-analysis scripts written by the Henkelman group were used to compare the Bader charge on each ion within the structures and the oxygen band centre. Pymatgen-based scripts were used to analyse the lattice parameters and compare the final energies to the compounds in the materials project with the same elements.

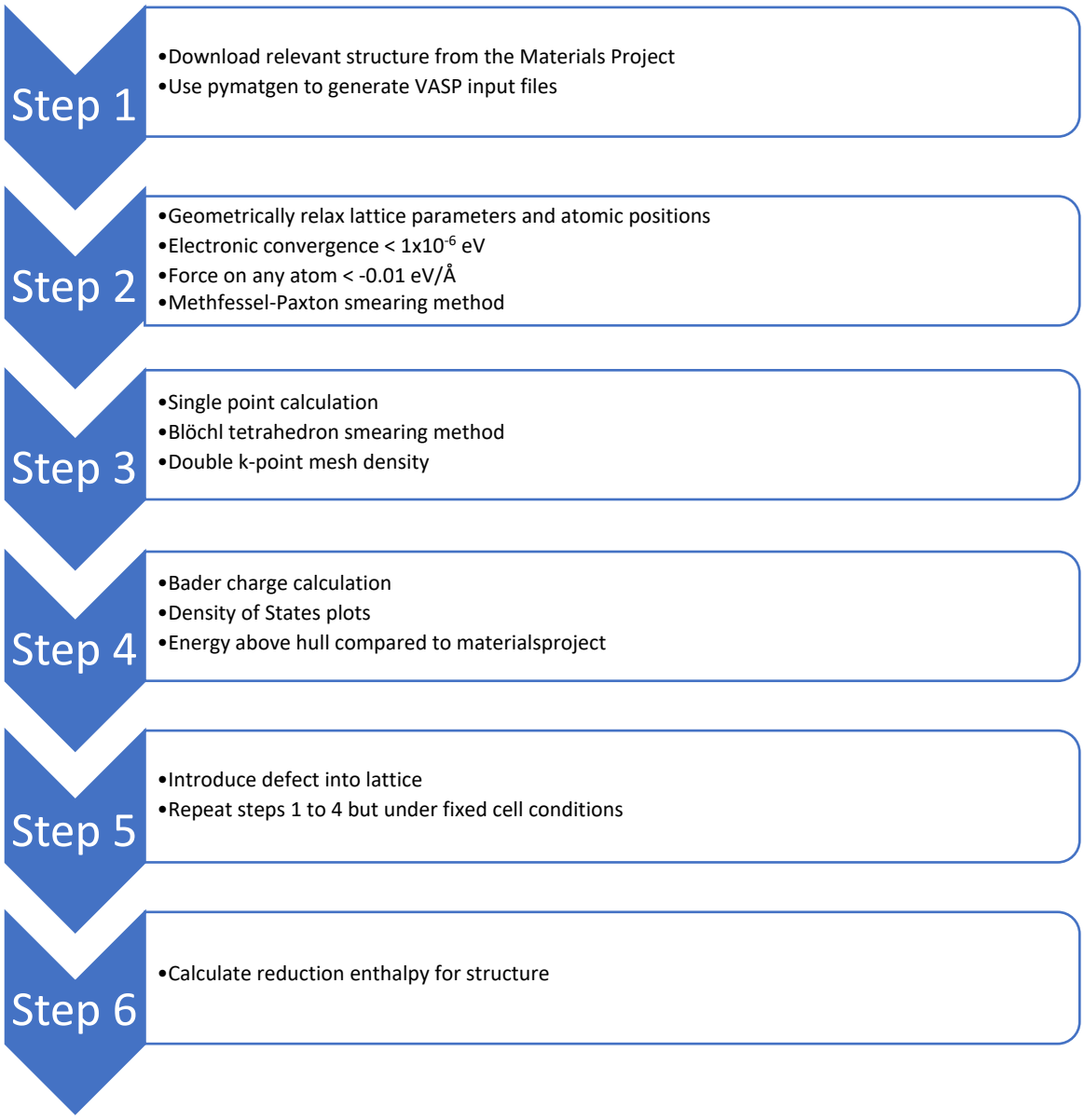

Figure 5-14. Typical DFT calculation workflow used for the simulations in this thesis.

6. Investigating the effect of antimony concentration on the fast redox kinetics of $SrCo_{1-x}Sb_xO_{3-\delta}$ for thermochemical energy storage, oxygen separation and water splitting

In this chapter, the feasibility of antimony doped strontium cobalt oxides for thermochemical redox applications in the temperature range 500 to 800 °C is investigated. The material stability when heating under inert atmospheres will be explored through thermogravimetric analysis and X-ray diffraction. Density functional theory calculations are also used to gain further understanding of the experimental observations. Results and discussions included within this chapter form part of a paper recently accepted in the Journal of the Electrochemical Society.

"**Wilson, G. E.,** Seymour, I. D., Cavallaro, A., Skinner, S. J., Aguadero, A.. Fast redox kinetics in $SrCo_{1-x}Sb_xO_{3-\delta}$ perovskites for thermochemical energy storage and oxygen separation, *J. Elec. Soc.* (Accepted)"

6.1. Introduction to $SrCo_{1-x}Sb_xO_{3-\delta}$

Strontium cobalt oxides have long been of interest in the solid oxide fuel cell community due to their fast mixed ionic and electronic conduction at intermediate temperatures, and topotactically exchange oxygen without changing crystal structure. [250]–[260] The strontium cobalt perovskite structure, $SrCoO_{3-\delta}$, can accommodate a large range of oxygen non-stoichiometry ($0< \delta<0.71$) at high temperatures. [261] Although upon slowly cooling under ambient conditions the standard cubic $Pm\bar{3}m$ structure separates into the $BaNiO_3$ 2H-type rhombohedral $Sr_6Co_5O_{15}$ phase and a minority Co_3O_4 spinel (Appendix B - Figure B-1). [262] The rhombohedral structure is a one-dimensional series of four face sharing CoO_6 octahedra disrupted by a Co oxide triangular prism (Figure 6-1a). [262] This phase separation is undesirable since it has been shown the total conductivity to be approximately 5x lower compared to the cubic polymorph. [263] This is due to the cubic polymorph with the corner sharing octahedra having 180 ° Co-O-Co bond angles allowing for better orbital overlap and thus charge transfer between the Co-d and O-p orbitals. [263]

Substituting cobalt with larger radii donor dopants with a fixed valency has been heavily reported to stabilise the 3C perovskite phase [147] at room temperature by promoting the high electrostatic repulsion of B-site cations. [264]–[269] This induces a corner sharing polyhedral network rather than face-sharing disposition. Furthermore, the inclusion of these dopants lowers the structure's Goldschmidt tolerance factor and reduce the oxidation state of the cobalt to a more favourable 3+. This contributes to the stabilisation of the 3C perovskite phase at room temperature, but ultimately forms the tetragonal *P*4*mmm* polymorph due to vacancy ordering within equatorial and axial oxygens.[265] The commonly reported transition metals (Table 6-1) have an ionic radii not too dissimilar from cobalt thereby demonstrating a solubility within cobalt of up to 20%, with 0 to 10% stabilising the tetragonal phase, and 10 to 20% stabilising the 3C cubic phase. The inclusion of greater concentrations is not necessarily beneficial since nearly every dopant shows lower total conductivity due to the fixed valency cations disrupting the Co-O-Co electron conduction paths. [253], [254], [256], [270], [271] Furthermore, the increased concentration lowers the number of oxygen vacancies within the structure to accommodate the increase in cation charge.

Table 6-1. Commonly investigated non-redox-active B-site dopants for strontium cobalt oxide compounds.

Transition Metal Ion	**Ionic radii** [272]	**Ref.**
Co^{4+}	0.530	
Sc^{3+}	0.745	[273], [274]
Sn^{4+}	0.690	[275]
Ti^{4+}	0.605	[276]
Nb^{5+}	0.640	[277], [278]
Ta^{5+}	0.640	[258], [279]
Sb^{5+}	0.600	[271], [280]–[282]
Mo^{6+}	0.590	[253], [283]

Ezbiri et al. used density functional theory identified cubic $SrCoO_3$ at the top of a Sabatier plot for thermochemical oxygen separation. The structure was proposed to have optimal energetics for both vacancy formation and oxygen incorporation.[284] The redox behaviour was demonstrated experimentally through thermogravimetric analysis; however the work was not expanded to understand the fundamentals of the kinetics. Therefore, in this chapter the effect

of B-site doping on the redox kinetics is studied for the well-reported $SrCo_{1-x}Sb_xO_{3-\delta}$ compound. Herein, the Sb concentration is increased incrementally from 5 to 20% and understood using a combination of experimental and computational methods. Thermogravimetric analysis and *in situ* high temperature XRD are used to observe the redox cyclability and first principles modelling to understand the effect of the dopant on the local electronic structure and vacancy formation energy. The $SrCoO_3$ compound without Sb was not investigated experimentally due to its difference in crystal structure forming an unfair comparison between the compounds.

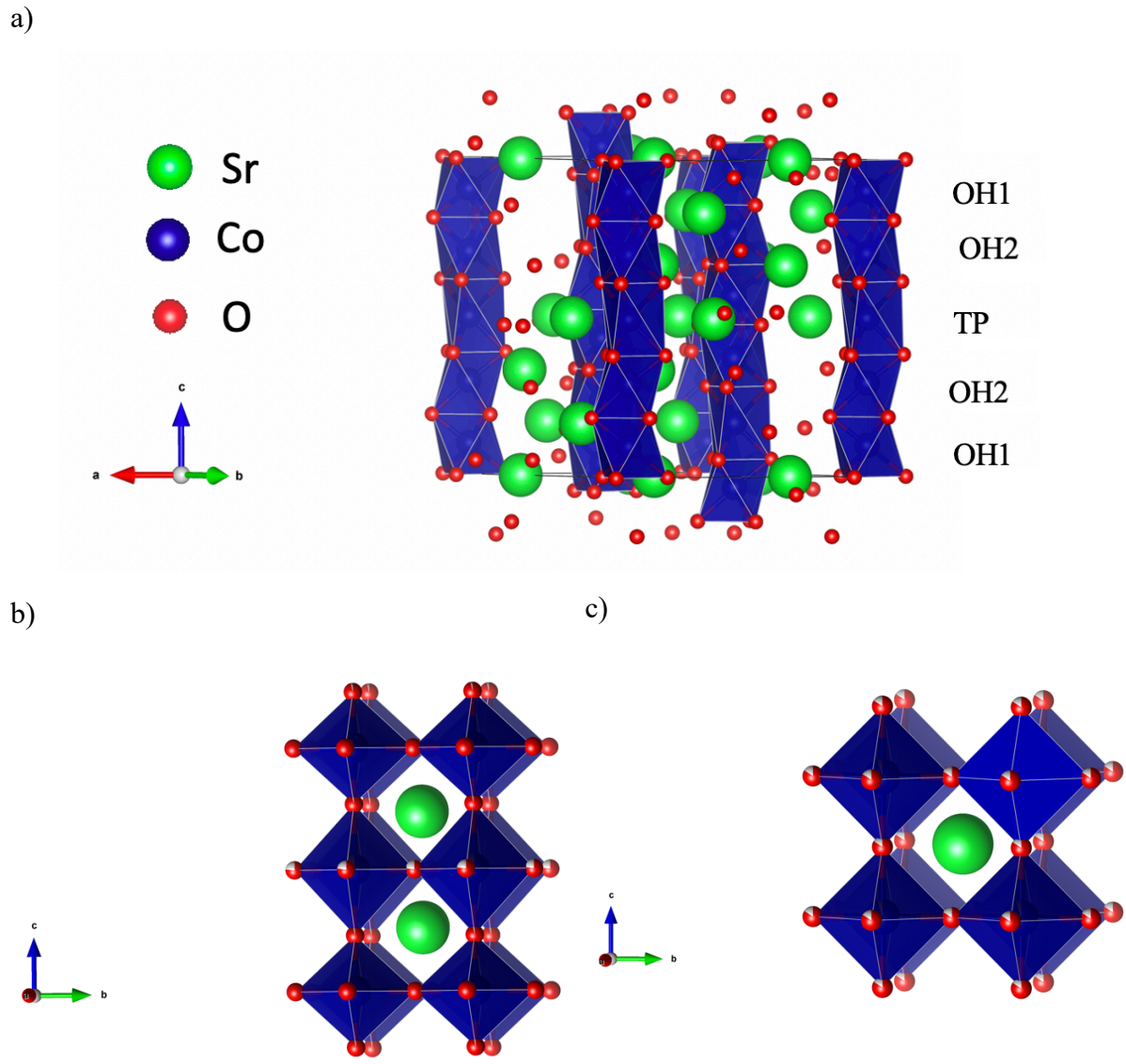

Figure 6-1. Strontium cobalt oxide polymorphs. a) 2H face-sharing octahedra polymorph, b) P4mmm tetragonal structure, c) 3C cubic polymorph.

6.2. Results and Discussion

$SrCo_{1-x}Sb_xO_{3-\delta}$ (x = 0.05, 0.10 and 0.20) powders were synthesised using a nitrate-citrate method, as described in section 4.2 and previously reported.[265], [285], [286] Stoichiometric ratios of precursor powders $Sr(NO_3)_2$ (>99%, Sigma Aldrich), $Co(NO_3)_2 \cdot 6H_2O$ (98-102%, Alfa Aesar) and Sb_2O_3 (99%, Alfa Aesar) were weighed and added to a stirring solution of 0.1 M citric acid (aq. 1% (v/v) 68% nitric acid). The solution was heated to a nominal temperature of 60 °C resulting in complete dissolution, followed by heating to 300 °C to promote the sol-gel reaction. The crude gel was decomposed at 600 °C for 12 hours before further calcination steps at 900, 1000 and 1100 °C for 12, 24 and 24 hours, respectively, with intermediary grinding stages using a pestle and mortar.

a) b)

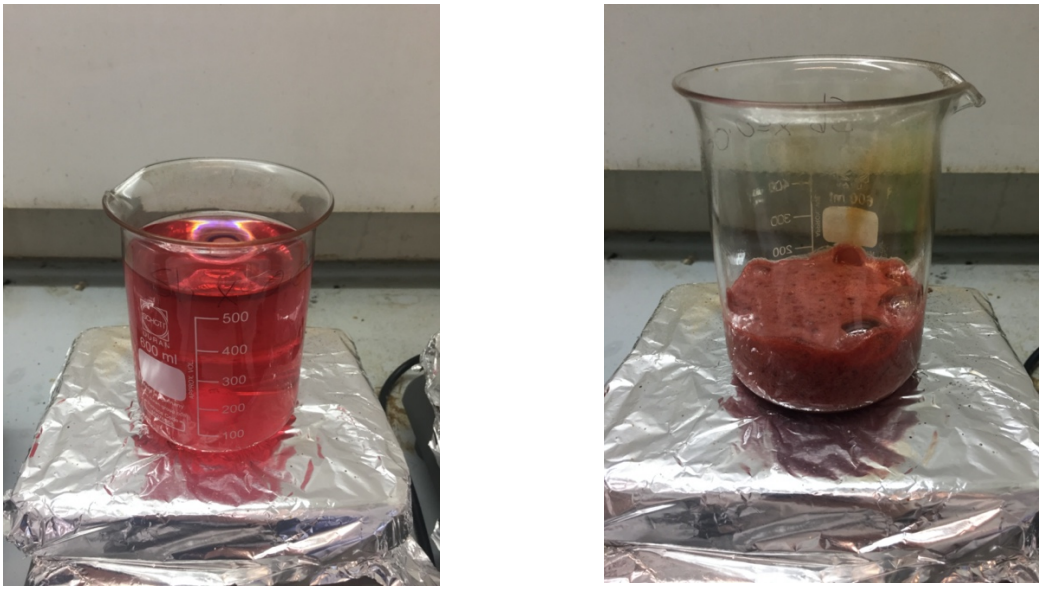

Figure 6-2. a) Stirring solution of Sr, Co and Sb nitrate salts in citric acid, b) Subsequent gel formed upon polymerisation.

6.2.1. Initial powder characterisation

The crystal structure of the synthesised powders was characterised using X-Ray powder diffraction. A Panalytical MPD was used with Cu-Kα radiation (λ = 1.542 Å) in a Bragg-Brentano setup. All measurements used the following parameters; 20° < 2θ < 80° and 0.04° step size with 100 seconds per step. Figure 6-3 shows the XRD patterns for the synthesised

materials used in this chapter. In agreement with previous literature reports, the inclusion of Sb stabilises the $P4mmm$ structure at low concentrations and the $Pm\bar{3}m$ structure at higher concentrations above 10%. [265] Refined lattice parameters are displayed in Table 6-2. Refined lattice parameters for the SrCo1-xSbxO3-δ.The lattice parameters are observed to increase with additional Sb incorporation in agreement with previous structural investigations. [282]

a)

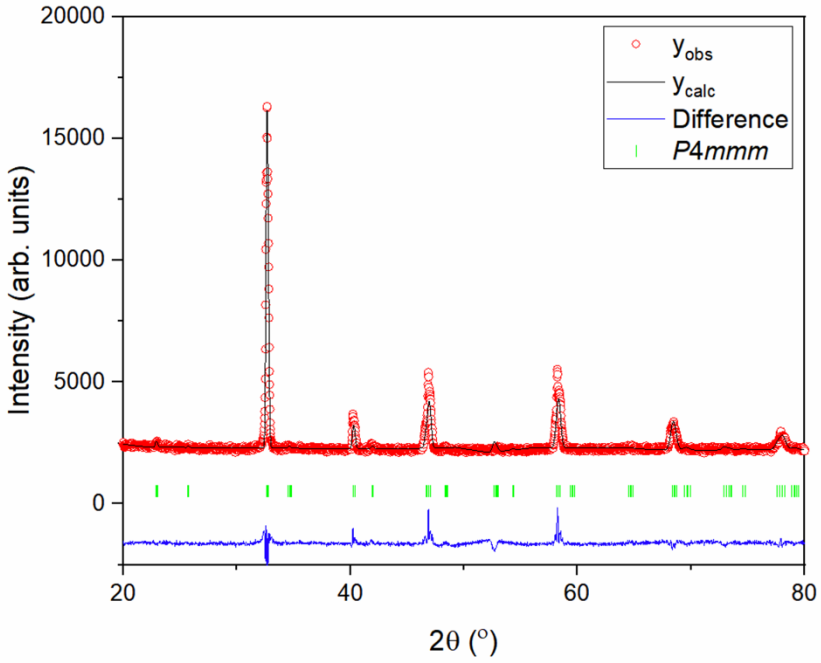
20000
15000
10000
5000
0
Intensity (arb. units)
20
40
60
80
2θ (°)
y_{obs}
y_{calc}
Difference
P4mmm

b)

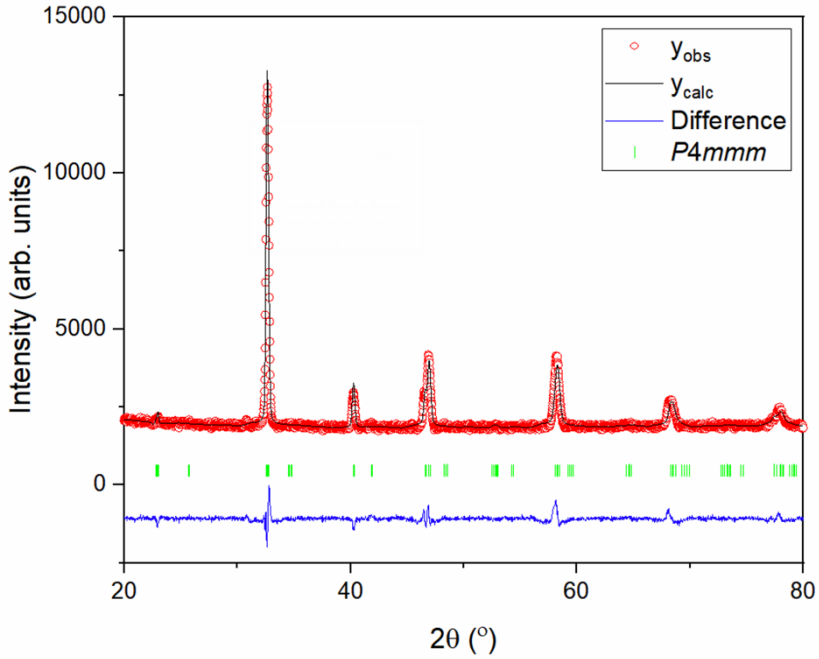
15000
10000
5000
0
Intensity (arb. units)
20
40
60
80
2θ (°)
y_{obs}
y_{calc}
Difference
P4mmm

c)

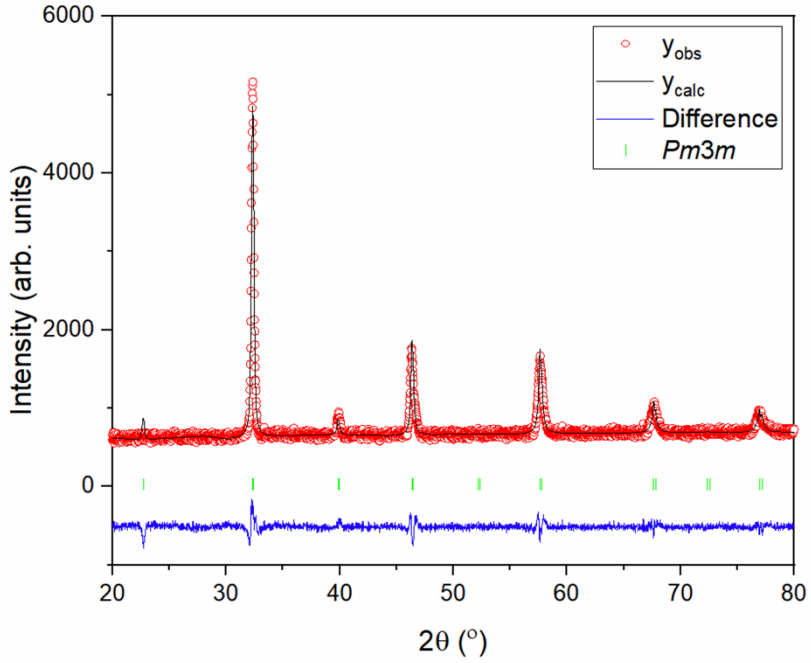

Figure 6-3. XRD diffractograms of the different Sb-doped SrCoO3 compounds, a) $SrCo_{0.95}Sb_{0.05}O_{3-\delta}$, b) $SrCo_{0.90}Sb_{0.10}O_{3-\delta}$ and c) $SrCo_{0.80}Sb_{0.20}O_{3-\delta}$.

Table 6-2. Refined lattice parameters for the $SrCo_{1-x}Sb_xO_{3-\delta}$.

	$SrCo_{0.95}Sb_{0.05}O_{3-\delta}$	**$SrCo_{0.90}Sb_{0.10}O_{3-\delta}$**	**$SrCo_{0.80}Sb_{0.20}O_{3-\delta}$**
***a* (Å)**	3.869(3)	3.8702(9)	3.9150(7)
***c* (Å)**	7.781(8)	7.796(3)	-
Cell Volume (Å^3)	116.79(2)	116.777(6)	60.01(2)
χ^2	2.53	1.86	1.62

A JEOL 6010LA scanning electron microscope (SEM) was used to assess the particle morphology. Figure 6-4a shows the powders have a wide range of sizes. Clusters of particles are seen to form of sizes greater than 50 µm, whereas Figure 6-4b shows the particles can be less than 5µm with smooth surfaces.

a)

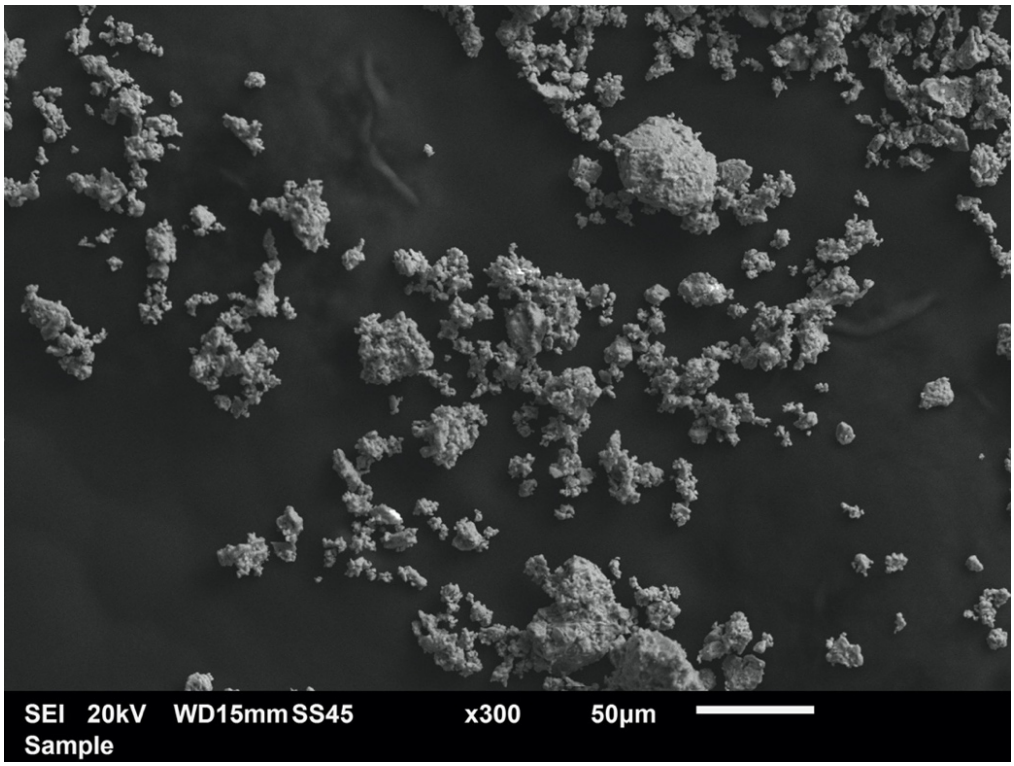

b)

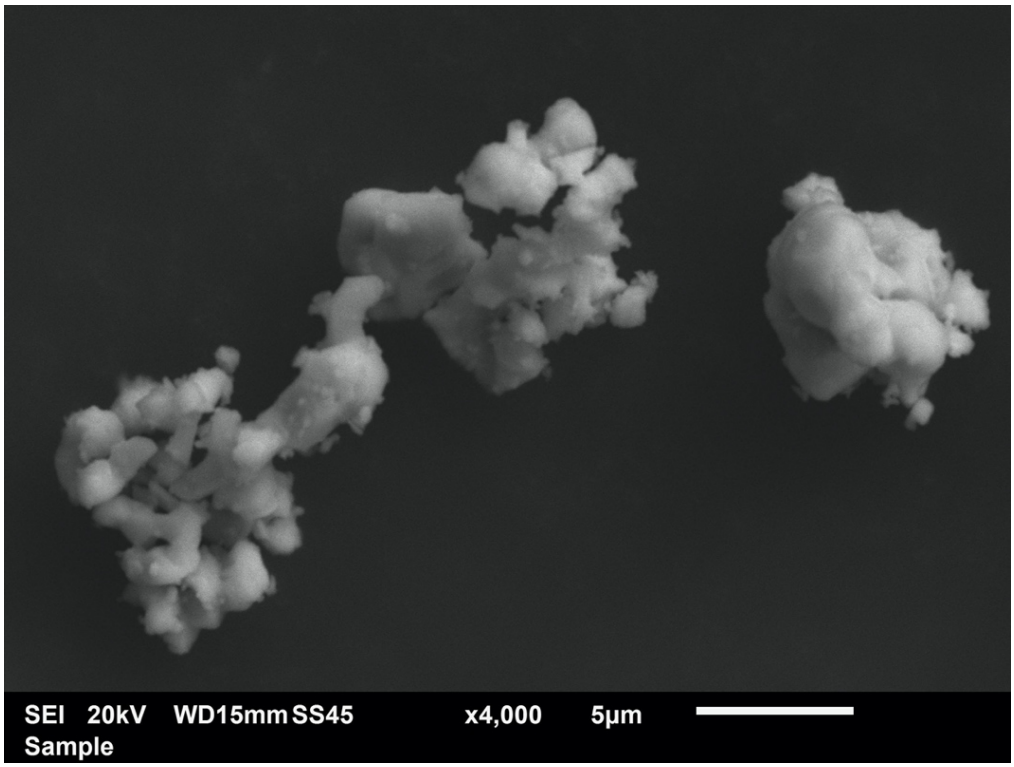

Figure 6-4. Scanning electron micrographs of synthesis $SrCo_{0.95}Sb_{0.05}O_3$ powder showing a) the size distribution and b) increased magnification of the particle.

6.2.2. Thermal Behaviour under low P_{O_2}

The thermal behaviour of the Sb-substituted has been well characterised under ambient oxygen partial pressures due to its interest as a solid oxide fuel cell cathode. [265], [285]–[287] However, the understanding and behaviour under low P_{O_2} (approximately 10^{-5} atm) is still lacking and crucial for use as thermochemical redox materials.

Here, the thermal behaviour and redox cyclability of the powders were investigated using a simultaneous thermal analyser (STA) (Netzsch 449c F5) under a dry argon atmosphere. As mentioned in section 5.4, this instrument combines thermogravimetric analysis (TGA) in tandem with differential scanning calorimetry (DSC) and allows the investigation of mass loss as well as possible phase transition behaviour or redox processes. Furthermore, the coupling of the STA with an oxygen analyser allows direct measurement of the reaction atmosphere and oxygen evolution.

Figure 6-5a to Figure 6-5c show the results from the thermal analysis. Initial non-stoichiometry values were obtained from previously published X-Ray Absorption Near Edge Spectroscopy experiments.[241] The authors compared the Co band edge to a calibration curve formed by a set of standard compounds with known Co oxidation states. The changes in non-stoichiometry were calculated using equation 6.1.

$$\Delta\delta = \frac{\Delta m \cdot M_s}{m_0 \cdot M_O} \tag{6.1}$$

The TGA (Figure 6-5a) shows the mass loss starts between 300 and 400 °C, coinciding with the increase in oxygen signal and a broad endothermic large endothermic energy uptake. All samples show a large initial peak just above 400 °C that coincides with the steepest mass loss gradient in (Figure 6-5a). This mass loss can be attributed to lattice reduction. This reduction reaction starts at slightly lower temperatures than those previously observed under compressed air due to the lower oxygen partial pressure.[265] Above 600 °C the mass loss slows before further reduction. Previously, these features were thought to be related to the phase transitions between the tetragonal to cubic perovskite polymorphs when heating under air (P_{O_2} = 0.21 atm).[265] As the vacancy concentration increases and reduction of the B-site cation causes an

increase in ionic radii. As a consequence, the Goldschmidt tolerance factor decreases and favours a crystal structure transformation to cubic symmetry.

Figure 6-5d compares the total oxygen production and production rate (initial peak) for each of the compounds up to 800 °C. $SrCo_{0.95}Sb_{0.05}O_{3-\delta}$ and $SrCo_{0.90}Sb_{0.10}O_{3-\delta}$ had similar oxygen production rates compared to those reported by Ezbiri *et al.* for $SrCoO_{3-\delta}$. [284] The inclusion of the antimony donor dopant increasing the average cobalt valency closer to 4+ and reduces the number of inherent oxygen vacancies present from synthesis to accommodate this change in charge. [265], [288] This can possibly allow for larger oxygen evolution volumes by the potential to introduce more vacancies within the structure before phase decomposition. However, as seen in Figure 6-5d the oxygen evolution is observed to decrease.

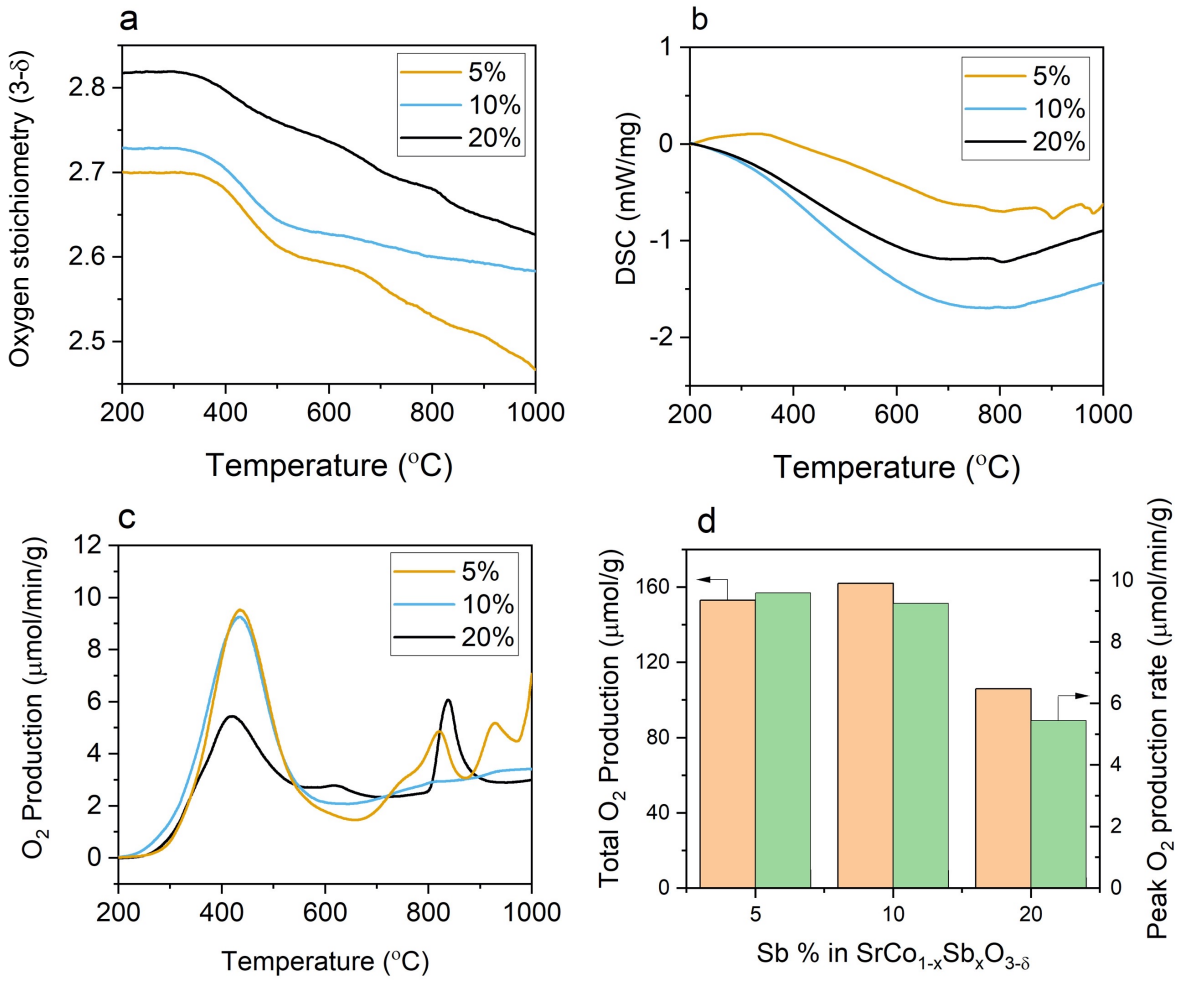

Figure 6-5. Thermal analysis of $SrCo_{1-x}Sb_xO_{3-\delta}$ showing a) thermogravimetric signal converted to oxygen stoichiometry, b) DSC signal, c) O_2 production detected in the exhaust stream. d) peak rate and total volume of O_2 production as a function of Sb concentration.

The room temperature diffractograms agree with the previous structures in Figure 6-3, except trace presences of the antimony and cobalt oxides in the $SrCo_{0.95}Sb_{0.05}O_{3-\delta}$ sample due to this being a new batch of synthesised powder. The diffraction peaks shift to lower angles as temperature increases, suggesting an expansion in the crystal lattice. For the $SrCo_{0.95}Sb_{0.05}O_{3-\delta}$ sample in Figure 6-6a, the (101) reflection splits above 400 °C coinciding with the rapid oxygen loss in Figure 6-4a. The splitting of the peak could be related to the formation of the brownmillerite phase as the oxygen stoichiometry approaches the $ABO_{2.5}$ formula, as observed by other authors when heating $SrFeO_3$ perovskites under argon. [289] Transformations to the (101) reflection were also observed with the $SrCo_{0.90}Sb_{0.10}O_{3-\delta}$ compound in Figure 6-6b. However, another explanation could be the reduction and phase separation of Sb_2O_3 identified by peak matching the increased reflections at 27.5 and 33 ° denoted by the heart (♥) symbol. Additionally, this could coincide with the further endothermic DSC peaks and the increase in oxygen evolution in Figure 6-4b and Figure *6-4*c respectively. $SrCo_{0.80}Sb_{0.20}O_{3-\delta}$ does not observe the antimony oxide reflections in the XRD (Figure 6-6c), however the increase the oxygen evolution occurs above 800 °C beyond the measured range of the HT-XRD. The isothermal redox cycling experiments discussed later in this report, had a maximum temperature of 800 °C and therefore absent from this kinetic study. Density functional theory is used in the next chapter to help understand the defect formation energy of these compounds.

a)

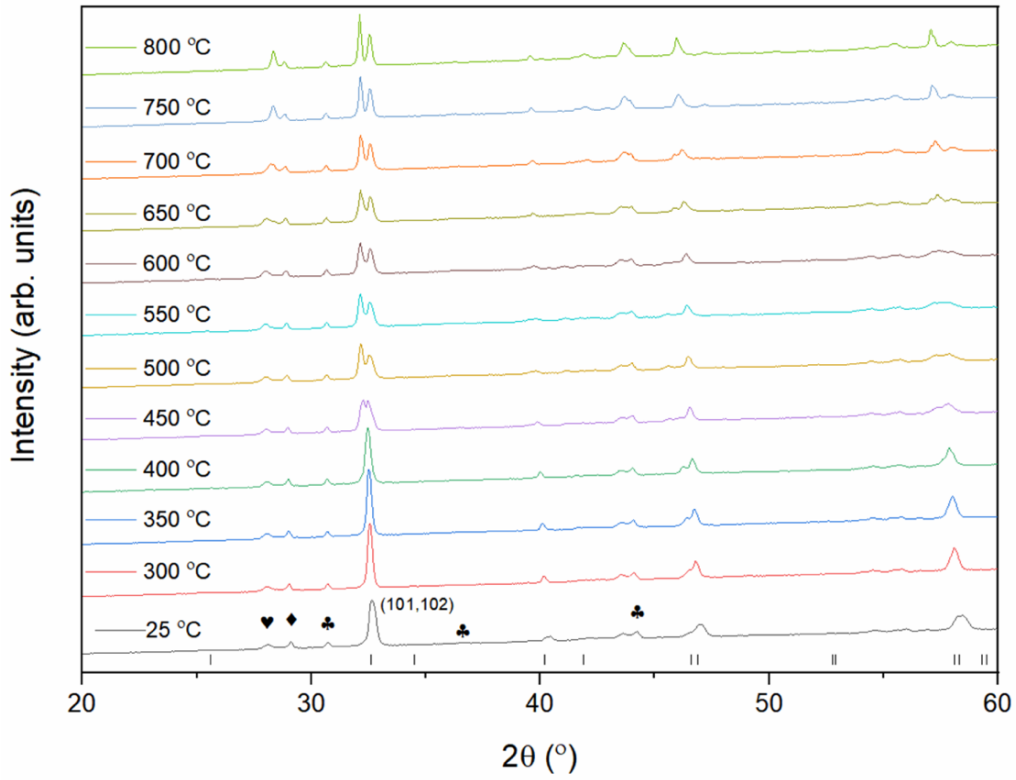
800 °C
750 °C
700 °C
650 °C
600 °C
550 °C
500 °C
450 °C
400 °C
350 °C
300 °C
25 °C
(101,102)
♥
♦
♣
Intensity (arb. units)
20
30
40
50
60
2θ (°)

b)

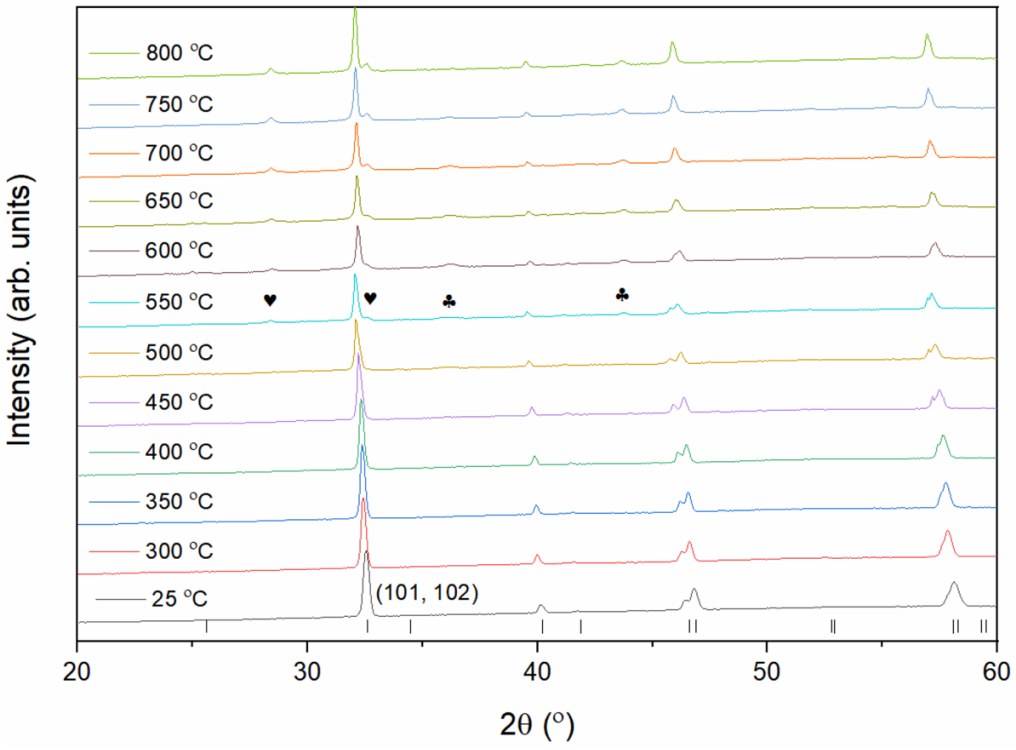
800 °C
750 °C
700 °C
650 °C
600 °C
550 °C
500 °C
450 °C
400 °C
350 °C
300 °C
25 °C
(101, 102)
♥
♣
Intensity (arb. units)
20
30
40
50
60
2θ (°)

c)

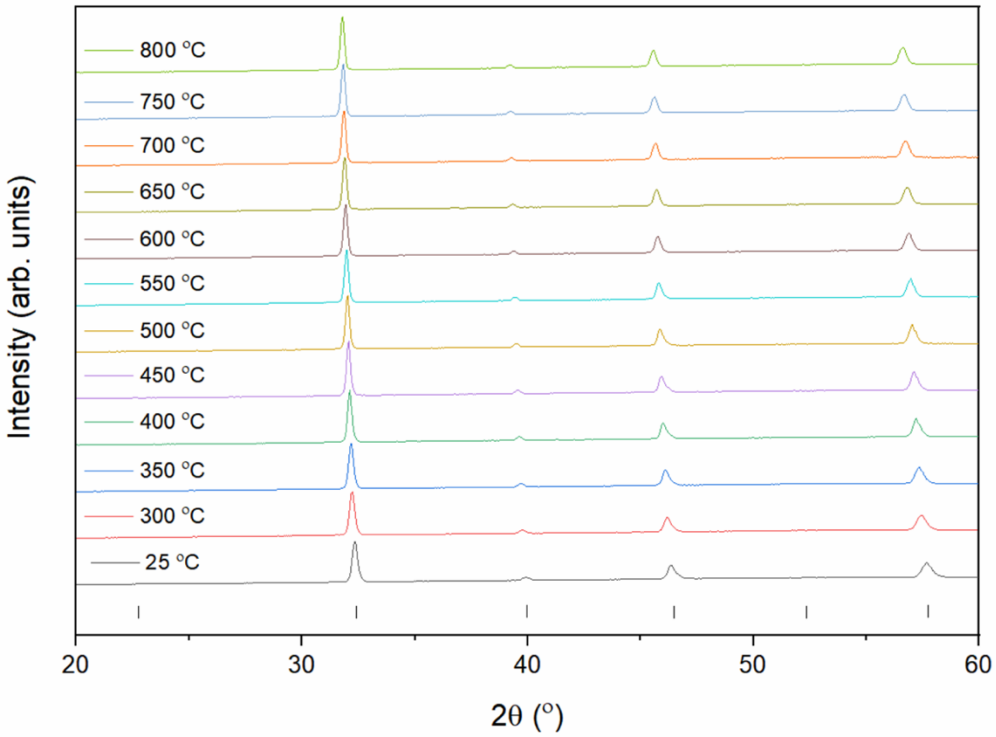

Figure 6-6. HT-XRD patterns collected at 50 °C intervals up to 800 °C for a) 5% Sb, b) 10% Sb and c) 20% Sb compounds. The splitting of the (101) peak is observed above 400 °C in a). References for the *P*4*mmm and* $Pm\bar{3}m$ space groups' Bragg reflections are displayed beneath the 25 °C diffractograms. Symbols denote the following: ♥ - Sb_2O_3, ♦ - Sb_2O_5, ♣ - Co_3O_4.

6.2.3. Defect Formation Thermodynamics

Spin-polarized density functional theory calculations, as previously described in section 5.6.11, were performed on undoped $SrCoO_3$ structures. An initial undoped *P*4*mmm* $SrCoO_3$ structure was obtained from the Materials Project [227] (mp-1273854). The lattice parameters and atoms within the structure were geometrically relaxed until it found a local energy minimum. The number of unit cells was increased to encompass a larger number of unit cells more appropriate for dilute defect calculations. Sb substitution was investigated by replacing 1, 2, or 4 Co cations with a Sb dopants in a 32 formula unit $SrCoO_3$ supercell corresponding to B-site concentrations of 3.125%, 6.25% and 12.5% and the structures $SrCo_{0.9675}Sb_{0.03125}O_3$, $SrCo_{0.9375}Sb_{0.0625}O_3$ and $SrCo_{0.875}Sb_{0.125}O_3$ respectively. Since Sb inclusion experimentally changes the lattice parameter (Table 6-2), it was appropriate in this situation allow the full geometric relaxation of the structure. Subsequent single-point calculations were carried out using a denser 4x4x4 gamma-centred k-point mesh and a Blöchl-tetrahedron smearing

algorithm to provide accurate final energies and more refined density of states plots. Figure 6-7 shows the outputted geometrically relaxed structures for increasing Sb concentration

Figure 6-8 shows the density of states for each of the simulated compounds. It is observed for structures below 25% the oxygen p band centre moves closer towards the Fermi energy. Previous studies have used this descriptor to reason improved oxygen evolution properties and anionic redox.[228], [229], [290] If the O 2p non-bonding band moves closer to the Fermi energy compared to the transition metal band, electrons spill-over to form $(O_2)^{n-}$ species that react through reductive elimination and evolve oxygen gas. [291] This aligns with the slightly earlier onset of oxygen evolution observed in the Sb 10% compound versus the 5% Sb compound (Figure 6-5a). The presence of more electronegative cations, such as Sb, can shift the oxygen band centre closer to the Fermi energy.[292] Furthermore, previous authors relate a higher oxygen band centre to greater oxygen diffusion rates due to lower vacancy formation energies and more facile charge transfer networks.[231] This was not observed experimentally whereby Aguadero *et al.* reported worsening oxygen migration with increased Sb-concentration.[265] Although the lowering of oxygen migration performance in these studies was attributed to the reduction in oxygen vacancy concentration.

a)

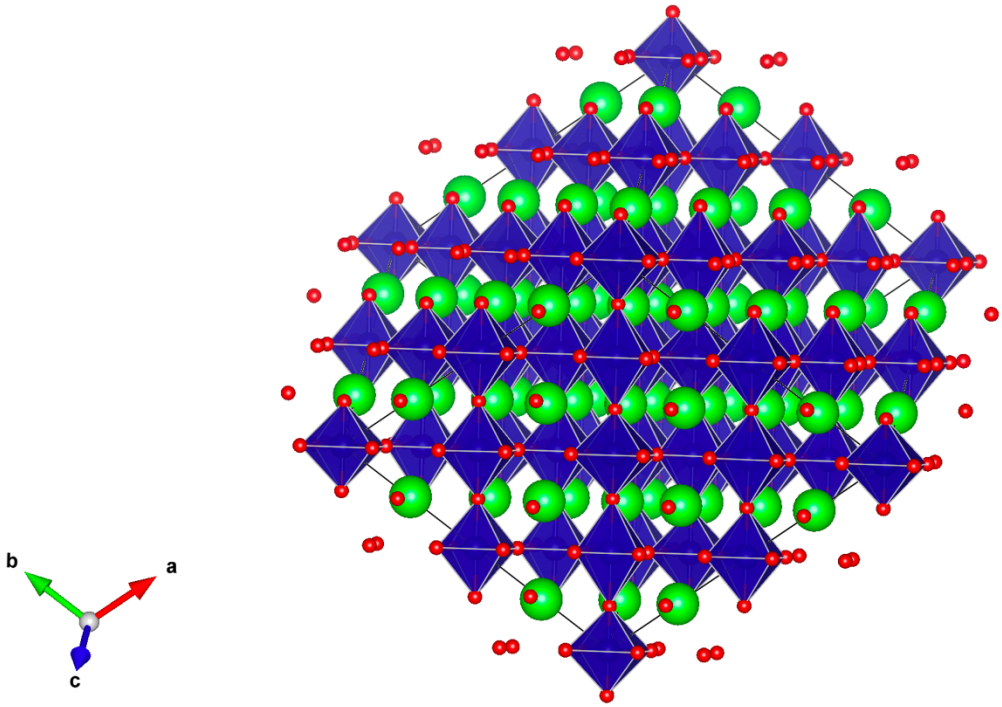

b)

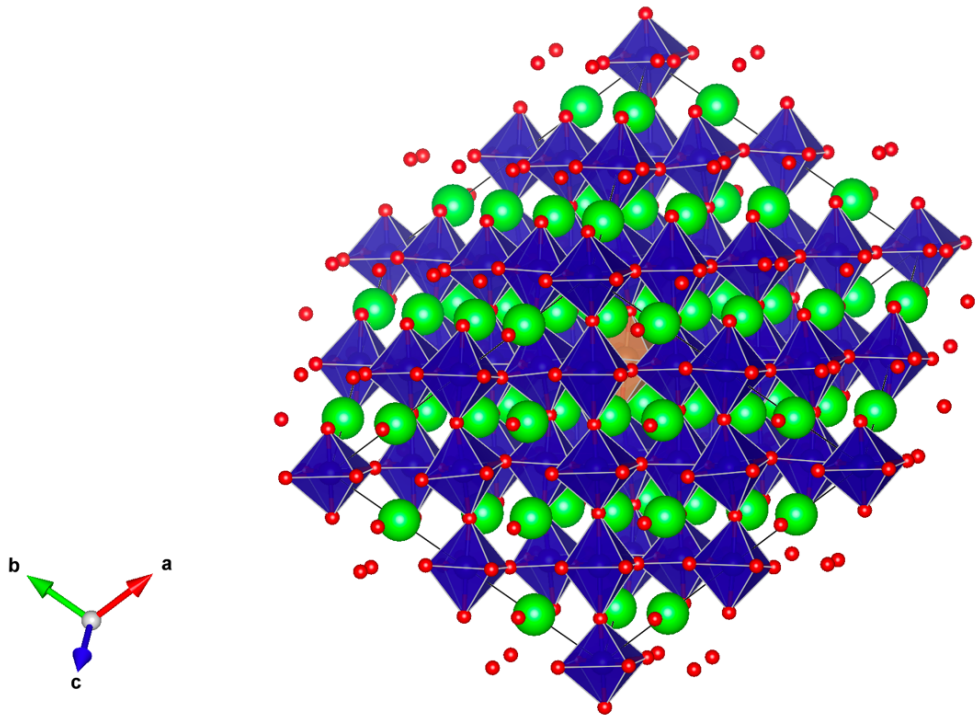

c)

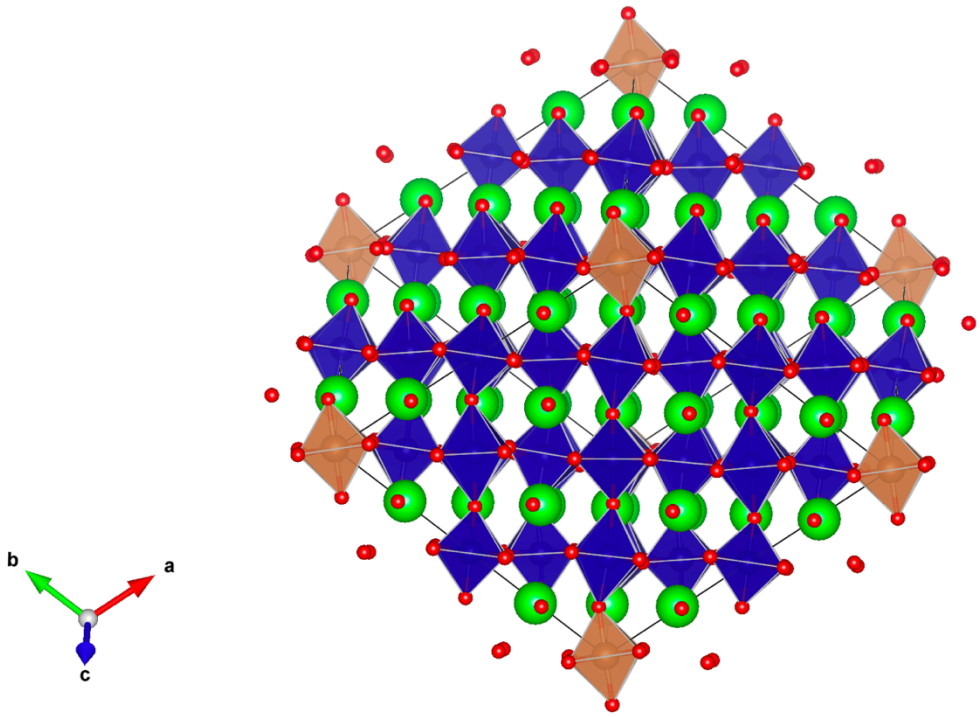

d)

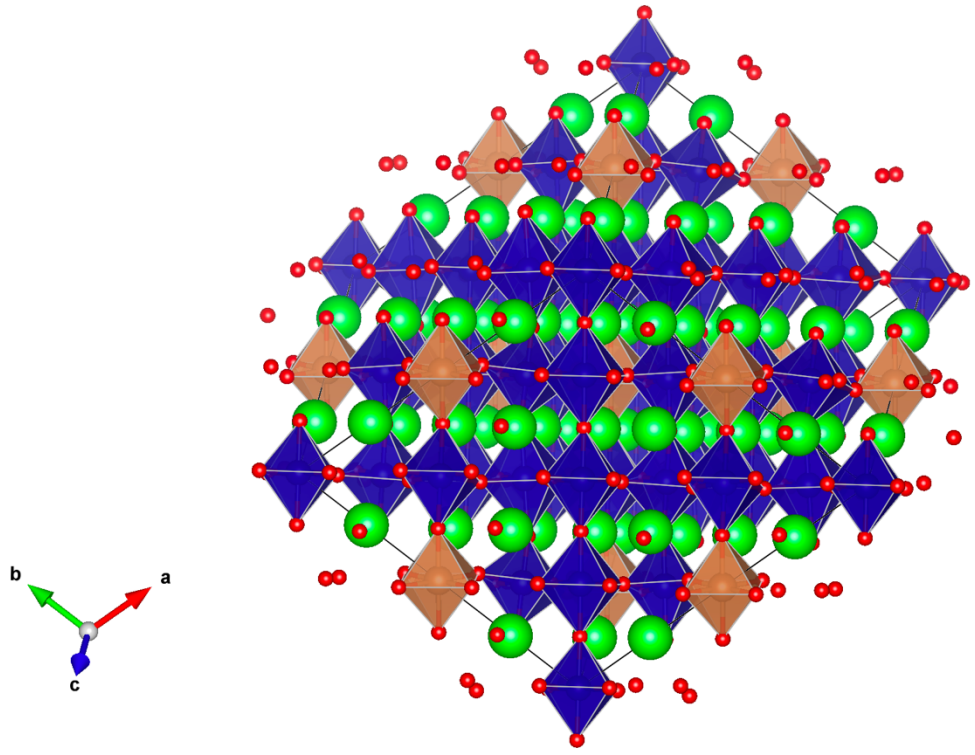

Figure 6-7. Geometrically relaxed structures for the a) 0%, b) 3.125%, c) 6.25% and d) 25% Sb-doped $SrCoO_3$ compounds.

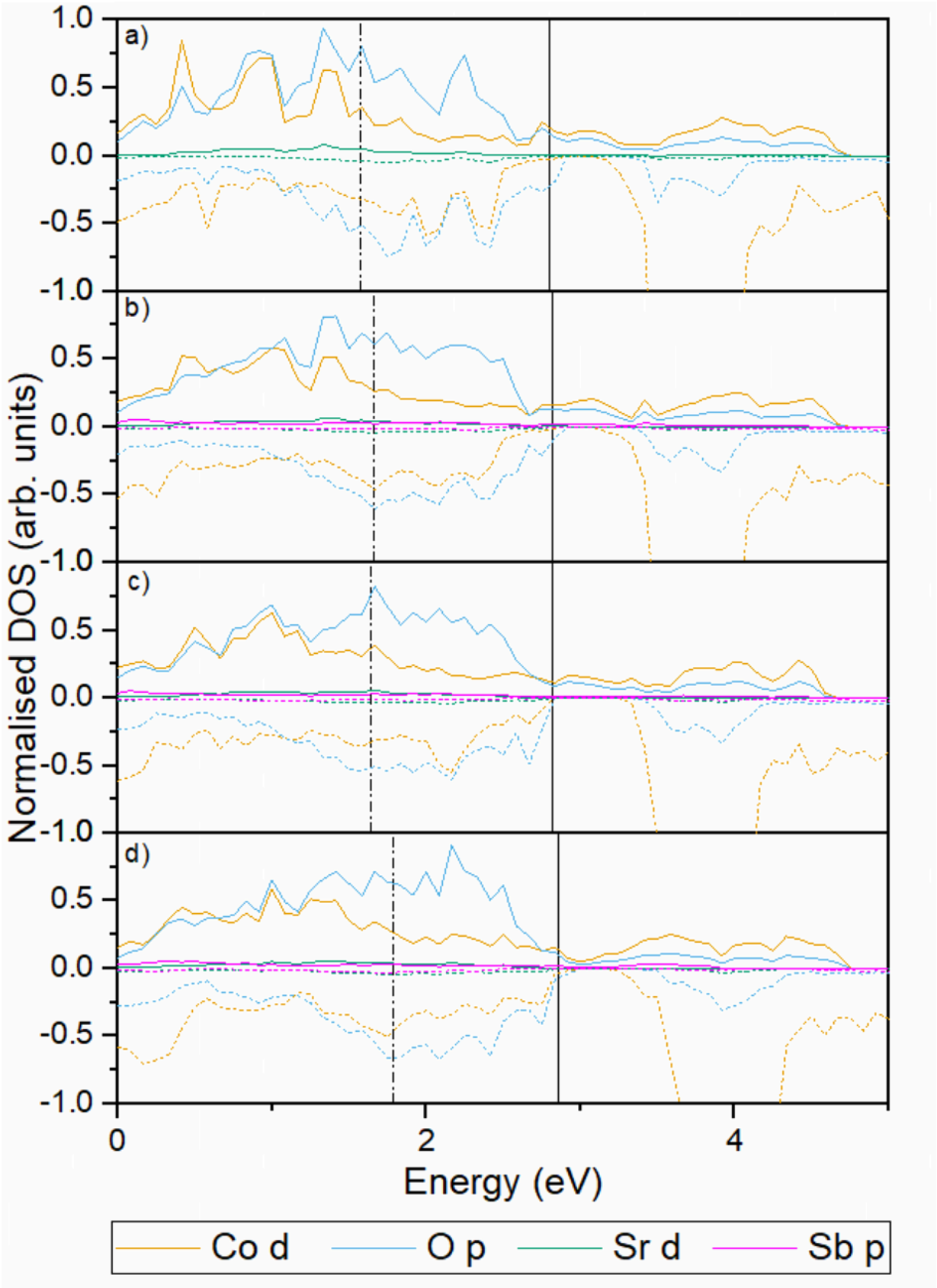

Figure 6-8. Density of states plots for the a) 0%, b) 3.125%, c) 6.25% and d) 25% Sb-doped $SrCoO_3$ compounds. The vertical lines display the position of the Fermi energy (solid) and oxygen p band centre (dashed).

The reduction enthalpy at 0 K, ΔH_{red}, was calculated using equation 6.2. The oxygen molecule energy was computed through geometric relaxation of the molecule within a 12x12x12 Å rhombohedral box. Oxygen vacancies were introduced at different coordination spheres to the Sb dopant to simulate the Sb-O-Co and Co-O-Co environments and the spatial effect of the antimony on the vacancy formation energy.

$$\Delta H_{red} = E_{ABO_{3-\delta}} + \frac{1}{2}E_{O_2} - E_{ABO_3} \quad (6.2)$$

where E_{ABO_3}, $E_{ABO_{3-\delta}}$ and E_{O_2} are the relaxed energies of the pristine, vacancy-defected and oxygen gas structures respectively.

Figure 6-9 shows the vacancy formation energy for each Sb concentration with respect to the coordination sphere from the Sb cation. Overall, the oxygen vacancy formation energy increases with respect to Sb concentration from 0.5 eV/ O atom for the $SrCoO_3$ structure to 0.7 eV/ O atom for the 12.5% Sb concentration. This is observed with the onset of oxygen evolution occurring at higher temperatures in the TGA experiments (Figure 6-5c).

Furthermore, it is seen that reduction enthalpy is significantly less in the second and third coordination spheres compared to those directly bonding to the Sb. Tahini *et al.* observed a similar behaviour when computationally investigating Nb doped $SrCoO_3$. [293] If the oxygens in the first coordination are considered "fixed", due to the higher reduction enthalpy, the number of reducible oxygens in the structure diminishes with increasing Sb-concentration thereby reducing the inherent oxygen non-stoichiometry as observed by experiment. Moreover, the difference in oxygen vacancy formation with different oxygen environments could help explain the additional oxygen evolution peaks observed as temperature increases. (Figure 6-5c).

These reduction enthalpies are significantly lower than those required to support thermochemical water splitting as proposed by Meredig and Wolverton ($\Delta H_O > 2.5$ eV). [294] However, the large oxygen non-stoichiometry could be of interest for alternative processes such as thermochemical energy storage [295]–[300] or oxygen separation. [301]–[303] In a similar process, the topotactic oxygen exchange metal oxides is facilitated by the atmosphere switching between inert and compressed air. Upon reoxidation the exothermic release of

energy can be used to drive work processes. Perovskites have been of increasing interest in this field due to their wide chemical flexibility that allows tuning and optimization of reaction kinetics, storage capabilities and structural stability.

a)

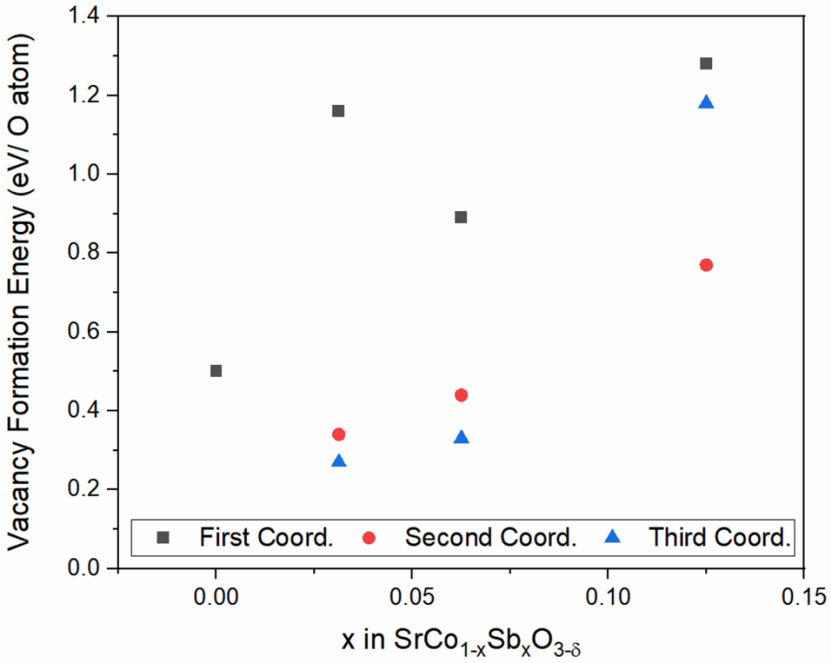

b)

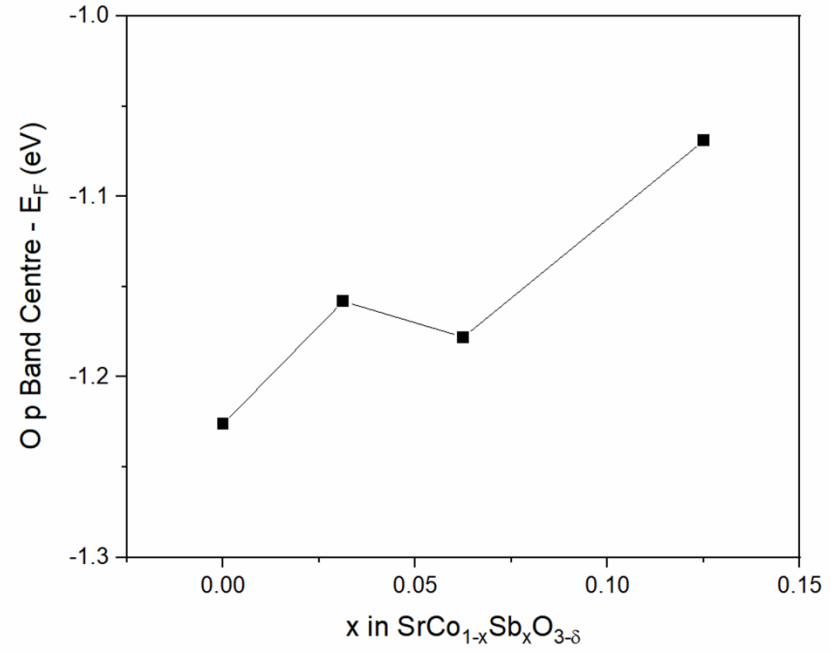

Figure 6-9. a) Computed oxygen vacancy formation enthalpy as a function of Sb concentration and coordination sphere with dopant cation. b) Relationship between O p band centre and Sb concentration within the structure.

6.2.4. Isothermal Redox Cycling

The isothermal redox kinetics between 500 and 800 °C were probed simultaneously by TGA and DSC. At the target temperature, the powders were redox cycled by switching the gas atmosphere between nitrogen (~10^{-4} atm) and compressed air (0.21 atm). Three cycles were completed on each powder before cooling to room temperature. Figure 6-10 shows an example of the redox cycling for the 10% Sb sample at 600 °C. Further cycling data is presented in Appendix B.

The mass loss when heating under nitrogen is demonstrated again as shown in the section 6.2.2. Upon switching gas atmosphere, mass increase and exothermic DSC spikes are indicative of the re-oxidation of the material. The opposite is observed when switched to nitrogen for the demonstration of the reduction reaction. The integral of the DSC peaks is a direct measurement of the energy stored and released during the redox processes.

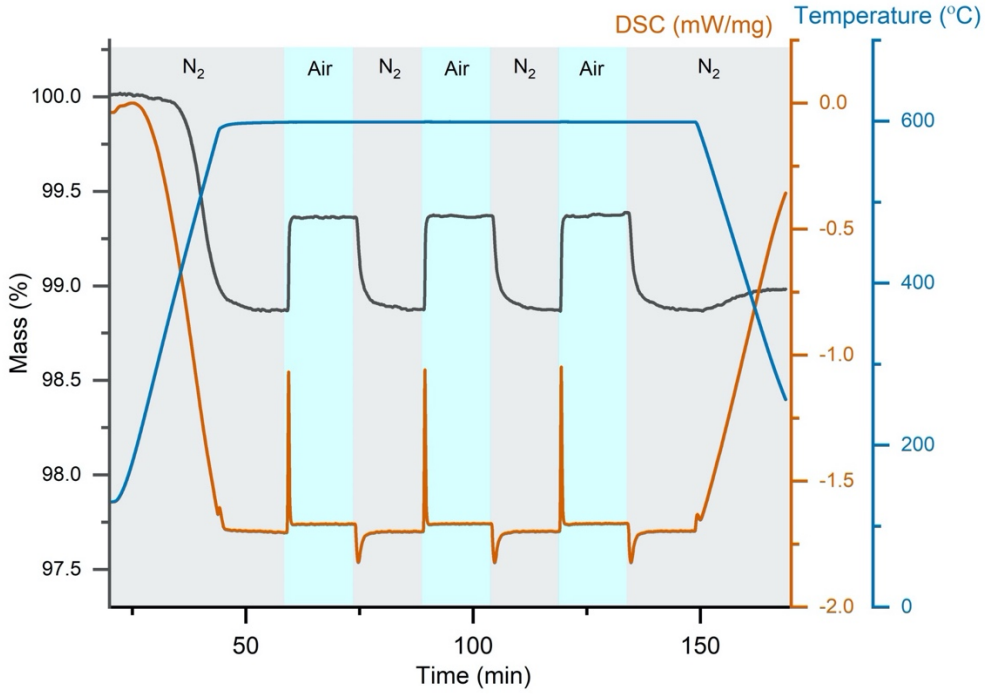

Figure 6-10. $SrCo_{0.9}Sb_{0.1}O_{3-\delta}$ isothermal redox cycling experiment at 600 °C.

The kinetic behaviour of the redox processes was investigated by plotting the reaction conversion versus time. Figure 6-11 and Figure *6-12* show the isothermal behaviour for the reduction and oxidation reaction respectively. The oxidation reaction is much faster, for all

compounds, compared to the reduction reaction. Each process can be deconvoluted into a surface reaction (initial gradient) and diffusion of oxygen through the bulk contribution (decaying tail). Pan *et al.* had previously reported oxygen diffusion to be the limiting factor of strontium cobalt oxide performance for low temperature electrochemical oxygen evolution. [304] Here, we observe a similar case whereby the higher doped samples demonstrate slower decays in the conversion graphs for reduction performance. Aguadero *et al.* previously showed the worsening of oxygen migration with increasing Sb-concentration due to lowering of oxygen vacancy concentration. [265] As previously discussed, additional Sb cations increases the number of Sb-O-Co bonds that require a greater energy to form a vacancy within the lattice. This greater vacancy formation energy will also hinder the oxygen ion migration through the lattice.[305]

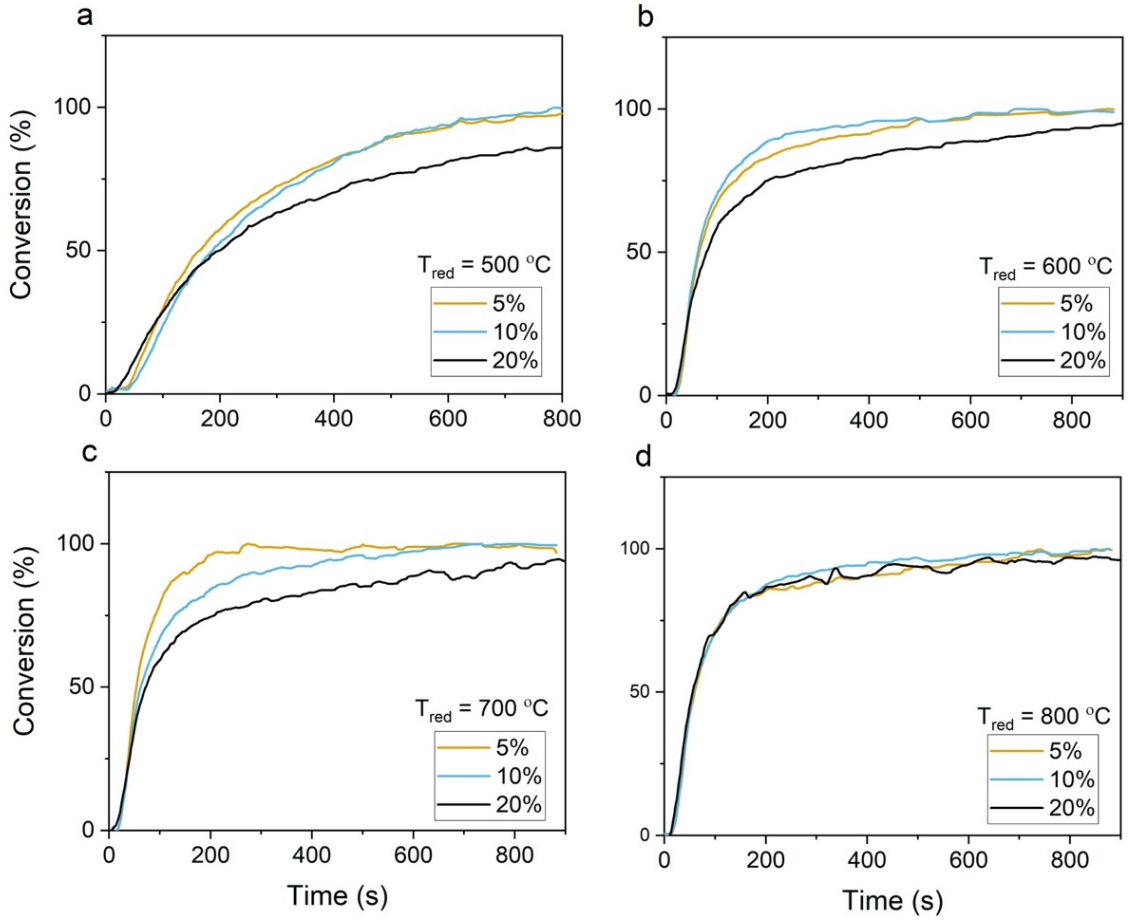

Figure 6-11. Comparison between reduction reaction conversions for different Sb concentrations at increasing temperatures.

Furthermore, the surface redox kinetics of metal oxides has been proposed to be related to the filling of the transition metal e_g* shell. The e_g* and O 2p orbitals in octahedral coordinations

overlap to form σ bonds that allow fast electron transfer (Section 2.3). Suntivich *et al.* found an optimal orbital filling of 1.2 for oxygen evolution reactions.[306] Previous XANES measurements suggest the antimony dopant affects the local cobalt cations by lowering the crystal field splitting energy that allows an intermediate spin (IS) state to be adopted (Co^{3+} d^6 IS t_{2g}^5 e_g^1).[287] Using previously published oxidation states obtained from XANES, the number of e_g* electrons is estimated and displayed in Figure 6-13a. This figure shows the number of electrons is close to the ideal 1.2 filling and increasing the temperature makes this more favourable. Although caution is advised since further reduction of the lattice, to achieve the ideal filling, may make the structure unable to accommodate so many vacancies, thus causing phase degradation as seen by the high-temperature XRD in section 6.2.2.

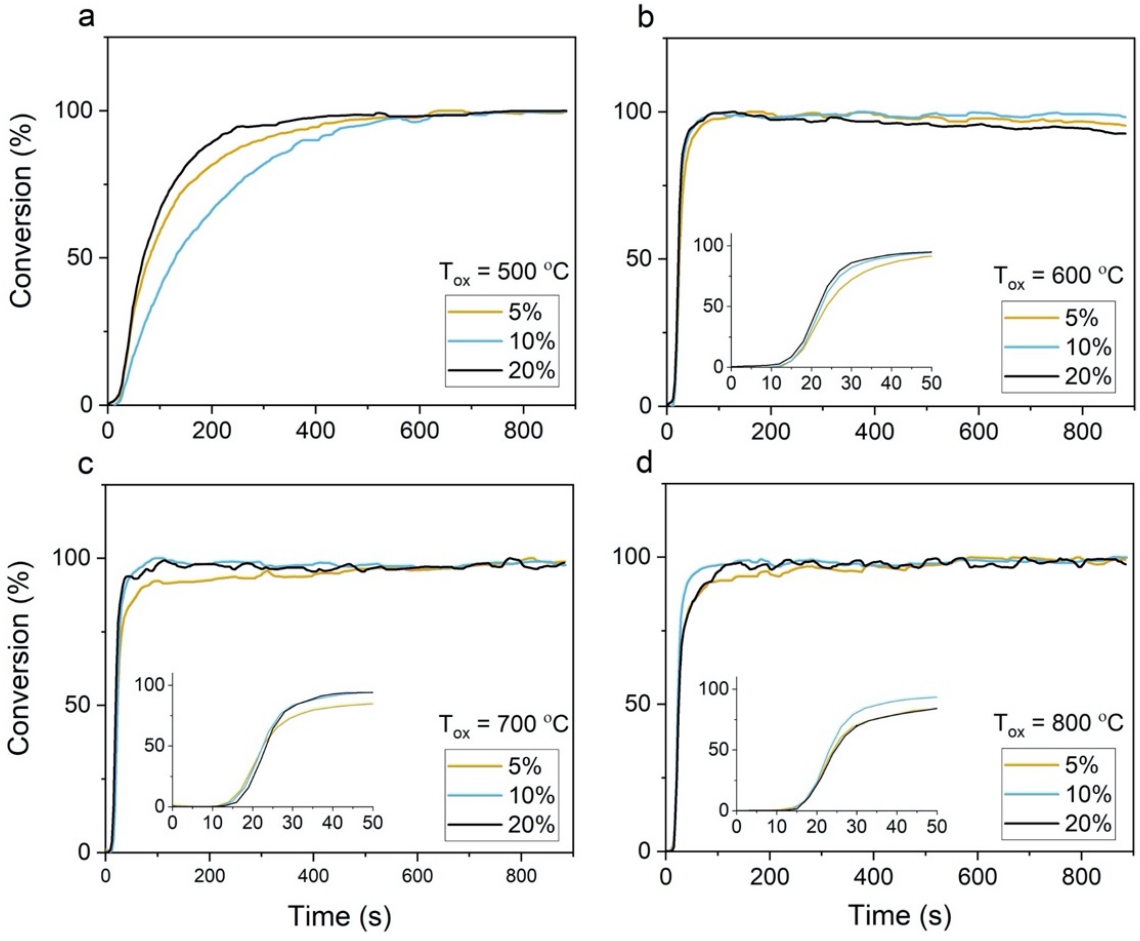

Figure 6-12. Comparison between oxidation reaction conversions for different Sb concentrations at increasing temperatures.

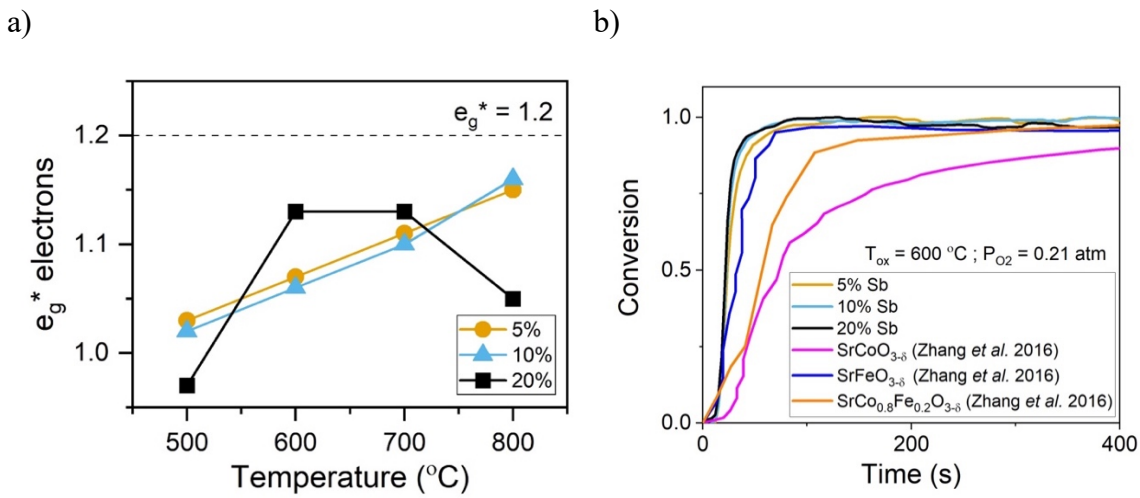

Figure 6-13. a) Predicted number of e_g^* electrons and as a function of temperature for each of the $SrCo_{1-x}Sb_xO_{3-\delta}$ compounds, b) comparison between oxidation reaction conversion at 600 °C of the $SrCo_{1-x}Sb_xO_{3-\delta}$ against oxygen separation materials reported within the literature. [260]

Figure 6-13b compares the oxidation reaction conversion rate of the Sb compounds against previous reported materials by Zhang *et al.*[307] As seen the in the figure the Sb-compounds have a faster completion compared to $SrCoO_3$. Furthermore, it exceeds the rate of the oxygen separation material benchmark $SrFeO_3$. This provides further evidence to the beneficial electron configuration induced by the Sb-incorporation. The reduced Fe^{3+} d^5 HS configuration that has two electrons in the e_g orbitals, whereas in the absence of antimony, Co^{3+} was reported to be in the LS configuration with no e_g electrons.

6.2.5. Thermochemical oxygen separation and energy storage performance

The volume of oxygen exchanged is the figure of merit for oxygen separation technologies, in a similar way to hydrogen production for thermochemical water splitting metal oxides. A theoretical maximum exchange volume can be calculated by considering the maximum and minimum oxygen stoichiometries in the isothermal gas switching experiments. Figure 6-14a compares the theoretical volumes exchanged under a temperature swing condition utilising the highest T_{red} of 800 °C. It is no surprise that the volumes exchanged increase as the oxidation temperature is lowered. Furthermore, the volumes exchanged decreases with increased Sb concentration reemphasising the effects of increasing the strong Sb-O-Co bonds concentration. However, temperature swing conditions can potentially lower the overall process efficiency

due to additional energy requirements to reheat the material.[164], [308] Therefore Figure 6-14b compares the volumes exchanged under isothermal conditions (T_{red}=T_{ox}). It is observed the oxygen exchange volumes are only significantly improved if T_{red}-T_{ox} > 100 °C. Although the isothermal volumes are reduced, they are still in comparable ranges to other literature materials, $SrCo_{0.85}Fe_{0.15}O_{3-\delta}$ (1.05 cm^3/g at 500 °C and 0.78 cm^3/g at 600 °C). [309]

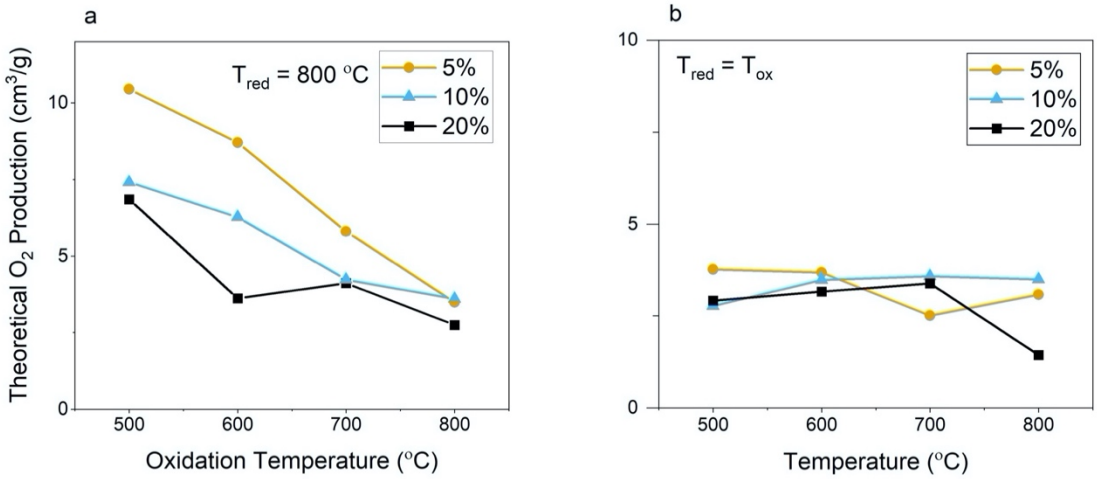

Figure 6-14. Theoretical oxygen exchange volumes for $SrCo_{1-x}Sb_xO_{3-\delta}$ compounds under a) temperature-swing conditions T_{red} = 800 °C, and b) isothermal conditions T_{red}=T_{ox}.

The integral of the DSC signal provides a direct measurement of the energy stored and released throughout the redox reactions. The energy stored and released by the 10 and 20% compounds generally increases with temperature whereas the 5% doped compound observes little change or slight decreases (Figure 6-15). This could be related to the 5% sample undergoing a phase decomposition as observed by HT-XRD (Figure 6-6a). Furthermore, above 700 °C, the 10% sample demonstrates a decrease in energy stored. This coincides with the orthorhombic phase forming within this compound. This suggests it is important to suppress phase decomposition for improved thermochemical energy storage performance. The energy storage and kinetics were observed to be reasonably consistent over a small number of cycles (Figure 6-15c and Figure *6-15*d), therefore suggesting material performance is maintained despite possible degradation. However, when comparing the energy values with literature materials of Co_3O_4 has an order of magnitude larger (844 kJ/kg).[115], [117], [310] Therefore, this family of materials are better placed for thermochemical oxygen separation.

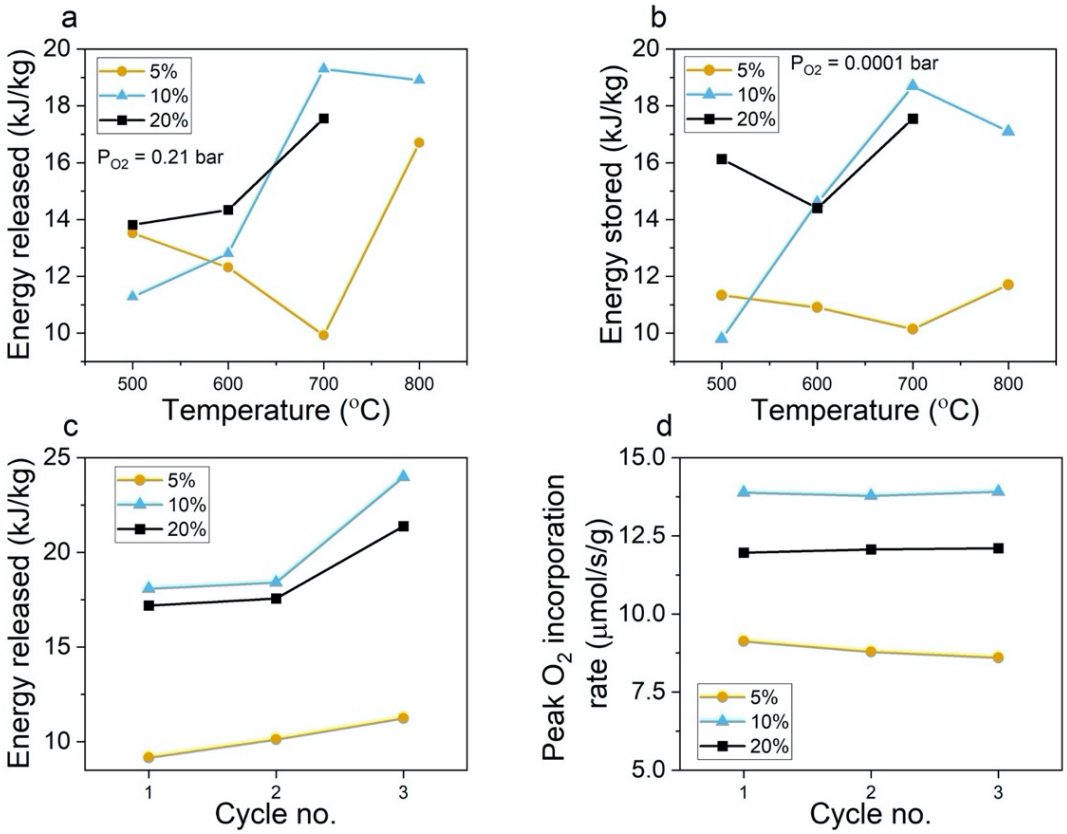

Figure 6-15. Comparisons generated from the DSC signal to show temperature and Sb effects on a) energy released, b) energy stored, and cyclability of c) energy storage and d) oxygen incorporation kinetics.

The topotactic oxygen exchange of these materials under ambient pressures was well studied for these materials due to their interest as solid oxide fuel cell cathodes.[280]–[282] SEM images do not demonstrate any distinct sintering or surface degradation features (Figure 6-16). However, upon cooling in nitrogen, post-cycling XRD analysis observed secondary peaks for the 5 and 10% Sb samples (Figure 6-17a and Figure *6-17*b). The quality of these diffractograms is diminished due to the small amount of powder. These peaks could be contributions from $SrCo_6O_{11}$, $Sr_6Co_5O_{15}$ or $Sr_2Sb_2O_7$ phases, that had been identified as possible decomposition products by DFT calculations. Alternatively, they could be due to the decomposition into cobalt and antimony oxides as seen in the high temperature XRD. The 20% Sb sample did not observe any degradation due to the temperature not exceeding 800 ºC above which the initial DSC suggested a phase decomposition.

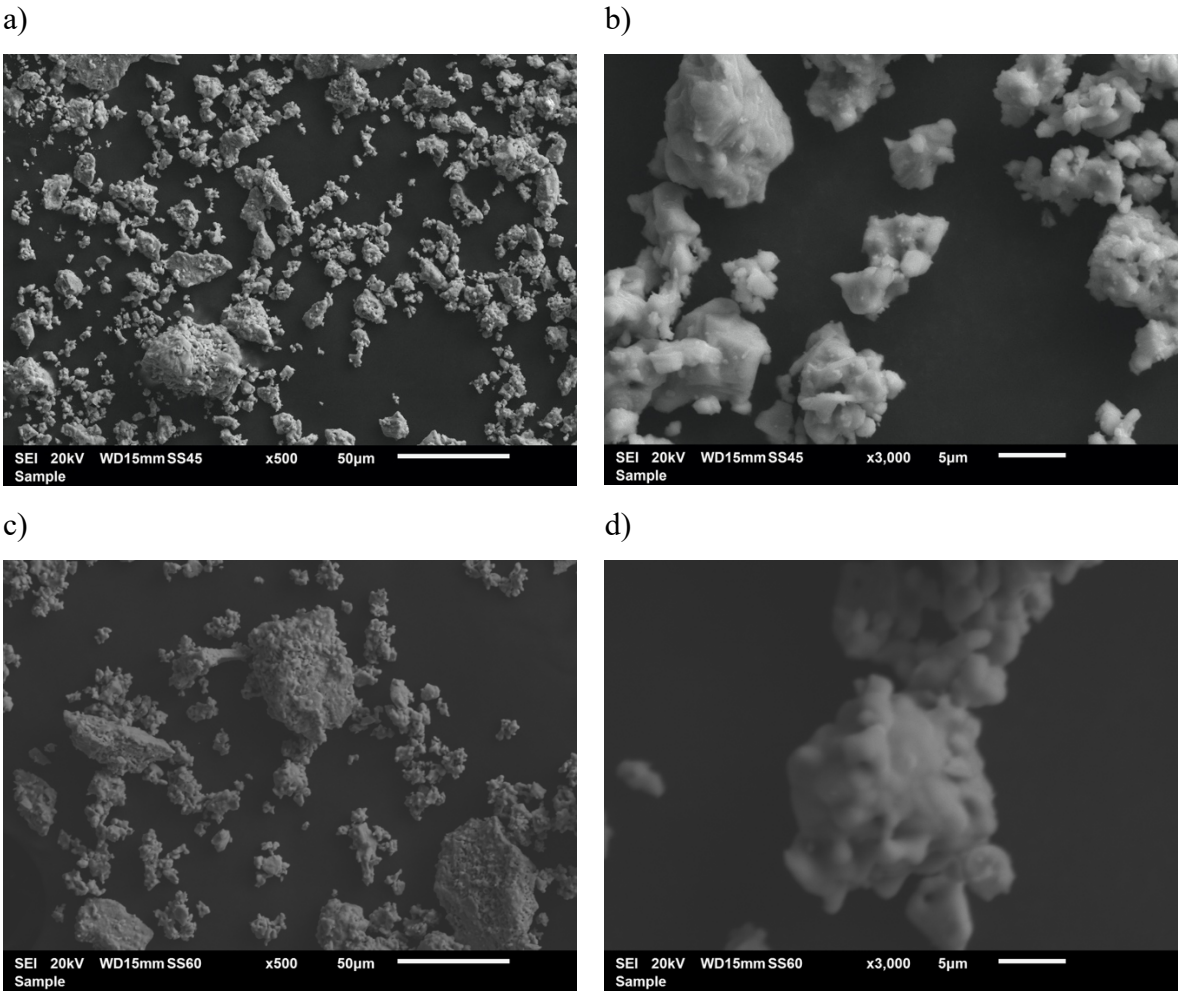

Figure 6-16. Scanning electron micrographs of the a) and b) 5% Sb compound and the c) and d) 20% Sb sample after isothermal redox cycling at 800 ºC.

Additional studies undertaken in tandem with this thesis demonstrated the materials instability under humid atmospheres. Cavallaro *et al.* treated 5% Sb powder with H_2O and used LEIS and XPS surface analysis techniques in combination with TGA to show the Sr surface enrichment that slows the redox kinetics. [311] This is important when designing for application since concentrated solar power plants would sensibly be situated in hot countries that can also have high humidity.

a)

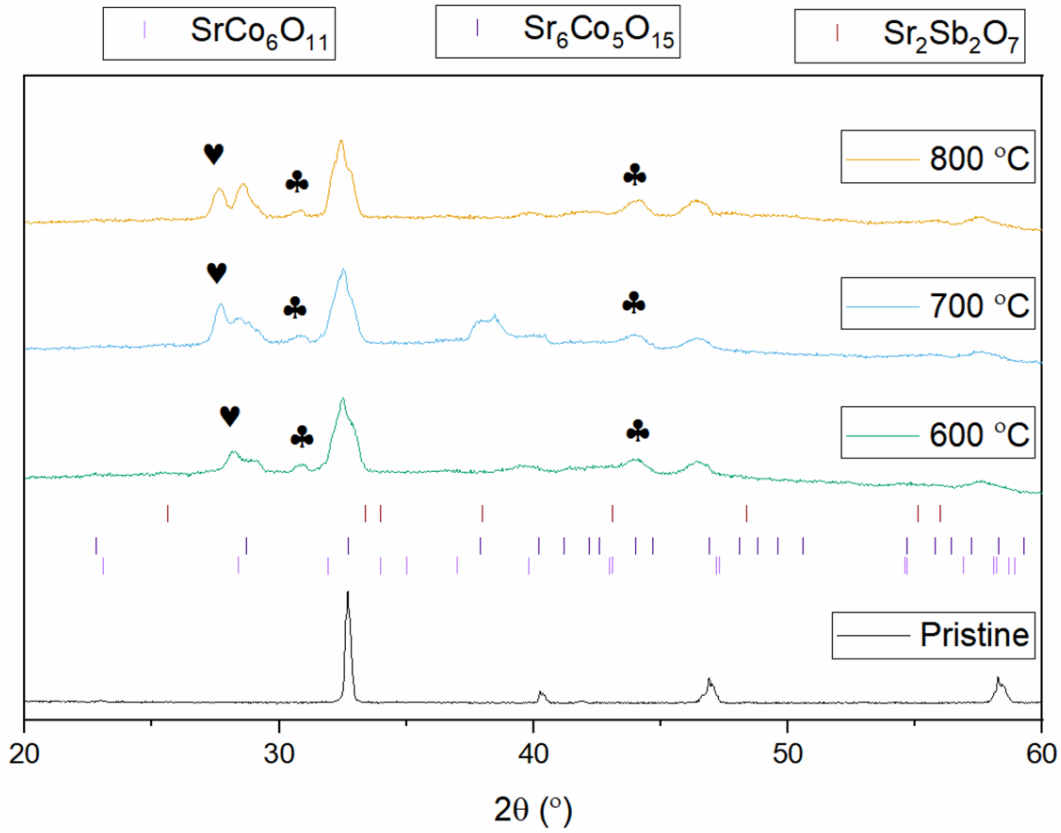
SrCo6O11
Sr6Co5O15
Sr2Sb2O7
800 °C
700 °C
600 °C
Pristine
20
30
40
50
60
2θ (°)

b)

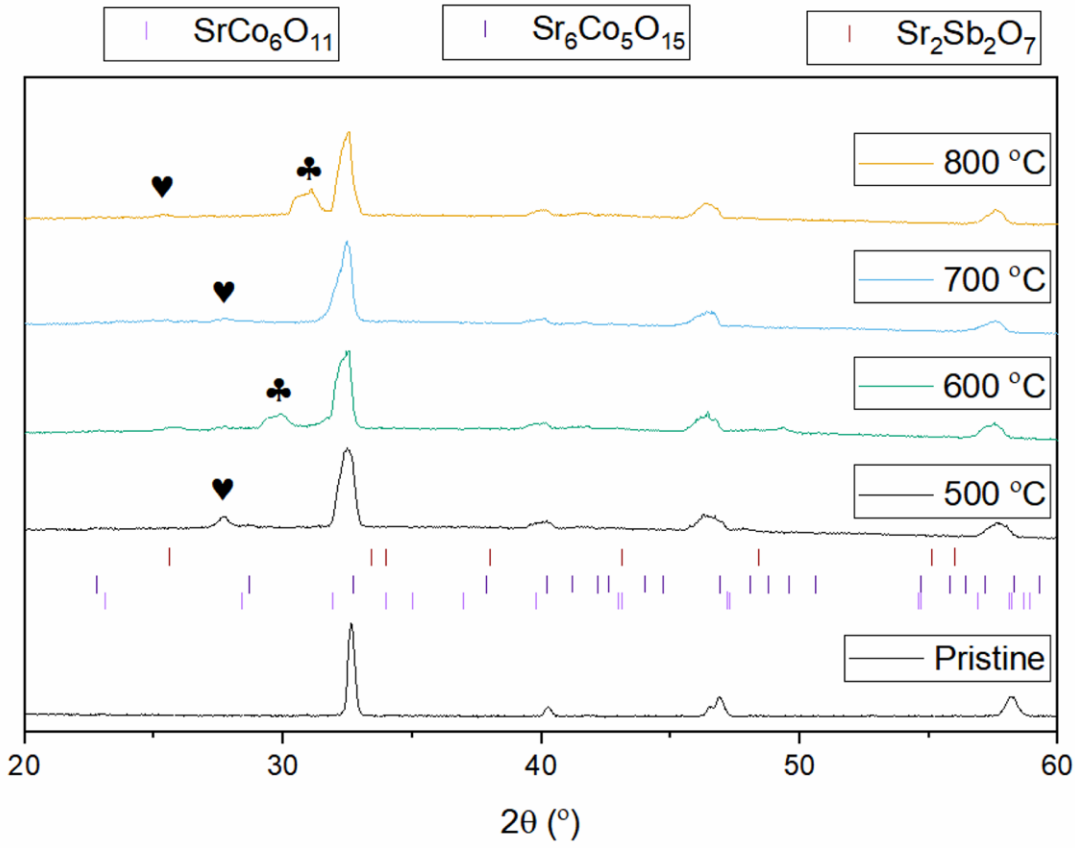
SrCo6O11
Sr6Co5O15
Sr2Sb2O7
800 °C
700 °C
600 °C
500 °C
Pristine
20
30
40
50
60
2θ (°)

c)

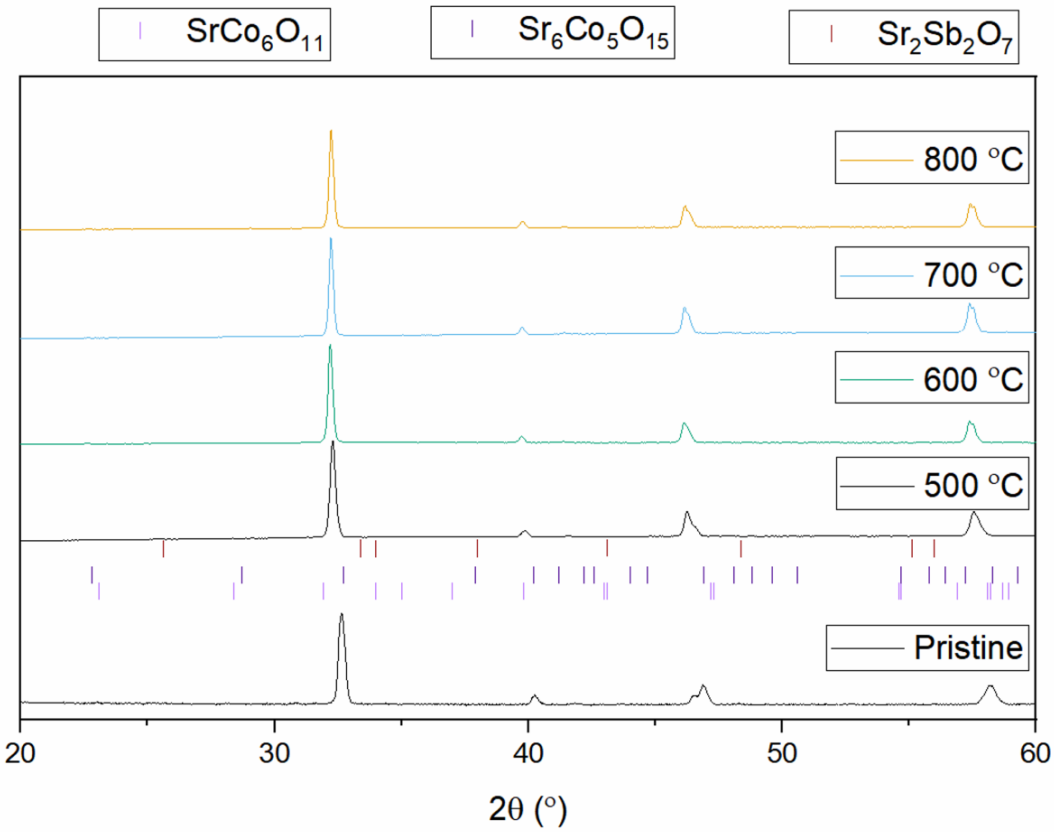

Figure 6-17. Post-cycling XRD patterns for a) 5%, b) 10% and c) 20% Sb compounds. Reference peaks for the $SrCo_6O_{11}$, $Sr_6Co_5O_{15}$ and $Sr_2Sb_2O_7$ peaks are shown below the diffractograms of the powder cycles at 500 °C. Symbols denote the following: ♥ - Sb_2O_3, ♦ - Sb_2O_5, ♣ - Co_3O_4.

6.2.6. Thermochemical Water Splitting

The 20% Sb containing sample was ambitiously tested for thermochemical water splitting using the rig described in section 5.5. This sample was chosen since it demonstrated the most crystallographic stability whilst maintaining fast kinetics. The sample was heated to 800 °C before cooling to 400 °C and humidifying the gas flow to a level of 50% relative humidity. Figure 6-18 shows the gas production over the course of the thermochemical water splitting cycle. In agreement with the previous oxygen evolution measurements, the detected oxygen level starts increasing at approximately 300 °C. The oxygen production volume rates were significantly higher than the original TGA experiment, 50 µmol/min/g versus 10 µmol/min/g (Figure 6-5c). Upon introduction of humidified gas, the hydrogen signal increases to a maximum rate of approximately 4 µmol/min/g. In comparison with other published materials,

this is a comparative hydrogen production rate to ceria at 1000 °C (6 µmol/min/g).[155] This result is encouraging since the thermochemical cycling occurs at significantly lower temperatures compared to the benchmark material ceria. However, upon trying a second cycle there is negligible oxygen and hydrogen production.

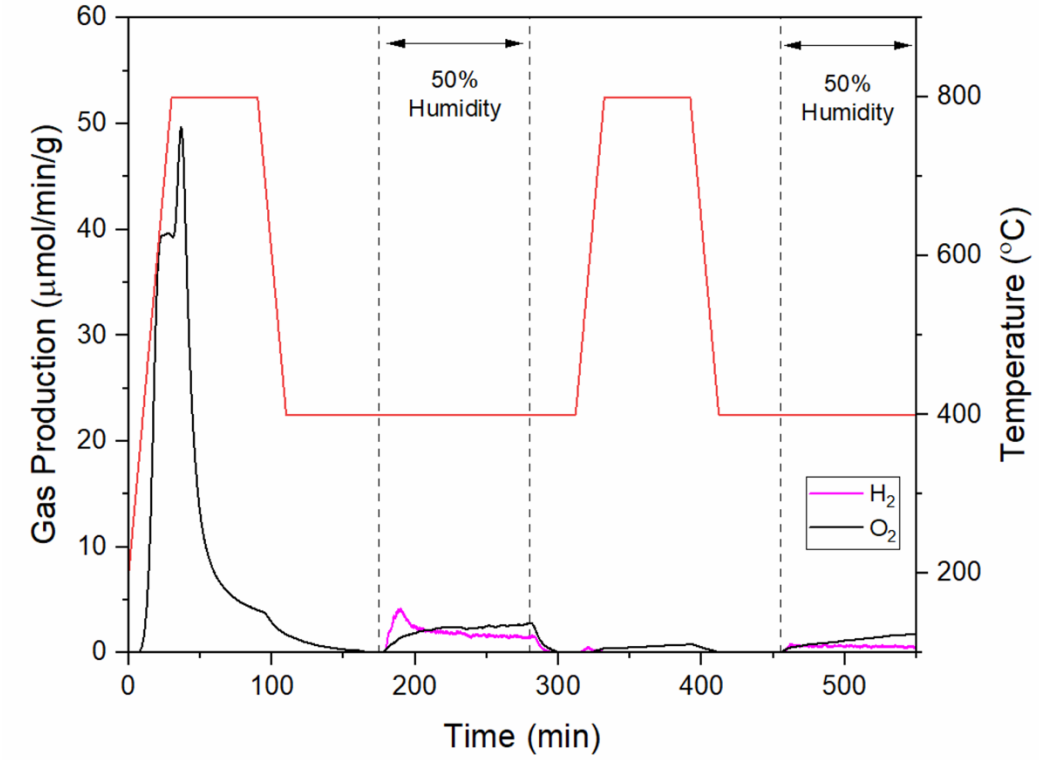

Figure 6-18. Hydrogen and oxygen production detected throughout a thermochemical water splitting cycle run between 800 and 400 °C.

Initial observations thought the increased oxygen evolution could be due to a lower P_{O_2} since the lack of ability to evacuate and backfill was compensated by a longer purge gas time to achieve a low constant oxygen signal. However, it would be a drastic decrease to cause a 10x increase in oxygen production. Furthermore, it was surprising the material was reoxidising and producing hydrogen since the computed reduction enthalpy was found to be much lower than the value expected to drive the splitting reactions. It is possible the large temperature swing and pH_2O could drive the splitting reaction, however post-operando XRD analysis revealed there is likely another reason. The XRD pattern revealed the severe degradation of the perovskite phase in the water splitting reactor (Figure 6-19). Peak indexing revealed the presence of $CoAl_2O_4$, CoO and SrO within the XRD pattern. There was only a minor presence of the parent perovskite phase remaining in the pattern. It is likely the perovskite undergoes a

reaction with the Al_2O_3 reaction chamber in a similar way to the previously reported hercynite system that forms the $CoAl_2O_4$ spinel phase whilst releasing oxygen as a further product (Eq. 6.3). [119] The oxygen produced could be the reason for the difference in oxygen production levels in this experiment. It is likely this spinel phase is active in water splitting. Although unlike the previous hercynite studies, where the phase reforms the doped iron oxide phase, since the temperature in this reaction is much lower, there is neither the thermal energy or high oxygen partial pressure to reform the perovskite phase therefore leaving SrO and CoO present. Cavallaro *et al.* also noticed the degradation of the Sb-doped strontium cobalt oxides under low P_{O_2} and humid environments to form SrO and Co-rich phases.[311] Furthermore, SEM images revealed near complete sintering of the powder in the reactor tube and change of the surface after the water splitting experiment in agreement with previous literature reports (Figure 6-20). [311] Therefore searching for a more stable metal oxide for thermochemical water splitting is important for endured performance.

$$SrCoO_3 + Al_2O_3 \rightarrow CoAl_2O_4 + SrO + \frac{1}{2}O_2 \tag{6.3}$$

$$CoAl_2O_4 + H_2O \rightarrow CoO + Al_2O_3 + H_2 + \frac{1}{2}O_2 \tag{6.4}$$

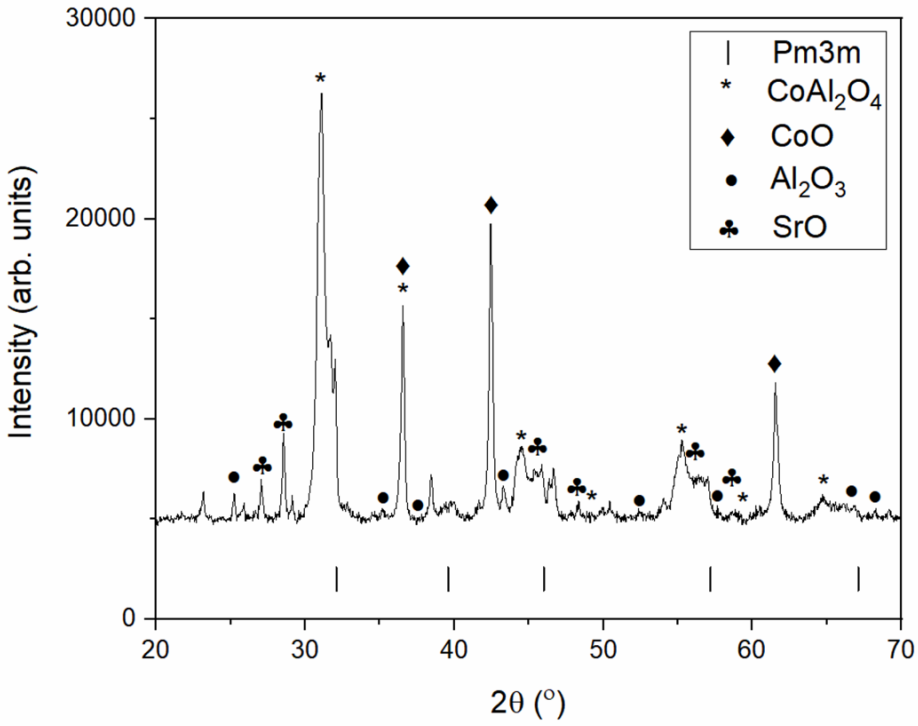

Figure 6-19. XRD pattern of Sb 20% compound post thermochemical water splitting.

a)

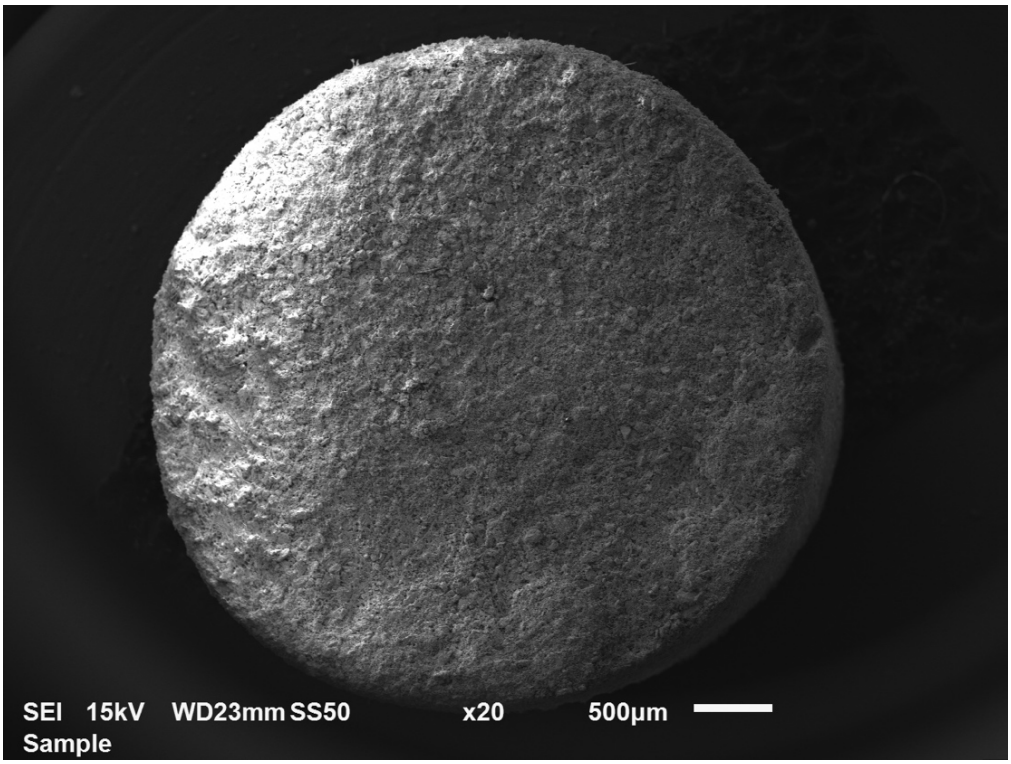

b)

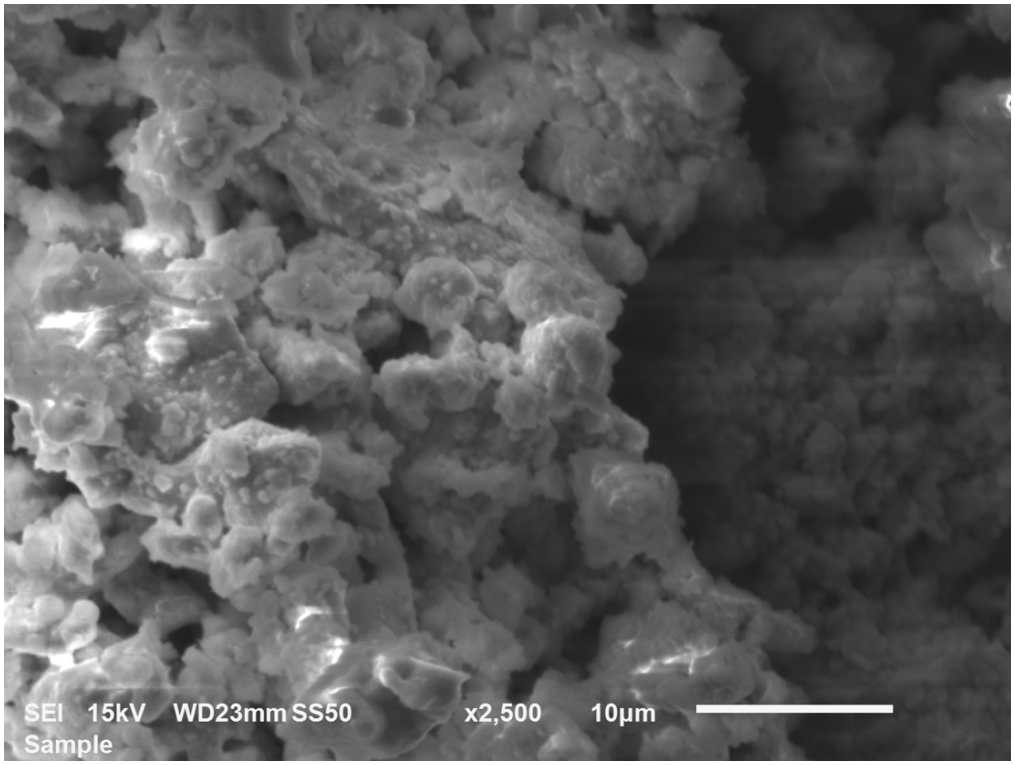

Figure 6-20. Scanning electron micrographs of the Sb 20% compound after thermochemical water splitting experiment cycling between 800 and 400 °C.

6.3. Conclusions

To conclude the work covered in this chapter, antimony-doped strontium cobalt oxides were investigated for thermochemical redox reactions. $SrCoO_3$ was previously proposed as a promising material for thermochemical oxygen separation due to its favourable thermodynamics. The introduction of Sb on the B-site was observed to improve the oxygen mobility and surface reactions under operation as a SOFC cathode. Here we investigated the effect of increasing the Sb concentration by probing the thermodynamics of oxygen defect formation computationally and related this to experimental thermal analysis results. It is suggested from computational thermodynamic values and DSC results that this compound would be better suited to thermochemical oxygen separation (0.5 to 1.3 eV/ O atom). Subsequent isothermal cycling experiments revealed rapid redox kinetics between 500 and 800 °C under alternating N_2 and compressed air atmospheres, exceeding that of $SrFeO_3$ and $SrCoO_3$ previously reported within literature.

Through the combination of experimental and computational methods, it is postulated Sb influences the neighbouring cobalt cations within the structure, by lowering the crystal field splitting to change the electronic configuration to an intermediate spin state. Thus, making oxygen evolution more favourable due to increasing the e_g* electrons close to 1 – nearer the preferred filling of 1.2. Although further increased incorporation of Sb limits the ultimate amount of oxygen exchange due to the increased concentration of strong Sb-O covalent bonds and slower oxygen migration within the lattice.

The fast redox kinetics is not translated over to thermochemical water splitting systems due to the material instability against conventional reactor materials such as Al_2O_3 under thermal reduction conditions to produced $CoAl_2O_4$. This phase was observed to produce hydrogen, however, did not reform the original strontium cobalt perovskite and therefore could not be thermochemically cycled. It was suggested the search for more stable perovskite materials for thermochemical water splitting should continue and the $SrCo_{1-x}Sb_xO_{3-\delta}$ compounds are better suited for oxygen separation technologies.

7. Investigating the effect of iron concentration in $(La_{0.8}Sr_{0.2})_{0.95}Cr_{1-x}Fe_xO_{3-\delta}$ for thermochemical water splitting

In this chapter we present our study on the understanding of the ratio between chromium and iron content on the B-site of $(La_{0.8}Sr_{0.2})_{0.95}Cr_{1-x}Fe_xO_{3-\delta}$ compounds. These commercial powders are known for their high stability over a wide range of partial pressures from their previous use as oxygen transport membrane materials [265] Here, we use similar techniques to the previous chapter to understand their feasibility for thermochemical water splitting catalysts.

7.1. Introduction to $(La_{0.8}Sr_{0.2})_{0.95}Cr_{1-x}Fe_xO_{3-\delta}$

Lanthanum chromium-based perovskites have been of interest for several years for use as oxygen transport membranes due to their high stability over a wide range of oxygen partial pressures. [312] Oxygen transport membranes operate as dense ceramics whereby oxygen is transported across a chemical potential gradient from the high P_{O_2} side (P_{O_2} = 0.21 atm) to a low P_{O_2} side (P_{O_2} = 10^{-20} atm) where it takes part in reactions as an oxidising agent (Figure 7-1). Additionally, materials used for this technology require fast mixed ionic and electronic conduction properties. This allows for the improvement in speed at which in bulk oxygen diffuses across the membrane, and allows for the accommodation of thicker yet more robust and industrially manageable structures. [313]

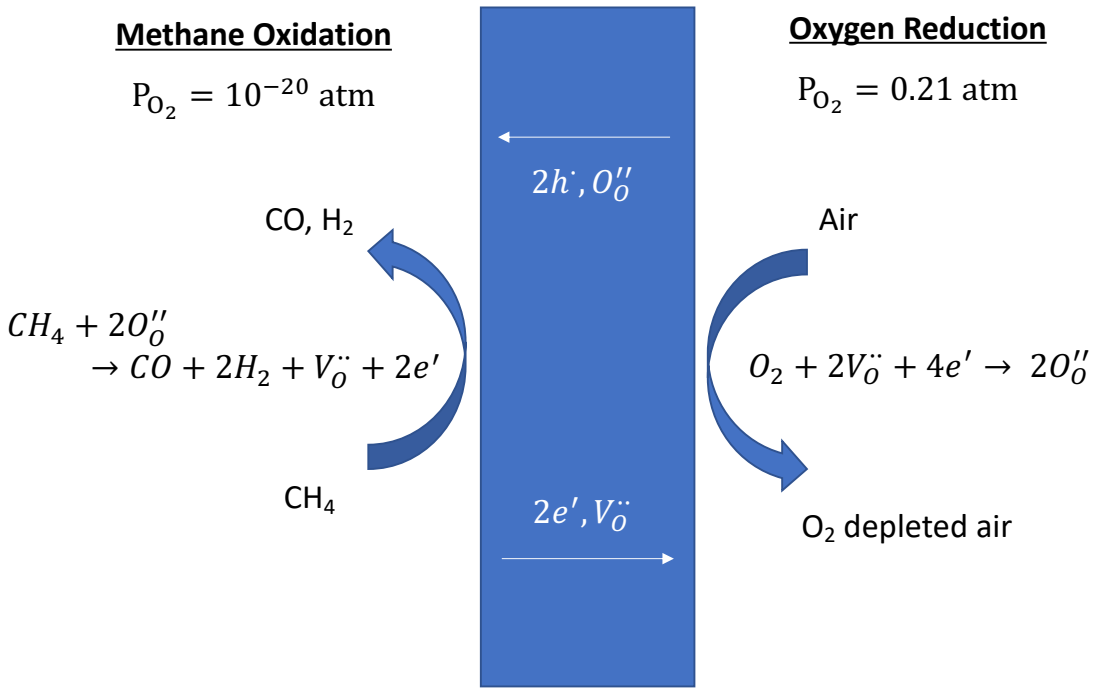

Figure 7-1. Schematic demonstrating the principles of an oxygen transport membrane.

The ionic and electronic conductivity of $LaCrO_3$ is improved by the inclusion of acceptor dopants onto the A-site due to the introduction of oxygen vacancies and holes. [314] Strontium dopants had been included to improve the performance of the chromates in terms of densification, but also the electronic conductivity. [315] Devi *et al.* proposed a 20% Sr concentration for optimal electronic conductivity. [316] Furthermore, Ramos and Atkinson also demonstrated doping with strontium improved the surface exchange and bulk diffusivity within this class of perovskites, due to the improvement of the p-type conduction and increase in probability of oxygen vacancies being present within the lattice. [317] Xiong *et al.* showed the substitution of later first row transition metals onto the B-site promotes electronic charge compensation by oxidising chromium to the 4+ state within the lattice.[318] The ionisation energy of the transition metals substituents in this study suggest it is more favourable for the chromium to compensate the charge rather than Fe or Ni. The increase in chromium oxidation state in Fe substituted compounds the was confirmed by Lü *et al.* using Mössbauer spectroscopy.[319] The features within the spectra revealed the presence of $Fe^{3+}O_6$ octahedra within the structure. Upon heating in low P_{O_2} $Fe^{3+}O_5$ pentahedra were formed suggesting a Cr^{4+}/Cr^{3+} redox couple. Furthermore, Shen *et al.* demonstrated inclusion of Fe cations on the B-site can improve in the oxygen diffusivity and surface exchange rate through the increased presence of oxygen vacancies within the structure. [320]

Lanthanum chromate perovskites have demonstrated redox cyclability by use as a methane oxidation catalysts.[321]–[323] Recently, B-site substituted lanthanum chromate perovskites have been reported for thermochemical splitting reactions with comparable gas production volumes and kinetics to ceria. [160], [324], [325] Increased concentrations of Mn or Co on the B-site improved the oxygen evolution performance, however at a cost of the thermodynamic favourability for re-oxidation. [325] Carrillo *et al.* took advantage of the lanthanum chromates stability under high temperatures, to perform several short thermochemical cycles under isothermal conditions (T_{red}=T_{ox}). [160] The authors noticed similar patterns to Bork *et al.* [325] where lower oxygen volumes are produced with higher chromium concentration, however it was observed oxidation kinetics improved, peaking with the composition $La_{0.6}Sr_{0.4}Cr_{0.85}Mn_{0.15}O_3$. Naturally, it was of interest to investigate the Fe incorporation since this lies in between Mn and Co on the top row of the transition metal group. In this chapter we will investigate the $(La_{0.8}Sr_{0.2})_{0.95}Cr_{1-x}Fe_xO_{3-\delta}$ (x= 0.1, 0.2 and 0.3) perovskites for thermochemical water splitting to try and understand the effect of Fe concentration on the performance.

7.2. Results and Discussion

7.2.1. Initial powder characterisation

Three compositions of $(La_{0.8}Sr_{0.2})_{0.95}Cr_{1-x}Fe_xO_{3-\delta}$ (x = 0.1, 0.2 and 0.3) powders were supplied by Praxair inc. X-ray diffraction was used to determine the starting crystal structure of the powders. Each of the structures was refined to a $R\bar{3}c$ structure in agreement with previous reports (Figure 7-2 to Figure *7-4*). [326], [327] It must be noted there are minor traces of a $SrCrO_4$ secondary phase in this batch of powders as spotted previously by Shen. [327] This phase is identified by the presence of three peaks between 25 and 30°. This is further confirmed by XPS analysis where it is observable the increased presence of Sr 3d surface peaks and Cr^{6+} peaks in the Cr 2p spectra (Figure 7-5 and Figure *7-6*). Other authors have reported this secondary phase, but it is removed upon heating the compounds. [328], [329] Bork *et al.* also noted the presence of this impurity phase but suggested it is removed after thermochemical cycling at 1200/800 °C. [325] However, Russo *et al.* have reported the presence of Cr^{6+} at the surface of Sr-free $LaCrO_3$ compounds therefore suggesting a small concentration maybe within the perovskite lattice.[330]–[332]

The refinement results suggested a lengthening of the lattice parameters with increased Fe content (Table 7-1). Although the reliability parameters indicate a non-perfect fitting due to the presence of the $SrCrO_4$ secondary phase, some trends can still be observed. The ionic radii of iron ions are larger than chromium ions due to increased d-orbital filling. This could be the cause for the *c* lattice parameter to increase by approximately 0.04 Å between compositions. The difference between the chromium and iron cations is in a similar range of 0.03 Å (Cr^{3+} =0.615 Å, Fe^{3+} = 0.645 Å). [333] However the *a* lattice parameter only expands by an order of magnitude less. The anisotropic expansion of the *c*-direction could be due to changes with oxidation state of the Cr within the structure. As mentioned when introducing the perovskite in the in the previous section, the B-site cation is usually a transition metal that can be in many different oxidation states. Some authors suggest the chromium is partially oxidised to a 3/4+ state upon the introduction of Sr-acceptor cations. [318], [319], [334] Although, the higher Cr valence state would have a lower ionic radius. The Goldschmidt tolerance factor does decrease with increasing Fe content (Table 7-1) and the discrepancy between the change in lattice parameters could be due to a cooperative octahedra tilting one of the directions, however further experiments would be required to confirm this theory.

An alternative explanation for the increased lattice parameters could be due to the presence of inherent oxygen vacancies within the structure from synthesis. The negative charged imposed by strontium acceptor dopants are compensated by positive defects such as holes or oxygen vacancies. Oxygen vacancies can acquire a larger space within the crystal lattice. [335] Previous Mossbauer spectroscopy experiments observed the presence of square pyramidal $Fe^{3+}O_5$ features within these perovskites. [319] The increase in iron concentration would make these features more abundant. Furthermore, this correlates with the increase in ionic conductivity of these perovskites with increased iron content.[320] Mössbauer spectroscopy is not able to be used to understand the chromium concentration. An attempt at quantifying the initial oxygen stoichiometry, i.e. inherent vacancies present within the lattice, was made through 5% H_2:Ar thermogravimetric analysis. However, since these perovskites are stable in reducing atmosphere, it was unable to accurately quantify the oxygen since the TGA was unable to reach the temperatures required to reduce the perovskite to its constituent metal oxides. Ideally a technique like neutron diffraction would be used to determine the oxygen content through the Rietveld refinement of this phase. Furthermore, it could reveal more insights into the presence of B-site cations and oxygen coordination within the structure.

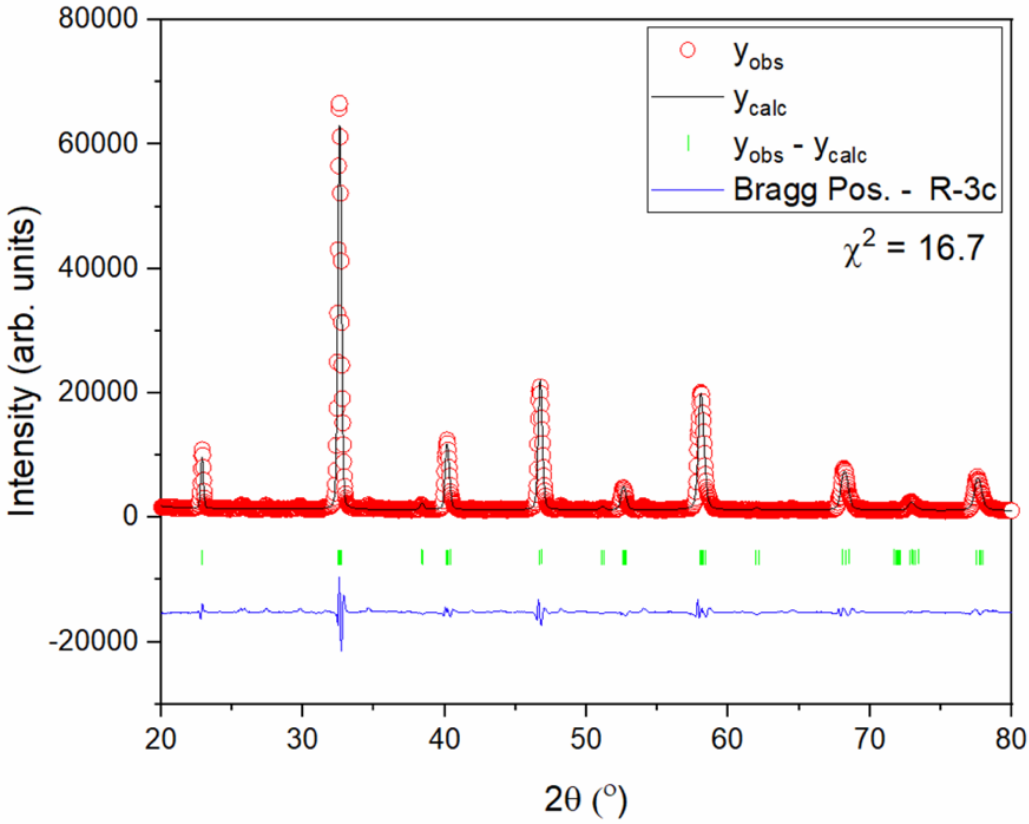

Figure 7-2. Le Bail refinement of LSCrF-8273 pristine powder with a $R\bar{3}c$ space group.

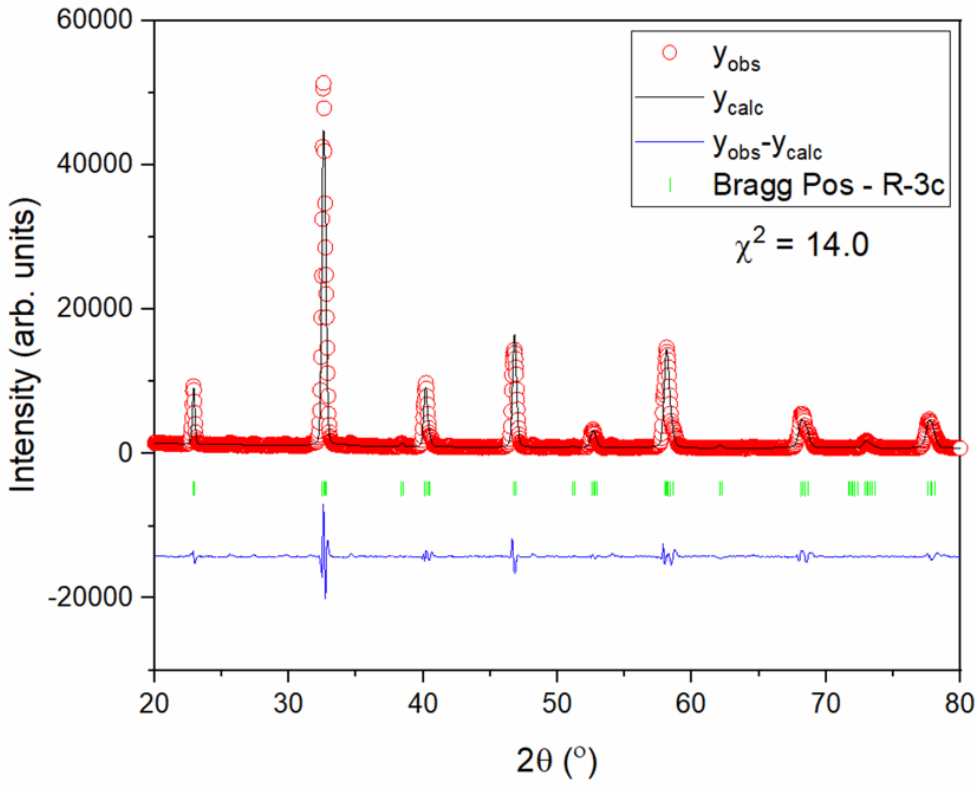

Figure 7-3. Le Bail refinement of LSCrF-8282 pristine powder with a $R\bar{3}c$ space group.

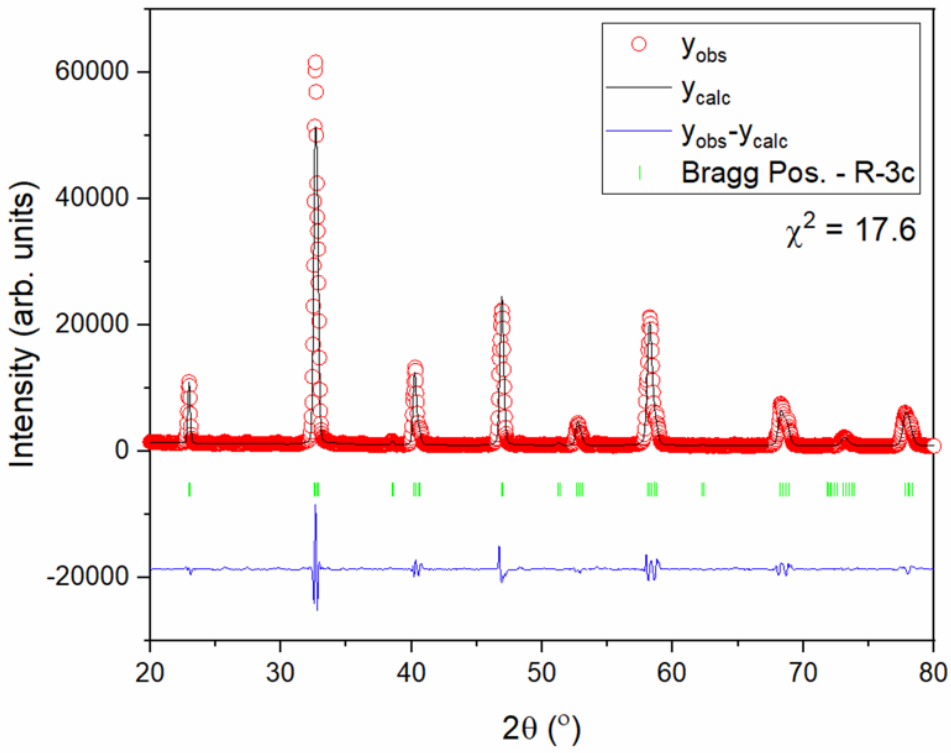

Figure 7-4. Le Bail refinement of LSCrF-8291 pristine powder with a $R\bar{3}c$ space group.

Table 7-1. Outputted lattice parameters from Le Bail refinement of LSCrF powders.

	LSCrF - 8273	**LSCrF - 8282**	**LSCrF – 8291**
a (Å)	5.506(1)	5.5038(0)	5.494(1)
c (Å)	13.424(7)	13.3828(5)	13.3414(4)
Cell Volume (Å^3)	352.5(2)	351.0(2)	348.7(2)
χ^2	16.7	14.0	17.6
Goldschmidt tolerance factor	0.923	0.925	0.927

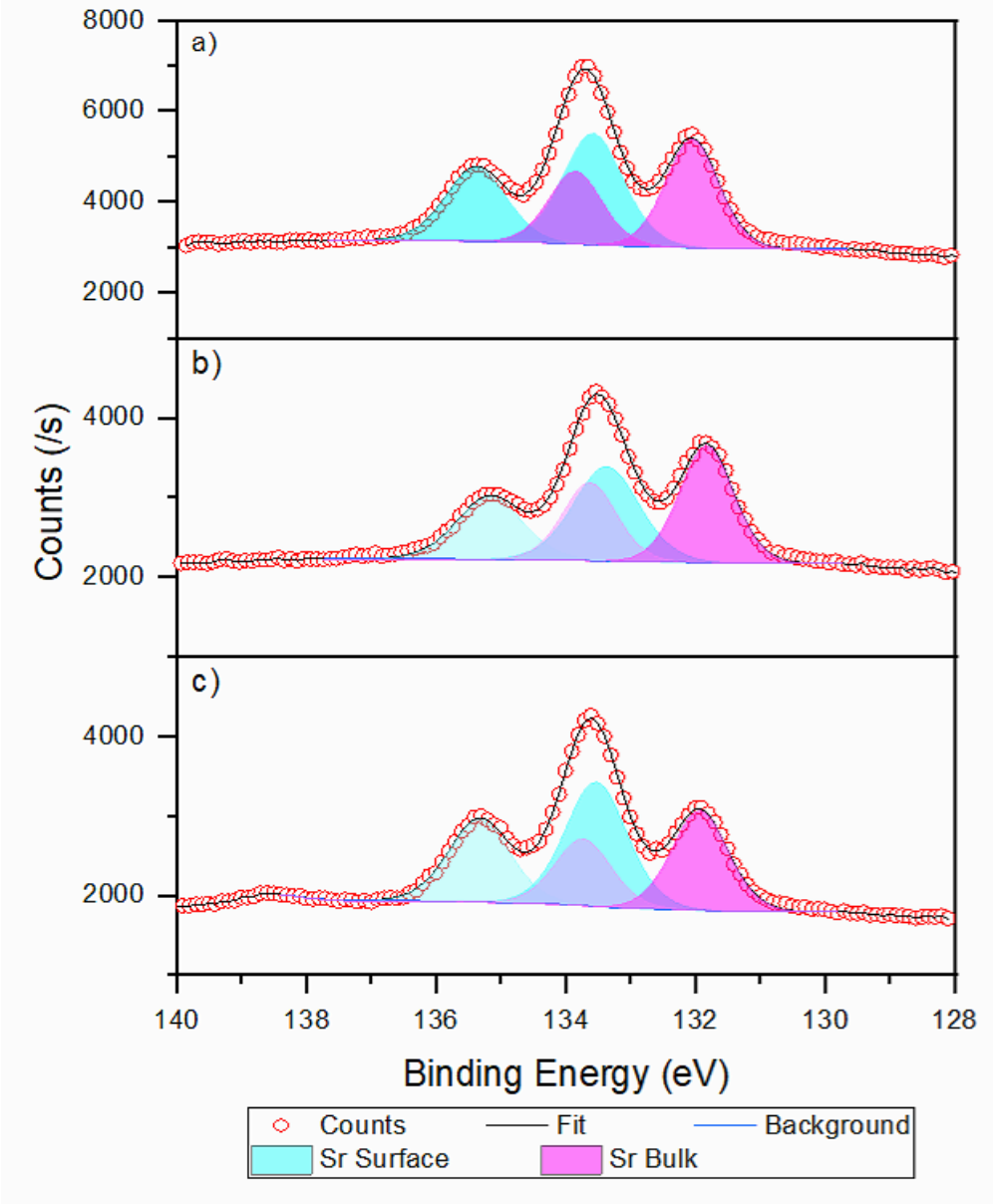

Figure 7-5. XPS Spectra for the Sr 3d level for a) LSCrF-8273, b) LSCrF-8282 and c) LSCrF-8291.

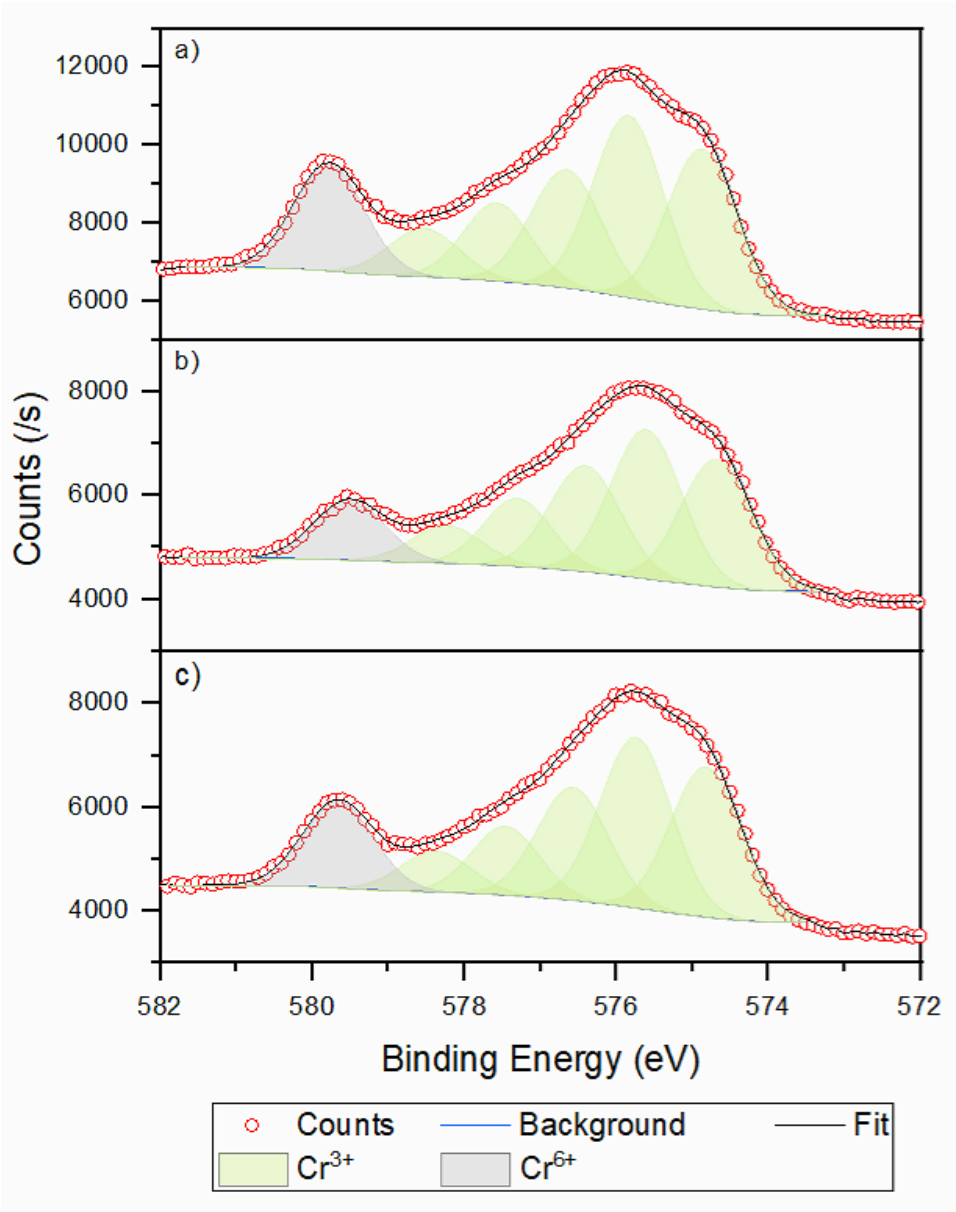

Figure 7-6. XPS Spectra for the Cr 2p level for a) LSCrF-8273, b) LSCrF-8282 and c) LSCrF-8291.

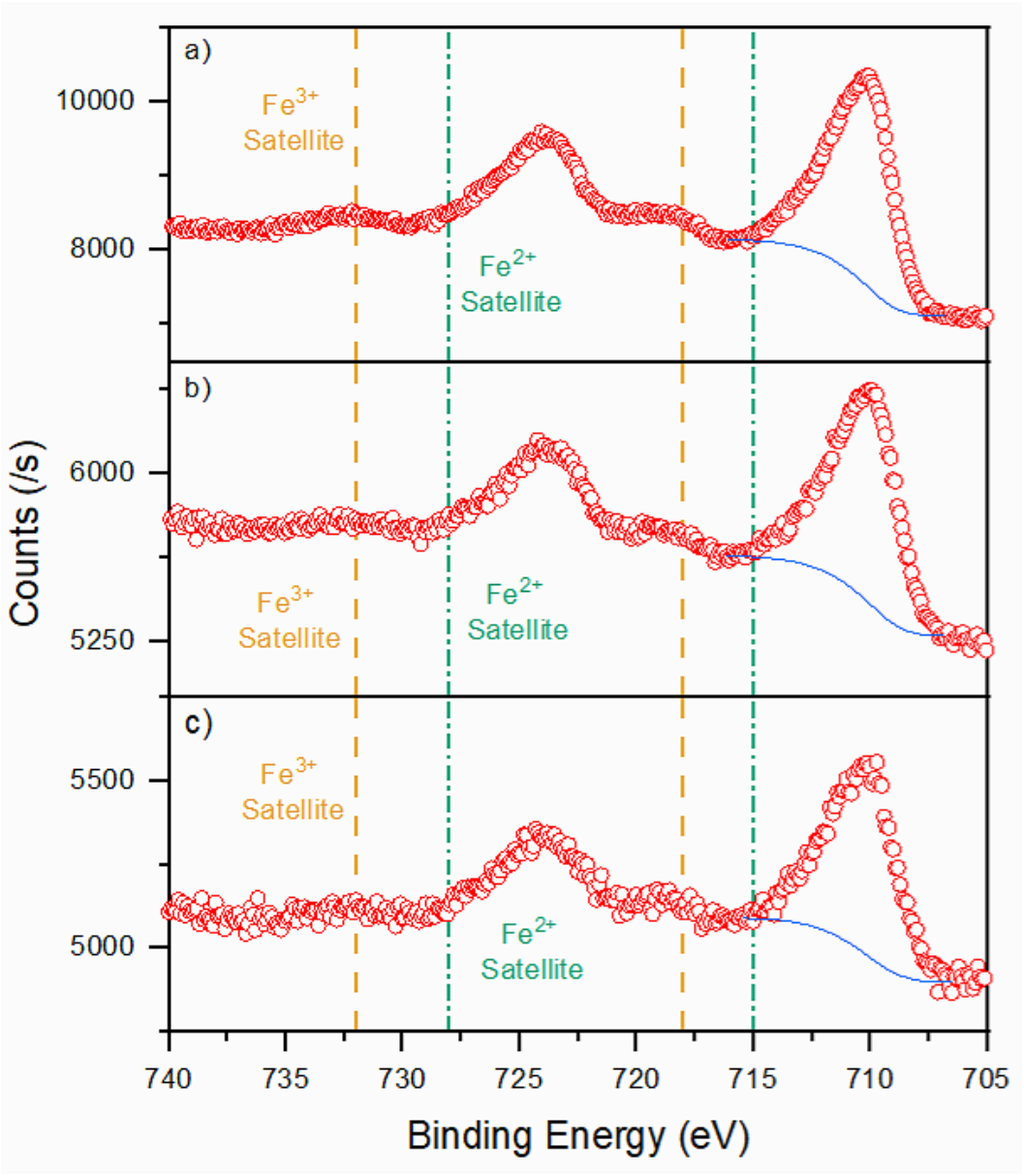

Figure 7-7. XPS Spectra for the Fe 2p level for a) LSCrF-8273, b) LSCrF-8282 and c) LSCrF-8291.

Secondary electron micrographs revealed the powders to composed of 100 μm compacted spheres (Figure 7-8a). These spheres are structurally stable when manoeuvring the powder between vessels however a small amount of force can cause the powders to break into its constituent particles. Upon inspection by higher magnification the spheres revealed a high surface roughness that can be beneficial to providing a large active area for redox reactions (Figure 7-8b).

a)

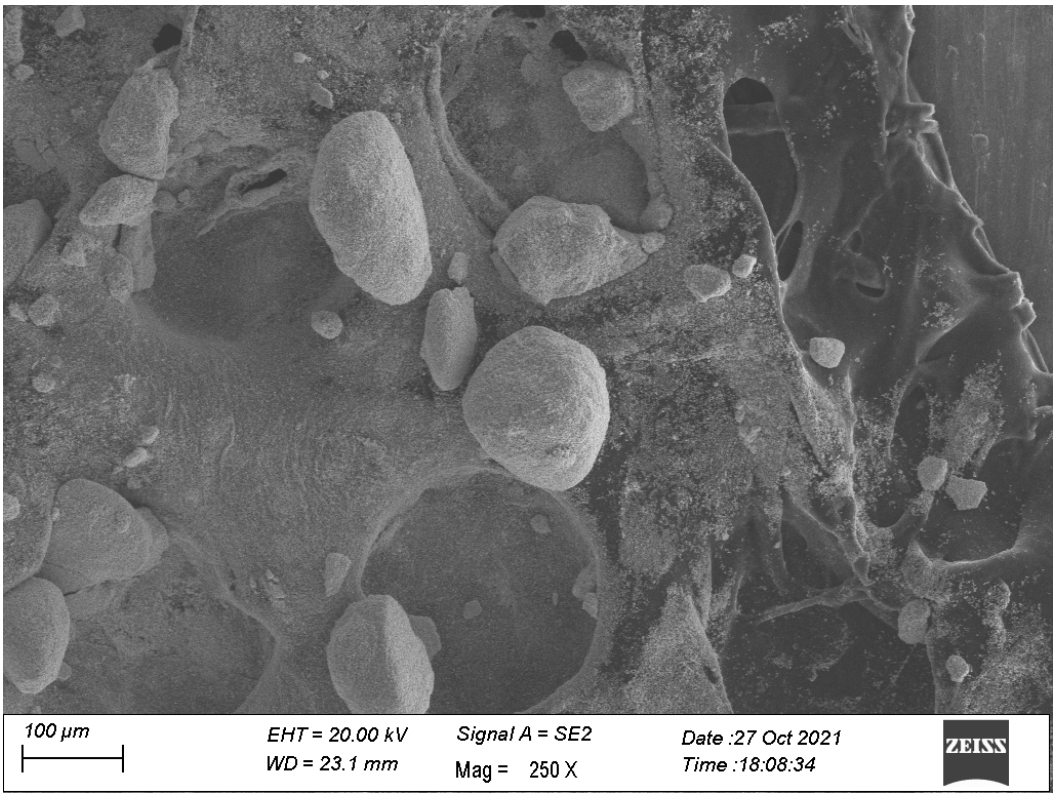

b)

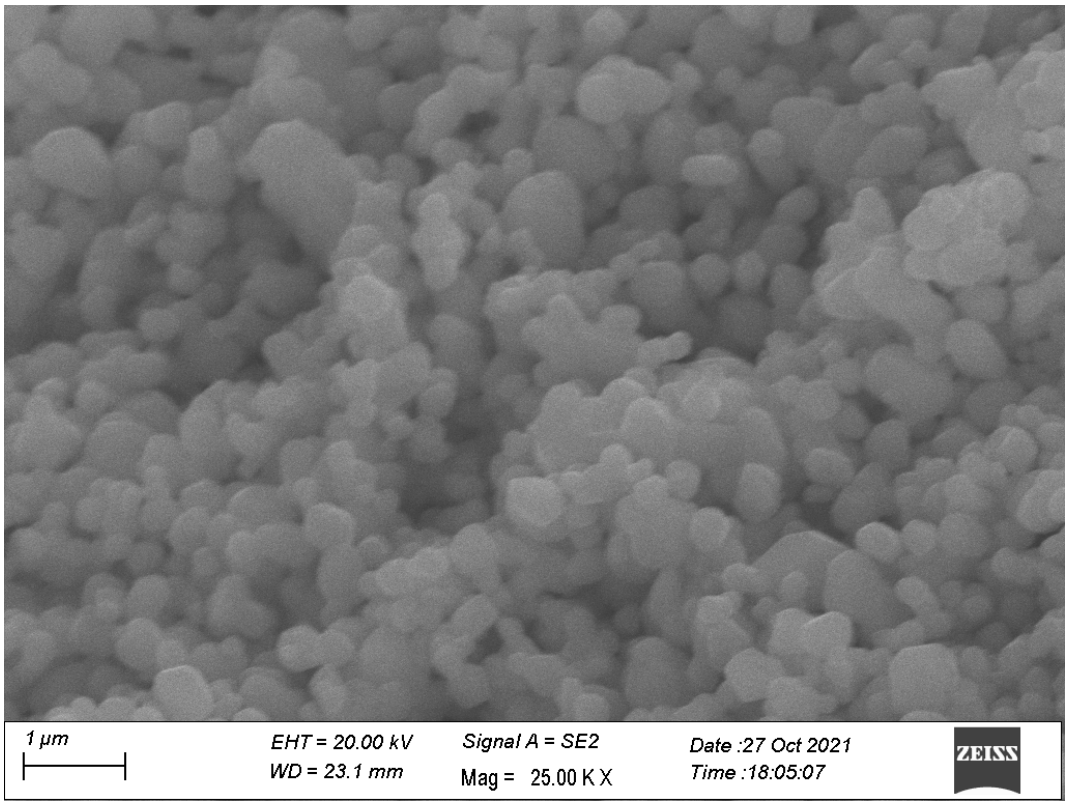

Figure 7-8. Secondary electron micrographs of the LSCrF-8282 powder.

7.2.2. Thermal Behaviour under low P_{O_2}

The thermal reduction of each powder was investigated using simultaneous thermal analysis (TGA-DSC) coupled with an oxygen sensor to measure the evolved oxygen. Approximately 50 mg of each powder was heated to 1450 °C under a flowing 100 ml min^{-1} nitrogen environment at a rate of 20 °C/min.

Figure 7-9 shows the oxygen evolution from the LSCrF powders. The oxygen starts to be detected at approximately 800 °C, significantly higher than the Sb-substituted strontium cobalt oxides reported in the previous chapter (300 to 400 °C). However, the production rates and volumes are much lower – approximately 1/3 in comparison (Figure 6-5c). This is most likely due to the increased stability of the perovskites and lowered reducibility of the B-site cations present within the structures. There is a clear dependence on the Fe concentration with the oxygen evolution volumes and rates (Figure 7-10). With higher Fe concentrations having larger and faster oxygen evolution. On initial inspection this could be due to the Fe-O bonds being relatively facile to break compared to the Cr-O bonds. An observation that was previously observed for Mn and Co substituted $LaCrO_3$ perovskites. [160], [325]

DFT was used to help understand the Fe dependence on oxygen evolution. In similar practice to the previous chapter, spin polarised DFT+U calculations were performed using the PBE functional within VASP (U_{Cr} = 3.7 eV). The undoped $LaCrO_3$ structure was taken from the materialsproject (mp-19357), and PAW pseudopotentials were used consistent with those reported in the database. The lattice parameters and atomic positions were relaxed using a plane wave cut off of 520 eV, electronic convergence of $1x10^{-6}$ eV and force convergence of 0.01 eV/Å. An initial 2×2×2 gamma-centred k-point mesh was used to sample the Brillouin zone. The primitive unit cell was expanded to include 16 formula units ($La_{16}Cr_{16}O_{48}$) and Fe cations replaced Cr to form substitution contents of 0.0625%, 0.125% and 0.25% of the B-site (1, 2 and 4 Fe cations respectively). These structures were run using the same parameters as the $LaCrO_3$ structure but with a U correction of 5.3 eV. The final energies were calculated using single-point calculations with the Blöchl tetrahedron method and a 4x4x4 gamma-centered k-point mesh. Figure 7-11 displays the geometrically relaxed structures.

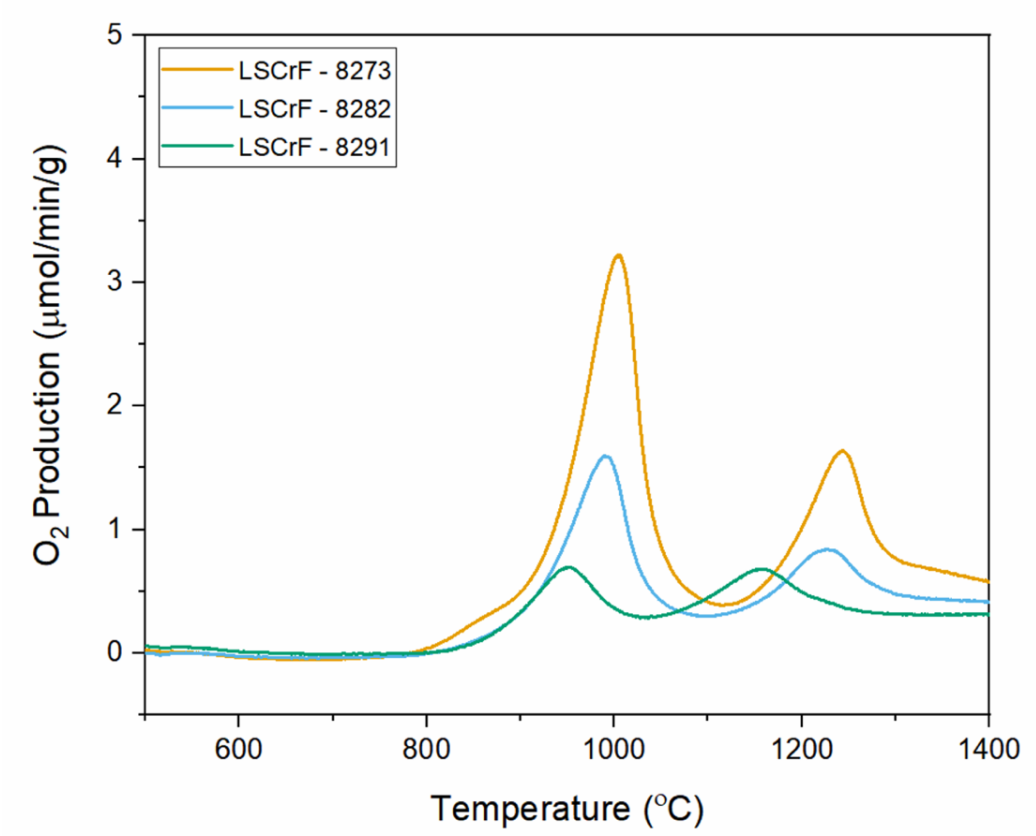

Figure 7-9. Oxygen evolution from the LSCrF powders heating at 20 °C/min.

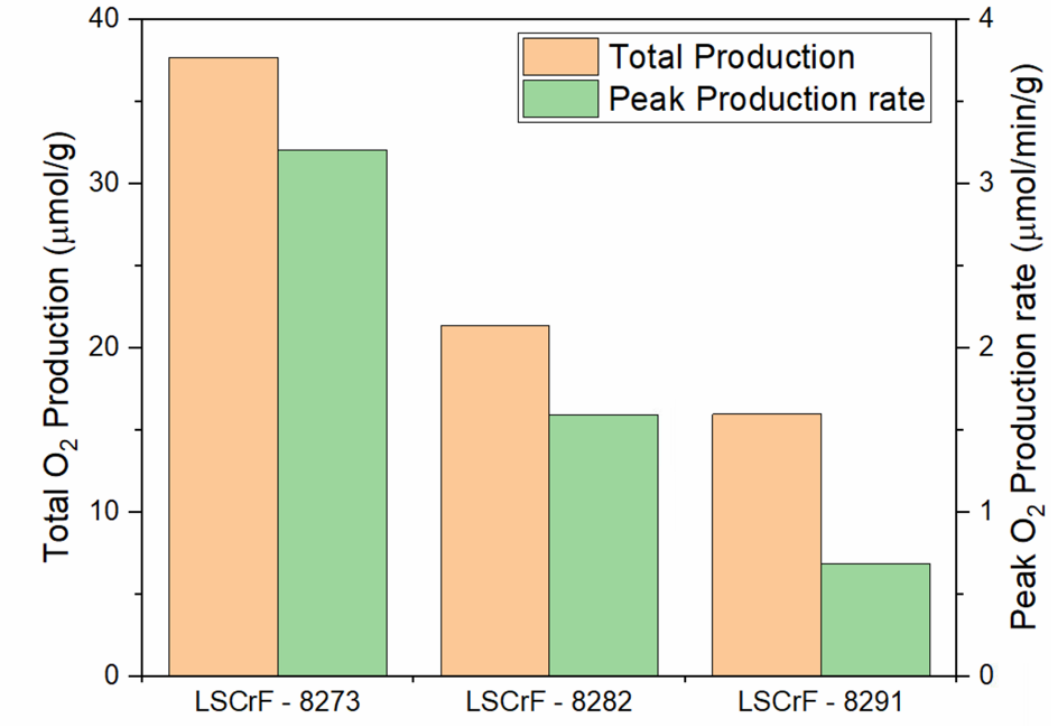

Figure 7-10. Comparisons between the total oxygen production and peak oxygen production of the LSCrF powders up to 1200 °C.

a)

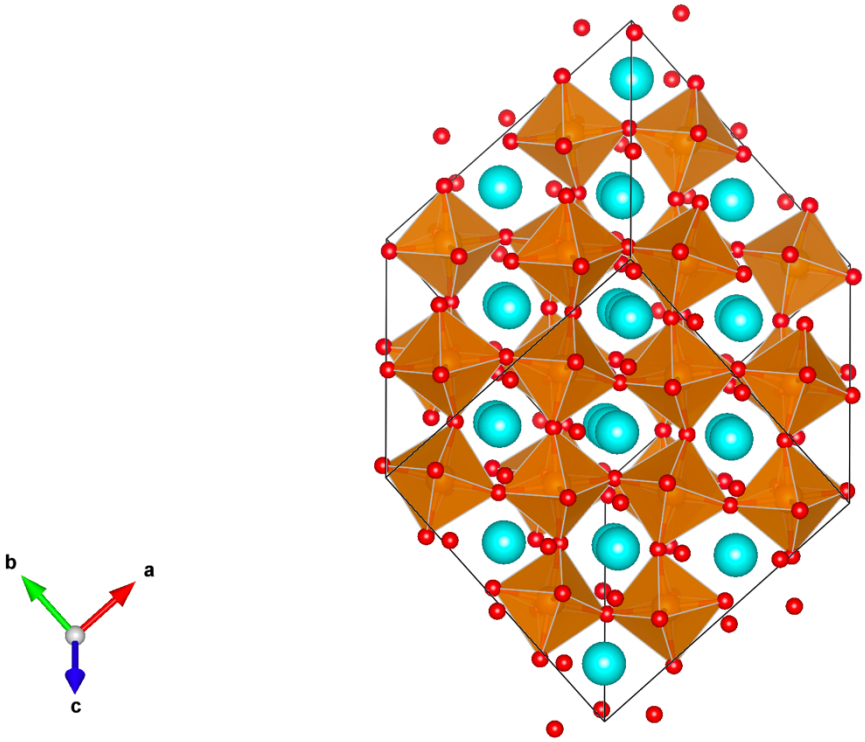

b)

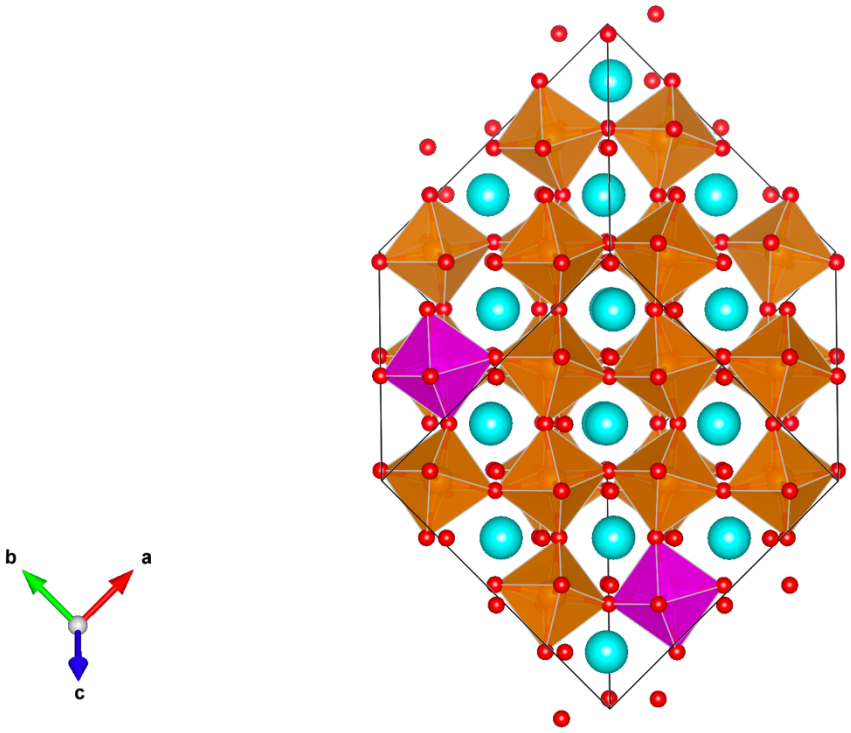

c)

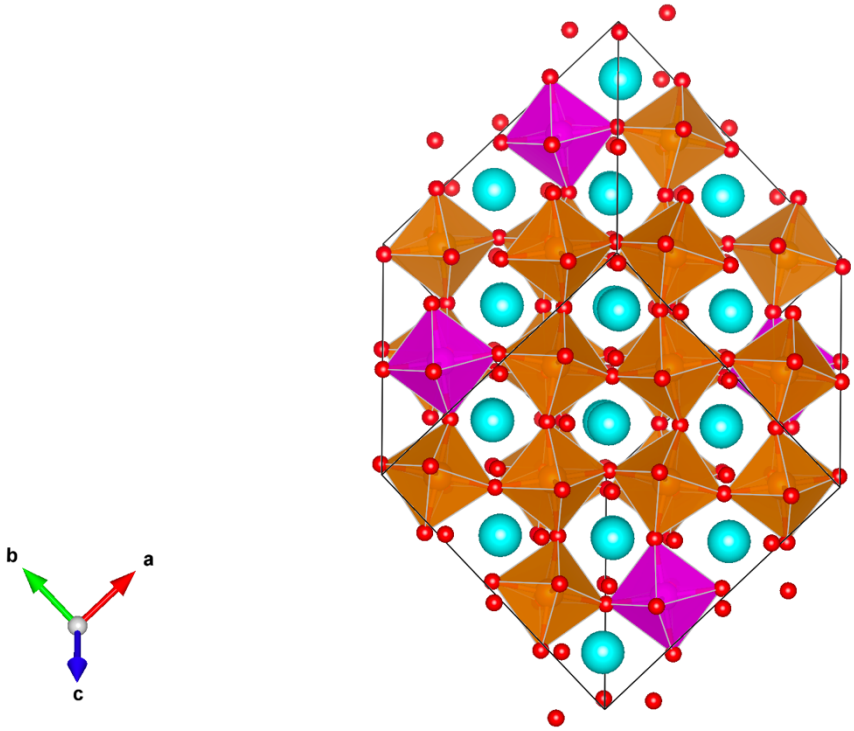

d)

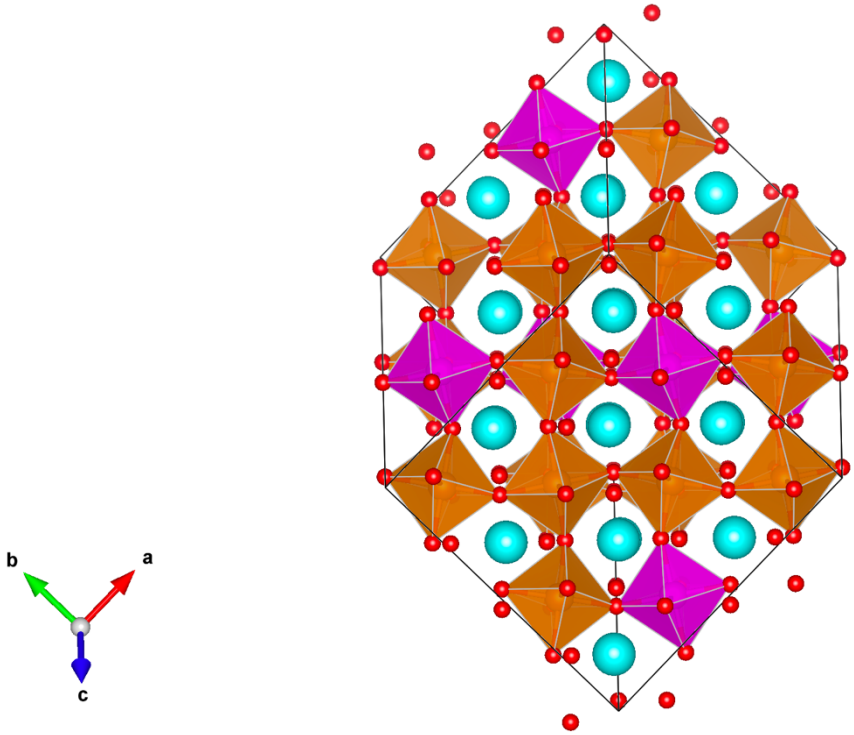

Figure 7-11. Geometrically relaxed structures of the $LaCrO_3$ structures with a) 0%, b) 6.25%, c) 12.5% and d) 25% Fe substituted onto the B-site.

Single oxygen vacancies were introduced separately from the first and second coordination spheres of the Fe and the atomic positions relaxed with fixed lattice parameters. The reduction enthalpy was calculated using the same equation as previous chapter. (Equation 6.2). Figure 7-12 displays the oxygen vacancy formation energy with respect to Fe concentration and coordination sphere. It is observed that the vacancy formation energy is approximately 0.6 eV/O atom lower in the first coordination sphere to the Fe cation. Beyond the first coordination sphere the formation energy shows little change. Therefore the differences in the oxygen evolution from these materials can be attributed to the abundance of Fe-O bonds within the structure. Figure 7-13 displays the density of states plots for each of the Fe-doped $LaCrO_3$ structures. The density of states of the undoped structure predicts the Fermi energy to sit just above the valence band edge in agreement with the p-type conduction behaviour of this material. [317] The band gap is observed to be in the region of 2.4 eV in agreement with other first principle reports.[336] However, this is slightly lower than the experimental value of 3.4 eV.[337] Upon introduction of iron into the structure, Fe d states appear just below conduction band edge lowering the band gap in agreement with previous reports. [337]–[339] This can have a secondary effect of shifting the oxygen states closer to the conduction band making reduction more facile.[340], [341]

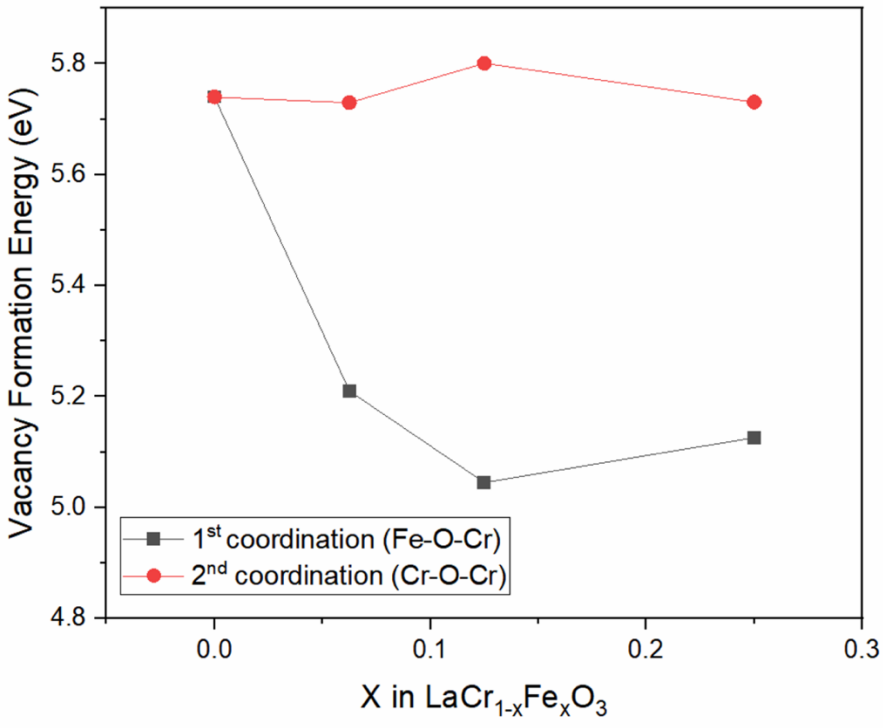

Figure 7-12. Oxygen vacancy formation energy for $LaCr_{1-x}Fe_xO_3$ as function of Fe content a spatial coordination to the Fe cation within the structure.

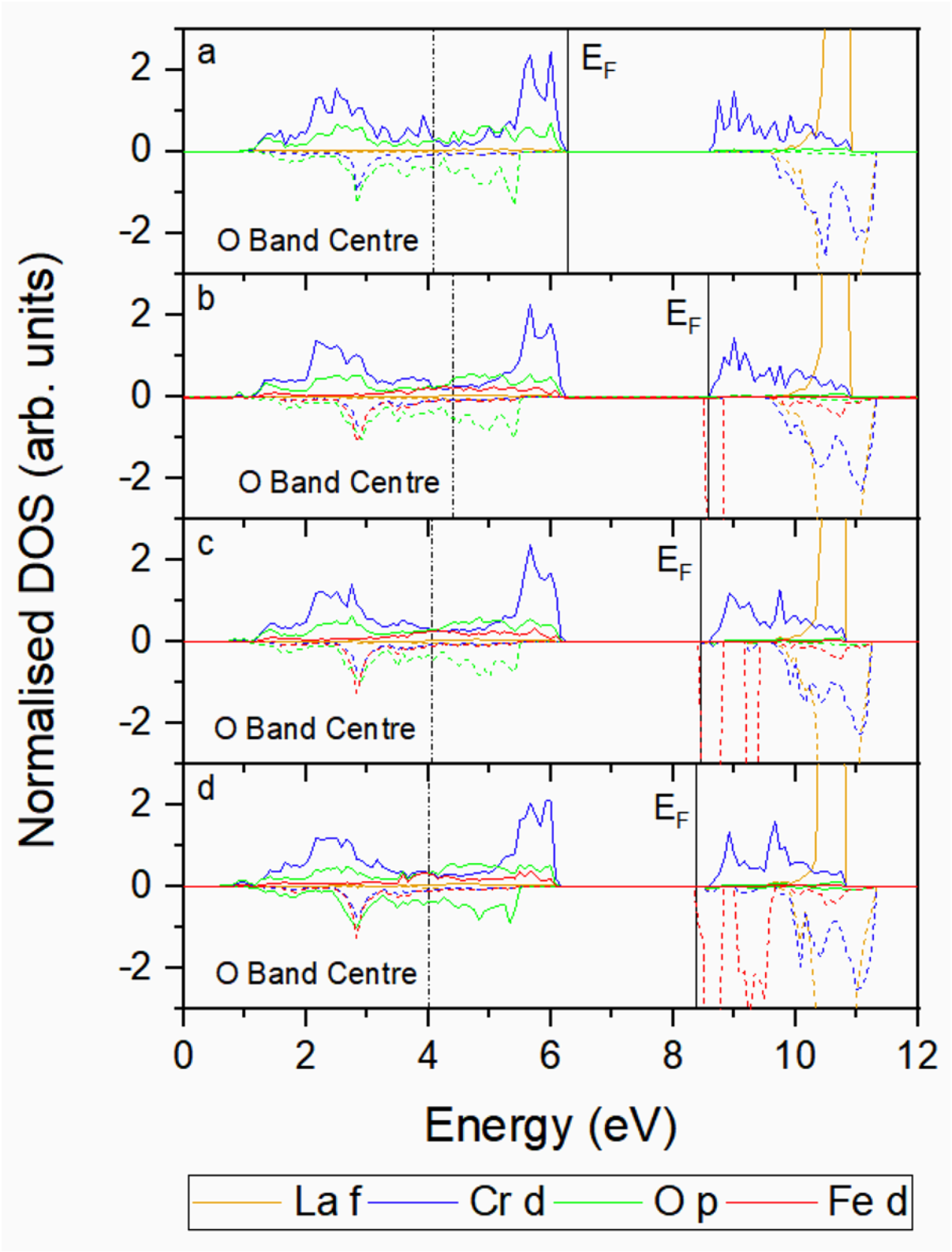

Figure 7-13. DOS plots for a) 0%, b) 6.25%, c) 12.5% and d) 25% Fe content on $LaCr_{1-x}Fe_xO_3$.

The reduction enthalpies displayed in for this compound are significantly greater than those needed for thermochemical water splitting. Although, the strontium present in the experimental compounds was not accounted for within the structure since it would provide a large

configurational problem to try and simulate. It is expected this acceptor ion would likely influence the electronic structure and cation oxidation states and make vacancy formation more favourable as commonly reported in the literature.[342] The experimental thermodynamic were attempted to be investigated by TGA. The powders were held at temperatures between of 800 and 1200 °C with incremental increases of oxygen partial pressure from 10^{-5} to 0.02 atm. However, the mass was unable to be stabilised despite extended time holds of up to 2 hours. Fortunately, literature sources report the oxygen non-stoichiometry of similar materials ($La_{0.9}Sr_{0.1}CrO_3$, $La_{0.7}Sr_{0.3}CrO_3$ and $La_{0.75}Sr_{0.25}Cr_{0.5}Fe_{0.5}O_3$). [343], [344]

Figure 7-14a and b display the partial molar enthalpy and entropies of these materials respectively in comparison with previously reported thermochemical water splitting materials.[126], [345] The increasing concentration of strontium on the A-site from 10% to 30% in lanthanum chromate perovskites lowers both reduction enthalpy and entropy values. As previously discussed, this could be due to the ionic compensation of the acceptor dopant charge promoting the oxidation state of the Cr to the more unfavourable 4+ state. This effect has been observed in other lanthanum-based perovskites – particularly $LaMnO_3$ and $LaFeO_3$. [346]–[348] Some authors suggest the strontium moves the oxygen band centre closer to the Fermi energy thus allowing more facile electron transfer in the reduction reaction.[342] Furthermore, comparing $La_{0.7}Sr_{0.3}CrO_3$ and $La_{0.75}Sr_{0.25}Cr_{0.5}Fe_{0.5}O_3$, we observe the introduction of iron onto the B-site to further lower the reduction enthalpy and entropy, but also expands the oxygen non-stoichiometry that can be accommodated within the perovskite. This agrees with theoretical calculations by Bork *et al.* who observed lowering of thermodynamic driving force for reduction with increased Mn concentration in $La_{0.6}Sr_{0.4}Cr_{1-x}Mn_xO_{3-\delta}$. [349] This further corroborates the TGA results for increased oxygen production with higher Fe content in Figure 7-9. The thermodynamic values of the powders investigated in this chapter can be roughly estimated through linear interpolation of the partial molar enthalpy and entropy values for a given value of δ presented in Figure 7-14a and b. A non-stoichiometry of 0.1 was chosen here to be comparable with benchmark thermochemical redox perovskites. The interpolated vales are presented in Table 7-2. Despite being lower than the benchmark material ceria, the predicted enthalpies are in the suitable range for thermochemical water splitting outlined by Meredig and Wolverton. [294]

On the other hand, the entropy values should be approached with caution. The interpolation window is narrow thus suggesting very similar values for each of the perovskites. When considering the configurational entropy term, increasing the iron content would be expected to increase the entropy within the system if randomly distributed randomly over the lattice. Furthermore, Bork *et al.* predicted an increase in entropy for increasing Mn concentration in $La_{0.6}Sr_{0.4}Cr_{1-x}Mn_xO_{3-\delta}$. [349] Here, we observe a decrease in entropy as the perovskite goes from $La_{0.7}Sr_{0.3}CrO_3$ to $La_{0.75}Sr_{0.25}Cr_{0.5}Fe_{0.5}O_3$. Although the slight differences in La to Sr ratio could play a factor, as well as the A-site deficiency present within the powders. However there is the possibility of Fe and Cr ordering or vacancy clusters, being present in the lattice, that will consequently lower the randomness. Ultimately, it is crucial for future work to determine these thermodynamic quantities for the LSCrF powders in this study. Other methods such as coulometric titration can be used as an alternative method to understand the non-stoichiometry over a wider range of oxygen partial pressures from 10^{-5} to 10^{-20} atm.

a)

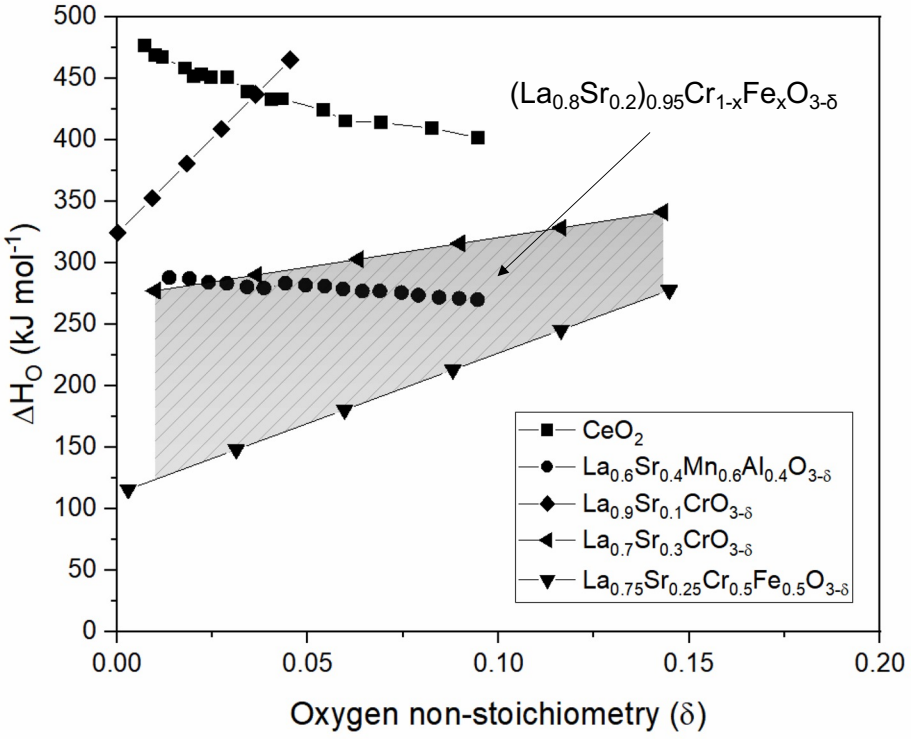

b)

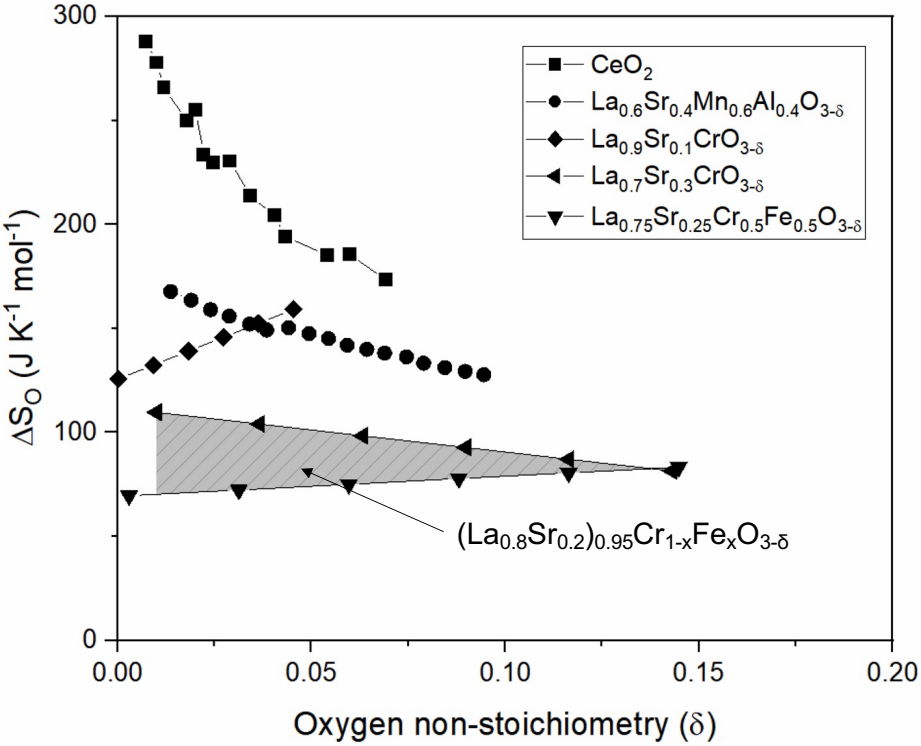

Figure 7-14. Partial molar enthalpy and entropy for lanthanum chromium-based perovskites and other thermochemical water splitting materials reported within literature. [126], [345]

Table 7-2. Interpolated partial molar enthalpy and entropy values for the LSCrF powders used in this study.

Fe content	ΔH_O (kJ mol^{-1})	ΔS_O (J K^{-1} mol^{-1})
0.1	301.91	88.17
0.2	283.09	85.87
0.3	264.27	83.58

7.2.3. Crystallographic and Morphological stability

The crystallographic stability of the compounds through the reduction reaction was measured by *in-situ* high temperature XRD under flowing nitrogen gas. The diffractograms were collected over a range of 20 to 60 ° at 100 °C intervals up to 1200 °C. The patterns at each temperature interval are shown in Figure 7-15. Each of the compounds demonstrated high crystallographic stability with no obvious deviations from the original $R\bar{3}c$ crystal structure. The peaks shift to lower angles in agreement with usual high temperature measurements due to lattice thermal expansion (increase in interplanar distance, d) (Equation 6.1). The lattice parameters were refined using FULLPROF software.[350]

$$\frac{n\lambda}{2d} = sin\theta \tag{6.1}$$

The lattice parameters were plotted as a function of temperature (Figure 7-16a and b). A linear fit was applied to each of the lattice parameters. Above 800 °C a contribution from the chemical expansion of the lattice would cause a deviation away from the linear fit due to the increased formation of oxygen vacancies within the structure. However, there is no obvious deviation for any of the compounds tested. This could be due to the possible low oxygen vacancy concentrations within the structure. The step could be better resolved with narrower temperature steps.

Albeit the thermal expansion of the compounds was observed to be larger than the $La_{0.8}Sr_{0.2}CrO_3$ compound reported in the literature, TEC=8.92x10^{-6} K^{-1}.[329] Larger thermal expansion values are observed with increased Fe concentration. This correlates well with the

increase in oxygen evolution rates observed with the TGA data suggesting a chemical expansion of the lattice.

Furthermore, the thermal expansion of the material was not isotropic. The *c* lattice parameter was observed to have a greater thermal expansion of approximately $2x10^{-4}$ Å/°C, however the *a* lattice parameter was observed to have a expansion of approximately $5x10^{-5}$ Å/°C. The anisotropy within the structures could suggest more favourable vacancy sites and vacancy ordering occurring within the lattice. One hypothesis could be the presence of the square pyramidal FeO_5 coordinations that had been observed by Mossbauer spectroscopy.[319] The formation of vacancies on these features can induce a square planar FeO_4 coordination. With vacancies above and below the central transition metal this can order the expansion along one direction. Alternatively, Chen and Grande have attributed anisotropic lattice expansions in $R\bar{3}c$ crystal structures of $La_{1-x}Sr_xFeO_3$ compounds to the straightening of antiferrodistorted octahedra within the lattice induced by increased vacancy concentration as the iron reduces for the 4+ to 3+ state. [351]

The presence of the $SrCrO_4$ peaks present between 25 and 35° in the pristine powder were observed to diminish upon heating in the nitrogen environment. This was also observed by Bork *et al.*. [325] Gupta *et al.* noticed the evolution of iron and chromium rich oxide phases after heating the LSCrF-8273, 8282 and 8291 compounds to 1400 °C under reducing atmospheres. [352] However, the conditions applied during this test are not as reducing, therefore this phase in not observed.

a)

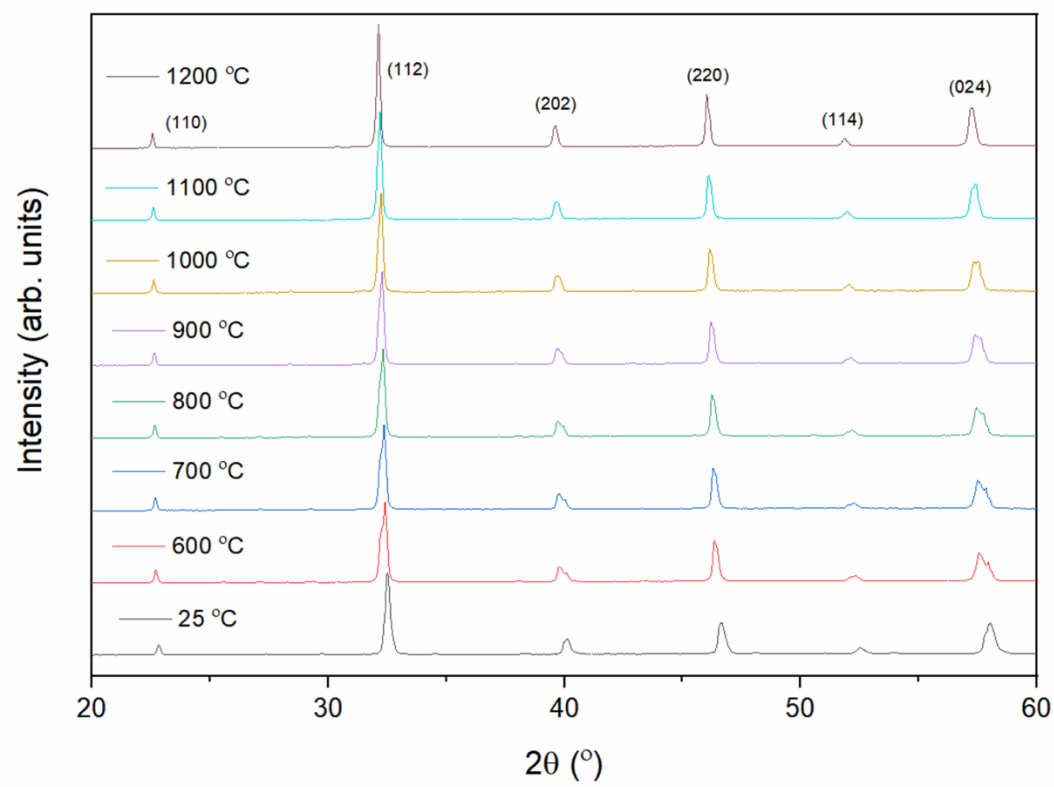
1200 °C
1100 °C
1000 °C
900 °C
800 °C
700 °C
600 °C
25 °C
(110)
(112)
(202)
(220)
(114)
(024)
Intensity (arb. units)
20
30
40
50
60
2θ (°)

b)

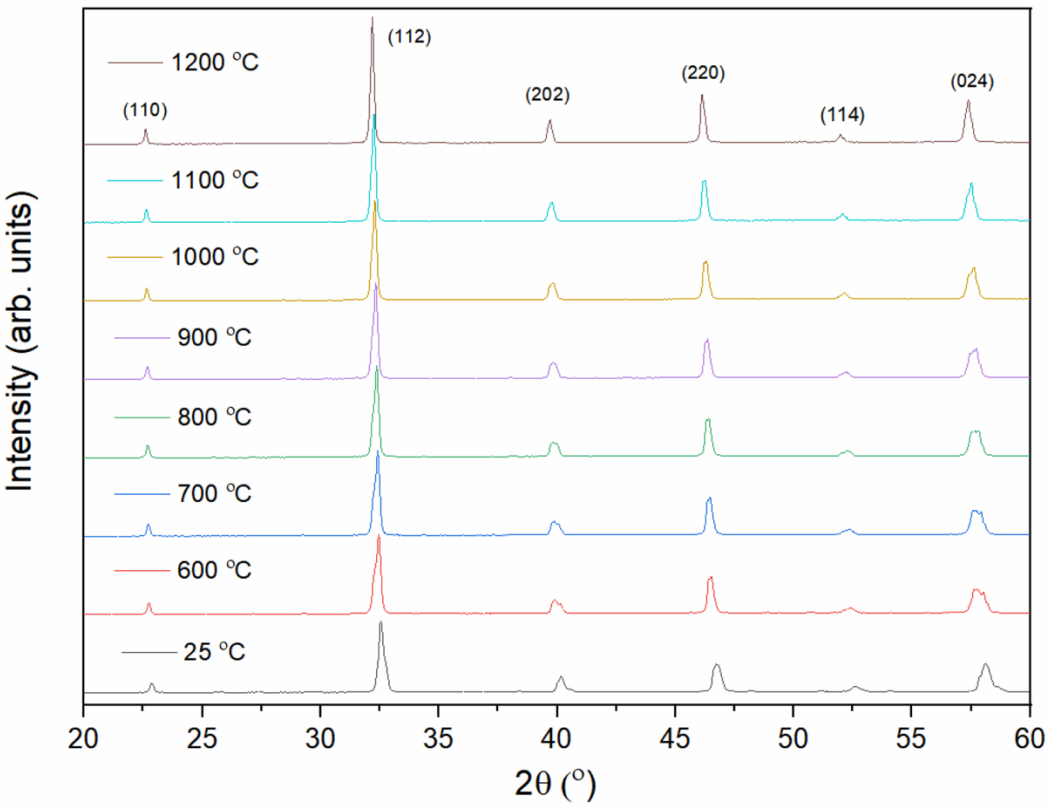
1200 °C
1100 °C
1000 °C
900 °C
800 °C
700 °C
600 °C
25 °C
(110)
(112)
(202)
(220)
(114)
(024)
Intensity (arb. units)
20
25
30
35
40
45
50
55
60
2θ (°)

c)

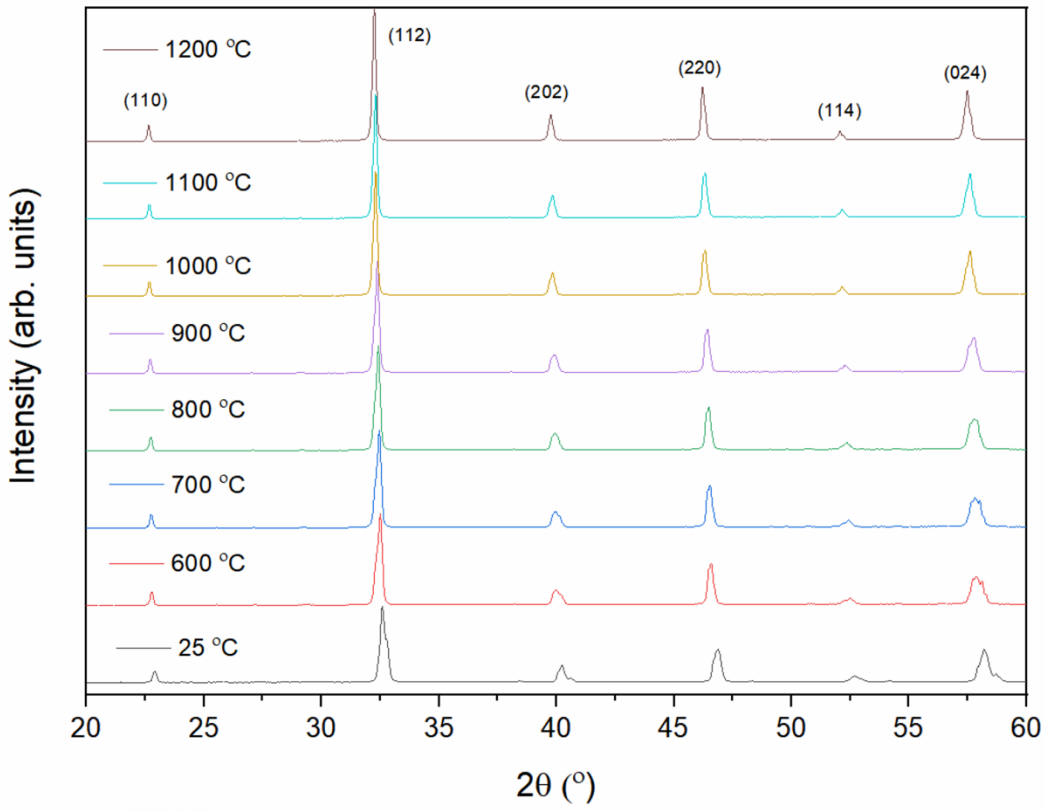

Figure 7-15. High temperature X-ray diffraction under nitrogen up to 1200 °C in 100 °C intervals for a) LSCrF-8273, b) LSCrF-8282 and c) LSCrF-8291.

a)

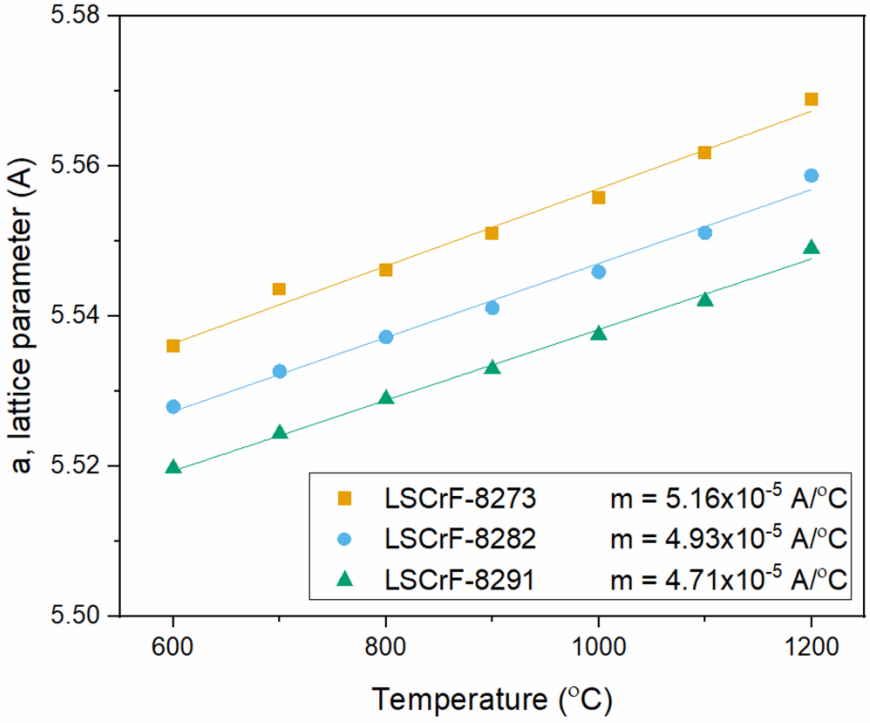
5.58
5.56
5.54
5.52
5.50
a, lattice parameter (A)
600
800
1000
1200
Temperature (°C)
LSCrF-8273 m = 5.16x10-5 A/°C
LSCrF-8282 m = 4.93x10-5 A/°C
LSCrF-8291 m = 4.71x10-5 A/°C

b)

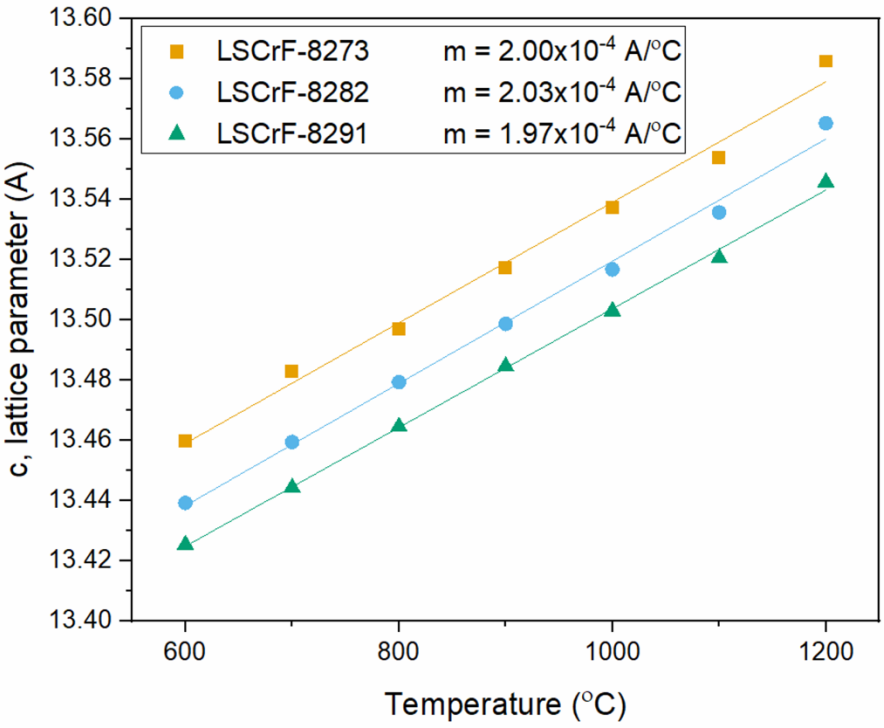
13.60
13.58
13.56
13.54
13.52
13.50
13.48
13.46
13.44
13.42
13.40
c, lattice parameter (A)
600
800
1000
1200
Temperature (°C)
LSCrF-8273 m = 2.00x10-4 A/°C
LSCrF-8282 m = 2.03x10-4 A/°C
LSCrF-8291 m = 1.97x10-4 A/°C

c)

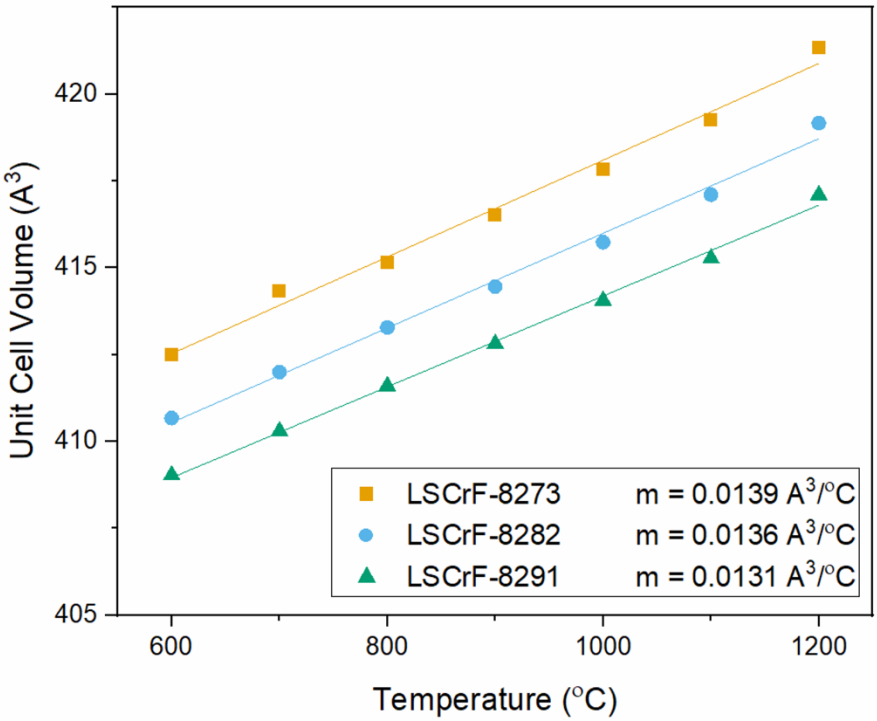

Figure 7-16. Lattice parameters and cell volume as a function of temperature for the LSCrF powders.

Small amounts of powder (<0.1g) were heated to 800, 1000 and 1200 °C and held for 2 hours under a flowing argon environment to allow the use of *ex-situ* techniques for the understanding of the material behaviour during the reduction reaction. Scanning electron microscopy was used to understand the morphological stability of the powders after heating as a function of reduction temperature. The spherical powder structures remained in the size region of 100 µm (Figure 7-17). The surface roughness of these macrospheres was retained throughout all heating temperatures (Figure 7-18). This suggests there were minimal signs of sintering within the first reduction step. However, it is observed greater amounts of electron charging during the electron microscopy thus suggesting the electronic conductivity has decreased.

a)

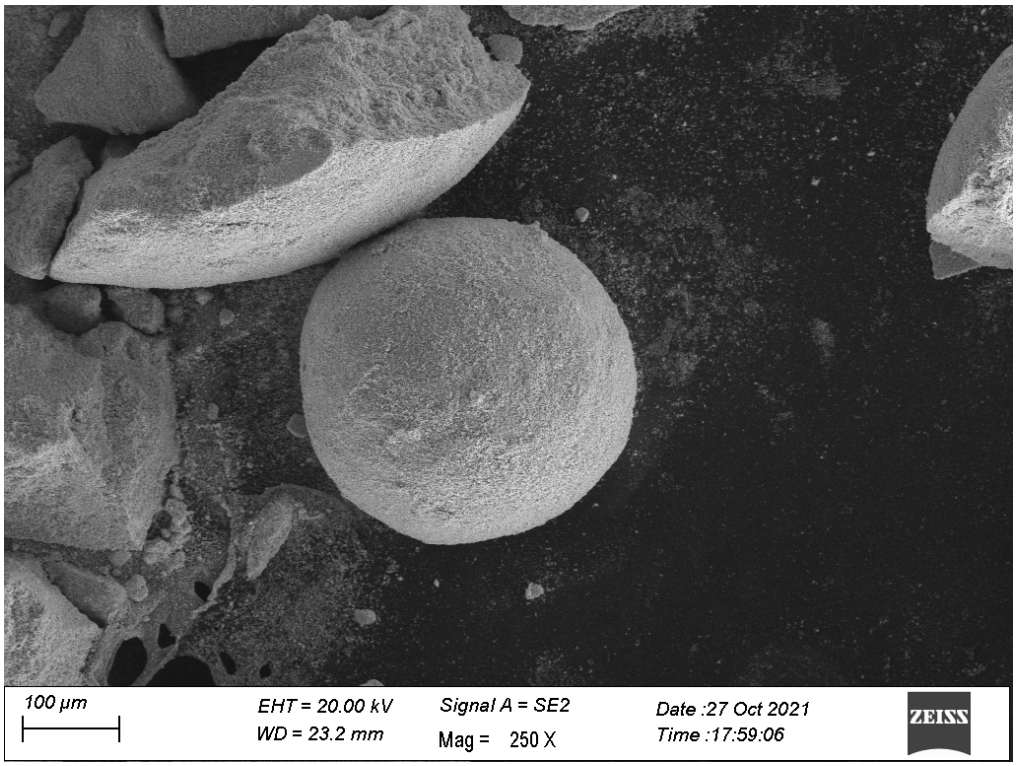

b)

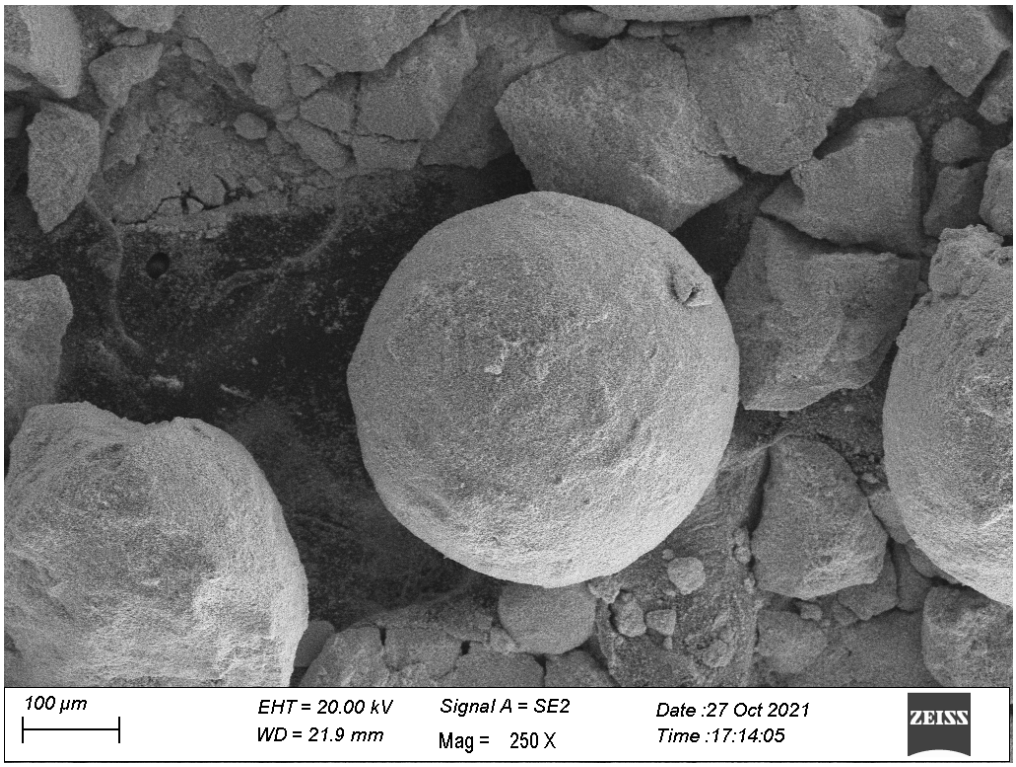

Figure 7-17. Secondary electron image showing the macrosphere structure of the a) LSCrF-8273 and b) LSCrF-8282 powders after heating to 1200 °C for 2 hours under flowing argon.

a)

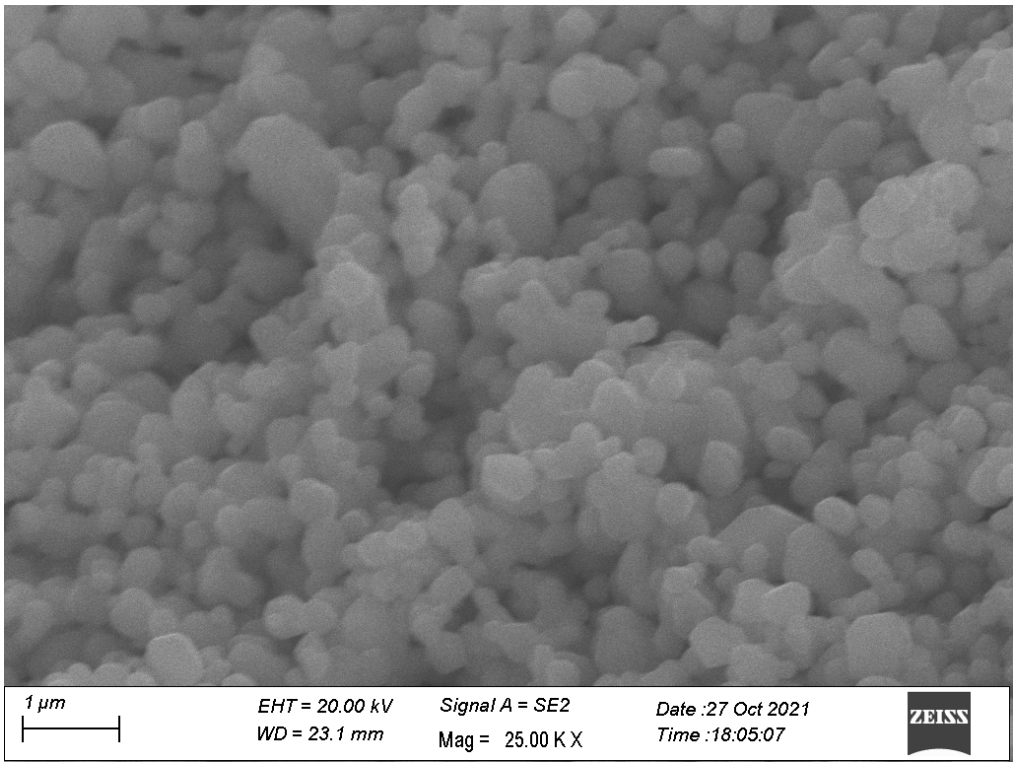
1 µm
EHT = 20.00 kV
WD = 23.1 mm
Signal A = SE2
Mag = 25.00 K X
Date :27 Oct 2021
Time :18:05:07
ZEISS

b)

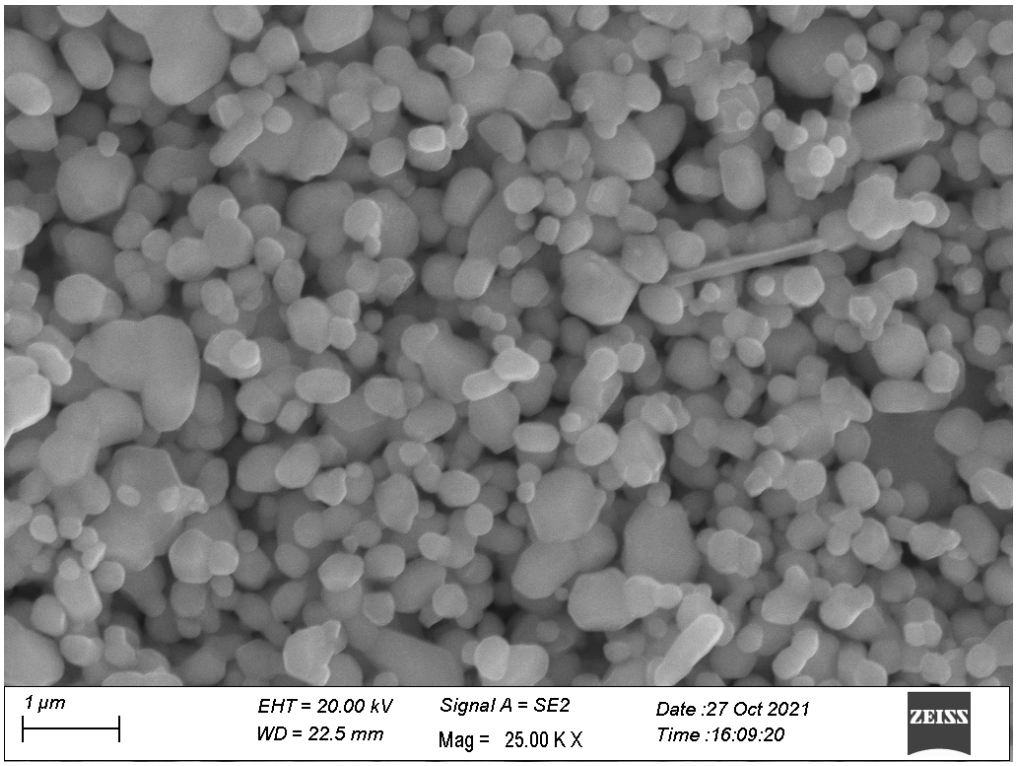
1 µm
EHT = 20.00 kV
WD = 22.5 mm
Signal A = SE2
Mag = 25.00 K X
Date :27 Oct 2021
Time :16:09:20
ZEISS

c)

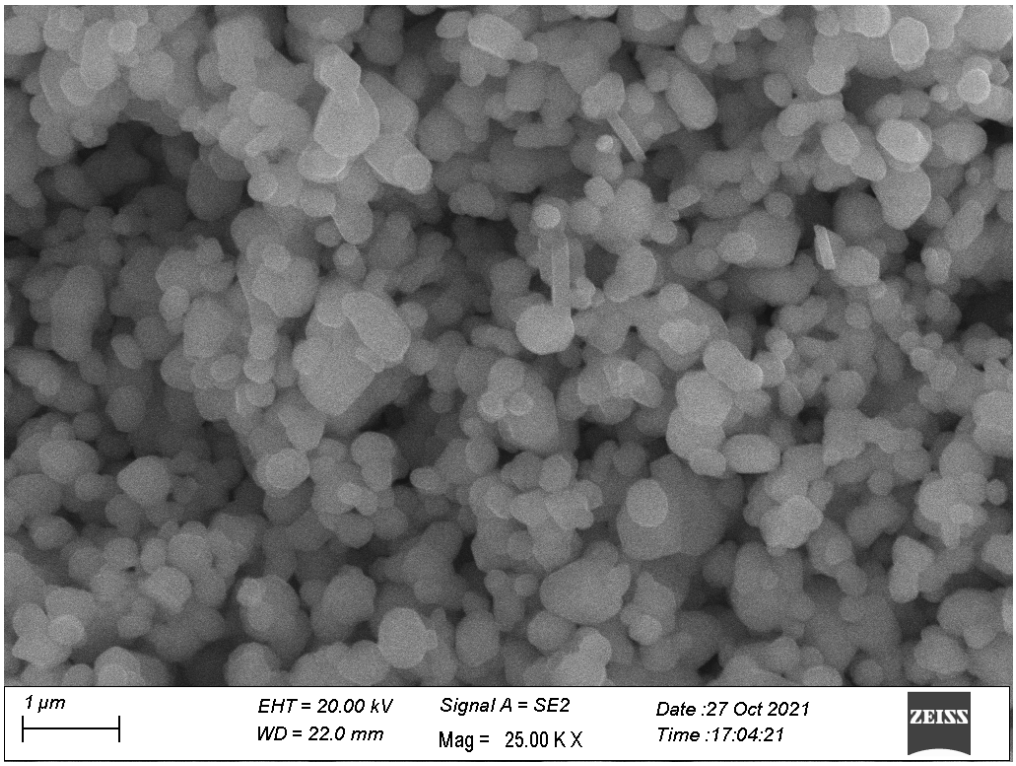

d)

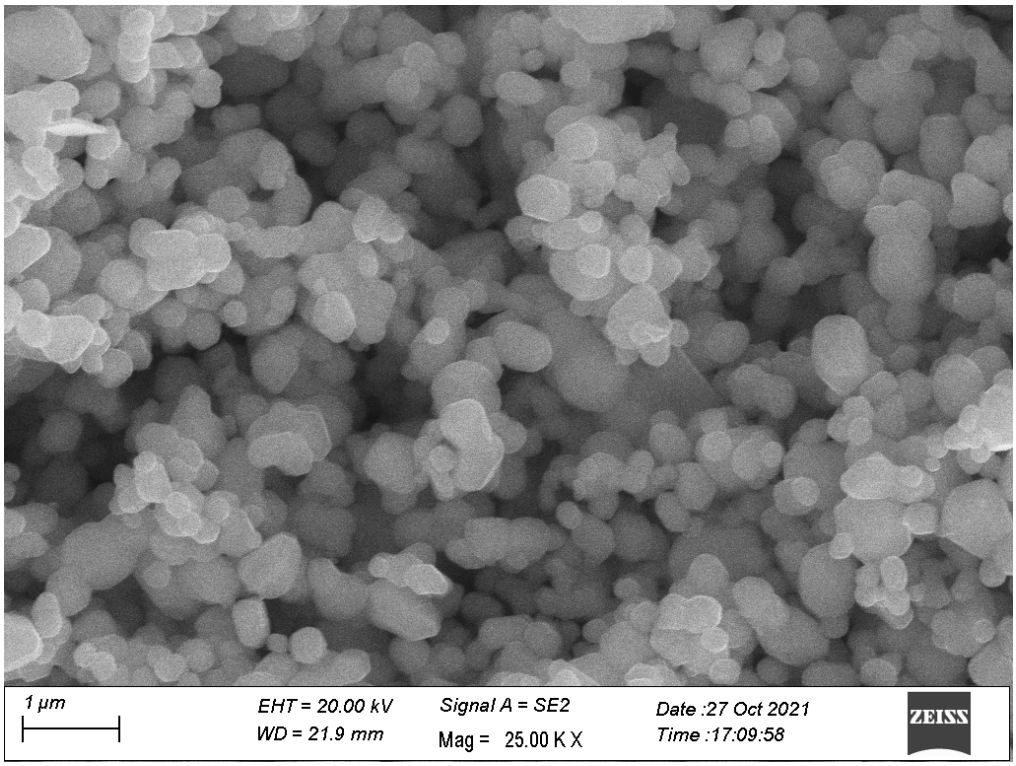

Figure 7-18. Secondary electron micrographs of the LSCrF-8282 powder surface a) as-received and heating under flowing argon for two hours at b) 800 °C, c) 1000 °C and d) 1200 °C.

7.2.4. Thermochemical Water Splitting

Each of the LSCrF powders were investigated for thermochemical water splitting. The water splitting experiments were conducted using the experimental rig described in Chapter 5. Approximately 0.1g of powder was loaded into the alumina reaction tube and purged overnight with argon gas at 200 ml/min. A mass spectrometer was used to analyse the exhaust gases with a mass:charge ratio of 2, 18, 32 and 40, corresponding to hydrogen, water, oxygen and argon respectively. The mass spectrometer current was converted to gas flow rates using calibration of 2% O_2 in argon and 5% H_2 in Argon. Each of the powders were heated to 1200 °C for 1 hour and subsequently cooled to the oxidation temperature of 800 °C for 3 hours in line with the experimental conditions Bork *et al*. used for cobalt substituted lantahanum chromatates.[325] During the oxidation steps the gas was humidified to 50% using de-ionised water. The cycle was repeated using the same reduction conditions, however the oxidation step was extended to overnight (approx. 17 hours) to try and observe the time taken for the oxidation reaction to reach equilibrium i.e. the hydrogen signal returns to 0. As mentioned in chapter 5, due to the setup being completed late into the experimental window of the PhD project, these results are used to provide an indication of water splitting ability. Further testing will be conducted during a subsequent postdoc position to investigate further different temperatures and humidity.

Figure 7-19 to Figure *7-21* show the gas production under a 1200/800 °C redox cycle with 50% humidity. The initial reduction step for each powder shows similar oxygen evolution volumes to those observed by TGA in Figure 7-10 (Table 7-3). The differences could be due to the longer purge time in this experiment that can induce a lower starting oxygen partial pressure or differences in the effectiveness of heat transfer to powder between the two methods, thus producing different reduction extents. The oxygen production levels returned to zero by the end of the reduction isotherm with no further oxygen evolved during cooling to 800 °C. Upon introduction of humidified gas to the gas flow there is a near instantaneous increase in the hydrogen signal up to 9.5 μmol/min/g, 6 μmol/min/g and 2.5 μmol/min/g for the LSCrF 8273, 8282 and 8291 powders respectively. These rates exceeded those observed by $Ce_{0.75}Zr_{0.25}O_{2-\delta}$ reduced at 1400 °C and reoxidised at 800 °C using the same experimental setup. (Figure 7-22). The H_2 production rate of the LSCrF-8273 powder had peak production rate nearly double the doped ceria compound (9.40 μmol/min/g vs 3.25μmol/min/g), despite having a 200 °C lower reduction temperature. Furthermore, the hydrogen produced by these compounds over two hours exceeds the values of other lanthanum chromates ($La_{0.6}Sr_{0.4}Cr_{0.8}Co_{0.2}O_{3-\delta}$) tested under

the same redox temperatures and oxidant concentration (157 μmol/g for x=0.2). [325] This could be due to the replacement of the cobalt with the less reducible Fe cation, and lower strontium concentration in the lattice, increasing the reduction enthalpy and therefore favouring the splitting reaction.

Table 7-3. Gas evolution volumes for the LSCrF compounds over two cycles at 1200 and 800 °C.

LSCrF Compound	Cycle	O_2 Evolved (μmol/g)	Peak O_2 production rate (μmol/min/g)	H_2 Production over 120 mins (μmol/g)	Peak H_2 production rate (μmol/min/g)
8273	1st	114.62	6.03	334.00	9.40
	2nd	0	0	209.84	4.47
8282	1st	90.74	5.10	289.91	5.32
	2nd	18.96	0.82	330.37	5.76
8291	1st	70.53	3.53	190.25	2.13
	2nd	9.18	0.38	215.99	3.00

However, in comparison with the oxygen evolved from the lattice, the expected ratio between H_2 and O_2 is 2:1. This is not observed in this case for either the production rates or production volume, thus suggesting imperfect splitting performance (Table 7-3). Interestingly it is observed the hydrogen production never returns to zero, further suggesting an incomplete reaction. However, Carrillo *et al.* observed this behaviour when isothermally cycling $La_{0.6}Sr_{0.4}Cr_{0.85}Mn_{0.15}O_{3-\delta}$ at 1400 °C. [160] The authors attributed this to thermolysis at the sample surface, however this might be unlikely in these results since the oxidation temperature is 600 °C lower. At this temperature the equilibrium concentrations of hydrogen are negligible. Furthermore, there was no observed increase in the oxygen signal recorded by the mass spectrometer.

The redox cycle was repeated to observe durability of the material; however, the hydrogen production rates and volumes were observed to significantly decrease for the LSCrF-8273 powder (Figure 7-19). Although these results are encouraging and prove thermochemical redox behaviour, further investigations are warranted with repeat experiments at different

temperatures and humidity conditions for improved reliability and better understanding of the kinetic behaviour.

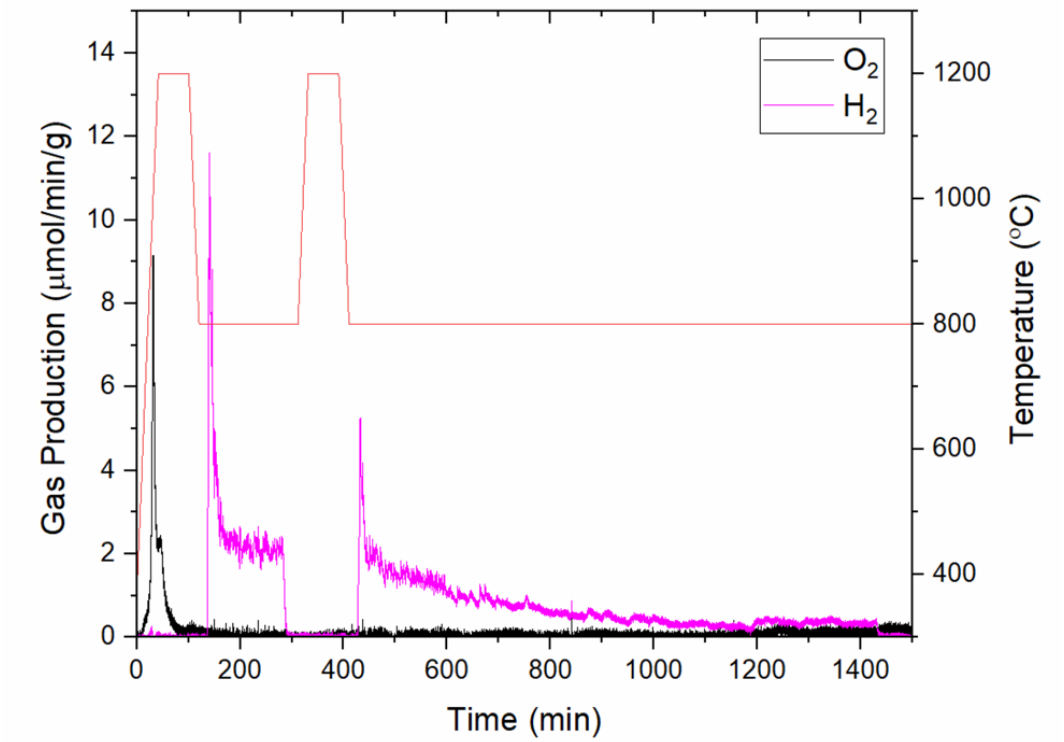

Figure 7-19. Gas evolution from LSCrF-8273 throughout the 1200-800 °C thermochemical water splitting cycle.

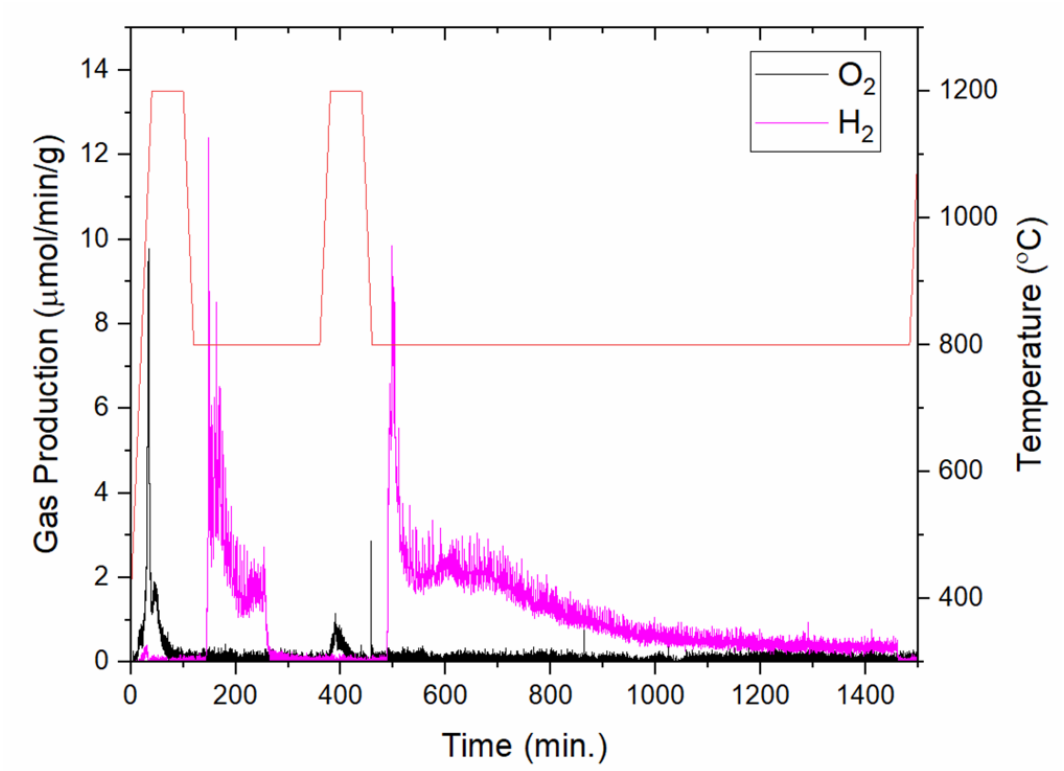

Figure 7-20. Gas evolution from LSCrF-8282 throughout the 1200-800 °C thermochemical water splitting cycle.

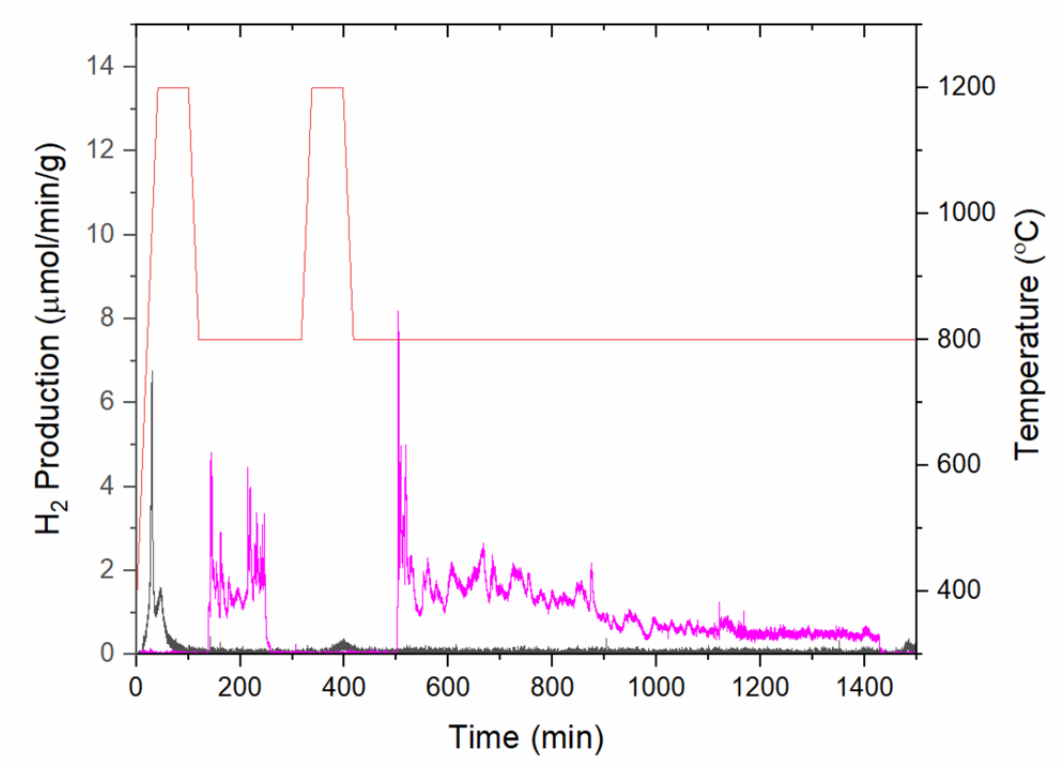

Figure 7-21. Gas evolution from LSCrF-8291 throughout the 1200-800 °C thermochemical water splitting cycle.

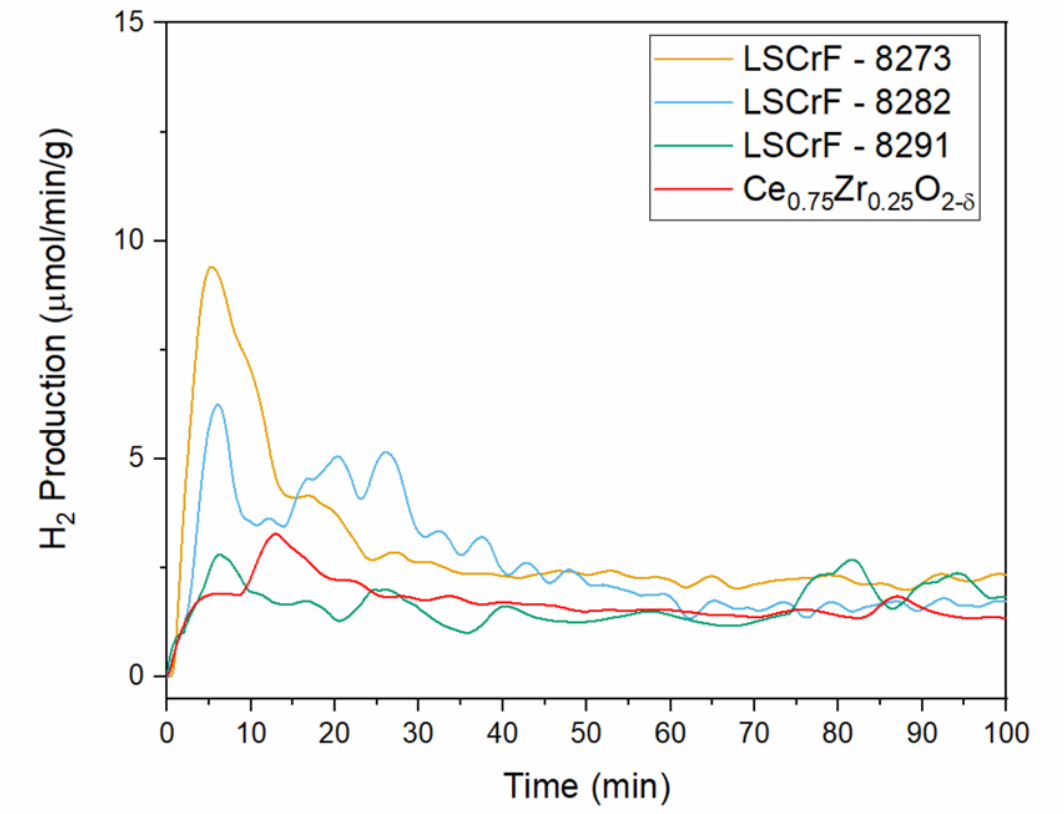

Figure 7-22. Comparison between H_2 evolution of the LSCrF powders (T_{red} = 1200 °C; T_{ox} = 800 °C) and $Ce_{0.75}Zr_{0.25}O_2$ (T_{red} = 1400 °C; T_{ox} = 1000 °C). The signals have been smoothed using an adjacent-average method for enhanced clarity.

The drop in gas production in the second redox cycle suggests a degradation occurring within the material. XRD and SEM were used to understand if there has been any crystallographic or morphological degradation. Bork *et al.*'s investigation into Co substituted $LaCrO_3$ perovskites reported no change in the particle size [325], whereas Carrillo *et al*. reported degradation over fifteen cycles that was attributed to the sintering of the sample. However these samples where ran isothermally at much higher temperatures of 1400 °C, [160] close to the sintering temperature used for making dense $LaCrO_3$ oxygen transport membranes.[194], [320] The SEM images for these samples are in agreement with Bork *et al.* whereby no obvious signs of sintering are observed, since the macrospheres remain in the region of 100 µm (Figure 7-23a,c,e). The long thin features present in the micrograph are residual alumina wool used to hold the sample in the reactor tube. After inspection at higher magnification, the structures have maintained their surface roughness further suggesting minimal sintering effects. (Figure 7-23 b,d,f).

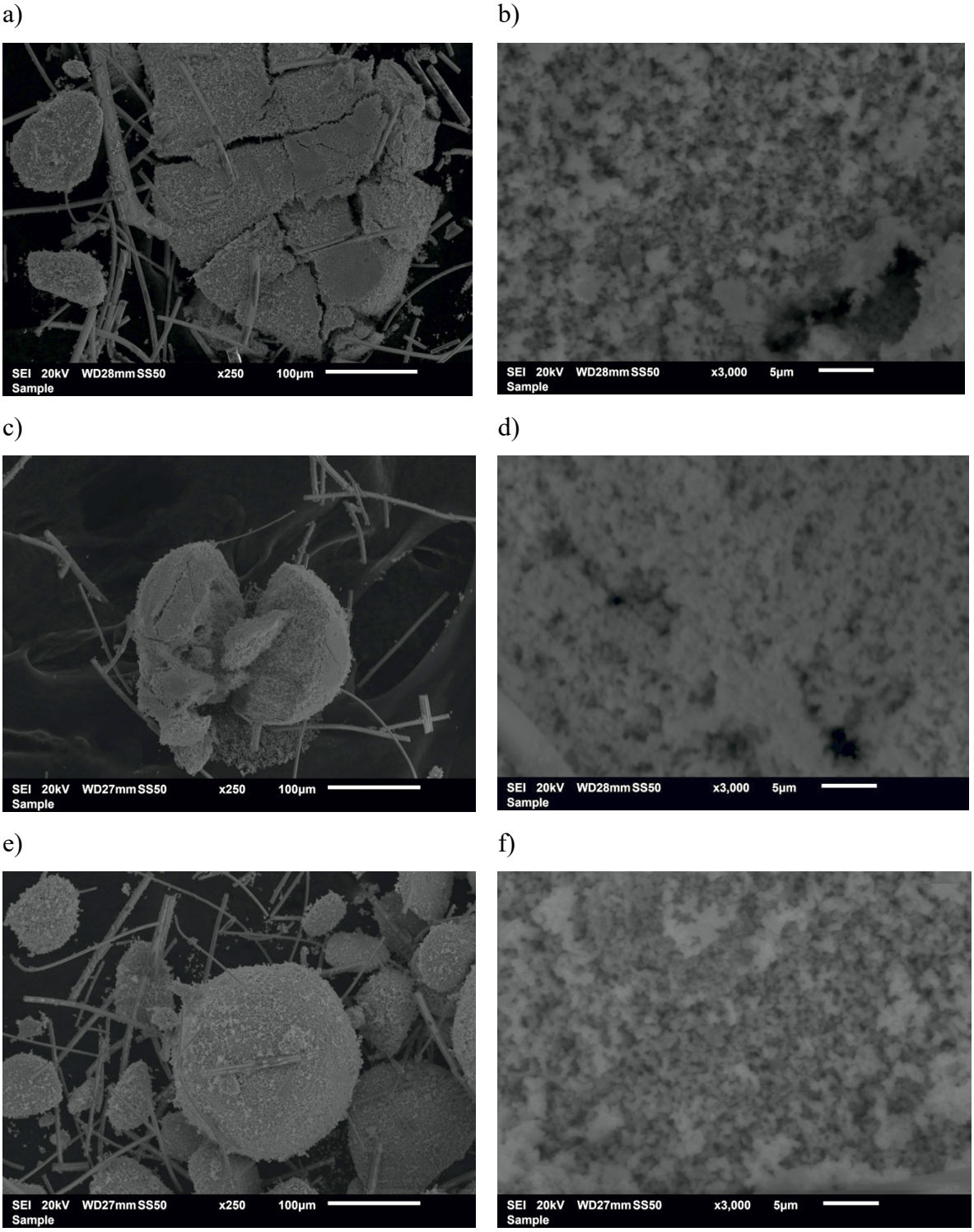

Figure 7-23. Secondary electron micrographs of a,b) LSCrF-8273, c,d) LSCrF-8282, and e,f) LSCrF-8291 powders after thermochemical water splitting cycles at 1200/800 °C.

XRD revealed the presence of the same rhombohedral perovskite phase with $R\bar{3}c$ space group. (Figure 7-24) – confirming the structural stability of the compounds. Le Bail refinement was used to understand the changes in lattice parameter that may have occurred during the

thermochemical cycling. Cubic perovskite phases ($Pm\bar{3}m$) were attempted as part of the refinement process due to the potential of vacancy induced antiferrodistortive octahedra tilting corrections [351], however no better fitting statistics were achieved. In theory, no change should be observed if compound has been fully reoxidised to the initial stoichiometry. However, the lattice parameters displayed in Table 7-4 are increased suggesting an expanded unit cell. Since this was conducted at room temperature, the unit cell parameters are only affected by the chemical expansion of the lattice. Here the presence of thermally induced vacancies and reduced cations that have not been rectified in the oxidation step could explain the increase. However, the accuracy of the refinement is not perfect. The refinement process was only conducted for the perovskite phase, hence the large reliability factors. The diffractograms revealed additional peaks that were matched to Al_2O_3 and $Sr(OH)_2$. Sabarou *et al.* also noticed the stable nature of the LSCrF-8291 compound but also the presence of Sr rich phases by XRD after heat treatment under humid hydrogen at 850 °C. [353]

As mentioned in the SEM micrographs, alumina is residue from the wool sample holder. On the other hand, comparing the in-situ diffractograms in section 7.2.3 (Figure 7-15) under flowing inert environment, it is highly likely the $Sr(OH)_2$ is a secondary phase that has formed during the oxidation step. Surface hydroxides have been widely reported in the SOFC community for the degradation of the cathode performance by increasing the ohmic resistance.[354] This is related to the atomic redistribution of strontium acceptor ions towards the surface of the materials as a response to temperature and environment. [355]–[357] This surface phenomena is further explored in the next section.

a)

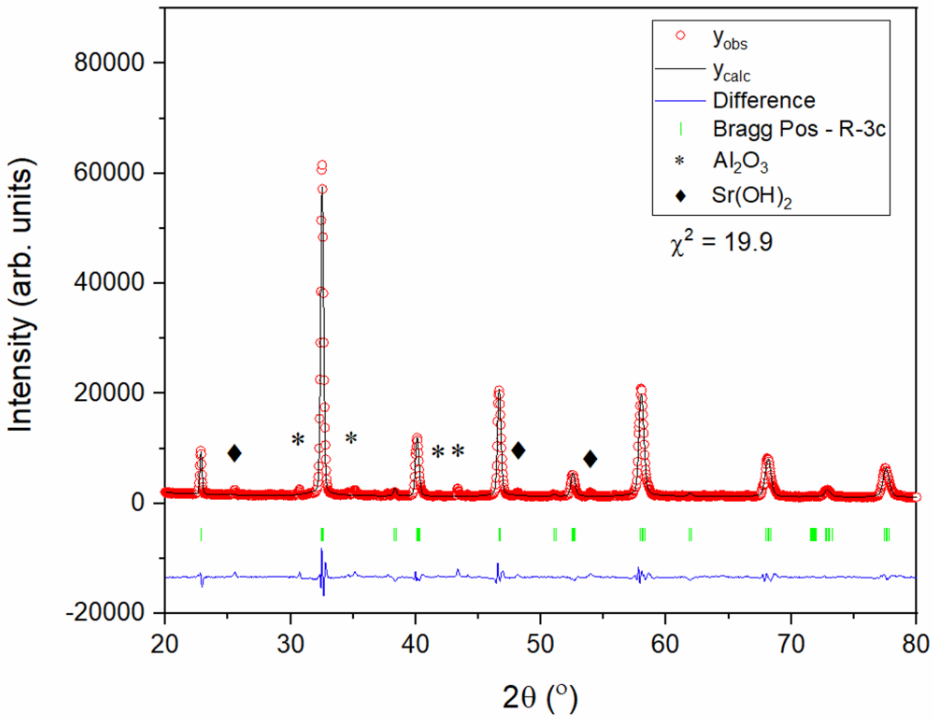
Intensity (arb. units)
2θ (°)
y_obs
y_calc
Difference
Bragg Pos - R-3c
Al2O3
Sr(OH)2
χ2 = 19.9

b)

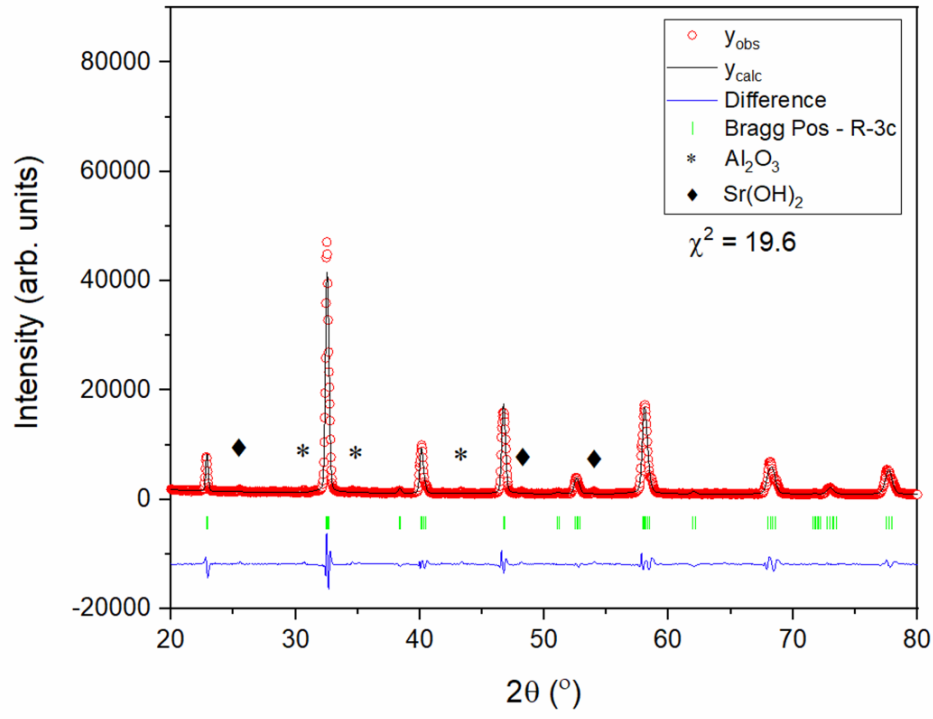
Intensity (arb. units)
2θ (°)
y_obs
y_calc
Difference
Bragg Pos - R-3c
Al2O3
Sr(OH)2
χ2 = 19.6

c)

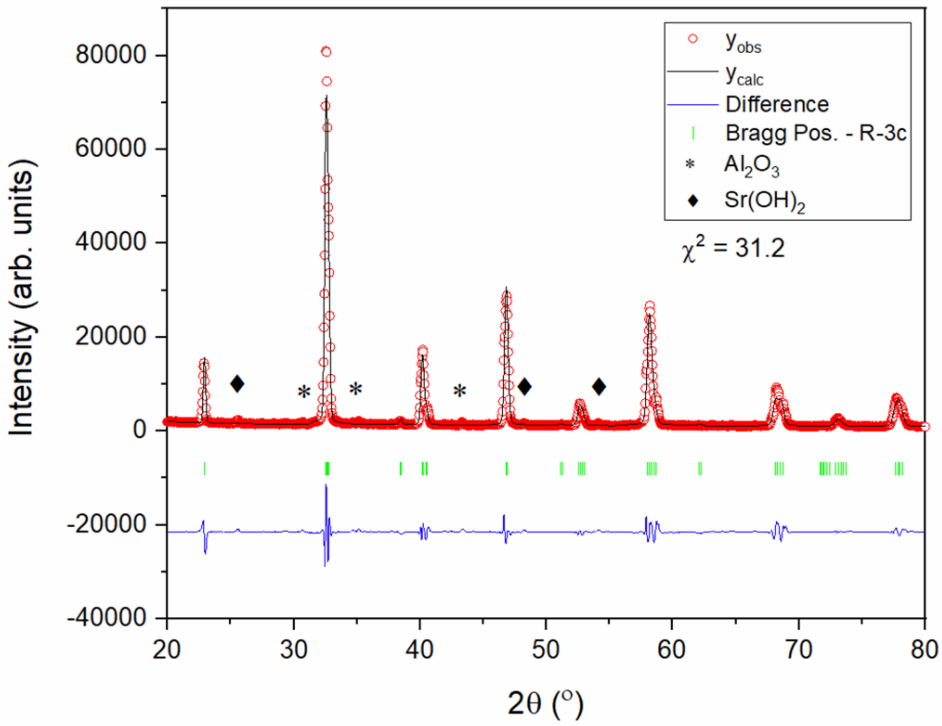

Figure 7-24. XRD diffractograms for a) LSCrF-8273, b) LSCrF-8282 and c) LSCrF-8291 compounds after 1200/800 °C thermochemical water splitting cycles.

Table 7-4. Lattice parameters and fitting results for the Le Bail refinement of the LSCrF compounds after thermochemical water splitting cycles.

	LSCrF - 8273	**LSCrF - 8282**	**LSCrF – 8291**
a (Å)	5.5127(2)	5.509(2)	5.502(1)
c (Å)	13.446(8)	13.405(0)	13.365(8)
Cell Volume (Å^3)	353.8(3)	352.4(3)	350.4(2)
Increase in Cell Volume (%)	0.387	0.384	0.470
χ^2	19.9	19.6	31.2

7.2.5. Surface Instability under low P_{O_2}

The previous section showed each of the compositions appear mostly crystallographically and morphologically stable throughout the water splitting cycle, however the formation of $Sr(OH)_2$ secondary phase on the surface is abundant enough to be detected by XRD. It is postulated that this secondary phase can be the source of degradation of the thermochemical water splitting performance. Surface sensitive techniques such as XPS and LEIS were used to understand the formation of this phase. Small amounts of each powder were heated to 800, 1000 and 1200 °C under Argon for 2 hours to understand whether the formation is thermally driven. XPS was used to understand the changes in oxidation state within the compounds as well as the changes in bonding environments near the surface. The XPS spectra of the core levels were obtained for all the components within the compounds using an identical experimental method to the core levels of the pristine materials.

Figure 7-25 shows the Sr 3d core level as a function of thermal history for each compound. As the samples are heated from room temperature to 800 °C under argon, the amount of surface strontium appears to decrease with respect to the bulk level. The surface strontium level could be contributed by the presence of species such as SrO or $Sr(OH)_2$. The lowering of this level's abundance could be due to the removal of the $SrCrO_4$ phase from the surface as it is dissolved within the perovskite lattice.[358] However, heating to 1200 °C leads to the surface strontium increasing again. This could be due to strontium segregating from the bulk to the surface within the structure. The ratio of Sr $3d_5$ to La $3d_5$ was inspected for each of the compounds (Figure 7-26). In agreement with the observations of the Sr 3d core level, the ratio remains unchanged up to 800 °C but significantly increases at 1200 °C. This suggests the Sr is moving towards the surface at the expense of lanthanum. A more accurate observation of this phenomena is acquired using LEIS.

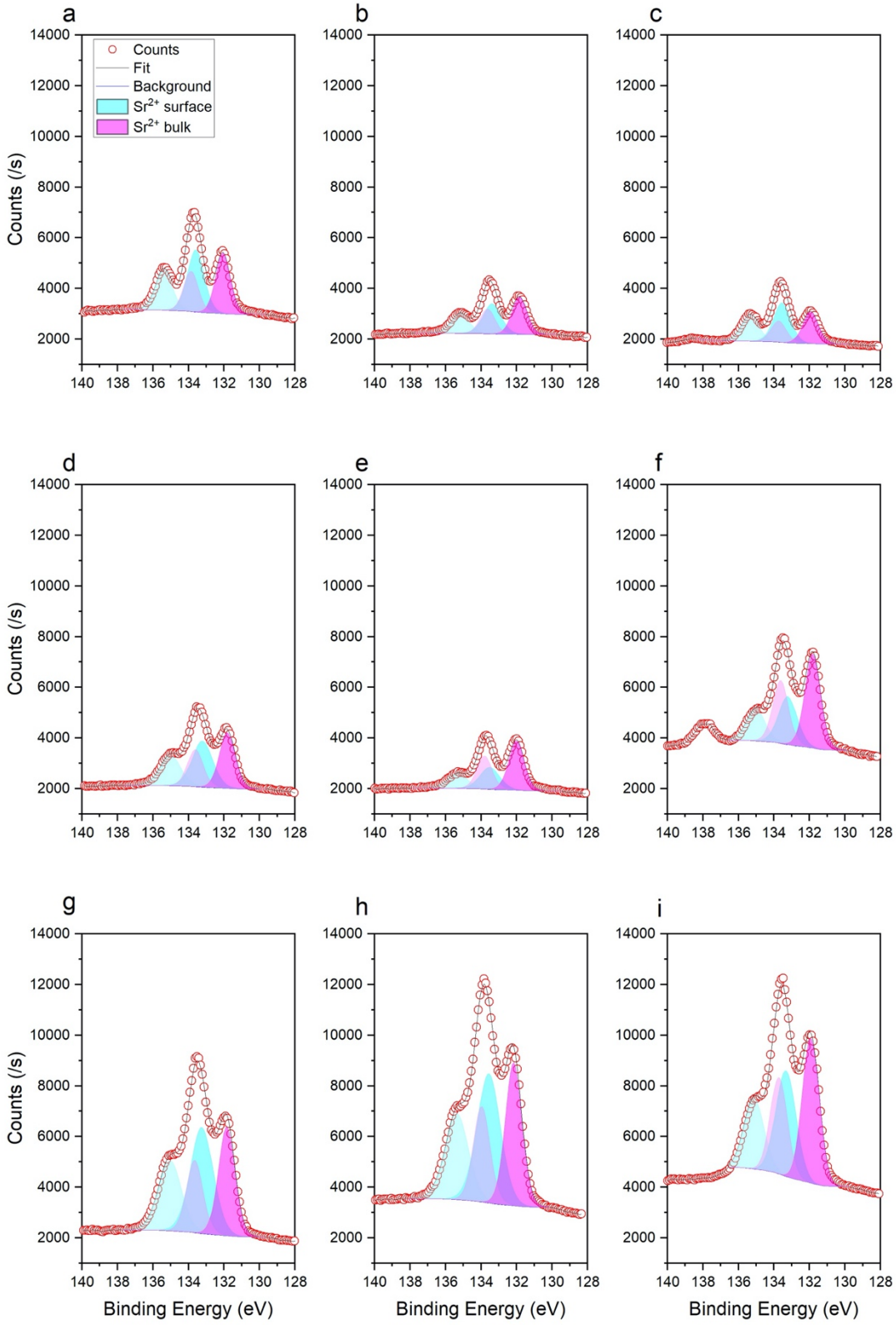

Figure 7-25. XPS spectra of the Sr 3d core level at RT (first row), 800 (second row) and 1200 (third row), for the LSCrF compounds 8273 (first column a, d, g), 8282 (second column b, e, h) and 8291 (third column c, f, i).

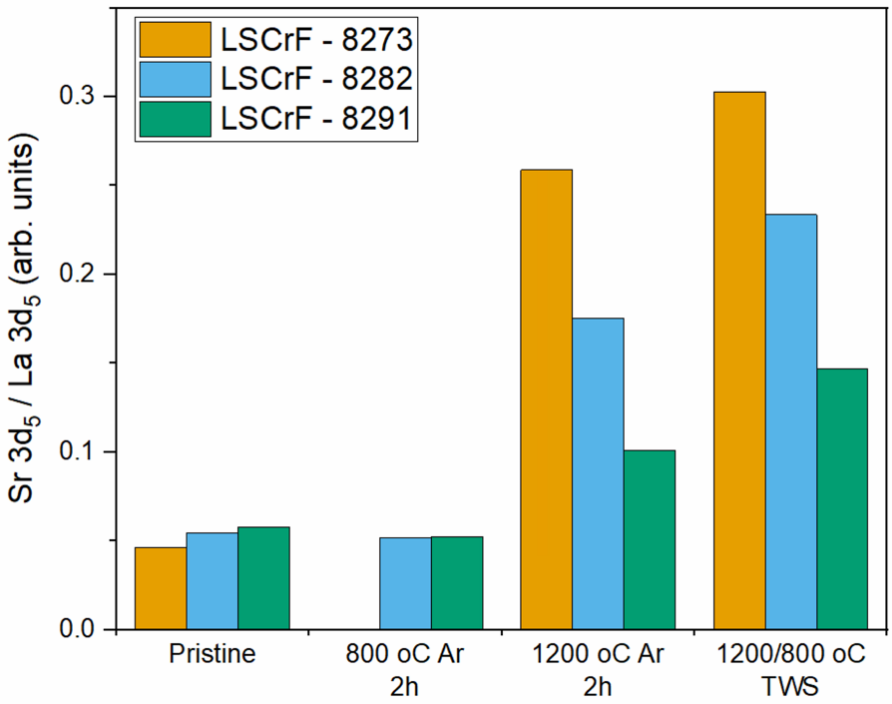

Figure 7-26. Ratio of Sr 3d5 to La 3d5 core level peaks in the LSCrF powders as a function of thermal history.

LEIS was used to probe the species present on the outermost atomic layer. A small amount of powder was loaded into the sample holder and uniaxial pressure applied to create a flat surface. A 6 keV Ne^+ beam was rastered over a 1 mm^2 area to detect the constituent elements present within the structure. This energy is slightly higher than the normal reported 5 keV beam to provide sufficient resolution between the neighbouring Cr and Fe peaks.[359], [360] Although with the use of the heavier primary ion Ne^+ beam information is lost regarding lower mass species e.g. oxygen presence. However this data could be inaccurate due to the instrument operating under high vacuum that promotes the outgassing of the sample. A 1 keV Ar^+ beam was used to sputter the surface after each analysis step to reveal a depth profile into the material. The sputter beam was rastered over an area of 1.5 mm^2, intentionally larger to ensure no edge effects. The depth profiling was repeated until the total dose received by the surface was approximately $15x10^{15}$ ions/cm^2. The fraction of A-site element and fraction of B-site elements were calculated using Equations 7.1 and 7.2 respectively.

$$f(X) = \frac{C_X}{C_{La} + C_{Sr}} \tag{7.1}$$

$$f(Y) = \frac{C_Y}{C_{Cr} + C_{Fe}} \tag{7.2}$$

where C_X denotes the concentration of the respective element.

Figure 7-27 shows the changes in the fraction of Sr and La on the A-site for each compound as the reduction temperature increases. The first row (Figure 7-27a, b, c) shows the results from pristine samples that have undergone no prior heat treatment. The ratio of La to Sr is near identical to the nominal synthesis composition, 80:20. This remains the same up to 800 °C (Figure 7-27d, e, f, second row) (except for the 8291 compound) above which the concentration of strontium starts to increase, in agreement with the XPS data. Furthermore, the extent at which strontium is present at the surface is dependent on the Fe content within the compound. The higher 8273 and 8282 compounds appeared to have significantly higher Sr content at the surface, however none of the compounds returned to the bulk stoichiometry within the measured depth profile. These observations can strongly suggest there could be a relationship between the oxygen vacancy concentration at the extent of Sr segregation. The cause of strontium segregation has been discussed extensively with the effects of elastic lattice strain and electrostatic potentials being the main two contributing factors.[361] Sr^{2+} has a larger ionic radius compared to La^{3+} in the XII coordinated site (1.44 vs 1.36 Å).[272] This causes strain on the A-site that can be alleviated by the rearrangement of cations, thus lowering the overall energy of the system.[361] At high temperatures there is sufficient thermal energy to allow cation migration throughout the structure. The perovskite phase is compiled of an ionic lattice with an AO-BO_2-AO stacking sequence. In lanthanum-based perovskites, these layers have overall nominal charges of +1 and -1 respectively. At the surface this causes a polar charge that can attract oppositely charged ions. This surface charge is typically neutralised by the reaction with the gaseous atmosphere to form surface passivating secondary phases. [354], [362] A DFT investigation into the Sr segregation of LSCF suggested the Bader charge on the on SrO layer is lower than that of LaO layer thus migration of strontium lowers the surface charge. [363]

Here, a greater effect from the electrostatic contribution is observed. The increased concentration of oxygen vacancies can cause further build-up of positive charge at the surface that attract the Sr'_{La} towards the surface. [364], [365] In this case the strontium at the surface

reacts with the steam to form $Sr(OH)_2$. Sha *et al.* recently reported Sr segregation in the LSCrF-8255 compound when investigating the surface exchange and oxygen diffusion measurements.[194] Although these experiments were carried out below 800 °C in oxygen rich environments, the concentration of thermally induced vacancies at the surface is lower, therefore suggesting there is still an elastic contribution. Sha later expanded on their work to demonstrate enhanced oxygen diffusion and surface exchange under humid environments due to the facile formation of hydroxyls on the strontium rich surface.[366]

The trends on the B-site fractions are less clear. Even at room temperature (first row, Figure 7-28), there is significant intermixing of the Cr and Fe within the compounds, as the structures deviate significantly from the nominal compositions. The intermixing becomes more apparent with temperature with the Cr concentration decreasing in the 8282 and 8291 compounds. It has been well-reported in metallurgy and other Cr-containing perovskites, that chromium oxide is volatile under air at temperatures greater than 900 °C. [367] This is likely to be more favourable at higher temperatures under the lower oxygen partial pressures present in this study. Alternatively, the formation of Fe and Cr rich spinel phases has been reported for LSCrF compounds. [194], [353], [366] The formation of these phases were not in high enough concentration to be detected by XRD, therefore other techniques such as STEM-EDX would be required to prove their presence.

XPS of the Cr and Fe core levels did not reveal any conclusive information regarding changes to oxidation state or bonding environments, except for the reduction intensity of the Cr^{6+} peak attributed to the $SrCrO_4$ phase. The Cr^{6+} concentration was also observed to decrease upon annealing at 700 °C under a reducing atmosphere. [368] This secondary phase has been previously suggested to melt and act as a sintering aid for these compounds. [369] Sabarou *et al.* suggested the $SrCrO_4$ phase could decompose to form SrO and the volatile CrO_3 phases. [370] This could explain the presence of Sr at the surface and loss of Cr; however, the depth profile from LEIS ascertains the origin of these elements from within the bulk.

The redistribution and loss of these elements are evidently an issue when considering the long-term performance of these materials. Surface analysis techniques have been rarely reported in the thermochemical papers and deactivation in perovskite materials is mainly attributed to sintering of particles and loss of active surface area. However, some materials that overlap the

thermochemical redox and SOFC cathode fields have reported Sr segregation and deactivation of their surface exchange, namely $La_{1-x}Sr_xMnO_3$. [365], [371] It is possible that Sr-segregation could be a limiting factor in these materials, however further experiments are required to be certain.

Different methods to mitigate the segregation in perovskite materials have been proposed. The doping with isovalent cations of greater ionic radii can help alleviate the strain within the lattice, [372]as well as changing the electrostatics by the introduction of lower reducibility cations at the surface to prevent build-up of surface vacancies. [373] Altering either the elastic or electrostatic contribution usually negatively effects the other, therefore it is tricky to design the perfect material for prevent Sr segregation and is often a trade-off between the two. [361] Furthermore, the requirements for thermochemical water splitting materials need to be considered e.g. lower reducible surface means lower vacancies and lower fuel production.

Interestingly, the Sr-segregation in perovskites has facilitated phase reconstruction of these materials at the surface to $SrO{\bullet}ABO_3$ layered perovskite phases, called Ruddlesden-Popper phases. [374], [375] The techniques used in this chapter would be unable to determine the presence of this phase reconstruction, however these layered perovskites have been widely spoken about but minimally reported for thermochemical water splitting due to their fast oxygen migration and ability to exchange large oxygen stoichiometries. The next chapter delves further into this class of materials and uses high throughput computational methods to screen suitable candidates.

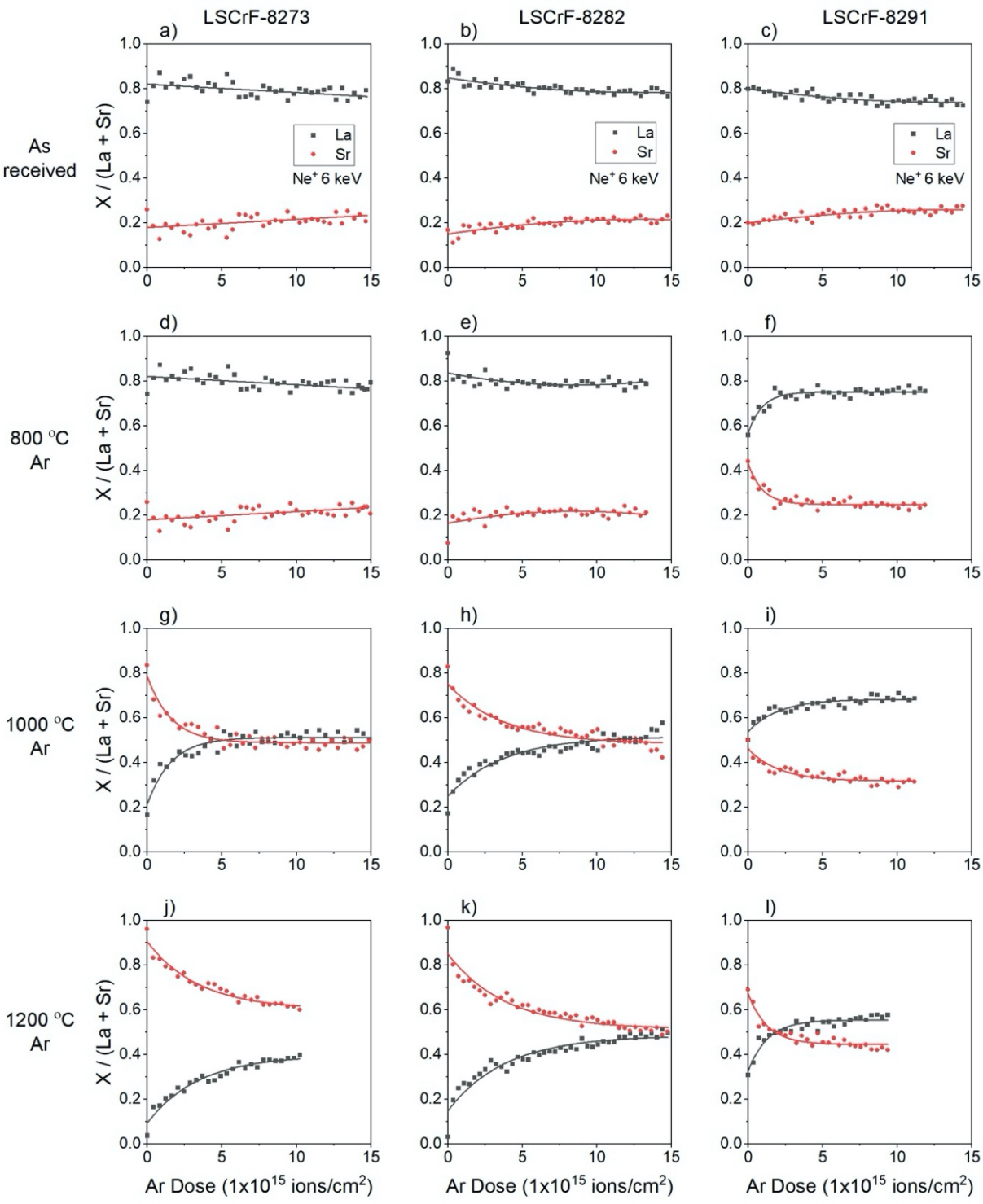

Figure 7-27. LEIS depth profiles of A-site cations at RT (first row), 800 (second row), 1000 (third row) and 1200 °C (fourth row), for the LSCrF compounds 8273 (first column a, d, g, j), 8282 (second column b, e, h, k) and 8291 (third column c, f, i, l).

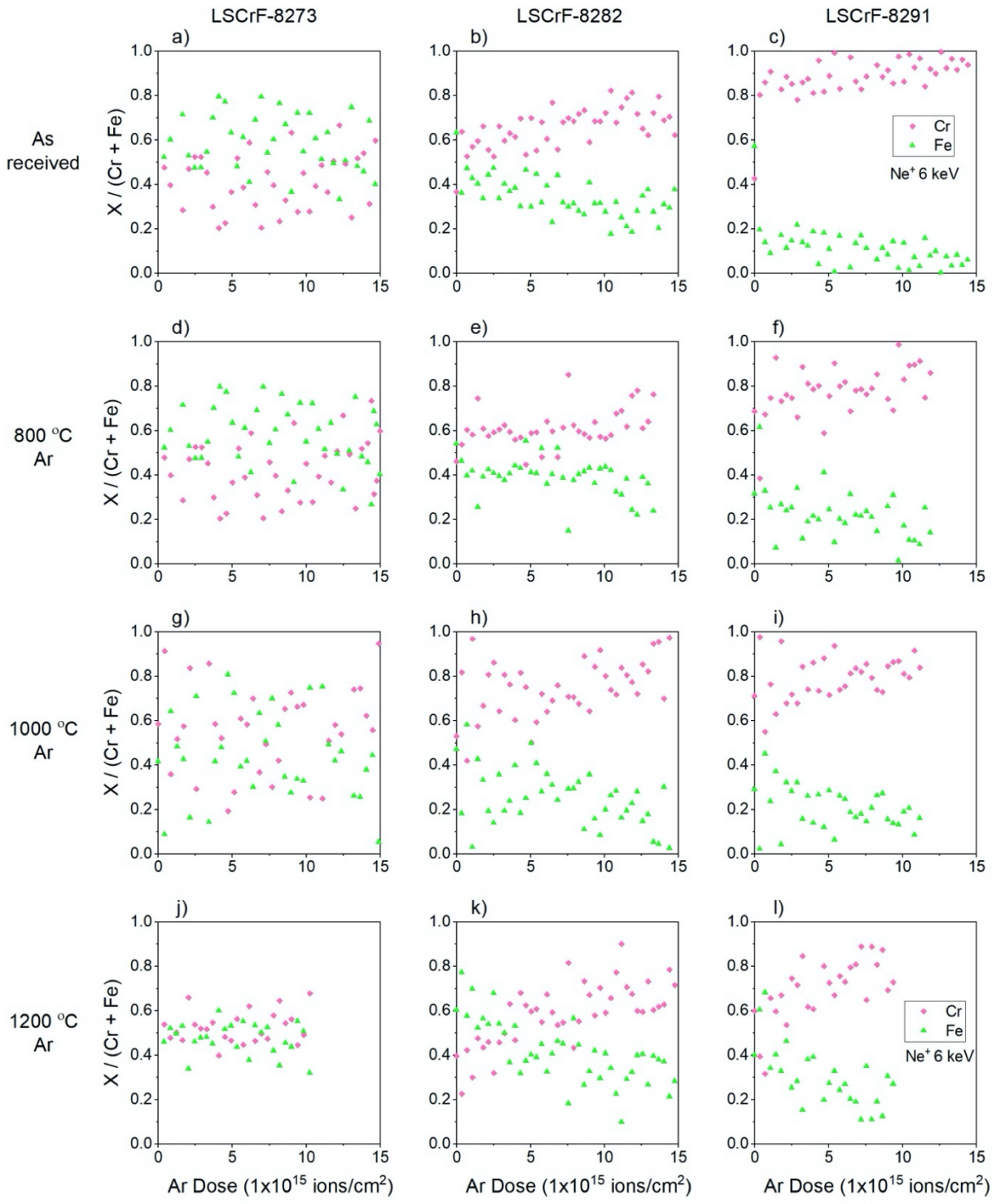

Figure 7-28. LEIS depth profiles of B-site cations at RT (first row), 800 (second row), 1000 (third row) and 1200 °C (fourth row), for the LSCrF compounds 8273 (first column a, d, g, j), 8282 (second column b, e, h, k) and 8291 (third column c, f, i, l).

7.3. Conclusion

An investigation in to $(La_{0.8}Sr_{0.2})_{0.95}Cr_{1-x}Fe_xO_{3-\delta}$ (x = 0.1, 0.2 and 0.3) perovskites was carried out to understand their applicability to thermochemical water splitting. These materials have previously reported high thermochemical stabilities over a wide range of materials whilst accommodating oxygen non-stoichiometry within their structure. This reputation alongside the analogous Co and Mn lanthanum chromate structures demonstrating good performance in literature, suggested that the iron compounds should perform equally well.

Initial characterisations and thermal analysis under low oxygen partial pressures revealed increased Fe content favoured greater oxygen evolution rates and volumes (36 μmol/g versus 16 μmol/g for LSCrF-8273 and LSCrF-8291 respectively). First principle modelling methods were used to understand the transition metal-oxygen bond was easier to break in direct coordination with the iron cation. Despite this all of the compounds had estimated thermodynamic quantities that aligned with favourable thermochemical water splitting conditions. This was demonstrated through the successful splitting of water molecules in modest 1200/800 °C temperatures - exceeding production rates compared to $Ce_{0.75}Zr_{0.25}O_{2-\delta}$ (9.4 μmol/min/g versus 3.0 μmol/min/g for LSCrF-8273 versus $Ce_{0.75}Zr_{0.25}O_{2-\delta}$ respectively). Although the low surface stability of the compounds during the reduction reaction prevented the material from observing multiple redox cycles. Surface sensitive techniques novel to the thermochemical water splitting field such as LEIS and XPS were used to characterise strontium segregation and loss of volatile Cr at the surface that leads to the reduction in performance.

8. Screening of new n=1 Ruddlesden-Popper materials for thermochemical water splitting by reduction thermodynamics

In this chapter, we report the results from a screening of all possible first order Ruddlesden-Popper oxides for thermochemical water splitting based on thermodynamic parameters previously reported within literature. As mentioned at the end of the chapter 7, surface instability of perovskite materials can lead to the reconstruction into Ruddlesden-Popper (RP) layered perovskite phases. However, these phases have been reported to be able to act as fast oxygen conductors and exchange gases with its environment. Although, not a large number of RP phases have been reported for thermochemical water splitting. Motivation is drawn from previous screening efforts by Emery *et al*. who investigated the perovskite family of materials. [241] The work in this chapter uses density functional theory to screen all possible n=1 Ruddlesden-Popper using DFT to predict oxygen defect formation energies we hope to narrow down the family of materials for further experimental testing. The computational work reported in this chapter was completed under the guidance of Dr Ieuan Seymour, who taught the concepts of DFT and guided the calculations.

8.1. Introduction to Ruddlesden-Popper Oxides

Ruddlesden-Popper oxides are a perovskite-like structure that have been of interest in the SOFC community due to their stable structures and mixed ionic and electronic conduction. [376] Originally, proposed by Ruddlesden and Popper in 1957 [377], the structures are formed of n perovskite layers interrupted by an AO rock salt layer. Figure 8-1 demonstrates that different structures can be formed depending on the order of n. Albeit, the most investigated structure is the n=1 structure with the generic formula $A_2BO_{4\pm\delta}$ due to their higher ionic conductivities due to wide range of oxygen defects. [378] Importantly the oxygen non-stoichiometry (δ) value can be positive or negative. This is by means of vacancies forming within the perovskite layer or by the accommodation of oxygen interstitials within the rock salt layer.[379]

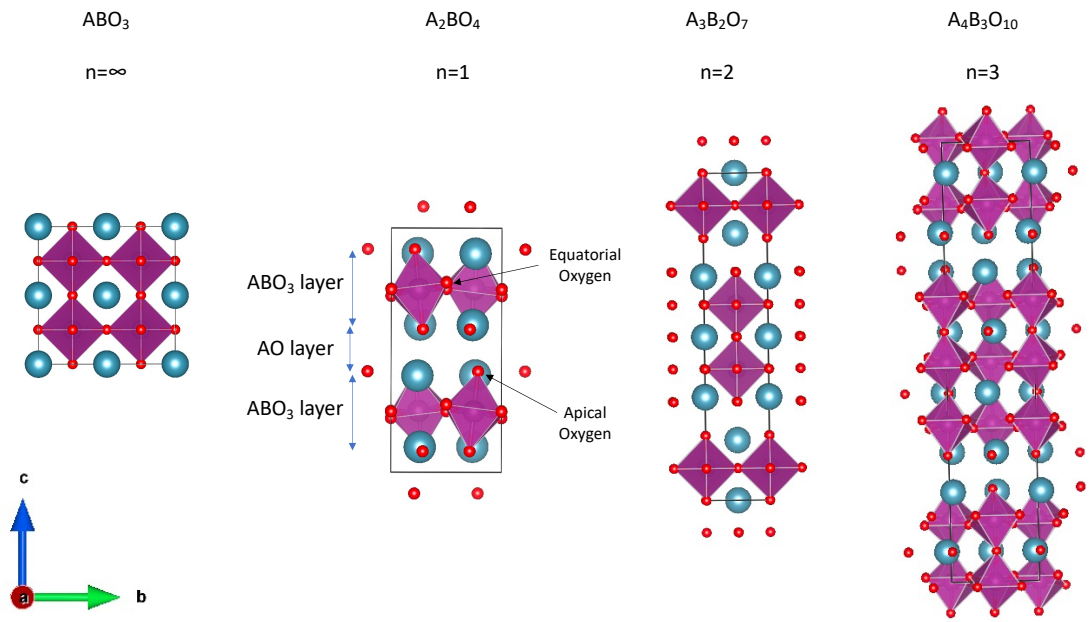

Figure 8-1. Possible Ruddlesden-Popper structures as a function of n.

These oxygen interstitials contribute to the fast oxygen ion conduction within SOFC cathodes. $La_2NiO_{4+\delta}$ has been shown to have faster oxygen diffusion properties at lower temperatures compared to the better reported SOFC LSCF compounds. [380]–[382] Chroneos *et al.* computationally confirmed this was due to oxygen interstitials having a lower activation energy through a interstitialcy conduction mechanism within the rock salt layer. [383] This was further backed up by Burriel *et al.* who demonstrated fast oxygen ion diffusion only occurs in the planes parallel to the rock salt layer. [384] Despite good ionic conduction, the electronic conductivity in the undoped materials is poor for MIECs (Nd_2NiO_4 = 50 S/cm vs $La_{0.6}Sr_{0.4}CoO_3$ = 1600 S/cm between 500 and 700 °C).[385] Similar to the lanthanum chromates, strontium acceptor doping has been investigated to improve the electronic conduction of La_2NiO_4 by increasing the B-site oxidation state.[380], [386] On the other hand, this lowers the concentration of charge compensating oxygen interstitials within the structure, although does promote the presence of oxygen vacancies at more reducing conditions (higher temperature or lower oxygen partial pressure).[387], [388] Aguadero *et al.* demonstrated that high pressure synthesis conditions can be altered to tune large oxygen non-stoichiometry (δ=0.31) within the $La_2CoO_{4+\delta}$ structure. [389] This is significantly higher than most non-stoichiometry values of perovskites for thermochemical water splitting ($\delta \approx 0.1$) and if exploited would result in large productions volumes. Importantly, RP oxides have been reported to have high chemical stability compared to perovskite materials. [390]

Over the years, a handful of RP-214 materials have been proposed for thermochemical water splitting although to no true comparison with ceria. [158], [173] However more recently, there have been reports of RP n=1 structures for thermochemical water splitting that undergo phase changes throughout the redox cycle ($Ce_xSr_{2-x}MnO_4$).[391] Studies on this material were expanded by Begereson-Keller *et al.* [392] who outline the thermodynamic properties of these compounds to be in line with the LSMA compounds proposed by Takacs *et al.*.[159] In this chapter we aim to apply computational screening methods to try and identify some RP n=1 compounds that will be suitable for thermochemical water splitting.

8.2. Screening criteria

This screening study has the aim of being comprehensive over all possible A and B site combinations of known oxidation states with reported Shannon ionic radii.[272] The database compiled by Professor Grimes' group at Imperial College London was used as the primary input with 167 unique entries.[393] A full copy of the database is provided in appendix D. This led to a possible initial 27,889 possible combinations.

The first two screening parameter were to remove combinations that contained possible radioactive or toxic elements (Ac, Am, Bk, Cd, Cm, Fr, Hg, No, Np, Pa, Pb, Pm, Pu, Tc, U). Despite their use in batteries and perovskite solar cells respectively, Cd and Pb were chosen to be non-suitable elements for this study. Cobalt and Nickel were included due to the common use within SOFC materials.

The third screening was to determine charge neutral compounds when $\delta=0$. This will remove all possible structures that do not have the following oxidation states combinations; A=1+ and B = 6+, A=2+ and B = 4+, A = 3+ and B = 2+. Since δ is not expected to be large, it is likely the structures will remain stable upon redox reactions.

The next screening parameter is based on the possible bond coordination of the cation. The A-site cation must have a coordination of IX whereas the B-site cation sits within a BO_6 octahedra, and therefore needs a coordination of VI. The next two parameters predict the likelihood a perovskite layer will form. This is dependent on the criteria outlined by the Goldschmidt tolerance factor. (Equation 8.1) [394] Usually with perovskite structures, the A-site cation is

larger than the B-site cation. If the Goldschmidt tolerance is between 0.7 and 1.1 it is likely a perovskite will form. If the tolerance is equal to 1 a perfect cubic perovskite will form. Below t=1 value the structure will deviate into a tetragonal or orthorhombic structure by accommodating tilting of the octahedra. Above t=1, a hexagonal face sharing structure is preferential, however since the n=1 RP structure does not allow face-sharing octahedra, an upper limit of 1.05 is set.

$$t = \frac{r_A + r_O}{\sqrt{2}(r_B + r_O)} \tag{8.1}$$

where r_X is ionic radius, and X denotes whether it is A-site, B-site or oxygen.

The final screening parameter of the initial section identifies if there is an active redox couple present on either the A-site or B-site. It is common for the B-site cation to be the redox active element since it has the greater bond-overlap with the oxygen, however it was recently reported that the inclusion of a redox active element on the A-site can have entropic benefits on the water splitting thermodynamics.[168] Those structures with a cation stable in a higher oxidation state than that at neutral stoichiometry will be investigated for interstitial based redox reactions, whereas those with a lower oxidation state will be investigated for vacancy based redox reactions. Separate vacancy energy formation calculations will be carried out considering both, the apical and the equatorial oxygen sites.

The parameters described up to this point were all possible to be carried out using simple hand calculations, although further efforts through DFT can be used to quantify structural stabilities and defect formation enthalpies. In a similar way to Emery *et al.* [167], we outline a maximum energy above the hull value, and a reduction enthalpy window. The energy above hull limit is set as 60 meV. This is equal to the computed value for La_2CoO_4 - a structure that can be easily synthesised within the laboratory.[389] Furthermore, the reduction enthalpy window was set to be $2.5 < \Delta H < 5$ eV, in agreement with Emery *et al.*'s original basis of Meredig and Wolverton's thermodynamic criterion.[62], [241] Other authors have proposed slightly different thermodynamic windows. Deml *et al.* used a window based on the simulation of $La_{1-x}Sr_xMn_{1-y}Al_yO_3$ structures that were experimentally proven to have similar splitting performances to ceria.[395] Recently Gautam *et al*. proposed a narrower window of 3.1 to 4.2 eV when reviewing A-site reducible perovskite materials. [396] Here, the wider window was

chosen to try and observe high numbers of new materials since the Ruddlesden-Popper materials have been scarcely researched for thermochemical water splitting.

8.3. Computational Results and Discussion

The screening parameters implemented prior to the DFT calculations minimised the number of simulations. The initial number of possible compounds is 27,889. Figure 8-2 shows the reduction in number of possible candidates after each screening parameter. It is clear that the largest reduction was due to the charge neutral parameter that limited the possible combinations. Furthermore, the bond coordination and tolerance factors parameters also reduced the number of candidates significantly. There were 238 possible compounds identified for vacancy redox reactions, and 325 for interstitial based systems. These candidates were taken forward to DFT screening.

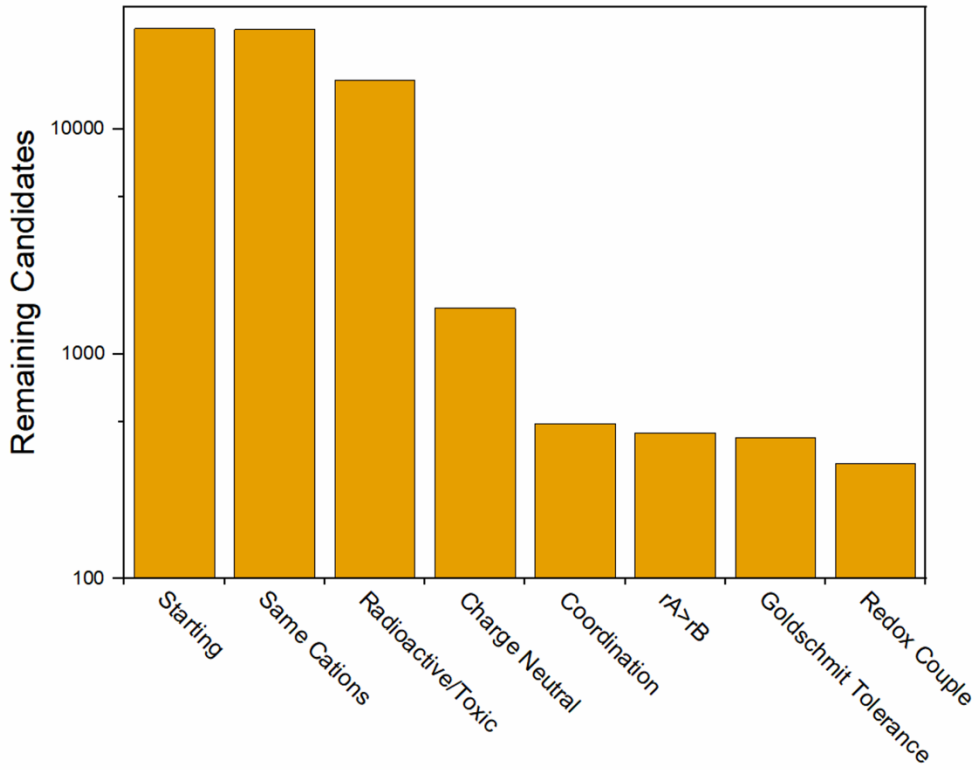

Figure 8-2. Reduction in number of potential vacancy-supporting compounds after initial screening parameters were applied.

Figure 8-3a and Figure 8-3b compare the abundancy of different metal ion groups on the A-site and B-sites respectively. Rare earth elements are the most abundant group of the A-site elements. This is likely due their ionic radii being larger than most B-site compatible elements thus also satisfying the Goldschmidt tolerance factor criterion. Furthermore, these elements usually have 2+ or 3+ oxidation states that have combinations to support the Ruddlesden-Popper structures. Secondly, alkaline earth metals are also abundant with their 2+ oxidation state. Furthermore, the transition metal is overwhelmingly likely to be on the B-site element. These are seen for both vacancy supporting and interstitial supporting structures. The combination of alkaline earth metal or rare-earth elements and transition metal is commonly seen with a lot of perovskite or layered perovskite materials reported within the literature.

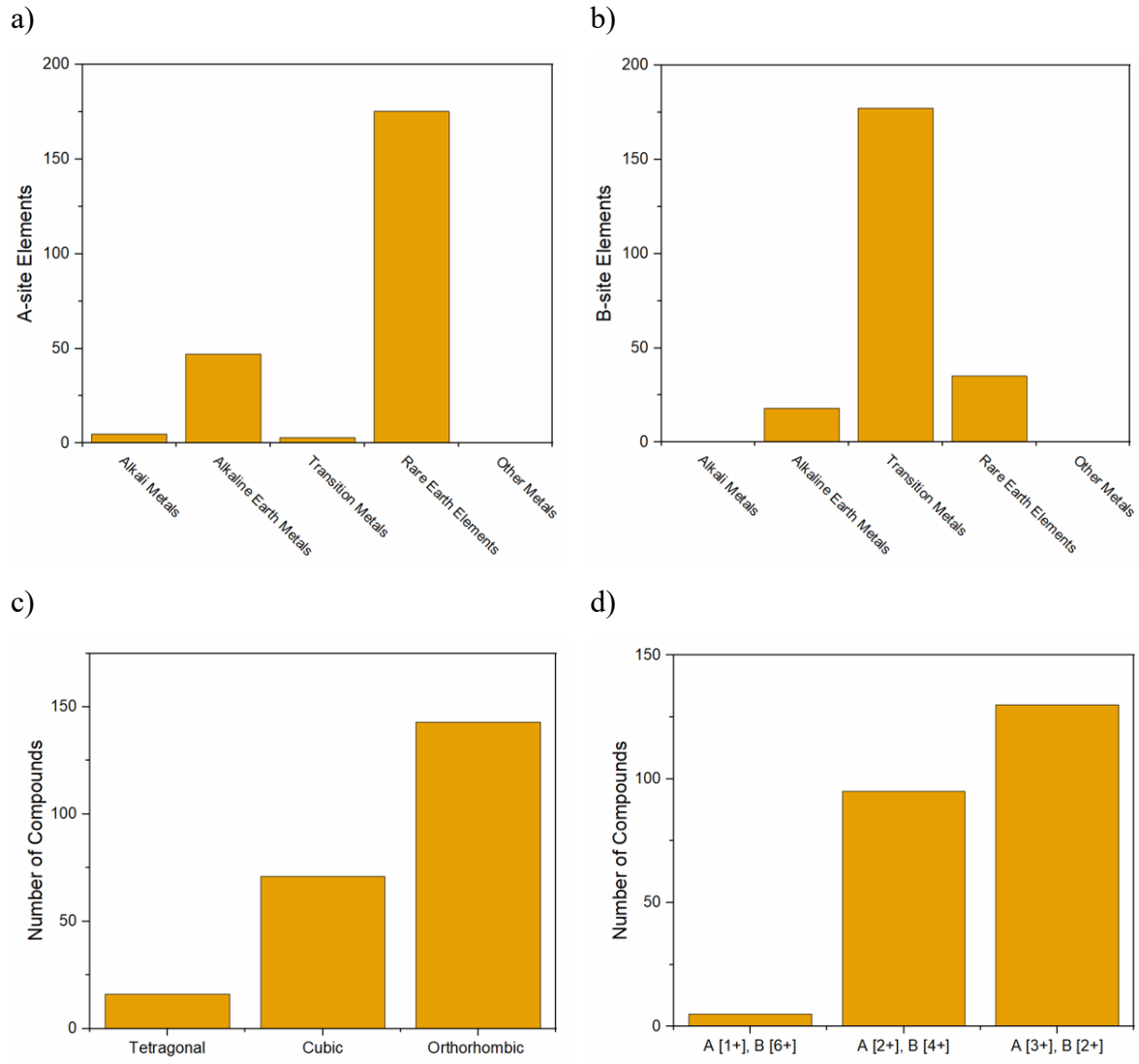

Figure 8-3. Comparisons of prospective vacancy supporting compounds properties prior after initial screening parameters.

The Goldschmidt tolerance factor also predicted a high number of orthorhombic based structures. The metal oxide octahedra in these structures undergo tilting to accommodate the

mismatch in ionic radii of the A-site and B-site commonly the *Bmab* space group. The presence of the rock salt layer could accommodate any strain that is introduced from this tilting effect. Commonly the RP K_2NiF_4 structure has the tetragonal *I*4/*mmm* structure. Introduction of dopant elements and changes in oxygen stoichiometry can force phase transitions to occur between these two polymorphs. [397], [398]

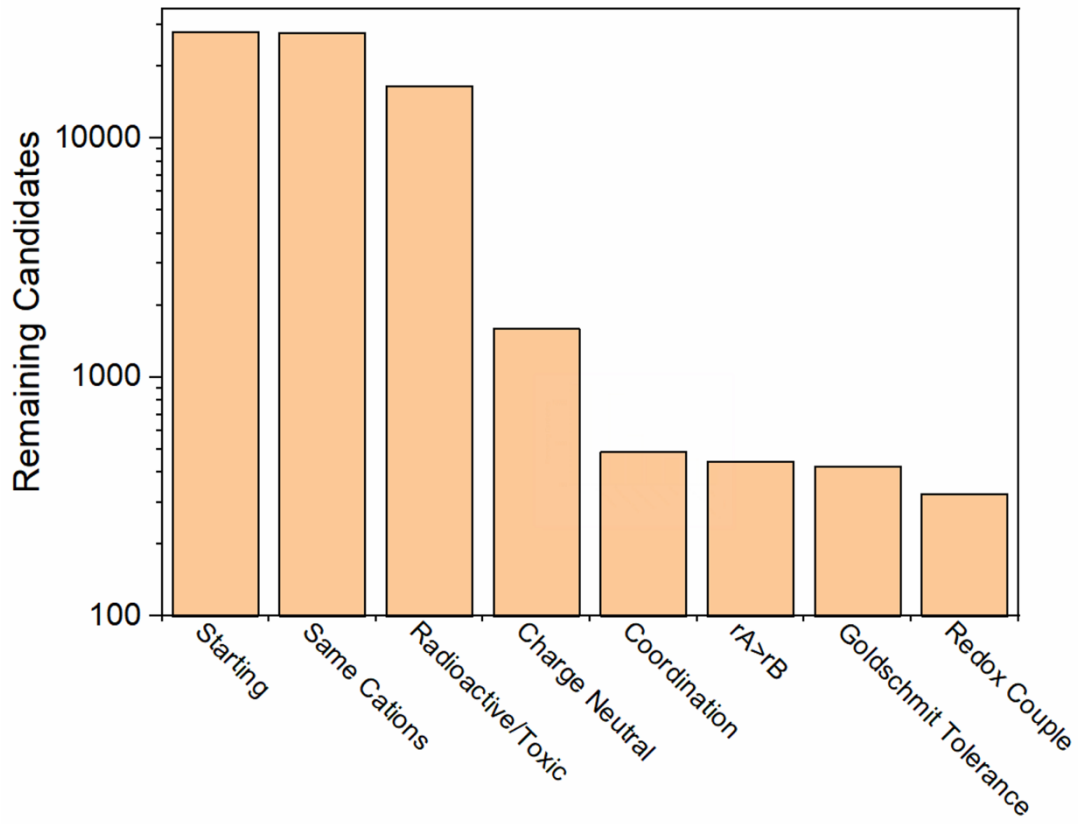

Figure 8-4. Reduction in number of potential interstitial candidates after initial screening parameters were applied.

Pymatgen-based scripts were used to rapidly formulate input files based on a 4-formula unit La_2NiO_4 *I*4/*mmm* structure from the materialsproject (mp-21326). Each structure was duplicated using two magnetic configurations that were set in the input file to understand the effect of spin on the stability of these structures. Firstly, ferromagnetic alignment on the B-site cation and secondly anti-ferromagnetic alignments whereby the spin is altered along 180° B-O-B bonds. The structures underwent a full geometric relaxation of both atomic positions and lattice parameters using the plane wave basis set codes implemented with VASP. An energy cut-off of 520 eV and k-point mesh of 4x4x2 were used for the high-throughput calculations.

This was determined through initial convergence testing of the La_2NiO_4 structure. (Appendix D)

Python scripts were used to check the electronic and force convergence, before extracting information regarding the energies, lattice parameters, band centre and oxygen Bader charge. The final energies were compared with structures present within the materialsproject to determine the energy above hull. This can lead to a source of error if there are not structure with a certain element in the structure present within the materialsproject since the energy above the hull is a comparative value.

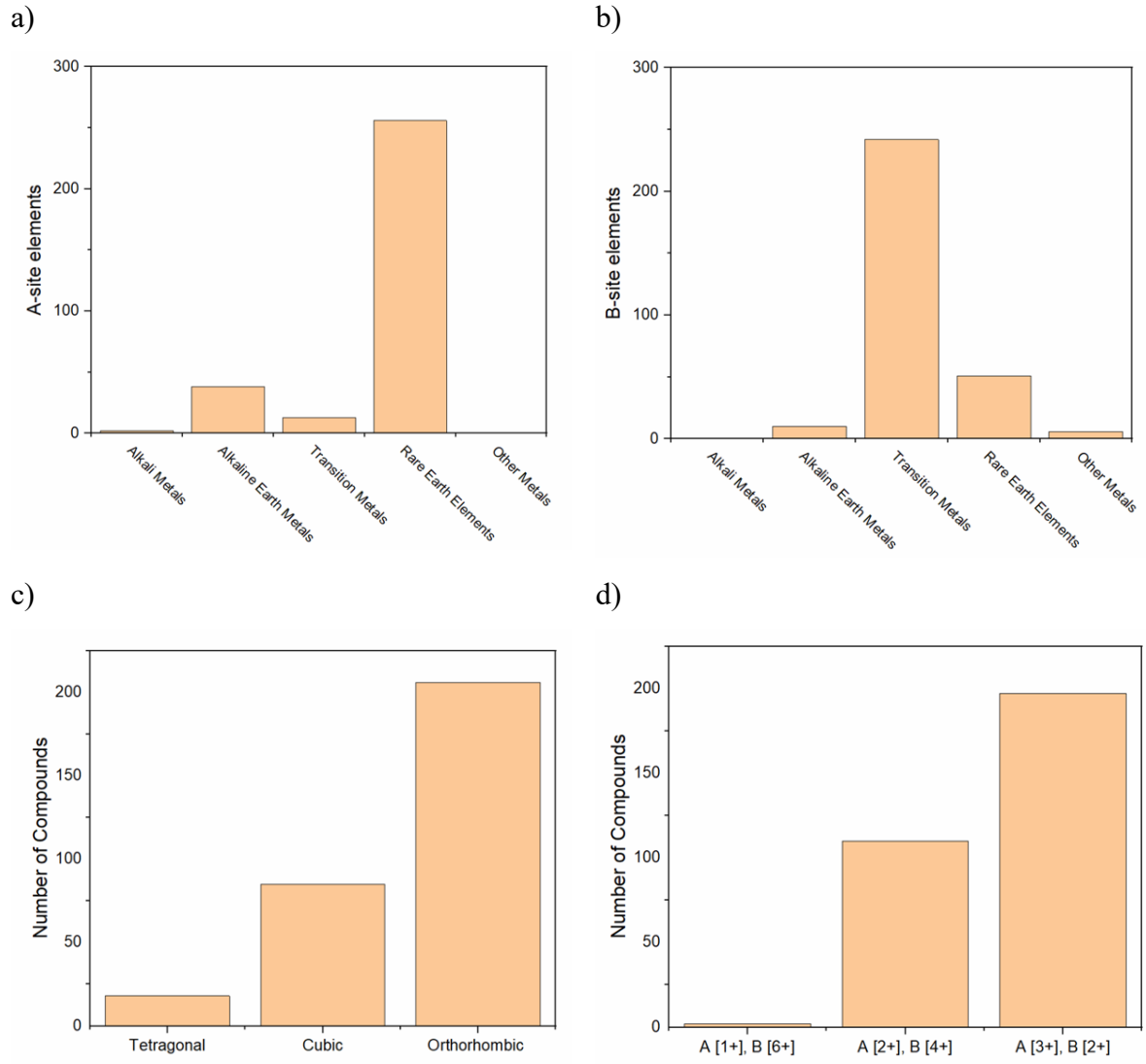

Figure 8-5. Comparisons of prospective interstitial supporting compounds properties prior after initial screening parameters.

8.3.1. Stable compounds

The initial DFT screening suggested 53 “synthesisable” structures that were able to accommodate oxygen vacancies within the structure. This screening step also predicted 44 stable structures that can accommodate an interstitial within the structure. Experimentally observed structures such as La_2CoO_4, La_2NiO_4, and La_2CuO_4 made it through the interstitial screen as well as Sr- and Ca-based vacancy structures that have been investigated for their magnetic properties.[389], [399]–[402]

Figure 8-6a and Figure *8-7*a show most synthesisable structures have an alkaline earth metal on the A-site and consequently a B-site element with 4+ oxidation state (Figure 8-6b). The B-site elements were exclusively transition metals. The high number of this combination is likely due to the abundance of 3/4/5+ redox couples in the transition metal group. The number of 3+ A-site elements increases for the interstitial compounds (Figure 8-7b). This is likely due to the 2/3+ redox couple being more abundant than a 1/2+ redox couple required for vacancies to be present in these structures.

This screening is not necessarily definitive for a couple of reasons. Firstly, the “synthesisability” limit was set to equal that of an experimental structure. The DFT calculations are run at 0K and therefore are not at synthesis conditions. Changing the temperature and chemical potential of oxygen in the synthesis atmosphere can change the favourability of formation of some compounds. Secondly, the convex hulls that these structures are compared to are from structures present within the materialsproject database. Therefore, the accuracy of the convex hull is related to the number of database entries with the same elements. This was noticed in this experiment by the large number of Yb-based compounds that were found to sit on the convex hull. This result could be true to reality; however they are not reported on large crystallographic databases such as ICSD, and to best knowledge not reported within literature. Therefore, a cautious approach is advised until the structures are synthesised.

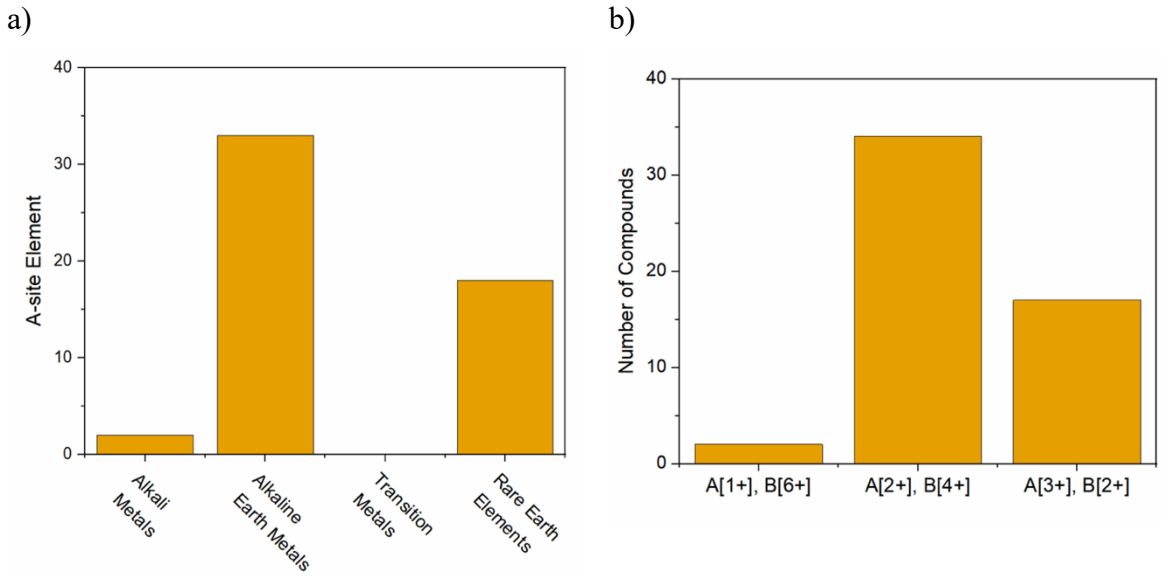

Figure 8-6. Comparisons of a) A-site elements and b) Cation oxidation states of stable RP-214 structures that are able to support the formation of oxygen vacancies.

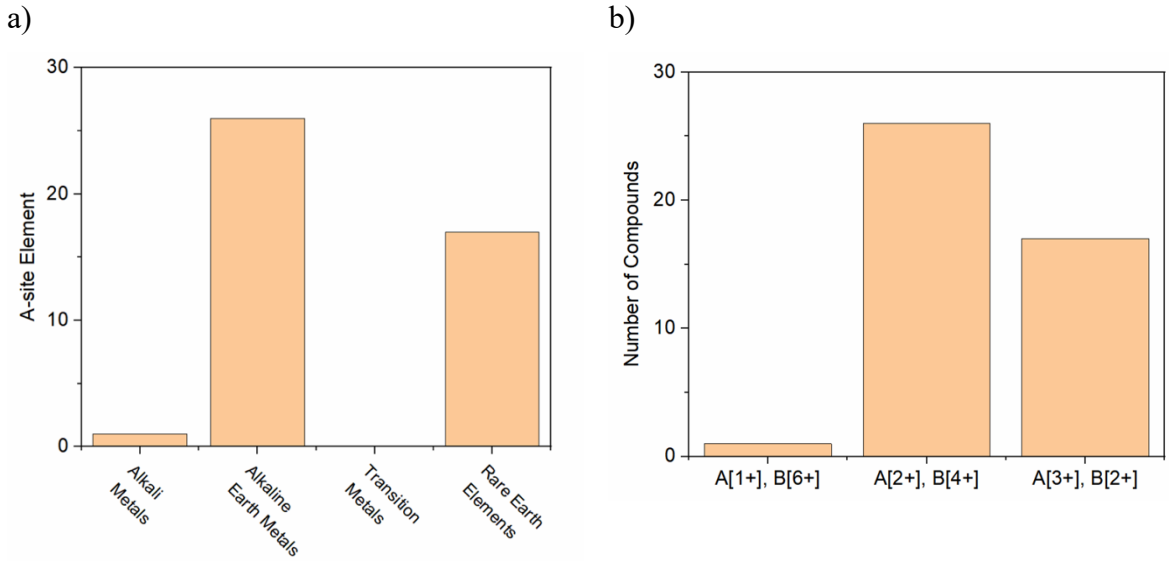

Figure 8-7. Comparisons of a) A-site elements and b) Cation oxidation states of stable RP-214 structures that are able to support the formation of oxygen interstitials.

8.3.2. Thermodynamically favourable compounds

The defect formation energies were calculated for the predicted stable structures. The addition or subtraction of an oxygen ion from this structure would be equivalent to a non-stoichiometry of ±0.25. This lies between the values of the benchmark cerium oxide materials ($\delta \approx 0.075$)

and the screening studies by Emery *et al.* (δ=0.5). It would be best practice to see how the formation energy converges with supercell time. However, this would significantly increase the computational expense of this screening study and other authors have reported the supercell size has little effect on the defect formation enthalpy.[241]

Figure 8-8 outlines the position of the defects introduced within the A_2BO_4 structure. Interstitial oxygen anions were introduced in the rock salt layer at a position of (0.5, 0.5, 0.5) in the middle of the four octahedra. Two types of vacancies were introduced within the structures. Apical vacancies were introduced at the oxygen as close to the position (0.75, 0.25, 0.57) and the equatorial vacancy was introduced at the oxygen nearest (0.5, 0.5, 0.25). During the computation of the defected structures, the lattice parameters were constrained whilst the atomic positions were relaxed until the electronic convergence was below $1x10^{-6}$ eV and force converged below 0.01 eV/A. The reduction enthalpy was calculated for the vacancy and interstitial compounds by equations 8.3 and 8.4 respectively.

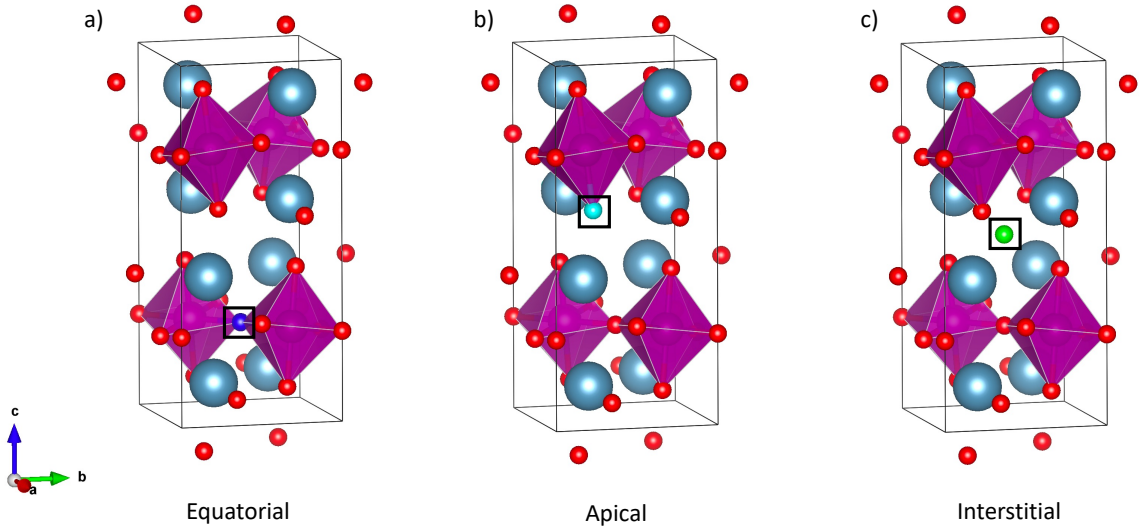

Figure 8-8. Locations of the different defects introduced in the RP-214 structure.

$$\Delta H_{red} = E_{A_2BO_{3.75}} + \frac{1}{2}E_{O_2} - E_{A_2BO_4} \quad (8.3)$$

$$\Delta H_{red} = E_{A_2BO_4} + \frac{1}{2}E_{O_2} - E_{A_2BO_{4.25}} \quad (8.4)$$

Figure 8-9 shows the relationship between the reduction enthalpy and those stable Ruddlesden-Popper that are theoretically able to support vacancies. The compounds are grouped with respect to the A-site cation with increasing atomic number towards the right-hand side of the figure. The B-site cations within the groups are also arranged with respect to atomic number. Both apical and equatorial vacancies are displayed in this figure for comparison between the two types of point defects. Furthermore, the window identified by Emery *et al.* is displayed to easily identify which compounds have favourable thermochemical water splitting thermodynamics.

Some trends are instantly noticeable, in particular the decrease in reduction enthalpy as the B-site cation progresses across the rows to higher atomic number. Linear trend lines are drawn to guide the eyes; however, the trend discontinues at the end of the row. Progression across a row in the periodic table usually has trends of decreasing atomic radius and increasing electronegativity. The latter has been discussed in explanations of decreasing vacancy formation energies in perovskite materials.[292], [403] Earlier transition metals in the row form stronger polar-covalent bonds and as the row progresses, d-orbitals filling increases to the point where fully occupied orbitals will start to repel oxygen lone pairs and weaken the bond. [404] Furthermore this translates the oxygen p-band centre closer to the Fermi energy therefore lowering the energy requirement for electrons to move from oxygen states to the transition metal. Discrepancies in the trend can be explained through electron configurations. Pavone *et al.* investigated the effect of B-site transition metal on the reduction enthalpies of La-based perovskites materials. [242] The reduction enthalpy decreased across the row from Cr to Co except for $LaFeO_3$. Here we observe a similar trend for Sr and Ca based RP-214 materials as seen in Figure 8-9 that can be explained from electron configuration symmetry. Cr4+ has 2 d-orbital electrons and the gain of an electron from the lattice reduction will complete the three half-filled orbitals with higher stability. On the other hand, Mn4+ already has three half-filled orbitals therefore it will require greater energy to disrupt this configuration (Figure 8-10).

It is observed that the A-site does not have as strong effect on the reduction enthalpy compared to the B-site cation. Changing the A-site from Ca to Sr or Ba in vanadium- or iron-based compounds is seen to slightly decrease the reduction enthalpy. The increase in the ionic radii of these elements could play an effect in reduction of the lattice by increasing the Goldschmidt tolerance factor closer to the ideal perovskite. This can lead to less distorted octahedra with

better TM 3d – O 2p orbital overlap and more facile charge transfer during the reduction reaction.

Furthermore, another prominent observation is the difference between a vacancy forming on the apical site being different from the equatorial site. The equatorial site is coordinated to two B-site cations that can accommodate a charge redistribution from the reduction reaction. In contrast the apical oxygen is coordinated to a single B-site cation. Therefore, the coordinated cation would require a larger change in oxidation state, or for it to be rapidly distributed over the lattice.

Table 8-1 lists all the compounds with a reduction enthalpy that is predicted to be favourable for thermochemical water splitting in-line with Emery *et al.*.[241] Further information is provided regarding the energy above hull and structural information. The structures present in the ICSD are also recorded. The materials fall within the narrower window defined by Gautam *et al.* are highlighted within the table.[396] The screening study found primarily alkaline earth metal-based compounds from abundant elements such as Ca, Mn and Cr.[405] Further structures containing precious metals were also predicted such as Rh, Ir and Pd. These elements are notoriously good catalytic materials for a variety of reactions however would significantly increase cost. [406]

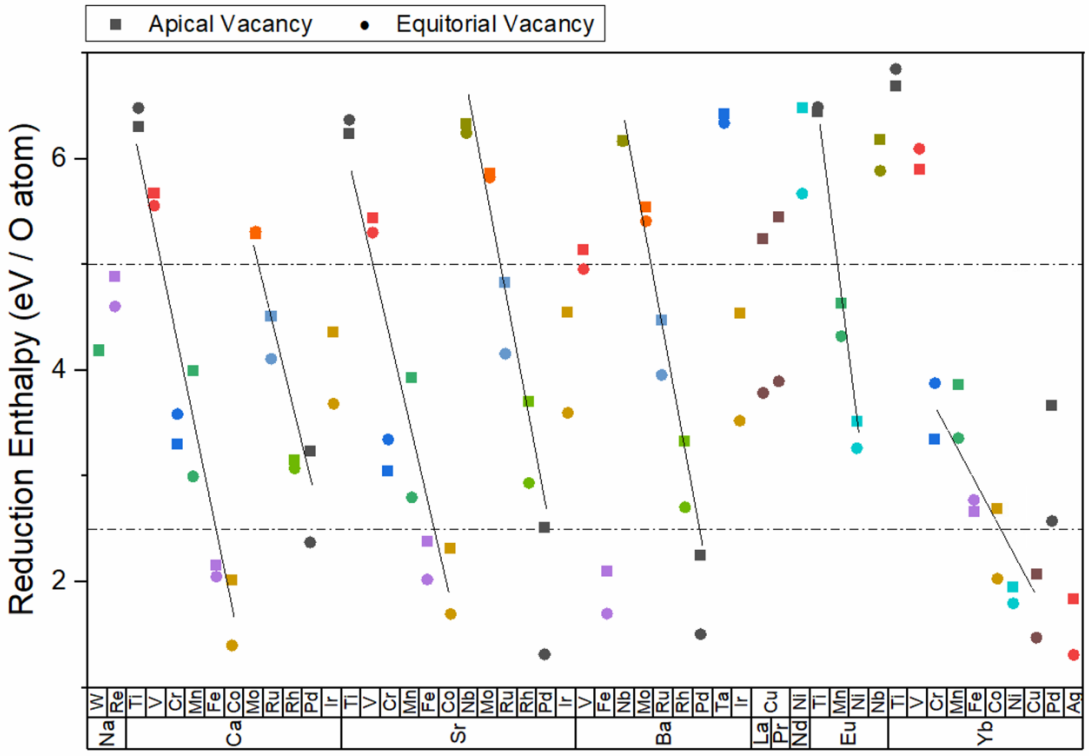

Figure 8-9. Reduction enthalpy of oxygen vacancy supporting thermodynamically stable RP-214 compounds. The compounds are grouped with common A-site cations and arrange B-sites with increasing atomic number. The colours are unique to B-site elements.

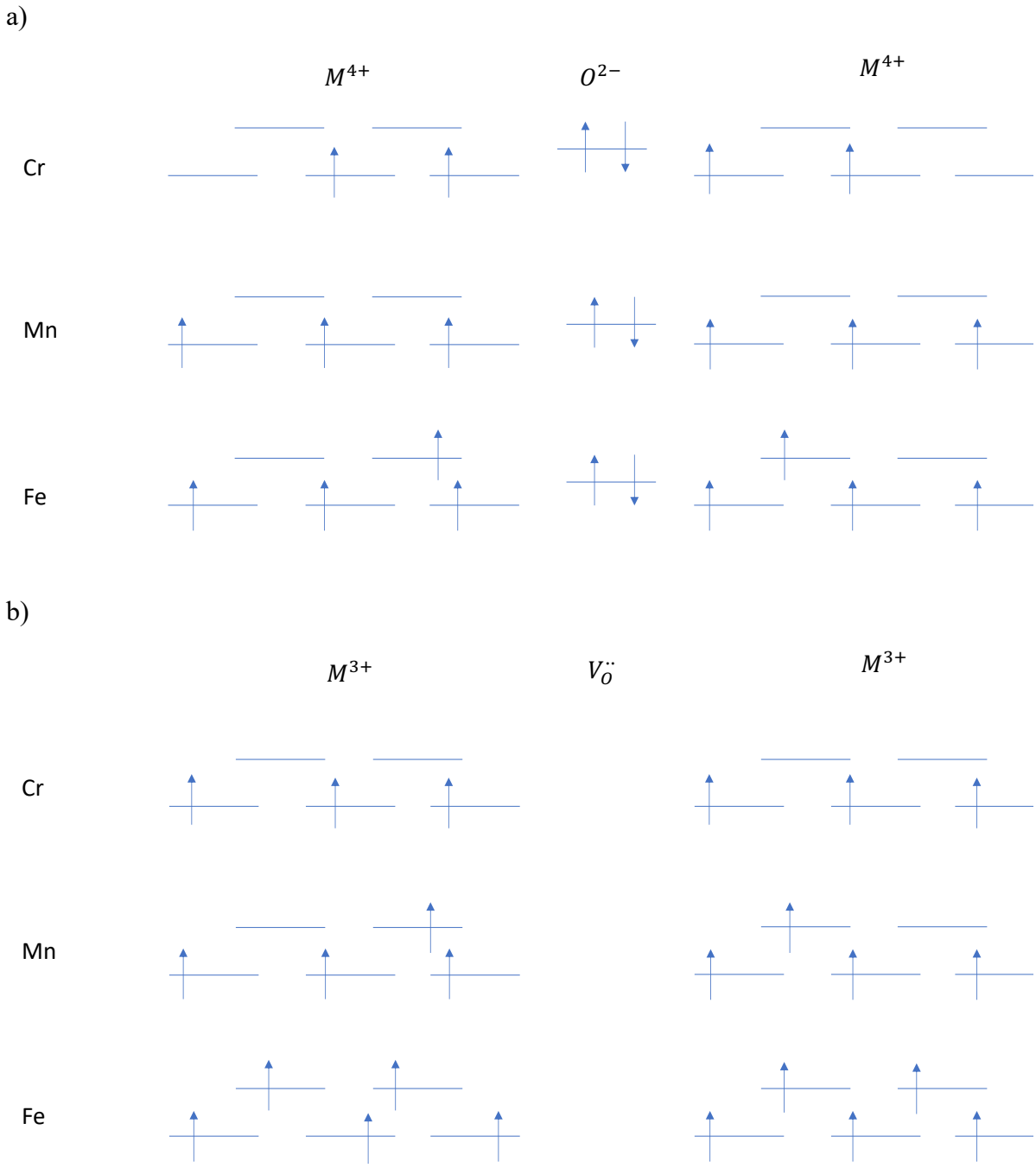

Figure 8-10. Electron configurations of a B-O-B bond in Sr_2MO_4 (M=Cr to Fe) in the a) oxidised state (δ=0) and b) reduced state. (δ = -0.25) after the vacancy has been formed.

Figure 8-11 shows the trends for reduction enthalpy in the interstitial-supporting compounds. The reduction enthalpies for removing an interstitial from the lattice are much lower compared to the vacancy supporting compounds to the point where the reduction enthalpy is negative, therefore suggesting instability of interstitials within the lattice. Furthermore, the similar B-site periodic trend is observed with the reduction enthalpy lowering with higher atomic number.

Similarly, to the vacancy defects, discrepancies can try to be explained through electron configuration. The reduction enthalpy for $La_2MO_{4.25}$ and $Pr_2MO_{4.25}$ (M = Co, Ni or Cu) follows a "V" shape with the minima observed for the nickelate compound. In their stoichiometric compounds (δ=0), the Co^{2+} and Ni^{2+} cations had been observed to be present in the high spin electron configuration (Figure 8-12b).[407]–[409] However, upon oxidation to the Ni^{3+} or Co^{3+} states, a mixture of high-spin and low-spin configurations are present (Figure 8-12a). Considering the Co^{3+}-HS to Co^{2+}-HS reduction, involves the removal of unpaired elections from the structure that would likely be energetically favourable. However, Co^{3+}-LS to Co^{2+}-HS reduction, breaks the electron degeneracy and would likely require significantly higher energy. Conversely, with the reduction of Ni^{3+} will have more favourable electron filling. Ni^{3+}-LS to Ni^{2+}-HS state, the electron would preferentially fill the second e_g orbital than pair with the first e_g orbital, whereas in the Ni^{3+}-HS to Ni^{2+}-HS states, the electron completes the pairing of the t_{2g} electron shells. Both of these processes are likely more favourable than the Co^{3+} reduction. On the other hand, the La_2CuO_4 shows an increase in reduction enthalpy versus the La_2NiO_4 compound due to the disruption of half-filled e_g orbitals. However, the Cu^{3+} is difficult to stabilise therefore the solubility of oxygen interstitials within this compound is expected to be limited [410], although this can be manipulated by synthesis conditions. [411]

This screening study only found three potential compounds that could support thermochemical water splitting through an interstitial mechanism – Ba_2NbO_4, Ba_2TaO_4 and Sr_2NbO_4. Neither of the compounds were found to be present on the ICSD database or reported within literature. The energy above hull of these compounds were much higher than the vacancy counterparts. It remains of interest to see whether these compounds can be synthesised since the Nb and Ta would be required to primarily occupy the 4^+ oxidation state – one that is most definitely unfavourable as a d^1 electron configuration.

It is interesting to see the La_2CoO_4 and Pr_2CoO_4 structures being relatively close to the ideal thermodynamic window. The lanthanum variant has been studied for fuel cell cathodes due to their affinity to be oxidised with interstitials leading to fast kinetics.[412] It is likely that thermochemical water splitting with these compounds could be driven by shifting the thermodynamics with high humidity atmospheres. Alternatively substituting the B-site cation with "fixed" oxidation state cations could increase the reduction enthalpy, as seen with the strontium cobalt oxides in chapter 6.

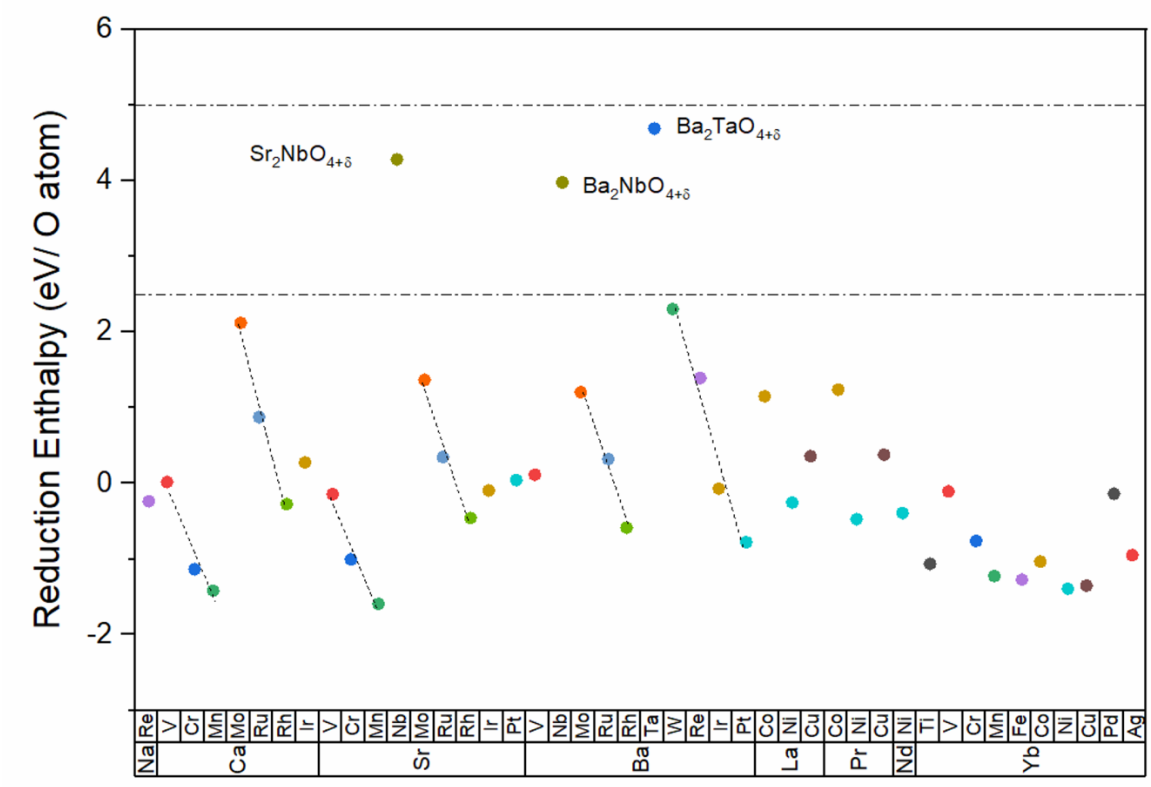

Figure 8-11. Reduction enthalpy of oxygen interstitial supporting thermodynamically stable RP-214 compounds. The compounds are grouped with common A-site cations and arrange B-sites with increasing atomic number. The colours are unique to B-site elements.

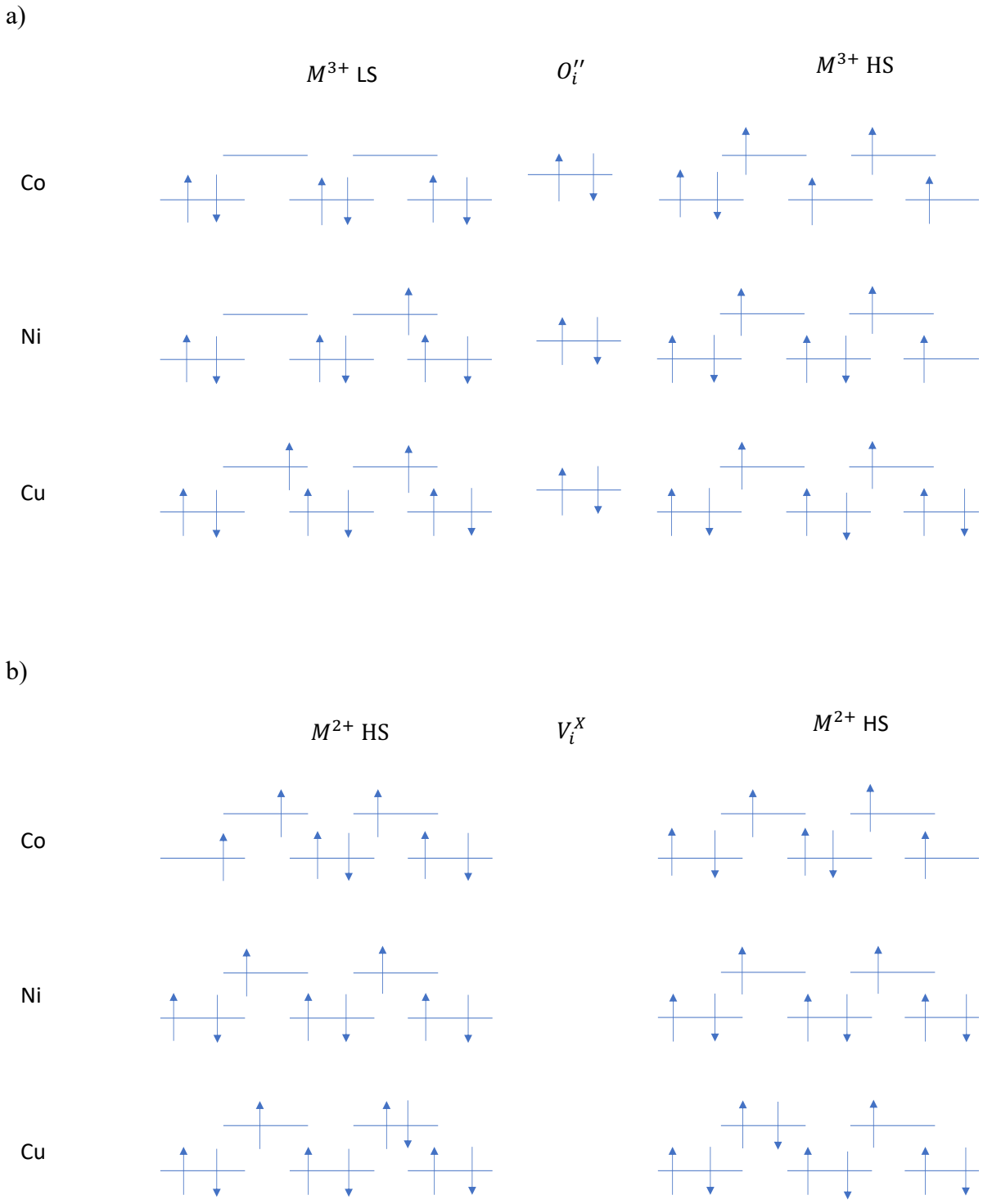

Figure 8-12. B-site element electron configurations of a) oxidised $La_2MO_{4.25}$ and b) reduced La_2MO_4 (M=Co, Ni or Cu) after the oxygen interstitial has been removed. Both spin configurations are shown here as a short comparison.

Table 8-1. List of Ruddlesden-Popper metal oxides favourable for thermochemical water splitting using vacancy point defects.

	Energy Above Hull (meV/atom)	Reduction Enthalpy (eV/O atom)		Space Group	Lattice Parameters (Å)			Present in ICSD	Ref.
		Apical	Equatorial		*a*	*b*	*c*		
Na_2WO_4	49.625	4.188	-	*P*4_2/*ncm*	5.537	5.537	12.212		
Na_2ReO_4	56.541	4.889	4.605	*P*4_2/*ncm*	5.507	5.507	11.849		
Ca_2CrO_4	33.268	3.299	3.587	*P*2_1/*c*	5.439	5.439	11.628	✓	[413]
Ca_2MnO_4	9.912	3.958	2.928	*P*4_2/*ncm*	5.353	5.354	11.780	✓	[414]–[417]
Ca_2RuO_4	39.160	4.516	4.109	*P*4_2/*ncm*	5.550	5.550	11.818	✓	[418]
Ca_2RhO_4	56.131	3.153	3.072	*P*4_2/*ncm*	5.490	5.490	12.027		
Ca_2PdO_4	0.000	3.231	2.374	*P*2_1/*c*	5.719	5.322	12.186		
Ca_2IrO_4	57.416	4.363	3.686	*P*4_2/*ncm*	5.478	5.478	12.151	✓	[419]
Sr_2CrO_4	16.329	3.046	3.347	*P*4_2/*ncm*	5.474	5.474	12.612	✓	[420]
Sr_2MnO_4	0.000	3.934	2.798	*I*4/*mmm*	5.437	5.437	12.614	✓	[416], [421]
Sr_2RuO_4	0.000	4.827	4.157	*P*4_2/*ncm*	5.566	5.566	12.796	✓	[422]–[424]
Sr_2RhO_4	18.486	3.701	2.936	*P*4_2/*ncm*	5.578	5.578	12.797	✓	[424]–[427]
Sr_2PdO_4	0.000	2.514	1.314	*P*4_2/*ncm*	5.687	5.688	12.580		
Sr_2IrO_4	17.602	4.549	3.598	*P*4_2/*ncm*	5.567	5.567	12.889	✓	[424], [427]–[429]
Ba_2VO_4	28.874	5.141	4.957	*I*4/*mmm*	5.788	5.787	13.176		
Ba_2RuO_4	3.862	4.475	3.957	*Cmce*	5.717	5.717	13.536		
$Ba2RhO_4$	2.145	3.329	2.704	*P*4_2/*ncm*	5.757	5.757	13.427		
Ba_2IrO_4	17.082	4.542	3.523	Cmce	5.727	5.727	13.660	✓	[430]
La_2CuO_4	54.162	5.247	3.787	*P*4_2/*ncm*	5.466	5.465	13.088	✓	[431], [432]
Pr_2CuO_4	58.283	5.447	3.897	*P*4_2/*ncm*	5.436	5.436	12.945	✓	[433]
Eu_2MnO_4	0.000	4.638	4.323	*P*4_2/*ncm*	5.588	5.585	12.160		
Eu_2NiO_4	16.230	3.520	3.264	*P*4_2/*ncm*	5.475	5.472	12.096		
Yb_2CrO_4	7.246	3.347	3.878	*C*2/*m*	5.330	5.329	11.538		
Yb_2MnO_4	0.000	3.861	3.359	*P*4_2/*ncm*	5.297	5.297	11.494		
Yb_2FeO_4	0.000	2.658	2.775	*P*2_1/*c*	5.411	5.410	11.320		
Yb_2CoO_4	0.000	2.687	2.028	*P*-1	5.250	5.266	11.415		
Yb_2PdO_4	0.000	3.667	2.574	*P*2_1/*c*	5.833	4.968	12.161		

Table 8-2. List of Ruddlesden-Popper metal oxides favourable for thermochemical water splitting using institial point defects.

	Energy Above Hull (meV/atom)	Reduction Enthalpy (eV/O atom)	Space Group	Lattice Parameters (Å)			Present in ICSD	Ref.
				a	b	c		
$Sr_2NbO_{4.25}$	61.779	4.286	*P*-4	5.798	5.798	12.636		
$Ba_2TaO_{4.25}$	81.864	4.694	*P*-42*m*	5.828	5.828	13.542		
$Ba_2NbO_{4.25}$	53.418	3.980	*P*-42*m*	5.887	5.887	13.467		

8.3.3. Descriptors for thermochemical water splitting materials

There have been a number of techniques used to predict the reduction enthalpy of metal oxides from simple computationally derived descriptors. The purpose is to allow faster screening of materials and improve material predictions. One common descriptor is the oxygen p-band centre with respect to the Fermi energy.[340], [434]–[436] Transition metal cations in octahedral complexes split electron states into five d-orbitals that spatially overlap with oxygen p-orbitals. The translational symmetry of the oxide lattice causes the formation of separated metal d and oxygen p bands. The overlap of these states can be quantified through density of states plots with the degree of overlap related to the degree of bond covalency.[292] The closer values to the fermi energy i.e. less negative, suggests there is a lower charge transfer gap for electrons to move from the oxygen 2p band to the Fermi energy and liberate an oxygen from the structure. As mentioned in chapter 5, this has been extended to other parameters such as oxygen migration. [231] Higher band centres will have more favourable oxygen migration properties due to the lower vacancy formation enthalpies and the weaker metal-oxygen bonds having increased flexibility.[231]

Here the oxygen p-band centre is tested as a descriptor for the reduction enthalpy of Ruddlesden-Popper materials. The band centre was calculated for the most oxidised phase for both sets of vacancy and interstitial supporting compounds (A_2BO_4 and $A_2BO_{4.25}$ respectively). Figure 8-13 shows a comparison between the reduction enthalpy and the oxygen p band centre. The reduction enthalpy is displayed for each investigated point defect. Correlations were investigated using Pearson's correlation coefficient whereby a value closer to 1 or -1 represents

a stronger positive or negative correlation respectively. Here a negative correlation is observed between reduction enthalpy and oxygen band centre. However, the low Pearson r value in Figure 8-13 suggests that the oxygen p band centre is a poor descriptor for all point defects in these structures (r=-0.0697). However, when considering solely interstitial defects the correlation become much stronger (r=-0.85468). The correlation between reduction enthalpy and band centre for Ruddlesden-Popper oxides was previously reported by Xie *et al.* although the authors reported a linear fit for all defects for $La_{2-x}Sr_xMO_{4\pm\delta}$ (M=Co, Ni and Cu) structures. [228] Here we consider a larger number of A-site and B-site configurations that potentially expand the scatter range compared to the previous literature.

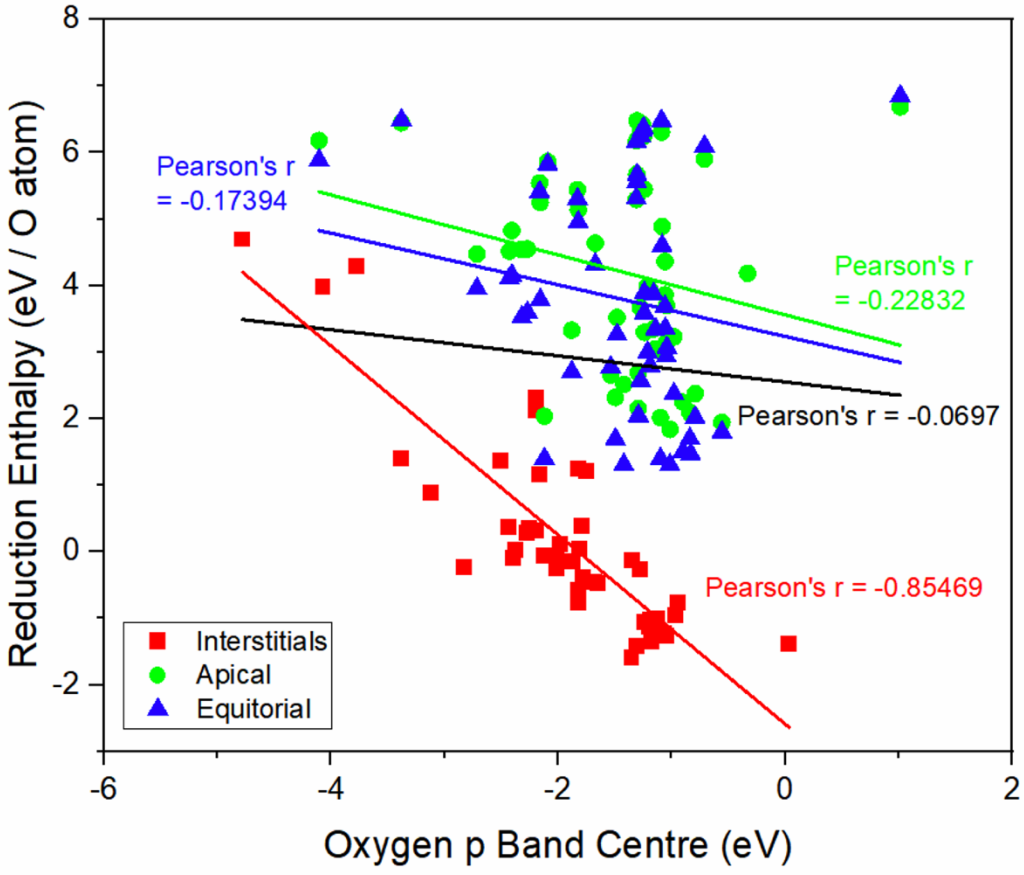

Figure 8-13. Comparison between reduction enthalpy and oxygen p band centre for the n=1 Ruddlesden-Popper phases.

Another descriptor reported within the literature is the charge delocalisation before and after an oxygen ion has been removed from the structure. [404], [437], [438] Equation 8.5 calculates the delocalisation, γ, from the average Bader charges on the oxygen within the reduced and oxidised structures.

$$\gamma = (N-1)\frac{\langle q_{o,reduced}\rangle - \langle q_{o,oxidised}\rangle}{\langle q_{o,oxidised}\rangle} \quad (8.5)$$

Where N is the number of oxygens in the oxidised structure, $\langle q_{o,X}\rangle$ is the average oxygen Bader charge in structure X.

This descriptor originated to understand the oxygen migration trends within SOFC materials. The hybridisation between metal 3d and oxygen 2p bands partially delocalises the charge over the oxygen sublattice.[404], [437], [438] Higher levels of delocalisation suggests greater charge spreading and minimising the repulsion from the oxygen defect and ease at which the defect can be accommodated by the lattice. This descriptor is relevant in this case since most metal oxide compounds used in this application exhibit a small polaron hopping charge transfer behaviour. This means the two electrons remaining after the vacancy formation will associate with the neighbouring transition metals and would be localised rather than delocalised in a band. These then move through the structure with the oxygen defect by ambipolar diffusion to maintain charge neutrality.

Figure 8-14 demonstrates the comparison between reduction enthalpy and charge delocalisation of the screened Ruddlesden-Popper compounds. Similar to the oxygen p band centre, a strong negative correlation is observed when considering all oxygen species in good agreement with original descriptor reports. [404], [437], [438] This demonstrates an improvement over the oxygen p band centre, however, when considering the correlation of individual point defect species, the strength of the correlation worsens for interstitial defects. Although, the correlations for both vacancy defects are stronger. Despite the improvements, this descriptor is more computationally expensive since it still requires the calculation of two structures - oxidised and reduced. Although additional information regarding the changes in charge distribution over lattice can lead to interesting observations, this would not save any computational time in a screening study.

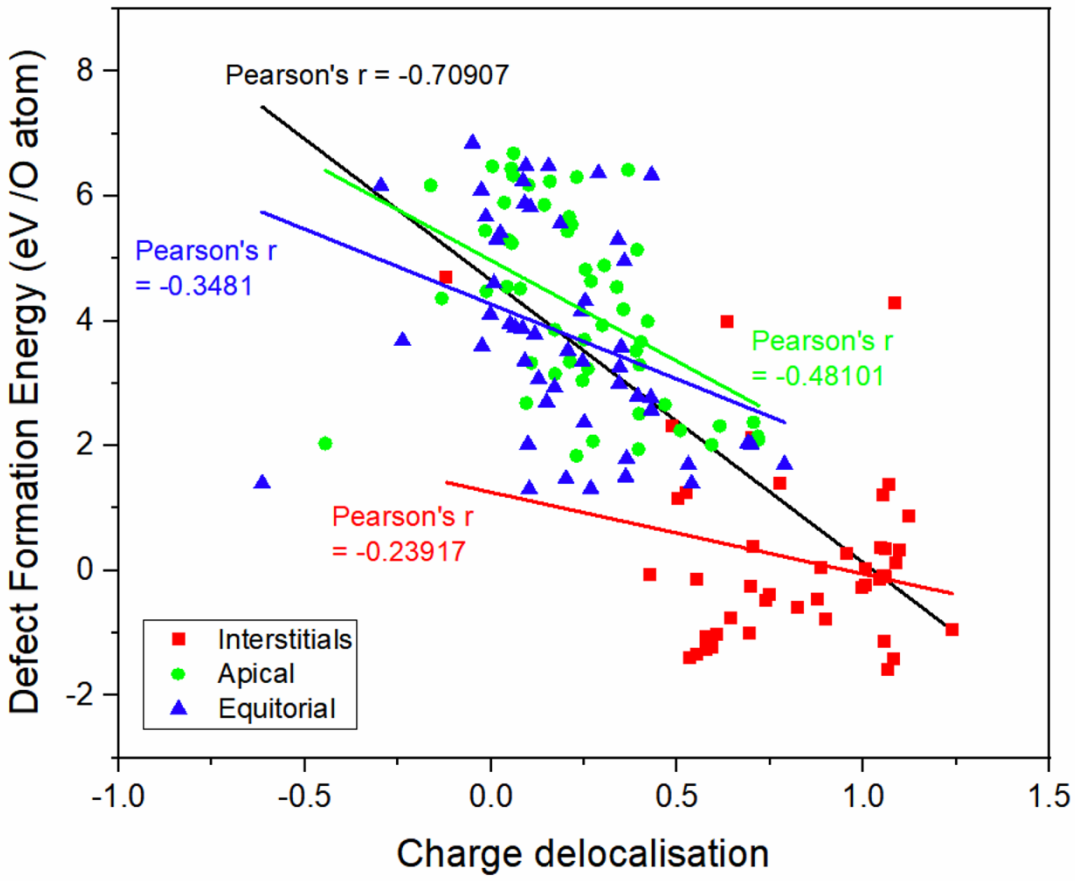

Figure 8-14. Comparison between reduction enthalpy and charge delocalisation for the n=1 Ruddlesden-Popper phases.

As an alternative, this work investigated a new simple descriptor based on the lattice enthalpy. This value is well-reported in chemistry textbooks as the energy required to dissociate an ionic lattice into its gaseous constituent elements. The lattice enthalpy is proportional to the electrostatic potential between oppositely charged ions. The enthalpy was originally quantified by the Born-Landé equation to include a proportionality equation based on the Madelung constant of the ions. Since this is dependent on the crystallographic structure, Kapustinskii later revisited the model and proposed a simplification to make it universally applicable to all ionic lattices. [439]

The relationship between lattice enthalpy and reduction enthalpy is observed through the simple electrostatic attraction (Equation 8.6). Bader charge was used as inputs to the equations, alongside the average distance between the B-site and oxygen ion of interest, as determined by using VESTA to inspect the outputted structures. The A-site is considered to have a "fixed" oxidation state, therefore only B-site and oxygen interactions are calculated for simplicity. It is

acknowledged that A-site interactions can improve the model sophistication and is considered for future work.

$$\Delta H_{latt} \propto \frac{\langle q_B \rangle \cdot q_o}{\langle r_{B-O} \rangle} \tag{8.6}$$

Figure 8-15 compares reduction enthalpy with the electrostatic potential between B-site cation and the oxygen ion to be removed from the structure. It is seen that a stronger lattice enthalpy has a higher reduction enthalpy. The model has strongest correlation between the tested descriptors (r = -0.81761). This descriptor predicts Ruddlesden-Popper structures with an electrostatic potential between -0.8 and -1.3 will have a reduction enthalpy suitable for thermochemical water splitting in line with Emery's prediction window. Although the spread in the data is quite large at these boundaries (up to 4 eV). This could be due to increased interaction from the A-site cation not captured in this calculation.

Crucially, when considering the oxygen defect species independently, all point defect species follow the correlation with a stronger value compared to the previous two descriptors. Therefore this suggests the electrostatic potential may act as a universal descriptor for all defect species. Furthermore, the computational requirement for this model only requires a single structure calculation, therefore allowing faster material discovery. This model can be further validated by extending it to higher order Ruddlesden-Popper orders (n>1) and perovskite materials.

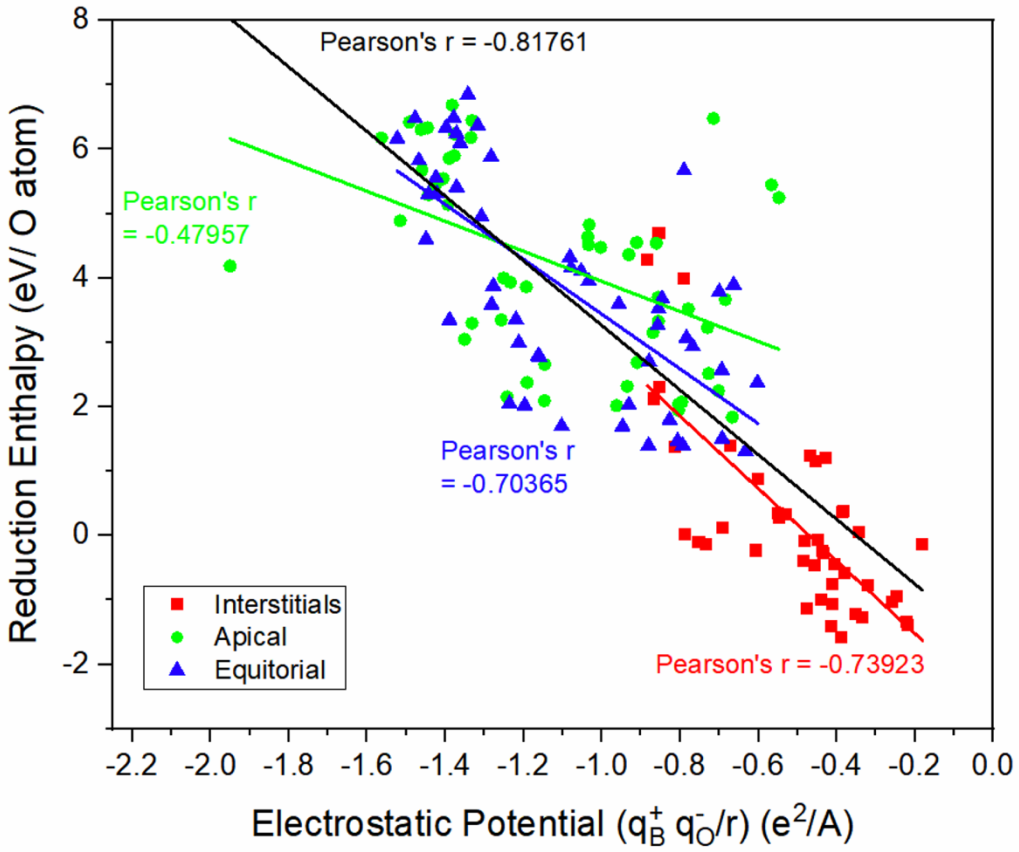

Figure 8-15. Comparison between reduction enthalpy and ionic electrostatic potential for the n=1 Ruddlesden-Popper phases.

Further screening models have been proposed by Deml *et al.* and later Wexler *et al.* in which numerous parameters are required to form parametric equations that accurately fit calculated vacancy formation energies.[154], [213], [440] These parameters were based on simple outputs such as formation enthalpy, oxygen band centre, band gap, energy above hull. Deml combine the band gap and oxide formation enthalpy to accurately describe the reduction enthalpy of $LaBO_3$ oxides. [154] Deml later expanded on their work to include oxygen p band centre and electronegativity.[213] These improvements to the model led to the accurate description of other metal oxide crystallographic structures e.g. fluorites, rock salts and spinels. Wexler's model was developed using simple binary metal oxides and translated well to more complex perovskites, but did not have a significant improvement over Deml's model. [211] The more complex models may provide a more accurate fit, however, the input parameters are not necessarily simple to acquire. For example, band gap energies are notoriously tricky to predict using DFT methods. Furthermore, the energy above hull is based on a comparison to compounds present in known databases. Although other databases beyond the materialsproject, maybe more populated, e.g. A-Flow and the Open Quantum Materials Database (OQMD),

some elements may not be as abundantly reported. Interestingly, Wexler *et al.* used the more sophisticated SCAN+U method rather than the more conventional GGA+U method. [211] Other studies have reported SCAN+U to accurately model redox thermodynamics of transition metal oxides. [441] A good extension of the work covered in this chapter would be to re-run the calculations using the SCAN+U method to observe if the same trends are observed, therefore providing validation to the proposed descriptor.

In the following chapter, experimental validation is carried out by investigating the thermochemical redox performance of the Ca_2MnO_4 compound. This material is composed of abundant constituent elements and was observed to have reduction enthalpies of 3.958 and 2.928 eV/O atom for the apical and oxygen sites respectively. Furthermore, the low energy above the hull suggested the compound is easily synthesised under laboratory conditions. These properties made is an interesting choice to compound to carry on to further testing.

8.4. Conclusions

In summary, this chapter used computational methods to screen the n=1 Ruddlesden-Popper metal oxide family to find potential compounds with favourable thermodynamics for thermochemical water splitting ($2.5< \Delta H_{red} <5$ eV/ O atom). Starting from 27,889 candidates, initial screens based on common perovskite crystallographic principles, a smaller set of compounds were simulated using density functional theory. Structures predicted to be synthesisable using an experimental based assumption for the energy above hull were further investigated by introducing defects into the structure from which the reduction enthalpy was calculated. This outlined a possible 27 compounds suitable for thermochemical water splitting via a vacancy mechanism and a further 3 compounds using an interstitial mechanism, of which several structures are predicted that have not previously been reported in inorganic crystallographic databases. Furthermore, the reduction enthalpy for the compounds in this dataset was compared against simple descriptors known in the literature (Oxygen p band centre and charge delocalisation). After observing good correlations with these descriptors, this chapter proposed a new simple descriptor based on the ionic lattice enthalpy. This descriptor demonstrated better universality for all oxygen defect species all oxygen defect species within the RP n=1 structure by reporting stronger Pearson's correlation values of -0.82.

9. Investigating Ca_2MnO_4 for thermochemical water splitting

Previously chapter 8 screened the n=1 Ruddlesden-Popper family for potential candidates for thermochemical water splitting. Ca_2MnO_4 was found to have favourable thermodynamics and stability values that suggested it is easily synthesisable under laboratory conditions. Furthermore, the elemental abundance of Ca and Mn drive motivation for this compound to be chosen for investigation.[405] This chapter will outline the additional computational understanding by outlining more detail into the defect formation energy as well as proposing an energy landscape for the water splitting reaction. Experiments are used to demonstrate the thermochemical water splitting performance and understand changes to crystallographic and chemical behaviour over the course of the redox cycle. The computational work reported in this chapter was completed under the guidance of Dr Ieuan Seymour, who taught the concepts of DFT and guided the calculations.

9.1. Previous investigations into Ca2MnO4

Both calcium and manganese containing compounds have been investigated for thermochemical water splitting or thermochemical energy storage technologies.[152], [155], [161], [438]–[443] Ca-doped $LaMnO_3$ has been studied to improve the oxygen production volumes during the reduction reaction. [153] This makes the oxygen vacancy formation more facile, however above 40% Ca inclusion the re-oxidation began to depreciate. $CaMnO_3$ has been one of the leading perovskite materials investigated for thermochemical energy storage due to its high energy density as an account of its ability to exchange oxygen within its lattice. [443], [444] Furthermore, it has been shown to be able to accommodate a wide range of different dopants into the structure to tune its thermochemical performance. [448], [449] Recently, $CaMn_{0.5}Ti_{0.5}O_{3-\delta}$ has been reported to demonstrate thermochemical water splitting with large production volumes and exceptional kinetics peaking at 5 μmol/min/g. [450] The inclusion of the relatively "redox inactive" Ti^{4+} increased the reduction enthalpy and entropy to being more favourable for the splitting reactions. However, $CaMnO_3$ has been observed to decompose into Ca_2MnO_4 and $CaMn_2O_4$ phases at temperatures above 1300 K under N_2. [451]

Ca_2MnO_4 has not been previously studied for thermochemical water splitting. Although it is a material that has been studied for dielectric and superconducting properties.[452], [453] The oxygen stoichiometric structure forms a $I4_1/acd$ tetragonal structure formed of alternate layers of rock-salt/perovskite ($CaO{\bullet}CaMnO_3$).[454] This phase has previously been reported to be stable with oxygen non-stoichiometry by vacancy defects up to values of δ=0.5 with assistance of a metal Ti reducing agent. [455], [456] In this chapter, the Ca_2MnO_4 is successfully synthesised, characterised and experimentally tested for thermochemical water splitting performance.

9.2. Results and Discussion

9.2.1. Defect formation energies

As part of the screening study in the previous chapter, the Ca_2MnO_4 (CMO-214) structure was determined to have a suitable defect formation energy for thermochemical water splitting. This material was calculated to have an anti-ferromagnetic arrangement of the manganese cations within the structure in agreement with previous structural characterisations of the compound. [457] This was attributed to the super-exchange between the manganese and oxygen ions. According to Goodenough-Kanamori rules, half-filled transition metal orbitals will interact with the filled oxygen p-orbitals along Mn-O-Mn 180° bond angles coordination to give an antiferromagnetic sub-lattice. Furthermore, the energy above hull of this compounds was 9.9 meV/atom compared to other Ca and Mn-based compounds within the materials project. [240] This is much lower than the imposed stability limit of 60 meV/atom for the experimentally synthesisable La_2CoO_4. [389] This strongly suggested it is synthesisable under simple laboratory conditions.

The defect energies were calculated in the previous section as part of the screening study. These were computationally compared to the analogous perovskite structure that has been commonly reported within literature. The comparison between reduction enthalpies is displayed in Table 9-1. The $CaMnO_3$ reduction enthalpy is 1.14 eV/atom is in a similar range to the experimental values of the cubic phase reported by Mastronado *et al.* [458] On the other hand, the over two-fold increase in reduction enthalpy for the Ruddlesden-Popper phase to 2.99 eV/O atom, aligns with similar improvement reported by Qian *et al.* for the inclusion of Ti^{4+} within the structure.

[450] However, the oxygen p band centre is further from the Fermi energy in the perovskite phase (-1.60 eV), compared to the Ruddlesden-Popper (-1.30), further suggesting the oxygen p-band descriptor is not applicable for vacancy defects in these materials.

Furthermore, there is an approximate 1 eV/O atom energy difference between a vacancy forming on the equatorial and apical oxygen sites. Trying to further understand this disparity, the magnetic moments of the structures were investigated to calculate the oxidations state of the B-site cation. The pristine structures all had a magnetic moment of 2.988μ_B which is in agreement with experimental values for Mn^{4+} d^3 cations.[459] Upon introducing an oxygen vacancy in the equatorial position (Figure 9-1a) the two adjacent Mn cations are reduced to Mn^{3+} d^4 – indicated by an increase in magnetic moment to 3.576. However, for the vacancy forming on the apical site, the calculations predict a difference whereby a $Mn^{4+}O_5$ square pyramidal structure forms, yet the charge is transferred to structurally unperturbed adjacent Mn cations. The apical site is only bonded to one B-site cation. For reduction to occur either this cation would need to be undergo double reduction or for the charge to be transferred to other cations. The difficulty of both these processes could explain the larger vacancy formation energy. Furthermore, the apical vacancy will disrupt the CaO rock salt layer that is likely to be more ionic in nature with a larger lattice enthalpy. This is supported by the increased Bader charge calculated to be on the apical sites. (Table 9-1).

Table 9-1. Comparison of reduction enthalpy, oxygen band centre and oxygen charge for the perovskite and n=1 Ruddlesden-Popper calcium manganate phases.

	Reduction Enthalpy (eV / O atom)		**Oxygen p Band Centre (eV)**	**Average Oxygen Charge (e)**		
	Equatorial	**Apical**		**Overall**	**Equatorial**	**Apical**
$CaMnO_3$	1.14		-1.60	-1.17		
Ca_2MnO_4	2.93	3.96	-1.30	-1.24	-1.20	-1.28

a)

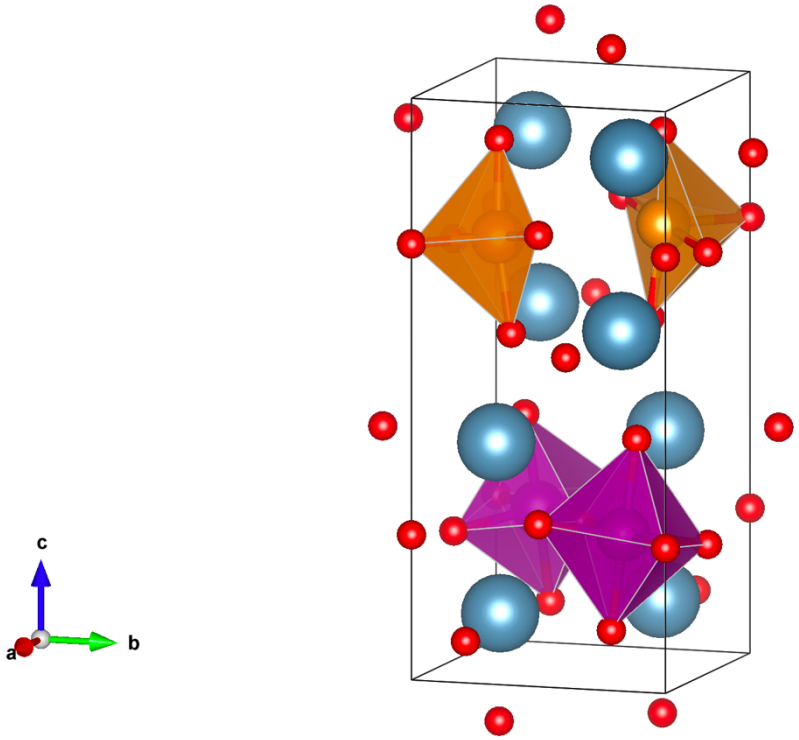

b)

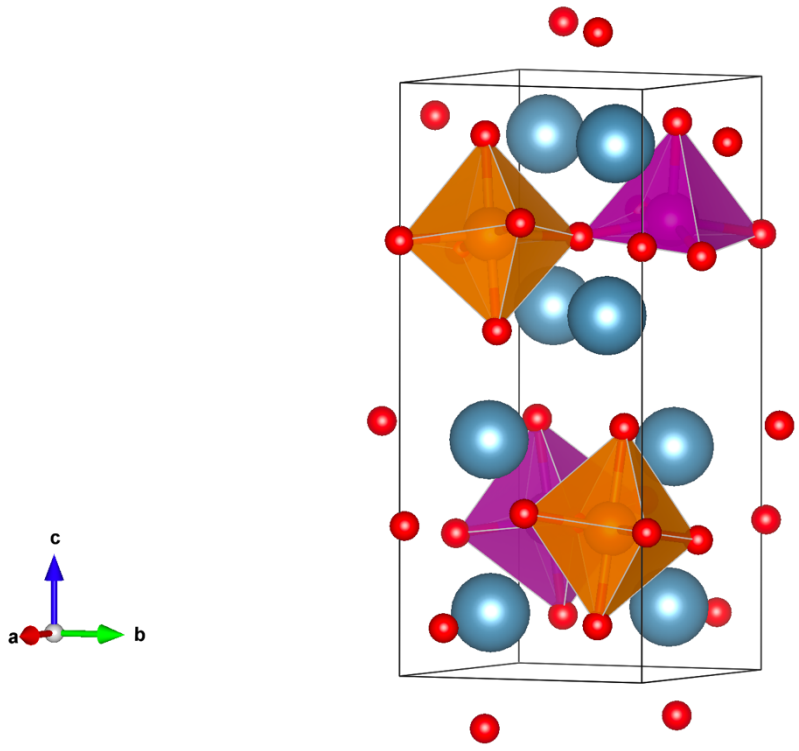

Figure 9-1. Ca_2MnO_4 structures with an oxygen vacancy introduced on the a) equatorial and b) apical lattice sites. The orange octahedra indicate the manganese ions with increased magnetic moment indicating a decrease in oxidation state.

9.2.2. Initial Powder Characterisation

Ca_2MnO_4 samples were synthesised using the sol-gel method as previously reported in the literature. [455], [456] Stoichiometric amounts of $Ca(NO_3)_2 \bullet 4H_2O$ (99%) and MnO_2 (99%) powders were dissolved in HNO_3 before citric acid and ethylene glycol were added in a 2:4:1 molar ratio with nitrates respectively. The solution was stirred on a hot plate heated to 300 °C to promote the sol-gel reaction. At the onset of gelation (Figure 9-2a), the beaker was removed from the hot plate and cooled. The gel was crushed before decomposing at 600 °C for 12 hours. The decomposed ash was ground using a pestle and mortar before being reheated at 1000 °C for 12 hours and 1200 °C for 24 hours with intermediate grinding. The final product was a fine black powder (Figure 9-2b).

a) b)

Figure 9-2. Images of the Ca_2MnO_4 synthesis process showing a) formed gel of metal nitrate solutions and b) final powder state.

X-Ray diffraction was used to confirm the crystal structure of the synthesised phase. Le Bail refinement was conducted to determine the lattice parameters. Figure 9-3 shows the

diffractogram with the structure fitted to the $I4_1/acd$ tetragonal phase in agreement with previous literature reports. [454], [457] This phase is a subsidiary of the *I*4/*mmm* RP phase, however due to the tilting of the MnO_6 octahedra cause a displacement of the oxygen anions within the structure that arise to special reflections of the (211), (213), (215) and (217) planes.[454]

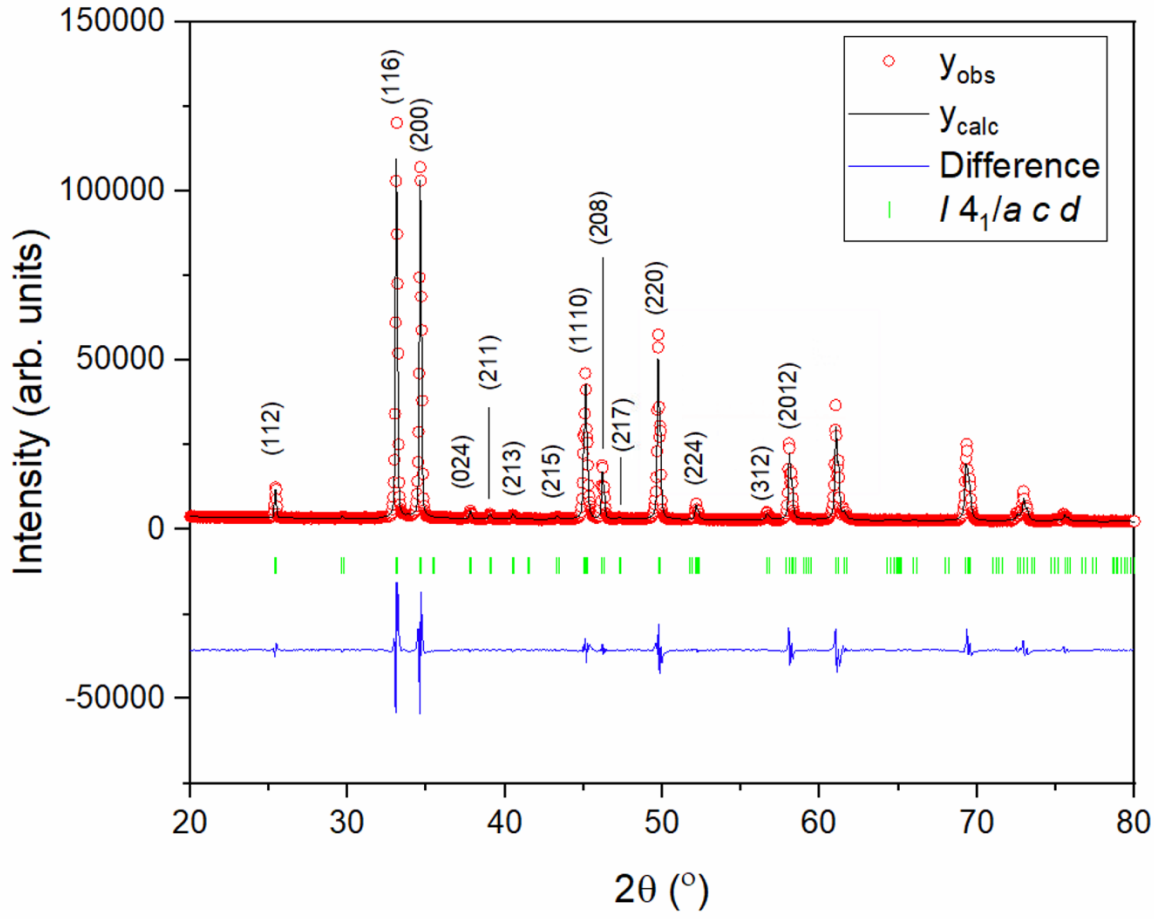

Figure 9-3. XRD diffractogram of the synthesised Ca_2MnO_4 powder.

Table 9-2. Lattice parameters for the synthesised Ca_2MnO_4 compared to reference literature data.

	Ca_2MnO_4 (This work)	**Ca_2MnO_4 (ref. [414])**
a (Å)	5.18507(6)	5.18847(3)
c (Å)	24.1082(5)	24.12907(14)
Cell Volume (Å^3)	648.1(2)	649.54

XPS data was used to understand the chemical nature of the surface of the powders. Each of the core levels of the constituent elements with Ca_2MnO_4 were scanned individually. Both the calcium 2p and oxygen 1s spectra were fitted with two components corresponding to the bulk and surface states (Figure 9-4a and Figure *9-4*b). The Mn 2p and 3s spectra were collected to try and determine the oxidation state of manganese. This is difficult with peak fitting the 2p spectra, however the unique split peak feature of the 2p3/2 peak has previously been used as a strong indication of Mn4+ in manganese oxide (Figure 9-4c).[460] Furthermore, the peak separation in the Mn 3s spectra can be used to determine oxidation state. Peak separation in the region of 4.7 eV can usually be attributed to the 4+ oxidation state. [461] Here the separation is slightly lower, that can suggest the oxidation state to Mn5+ (Figure 9-4d).

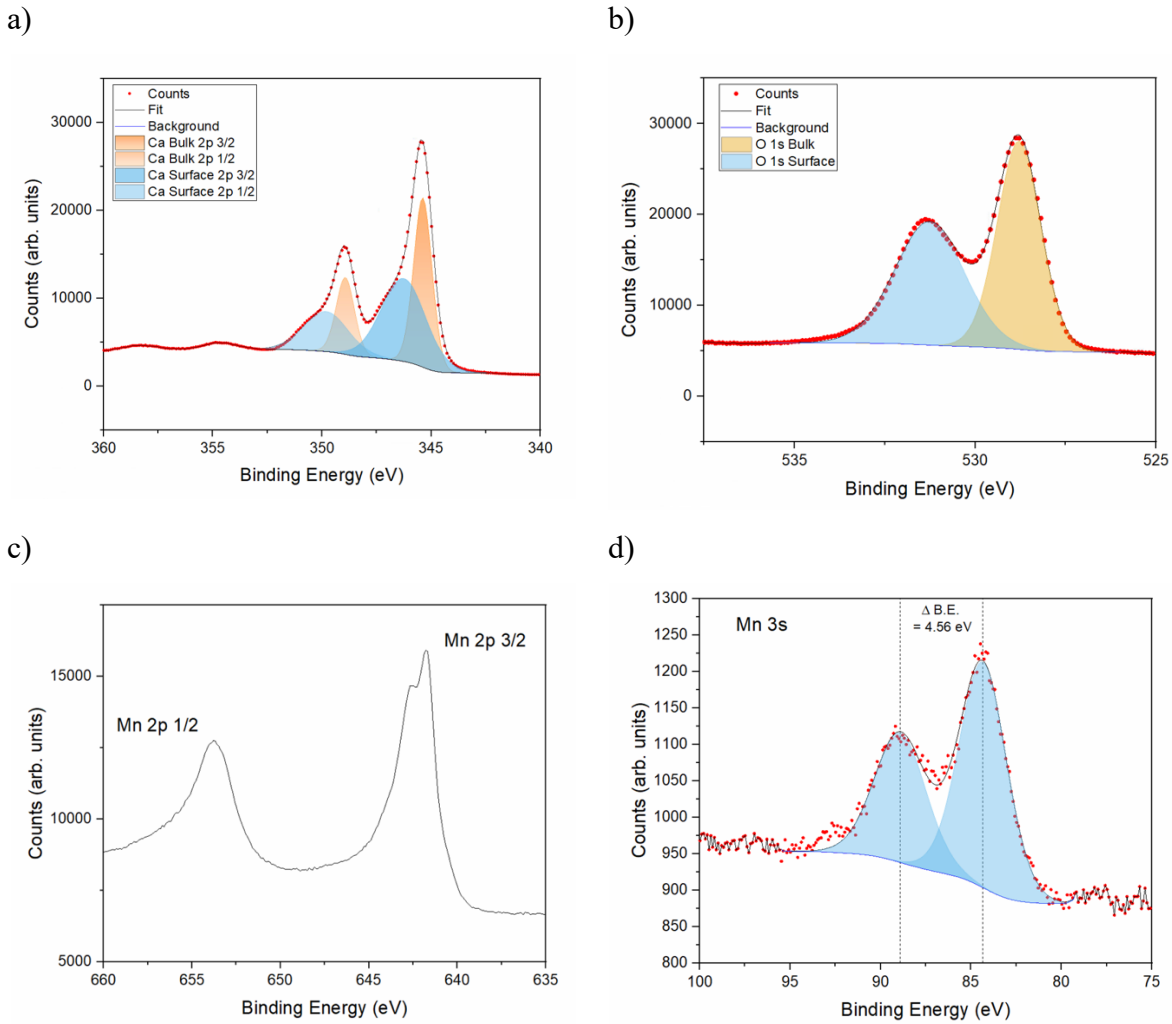

Figure 9-4. XPS spectra obtained for the Ca_2MnO_4. a) Ca 2p, b) O 1s, c) Mn 2p and d) Mn 3s core level spectra.

Secondary electron images revealed the powder size and morphology (Figure 9-5). A JEOL 6010 SEM was used with a 20 kV accelerating voltage and working distance of 27 mm. Similar to the LSCrF powders in chapter 7, the powder can form macrostructures of in the region of 50 μm. Further magnification on one of these structures can reveal a highly porous with a large surface area for gas exchange (Figure 9-5b).

a)

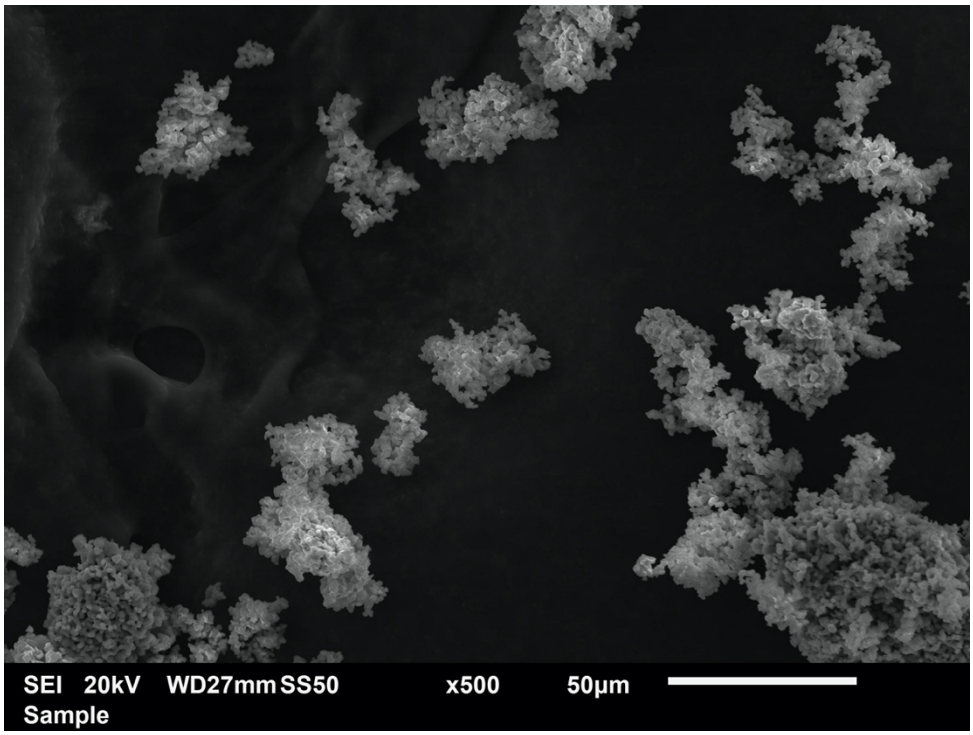

b)

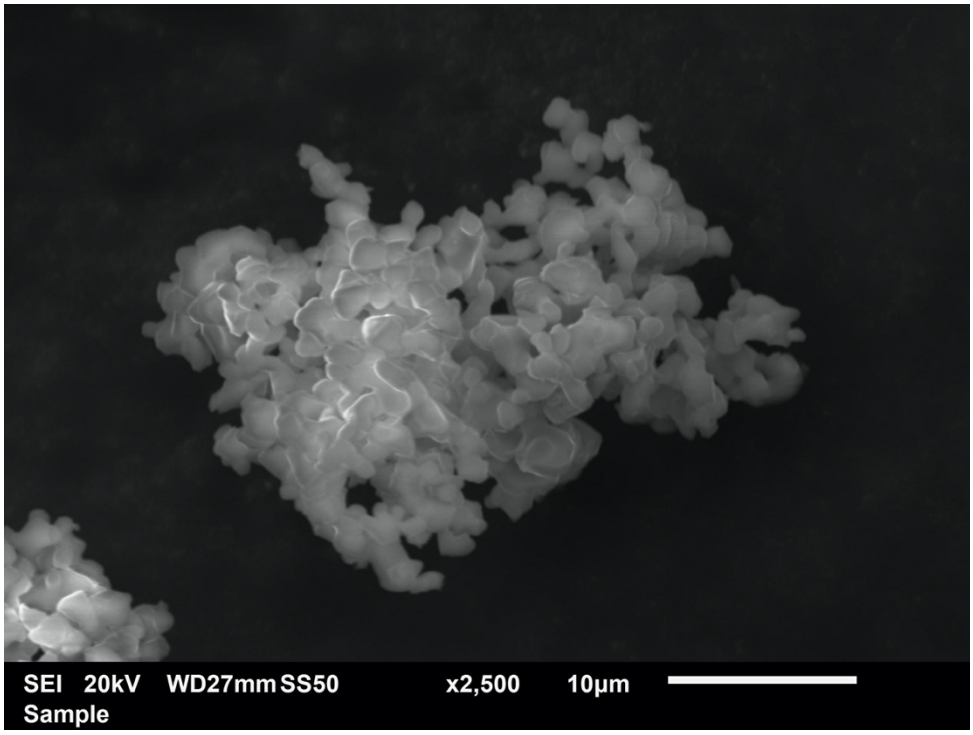

Figure 9-5. Secondary electron images of the synthesised Ca_2MnO_4 powder.

9.2.3. Thermal Behaviour under low P_{O_2}

The thermal behaviour of the powder was investigated using TGA-DSC to heat the powder to 1400 °C under 100 ml/min of flowing argon. The oxygen in the exhaust gas was measured using the same electrochemical sensor as the studies in the previous chapters. The chamber was evacuated and back filled twice to achieve an oxygen partial pressure in the region of 20 ppm. The heating rate was fixed to 20 °C/min.

Figure 9-6a shows the mass change and DSC signal as a function of temperature. Below 600 °C there is a small mass loss observed before the signal stabilising until 800 °C. This initial mass loss was originally thought to be related to oxygen interstitials evolving from the lattice since the Mn 3s XPS spectra due to XPS suggesting the presence of Mn^{5+}. However, this was later dismissed due to no increase in the oxygen signal. Instead, the initial mass loss could be attributed to adsorbed carbon or moisture on the surface of the material. The calculations for the oxygen stoichiometry used the stabilised mass just after 600 °C and assumed complete stoichiometry.

Above 800 °C thermal reduction is initiated, indicated by a decrease in the mass signal and a consequent increase in the oxygen detected in the exhaust stream (Figure 9-6b). This steadily continues until 1100 °C where the oxygen production slows, however the mass continues to decrease. At 1350 °C there is a sharp decrease in the mass and rapid increase in the oxygen production signal. The DSC signal noise provides indication that the phase may start melting above this temperature. This was later confirmed upon the extraction of the sample from the instrument.

The oxygen production rates prior to melting are larger to than the rates observed by LSCrF-8273 powder in chapter 7 (Figure 7-9). Production rate at 1000 ° is 3.9 μmol/min/g Ca_2MnO_4 versus 2.6 μmol/min/g LSCrF-8273. Furthermore, the oxygen production only shows one broad production rather numerous peaks. This suggests just a singular reduction process is occurring upon heating. The maximum oxygen non-stoichiometry calculated for this heating program prior to melting was approximately 3.75. Previous authors have reported this compound's ability to accommodate oxygen non-stoichiometries (δ=0.5), however this was using a Ti metal reducing agent and lower temperatures. [456]

a)

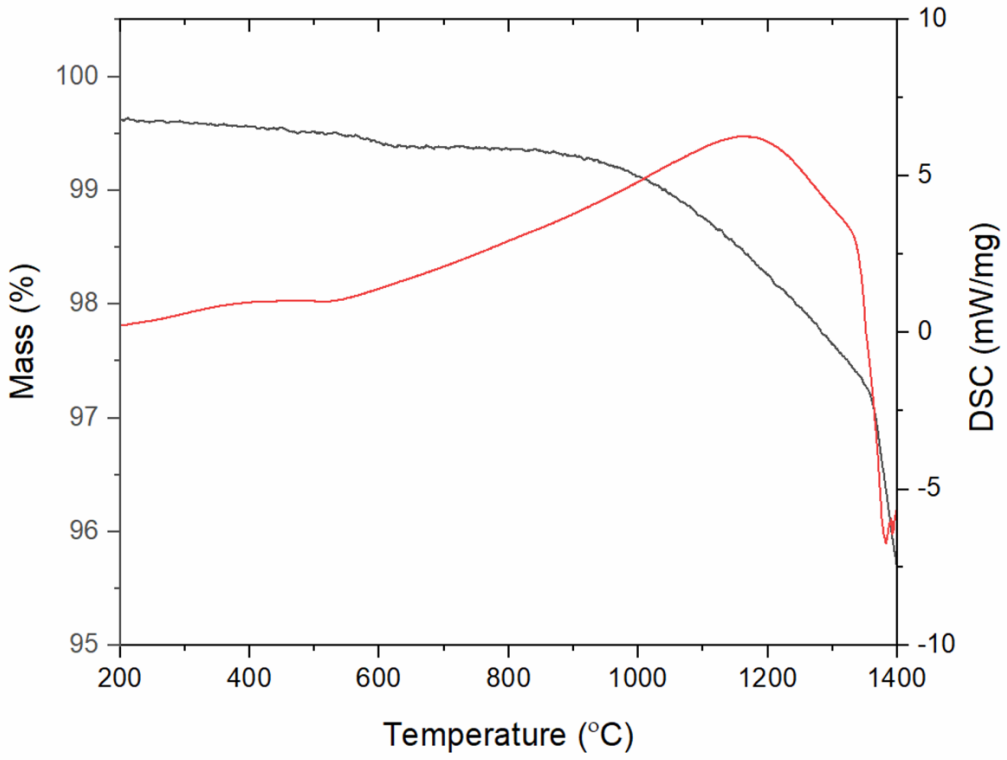

b)

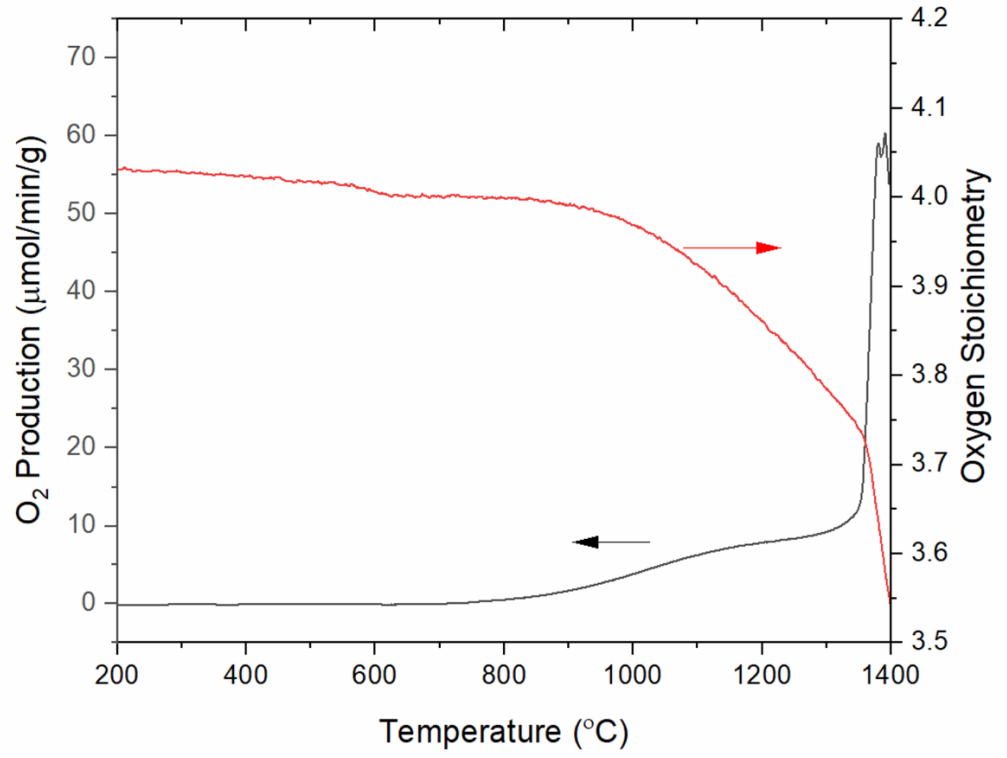

Figure 9-6. Thermal analysis results from heating Ca_2MnO_4 under an argon environment. a) Mass % and DSC signal as a function of temperature, b) O_2 detected in the exhaust stream and oxygen stoichiometry converted from the mass loss.

The thermal stability of the Ca_2MnO_4 under inert gas flow was analysed using HT-XRD. The sample was heated under nitrogen flow up to 1200 °C in an Anton-Paar HTK1200N environment chamber. The powder samples were placed on an alumina sample holder and flattened using a glass slide. The samples were heated to the target temperature and held for 20 mins before scanning the range 20 to 60° with a step size of 0.034°. The lattice parameters were refined using Le Bail method and FULLPROF software. [350]

The compound observed good thermal stability by retaining the $I4_1/acd$ tetragonal space group until exceeding 1100 °C (Figure 9-7). Above this temperature secondary phase peaks appear between 35 and 40° and 50 and 55°. These peaks were matched to the $CaMn_2O_4$ spinel phase that had been observed to form when heating $CaMnO_3$ to high temperatures. [451], [462] The presence of this phase can be confirmed visually by the presence of reddish-brown spots on the black powders (Figure 9-8). Leonowicz *et al*. suggested that this phase forms as part of a decomposition reaction alongside CaO as a secondary product.[462] Reinspecting the TGA data and calculating the predicted oxygen evolution from the change in mass, a discrepancy is observed above 1100 °C whereby the mass loss does not align with the oxygen production. This could be due to volatility of the metal oxide or its decomposition products, however this has not been previously reported.

An interesting observation of the high temperature XRD was observed from inspecting the refined lattice parameters. Ca_2MnO_4 undergoes a negative thermal expansion along the c-axis up to 800 °C. This has previously been reported in air atmospheres and related to the straightening of MnO_6 octahedra and a phase transition to the *I*4/*mmm* structure.[454], [463] This structural transition has been reported for other RP phases, namely Sr_2RhO_4 – interestingly another potential thermochemical water splitting structure identified by the screening study in chapter 8. [464] This transition in the Ca_2MnO_4 appears to coincide with the oxygen evolution occurring from the lattice. It is therefore thought less tilted octahedra can allow for greater Mn 3d and O 2p bond overlap in the structure, therefore allowing more facile electron transfer. This has been postulated with the B-site doped $SrCoO_3$ discussed in chapter 6. Once in the positive thermal expansion region, the rate of c-axis expansion appears to increase with temperature. This is due to chemical expansion from the formation of Mn^{3+} HS ions within the structure that are 20% larger than the oxidised Mn^{4+} (0.645 vs. 0.53 Å respectively).[272]

Furthermore, the increase in expansion could be due to the formation of HS d^4 Mn^{3+} ions that are Jahn-Teller active and can lead to an elongated structure within the lattice. [465]

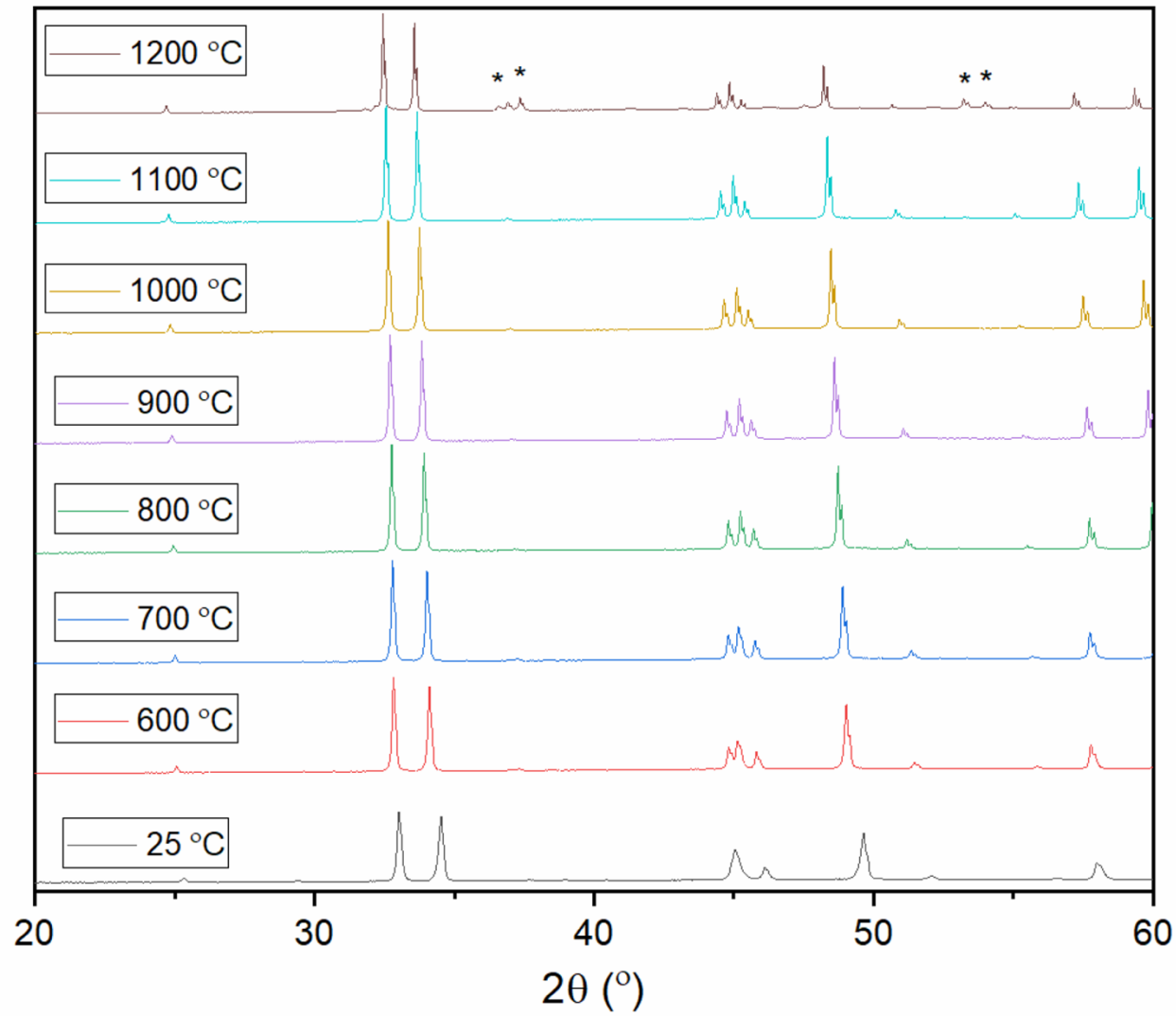

Figure 9-7. High temperature X-ray diffractograms between 600 and 1200 °C of Ca_2MnO_4 under a nitrogen flow. Asterisks indicate the presence of $CaMn_2O_4$ spinel phase forming at high temperatures.

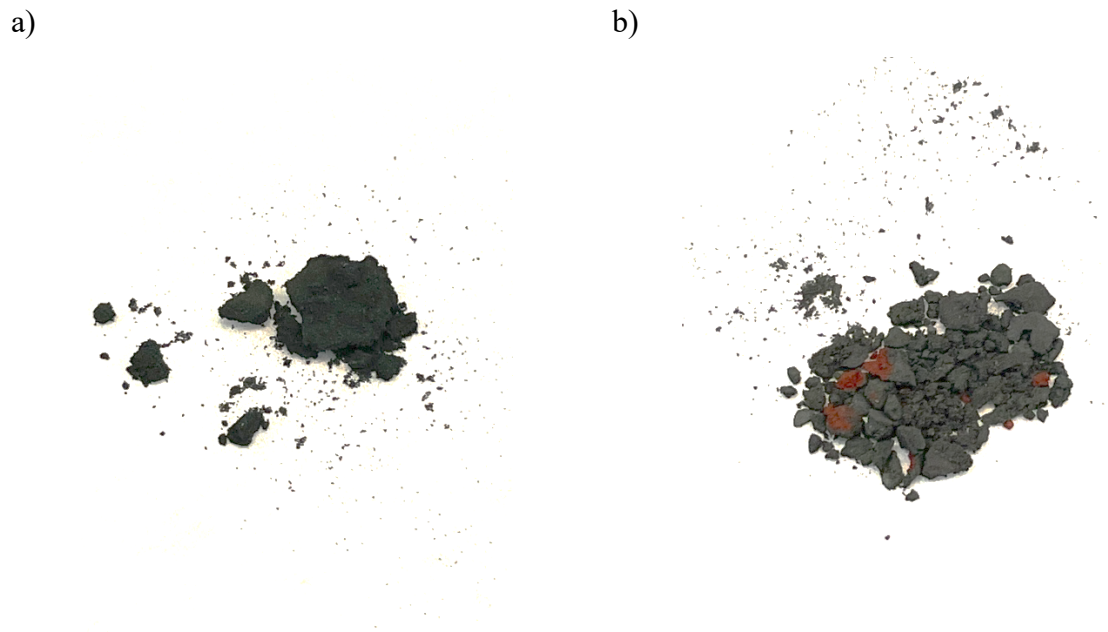

Figure 9-8. Contrast enhanced images of the $Ca2MnO_4$ powders heated under inert gas flow to a) 1000 °C and b) 1200°C. Presence of the $CaMn_2O_4$ spinel phase is observed by the reddish-brown spots in b).

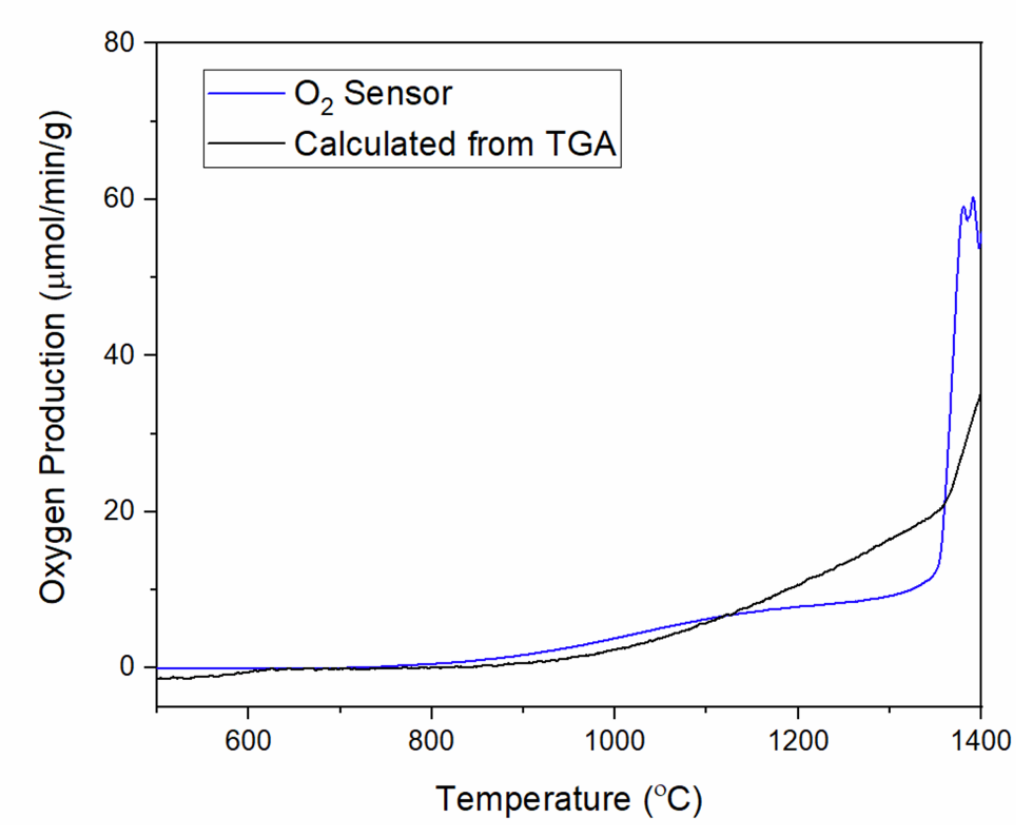

Figure 9-9. Comparison between the oxygen evolution for Ca_2MnO_4 measured directly from the exhaust gas and calculated production from the TG mass signal.

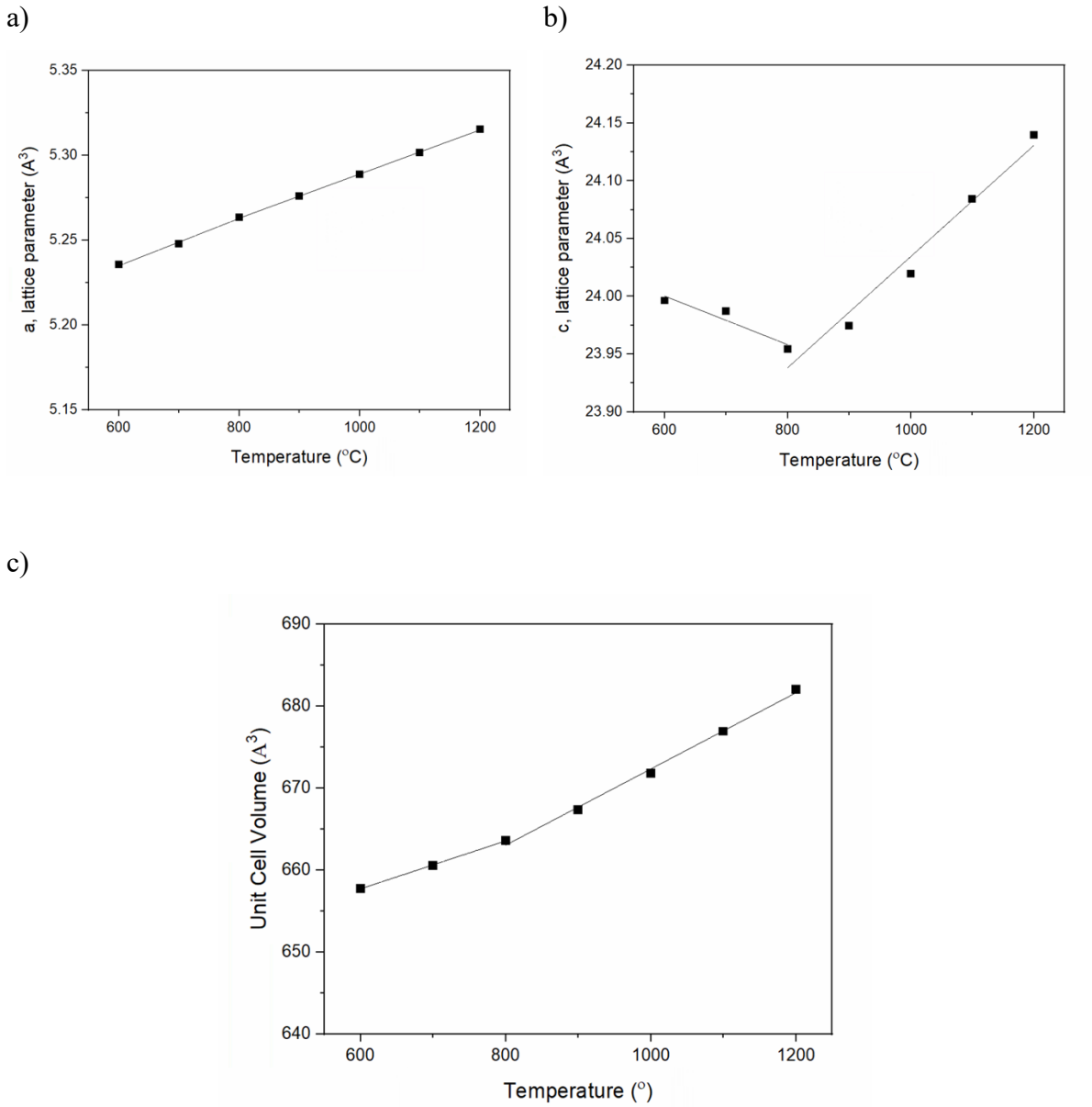

Figure 9-10. Lattice parameters outputted from the high-temperature X-ray diffraction of Ca_2MnO_4 under nitrogen gas.

9.2.4. Thermochemical Water Splitting

The thermochemical water splitting performance was measured using the reactor described in chapter 5. Approximately 0.1 g of powder was loaded into the alumina reactor tube and purged with argon overnight to achieve a low constant P_{O_2} of approximately 10^{-4} atm. The oxygen and hydrogen signals were detected using a quadruple mass spectrometer over the duration of the reaction. The redox cycling was conducted under a temperature swing operation between 1000 and 800 °C. This upper temperature was set to avoid the decomposition of the phase to

$CaMn_2O_4$. Reoxidation was performed under 50% humidity to maintain consistency with the LSCrF experiments. As mentioned in the previous experimental chapters, this water splitting reactor was completed late into the experimental window of the PhD and the data is presented to demonstrate hydrogen production capability. Further optimisation of the reactor will be undertaken during subsequent postdoc placement.

The gas production shown in Figure 9-11 agrees with the oxygen evolved in the thermal analysis experiments. The oxygen production occurs at approximately 800 °C and increases up to 1000 °C at which the isotherm causes the decrease in production. Despite the 60-minute isotherm and cooling, the gas production appears to not reach equilibrium (i.e. returns to zero), therefore suggesting slow oxygen diffusion within the material.

Upon introduction of humidity to the reduced material, the hydrogen signal increases to approximately 1.6 μmol/min/g. This value is comparable to the LSCrF-8291 compound, however, this is lower than other perovskites reported within the literature. Furthermore, the production stays constant for the reoxidation window but never returns to zero suggesting equilibrium is not reached. The oxygen signal increases later on in the oxidation cycle suggesting some thermolysis may occur on the sample surface. However, some confidence is gained that the oxygen has been reincorporated into the lattice, since a small increase in the oxygen signal is observed upon reheating to 1000 °C.

Interestingly the oxygen production rate and volume in the first reduction step (Table 9-3) was significantly higher than the TGA experiment (Figure 9-6). This was observed with the $SrCo_{0.8}Sb_{0.2}O_{3-\delta}$ in the chapter 6, due to the reaction with the alumina tube and sample holder. Post thermochemical water splitting characterisation by XRD revealed no obvious formation of secondary phases with only Al_2O_3 present from the alumina wool sample holder (Figure 9-12), so the difference could be more related to the difference in heating conditions between the TGA and water splitting rig. The Le Bail refined lattice parameters determine the cell volume remains slightly larger than the synthesised powder probably due to the presence of residual reduced Mn cations within the structure.

Table 9-3. Gas production volumes for Ca_2MnO_4 thermochemical water splitting cycle between 1000 and 800 °C and 50% humidity.

	O_2 Evolved (µmol/g)	**Peak O_2 production rate (µmol/min/g)**	**H_2 Production over 120 mins (µmol/g)**	**Peak H_2 production rate (µmol/min/g)**
Ca_2MnO_4	227.94	9.24	78.21	1.61

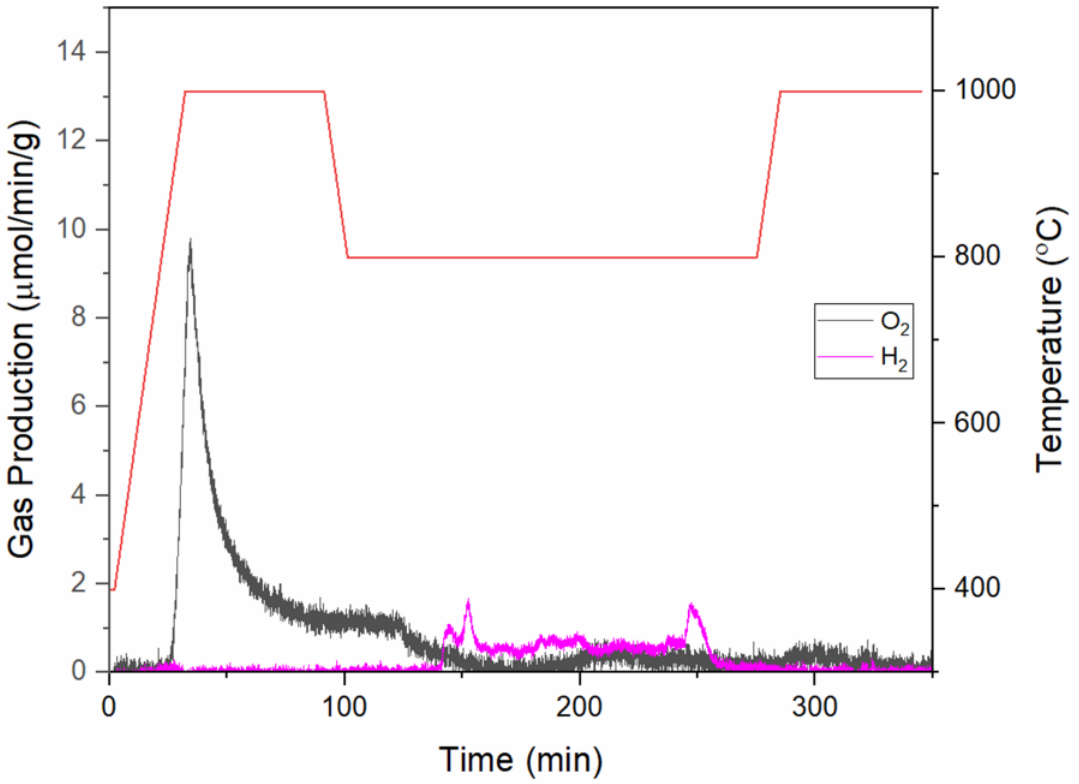

Figure 9-11. Gas production of the 1000/800 °C thermochemical water splitting cycle for Ca_2MnO_4.

In order to gain further understanding of the thermochemical redox cycle, a small amount of powder was heated to 1000 °C for 1 hour under an argon flow. This powder was then investigated using SEM and XPS to understand changes in morphology and surface chemistry. Secondary electron images were taken using a JEOL 6010 SEM with a 20 kV accelerating voltage. The "macro" structures remained in the range of 50 µm, although further magnification demonstrated the porous microstructure had been decreased upon heating (Figure 9-13b). Further sintering was observed with the increased timescales at elevated temperatures of the water splitting sample (Figure 9-13c). The sintering effect causes a

reduction in the active gas-solid surface area available for reactions and can lower the kinetics of the process. This has been reported within the literature as the cause for deactivation. [156] The inclusion of redox stable cations such as Mg^{2+} has been shown to limit sintering.[466] However, the increased stability and aliovalent nature could have underlying effects on other properties such as oxygen migration and vacancy formation energetics.

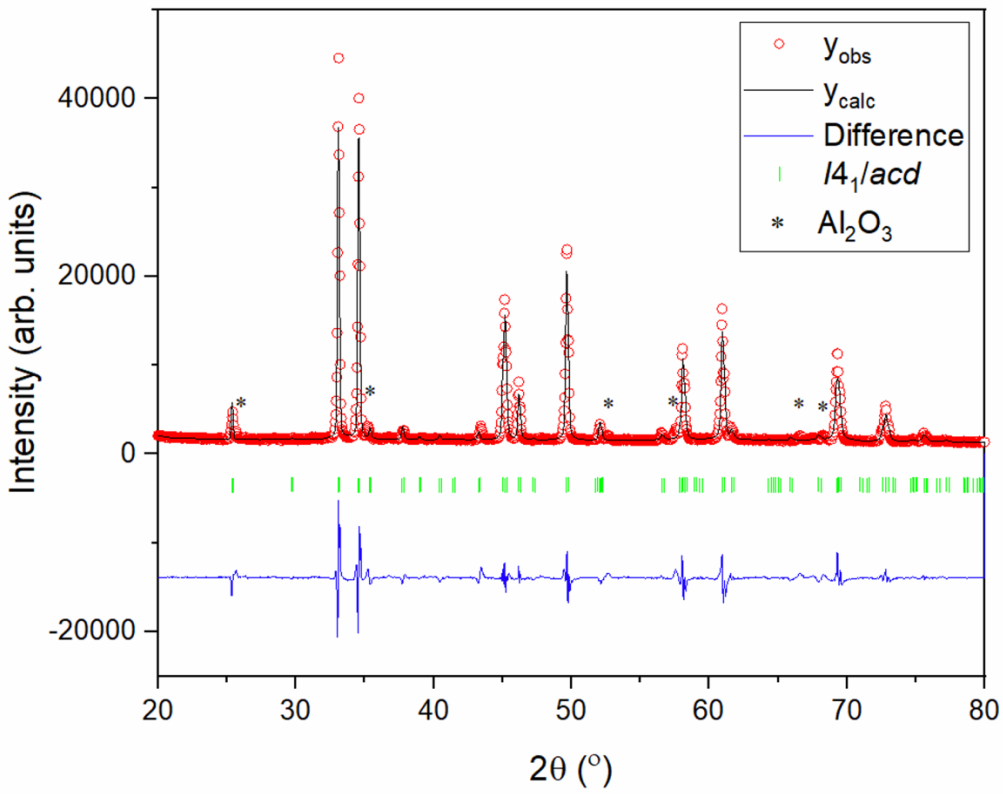

Figure 9-12. X-ray diffractogram of Ca_2MnO_4 after thermochemical water splitting cycle at 1000 and 800 °C.

Table 9-4. Comparison of lattice parameters of the synthesised Ca_2MnO_4 and post thermochemical water splitting cycle powder.

	Ca_2MnO_4 (Pristine)	**Ca_2MnO_4 (1000/800 TWS)**
a (Å)	5.18507(6)	5.1906(1)
c (Å)	24.1082(5)	24.065(1)
Cell Volume (Å^3)	648.1(2)	648.4(4)

a)

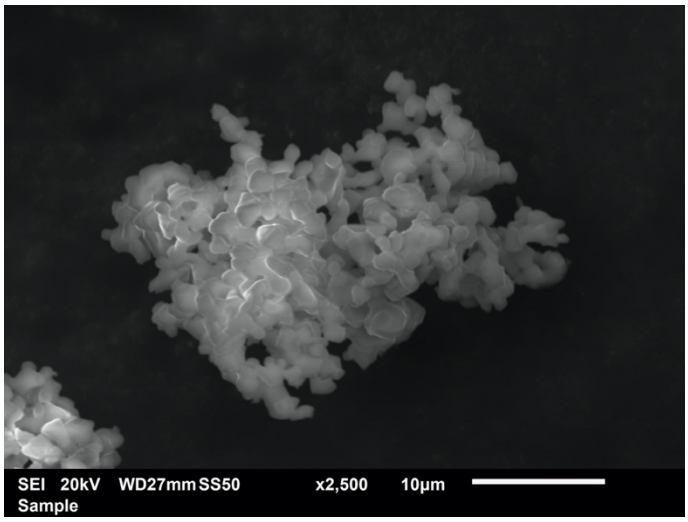

b)

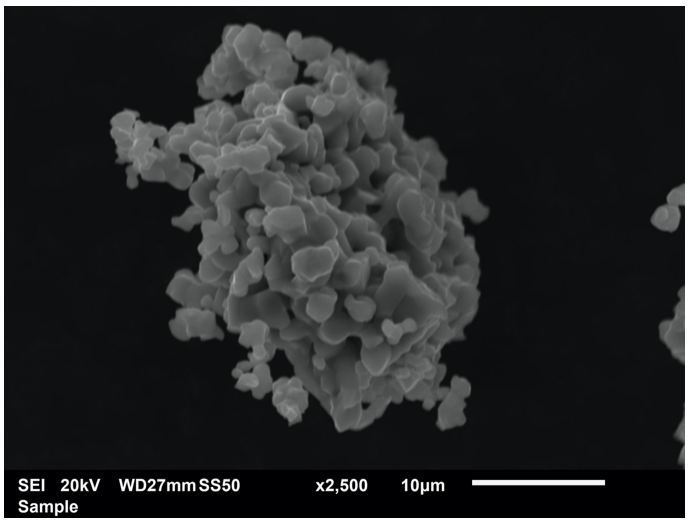

c)

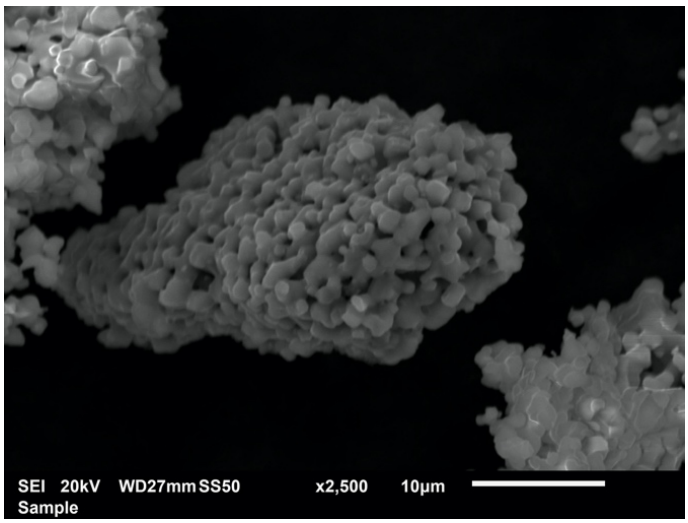

Figure 9-13. Secondary electron micrographs of the Ca_2MnO_4 powder after a) synthesis, b) heating to 1000 °C under Argon and c) after thermochemical water splitting at 1000/800 °C.

XPS analysed the core levels of the manganese cation before and after the reoxidation under steam. Figure 9-14a and c the Mn 2p spectra before and after steam respectively. The distinct peak shape of the 2p3 level related to the Mn^{4+} ion (Figure 9-4d) is not observed, thus confirming the reduction of the lattice. The thermochemical water splitting sample could display a slight reformation of the peak shape, however remains inconclusive. The Mn 3s spectra shown in Figure 9-14b and Figure *9-14*d show the peak an increase in the multiplet splitting suggesting a shift to lower oxidation states. Figure 9-14b does not reach the separation of the reference Mn_2O_3 (5.5 eV), suggesting a mixed 3/4+ oxidation state is present in the $Ca_2MnO_{4-\delta}$ and not complete reduction to the $Ca_2MnO_{3.5}$ or phase decomposition to $CaMn_2O_4$. However, upon inspection of the water splitting sample, it is difficult to accurately determine the peak splitting. A secondary component matched to a barium contaminant contributes to the area of the higher binding energy peak. It is postulated the barium source is from the alumina wool used to hole the sample in the reactor tube, however further experiments are required to prove this theory.

From the inspection of the Ca 2p and O 1s XPS spectra, the concentration of surface species is observed to increase after the oxidation step with steam (Figure 9-15). This can be attributed to calcium hydroxide phases that may form on the surface with upon introduction of humidified gas. Hydroxyl groups fill the surface vacancies upon the reintroduction of steam. Subsequent charge transfer from one of the hydroxyl groups to the reduced transition metal cation breaks one of the surface hydroxyl groups to allow facile surface diffusion of the proton. Previous authors have tried to calculate the surface reaction mechanisms of steam with reduced metal oxides. [467], [468] The diffusing proton reduces another hydroxyl group to form a hydrogen that desorbs from the surface. The charge transfer step is calculated to be the rate determining step for both ceria and $LaMnO_3$ surfaces. [467], [468] The decomposition of $Ca(OH)_2$ has been a heavily studied thermochemical energy storage.[469], [470] The hydrated phase is highly stable and thermodynamically drives the oxidation reaction with fast kinetics [471]–[473] The increased stability of the $Ca(OH)_2$ phase could suggest there is an increased energy requirement to decompose the surface hydroxyls during oxidation reaction. Zhao *et al.* suggested the destabilising of this hydroxyl group can accelerate the water splitting kinetics. [468]

Alternatively, surface analysis techniques such as LEIS have reported Ruddlesden-Popper oxides to have AO-terminated surfaces with an absence of the B-site cation in the first atomic

layer.[474] This cation is the redox active species within the compound and its lack of surface presence could explain the slower reaction kinetics. However, authors have shown the AO terminated surface can still be active in gas-solid reactions.[475], [476] The introduction of a redox active species onto the A-site, such as in the case of $Ce_xSr_{2-x}MnO_4$ [392], could be a good avenue to explore for accelerating the splitting reaction. Furthermore, it could be interesting to explore surface modifications of the RP phase through processes such as ex-solution. This involves the formation of socketed metal nanoparticles on the surface of the metal oxides to have catalytic effect on the splitting reaction and has been seen to improve the splitting reaction for perovskite compounds.[169]

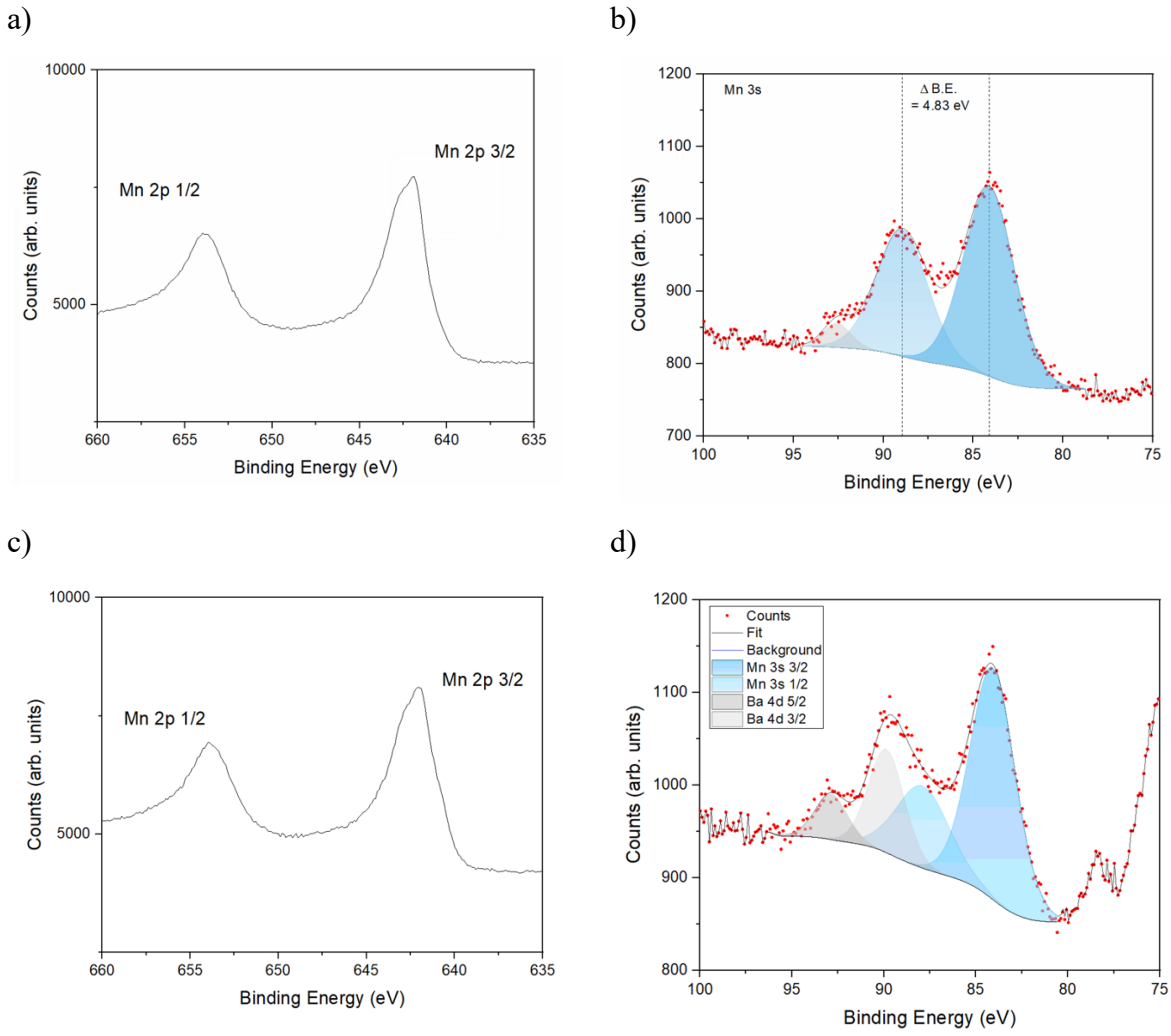

Figure 9-14. XPS spectra of the Mn core levels for Ca_2MnO_4 powder after a,b) heating to 1000 °C under argon and c,d) thermochemical water splitting at 1000/800 °C.

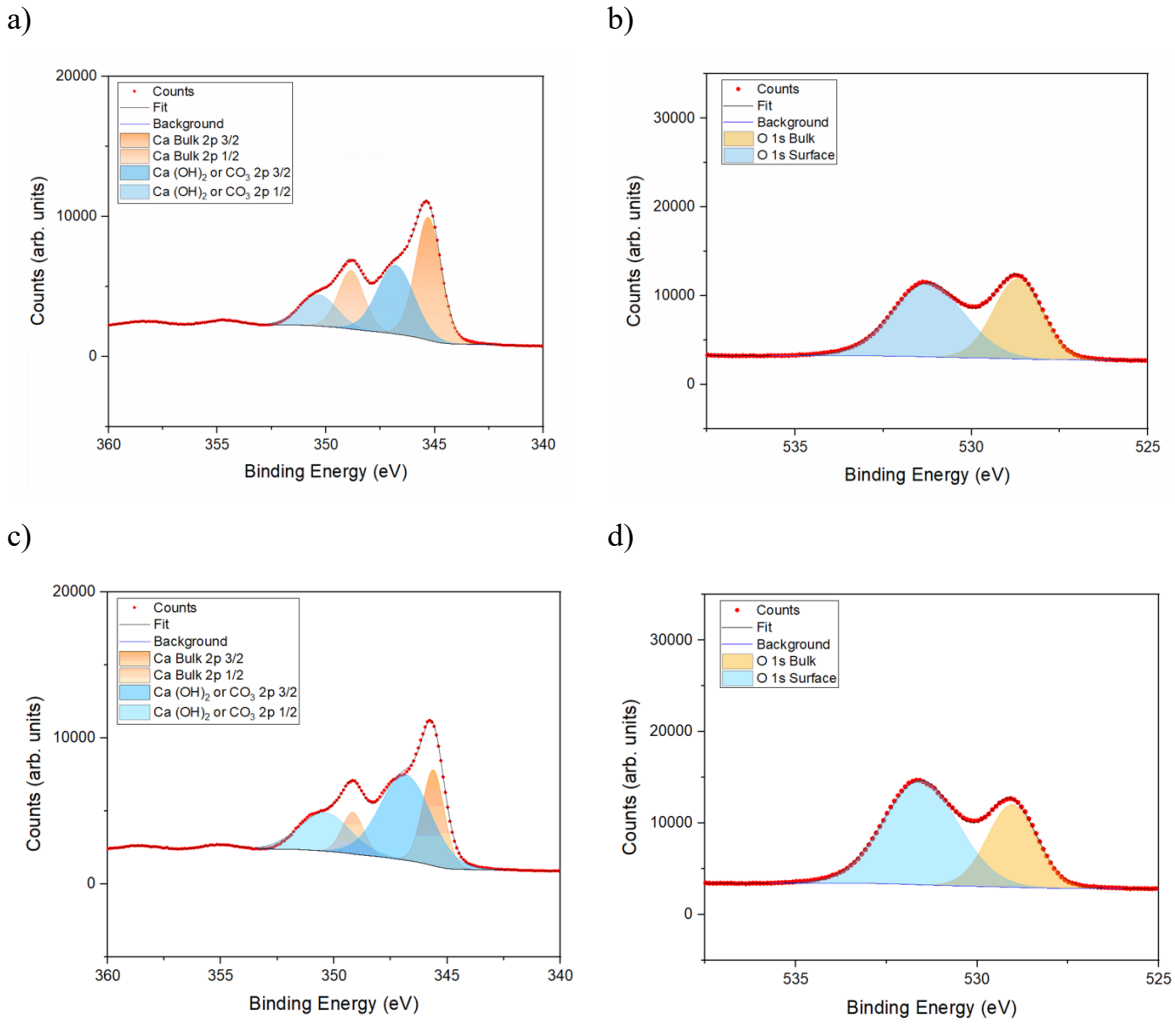

Figure 9-15. XPS spectra of the Ca 2p and O 1s core levels for Ca_2MnO_4 powder after a,b) heating to 1000 °C under argon and c,d) thermochemical water splitting at 1000/800 °C.

9.3. Conclusions

Ca_2MnO_4 was identified by computational screening to have favourable reduction enthalpy for thermochemical water splitting (2.93 eV/ O atom). In this chapter, Ca_2MnO_4 was further investigated using computational and experimental methods to confirm thermochemical water splitting behaviour. This compound composed of abundant elements was synthesised using sol-gel method to form a $I4_1/acd$ crystal structure. Thermal analysis methods confirmed oxygen evolution under an inert gas flow was onset by heating to temperatures greater than 800 °C. Production rates were in similar ranges to those of LSCrF materials reported in previous chapters (3.9 µmol/min/g Ca_2MnO_4 versus 2.6 µmol/min/g LSCrF-8273 at 1000 ° C). In-situ XRD provided further confirmation of crystallographic stability up 1100 °C. Ca_2MnO_4

was heated to 1000 °C under flowing argon, before reoxidising under 50% humidity at 800 °C. However, the reoxidation kinetics were observed to be sluggish compared to literature reported materials (1.61 μmol/min/g versus 3.0 μmol/min/g for Ca_2MnO_4 versus $Ce_{0.75}Zr_{0.25}O_{2-\delta}$ respectively). XPS and SEM attributed this to a combination of particle sintering and formation of stable surface hydroxyls that limits the reactive area and slows the electron transfer during reoxidation. Further improvements to these materials should focus on improving the reoxidation reaction by through doping strategies to destabilise the surface hydroxyls and limiting particle sintering.

10. Conclusions

Thermochemical water splitting is a green hydrogen production technique that uses concentrated solar energy to heat metal oxides and facilitate thermal reduction and consequent oxygen release. Reduced metal oxides react with steam resulting in reoxidation and production of hydrogen. Current trends in research are to lower the temperatures required for thermal reduction without compromising hydrogen production volumes or rates, and this has led to the research of different metal oxide families such as perovskites. This thesis continues the research into perovskite materials through combining experimental and first principal techniques.

Initially, $SrCo_{1-x}Sb_xO_3$ perovskites were investigated due to their previous reports of rapid exchange of large oxygen volumes. Although despite its large oxygen evolution volumes, the thermodynamics for water splitting were unfavourable. However, the material was found to have better performance as an oxygen separation material. The inclusion of antimony was observed to improve the redox kinetics by lowering crystal field splitting of the cobalt cations to induce a more favourable electron configuration ($e_g^* = 1.2$) that exceeds the redox kinetics of current oxygen separation materials.

Secondly, previous studies on lanthanum chromium perovskites are expanded by investigating the effect of Fe concentration within the $(La_{0.8}Sr_{0.2})_{0.95}Cr_{1-x}Fe_xO_{3-\delta}$ structure. Oxygen evolution was observed to increase with additional Fe content. DFT calculations outline Fe-O bonds have a lower reduction enthalpy compared to Cr-O and consequently increased Fe concentration leads to greater oxygen evolution volumes up to 36 μmol/g. These materials demonstrated hydrogen production via thermochemical water splitting; however surface analysis techniques revealed an increase in Sr segregating towards the surface that mitigated further production. The reduction extent strongly correlated with vacancy concentration suggesting an electrostatic driving force within the sample. These strontium enriched surfaces had previously been reported to undergo recrystallisation to layered perovskite Ruddlesden-Popper phases. The phases are known for their oxygen exchange properties however are relatively underexplored for thermochemical water splitting.

This work completed a comprehensive screening study based on simple and well-known crystallographic principles and DFT simulations of over 27,000 possible A_2BO_4 structures to find potential candidates to proceed with experimental testing. 30 candidate materials were predicted to have favourable thermodynamics to support thermochemical water splitting. From which, Ca_2MnO_4, was investigated experimentally due its abundant constituent elements. This compound was synthesised and characterised using a suite of different analytical techniques. Importantly, the powder compound was observed to produce hydrogen during a 1000/800 °C redox cycle thereby providing validation to the computational screening of Ruddlesden-Popper oxides. There is plenty of scope to pursue with investigating Ca_2MnO_4 compounds and Ruddlesden-Popper oxides for thermochemical water splitting with doping strategies to further enhance the performance.

11. Future Work

Further work regarding the results covered in this thesis can be split into two categories: initial and prospective. Firstly, further characterisation of the redox thermodynamics, ΔH_O and ΔS_O, should be completed to provide better design of experimental parameters and materials performance. Furthermore, the ability of having a reliable experimental setup to test the thermodynamics can provide further validation to the RP-screening study. Alternative methods such as coulometric titration can provide data at lower oxygen partial pressures ($<10^{-15}$ atm), however an interesting report by Carrillo and Scheffe outlines a protocol to experimentally determine thermodynamic parameters by monitoring hydrogen production and consumption as the P_{O_2} is changed by altering the water content in the gas flow.[477] This is interesting due to its ability to simultaneously demonstrate water splitting performance alongside recording the thermodynamic information. This experimental protocol can be relatively straight forwards to implement with the rig used in this thesis and given the time to research should be fruitful for the materials discussed as part of this project.

Following on from the thermodynamic characterisation, optimal cycling parameters can be determined, and the durability of the materials can be further understood. The degradation effects of the perovskite materials can be explored as a function of temperature, time, or oxygen partial pressure since there was a clear dependence on the vacancy concentration. Furthermore, corroboration with known perovskite thermochemical materials such as LSM would provide stronger basis of the nature of this degradation mechanism.

Regarding the Ruddlesden-Popper materials outlined by the screening study, it could be easy to try and synthesise and test the compounds. However a more interesting route would be to undertake a fundamental study into the difference between the interstitial and vacancy-mediated surface reactions between steam and reduced oxides. First principles studies on the surface reaction mechanisms have previously been reported for ceria and $LaMnO_3$ and can provide a good basis from which to start. An extension to this would be interesting to simulate and understand the effect of crystal anisotropy and surface termination on the splitting reaction in the Ruddlesden-Popper oxides, since both factors have been shown to affect the catalytic performance. [360], [478]–[480]

This thesis demonstrated the thermochemical water splitting performance of both perovskite and Ruddlesden-Popper oxides. These two related materials have been investigated previously as heterostructures for enhanced oxygen surface exchange. [481]–[484] The interfaces between the two phases have been attributed for the improved oxygen exchange and other knowledge from the solid oxide cells field relating to triple phase boundary decoration can further optimise the material performance.

References

[1] W. F. Ruddiman, “The anthropocene,” *Annual Review of Earth and Planetary Sciences*, vol. 41, pp. 45–68, May 2013, doi: 10.1146/annurev-earth-050212-123944.

[2] S. L. Lewis and M. A. Maslin, “Defining the Anthropocene,” *Nature 2015 519:7542*, vol. 519, no. 7542, pp. 171–180, Mar. 2015, doi: 10.1038/nature14258.

[3] IEA, “Global Energy Review 2021,” Paris, 2021.

[4] R. A. Huggins, *Energy Storage*. Springer, 2016. doi: 10.1007/978-3-319-21239-5_1.

[5] T. Chen *et al.*, “Applications of Lithium-Ion Batteries in Grid-Scale Energy Storage Systems,” *Transactions of Tianjin University*, vol. 26, no. 3, pp. 208–217, 2020, doi: 10.1007/S12209-020-00236-W/

[6] P. Nikolaidis and A. Poullikkas, “A comparative overview of hydrogen production processes,” *Renewable and Sustainable Energy Reviews*, vol. 67, pp. 597–611, 2017, doi: https://doi.org/10.1016/j.rser.2016.09.044.

[7] “What impact did COP26 have on public opinion? | YouGov.” https://yougov.co.uk/topics/politics/articles-reports/2021/11/22/what-impact-did-cop26-have-public-opinion (accessed Mar. 06, 2022).

[8] “A sustainable pathway for the global energy transition”, Accessed: Mar. 06, 2022. [Online]. Available: www.hydrogencouncil.com.

[9] F. Eljack and M.-K. Kazi, “Prospects and Challenges of Green Hydrogen Economy via Multi-Sector Global Symbiosis in Qatar,” *Frontiers in Sustainability*, vol. 0, p. 14, Jan. 2021, doi: 10.3389/FRSUS.2020.612762.

[10] K. H. Delgado, L. Maier, S. Tischer, A. Zellner, H. Stotz, and O. Deutschmann, “Surface Reaction Kinetics of Steam- and CO_2-Reforming as Well as Oxidation of Methane over Nickel-Based Catalysts,” *Catalysts*, vol. 5, no. 2, pp. 871–904, 2015, doi: 10.3390/catal5020871.

[11] M. Ball and M. Weeda, “The hydrogen economy – Vision or reality?,” *International Journal of Hydrogen Energy*, vol. 40, no. 25, pp. 7903–7919, Jul. 2015, doi: 10.1016/J.IJHYDENE.2015.04.032.

[12] “Hydrogen generation could become $1 trillion market: Goldman Sachs.” https://www.cnbc.com/2022/02/23/hydrogen-generation-could-become-1-trillion-market-goldman-sachs.html (accessed Mar. 06, 2022).

[13] S. Trasatti, “Water electrolysis: who first?,” *Journal of Electroanalytical Chemistry*, vol. 476, no. 1, pp. 90–91, Oct. 1999, doi: 10.1016/S0022-0728(99)00364-2.

[14] S. Shiva Kumar and V. Himabindu, “Hydrogen production by PEM water electrolysis – A review,” *Materials Science for Energy Technologies*, vol. 2, no. 3, pp. 442–454, Dec. 2019, doi: 10.1016/J.MSET.2019.03.002.

[15] K. Scott, “Chapter 1 Introduction to Electrolysis{,} Electrolysers and Hydrogen Production,” in *Electrochemical Methods for Hydrogen Production*, The Royal Society of Chemistry, 2020, pp. 1–27. doi: 10.1039/9781788016049-00001.

[16] C. Li and J. B. Baek, “The promise of hydrogen production from alkaline anion exchange membrane electrolyzers,” *Nano Energy*, vol. 87, p. 106162, Sep. 2021, doi: 10.1016/J.NANOEN.2021.106162.

[17] S. Shiva Kumar and V. Himabindu, “Hydrogen production by PEM water electrolysis – A review,” *Materials Science for Energy Technologies*, vol. 2, no. 3, pp. 442–454, 2019, doi: https://doi.org/10.1016/j.mset.2019.03.002.

[18] Y. Guo, G. Li, J. Zhou, and Y. Liu, “Comparison between hydrogen production by alkaline water electrolysis and hydrogen production by PEM electrolysis,” *IOP Conference Series: Earth and Environmental Science*, vol. 371, no. 4, p. 042022, Dec. 2019, doi: 10.1088/1755-1315/371/4/042022.

[19] “Critical metals in the path towards the decarbonisation of the EU energy sector - Publications Office of the EU.” https://op.europa.eu/en/publication-detail/-/publication/505c089c-7655-4546-bd17-83f91d581190/language-en (accessed Mar. 06, 2022).

[20] C. Gupta, P. H. Maheshwari, and S. R. Dhakate, “Development of multiwalled carbon nanotubes platinum nanocomposite as efficient PEM fuel cell catalyst,” *Materials for Renewable and Sustainable Energy*, vol. 5, no. 1, pp. 1–11, Feb. 2016, doi: 10.1007/S40243-015-0066-5/

[21] M. Kim, “Progress towards lower-cost proton exchange membrane fuel cells,” *Scilight*, vol. 2021, no. 14, p. 141110, Apr. 2021, doi: 10.1063/10.0004268.

[22] L. Mølmen, K. Eiler, L. Fast, P. Leisner, and E. Pellicer, “Recent advances in catalyst materials for proton exchange membrane fuel cells,” *APL Materials*, vol. 9, no. 4, p. 040702, Apr. 2021, doi: 10.1063/5.0045801.

[23] J. B. Hansen, “Solid oxide electrolysis – a key enabling technology for sustainable energy scenarios,” *Faraday Discussions*, vol. 182, no. 0, pp. 9–48, Nov. 2015, doi: 10.1039/C5FD90071A.

[24] M. A. Laguna-Bercero, “Recent advances in high temperature electrolysis using solid oxide fuel cells: A review,” *Journal of Power Sources*, vol. 203, pp. 4–16, 2012, doi: https://doi.org/10.1016/j.jpowsour.2011.12.019.

[25] E. E. (Stathis) Michaelides, *Green Energy and Technology*. Springer, 2012. doi: 10.2174/97816080528511120101.

[26] J. D. Holladay, J. Hu, D. L. King, and Y. Wang, “An overview of hydrogen production technologies,” *Catalysis Today*, vol. 139, no. 4, pp. 244–260, Jan. 2009.

[27] N. Getoff, “Photoelectrochemical and photocatalytic methods of hydrogen production: A short review,” *International Journal of Hydrogen Energy*, vol. 15, no. 6, pp. 407–417, Jan. 1990, doi: 10.1016/0360-3199(90)90198-8.

[28] C. Acar, I. Dincer, and G. F. Naterer, “Review of photocatalytic water-splitting methods for sustainable hydrogen production,” *International Journal of Energy Research*, vol. 40, no. 11, pp. 1449–1473, Sep. 2016, doi: 10.1002/ER.3549.

[29] T. Bak, J. Nowotny, M. Rekas, and C. C. Sorrell, “Photo-electrochemical properties of the TiO2-Pt system in aqueous solutions,” *International Journal of Hydrogen Energy*, vol. 27, no. 1, pp. 19–26, 2002, doi: https://doi.org/10.1016/S0360-3199(01)00090-8.

[30] C. Acar, I. Dincer, and C. Zamfirescu, “A review on selected heterogeneous photocatalysts for hydrogen production,” *International Journal of Energy Research*, vol. 38, no. 15, pp. 1903–1920, Dec. 2014, doi: 10.1002/ER.3211.

[31] V. M. Aroutiounian, V. M. Arakelyan, and G. E. Shahnazaryan, “Metal oxide photoelectrodes for hydrogen generation using solar radiation-driven water splitting,” *Solar Energy*, vol. 78, no. 5, pp. 581–592, 2005, doi: https://doi.org/10.1016/j.solener.2004.02.002.

[32] L. A. Weinstein, J. Loomis, B. Bhatia, D. M. Bierman, E. N. Wang, and G. Chen, “Concentrating Solar Power,” *Chemical Reviews*, vol. 115, no. 23, pp. 12797–12838, Dec. 2015, doi: 10.1021/acs.chemrev.5b00397.

[33] M. Romero and A. Steinfeld, “Concentrating solar thermal power and thermochemical fuels,” *Energy & Environmental Science*, vol. 5, no. 11, p. 9234, Oct. 2012, doi: 10.1039/c2ee21275g.

[34] J. Lédé, F. Lapicque, and J. Villermaux, “Production of hydrogen by direct thermal decomposition of water,” *International Journal of Hydrogen Energy*, vol. 8, no. 9, pp. 675–679, Jan. 1983, doi: 10.1016/0360-3199(83)90175-1.

[35] J. Scheffe, D. Mccord, and D. Gordon, “Hydrogen (or Syngas) Generation-Solar Thermal Chemical Energy Storage”.

[36] K. Onuki, S. Kubo, A. Terada, N. Sakaba, and R. Hino, “Thermochemical water-splitting cycle using iodine and sulfur,” *Energy & Environmental Science*, vol. 2, no. 5, pp. 491–497, May 2009, doi: 10.1039/B821113M.

[37] S. Kubo *et al.*, “A demonstration study on a closed-cycle hydrogen production by the thermochemical water-splitting iodine–sulfur process,” *Nuclear Engineering and Design*, vol. 233, no. 1–3, pp. 347–354, Oct. 2004, doi: 10.1016/J.NUCENGDES.2004.08.025.

[38] C. Sattler, M. Roeb, C. Agrafiotis, and D. Thomey, “Solar hydrogen production via sulphur based thermochemical water-splitting,” *Solar Energy*, vol. 156, pp. 30–47, Nov. 2017, doi: 10.1016/J.SOLENER.2017.05.060.

[39] M. Roeb *et al.*, “Sulphur based thermochemical cycles: Development and assessment of key components of the process,” *International Journal of Hydrogen Energy*, vol. 38, no. 14, pp. 6197–6204, May 2013, doi: 10.1016/J.IJHYDENE.2013.01.068.

[40] A. Steinfeld, “Solar thermochemical production of hydrogen—a review,” *Solar Energy*, vol. 78, no. 5, pp. 603–615, 2005, doi: 10.1016/j.solener.2003.12.012.

[41] R. Schäppi *et al.*, “Drop-in fuels from sunlight and air,” *Nature*, vol. 601, no. 7891, pp. 63–68, 2022, doi: 10.1038/s41586-021-04174-y.

[42] A. J. Carrillo, J. González-Aguilar, M. Romero, and J. M. Coronado, “Solar Energy on Demand: A Review on High Temperature Thermochemical Heat Storage Systems and Materials,” *Chemical Reviews*, vol. 119, no. 7, pp. 4777–4816, Apr. 2019, doi: 10.1021/acs.chemrev.8b00315.

[43] R. Schäppi *et al.*, “Drop-in fuels from sunlight and air,” *Nature*, vol. 601, no. 7891, pp. 63–68, 2022, doi: 10.1038/s41586-021-04174-y.

[44] D. Marxer *et al.*, “Demonstration of the Entire Production Chain to Renewable Kerosene via Solar Thermochemical Splitting of H_2O and CO_2,” *Energy & Fuels*, vol. 29, no. 5, pp. 3241–3250, May 2015, doi: 10.1021/acs.energyfuels.5b00351.

[45] “Synhelion | Solar fuels move the world toward net zero.”

[46] “Heliogen – Replacing Fossil Fuels with Concentrated Sunlight.”

[47] R. S. El-Emam and H. Özcan, “Comprehensive review on the techno-economics of sustainable large-scale clean hydrogen production,” *Journal of Cleaner Production*, vol. 220, pp. 593–609, 2019, doi: https://doi.org/10.1016/j.jclepro.2019.01.309.

[48] S. S. Batsanov and A. S. Batsanov, “Crystal Structure: Real,” in *Introduction to Structural Chemistry*, Dordrecht: Springer Netherlands, 2012, pp. 329–356. doi: 10.1007/978-94-007-4771-5_6.

[49] J. Maier, “Defect Chemistry: Composition, Transport, and Reactions in the Solid State; Part I: Thermodynamics,” *Angewandte Chemie International Edition in English*, vol. 32, no. 3, pp. 313–335, 1993, doi: https://doi.org/10.1002/anie.199303133.

[50] H. L. Tuller and S. R. Bishop, “Point Defects in Oxides: Tailoring Materials Through Defect Engineering,” *Annual Review in Materials Research*, vol. 41, pp. 369–398, Jul. 2011, doi: 10.1146/ANNUREV-MATSCI-062910-100442.

[51] F. A. Kröger and H. J. Vink, “Relations between the Concentrations of Imperfections in Crystalline Solids,” *Solid State Physics - Advances in Research and Applications*, vol. 3, no. C, pp. 307–435, Jan. 1956, doi: 10.1016/S0081-1947(08)60135-6.

[52] J. Schoonman, *CRC Handbook of Solid State Electrochemistry: Defect chemistry in solid state electrochemistry*. CRC HPress, 1997.

[53] Z. Zakaria, S. H. Abu Hassan, N. Shaari, A. Z. Yahaya, and Y. Boon Kar, “A review on recent status and challenges of yttria stabilized zirconia modification to lowering the temperature of solid oxide fuel cells operation,” *International Journal of Energy Research*, vol. 44, no. 2, pp. 631–650, 2020, doi: https://doi.org/10.1002/er.4944.

[54] R. J. Martín-Palma and J. M. Martínez-Duart, “Chapter 3 - Review of Semiconductor Physics,” in *Nanotechnology for Microelectronics and Photonics (Second Edition)*, Second Edition., R. J. Martín-Palma and J. M. Martínez-Duart, Eds. Elsevier, 2017, pp. 51–80. doi: https://doi.org/10.1016/B978-0-323-46176-4.00003-1.

[55] G. George, S. Rao Ede, and Z. Luo, *Fundamentals of Perovskite Oxides: Synthesis, Structure, Properties and Applicationsd*. CRC Press, 2020.

[56] W. T. Hong, M. Risch, K. A. Stoerzinger, A. Grimaud, J. Suntivich, and Y. Shao-Horn, “Toward the rational design of non-precious transition metal oxides for oxygen electrocatalysis,” *Energy Environ. Sci.*, vol. 8, no. 5, pp. 1404–1427, 2015, doi: 10.1039/C4EE03869J.

[57] F. A. Cotton, “I - Ligand field theory,” *Journal of Chemical Education*, vol. 41, no. 9, p. 466, Sep. 1964, doi: 10.1021/ed041p466.

[58] M. Pavone, A. M. Ritzmann, and E. A. Carter, “Quantum-mechanics-based design principles for solid oxide fuel cell cathode materials,” *Energy Environ. Sci.*, vol. 4, no. 12, pp. 4933–4937, 2011, doi: 10.1039/C1EE02377B.

[59] A. B. Muñoz-García, A. M. Ritzmann, M. Pavone, J. A. Keith, and E. A. Carter, “Oxygen Transport in Perovskite-Type Solid Oxide Fuel Cell Materials: Insights from Quantum Mechanics,” *Accounts of Chemical Research*, vol. 47, no. 11, pp. 3340–3348, Nov. 2014, doi: 10.1021/ar4003174.

[60] C. Yang and A. Grimaud, “Factors Controlling the Redox Activity of Oxygen in Perovskites: From Theory to Application for Catalytic Reactions,” *Catalysts*, vol. 7, no. 5, 2017, doi: 10.3390/catal7050149.

[61] M. Takacs, J. R. Scheffe, and A. Steinfeld, “Oxygen nonstoichiometry and thermodynamic characterization of Zr doped ceria in the 1573-1773 K temperature range.,” *Phys Chem Chem Phys*, vol. 17, no. 12, pp. 7813–7822, Mar. 2015, doi: 10.1039/c4cp04916k.

[62] B. Meredig and C. Wolverton, “First-principles thermodynamic framework for the evaluation of thermochemical H_2O-or CO_2-splitting materials,” *PHYSICAL REVIEW B*, vol. 80, p. 245119, 2009, doi: 10.1103/PhysRevB.80.245119.

[63] A. A. Emery, C. Wolverton, and S. Characteristic, “Data Descriptor: High-throughput DFT calculations of formation energy, stability and oxygen vacancy formation energy of ABO_3 perovskites Background & Summary,” 2017, doi: 10.1038/sdata.2017.153.

[64] C. L. Muhich *et al.*, “Efficient generation of H_2 by splitting water with an isothermal redox cycle.,” *Science*, vol. 341, no. 6145, pp. 540–542, Aug. 2013, doi: 10.1126/science.1239454.

[65] H. Kong, Y. Hao, and H. Jin, “Isothermal versus two-temperature solar thermochemical fuel synthesis: A comparative study,” *Applied Energy*, vol. 228, pp. 301–308, Oct. 2018, doi: 10.1016/J.APENERGY.2018.05.099.

[66] R. Bader, L. J. Venstrom, J. H. Davidson, and W. Lipiński, “Thermodynamic Analysis of Isothermal Redox Cycling of Ceria for Solar Fuel Production,” *Energy & Fuels*, vol. 27, no. 9, pp. 5533–5544, Sep. 2013, doi: 10.1021/ef400132d.

[67] R. J. Carrillo and J. R. Scheffe, “Beyond Ceria: Theoretical Investigation of Isothermal and Near-Isothermal Redox Cycling of Perovskites for Solar Thermochemical Fuel Production,” *Energy and Fuels*, 2019, doi: 10.1021/ACS.ENERGYFUELS.9B02714/SUPPL_FILE/EF9B02714_SI_001.PDF.

[68] R. J. Carrillo and J. R. Scheffe, “Advances and trends in redox materials for solar thermochemical fuel production,” *Solar Energy*, 2017, doi: 10.1016/j.solener.2017.05.032.

[69] V. N. Tikhonovich, O. M. Zharkovskaya, E. N. Naumovich, I. A. Bashmakov, V. V Kharton, and A. A. Vecher, “Oxygen nonstoichiometry of $Sr(Co,Fe)O_{3-\delta}$ based perovskites: I. Coulometric titration of $SrCo_{0.85}Fe_{0.10}Cr_{0.05}O_{3-\delta}$ by the two-electrode technique,” *Solid State Ionics*, vol. 160, no. 3–4, pp. 259–270, 2003, doi: 10.1016/S0167-2738(03)00187-5.

[70] R. J. Panlener, R. N. Blumenthal, and J. E. Garnier, “A thermodynamic study of nonstoichiometric cerium dioxide,” *Journal of Physics and Chemistry of Solids*, vol. 36, no. 11, pp. 1213–1222, 1975, doi: 10.1016/0022-3697(75)90192-4.

[71] B. Bulfin, F. Call, J. Vieten, M. Roeb, C. Sattler, and I. v Shvets, “Oxidation and Reduction Reaction Kinetics of Mixed Cerium Zirconium Oxides,” *Journal of Physical Chemistry C*, vol. 120, pp. 2027–2035, 2016, doi: 10.1021/acs.jpcc.5b08729.

[72] S. Ackermann, L. Sauvin, R. Castiglioni, J. L. M. Rupp, J. R. Scheffe, and A. Steinfeld, “Kinetics of CO_2 Reduction over Nonstoichiometric Ceria,” *The Journal of Physical Chemistry C*, vol. 119, no. 29, pp. 16452–16461, Jul. 2015, doi: 10.1021/acs.jpcc.5b03464.

[73] M. Fu, L. Wang, T. Ma, H. Ma, H. Xu, and X. Li, “Mechanism of CO production around oxygen vacancy of $LaMnO_3$: an efficient and rapid evaluation of the doping effect on the kinetics and thermodynamic driving force of CO_2 -splitting,” *Journal of Materials Chemistry A*, vol. 8, no. 4, pp. 1709–1716, Jan. 2020, doi: 10.1039/C9TA09764C.

[74] A. H. McDaniel *et al.*, “Sr- and Mn-doped $LaAlO_{3-\delta}$ for solar thermochemical H2 and CO production,” *Energy & Environmental Science*, vol. 6, no. 8, p. 2424, Jul. 2013, doi: 10.1039/c3ee41372a.

[75] T. C. Davenport, M. Kemei, M. J. Ignatowich, and S. M. Haile, “Interplay of material thermodynamics and surface reaction rate on the kinetics of thermochemical hydrogen production,” *International Journal of Hydrogen Energy*, vol. 42, no. 27, pp. 16932–16945, Jul. 2017, doi: 10.1016/J.IJHYDENE.2017.05.184.

[76] T. C. Davenport, C.-K. Yang, C. J. Kucharczyk, M. J. Ignatowich, and S. M. Haile, “Maximizing fuel production rates in isothermal solar thermochemical fuel production,” *Applied Energy*, vol. 183, pp. 1098–1111, Dec. 2016, doi: 10.1016/J.APENERGY.2016.09.012.

[77] H. Téllez, J. Druce, J. E. Hong, T. Ishihara, and J. A. Kilner, “Accurate and precise measurement of oxygen isotopic fractions and diffusion profiles by selective attenuation of secondary ions (SASI),” *Analytical Chemistry*, vol. 87, no. 5, pp. 2907–2915, Mar. 2015, doi: 10.1021/AC504409X/ASSET/IMAGES/AC504409X.SOCIAL.JPEG_V03.

[78] R. A. de Souza, J. Zehnpfenning, M. Martin, and J. Maier, “Determining oxygen isotope profiles in oxides with Time-of-Flight SIMS,” *Solid State Ionics*, pp. 1465–1471, 2005, doi: 10.1016/j.ssi.2005.03.012.

[79] C. B. Gopal and S. M. Haile, “An electrical conductivity relaxation study of oxygen transport in samarium doped ceria,” *Journal of Materials Chemistry A*, vol. 2, no. 7, pp. 2405–2417, Jan. 2014, doi: 10.1039/C3TA13404K.

[80] J. A. Lane and J. A. Kilner, “Measuring oxygen diffusion and oxygen surface exchange by conductivity relaxation,” *Solid State Ionics*, vol. 136–137, pp. 997–1001, Nov. 2000, doi: 10.1016/S0167-2738(00)00554-3.

[81] F. Chiabrera *et al.*, “Visualizing local fast ionic conduction pathways in nanocrystalline lanthanum manganite by isotope exchange-atom probe tomography,” *Journal of Materials Chemistry A*, vol. 10, no. 5, pp. 2228–2234, Feb. 2022, doi: 10.1039/D1TA10538H.

[82] A. Kushima, D. Parfitt, A. Chroneos, B. Yildiz, J. A. Kilner, and R. W. Grimes, “Interstitialcy diffusion of oxygen in tetragonal $La_2CoO_{4+\delta}$.,” *Phys Chem Chem Phys*, vol. 13, no. 6, pp. 2242–2249, Feb. 2011, doi: 10.1039/c0cp01603a.

[83] D. Parfitt, A. Kordatos, P. P. Filippatos, and A. Chroneos, “Diffusion in energy materials: Governing dynamics from atomistic modelling,” *Applied Physics Reviews*, vol. 4, no. 3, p. 31305, Sep. 2017, doi: 10.1063/1.5001276.

[84] S. Ackermann, J. R. Scheffe, and A. Steinfeld, “Diffusion of Oxygen in Ceria at Elevated Temperatures and Its Application to H_2O/CO_2 Splitting Thermochemical Redox Cycles,” *The Journal of Physical Chemistry C*, vol. 118, no. 10, pp. 5216–5225, Mar. 2014, doi: 10.1021/jp500755t.

[85] R. N. Blumenthal and R. L. Hofmaier, “The Temperature and Compositional Dependence of the Electrical Conductivity of Nonstoichiometric CeO_{2-x},“ *Journal of The Electrochemical Society*, vol. 121, no. 1, p. 126, 1974, doi: 10.1149/1.2396805.

[86] R. N. Blumenthal and R. K. Sharma, “Electronic conductivity in nonstoichiometric cerium dioxide,” *Journal of Solid State Chemistry*, vol. 13, no. 4, pp. 360–364, 1975, doi: https://doi.org/10.1016/0022-4596(75)90152-8.

[87] C.-K. Yang, Y. Yamazaki, A. Aydin, and S. M. Haile, “Thermodynamic and kinetic assessments of strontium-doped lanthanum manganite perovskites for two-step thermochemical water splitting,” *Journal of Materials Chemistry A*, vol. 2, no. 33, pp. 13612–13623, Jul. 2014, doi: 10.1039/C4TA02694B.

[88] E. Navickas *et al.*, “Fast oxygen exchange and diffusion kinetics of grain boundaries in Sr-doped $LaMnO_3$ thin films,” *Phys. Chem. Chem. Phys. Phys. Chem. Chem. Phys*, vol. 17, no. 17, pp. 7583–8284, 2015.

[89] H. A. Hansen and C. Wolverton, "Kinetics and Thermodynamics of H_2O Dissociation on Reduced CeO_2 (111)," *The Journal of Physical Chemistry C*, vol. 118, no. 47, pp. 27402–27414, Nov. 2014, doi: 10.1021/jp508666c.

[90] M. Fu, H. Xu, and X. Li, "Mechanism of oxygen vacancy assisted water-splitting of $LaMnO_3$: inorganic perovskite prediction for fast solar thermochemical H_2 production," *Inorganic Chemistry Frontiers*, vol. 7, no. 12, pp. 2381–2387, 2020, doi: 10.1039/D0QI00338G.

[91] C.-K. Yang, Y. Yamazaki, A. Aydin, and S. M. Haile, "Thermodynamic and kinetic assessments of strontium-doped lanthanum manganite perovskites for two-step thermochemical water splitting," *Journal of Materials Chemistry A*, vol. 2, no. 33, pp. 13612–13623, 2014, doi: 10.1039/C4TA02694B.

[92] S. Dey, B. S. Naidu, and C. N. R. Rao, "Beneficial effects of substituting trivalent ions in the B-site of $La_{0.5}Sr_{0.5}Mn_{1-x}A_xO_3$ (A = Al, Ga, Sc) on the thermochemical generation of CO and H_2 from CO_2 and H_2O," *Dalton Transactions*, vol. 45, pp. 2430–2435, 2016, doi: 10.1039/c5dt04822b.

[93] B. Bulfin *et al.*, "Thermodynamics of CeO_2 Thermochemical Fuel Production," *Energy & Fuels*, vol. 29, pp. 1001–1009, 2015, doi: 10.1021/ef5019912.

[94] B. Bulfin, J. Vieten, C. Agrafiotis, M. Roeb, and C. Sattler, "Applications and limitations of two step metal oxide thermochemical redox cycles; a review," *J. Mater. Chem. A*, vol. 5, pp. 18951–18966, 2017, doi: 10.1039/c7ta05025a.

[95] B. D. Ehrhart, C. L. Muhich, I. Al-Shankiti, and A. W. Weimer, "System efficiency for two-step metal oxide solar thermochemical hydrogen production – Part 1: Thermodynamic model and impact of oxidation kinetics," *International Journal of Hydrogen Energy*, vol. 41, no. 44, pp. 19881–19893, Nov. 2016, doi: 10.1016/J.IJHYDENE.2016.07.109.

[96] C. L. Muhich, S. Blaser, M. C. Hoes, and A. Steinfeld, "Comparing the solar-to-fuel energy conversion efficiency of ceria and perovskite based thermochemical redox cycles for splitting H_2O and CO_2," *International Journal of Hydrogen Energy*, vol. 43, no. 41, pp. 18814–18831, Oct. 2018, doi: 10.1016/J.IJHYDENE.2018.08.137.

[97] I. Ermanoski, "Maximizing efficiency in two-step solar-thermochemical fuel production," *Energy Procedia*, vol. 69, pp. 1731–1740, 2015, doi: 10.1016/j.egypro.2015.03.141.

[98] A. de la Calle and A. Bayon, “Annual performance of a thermochemical solar syngas production plant based on non-stoichiometric CeO_2,” *International Journal of Hydrogen Energy*, vol. 44, no. 3, pp. 1409–1424, Jan. 2019, doi: 10.1016/J.IJHYDENE.2018.11.076.

[99] A. Gallo, A. Marzo, E. Fuentealba, and E. Alonso, “High flux solar simulators for concentrated solar thermal research: A review,” *Renewable and Sustainable Energy Reviews*, vol. 77, pp. 1386–1402, 2017, doi: 10.1016/j.rser.2017.01.056.

[100] N. P. Siegel, J. E. Miller, I. Ermanoski, R. B. Diver, E. B. Stechel, and Stechel, E. B., “Factors Affecting the Efficiency of Solar Driven Metal Oxide Thermochemical Cycles,” *Industrial & Engineering Chemical Research*, vol. 52, pp. 3276–3286, 2013, doi: 10.1021/ie400193q.

[101] S. Abanades, P. Charvin, F. Lemont, and G. Flamant, “Novel two-step SnO_2/SnO water-splitting cycle for solar thermochemical production of hydrogen,” *International Journal of Hydrogen Energy*, vol. 33, no. 21, pp. 6021–6030, Nov. 2008, doi: 10.1016/J.IJHYDENE.2008.05.042.

[102] A. Steinfeld, “Solar hydrogen production via a two-step water-splitting thermochemical cycle based on Zn/ZnO redox reactions,” *International Journal of Hydrogen Energy*, vol. 27, no. 6, pp. 611–619, Jun. 2002, doi: 10.1016/S0360-3199(01)00177-X.

[103] C. Perkins, P. R. Lichty, and A. W. Weimer, “Thermal ZnO dissociation in a rapid aerosol reactor as part of a solar hydrogen production cycle,” *International Journal of Hydrogen Energy*, vol. 33, no. 2, pp. 499–510, Jan. 2008, doi: 10.1016/J.IJHYDENE.2007.10.021.

[104] J. R. Scheffe and A. Steinfeld, “Oxygen exchange materials for solar thermochemical splitting of H_2O and CO_2: a review,” *Materials Today*, vol. 17, no. 7, pp. 341–348, 2014, doi: 10.1016/j.mattod.2014.04.025.

[105] I. Alxneit, “Assessing the feasibility of separating a stoichiometric mixture of zinc vapor and oxygen by a fast quench – Model calculations,” *Solar Energy*, vol. 82, no. 11, pp. 959–964, Nov. 2008, doi: 10.1016/J.SOLENER.2008.05.009.

[106] S. Abanades, “Metal Oxides Applied to Thermochemical Water-Splitting for Hydrogen Production Using Concentrated Solar Energy,” *ChemEngineering*, vol. 3, no. 3, p. 63, Jul. 2019, doi: 10.3390/chemengineering3030063.

[107] Y. Lu, L. Zhu, C. Agrafiotis, J. Vieten, M. Roeb, and C. Sattler, “Solar fuels production: Two-step thermochemical cycles with cerium-based oxides,” *Progress in Energy and Combustion Science*, vol. 75, p. 100785, Nov. 2019, doi: 10.1016/J.PECS.2019.100785.

[108] T. Nakamura, “Hydrogen production from water utilizing solar heat at high temperatures,” *Solar Energy*, vol. 19, no. 5, pp. 467–475, 1977, doi: 10.1016/0038-092X(77)90102-5.

[109] P. Charvin, S. Abanades, G. Flamant, and F. Lemort, “Two-step water splitting thermochemical cycle based on iron oxide redox pair for solar hydrogen production,” *Energy*, vol. 32, no. 7, pp. 1124–1133, Jul. 2007, doi: 10.1016/J.ENERGY.2006.07.023.

[110] E. N. Coker, J. A. Ohlhausen, A. Ambrosini, and J. E. Miller, “Oxygen transport and isotopic exchange in iron oxide/YSZ thermochemically-active materials via splitting of $C(^{18}O)_2$ at high temperature studied by thermogravimetric analysis and secondary ion mass spectrometry,” *Journal of Materials Chemistry*, vol. 22, no. 14, pp. 6726–6732, Mar. 2012, doi: 10.1039/C2JM15324F.

[111] E. N. Coker, A. Ambrosini, M. A. Rodriguez, and J. E. Miller, “Ferrite-YSZ composites for solar thermochemical production of synthetic fuels: in operando characterization of CO_2 reduction,” *Journal of Materials Chemistry*, vol. 21, no. 29, pp. 10767–10776, Jul. 2011, doi: 10.1039/C1JM11053E.

[112] T. Kodama, Y. Nakamuro, and T. Mizuno, “A Two-Step Thermochemical Water Splitting by Iron-Oxide on Stabilized Zirconia,” *Journal of Solar Energy Engineering*, vol. 128, no. 1, pp. 3–7, Feb. 2006, doi: 10.1115/1.1878852.

[113] M. D. Allendorf, R. B. Diver, N. P. Siegel, and J. E. Miller, “Two-Step Water Splitting Using Mixed-Metal Ferrites: Thermodynamic Analysis and Characterization of Synthesized Materials,” *Energy & Fuels*, vol. 22, no. 6, pp. 4115–4124, Nov. 2008, doi: 10.1021/ef8005004.

[114] T. Kodama and N. Gokon, “Thermochemical Cycles for High-Temperature Solar Hydrogen Production,” 2007, doi: 10.1021/cr050188a.

[115] C. Agrafiotis, M. Roeb, M. Schmücker, and C. Sattler, “Exploitation of thermochemical cycles based on solid oxide redox systems for thermochemical storage of solar heat. Part 1: Testing of cobalt oxide-based powders,” *Solar Energy*, vol. 102, pp. 189–211, Apr. 2014, doi: 10.1016/j.solener.2013.12.032.

[116] M. Neises, S. Tescari, L. De Oliveira, M. Roeb, C. Sattler, and B. Wong, “Solar-heated rotary kiln for thermochemical energy storage,” 2012, doi: 10.1016/j.solener.2012.07.012.

[117] K. N. Hutchings, M. Wilson, P. A. Larsen, and R. A. Cutler, “Kinetic and thermodynamic considerations for oxygen absorption/desorption using cobalt oxide,” *Solid State Ionics*, vol. 177, no. 1–2, pp. 45–51, Jan. 2006, doi: 10.1016/j.ssi.2005.10.005.

[118] A. J. Carrillo *et al.*, “Thermochemical energy storage at high temperature via redox cycles of Mn and Co oxides: Pure oxides versus mixed ones,” *Solar Energy Materials and Solar Cells*, vol. 123, pp. 47–57, 2014, doi: 10.1016/J.SOLMAT.2013.12.018.

[119] J. R. Scheffe, J. Li, and A. W. Weimer, “A spinel ferrite/hercynite water-splitting redox cycle,” *International Journal of Hydrogen Energy*, vol. 35, pp. 3333–3340, 2010, doi: 10.1016/j.ijhydene.2010.01.140.

[120] A. Aguadero *et al.*, “Materials development for intermediate-temperature solid oxide electrochemical devices,” *Journal of Materials Science*, vol. 47, no. 9, pp. 3925–3948, May 2012, doi: 10.1007/s10853-011-6213-1.

[121] J. L. Ayastuy, A. Iglesias-González, and M. A. Gutiérrez-Ortiz, “Synthesis and characterization of low amount tin-doped ceria ($Ce_XSn_{1-X}O_{2-\delta}$) for catalytic CO oxidation,” *Chemical Engineering Journal*, vol. 244, pp. 372–381, 2014, doi: 10.1016/J.CEJ.2014.01.077.

[122] J. A. Rodriguez, D. C. Grinter, Z. Liu, R. M. Palomino, and S. D. Senanayake, “Ceria-based model catalysts: Fundamental studies on the importance of the metal-ceria interface in CO oxidation, the water-gas shift, CO_2 hydrogenation, and methane and alcohol reforming,” *Chemical Society Reviews*, vol. 46, no. 7. Royal Society of Chemistry, pp. 1824–1841, 2017. doi: 10.1039/c6cs00863a.

[123] S. Abanades and G. Flamant, “Thermochemical hydrogen production from a two-step solar-driven water-splitting cycle based on cerium oxides,” *Solar Energy*, vol. 80, no. 12, pp. 1611–1623, 2006, doi: 10.1016/j.solener.2005.12.005.

[124] W. C. Chueh and S. M. Haile, “A thermochemical study of ceria: exploiting an old material for new modes of energy conversion and CO_2 mitigation,” *Philosophical Transactions of the Royal Society of London A: Mathematical, Physical and Engineering Sciences*, vol. 368, no. 1923, 2010.

[125] W. C. Chueh *et al.*, “High-Flux Solar-Driven Thermochemical Dissociation of CO_2 and H_2O Using Nonstoichiometric Ceria,” *Science,* vol. 330, no. 6012, pp. 1797–1801, Dec. 2010, doi: 10.1126/science.280.5362.425.

[126] R. J. Panlener, R. N. Blumenthal, and J. E. Garnier, “A thermodynamic study of nonstoichiometric cerium dioxide,” *Journal of Physics and Chemistry of Solids*, vol. 36, no. 11, pp. 1213–1222, 1975, doi: 10.1016/0022-3697(75)90192-4.

[127] B. Bulfin *et al.*, “Statistical thermodynamics of non-stoichiometric ceria and ceria zirconia solid solutions,” *Physical Chemistry Chemical Physics*, vol. 18, no. 33, pp. 23147–23154, Aug. 2016, doi: 10.1039/C6CP03158G.

[128] B. Bulfin *et al.*, “Thermodynamics of CeO_2 Thermochemical Fuel Production,” *Energy & Fuels*, vol. 29, pp. 1001–1009, 2015, doi: 10.1021/ef5019912.

[129] R. J. Carrillo and J. R. Scheffe, “Advances and trends in redox materials for solar thermochemical fuel production,” *Solar Energy*, 2017, doi: 10.1016/j.solener.2017.05.032.

[130] S. Chuayboon, S. Abanades, and S. Rodat, “Syngas production via solar-driven chemical looping methane reforming from redox cycling of ceria porous foam in a volumetric solar reactor,” *Chemical Engineering Journal*, vol. 356, pp. 756–770, Jan. 2019, doi: 10.1016/J.CEJ.2018.09.072.

[131] P. Furler *et al.*, “Thermochemical CO_2 splitting via redox cycling of ceria reticulated foam structures with dual- scale porosities,” *Phys. Chem. Chem. Phys. Phys. Chem. Chem. Phys*, vol. 16, no. 16, pp. 10503–10511, 2014, doi: 10.1039/c4cp01172d.

[132] A. Haeussler *et al.*, “Recent progress on ceria doping and shaping strategies for solar thermochemical water and CO_2 splitting cycles,” *AIMS Materials Science 2019 5:657*, vol. 6, no. 5, pp. 657–684, 2019, doi: 10.3934/MATERSCI.2019.5.657.

[133] Q. Jiang, G. Zhou, Z. Jiang, and C. Li, “Thermochemical CO_2 splitting reaction with $Ce_xM_{1-x}O_{2-\delta}$ (M = Ti^{4+}, Sn^{4+}, Hf^{4+}, Zr^{4+}, La^{3+}, Y^{3+} and Sm^{3+}) solid solutions,” *Solar Energy*, vol. 99, pp. 55–66, Jan. 2014, doi: 10.1016/J.SOLENER.2013.10.021.

[134] R. R. Bhosale and G. D. Takalkar, “Nanostructured co-precipitated $Ce_{0.9}Ln_{0.1}O_2$ (Ln = La, Pr, Sm, Nd, Gd, Tb, Dy, or Er) for thermochemical conversion of CO_2,” *Ceramics International*, vol. 44, no. 14, pp. 16688–16697, Oct. 2018, doi: 10.1016/J.CERAMINT.2018.06.096.

[135] H. Kaneko *et al.*, “Reactive ceramics of CeO_2–MO_x (M=Mn, Fe, Ni, Cu) for H_2 generation by two-step water splitting using concentrated solar thermal energy,” *Energy*, vol. 32, no. 5, pp. 656–663, May 2007, doi: 10.1016/J.ENERGY.2006.05.002.

[136] R. Jacot, R. E. Mo, R. Michalsky, A. Steinfeld, and G. R. Patzke, “Trends in the phase stability and thermochemical oxygen exchange of ceria doped with potentially tetravalent metals,” *J. Mater. Chem. A*, vol. 5, pp. 19901–19913, 2017, doi: 10.1039/c7ta04063f.

[137] A. le Gal and S. Abanades, “Dopant Incorporation in Ceria for Enhanced Water-Splitting Activity during Solar Thermochemical Hydrogen Generation,” *Journal of Physical Chemistry*, vol. 116, pp. 13516–13523, 2012, doi: 10.1021/jp302146c.

[138] B. Bulfin, M. Lange, L. de Oliveira, M. Roeb, and C. Sattler, “Solar thermochemical hydrogen production using ceria zirconia solid solutions: Efficiency analysis,” *International Journal of Hydrogen Energy*, vol. 41, no. 42, pp. 19320–19328, Nov. 2016, doi: 10.1016/J.IJHYDENE.2016.05.211.

[139] A. le Gal and S. Abanades, “Catalytic investigation of ceria-zirconia solid solutions for solar hydrogen production,” *International Journal of Hydrogen Energy*, vol. 36, no. 8, pp. 4739–4748, Apr. 2011.

[140] A. Pappacena *et al.*, “New Insights into the Dynamics That Control the Activity of Ceria− Zirconia Solid Solutions in Thermochemical Water Splitting Cycles,” *The Journal of Physical Chemistry C*, vol. 121, pp. 17746–17755, 2017, doi: 10.1021/acs.jpcc.7b06043.

[141] A. Bonk *et al.*, “The effect of dopants on the redox performance, microstructure and phase formation of ceria,” *Journal of Power Sources*, vol. 300, pp. 261–271, Dec. 2015, doi: 10.1016/j.jpowsour.2015.09.073.

[142] C. Muhich and A. Steinfeld, “Principles of doping ceria for the solar thermochemical redox splitting of H_2O and CO_2,” *Journal of Materials Chemistry A*, vol. 5, no. 30, pp. 15578–15590, Aug. 2017, doi: 10.1039/C7TA04000H.

[143] Q. L. Meng, C. il Lee, T. Ishihara, H. Kaneko, and Y. Tamaura, “Reactivity of CeO_2 -based ceramics for solar hydrogen production via a two-step water-splitting cycle with concentrated solar energy,” *International Journal of Hydrogen Energy*, vol. 36, no. 21, pp. 13435–13441, Oct. 2011, doi: 10.1016/J.IJHYDENE.2011.07.089.

[144] C. il Lee, Q. L. Meng, H. Kaneko, and Y. Tamaura, “Solar hydrogen productivity of ceria-scandia solid solution using two-step water-splitting cycle,” *Journal of Solar Energy Engineering, Transactions of the ASME*, vol. 135, no. 1, Feb. 2013, doi: 10.1115/1.4006876/443613.

[145] M. Kang *et al.*, "CO_2 splitting via two step thermochemical reactions over doped ceria/zirconia solid solutions," *RSC Advances*, vol. 3, no. 41, pp. 18878–18885, Sep. 2013, doi: 10.1039/C3RA43742F.

[146] A. M. Glazer, "Simple ways of determining perovskite structures," *Acta Crystallographica Section A*, vol. 31, no. 6, pp. 756–762, Nov. 1975, doi: 10.1107/S0567739475001635.

[147] J. B. Goodenough and J. S. Zhou, "Localized to Itinerant Electronic Transitions in Transition-Metal Oxides with the Perovskite Structure," *Chemistry of Materials*, vol. 10, no. 10, pp. 2980–2993, 1998, doi: 10.1021/CM980276U.

[148] J. Irvine *et al.*, "Roadmap on inorganic perovskites for energy applications," *Journal of Physics: Energy*, vol. 3, no. 3, p. 031502, Jul. 2021, doi: 10.1088/2515-7655/ABFF18.

[149] M. Kubicek, A. H. Bork Ac, and J. L. M. Rupp, "Perovskite oxides – a review on a versatile material class for solar-to-fuel conversion processes," *J. Mater. Chem. A*, vol. 5, pp. 11983–12000, 2017, doi: 10.1039/c7ta00987a.

[150] J. R. Scheffe, D. Weibel, and A. Steinfeld, "Lanthanum–Strontium–Manganese Perovskites as Redox Materials for Solar Thermochemical Splitting of H_2O and CO_2," *Energy and Fuels*, vol. 27, no. 8, pp. 4250–4257, Aug. 2013, doi: 10.1021/EF301923H.

[151] M. J. Ignatowich *et al.*, "Impact of enhanced oxide reducibility on rates of solar-driven thermochemical fuel production," *MRS Communications*, vol. 7, pp. 873–878, 2017, doi: 10.1557/mrc.2017.108.

[152] S. Dey, B. S. Naidu, A. Govindaraj, and C. N. R. Rao, "Noteworthy performance of $La_{1-x}Ca_xMnO_3$ perovskites in generating H_2 and CO by the thermochemical splitting of H_2O and CO_2," *Phys. Chem. Chem. Phys*, vol. 122, no. 17, pp. 122–125, 2015, doi: 10.1039/c4cp04578e.

[153] L. Wang *et al.*, "Enhanced Thermochemical H_2 Production on Ca-Doped Lanthanum Manganite Perovskites Through Optimizing the Dopant Level and Re-oxidation Temperature," *Acta Metallurgica Sinica (English Letters)*, vol. 31, no. 4, pp. 431–439, Apr. 2018, doi: 10.1007/s40195-018-0715-7.

[154] A. M. Deml, V. Stevanović, C. L. Muhich, C. B. Musgrave, and R. O'Hayre, "Oxide enthalpy of formation and band gap energy as accurate descriptors of oxygen vacancy formation energetics," *Energy & Environmental Science*, vol. 7, no. 6, p. 1996, May 2014, doi: 10.1039/c3ee43874k.

[155] A. H. McDaniel *et al.*, "Sr- and Mn-doped $LaAlO_{3-\delta}$ for solar thermochemical H_2 and CO production," *Energy & Environmental Science*, vol. 6, no. 8, p. 2424, Jul. 2013, doi: 10.1039/c3ee41372a.

[156] S. Dey, B. S. Naidu, and C. N. R. Rao, "Beneficial effects of substituting trivalent ions in the B-site of $La_{0.5}Sr_{0.5}Mn_{1-x}A_xO_3$ (A = Al, Ga, Sc) on the thermochemical generation of CO and H_2 from CO_2 and H_2O," *Dalton Transactions*, vol. 45, no. 6, pp. 2430–2435, Feb. 2016, doi: 10.1039/C5DT04822B.

[157] L. Wang *et al.*, "Enhanced Thermochemical Water Splitting through Formation of Oxygen Vacancy in $La_{0.6}Sr_{0.4}BO_{3-\delta}$ (B=Cr, Mn, Fe, Co, and Ni) Perovskites," *Chempluschem*, vol. 83, no. 10, pp. 924–928, Oct. 2018, doi: 10.1002/cplu.201800178.

[158] A. Demont, S. S. Abanades, and E. Beche, "Investigation of Perovskite Structures as Oxygen-Exchange Redox Materials for Hydrogen Production from Thermochemical Two-Step Water-Splitting Cycles," *The Journal of Physical Chemistry C*, vol. 118, no. 24, pp. 12682–12692, Jun. 2014, doi: 10.1021/jp5034849.

[159] M. Takacs, M. Hoes, M. Caduff, T. Cooper, J. R. R. Scheffe, and A. Steinfeld, "Oxygen nonstoichiometry, defect equilibria, and thermodynamic characterization of $LaMnO_3$ perovskites with Ca/Sr A-site and Al B-site doping," *Acta Materialia*, vol. 103, pp. 700–710, Jan. 2016

[160] A. J. Carrillo, A. H. Bork, T. Moser, E. Sediva, Z. D. Hood, and J. L. M. Rupp, "Modifying $La_{0.6}Sr_{0.4}MnO_3$ Perovskites with Cr Incorporation for Fast Isothermal CO_2-Splitting Kinetics in Solar-Driven Thermochemical Cycles," *Advanced Energy Materials*, vol. 9, no. 28, p. 1803886, Jul. 2019, doi: 10.1002/AENM.201803886.

[161] S. Dey, B. S. Naidu, and C. N. R. Rao, "$Ln_{0.5}A_{0.5}MnO_3$ (Ln=Lanthanide, A= Ca, Sr) Perovskites Exhibiting Remarkable Performance in the Thermochemical Generation of CO and H_2 from CO_2 and H_2O," *Chemistry - A European Journal*, vol. 21, no. 19, pp. 7077–7081, May 2015, doi: 10.1002/chem.201500442.

[162] R. J. Carrillo, C. M. Hill, K. J. Warren, and J. R. Scheffe, "Oxygen Nonstoichiometry and Defect Equilibria of Yttrium Manganite Perovskites with Strontium A-Site and Aluminum B-Site Doping," *Journal of Physical Chemistry C*, vol. 124, no. 8, pp. 4448–4458, Feb. 2020, doi: 10.1021/ACS.JPCC.9B11308/

[163] D. R. Barcellos, M. D. Sanders, J. Tong, A. H. Mcdaniel, and R. P. O'hayre, "BaCe0.25Mn0.75O3-d - a promising perovskite-type oxide for solar thermochemical hydrogen production," *This journal is Cite this: Energy Environ. Sci*, vol. 11, p. 3256, 2018, doi: 10.1039/c8ee01989d.

[164] B. D. Ehrhart, C. L. Muhich, I. Al-Shankiti, and A. W. Weimer, "System efficiency for two-step metal oxide solar thermochemical hydrogen production – Part 1: Thermodynamic model and impact of oxidation kinetics," *International Journal of Hydrogen Energy*, vol. 41, no. 44, pp. 19881–19893, Nov. 2016, doi: 10.1016/J.IJHYDENE.2016.07.109.

[165] M. Ong, Q. Campbell, I. Dabo, and R. A. Jishi, "First-principles investigation of $BiVO_3$ for thermochemical water splitting," *International Journal of Hydrogen Energy*, vol. 44, no. 3, pp. 1425–1430, Jan. 2019, doi: 10.1016/J.IJHYDENE.2018.11.125.

[166] Z. Chen *et al.*, "Sr- and Co-doped $LaGaO_{3-\delta}$ with high O_2 and H_2 yields in solar thermochemical water splitting," *Journal of Materials Chemistry A*, vol. 7, no. 11, pp. 6099–6112, Mar. 2019, doi: 10.1039/C8TA11957K.

[167] A. A. Emery, J. E. Saal, S. Kirklin, V. I. Hegde, and C. Wolverton, "High-Throughput Computational Screening of Perovskites for Thermochemical Water Splitting Applications," *Chemistry of Materials*, vol. 28, no. 16, pp. 5621–5634, Aug. 2016, doi: 10.1021/acs.chemmater.6b01182.

[168] G. Sai Gautam, E. B. Stechel, and E. A. Carter, "Exploring Ca–Ce–M–O (M = 3d Transition Metal) Oxide Perovskites for Solar Thermochemical Applications," *Chemistry of Materials*, vol. 32, no. 23, pp. 9964–9982, Dec. 2020, doi: 10.1021/acs.chemmater.0c02912.

[169] A. J. Carrillo, K. J. Kim, Z. D. Hood, A. H. Bork, and J. L. M. Rupp, "$La_{0.6}Sr_{0.4}Cr_{0.8}Co_{0.2}O_3$Perovskite Decorated with Exsolved Co Nanoparticles for Stable CO_2 Splitting and Syngas Production," *ACS Applied Energy Materials*, vol. 3, no. 5, pp. 4569–4579, May 2020, doi: 10.1021/ACSAEM.0C00249/

[170] A. H. Bork, A. J. Carrillo, Z. D. Hood, B. Yildiz, and J. L. M. Rupp, "Oxygen Exchange in Dual-Phase $La_{0.65}Sr_{0.35}MnO_3$–CeO_2 Composites for Solar Thermochemical Fuel Production," *ACS Applied Materials & Interfaces*, vol. 12, no. 29, pp. 32622–32632, Jul. 2020, doi: 10.1021/acsami.0c04276.

[171] S. Mulmi *et al.*, "Thermochemical CO2splitting using double perovskite-type $Ba_2Ca_{0.66}Nb_{1.34-x}Fe_xO_{6-\delta}$," *Journal of Materials Chemistry A*, vol. 5, no. 15, pp. 6874–6883, Apr. 2017, doi: 10.1039/C6TA10285A.

[172] C. Ruan, Y. Tan, L. Li, J. Wang, X. Liu, and X. Wang, "A novel CeO_2-x SnO_2/$Ce_2Sn_2O_7$ pyrochlore cycle for enhanced solar thermochemical water splitting," *AIChE Journal*, vol. 63, no. 8, pp. 3450–3462, Aug. 2017, doi: 10.1002/aic.15701.

[173] M. M. Nair and S. Abanades, “Experimental screening of perovskite oxides as efficient redox materials for solar thermochemical CO_2 conversion,” *Sustainable Energy & Fuels*, vol. 2, p. 843, 2018, doi: 10.1039/c7se00516d.

[174] M. P. Pechini, “METHOD OF PREPARING DEAD AND ALKALINE EARTH TITANATES AND NIOBATES AND COATING METHOD USING THE SAME.” 1967.

[175] A. E. Danks, S. R. Hall, and Z. Schnepp, “The evolution of ‘sol–gel’ chemistry as a technique for materials synthesis,” *Mater. Horiz.*, 2016, doi: 10.1039/C5MH00260E.

[176] X. Gao *et al.*, “Efficient ceria nanostructures for enhanced solar fuel production via high-temperature thermochemical redox cycles,” *J. Mater. Chem. A*, vol. 4, pp. 9614–9624, 2016, doi: 10.1039/c6ta02187e.

[177] Y. Leng, “X-Ray Diffraction Methods,” in *Materials Characterization*, John Wiley & Sons, Ltd, 2013, pp. 47–82. doi: https://doi.org/10.1002/9783527670772.ch2.

[178] S. R. Stock, *Elements of X-Ray Diffraction*. Harlow, UNITED KINGDOM: Pearson Education, Limited, 2013. [Online]. Available: http://ebookcentral.proquest.com/lib/imperial/detail.action?docID=5174404

[179] D. Zagorac, H. Müller, S. Ruehl, J. Zagorac, and S. Rehme, “Recent developments in the Inorganic Crystal Structure Database: theoretical crystal structure data and related features,” *Journal of Applied Crystallography*, vol. 52, no. 5, pp. 918–925, Oct. 2019, doi: 10.1107/S160057671900997X.

[180] L. B. McCusker, R. B. Von Dreele, D. E. Cox, D. Louer, and P. Scardi, “Rietveld refinement guidelines,” *J. Appl. Cryst*, vol. 32, pp. 36–50, 1999.

[181] A. le Bail, “Whole powder pattern decomposition methods and applications: A retrospection,” *Powder Diffraction*, vol. 20, no. 4, pp. 316–326, Dec. 2005, doi: 10.1154/1.2135315.

[182] S. R. Stock and S. R. Stock, *Elements of X-Ray Diffraction: Pearson New International Edition PDF EBook*. Harlow, UNITED KINGDOM: Pearson Education, Limited, 2013.

[183] J. Rodriguez-Carvajal, “FULLPROF: A program for Rietveld refinement and pattern-matching analysis,” 1990.

[184] J. I. Goldstein, D. E. Newbury, J. R. Michael, N. W. M. Ritchie, J. H. J. Scott, and D. C. Joy, *Scanning Electron Microscopy and X-Ray Microanalysis*. 2018. doi: 10.1007/978-1-4939-6676-9_5.

[185] Y. Leng, “Scanning Electron Microscopy,” in *Materials Characterization*, John Wiley & Sons, Ltd, 2013, pp. 127–161. doi: https://doi.org/10.1002/9783527670772.ch4.

[186] Y. Leng, “Scanning Electron Microscopy,” in *Materials Characterization*, John Wiley & Sons, Ltd, 2013, pp. 127–161. doi: https://doi.org/10.1002/9783527670772.ch4.

[187] J. I. Goldstein, D. E. Newbury, J. R. Michael, N. W. M. Ritchie, J. H. J. Scott, and D. C. Joy, *Scanning Electron Microscopy and X-Ray Microanalysis*. New York, NY, UNITED STATES: Springer New York, 2017. [Online]. Available: http://ebookcentral.proquest.com/lib/imperial/detail.action?docID=6314883

[188] P. van der Heide, “X-Ray Photoelectron Spectroscopy: An Introduction to Principles and Practices,” *X-Ray Photoelectron Spectroscopy: An Introduction to Principles and Practices*, Nov. 2011, doi: 10.1002/9781118162897.

[189] P. van der Heide, “X-Ray Photoelectron Spectroscopy: An Introduction to Principles and Practices,” *X-Ray Photoelectron Spectroscopy: An Introduction to Principles and Practices*, 2011, doi: 10.1002/9781118162897.

[190] E. Smith, “An introduction to X-ray photoelectron spectroscopy.” Accessed: Feb. 04, 2022. [Online]. Available: https://www.nottingham.ac.uk/nmrc/documents/training-series/introduction-to-xps-principles.pdf

[191] M. C. Biesinger, B. P. Payne, A. P. Grosvenor, L. W. M. Lau, A. R. Gerson, and R. S. C. Smart, “Resolving surface chemical states in XPS analysis of first row transition metals, oxides and hydroxides: Cr, Mn, Fe, Co and Ni,” *Applied Surface Science*, vol. 257, no. 7, pp. 2717–2730, 2011, doi: 10.1016/J.APSUSC.2010.10.051.

[192] G. H. Major *et al.*, “Practical guide for curve fitting in x-ray photoelectron spectroscopy,” *Journal of Vacuum Science & Technology A: Vacuum, Surfaces, and Films*, vol. 38, no. 6, p. 061203, Oct. 2020, doi: 10.1116/6.0000377.

[193] G. H. Major *et al.*, “Practical guide for curve fitting in x-ray photoelectron spectroscopy,” *Journal of Vacuum Science \& Technology A*, vol. 38, no. 6, p. 61203, 2020, doi: 10.1116/6.0000377.

[194] Z. Sha, E. Cali, G. Kerherve, and S. J. Skinner, “Oxygen diffusion behaviour of A-site deficient $(La_{0.8}Sr_{0.2})_{0.95}Cr_{0.5}Fe_{0.5}O_{3-\delta}$ perovskites in humid conditions,” *Journal of Materials Chemistry A*, vol. 8, no. 40, pp. 21273–21288, Oct. 2020, doi: 10.1039/D0TA08899D.

[195] C. V Cushman *et al.*, “Low energy ion scattering (LEIS). A practical introduction to its theory, instrumentation, and applications,” *Anal. Methods*, vol. 8, no. 17, pp. 3419–3439, 2016, doi: 10.1039/C6AY00765A.

[196] H. H. Brongersma, M. Draxler, M. de Ridder, and P. Bauer, “Surface composition analysis by low-energy ion scattering,” *Surface Science Reports*, vol. 62, no. 3, pp. 63–109, 2007, doi: 10.1016/J.SURFREP.2006.12.002.

[197] A. Benninghoven, “Surface investigation of solids by the statical method of secondary ion mass spectroscopy (SIMS),” *Surface Science*, vol. 35, no. C, pp. 427–457, 1973, doi: 10.1016/0039-6028(73)90232-X.

[198] J. Druce, T. Ishihara, and J. Kilner, “Surface composition of perovskite-type materials studied by Low Energy Ion Scattering (LEIS),” *Solid State Ionics*, vol. 262, pp. 893–896, 2014, doi: 10.1016/J.SSI.2013.09.010.

[199] P. G. Laye, S. B. Warrington, T. M. Group, G. R. Heal, D. M. Price, and R. Wilson, *Principles of Thermal Analysis and Calorimetry*. The Royal Society of Chemistry, 2002. doi: 10.1039/9781847551764.

[200] P. Gabbott, “A Practical Introduction to Differential Scanning Calorimetry,” in *Principles and Applications of Thermal Analysis*, John Wiley & Sons, Ltd, 2008, pp. 1–50. doi: https://doi.org/10.1002/9780470697702.ch1.

[201] M. E. Brown, “Evolved Gas Analysis (EGA),” in *Introduction to Thermal Analysis: Techniques and Applications*, M. E. Brown, Ed. Dordrecht: Springer Netherlands, 2001, pp. 139–155. doi: 10.1007/0-306-48404-8_8.

[202] R. Ramamoorthy, P. K. Dutta, and S. A. Akbar, “Oxygen sensors: Materials, methods, designs and applications,” *Journal of Materials Science*, vol. 38, no. 21, pp. 4271–4282, 2003, doi: 10.1023/A:1026370729205.

[203] R. J. Carrillo, K. J. Warren, and J. R. Scheffe, “Experimental Framework for Evaluation of the Thermodynamic and Kinetic Parameters of Metal-Oxides for Solar Thermochemical Fuel Production,” *Journal of Solar Energy Engineering*, vol. 141, pp. 0210071–02100710, 2019, doi: 10.1115/1.4042088.

[204] A. J. Carrillo, A. H. Bork, T. Moser, E. Sediva, Z. D. Hood, and J. L. M. Rupp, “Modifying $La_{0.6}Sr_{0.4}MnO_3$ Perovskites with Cr Incorporation for Fast Isothermal CO_2 Splitting Kinetics in Solar-Driven Thermochemical Cycles,” *Advanced Energy Materials*, vol. 9, no. 28, p. 1803886, Jul. 2019, doi: 10.1002/aenm.201803886.

[205] A. J. Carrillo, K. J. Kim, Z. D. Hood, A. H. Bork, and J. L. M. Rupp, “$La_{0.6}Sr_{0.4}Cr_{0.8}Co_{0.2}O_3$ Perovskite Decorated with Exsolved Co Nanoparticles for Stable CO_2 Splitting and Syngas Production,” *ACS Applied Energy Materials*, vol. 3, no. 5, pp. 4569–4579, 2020, doi: 10.1021/ACSAEM.0C00249/

[206] A. H. Bork, M. Kubicek, M. Struzik, and J. L. M. Rupp, "Perovskite $La_{0.6}Sr_{0.4}Cr_{1-x}Co_xO_{3-d}$ solid solutions for solar-thermochemical fuel production: strategies to lower the operation temperature," *J. Mater. Chem. A*, vol. 3, pp. 15546–15557, 2015, doi: 10.1039/c5ta02519b.

[207] C. Perego and S. Peratello, "Experimental methods in catalytic kinetics," *Catalysis Today*, vol. 52, no. 2–3, pp. 133–145, 1999, doi: 10.1016/S0920-5861(99)00071-1.

[208] C. L. Song, J. X. Yi, and Y. Yan, "Detailed description of pulse isotopic exchange method for analyzing oxygen surface exchange behavior on oxide ion conductors," *Chinese Journal of Chemical Physics*, vol. 32, no. 4, pp. 474–484, 2019, doi: 10.1063/1674-0068/cjcp1811245.

[209] E. Hoffmann and V. Stroobant, *Mass spectrometry Mass spectrometry*, vol. 1040, no. 2. 2016.

[210] P. Vacuum, *6.3 Quadrupole mass spectrometers (QMS) - The Vacuum Technology Book*.

[211] R. B. Wexler, G. S. Gautam, E. B. Stechel, and E. A. Carter, "Factors Governing Oxygen Vacancy Formation in Oxide Perovskites," *J Am Chem Soc*, vol. 143, no. 33, pp. 13212–13227, Aug. 2021, doi: 10.1021/jacs.1c05570.

[212] A. M. Deml, V. Stevanović, A. M. Holder, M. Sanders, R. O'Hayre, and C. B. Musgrave, "Tunable oxygen vacancy formation energetics in the complex perovskite oxide $Sr_xLa_{1-x}Mn_yAl_{1-y}O_3$," *Chemistry of Materials*, vol. 26, no. 22, pp. 6595–6602, Nov. 2014, doi: 10.1021/CM5033755/

[213] A. M. Deml, A. M. Holder, R. P. O'Hayre, C. B. Musgrave, and V. Stevanović, "Intrinsic Material Properties Dictating Oxygen Vacancy Formation Energetics in Metal Oxides," *The Journal of Physical Chemistry Letters*, vol. 6, no. 10, pp. 1948–1953, May 2015, doi: 10.1021/acs.jpclett.5b00710.

[214] D. S. Sholl and J. A. Steckel, *Density functional theory : a practical introduction*. Wiley, 2009.

[215] P. Hohenberg and W. Kohn, "Inhomogeneous Electron Gas," *Physical Review*, vol. 136, no. 3B, pp. B864–B871, Nov. 1964, doi: 10.1103/PhysRev.136.B864.

[216] W. Kohn and L. J. Sham, "Self-Consistent Equations Including Exchange and Correlation Effects," *Physical Review*, vol. 140, no. 4A, pp. A1133–A1138, Nov. 1965, doi: 10.1103/PhysRev.140.A1133.

[217] J. P. Perdew and Y. Wang, “Accurate and simple analytic representation of the electron-gas correlation energy,” *Physical Review B*, vol. 45, no. 23, pp. 13244–13249, Jun. 1992, doi: 10.1103/PhysRevB.45.13244.

[218] J. P. Perdew, K. Burke, and M. Ernzerhof, “Generalized gradient approximation made simple,” *Physical Review Letters*, vol. 77, no. 18, pp. 3865–3868, 1996, doi: 10.1103/PhysRevLett.77.3865.

[219] L. Wang, T. Maxisch, and G. Ceder, “Oxidation energies of transition metal oxides within the GGA+U framework,” *Phys. Rev. B*, vol. 73, no. 19, p. 195107, May 2006, doi: 10.1103/PhysRevB.73.195107.

[220] V. I. Anisimov, J. Zaanen, and O. K. Andersen, “Band theory and Mott insulators: Hubbard U instead of Stoner I,” *Physical Review B*, vol. 44, no. 3, pp. 943–954, Jul. 1991, doi: 10.1103/PhysRevB.44.943.

[221] A. I. Liechtenstein, V. I. Anisimov, and J. Zaanen, “Density-functional theory and strong interactions: Orbital ordering in Mott-Hubbard insulators,” *Physical Review B*, vol. 52, no. 8, pp. R5467–R5470, Aug. 1995, doi: 10.1103/PhysRevB.52.R5467.

[222] S. Dudarev and G. Botton, “Electron-energy-loss spectra and the structural stability of nickel oxide: An LSDA+U study,” *Physical Review B - Condensed Matter and Materials Physics*, vol. 57, no. 3, pp. 1505–1509, 1998, doi: 10.1103/PhysRevB.57.1505.

[223] A. D. Becke, “A new mixing of Hartree–Fock and local density-functional theories,” *The Journal of Chemical Physics*, vol. 98, no. 2, pp. 1372–1377, 1993, doi: 10.1063/1.464304.

[224] M. C. Payne, M. P. Teter, D. C. Allan, T. A. Arias, and J. D. Joannopoulos, “Iterative minimization techniques for ab initio total-energy calculations: molecular dynamics and conjugate gradients,” *Reviews of Modern Physics*, vol. 64, no. 4, pp. 1045–1097, Oct. 1992, doi: 10.1103/RevModPhys.64.1045.

[225] D. Joubert, “From ultrasoft pseudopotentials to the projector augmented-wave method,” *Physical Review B - Condensed Matter and Materials Physics*, vol. 59, no. 3, pp. 1758–1775, 1999, doi: 10.1103/PhysRevB.59.1758.

[226] P. E. Blöchl, “Projector augmented-wave method,” *Physical Review B*, vol. 50, no. 24, pp. 17953–17979, Dec. 1994, doi: 10.1103/PhysRevB.50.17953.

[227] A. Jain *et al.*, “Commentary: The materials project: A materials genome approach to accelerating materials innovation,” *APL Materials*, vol. 1, no. 1. American Institute of Physics Inc., p. 11002, 2013. doi: 10.1063/1.4812323.

[228] Wei Xie, Yueh-Lin Lee, Yang Shao-Horn, and Dane Morgan, "Oxygen Point Defect Chemistry in Ruddlesden Popper Oxides $(La_{1-x}Sr_x)_2MO_{4\pm\delta}$ (M = Co, Ni, Cu)". *The Journal of Physical Chemistry Letters*, vol. 7, pp. 1939-1944, 2016, doi: 10.1021/acs.jpclett.6b00739

[229] Y.-L. Lee, D. Lee, X. R. Wang, H. N. Lee, D. Morgan, and Y. Shao-Horn, "Kinetics of Oxygen Surface Exchange on Epitaxial Ruddlesden–Popper Phases and Correlations to First-Principles Descriptors," *The Journal of Physical Chemistry Letters*, vol. 7, no. 2, pp. 244–249, Jan. 2016, doi: 10.1021/acs.jpclett.5b02423.

[230] S. Xu, R. Jacobs, and D. Morgan, "Factors Controlling Oxygen Interstitial Diffusion in the Ruddlesden–Popper Oxide $La_{2-x}Sr_xNiO_{4+\delta}$," *Chemistry of Materials*, vol. 30, no. 20, pp. 7166–7177, 2018, doi: 10.1021/acs.chemmater.8b03146.

[231] T. T. Mayeshiba and D. D. Morgan, "Factors controlling oxygen migration barriers in perovskites," *Solid State Ionics*, vol. 296, pp. 71–77, 2016, doi: https://doi.org/10.1016/j.ssi.2016.09.007.

[232] R. F. W. Bader, "A quantum theory of molecular structure and its applications," *Chemical Reviews*, vol. 91, no. 5, pp. 893–928, Jul. 1991, doi: 10.1021/cr00005a013.

[233] R. F. W. Bader, "The Quantum Mechanical Basis of Conceptual Chemistry," *Monatshefte für Chemie / Chemical Monthly*, vol. 136, no. 6, pp. 819–854, 2005, doi: 10.1007/s00706-005-0307-x.

[234] G. Henkelman, A. Arnaldsson, and H. Jónsson, "A fast and robust algorithm for Bader decomposition of charge density," *Computational Materials Science*, vol. 36, no. 3, pp. 354–360, 2006, doi: 10.1016/j.commatsci.2005.04.010.

[235] W. Tang, E. Sanville, and G. Henkelman, "A grid-based Bader analysis algorithm without lattice bias," *Journal of Physics Condensed Matter*, vol. 21, no. 8, p. 84204, 2009, doi: 10.1088/0953-8984/21/8/084204.

[236] A. Krawczuk and P. Macchi, "Charge density analysis for crystal engineering," *Chemistry Central Journal*, vol. 8, no. 1, p. 68, 2014, doi: 10.1186/s13065-014-0068-x.

[237] A. A. Emery and C. Wolverton, "High-throughput DFT calculations of formation energy, stability and oxygen vacancy formation energy of ABO_3 perovskites," *Sci Data*, vol. 4, p. 170153, Oct. 2017, doi: 10.1038/sdata.2017.153.

[238] S. Curtarolo *et al.*, "AFLOW: An automatic framework for high-throughput materials discovery," Aug. 2013, doi: 10.1016/j.commatsci.2012.02.005.

[239] S. Kirklin *et al.*, “The Open Quantum Materials Database (OQMD): assessing the accuracy of DFT formation energies,” *npj Computational Materials*, vol. 1, no. 1, p. 15010, 2015, doi: 10.1038/npjcompumats.2015.10.

[240] A. Jain *et al.*, “Commentary: The materials project: A materials genome approach to accelerating materials innovation,” *APL Materials*, vol. 1, no. 1. American Institute of Physics Inc., p. 11002, Jul. 18, 2013. doi: 10.1063/1.4812323.

[241] A. A. Emery, J. E. Saal, S. Kirklin, V. I. Hegde, and C. Wolverton, “High-Throughput Computational Screening of Perovskites for Thermochemical Water Splitting Applications,” *Chemistry of Materials*, vol. 28, no. 16, pp. 5621–5634, Aug. 2016, doi: 10.1021/acs.chemmater.6b01182.

[242] M. Pavone, A. M. Ritzmann, and E. A. Carter, “Quantum-mechanics-based design principles for solid oxide fuel cell cathode materials,” *Energy Environ. Sci.*, vol. 4, no. 12, pp. 4933–4937, 2011, doi: 10.1039/C1EE02377B.

[243] A. Goyal, P. Gorai, H. Peng, S. Lany, and V. Stevanović, “A computational framework for automation of point defect calculations,” *Computational Materials Science*, vol. 130, pp. 1–9, 2017, doi: https://doi.org/10.1016/j.commatsci.2016.12.040.

[244] K. Hoang and M. D. Johannes, “Defect chemistry in layered transition-metal oxides from screened hybrid density functional calculations,” *Journal of Materials Chemistry A*, vol. 2, pp. 5224–5235, 2014, doi: 10.1039/c4ta00673a.

[245] C. Freysoldt *et al.*, “First-principles calculations for point defects in solids,” *Reviews of Modern Physics*, vol. 86, p. 253, 2014, doi: 10.1103/RevModPhys.86.253.

[246] A. Alkauskas, M. D. McCluskey, and C. G. van de Walle, “Tutorial: Defects in semiconductors—Combining experiment and theory,” *Journal of Applied Physics*, vol. 119, no. 18, p. 181101, May 2016, doi: 10.1063/1.4948245.

[247] G. Kresse and J. Furthmüller, “Efficient iterative schemes for ab initio total-energy calculations using a plane-wave basis set,” *Physical Review B - Condensed Matter and Materials Physics*, vol. 54, no. 16, pp. 11169–11186, 1996, doi: 10.1103/PhysRevB.54.11169.

[248] P. E. Blöchl, “Projector augmented-wave method,” *Physical Review B*, vol. 50, no. 24, pp. 17953–17979, 1994, doi: 10.1103/PhysRevB.50.17953.

[249] S. P. Ong *et al.*, “Python Materials Genomics (pymatgen): A robust, open-source python library for materials analysis,” *Computational Materials Science*, vol. 68, pp. 314–319, 2013, doi: https://doi.org/10.1016/j.commatsci.2012.10.028.

[250] A. Aguadero *et al.*, “Materials development for intermediate-temperature solid oxide electrochemical devices,” *Journal of Materials Science*, vol. 47, no. 9, pp. 3925–3948, May 2012, doi: 10.1007/s10853-011-6213-1.

[251] A. Aguadero, C. de la Calle, D. Pérez-Coll, and J. A. Alonso, “Study of the Crystal Structure, Thermal Stability and Conductivity of $Sr(V_{0.5}Mo_{0.5})O_{3+\delta}$ as SOFC Material,” *Fuel Cells*, vol. 11, no. 1, pp. 44–50, Feb. 2011, doi: 10.1002/fuce.201000070.

[252] V. Cascos, A. Aguadero, G. Harrington, M. T. Fernández-Díaz, and J. A. Alonso, “Design of $Sr_{0.7}R_{0.3}CoO_{3-\delta}$ (R = Tb and Er) Perovskites Performing as Cathode Materials in Solid Oxide Fuel Cells,” *Journal of The Electrochemical Society*, vol. 164, no. 10, pp. 3019–3027, 2017, doi: 10.1149/2.0031710jes.

[253] A. Aguadero, D. Pérez-Coll, J. A. Alonso, S. J. Skinner, and J. Kilner, “A New Family of Mo-Doped $SrCoO_{3-\delta}$ Perovskites for Application in Reversible Solid State Electrochemical Cells,” *Chemistry of Materials*, vol. 24, no. 14, pp. 2655–2663, Jul. 2012, doi: 10.1021/cm300255r.

[254] F. Wang, Q. Zhou, T. He, G. Li, and H. Ding, “Novel $SrCo_{1-y}Nb_yO_{3-\delta}$ cathodes for intermediate-temperature solid oxide fuel cells,” *Journal of Power Sources*, vol. 195, no. 12, pp. 3772–3778, Jun. 2010, doi: 10.1016/J.JPOWSOUR.2009.12.081.

[255] J. Wang, T. Yang, Y. Wen, Y. Zhang, C. Sun, and K. Huang, “Performance and stability of $SrCo_{0.9}Nb_{0.1}O_{3-\delta}$-$(La_{0.60}Sr_{0.40})_{0.95}(Co_{0.20}Fe_{0.80})O_{3-\delta}$ bilayer cathode for intermediate-temperature solid oxide fuel cells,” *Journal of Power Sources*, vol. 414, pp. 24–30, Feb. 2019, doi: 10.1016/J.JPOWSOUR.2018.12.082.

[256] V. Cascos, R. Martínez-Coronado, and J. A. Alonso, “New Nb-doped $SrCo_{1-x}Nb_xO_{3-\delta}$ perovskites performing as cathodes in solid-oxide fuel cells,” *International Journal of Hydrogen Energy*, vol. 39, no. 26, pp. 14349–14354, 2014, doi: 10.1016/j.ijhydene.2014.03.100.

[257] P. Zeng, Z. Shao, S. Liu, and Z. P. Xu, “Influence of M cations on structural, thermal and electrical properties of new oxygen selective membranes based on $SrCo_{0.95}M_{0.05}O_{3-\delta}$ perovskite,” *Separation and Purification Technology*, vol. 67, no. 3, pp. 304–311, Jun. 2009, doi: 10.1016/J.SEPPUR.2009.03.047.

[258] M. Li, W. Zhou, V. K. Peterson, M. Zhao, and Z. Zhu, “A comparative study of $SrCo_{0.8}Nb_{0.2}O_{3-\delta}$ and $SrCo_{0.8}Ta_{0.2}O_{3-\delta}$ as low-temperature solid oxide fuel cell cathodes: effect of non-geometry factors on the oxygen reduction reaction,” *Journal of Materials Chemistry A*, vol. 3, no. 47, pp. 24064–24070, Nov. 2015, doi: 10.1039/C5TA07178J.

[259] S. Le *et al.*, "A novel Nb and Cu co-doped $SrCoO_{3-\delta}$ cathode for intermediate temperature solid oxide fuel cells," *International Journal of Hydrogen Energy*, vol. 45, no. 18, pp. 10862–10870, Apr. 2020, doi: 10.1016/J.IJHYDENE.2020.01.160.

[260] S. Huang, S. Feng, Q. Lu, Y. Li, H. Wang, and C. Wang, "Cerium and niobium doped $SrCoO_{3-\delta}$ as a potential cathode for intermediate temperature solid oxide fuel cells," *Journal of Power Sources*, vol. 251, pp. 357–362, Apr. 2014, doi: 10.1016/J.JPOWSOUR.2013.11.096.

[261] J. C. Grenier, S. Ghodbane, G. Demazeau, M. Pouchard, and P. Hagenmuller, "Le cobaltite de strontium $Sr_2Co_2O_5$: Caracterisation et proprietes magnetiques," *Materials Research Bulletin*, vol. 14, no. 6, pp. 831–839, 1979, doi: 10.1016/0025-5408(79)90145-4.

[262] W. T. A. Harrison, S. L. Hegwood, and A. J. Jacobson, "A Powder Neutron Diffraction Determination of the Structure of $Sr_6Co_5O_{15}$, Formerly Described as the Low-temperature Hexagonal Form of $SrCoO_3$," 1995.

[263] C. de la Calle, A. Aguadero, J. A. Alonso, and M. T. Fernández-Díaz, "Correlation between reconstructive phase transitions and transport properties from $SrCoO_{2.5}$ brownmillerite: A neutron diffraction study," *Solid State Sciences*, vol. 10, no. 12, pp. 1924–1935, 2008, doi: 10.1016/j.solidstatesciences.2008.03.015.

[264] A. Aguadero, D. Pérez-Coll, J. A. Alonso, S. J. Skinner, and J. Kilner, "A New Family of Mo-Doped $SrCoO_{3-\delta}$ Perovskites for Application in Reversible Solid State Electrochemical Cells," *Chemistry of Materials*, vol. 24, no. 14, pp. 2655–2663, Jul. 2012, doi: 10.1021/cm300255r.

[265] A. Aguadero, D. Pérez-Coll, C. de la Calle, J. A. Alonso, M. J. Escudero, and L. Daza, "$SrCo_{1-x}Sb_xO_{3-\delta}$ perovskite oxides as cathode materials in solid oxide fuel cells," *Journal of Power Sources*, vol. 192, no. 1, pp. 132–137, 2009, doi: 10.1016/j.jpowsour.2008.12.138.

[266] M. Li, W. Zhou, V. K. Peterson, M. Zhao, and Z. Zhu, "A comparative study of $SrCo_{0.8}Nb_{0.2}O_{3-\delta}$ and $SrCo_{0.8}Ta_{0.2}O_{3-\delta}$ as low-temperature solid oxide fuel cell cathodes: effect of non-geometry factors on the oxygen reduction reaction," *Journal of Materials Chemistry A*, vol. 3, no. 47, pp. 24064–24070, 2015, doi: 10.1039/C5TA07178J.

[267] F. Wang, Q. Zhou, T. He, G. Li, and H. Ding, "Novel $SrCo_{1-y}Nb_yO_{3-d}$ cathodes for intermediate-temperature solid oxide fuel cells," *Journal of Power Sources*, vol. 195, pp. 3772–3778, 2010, doi: 10.1016/j.jpowsour.2009.12.081.

[268] P. Zeng *et al.*, "Efficient stabilization of cubic perovskite $SrCoO_{3-\delta}$ by B-site low concentration scandium doping combined with sol–gel synthesis," *Journal of Alloys and Compounds*, vol. 455, no. 1–2, pp. 465–470, 2008, doi: 10.1016/J.JALLCOM.2007.01.144.

[269] Y. Shen, F. Wang, X. Ma, and T. He, "$SrCo_{1-y}Ti_yO_{3-\delta}$ as potential cathode materials for intermediate-temperature solid oxide fuel cells," *Journal of Power Sources*, vol. 196, no. 18, pp. 7420–7425, 2011, doi: 10.1016/J.JPOWSOUR.2011.04.025.

[270] X. Xu *et al.*, "Sc and Ta-doped $SrCoO_{3-\delta}$ perovskite as a high-performance cathode for solid oxide fuel cells," *Composites Part B: Engineering*, vol. 178, Dec. 2019, doi: 10.1016/J.COMPOSITESB.2019.107491.

[271] S.-F. Wang, H.-C. Lu, Y.-F. Hsu, C.-C. Huang, and C.-T. Yeh, "$SrCo_{1-x}Sb_xO_{3-\delta}$ cathode materials prepared by Pechini method for solid oxide fuel cell applications," *Ceramics International*, vol. 38, no. 7, pp. 5941–5947, 2012, doi: 10.1016/j.ceramint.2012.04.046.

[272] R. D. Shannon, "Revised effective ionic radii and systematic studies of interatomic distances in halides and chalcogenides," *Acta Crystallographica Section A*, vol. 32, no. 5, pp. 751–767, Sep. 1976, doi: 10.1107/S0567739476001551.

[273] P. Zeng *et al.*, "Efficient stabilization of cubic perovskite $SrCoO_{3-\delta}$ by B-site low concentration scandium doping combined with sol–gel synthesis," *Journal of Alloys and Compounds*, vol. 455, no. 1–2, pp. 465–470, May 2008, doi: 10.1016/J.JALLCOM.2007.01.144.

[274] H. A. Tahini, X. Tan, W. Zhou, Z. Zhu, U. Schwingenschlögl, and S. C. Smith, "Sc and Nb dopants in $SrCoO_3$ modulate electronic and vacancy structures for improved water splitting and SOFC cathodes," *Energy Storage Materials*, vol. 9, pp. 229–234, Oct. 2017, doi: 10.1016/J.ENSM.2017.01.005.

[275] Y. Chen, B. Qian, and Z. Shao, "Tin and iron co-doping strategy for developing active and stable oxygen reduction catalysts from $SrCoO_{3-\delta}$ for operating below 800 °C," *Journal of Power Sources*, vol. 294, pp. 339–346, Oct. 2015, doi: 10.1016/J.JPOWSOUR.2015.06.095.

[276] Y. Shen, F. Wang, X. Ma, and T. He, "$SrCo_{1-y}Ti_yO_{3-\delta}$ as potential cathode materials for intermediate-temperature solid oxide fuel cells," *Journal of Power Sources*, vol. 196, no. 18, pp. 7420–7425, Sep. 2011, doi: 10.1016/J.JPOWSOUR.2011.04.025.

[277] K. Zhang, R. Ran, L. Ge, Z. Shao, W. Jin, and N. Xu, "Systematic investigation on new $SrCo_{1-y}Nb_yO_{3-\delta}$ ceramic membranes with high oxygen semi-permeability," *Journal of Membrane Science*, vol. 323, no. 2, pp. 436–443, 2008, doi: 10.1016/j.memsci.2008.07.002.

[278] X. Jin, T. Yang, and K. Huang, "Defect structure, thermodynamic and transport properties of $SrCo_{0.9}Nb_{0.1}O_{2.5+\delta}$: A combined experimental and defect chemistry approach," *Solid State Ionics*, vol. 320, pp. 159–171, Jul. 2018, doi: 10.1016/j.ssi.2018.02.041.

[279] J. Wang, T. Yang, L. Lei, and K. Huang, "Ta-Doped $SrCoO_{3-\delta}$ as a promising bifunctional oxygen electrode for reversible solid oxide fuel cells: a focused study on stability," *J. Mater. Chem. A*, vol. 5, no. 19, pp. 8989–9002, May 2017, doi: 10.1039/C7TA02003A.

[280] A. Aguadero, C. de la Calle, J. A. Alonso, M. J. Escudero, M. T. Fernández-Díaz, and L. Daza, "Structural and Electrical Characterization of the Novel $SrCo_{0.9}Sb_{0.1}O_{3-\delta}$ Perovskite: Evaluation as a Solid Oxide Fuel Cell Cathode Material," *Chemistry of Materials*, vol. 19, no. 26, pp. 6437–6444, Dec. 2007, doi: 10.1021/cm071837x.

[281] A. Aguadero, J. A. Alonso, D. Pérez-Coll, C. de la Calle, M. T. Fernández-Díaz, and J. B. Goodenough, "$SrCo_{0.95}Sb_{0.05}O_{3-\delta}$ as Cathode Material for High Power Density Solid Oxide Fuel Cells," *Chemistry of Materials*, vol. 22, no. 3, pp. 789–798, Feb. 2010, doi: 10.1021/cm901423g.

[282] A. Aguadero, D. Pérez-Coll, C. de la Calle, J. A. Alonso, M. J. Escudero, and L. Daza, "$SrCo_{1-x}Sb_xO_{3-\delta}$ perovskite oxides as cathode materials in solid oxide fuel cells," *Journal of Power Sources*, vol. 192, no. 1, pp. 132–137, 2009, doi: 10.1016/j.jpowsour.2008.12.138.

[283] R. Wang, F. Jin, L. Ta, and T. He, "$SrCo_{1-x}Mo_xO_{3-\delta}$ perovskites as cathode materials for $LaGaO_3$-based intermediate-temperature solid oxide fuel cells," *Solid State Ionics*, vol. 288, pp. 32–35, May 2016, doi: 10.1016/J.SSI.2015.11.030.

[284] M. Ezbiri, K. M. Allen, M. E. Gàlvez, R. Michalsky, and A. Steinfeld, "Design Principles of Perovskites for Thermochemical Oxygen Separation," *ChemSusChem*, vol. 8, no. 11, pp. 1966–71, Jun. 2015, doi: 10.1002/cssc.201500239.

[285] A. Aguadero, C. de la Calle, J. A. Alonso, M. J. Escudero, M. T. Fernández-Díaz, and L. Daza, "Structural and Electrical Characterization of the Novel $SrCo_{0.9}Sb_{0.1}O_{3-\delta}$ Perovskite: Evaluation as a Solid Oxide Fuel Cell Cathode Material," *Chemistry of Materials*, vol. 19, no. 26, pp. 6437–6444, Dec. 2007, doi: 10.1021/cm071837x.

[286] A. Aguadero, J. A. Alonso, D. Pérez-Coll, C. de la Calle, M. T. Fernández-Díaz, and J. B. Goodenough, "$SrCo_{0.95}Sb_{0.05}O_{3-\delta}$ as Cathode Material for High Power Density Solid Oxide Fuel Cells ," *Chemistry of Materials*, vol. 22, no. 3, pp. 789–798, Feb. 2010, doi: 10.1021/cm901423g.

[287] A. Aguadero, M. Retuerto, F. Jiménez-Villacorta, M. T. Fernandez-Diaz, and J. A. Alonso, "Evolution of cobalt spin states and magnetic coupling along the $SrCo_{1-x}Sb_xO_{3-\delta}$ system: correlation with the crystal structure," *Phys. Chem. Chem. Phys.*, vol. 13, no. 28, pp. 12835–12843, 2011, doi: 10.1039/C1CP20849G.

[288] M. Li, W. Zhou, and Z. Zhu, "Comparative Studies of $SrCo_{1-x}Ta_xO_{3-\delta}$ (x=0.05–0.4) Oxides as Cathodes for Low-Temperature Solid-Oxide Fuel Cells," *ChemElectroChem*, vol. 2, no. 9, pp. 1331–1338, 2015, doi: 10.1002/CELC.201500157.

[289] J. Dou *et al.*, "A- and B-site Codoped $SrFeO_3$ Oxygen Sorbents for Enhanced Chemical Looping Air Separation," *ChemSusChem*, vol. 13, no. 2, pp. 385–393, Jan. 2020, doi: 10.1002/cssc.201902698.

[290] Y.-L. Lee, J. Kleis, J. Rossmeisl, Y. Shao-Horn, and D. Morgan, "Prediction of solid oxide fuel cell cathode activity with first-principles descriptors," *Energy & Environmental Science*, vol. 4, no. 10, p. 3966, Sep. 2011, doi: 10.1039/c1ee02032c.

[291] A. Grimaud, W. T. Hong, Y. Shao-Horn, and J. M. Tarascon, "Anionic redox processes for electrochemical devices," *Nature Materials*, vol. 15, no. 2. Nature Publishing Group, pp. 121–126, 2016. doi: 10.1038/nmat4551.

[292] L. Giordano, K. Akkiraju, R. Jacobs, D. Vivona, D. Morgan, and Y. Shao-Horn, "Electronic Structure-Based Descriptors for Oxide Properties and Functions," *Accounts of Chemical Research*, vol. 55, no. 3, pp. 298–308, Feb. 2022, doi: 10.1021/acs.accounts.1c00509.

[293] H. A. Tahini, X. Tan, W. Zhou, Z. Zhu, U. Schwingenschlögl, and S. C. Smith, "Sc and Nb dopants in $SrCoO_3$ modulate electronic and vacancy structures for improved water splitting and SOFC cathodes," *Energy Storage Materials*, vol. 9, pp. 229–234, Oct. 2017, doi: 10.1016/J.ENSM.2017.01.005.

[294] B. Meredig and C. Wolverton, "First-principles thermodynamic framework for the evaluation of thermochemical H_2O-or CO_2-splitting materials," *PHYSICAL REVIEW B*, vol. 80, p. 245119, 2009, doi: 10.1103/PhysRevB.80.245119.

[295] A. J. Carrillo, J. Gonzalez-Aguilar, M. Romero, and J. M. Coronado, “Solar Energy on Demand: A Review on High Temperature Thermochemical Heat Storage Systems and Materials,” *Chem. Rev.*, vol. 119, pp. 4777–4816, 2019, doi: 10.1021/acs.chemrev.8b00315.

[296] Z. Zhang, L. Andre, and S. Abanades, “Experimental assessment of oxygen exchange capacity and thermochemical redox cycle behavior of Ba and Sr series perovskites for solar energy storage,” *Solar Energy*, vol. 134, pp. 494–502, 2016, doi: https://doi.org/10.1016/j.solener.2016.05.031.

[297] L. Imponenti, K. J. Albrecht, R. Kharait, M. D. Sanders, and G. S. Jackson, “Redox cycles with doped calcium manganites for thermochemical energy storage to 1000 °C,” *Applied Energy*, vol. 230, pp. 1–18, Nov. 2018, doi: 10.1016/J.APENERGY.2018.08.044.

[298] R. Le Toquin, W. Paulus, A. Cousson, C. Prestipino, and C. Lamberti, “Time-Resolved in Situ Studies of Oxygen Intercalation into $SrCoO_{2.5}$, Performed by Neutron Diffraction and X-ray Absorption Spectroscopy,” *Journal of American Chemical Society*, vol. 128, pp. 13161–13174, 2006, doi: 10.1021/ja063207m.

[299] S. M. Babiniec, E. N. Coker, J. E. Miller, and A. Ambrosini, “Investigation of $La_xSr_{1-x}Co_yM_{1-y}O_{3-\delta}$ (M=Mn, Fe) perovskite materials as thermochemical energy storage media,” *Solar Energy*, vol. 118, pp. 451–459, 2015, doi: https://doi.org/10.1016/j.solener.2015.05.040.

[300] S. M. Babiniec, E. N. Coker, J. E. Miller, and A. Ambrosini, “Doped calcium manganites for advanced high-temperature thermochemical energy storage,” *International Journal of Energy Research*, vol. 40, no. 2, pp. 280–284, Feb. 2016, doi: 10.1002/er.3467.

[301] Q. Imtiaz, D. Hosseini, and C. R. Müller, “Review of Oxygen Carriers for Chemical Looping with Oxygen Uncoupling (CLOU): Thermodynamics, Material Development, and Synthesis,” *Energy Technology*, vol. 1, no. 11, pp. 633–647, 2013, doi: https://doi.org/10.1002/ente.201300099.

[302] E. Krzystowczyk, X. Wang, J. Dou, V. Haribal, and F. Li, “Substituted $SrFeO_3$ as robust oxygen sorbents for thermochemical air separation: correlating redox performance with compositional and structural properties,” *Physical Chemistry Chemical Physics*, vol. 22, no. 16, pp. 8924–8932, Apr. 2020, doi: 10.1039/d0cp00275e.

[303] J. Dou, E. Krzystowczyk, X. Wang, A. R. Richard, T. Robbins, and F. Li, "$Sr_{1-x}Ca_xFe_{1-y}Co_yO_{3-d}$ as facile and tunable oxygen sorbents for chemical looping air separation," *Journal of Physics: Energy*, vol. 2, no. 2, p. 25007, Apr. 2020, doi: 10.1088/2515-7655/ab7cb0.

[304] Y. Pan *et al.*, "Direct evidence of boosted oxygen evolution over perovskite by enhanced lattice oxygen participation," *Nature Communications*, vol. 11, no. 1, pp. 1–10, Dec. 2020, doi: 10.1038/s41467-020-15873-x.

[305] X. Mao *et al.*, "Computational Design and Experimental Validation of the Optimal Bimetal-Doped $SrCoO_{3-\delta}$ Perovskite as Solid Oxide Fuel Cell Cathode," *J Am Chem Soc*, vol. 143, no. 25, pp. 9507–9514, 2021, doi: 10.1021/JACS.1C03441/

[306] J. Suntivich, K. J. May, H. A. Gasteiger, J. B. Goodenough, and Y. Shao-Horn, "A perovskite oxide optimized for oxygen evolution catalysis from molecular orbital principles.," *Science*, vol. 334, no. 6061, pp. 1383–5, Dec. 2011, doi: 10.1126/science.1212858.

[307] Z. Zhang, L. Andre, and S. Abanades, "Experimental assessment of oxygen exchange capacity and thermochemical redox cycle behavior of Ba and Sr series perovskites for solar energy storage," *Solar Energy*, vol. 134, pp. 494–502, Sep. 2016, doi: 10.1016/J.SOLENER.2016.05.031.

[308] N. P. Siegel, J. E. Miller, I. Ermanoski, R. B. Diver, E. B. Stechel, and Stechel E. B., "Factors Affecting the Efficiency of Solar Driven Metal Oxide Thermochemical Cycles," *Industrial & Engineering Chemical Research*, vol. 52, pp. 3276–3286, 2013, doi: 10.1021/ie400193q.

[309] H. Ikeda, A. Tsuchida, J. Morita, and N. Miura, "$SrCo_xFe1_{-x}O_{3-\delta}$ Oxygen Sorbent Usable for High-Temperature Pressure-Swing Adsorption Process Operating at Approximately 300 °C," *Industrial & Engineering Chemistry Research*, vol. 55, no. 22, pp. 6501–6505, Jun. 2016, doi: 10.1021/acs.iecr.6b01284.

[310] A. J. Carrillo, J. L. M. Rupp, and J. M. Coronado, "CHAPTER 4: Redox Oxides for Thermochemical Energy Storage," in *Energy Storage and Conversion Materials*, 2019, pp. 136–187. doi: 10.1039/9781788012959-00136.

[311] A. Cavallaro *et al.*, "Analysis of H_2O-induced surface degradation in $SrCoO_3$ -derivatives and its impact on redox kinetics," *Journal of Materials Chemistry A*, vol. 9, no. 43, pp. 24528–24538, 2021, doi: 10.1039/D1TA04174F.

[312] S. Gupta, M. K. Mahapatra, and P. Singh, “Lanthanum chromite based perovskites for oxygen transport membrane,” *Materials Science and Engineering: R: Reports*, vol. 90, pp. 1–36, 2015, doi: 10.1016/J.MSER.2015.01.001.

[313] W. Bai *et al.*, “A comprehensive review on oxygen transport membranes: Development history, current status, and future directions,” *International Journal of Hydrogen Energy*, vol. 46, no. 73, pp. 36257–36290, Oct. 2021, doi: 10.1016/J.IJHYDENE.2021.08.177.

[314] D. Maiti, Y. A. Daza, M. M. Yung, J. N. Kuhn, and V. R. Bhethanabotla, “Oxygen vacancy formation characteristics in the bulk and across different surface terminations of $La_{1-x}Sr_xFe_{1-y}Co_yO_{3-\delta}$ perovskite oxides for CO_2 conversion,” *Journal of Materials Chemistry A*, vol. 4, no. 14, pp. 5137–5148, Mar. 2016, doi: 10.1039/C5TA10284G.

[315] K. P. Ong, P. Wu, L. Liu, and S. P. Jiang, “Optimization of electrical conductivity of $LaCrO_3$ through doping: A combined study of molecular modeling and experiment,” *Applied Physics Letters*, vol. 90, no. 4, p. 44109, 2007, doi: 10.1063/1.2431780.

[316] P. S. Devi and M. S. Rao, “Preparation, structure, and properties of strontium-doped lanthanum chromites: $La_{1-x}Sr_xCrO_3$,” *Journal of Solid State Chemistry*, vol. 98, no. 2, pp. 237–244, 1992, doi: 10.1016/S0022-4596(05)80231-2.

[317] T. Ramos and A. Atkinson, “Oxygen diffusion and surface exchange in $La_{1-x}Sr_xFe_{0.8}Cr_{0.2}O_{3-\delta}$ (x=0.2, 0.4 and 0.6),” *Solid State Ionics*, vol. 170, no. 3–4, pp. 275–286, 2004, doi: 10.1016/J.SSI.2004.03.001.

[318] H. Xiong, G. J. Zhang, J. Y. Zheng, and Y. Q. Jia, “Synthesis, crystal structure and electric conductivity of $La_{0.9}Ca_{0.1}Cr_{0.5}B_{0.5}O_3$ (B=Mn, Fe, Ni),” *Materials Letters*, vol. 51, no. 1, pp. 61–67, Oct. 2001, doi: 10.1016/S0167-577X(01)00265-8.

[319] M. F. Lü *et al.*, “Thermomechanical, transport and anodic properties of perovskite-type $(La_{0.75}Sr_{0.25})_{0.95}Cr_{1-x}Fe_xO_{3-\delta}$,” *Journal of Power Sources*, vol. 206, pp. 59–69, May 2012, doi: 10.1016/J.JPOWSOUR.2012.01.100.

[320] Z. Shen, J. A. Kilner, and S. J. Skinner, “Electrical conductivity and oxygen diffusion behaviour of the $(La_{0.8}Sr_{0.2})_{0.95}Cr_xFe_{1-x}O_{3-\delta}$ (x = 0.3, 0.5 and 0.7) A-site deficient perovskites,” *Physical Chemistry Chemical Physics*, vol. 20, no. 27, pp. 18279–18290, Jul. 2018, doi: 10.1039/C8CP02797H.

[321] S. Tao and J. T. S. Irvine, “Catalytic Properties of the Perovskite Oxide $La_{0.75}Sr_{0.25}Cr_{0.5}Fe_{0.5}O_{3-\delta}$ in Relation to Its Potential as a Solid Oxide Fuel Cell Anode Material,” *Chemistry of Materials*, vol. 16, no. 21, pp. 4116–4121, Oct. 2004, doi: 10.1021/CM049341S.

[322] M. S. S. Khine, L. Chen, S. Zhang, J. Lin, and S. P. Jiang, "Syngas production by catalytic partial oxidation of methane over $(La_{0.7}A_{0.3})BO_3$ (A = Ba, Ca, Mg, Sr, and B = Cr or Fe) perovskite oxides for portable fuel cell applications," *International Journal of Hydrogen Energy*, vol. 38, no. 30, pp. 13300–13308, Oct. 2013, doi: 10.1016/J.IJHYDENE.2013.07.097.

[323] C. Aliotta, L. F. Liotta, F. Deganello, V. la Parola, and A. Martorana, "Direct methane oxidation on $La_{1-x}Sr_xCr_{1-y}Fe_yO_{3-\delta}$ perovskite-type oxides as potential anode for intermediate temperature solid oxide fuel cells," *Applied Catalysis B: Environmental*, vol. 180, pp. 424–433, Jan. 2016, doi: 10.1016/J.APCATB.2015.06.012.

[324] A. J. Carrillo, K. J. Kim, Z. D. Hood, A. H. Bork, and J. L. M. Rupp, "$La_{0.6}Sr_{0.4}Cr_{0.8}Co_{0.2}O_3$ Perovskite Decorated with Exsolved Co Nanoparticles for Stable CO_2 Splitting and Syngas Production," *ACS Applied Energy Materials*, vol. 3, no. 5, pp. 4569–4579, 2020, doi: 10.1021/ACSAEM.0C00249/

[325] A. H. Bork, M. Kubicek, M. Struzik, and J. L. M. Rupp, "Perovskite $La_{0.6}Sr_{0.4}Cr_{1-x}Co_xO_{3-\delta}$ solid solutions for solar-thermochemical fuel production: strategies to lower the operation temperature," *Journal of Materials Chemistry A*, vol. 3, no. 30, pp. 15546–15557, Jul. 2015, doi: 10.1039/C5TA02519B.

[326] C. H. Wong, "Effects of Aging on ScSZ/LSCrF Dual-Phase Oxygen Transport Membrane for Syngas Production," London, 2017.

[327] Z. Shen, "Mass Transport in Mixed-Conducting LSCrF-ScSZ Dual Phase Composites for Oxygen Transport Membrane Applications," London, 2017.

[328] L. F. G. Setz, S. R. H. Mello-Castanho, R. Moreno, and M. T. Colomer, "PhysicoChemical characterization of strontium- and cobalt-doped lanthanum chromite powders produced by combustion synthesis," *International Journal of Applied Ceramic Technology*, vol. 6, no. 5, pp. 626–635, 2009, doi: 10.1111/J.1744-7402.2008.02302.X.

[329] P. Duran, J. Tartaj, F. Capel, and C. Moure, "Formation, sintering and thermal expansion behaviour of Sr- and Mg-doped $LaCrO_3$ as SOFC interconnector prepared by the ethylene glycol polymerized complex solution synthesis method," *J Eur Ceram Soc*, vol. 24, no. 9, pp. 2619–2629, Aug. 2004, doi: 10.1016/J.JEURCERAMSOC.2003.09.016.

[330] N. Russo, D. Fino, G. Saracco, and V. Specchia, "Studies on the redox properties of chromite perovskite catalysts for soot combustion," *Journal of Catalysis*, vol. 229, no. 2, pp. 459–469, Jan. 2005, doi: 10.1016/J.JCAT.2004.11.025.

[331] K. Rida, A. Benabbas, F. Bouremmad, M. A. Peña, E. Sastre, and A. Martínez-Arias, "Effect of calcination temperature on the structural characteristics and catalytic activity for propene combustion of sol–gel derived lanthanum chromite perovskite," *Applied Catalysis A: General*, vol. 327, no. 2, pp. 173–179, Aug. 2007, doi: 10.1016/J.APCATA.2007.05.015.

[332] K. Rida, A. Benabbas, F. Bouremmad, M. A. Peña, E. Sastre, and A. Martínez-Arias, "Effect of strontium and cerium doping on the structural characteristics and catalytic activity for C3H6 combustion of perovskite $LaCrO_3$ prepared by sol–gel," *Applied Catalysis B: Environmental*, vol. 84, no. 3–4, pp. 457–467, Dec. 2008, doi: 10.1016/J.APCATB.2008.04.031.

[333] R. D. Shannon, "Revised effective ionic radii and systematic studies of interatomic distances in halides and chalcogenides," *Acta Crystallographica Section A*, vol. 32, no. 5, pp. 751–767, 1976, doi: 10.1107/S0567739476001551.

[334] S. Miyoshi *et al.*, "Chemical stability of $La_{1-x}Sr_xCrO_3$ in oxidizing atmospheres," *Journal of Solid State Chemistry*, vol. 177, no. 11, pp. 4112–4118, Nov. 2004, doi: 10.1016/J.JSSC.2004.04.054.

[335] D. Marrocchelli, N. H. Perry, and S. R. Bishop, "Understanding chemical expansion in perovskite-structured oxides," *Physical Chemistry Chemical Physics*, vol. 17, no. 15, pp. 10028–10039, Apr. 2015, doi: 10.1039/C4CP05885B.

[336] J. Park *et al.*, "Assessing the Effects of Temperature and Oxygen Vacancy on Band Gap Renormalization in $LaCrO_{3-\delta}$: First-Principles and Experimental Corroboration," *ACS Appl. Mater. Interfaces*, vol. 13, pp. 17717–17725, 2021, doi: 10.1021/acsami.1c03503.

[337] O. Polat, Z. Durmus, F. M. Coskun, M. Coskun, and A. Turut, "Engineering the band gap of $LaCrO_3$ doping with transition metals (Co, Pd, and Ir)," *Journal of Materials Science*, vol. 53, no. 5, pp. 3544–3556, Mar. 2018, doi: 10.1007/S10853-017-1773-3/TABLES/3.

[338] R. S. Silva, F. Cunha, and P. Barrozo, "Raman spectroscopy of the Al-doping induced structural phase transition in $LaCrO_3$ perovskite," *Solid State Communications*, vol. 333, p. 114346, Jul. 2021, doi: 10.1016/J.SSC.2021.114346.

[339] T. Arima, Y. Tokura, and J. B. Torrance, "Variation of optical gaps in perovskite-type 3d transition-metal oxides," *PHYSICAL REVIEW B*, vol. 48, p. 17006, 1993.

[340] R. Jacobs, T. Mayeshiba, J. Booske, and D. Morgan, “Materials discovery and design principles for stable, high activity perovskite cathodes for solid oxide fuel cells,” *Advanced Energy Materials*, vol. 8, p. 1702708, 2018, [Online]. Available: https://arxiv.org/pdf/1801.06109.pdf

[341] L. Giordano, K. Akkiraju, R. Jacobs, D. Vivona, D. Morgan, and Y. Shao-Horn, “Electronic Structure-Based Descriptors for Oxide Properties and Functions,” *Accounts of Chemical Research*, vol. 55, no. 3, pp. 298–308, Feb. 2022, doi: 10.1021/acs.accounts.1c00509.

[342] M. Pavone, A. B. Muñoz-García, A. M. Ritzmann, and E. A. Carter, “First-Principles Study of Lanthanum Strontium Manganite: Insights into Electronic Structure and Oxygen Vacancy Formation,” *The Journal of Physical Chemistry C*, vol. 118, no. 25, pp. 13346–13356, Jun. 2014, doi: 10.1021/jp500352h.

[343] M. Oishi, K. Yashiro, K. Sato, J. Mizusaki, and T. Kawada, “Oxygen nonstoichiometry and defect structure analysis of B-site mixed perovskite-type oxide (La, Sr)(Cr, M)$O_{3-\delta}$ (M=Ti, Mn and Fe),” *Journal of Solid State Chemistry*, vol. 181, no. 11, pp. 3177–3184, 2008, doi: 10.1016/J.JSSC.2008.08.015.

[344] J. Mizusaki, S. Yamauchi, K. Fueki, and A. Ishikawa, “Nonstoichiometry of the perovskite-type oxide $La_{1-x}Sr_xCrO_{3-\delta}$,” *Solid State Ionics*, vol. 12, no. C, pp. 119–124, Mar. 1984, doi: 10.1016/0167-2738(84)90138-3.

[345] M. Ezbiri, M. Takacs, D. Theiler, R. Michalsky, and A. Steinfeld, “Tunable thermodynamic activity of $La_xSr_{1-x}Mn_yAl_{1-y}O_{3-d}$ ($0 < x < 1$, $0 < y < 1$) perovskites for solar thermochemical fuel synthesis,” *J. Mater. Chem. A*, vol. 5, pp. 4172–4182, 2017, doi: 10.1039/c6ta06644e.

[346] S. P. Jiang and J. G. Love, “Origin of the initial polarization behavior of Sr-doped $LaMnO_3$ for O_2 reduction in solid oxide fuel cells,” *Solid State Ionics*, vol. 138, no. 3–4, pp. 183–190, Jan. 2001, doi: 10.1016/S0167-2738(00)00806-7.

[347] C.-K. Yang, Y. Yamazaki, A. Aydin, and S. M. Haile, “Thermodynamic and kinetic assessments of strontium-doped lanthanum manganite perovskites for two-step thermochemical water splitting,” *Journal of Materials Chemistry A*, vol. 2, no. 33, pp. 13612–13623, 2014, doi: 10.1039/C4TA02694B.

[348] E. Bucher and W. Sitte, “Defect chemical analysis of the electronic conductivity of strontium-substituted lanthanum ferrite,” *Solid State Ionics*, vol. 173, no. 1–4, pp. 23–28, 2004, doi: 10.1016/J.SSI.2004.07.047.

[349] A. H. Bork, E. Povoden-Karadeniz, A. J. Carrillo, and J. L. M. Rupp, “Thermodynamic assessment of the solar-to-fuel performance of $La_{0.6}Sr_{0.4}Mn_{1-y}Cr_yO_{3-\delta}$ perovskite solid solution series,” *Acta Materialia*, vol. 178, pp. 163–172, Oct. 2019, doi: 10.1016/j.actamat.2019.07.022.

[350] J. Rodríguez-Carvajal, “Recent advances in magnetic structure determination by neutron powder diffraction,” *Physica B: Condensed Matter*, vol. 192, no. 1–2, pp. 55–69, Oct. 1993, doi: 10.1016/0921-4526(93)90108-I.

[351] X. Chen and T. Grande, “Anisotropic and nonlinear thermal and chemical expansion of $La_{1-x}Sr_xFeO_{3-\delta}$ (x = 0.3, 0.4, 0.5) perovskite materials,” *Chemistry of Materials*, vol. 25, no. 16, pp. 3296–3306, Aug. 2013, doi: 10.1021/CM401100C/

[352] S. Gupta, H. Sabarou, Y. Zhong, and P. Singh, “Role of chromium: Iron ratio and oxygen partial pressure on the processing and chemical stability of iron doped lanthanum strontium chromite based OTM,” *International Journal of Hydrogen Energy*, vol. 42, no. 40, pp. 25351–25358, Oct. 2017, doi: 10.1016/J.IJHYDENE.2017.08.140.

[353] H. Sabarou, R. Wang, and Y. Zhong, “The origin of the phase separation in $(La_{0.8}Sr_{0.2})_{0.95}(Cr_xFe_{1-x})O_{3\pm\delta}$ perovskites for oxygen transport membranes applications,” *Solid State Ionics*, vol. 349, Jun. 2020, doi: 10.1016/J.SSI.2020.115293.

[354] Z. Cai, M. Kubicek, J. Fleig, and B. Yildiz, “Chemical heterogeneities on $La_{0.6}Sr_{0.4}CoO_{3-\delta}$ thin films-correlations to cathode surface activity and stability,” *Chemistry of Materials*, vol. 24, no. 6, pp. 1116–1127, 2012, doi: 10.1021/CM203501U.

[355] Y. Yu *et al.*, “Effect of atmospheric CO2 on surface segregation and phase formation in $La_{0.6}Sr_{0.4}Co_{0.2}Fe_{0.8}O_{3-\delta}$ thin films,” *Applied Surface Science*, vol. 323, pp. 71–77, Dec. 2014, doi: 10.1016/J.APSUSC.2014.09.019.

[356] A. Heinsaar *et al.*, “Influence of Carbon Dioxide and Humidity on the Stability of $(La_{0.6}Sr_{0.4})_{0.99}Co_{1-x}Ti_xO_{3-\delta}$ Cathode,” *Journal of The Electrochemical Society*, vol. 169, no. 1, p. 014514, Jan. 2022, doi: 10.1149/1945-7111/AC4A53.

[357] K. Rida, A. Benabbas, F. Bouremmad, M. A. Peña, and A. Martínez-Arias, “Surface properties and catalytic performance of $La_{1-x}Sr_xCrO_3$ perovskite-type oxides for CO and C_3H_6 combustion,” *Catalysis Communications*, vol. 7, no. 12, pp. 963–968, Dec. 2006, doi: 10.1016/J.CATCOM.2006.04.011.

[358] R. Ianos *et al.*, “Comparative study regarding the formation of $La_{1-x}Sr_xCrO_3$ perovskite using unconventional synthesis methods,” *Journal of Thermal Analysis and Calorimetry*, vol. 94, no. 2, pp. 343–348, 2008,

[359] J. Druce, T. Ishihara, and J. Kilner, “Surface composition of perovskite-type materials studied by Low Energy Ion Scattering (LEIS),” *Solid State Ionics*, vol. 262, pp. 893–896, Sep. 2014, doi: 10.1016/J.SSI.2013.09.010.

[360] J. Druce *et al.*, “Surface termination and subsurface restructuring of perovskite-based solid oxide electrode materials,” *Energy & Environmental Science*, vol. 7, no. 11, pp. 3593–3599, Oct. 2014, doi: 10.1039/C4EE01497A.

[361] B. Koo, K. Kim, J. K. Kim, H. Kwon, J. W. Han, and W. Jung, “Sr Segregation in Perovskite Oxides: Why It Happens and How It Exists,” *Joule*, vol. 2, no. 8, pp. 1476–1499, Aug. 2018, doi: 10.1016/J.JOULE.2018.07.016.

[362] A. Staykov, S. Fukumori, K. Yoshizawa, K. Sato, T. Ishihara, and J. Kilner, “Interaction of SrO-terminated $SrTiO_3$ surface with oxygen, carbon dioxide, and water,” *Journal of Materials Chemistry A*, vol. 6, no. 45, pp. 22662–22672, Nov. 2018, doi: 10.1039/C8TA05177A.

[363] H. Ding, A. v. Virkar, M. Liu, and F. Liu, “Suppression of Sr surface segregation in $La_{1-x}Sr_xCo_{1-y}Fe_yO_{3-\delta}$: a first principles study,” *Physical Chemistry Chemical Physics*, vol. 15, no. 2, pp. 489–496, Dec. 2012, doi: 10.1039/C2CP43148C.

[364] W. Lee, J. W. Han, Y. Chen, Z. Cai, and B. Yildiz, “Cation size mismatch and charge interactions drive dopant segregation at the surfaces of manganite perovskites,” *J Am Chem Soc*, vol. 135, no. 21, pp. 7909–7925, May 2013, doi: 10.1021/JA3125349/

[365] T. T. Fister *et al.*, “In situ characterization of strontium surface segregation in epitaxial $La_{0.7}Sr_{0.3}MnO_3$ thin films as a function of oxygen partial pressure,” *Applied Physics Letters*, vol. 93, no. 15, p. 151904, Oct. 2008, doi: 10.1063/1.2987731.

[366] Z. Sha, E. Cali, Z. Shen, E. Ware, G. Kerherve, and S. J. Skinner, “Significantly Enhanced Oxygen Transport Properties in Mixed Conducting Perovskite Oxides under Humid Reducing Environments,” *Chemistry of Materials*, vol. 33, no. 21, pp. 8469–8476, Nov. 2021, doi: 10.1021/ACS.CHEMMATER.1C02909/

[367] H. C. GRAHAM and H. H. DAVIS, “Oxidation/Vaporization Kinetics of Cr_2O_3,” *Journal of the American Ceramic Society*, vol. 54, no. 2, pp. 89–93, 1971, doi: 10.1111/J.1151-2916.1971.TB12225.X.

[368] D. Chen *et al.*, “Revising the role of chromium on the surface of perovskite electrodes: Poison or promoter for the solid oxide electrolysis cell performance?,” *Journal of Catalysis*, vol. 381, pp. 520–529, Jan. 2020, doi: 10.1016/J.JCAT.2019.11.032.

[369] T. Wei, X. Liu, C. Yuan, Q. Gao, X. Xin, and S. Wang, “A modified liquid-phase-assisted sintering mechanism for $La_{0.8}Sr_{0.2}Cr_{1-x}Fe_xO_{3-d}$ - A high density, redox-stable perovskite interconnect for solid oxide fuel cells,” *Journal of Power Sources*, vol. 250, pp. 152–159, 2014, doi: 10.1016/j.jpowsour.2013.11.012.

[370] H. Sabarou, R. Wang, and Y. Zhong, “The origin of the phase separation in $(La_{0.8}Sr_{0.2})_{0.95}(Cr_xFe_{1-x})O_{3\pm\delta}$ perovskites for oxygen transport membranes applications,” *Solid State Ionics*, vol. 349, p. 115293, Jun. 2020, doi: 10.1016/J.SSI.2020.115293.

[371] W. Lee and B. Yildiz, “Factors that Influence Cation Segregation at the Surfaces of Perovskite Oxides,” *ECS Transactions*, vol. 57, no. 1, pp. 2115–2123, Oct. 2013, doi: 10.1149/05701.2115ECST/XML.

[372] B. Koo, J. Seo, J. K. Kim, and W. Jung, “Isovalent doping: a new strategy to suppress surface Sr segregation of the perovskite O_2-electrode for solid oxide fuel cells,” *Journal of Materials Chemistry A*, vol. 8, no. 27, pp. 13763–13769, Jul. 2020, doi: 10.1039/D0TA02870C.

[373] N. Tsvetkov, Q. Lu, L. Sun, E. J. Crumlin, and B. Yildiz, “Improved chemical and electrochemical stability of perovskite oxides with less reducible cations at the surface,” *Nature Materials*, vol. 15, no. 9, pp. 1010–1016, 2016, doi: 10.1038/NMAT4659.

[374] K. Szot and W. Speier, “Surfaces of reduced and oxidized $SrTiO_3$ from atomic force microscopy,” *PHYSICAL REVIEW B*, vol. 60, no. 8, 1999.

[375] H. Dulli, P. A. Dowden, S.-H. Liou, and E. W. Plummer, “Surface segregation and restructuring of colossal-magnetoresistant manganese perovskites La0.65Sr0.35MnO3,” *PHYSICAL REVIEW B*, vol. 62, no. 22, 2000,

[376] D. Lee and H. N. Lee, “Controlling Oxygen Mobility in Ruddlesden-Popper Oxides.,” *Materials (Basel)*, vol. 10, no. 4, Mar. 2017, doi: 10.3390/ma10040368.

[377] S. N. Ruddlesden and P. Popper, “New compounds of the K_2NiF_4 type,” *Acta Crystallographica*, vol. 10, no. 8, pp. 538–539, Aug. 1957, doi: 10.1107/S0365110X57001929.

[378] J. Song, D. Ning, B. Boukamp, J. M. Bassat, and H. J. M. Bouwmeester, “Structure, electrical conductivity and oxygen transport properties of Ruddlesden–Popper phases $Ln_{n+1}Ni_nO_{3n+1}$ (Ln = La, Pr and Nd; n = 1, 2 and 3),” *Journal of Materials Chemistry A*, vol. 8, no. 42, pp. 22206–22221, Nov. 2020, doi: 10.1039/D0TA06731H.

[379] V. V Kharton, A. P. Viskup, A. V Kovalevsky, E. N. Naumovich, and F. M. B. Marques, "Ionic transport in oxygen-hyperstoichiometric phases with K_2NiF_4-type structure," *Solid State Ionics*, vol. 143, no. 3–4, pp. 337–353, 2001, doi: 10.1016/S0167-2738(01)00876-1.

[380] S. J. Skinner and J. A. Kilner, "Oxygen diffusion and surface exchange in $La_{2-x}Sr_xNiO_{4+\delta}$," *Solid State Ionics*, vol. 135, no. 1–4, pp. 709–712, 2000, doi: 10.1016/S0167-2738(00)00388-X.

[381] J. A. Kilner and C. K. M. Shaw, "Mass transport in $La_2Ni_{1-x}Co_xO_{4+\delta}$ oxides with the K_2NiF_4 structure," *Solid State Ionics*, vol. 154–155, pp. 523–527, Dec. 2002, doi: 10.1016/S0167-2738(02)00506-4.

[382] C. N. Munnings, S. J. Skinner, G. Amow, P. S. Whitfield, and I. J. Davidson, "Oxygen transport in the $La_2Ni_{1-x}Co_xO_{4+\delta}$ system," *Solid State Ionics*, vol. 176, no. 23–24, pp. 1895–1901, Jul. 2005, doi: 10.1016/J.SSI.2005.06.002.

[383] A. Chroneos, D. Parfitt, J. A. Kilner, and R. W. Grimes, "Anisotropic oxygen diffusion in tetragonal $La_2NiO_{4+\delta}$: molecular dynamics calculations," *Journal of Materials Chemistry*, vol. 20, no. 2, pp. 266–270, 2009, doi: 10.1039/B917118E.

[384] M. Burriel *et al.*, "Influence of Crystal Orientation and Annealing on the Oxygen Diffusion and Surface Exchange of $La_2NiO_{4+\delta}$," *The Journal of Physical Chemistry C*, vol. 120, no. 32, pp. 17927–17938, Aug. 2016, doi: 10.1021/acs.jpcc.6b05666.

[385] A. Egger, E. Bucher, and W. Sitte, "Oxygen Exchange Kinetics of the IT-SOFC Cathode Material $Nd_2NiO_{4+\delta}$ and Comparison with $La_{0.6}Sr_{0.4}CoO_{3-\delta}$," *Journal of The Electrochemical Society*, vol. 158, no. 5, p. B573, Mar. 2011, doi: 10.1149/1.3569697/XML.

[386] T. Nakamura, K. Yashiro, K. Sato, and J. Mizusaki, "Electrical Conductivity and Thermoelectric Power of $La_{2-x}Sr_xNiO_{4+\delta}$," *ECS Trans*, vol. 16, p. 317, 2009, doi: 10.1149/1.3242246.

[387] D. M. Halat, M. T. Dunstan, M. W. Gaultois, S. Britto, and C. P. Grey, "Study of Defect Chemistry in the System $La_{2-x}Sr_xNiO_{4+\delta}$ by ^{17}O Solid-State NMR Spectroscopy and Ni K-Edge XANES," *Chemistry of Materials*, vol. 30, no. 14, pp. 4556–4570, 2018, doi: 10.1021/ACS.CHEMMATER.8B00747/

[388] T. Nakamura, K. Yashiro, K. Sato, and J. Mizusaki, "Oxygen nonstoichiometry and defect equilibrium in $La_{2-x}Sr_xNiO_{4+\delta}$," *Solid State Ionics*, vol. 180, no. 4–5, pp. 368–376, Apr. 2009, doi: 10.1016/J.SSI.2009.01.013.

[389] A. Aguadero, A. Alonso, and L. Daza, “Oxygen Excess in $La_2CoO_{4+\delta}$: A Neutron Diffraction Study,” *Zeitschrift für Naturforschung B*, vol. 63, pp. 615–622, 2008,

[390] M. Al Daroukh, V. V Vashook, H. Ullmann, F. Tietz, and I. A. Raj, “Oxides of the AMO_3 and A_2MO_4-type: structural stability, electrical conductivity and thermal expansion,” *Solid State Ionics*, vol. 158, no. 1–2, pp. 141–150, 2003, doi: 10.1016/S0167-2738(02)00773-7.

[391] D. R. Barcellos *et al.*, “Phase Identification of the Layered Perovskite $Ce_xSr_{2-x}MnO_4$ and Application for Solar Thermochemical Water Splitting,” *Inorganic Chemistry*, vol. 58, no. 12, pp. 7705–7714, Jun. 2019, doi: 10.1021/acs.inorgchem.8b03487.

[392] A. M. Bergeson-Keller, M. D. Sanders, and R. P. O’Hayre, “Reduction Thermodynamics of $Sr_{1-x}Ce_xMnO_3$ and $Ce_xSr_{2-x}MnO_4$ Perovskites for Solar Thermochemical Hydrogen Production,” *Energy Technology*, vol. 10, no. 1, Jan. 2022, doi: 10.1002/ENTE.202100515.

[393] I. C. L. Atomistic Simulation Group - Department of Materials, “Database of Ionic Radii.” http://abulafia.mt.ic.ac.uk/shannon/ptable.php (accessed Jul. 29, 2022).

[394] M. Johnsson and P. Lemmens, “Crystallography and Chemistry of Perovskites”.

[395] A. M. Deml, V. Stevanović, A. M. Holder, M. Sanders, R. O’Hayre, and C. B. Musgrave, “Tunable Oxygen Vacancy Formation Energetics in the Complex Perovskite Oxide $Sr_xLa_{1-x}Mn_yAl_{1-y}O_3$,” *Chemistry of Materials*, vol. 26, no. 22, pp. 6595–6602, Nov. 2014, doi: 10.1021/cm5033755.

[396] G. Sai Gautam, E. B. Stechel, and E. A. Carter, “Exploring Ca–Ce–M–O (M = 3d Transition Metal) Oxide Perovskites for Solar Thermochemical Applications,” *Chemistry of Materials*, vol. 32, no. 23, pp. 9964–9982, Dec. 2020, doi: 10.1021/acs.chemmater.0c02912.

[397] P. Ding *et al.*, “Review on Ruddlesden-Popper perovskites as cathode for solid oxide fuel cells,” *J. Phys. Mater*, vol. 4, p. 22002, 2021, doi: 10.1088/2515-7639/abe392.

[398] A. Grimaud, F. Mauvy, J. Marc Bassat, S. Fourcade, M. Marrony, and J. Claude Grenier, “Hydration and transport properties of the $Pr_{2-x}Sr_xNiO_{4+\delta}$ compounds as H^+-SOFC cathodes,” *Journal of Materials Chemistry*, vol. 22, no. 31, pp. 16017–16025, Jul. 2012, doi: 10.1039/C2JM31812A.

[399] V. v. Kharton, A. P. Viskup, E. N. Naumovkh, and F. M. B. Marques, “Oxygen ion transport in La_2NiO_4-based ceramics,” *Journal of Materials Chemistry*, vol. 9, no. 10, pp. 2623–2629, Jan. 1999, doi: 10.1039/A903276B.

[400] R. Hord *et al.*, “Transitions Between Lanthanum Cuprates: Crystal Structures of T′, Orthorhombic, and K_2NiF_4-type La_2CuO_4,” *Zeitschrift für anorganische und allgemeine Chemie*, vol. 637, no. 9, pp. 1114–1117, Jul. 2011, doi: 10.1002/ZAAC.201100176.

[401] J. C. Bouloux, J. L. Soubeyroux, G. le Flem, and P. Hagenguller, “Bidimensional magnetic properties of β-Sr_2MnO_4,” *Journal of Solid State Chemistry*, vol. 38, no. 1, pp. 34–39, Jun. 1981, doi: 10.1016/0022-4596(81)90469-2.

[402] K. Tezuka, M. Inamura, Y. Hinatsu, Y. Shimojo, and Y. Morii, “Crystal Structures and Magnetic Properties of $Ca_{2-x}Sr_xMnO_4$,” *Journal of Solid State Chemistry*, vol. 145, no. 2, pp. 705–710, Jul. 1999, doi: 10.1006/JSSC.1999.8290.

[403] W. T. Hong *et al.*, “Tuning the spin state in $LaCoO_3$ thin films for enhanced high-temperature oxygen electrocatalysis,” *Journal of Physical Chemistry Letters*, vol. 4, no. 15, pp. 2493–2499, Aug. 2013, doi: 10.1021/jz401271m.

[404] A. B. Muñoz-García, A. M. Ritzmann, M. Pavone, J. A. Keith, and E. A. Carter, “Oxygen Transport in Perovskite-Type Solid Oxide Fuel Cell Materials: Insights from Quantum Mechanics,” *Accounts of Chemical Research*, vol. 47, no. 11, pp. 3340–3348, Nov. 2014, doi: 10.1021/ar4003174.

[405] S. I. Dutch, “Periodic Tables of Elemental Abundance,” *In the Classroom 356 Journal of Chemical Education* •, vol. 76, no. 3, 1999,

[406] C. He, S. Desai, G. Brown, and S. Bollepalli, “PEM Fuel Cell Catalysts: Cost, Performance and Durability,” *The Electrochemical Society Interface*, 2005,

[407] M. Merz *et al.*, “Spin and orbital states in single-layered $La_{2-x}Ca_xCoO_4$ studied by doping-and temperature-dependent near-edge x-ray absorption fine structure,” *PHYSICAL REVIEW B*, vol. 84, p. 14436, 2011, doi: 10.1103/PhysRevB.84.014436.

[408] J. P. Tang, R. I. Dass, and A. Manthiram, “Comparison of the crystal chemistry and electrical properties of $La_{2-x}A_xNiO_4$ (A = Ca, Sr, and Ba),” *Materials Research Bulletin*, vol. 35, no. 3, pp. 411–424, 2000, doi: 10.1016/S0025-5408(00)00234-8.

[409] V. A. Cherepanov, A. R. Gilev, and E. A. Kiselev, “Electrotransport in the La_2NiO_4 -based solid solutions,” *Pure and Applied Chemistry*, vol. 91, no. 6, pp. 911–922, Jun. 2019, doi: 10.1515/PAC-2018-1001/

[410] C. Chaillout *et al.*, “The crystal structure of superconducting $La_2CuO_{4.032}$ by neutron diffraction,” *Physica C: Superconductivity*, vol. 158, no. 1–2, pp. 183–191, Apr. 1989, doi: 10.1016/0921-4534(89)90315-8.

[411] R. P. Rapp, A. Mehta, J. DiCarlo, and A. Navrotsky, "$La_2CuO_{4+\delta}$: Synthesis under high oxygen pressure and study of phase relations and energetics," *Journal of Materials Research*, vol. 9, no. 1, pp. 8–12, 1994, doi: 10.1557/JMR.1994.0008.

[412] T. Ghorbani-Moghadam, A. Kompany, M. M. Bagheri-Mohagheghi, and M. E. Abrishami, "High temperature electrical conductivity and electrochemical investigation of $La_{2-x}Sr_xCoO_4$ nanoparticles for IT-SOFC cathode," *Ceramics International*, vol. 44, no. 17, pp. 21238–21248, Dec. 2018, doi: 10.1016/J.CERAMINT.2018.08.171.

[413] L. P. Cao *et al.*, "High-pressure and high-temperature synthesis and physical properties of Ca_2CrO_4 solid," *AIP Advances*, vol. 6, no. 5, p. 55010, 2016, doi: 10.1063/1.4949008.

[414] C. Ablitt *et al.*, "Tolerance Factor Control of Uniaxial Negative Thermal Expansion in a Layered Perovskite," *Chemistry of Materials*, vol. 32, no. 1, pp. 605–610, Jan. 2020, doi: 10.1021/acs.chemmater.9b04512.

[415] I. D. Fawcett, J. E. S. IV, M. Greenblatt, M. Croft, and K. V Ramanujachary, "Structure, Magnetism, and Properties of Ruddlesden-Popper Calcium Manganates Prepared from Citrate Gels," *Chemistry of Materials*, vol. 10, no. 11, pp. 3643–3651, 1998, doi: 10.1021/cm980380b.

[416] K. Tezuka, M. Inamura, Y. Hinatsu, Y. Shimojo, and Y. Morii, "Crystal Structures and Magnetic Properties of $Ca_{2-x}Sr_xMnO_4$," *Journal of Solid State Chemistry*, vol. 145, no. 2, pp. 705–710, 1999, doi: 10.1006/JSSC.1999.8290.

[417] M. E. Leonowicz, K. R. Poeppelmeier, and J. M. Longo, "Structure determination of Ca_2MnO_4 and $Ca_2MnO_{3.5}$ by X-ray and neutron methods," *Journal of Solid State Chemistry*, vol. 59, no. 1, pp. 71–80, 1985, doi: 10.1016/0022-4596(85)90352-4.

[418] P. Steffens *et al.*, "High-pressure diffraction studies on Ca_2RuO_4," *Physical Review B - Condensed Matter and Materials Physics*, vol. 72, no. 9, p. 94104, 2005, doi: 10.1103/PHYSREVB.72.094104/

[419] D. Babel, W. Rüdorff, and R. Tschöpp, "Ternäre Oxide der Übergangsmetalle. VI. Erdalkaliiridium(IV)-oxide: Struktur von Dicalciumiridium(IV)-oxid, Ca_2IrO_4," *Zeitschrift für anorganische und allgemeine Chemie*, vol. 347, no. 5–6, pp. 282–288, 1966, doi: 10.1002/ZAAC.19663470509.

[420] T. Baikie, Z. Ahmad, M. Srinivasan, A. Maignan, S. S. Pramana, and T. J. White, "The crystallographic and magnetic characteristics of Sr_2CrO_4 (K_2NiF_4-type) and $Sr_{10}(CrO_4)_6F_2$ (apatite-type)," *Journal of Solid State Chemistry*, vol. 180, no. 5, pp. 1538–1546, 2007, doi: 10.1016/j.jssc.2007.02.023.

[421] J. C. Bouloux, J. L. Soubeyroux, G. Le Flem, and P. Hagenguller, "Bidimensional magnetic properties of β-Sr_2MnO_4," *Journal of Solid State Chemistry*, vol. 38, no. 1, pp. 34–39, 1981, doi: 10.1016/0022-4596(81)90469-2.

[422] Q. Huang *et al.*, "Neutron Powder Diffraction Study of the Crystal Structures of Sr_2RuO_4 and Sr_2IrO_4 at Room Temperature and at 10 K," *Journal of Solid State Chemistry*, vol. 112, no. 2, pp. 355–361, 1994, doi: 10.1006/JSSC.1994.1316.

[423] J. S. Gardner, G. Balakrishnan, and D. M. K. Paul, "Neutron powder diffraction studies of Sr_2RuO_4 and $SrRuO_3$," *Physica C: Superconductivity*, vol. 252, no. 3–4, pp. 303–307, 1995, doi: 10.1016/0921-4534(95)00495-5.

[424] M. V. R. Rao, V. G. Sathe, D. Sornadurai, B. Panigrahi, and T. Shripathi, "Metal to insulator transition in $Sr_2Ru_{1-x}Ir_xO_4$," *Journal of Physics and Chemistry of Solids*, vol. 61, no. 12, pp. 1989–1999, 2000, doi: 10.1016/S0022-3697(00)00193-1.

[425] B. Ranjbar and B. J. Kennedy, "Anisotropic thermal expansion in Sr_2RhO_4 – A variable temperature Synchrotron X-ray diffraction study," *Solid State Sciences*, vol. 49, pp. 43–46, 2015, doi: 10.1016/J.SOLIDSTATESCIENCES.2015.09.009.

[426] T. Vogt and D. J. Buttrey, "Temperature Dependent Structural Behavior of Sr_2RhO_4," *Journal of Solid State Chemistry*, vol. 123, no. 1, pp. 186–189, 1996, doi: 10.1006/JSSC.1996.0167.

[427] F. Ye *et al.*, "Structure symmetry determination and magnetic evolution in $Sr_2Ir_{1-x}Rh_x O_4$," *Physical Review B - Condensed Matter and Materials Physics*, vol. 92, no. 20, p. 201112, 2015, doi: 10.1103/PHYSREVB.92.201112/FIGURES/4/MEDIUM.

[428] K. Horigane *et al.*, "Magnetic phase diagram of $Sr_{2-x}La_xIrO_4$ synthesized by mechanical alloying," *Physical Review B*, vol. 97, no. 6, p. 64425, 2018, doi: 10.1103/PHYSREVB.97.064425/

[429] J. J. Randall, L. Katz, and R. Ward, "The Preparation of a Strontium-Iridium Oxide $Sr_2IrO_{4.12}$," *J Am Chem Soc*, vol. 79, no. 2, pp. 266–267, 2002, doi: 10.1021/JA01559A004.

[430] M. Isobe *et al.*, "Spin-Orbit Mott State in the Novel Quasi-2D Antiferromagnet Ba_2IrO_4," in *Journal of Physics: Conference Series*, 2012, pp. 1–4.

[431] A. Lappas and K. Prassides, "Oxygen-defect geometry in oxygen-rich $La_2Co_xCu_{1-x}O_{4+\delta}$ Layered Oxides," *Journal of Solid State Chemistry*, 1994, doi: 10.1006/jssc.1994.1009.

[432] R. Hord *et al.*, "Transitions Between Lanthanum Cuprates: Crystal Structures of T′, Orthorhombic, and K_2NiF_4-type La_2CuO_4," *Zeitschrift für anorganische und allgemeine Chemie*, vol. 637, no. 9, pp. 1114–1117, 2011, doi: 10.1002/ZAAC.201100176.

[433] M. S. Kaluzhskikh *et al.*, "High-temperature crystal structure and transport properties of the layered cuprates Ln_2CuO_4, Ln=Pr, Nd and Sm," *Journal of Solid State Chemistry*, vol. 184, no. 3, pp. 698–704, 2011, doi: 10.1016/J.JSSC.2011.01.035.

[434] Y. L. Lee, J. Kleis, J. Rossmeisl, S. H. Yang, and D. Morgan, "Prediction of solid oxide fuel cell cathode activity with first-principles descriptors," *Energy and Environmental Science*, vol. 4, no. 10, pp. 3966–3970, Oct. 2011, doi: 10.1039/c1ee02032c.

[435] Y.-L. Lee, D. Lee, X. R. Wang, H. N. Lee, D. Morgan, and Y. Shao-Horn, "Kinetics of Oxygen Surface Exchange on Epitaxial Ruddlesden–Popper Phases and Correlations to First-Principles Descriptors," *The Journal of Physical Chemistry Letters*, vol. 7, no. 2, pp. 244–249, Jan. 2016, doi: 10.1021/acs.jpclett.5b02423.

[436] W. Xie, Y.-L. Lee, Y. Shao-Horn, and D. Morgan, "Oxygen Point Defect Chemistry in Ruddlesden–Popper Oxides $(La_{1-x}Sr_x)_2MO_{4\pm\delta}$ (M = Co, Ni, Cu)," *The Journal of Physical Chemistry Letters*, vol. 7, no. 10, pp. 1939–1944, May 2016, doi: 10.1021/acs.jpclett.6b00739.

[437] M. Pavone, A. B. Muñoz-García, A. M. Ritzmann, and E. A. Carter, "First-Principles Study of Lanthanum Strontium Manganite: Insights into Electronic Structure and Oxygen Vacancy Formation," *The Journal of Physical Chemistry C*, vol. 118, no. 25, pp. 13346–13356, Jun. 2014, doi: 10.1021/jp500352h.

[438] H. A. Tahini, X. Tan, W. Zhou, Z. Zhu, U. Schwingenschlögl, and S. C. Smith, "Sc and Nb dopants in $SrCoO_3$ modulate electronic and vacancy structures for improved water splitting and SOFC cathodes," *Energy Storage Materials*, vol. 9, pp. 229–234, 2017, doi: 10.1016/J.ENSM.2017.01.005.

[439] A. F. Kapustinskii, "Lattice energy of ionic crystals," *Q. Rev. Chem. Soc.*, vol. 10, no. 3, pp. 283–294, 1956, doi: 10.1039/QR9561000283.

[440] R. B. Wexler, G. S. Gautam, E. B. Stechel, and E. A. Carter, "Factors Governing Oxygen Vacancy Formation in Oxide Perovskites," *J Am Chem Soc*, vol. 143, no. 33, pp. 13212–13227, Aug. 2021, doi: 10.1021/jacs.1c05570.

[441] G. Sai Gautam and E. A. Carter, "Evaluating transition metal oxides within DFT-SCAN and SCAN+U frameworks for solar thermochemical applications," *PHYSICAL REVIEW MATERIALS*, vol. 2, p. 95401, 2018, doi: 10.1103/PhysRevMaterials.2.095401.

[442] E. Mastronardo, X. Qian, J. M. Coronado, and S. Haile, "Fe-doped $CaMnO_3$ for thermochemical heat storage application," in *AIP Conference Proceedings*, Jul. 2019, vol. 2126, no. 1, p. 210005. doi: 10.1063/1.5117754.

[443] B. Bulfin *et al.*, "Redox chemistry of $CaMnO_3$ and $Ca_{0.8}Sr_{0.2}MnO_3$ oxygen storage perovskites," *Journal of Materials Chemistry A*, vol. 5, no. 17, pp. 7912–7919, May 2017, doi: 10.1039/C7TA00822H.

[444] L. Imponenti, K. J. Albrecht, R. Kharait, M. D. Sanders, and G. S. Jackson, "Redox cycles with doped calcium manganites for thermochemical energy storage to 1000 °C," *Applied Energy*, vol. 230, pp. 1–18, 2018, doi: https://doi.org/10.1016/j.apenergy.2018.08.044.

[445] J. R. Scheffe, D. Weibel, and A. Steinfeld, "Lanthanum–Strontium–Manganese Perovskites as Redox Materials for Solar Thermochemical Splitting of H_2O and CO_2," *Energy & Fuels*, vol. 27, no. 8, pp. 4250–4257, Aug. 2013, doi: 10.1021/ef301923h.

[446] A. Demont and S. Abanades, "High redox activity of Sr-substituted lanthanum manganite perovskites for two-step thermochemical dissociation of CO_2," *RSC Adv.*, vol. 4, pp. 54885–54891, 2014, doi: 10.1039/c4ra10578h.

[447] T. Cooper, J. R. Scheffe, M. E. Galvez, R. Jacot, G. Patzke, and A. Steinfeld, "Lanthanum Manganite Perovskites with Ca/Sr A-site and Al B-site Doping as Effective Oxygen Exchange Materials for Solar Thermochemical Fuel Production," *Energy Technology*, vol. 3, no. 11, pp. 1130–1142, Nov. 2015, doi: 10.1002/ente.201500226.

[448] S. M. Babiniec, E. N. Coker, J. E. Miller, and A. Ambrosini, "Doped calcium manganites for advanced high-temperature thermochemical energy storage," *International Journal of Energy Research*, vol. 40, no. 2, pp. 280–284, Feb. 2016, doi: 10.1002/er.3467.

[449] N. Galinsky, M. Sendi, L. Bowers, and F. Li, "$CaMn_{1-x}B_xO_{3-\delta}$ (B = Al, V, Fe, Co, and Ni) perovskite based oxygen carriers for chemical looping with oxygen uncoupling (CLOU)," *Applied Energy*, vol. 174, pp. 80–87, Jul. 2016, doi: 10.1016/J.APENERGY.2016.04.046.

[450] X. Qian *et al.*, "Outstanding Properties and Performance of $CaTi_{0.5}Mn_{0.5}O_{3-\delta}$ for Solar-Driven Thermochemical Hydrogen Production," *Matter*, vol. 4, no. 2, pp. 688–708, Feb. 2021, doi: 10.1016/J.MATT.2020.11.016/

[451] E. Bakken, T. Norby, and S. Stølen, "Nonstoichiometry and reductive decomposition of CaMnO3−δ," *Solid State Ionics*, vol. 176, no. 1–2, pp. 217–223, Jan. 2005, doi: 10.1016/J.SSI.2004.07.001.

[452] A. Graff and Y. Amouyal, “Effects of Lattice Defects and Niobium Doping on Thermoelectric Properties of Calcium Manganate Compounds for Energy Harvesting Applications,” *Journal of Electronic Materials 2015 45:3*, vol. 45, no. 3, pp. 1508–1516, Oct. 2015, doi: 10.1007/S11664-015-4089-6.

[453] F. Kawashima, X. Y. Huang, K. Hayashi, Y. Miyazaki, and T. Kajitani, “Structure and High-Temperature Thermoelectric Properties of the n-Type Layered Oxide $Ca_{2-x}Bi_x MnO_{4-\gamma}$,” *Journal of Electronic Materials 2009 38:7*, vol. 38, no. 7, pp. 1159–1162, Mar. 2009, doi: 10.1007/S11664-009-0700-Z.

[454] J. Takahashi and N. Kamegashira, “X-ray structural study of calcium manganese oxide by Rietveld analysis at high temperatures $Ca_2MnO_{4.00}$,” *Materials Research Bulletin*, vol. 28, no. 6, pp. 565–573, Jun. 1993, doi: 10.1016/0025-5408(93)90053-G.

[455] N. Chihaoui, R. Dhahri, M. Bejar, E. Dharhi, L. C. Costa, and M. P. F. Graça, “Electrical and dielectric properties of the $Ca_2MnO_{4-\delta}$ system,” *Solid State Communications*, vol. 151, no. 19, pp. 1331–1335, Oct. 2011, doi: 10.1016/J.SSC.2011.06.023.

[456] N. Chihaoui, M. Bejar, E. Dharhi, M. A. Valente, and M. P. F. Graa, “Effect of the oxygen deficiency on the physical properties of $Ca_2MnO_{4-\delta}$ compounds,” *Journal of Alloys and Compounds*, vol. 509, no. 36, pp. 8965–8969, Sep. 2011, doi: 10.1016/J.JALLCOM.2011.06.110.

[457] C. Autret *et al.*, “Structural investigation of Ca_2MnO_4 by neutron powder diffraction and electron microscopy,” *Journal of Solid State Chemistry*, vol. 177, no. 6, pp. 2044–2052, Jun. 2004, doi: 10.1016/J.JSSC.2004.02.012.

[458] E. Mastronardo, X. Qian, J. M. Coronado, and S. M. Haile, “The favourable thermodynamic properties of Fe-doped $CaMnO_3$ for thermochemical heat storage,” *Journal of Materials Chemistry A*, vol. 8, no. 17, pp. 8503–8517, May 2020, doi: 10.1039/D0TA02031A.

[459] I. D. Fawcett, J. E. Sunstrom IV, M. Greenblatt, M. Croft, and K. v. Ramanujachary, “Structure, Magnetism, and Properties of Ruddlesden-Popper Calcium Manganates Prepared from Citrate Gels,” *Chemistry of Materials*, vol. 10, no. 11, pp. 3643–3651, 1998, doi: 10.1021/cm980380b.

[460] M. C. Biesinger, B. P. Payne, A. P. Grosvenor, L. W. M. Lau, A. R. Gerson, and R. S. C. Smart, “Resolving surface chemical states in XPS analysis of first row transition metals, oxides and hydroxides: Cr, Mn, Fe, Co and Ni,” *Applied Surface Science*, vol. 257, no. 7, pp. 2717–2730, Jan. 2011, doi: 10.1016/J.APSUSC.2010.10.051.

[461] M. Fujiwara, T. Matsushita, and S. Ikeda, “Evaluation of Mn3s X-ray photoelectron spectroscopy for characterization of manganese complexes,” *Journal of Electron Spectroscopy and Related Phenomena*, vol. 74, no. 3, pp. 201–206, Nov. 1995, doi: 10.1016/0368-2048(94)02375-1.

[462] M. E. Leonowicz, K. R. Poeppelmeier, and J. M. Longo, “Structure determination of Ca_2MnO_4 and $Ca_2MnO_{3.5}$ by X-ray and neutron methods,” *Journal of Solid State Chemistry*, vol. 59, no. 1, pp. 71–80, Aug. 1985, doi: 10.1016/0022-4596(85)90352-4.

[463] P. Rocha-Rodrigues *et al.*, “Ca_2MnO_4 structural path: Following the negative thermal expansion at the local scale,” *PHYSICAL REVIEW B*, vol. 102, p. 104115, 2020, doi: 10.1103/PhysRevB.102.104115.

[464] B. Ranjbar and B. J. Kennedy, “Anisotropic thermal expansion in Sr_2RhO_4 – A variable temperature Synchrotron X-ray diffraction study,” *Solid State Sciences*, vol. 49, pp. 43–46, Nov. 2015, doi: 10.1016/J.SOLIDSTATESCIENCES.2015.09.009.

[465] J. A. Alonso, M. J. Martínez-Lope, M. T. Casais, and M. T. Fernández-Díaz, “Evolution of the Jahn-Teller Distortion of MnO_6 Octahedra in $RMnO_3$ Perovskites (R) Pr, Nd, Dy, Tb, Ho, Er, Y): A Neutron Diffraction Study,” *Inorganic Chemistry*, vol. 39, pp. 917–923, 2000, doi: 10.1021/ic990921e.

[466] A. Demont *et al.*, “Solar thermochemical conversion of CO_2 into fuel via two-step redox cycling of non-stoichiometric Mn-containing perovskite oxides,” *J. Mater. Chem. A*, vol. 3, no. 7, pp. 3536–3546, 2015, doi: 10.1039/C4TA06655C.

[467] M. Fu, H. Ma, X. Li, and H. Xu, “Mechanism and thermodynamic study of solar H_2 production on $LaFeO_3$ defected surface: Effect of H_2O to H_2 conversion ratio and kinetics on optimization of energy conversion efficiency,” *Journal of Cleaner Production*, vol. 268, p. 122293, Sep. 2020, doi: 10.1016/J.JCLEPRO.2020.122293.

[468] Z. Zhao, M. Uddi, N. Tsvetkov, B. Yildiz, and A. F. Ghoniem, “Redox Kinetics Study of Fuel Reduced Ceria for Chemical-Looping Water Splitting,” *Journal of Physical Chemistry C*, vol. 120, no. 30, pp. 16271–16289, Aug. 2016, doi: 10.1021/ACS.JPCC.6B01847.

[469] J. K. Rosemary, G. L. Bauerle, and T. H. Springer, “Solar Energy Storage Using Reversible Hydration-Dehydration of CaO-$Ca(OH)_2$,” *Journal of Energy*, vol. 3, no. 6, pp. 321–322, May 1979, doi: 10.2514/3.62440.

[470] I. Fujii, K. Tsuchiya, M. Higano, and J. Yamada, “Studies of an energy storage system by use of the reversible chemical reaction: CaO + H2O ⇌ $Ca(OH)_2$,” *Solar Energy*, vol. 34, no. 4–5, pp. 367–377, Jan. 1985, doi: 10.1016/0038-092X(85)90049-0.

[471] F. Schaube, L. Koch, A. Wörner, and H. Müller-Steinhagen, “A thermodynamic and kinetic study of the de- and rehydration of $Ca(OH)_2$ at high H_2O partial pressures for thermo-chemical heat storage,” *Thermochimica Acta*, vol. 538, pp. 9–20, Jun. 2012, doi: 10.1016/J.TCA.2012.03.003.

[472] A. K. Galwey and G. M. Laverty, “A kinetic and mechanistic study of the dehydroxylation of calcium hydroxide,” *Thermochimica Acta*, vol. 228, no. C, pp. 359–378, Nov. 1993, doi: 10.1016/0040-6031(93)80304-S.

[473] Y. A. Criado, M. Alonso, and J. C. Abanades, “Kinetics of the $CaO/Ca(OH)_2$ Hydration/Dehydration Reaction for Thermochemical Energy Storage Applications,” *Industrial and Engineering Chemistry Research*, vol. 53, no. 32, pp. 12594–12601, Aug. 2014, doi: 10.1021/IE404246P.

[474] M. Burriel *et al.*, “Absence of Ni on the outer surface of Sr doped La_2NiO_4 single crystals,” *Energy & Environmental Science*, vol. 7, no. 1, pp. 311–316, Dec. 2013, doi: 10.1039/C3EE41622D.

[475] T. Akbay, A. Staykov, J. Druce, H. Téllez, T. Ishihara, and J. A. Kilner, “The interaction of molecular oxygen on LaO terminated surfaces of La_2NiO_4,” *Journal of Materials Chemistry A*, vol. 4, no. 34, pp. 13113–13124, Aug. 2016, doi: 10.1039/C6TA02715F.

[476] J. Zhou, G. Chen, K. Wu, and Y. Cheng, “Interaction of La_2NiO_4 (100) surface with oxygen molecule: A first-principles study,” *Journal of Physical Chemistry C*, vol. 117, no. 25, pp. 12991–12999, Jun. 2013, doi: 10.1021/JP403094X/

[477] R. J. Carrillo, K. J. Warren, and J. R. Scheffe, “Experimental Framework for Evaluation of the Thermodynamic and Kinetic Parameters of Metal-Oxides for Solar Thermochemical Fuel Production,” *Journal of Solar Energy Engineering*, vol. 141, pp. 210071–2100710, 2019, doi: 10.1115/1.4042088.

[478] R. Bornovski, L. F. Huang, E. P. Komarala, J. M. Rondinelli, and B. A. Rosen, “Catalytic Enhancement of CO Oxidation on $LaFeO_3$ Regulated by Ruddlesden-Popper Stacking Faults,” *ACS Applied Materials and Interfaces*, vol. 11, no. 37, pp. 33850–33858, Sep. 2019, doi: 10.1021/ACSAMI.9B09404/

[479] M. Burriel *et al.*, “Influence of Crystal Orientation and Annealing on the Oxygen Diffusion and Surface Exchange of $La_2 NiO_{4+\delta}$,” *The Journal of Physical Chemistry C*, vol. 120, no. 32, pp. 17927–17938, Aug. 2016, doi: 10.1021/acs.jpcc.6b05666.

[480] Y. Chen *et al.*, “Segregated Chemistry and Structure on (001) and (100) Surfaces of $(La_{1-x}Sr_x)_2CoO_4$ Override the Crystal Anisotropy in Oxygen Exchange Kinetics,” *Chemistry of Materials*, vol. 27, no. 15, pp. 5436–5450, Aug. 2015, doi: 10.1021/ACS.CHEMMATER.5B02292.

[481] D. Lee, Y.-L. Lee, W. T. Hong, M. D. Biegalski, D. Morgan, and Y. Shao-Horn, “Oxygen surface exchange kinetics and stability of $(La,Sr)_2CoO_{4\pm\delta}/La_{1-x}Sr_xMO_{3-\delta}$ (M = Co and Fe) hetero-interfaces at intermediate temperatures,” *Journal of Materials Chemistry A*, vol. 3, no. 5, pp. 2144–2157, Jan. 2015, doi: 10.1039/C4TA05795C.

[482] J. Woo Han and B. Yildiz, “Mechanism for enhanced oxygen reduction kinetics at the $(La,Sr)CoO_{3-d}/(La,Sr)_2CoO_{4+d}$ hetero-interface,” *Energy & Environmental Science*, vol. 5, p. 8598, 2012, doi: 10.1039/c2ee03592h.

[483] N. Tsvetkov, Y. Chen, and B. Yildiz, “Reducibility of Co at the $La_{0.8}Sr_{0.2}CoO_3$ / $(La_{0.5}Sr_{0.5})_2CoO_4$ hetero-interface at elevated temperatures,” *Journal of Materials Chemistry A*, vol. 2, p. 14690, 2014, doi: 10.1039/c4ta01889c.

[484] M. Sase *et al.*, “Enhancement of Oxygen Surface Exchange at the Hetero-interface of $(La, Sr)CoO_3$ / $(La, Sr)_2CoO_4$ with PLD-Layered Films,” *Journal of The Electrochemical Society*, vol. 155, no. 8, p. B793, Jun. 2008, doi: 10.1149/1.2928612.

[485] W. W. Zhang, M. Chen, E. Povoden-Karadeniz, and P. V. Hendriksen, “Thermodynamic modeling of the Sr–Co–Fe–O system,” *Solid State Ionics*, vol. 292, pp. 88–97, Sep. 2016, doi: 10.1016/J.SSI.2016.05.011.

Appendix A – Supplementary information for Chapter 4

List of pseudopotentials used for elements in this study

Table A-1. Pseudopotentials used for the elements in compounds reported in this thesis. These are in agreement with those used in structures reported in the materialsproject database. [240]

Element	Pseudopotential	Element	Pseudopotential
O	O		
Li	Li_sv	Be	Be_sv
Na	Na_pv	Mg	Mg_pv
K	K_sv	Ca	Ca_sv
Rb	Rb_sv	Sr	Sr_sv
Cs	Cs_sv	Ba	Ba_sv
Sc	Sc_sv	Fe	Fe_pv
Ti	Ti_pv	Co	Co
V	V_sv	Ni	Ni_pv
Cr	Cr_pv	Cu	Cu_pv
Mn	Mn_pv	Zn	Zn
Y	Y_sv	Ru	Ru_pv
Zr	Zr_sv	Rh	Rh_pv
Nb	Nb_pv	Pd	Pd
Mo	Mo_pv	Ag	Ag
Hf	Hf_pv	Os	Os_pv
Ta	Ta_pv	Ir	Ir
W	W_pv	Pt	Pt
Re	Re_pv	Au	Au
Al	Al	Te	Te
Si	Si	Ga	Ga_d
P	P	Ge	Ge_d
S	S	As	As

In	In_d	Se	Se
Sn	Sn_d	Bi	Bi
Sb	Sb		
La	La	Tb	Tb_3
Ce	Ce	Dy	Dy_3
Pr	Pr_3	Ho	Ho_3
Nd	Nd_3	Er	Er_3
Sm	Sm_3	Tm	Tm_3
Eu	Eu	Yb	Yb
Gd	Gd	Lu	Lu_3

Appendix B – Supplementary information for Chapter 6

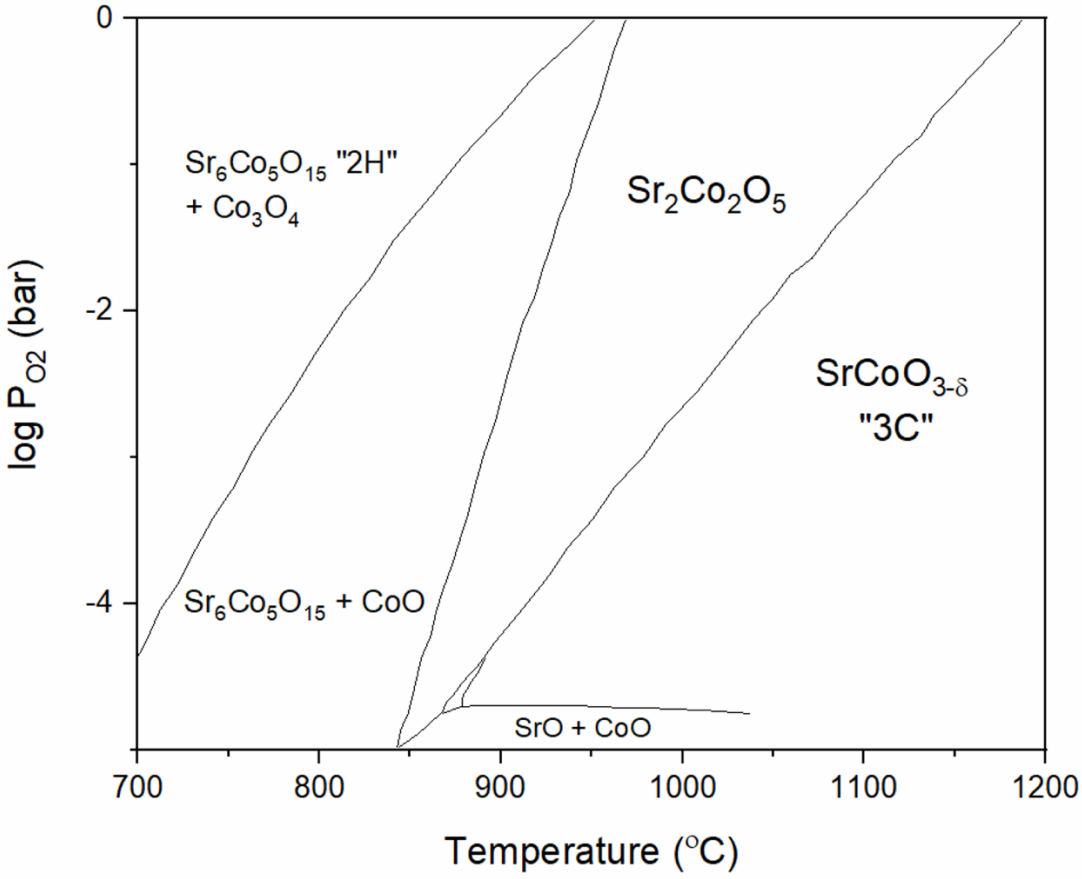

Figure B-1. Phase diagram of the $SrCoO_3$ compound. Adapted from [485].

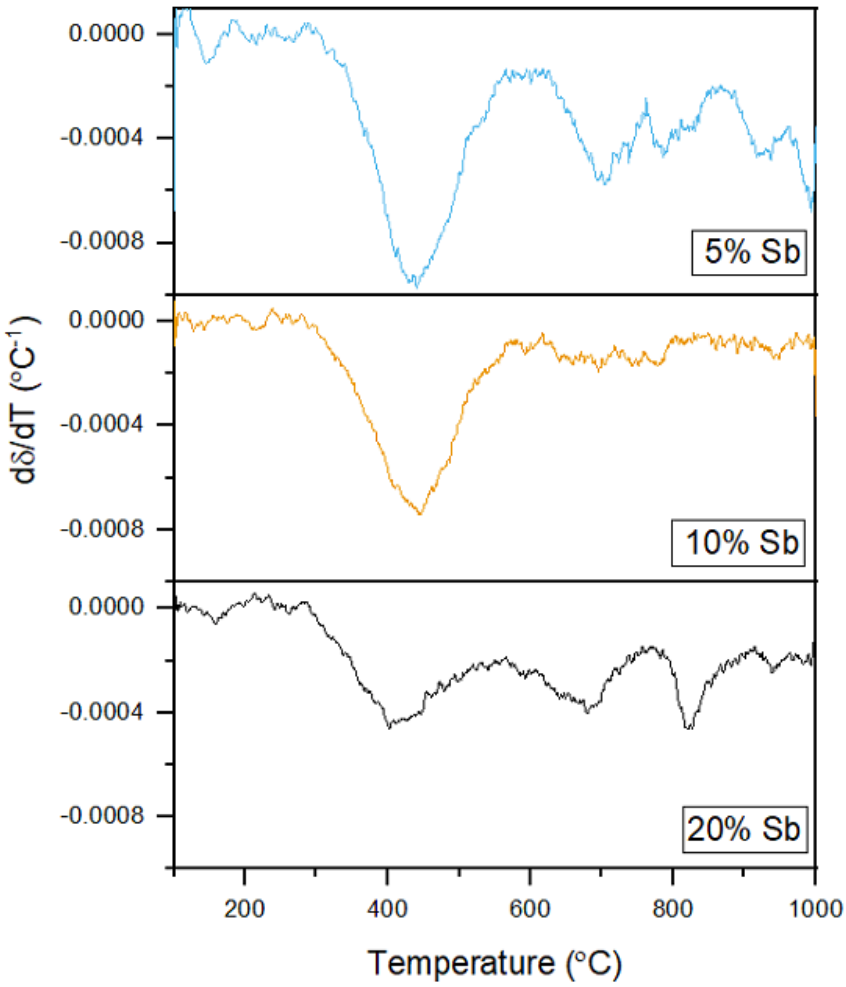

Figure B-1. First derivative of oxygen non-stoichiometry of the $SrCo_{1-x}Sb_xO_{3-\delta}$ compounds when heating under a dry argon environment.

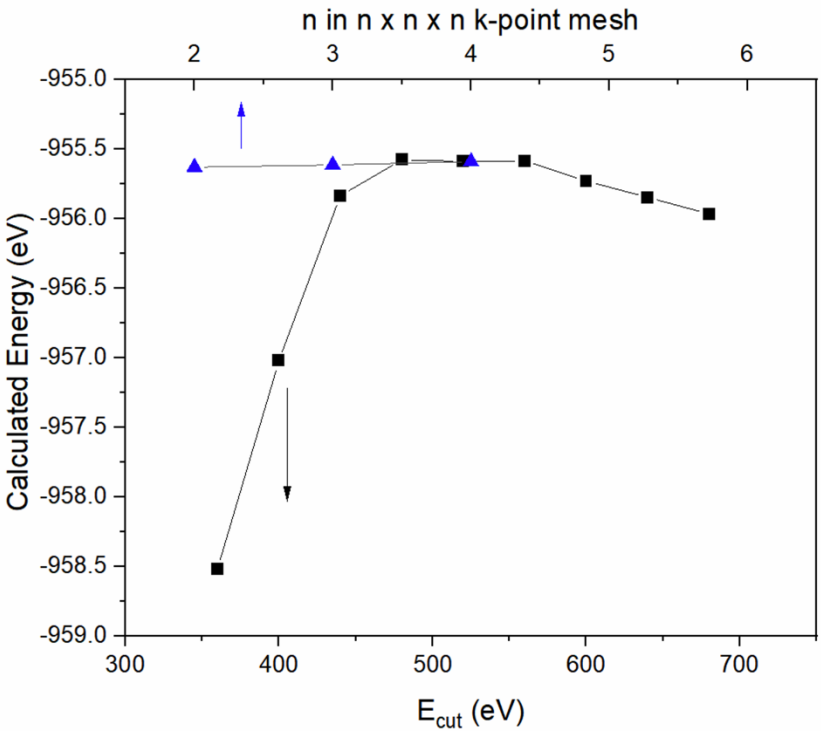

Figure B-2. Convergence testing results for the $SrCoO_3$ structure.

a)

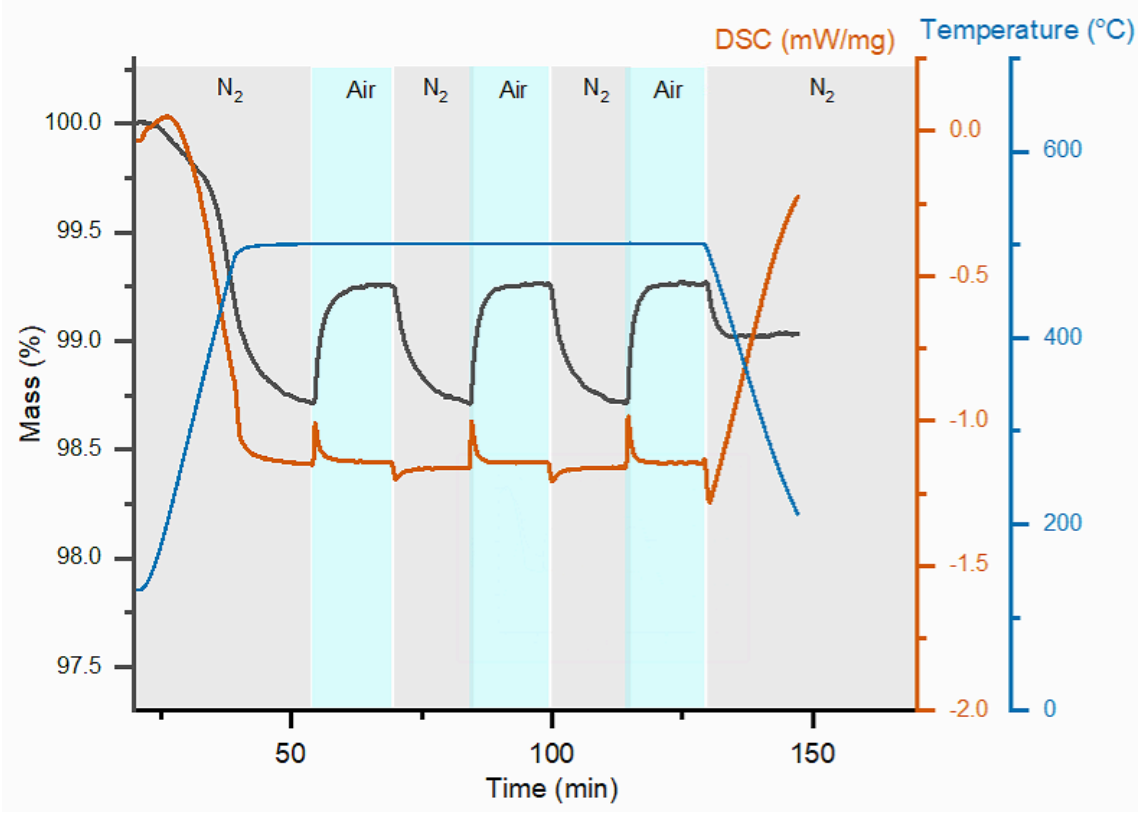
DSC (mW/mg)
Temperature (°C)
N2
Air
N2
Air
N2
Air
N2
100.0
99.5
99.0
98.5
98.0
97.5
Mass (%)
0.0
-0.5
-1.0
-1.5
-2.0
600
400
200
0
50
100
150
Time (min)

b)

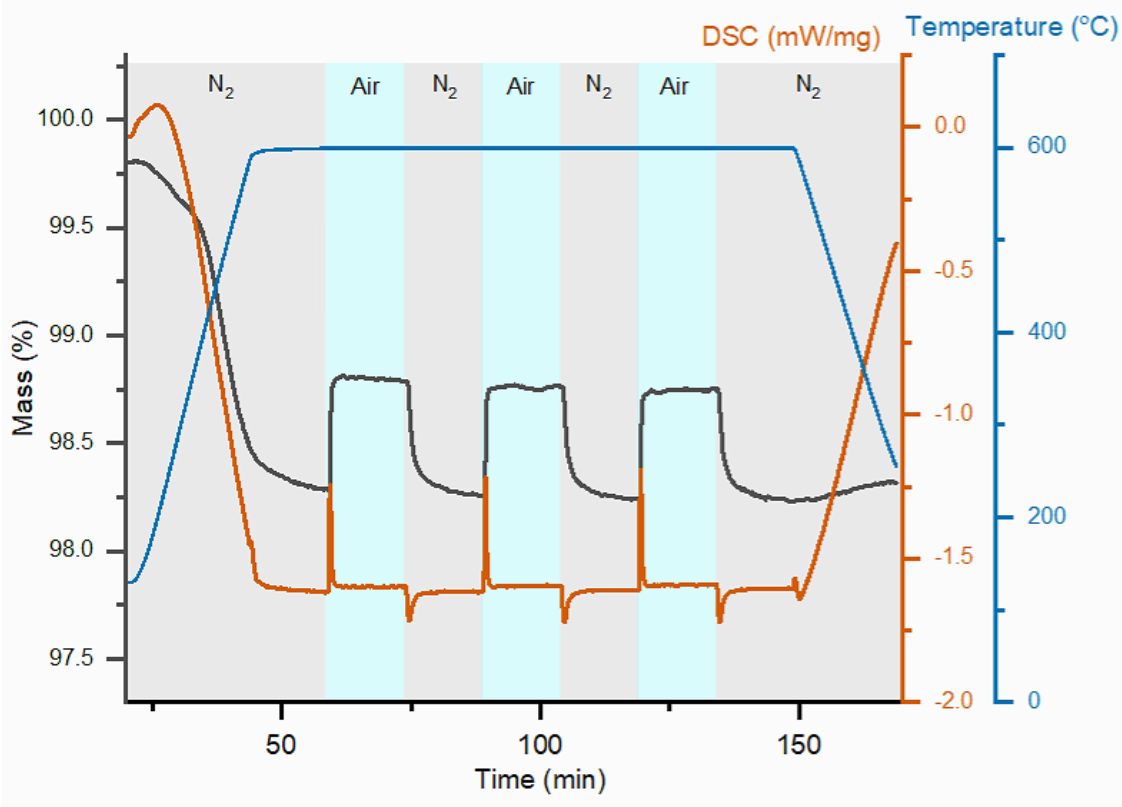
DSC (mW/mg)
Temperature (°C)
N2
Air
N2
Air
N2
Air
N2
100.0
99.5
99.0
98.5
98.0
97.5
Mass (%)
0.0
-0.5
-1.0
-1.5
-2.0
600
400
200
0
50
100
150
Time (min)

c)

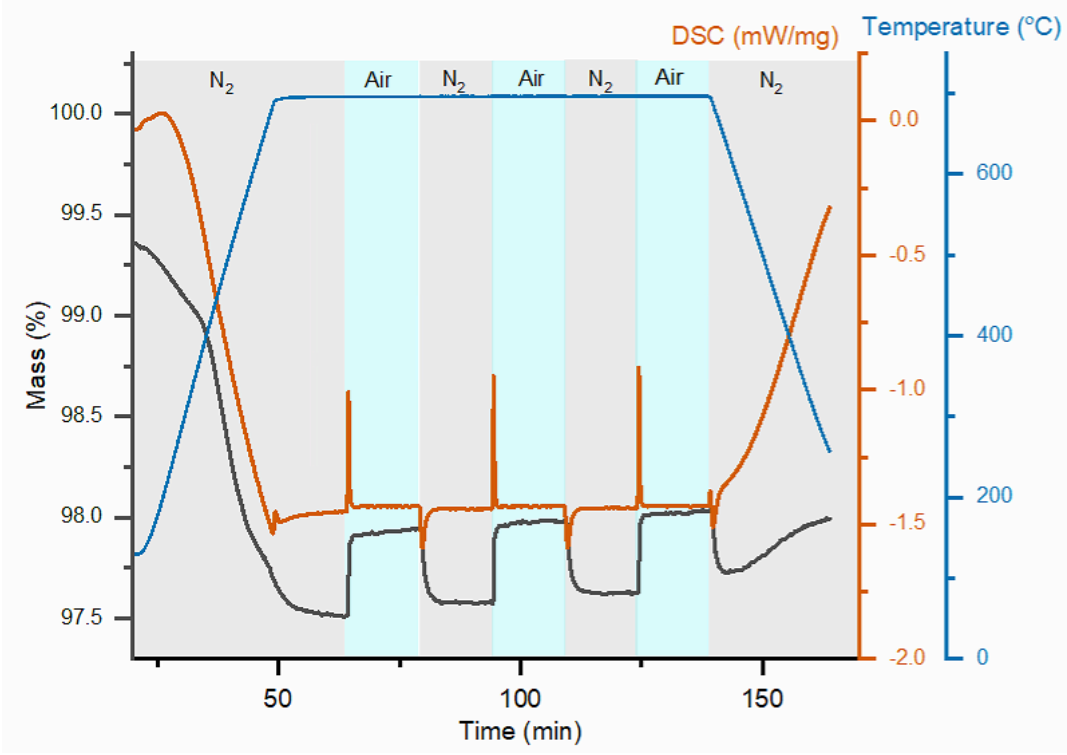

d)

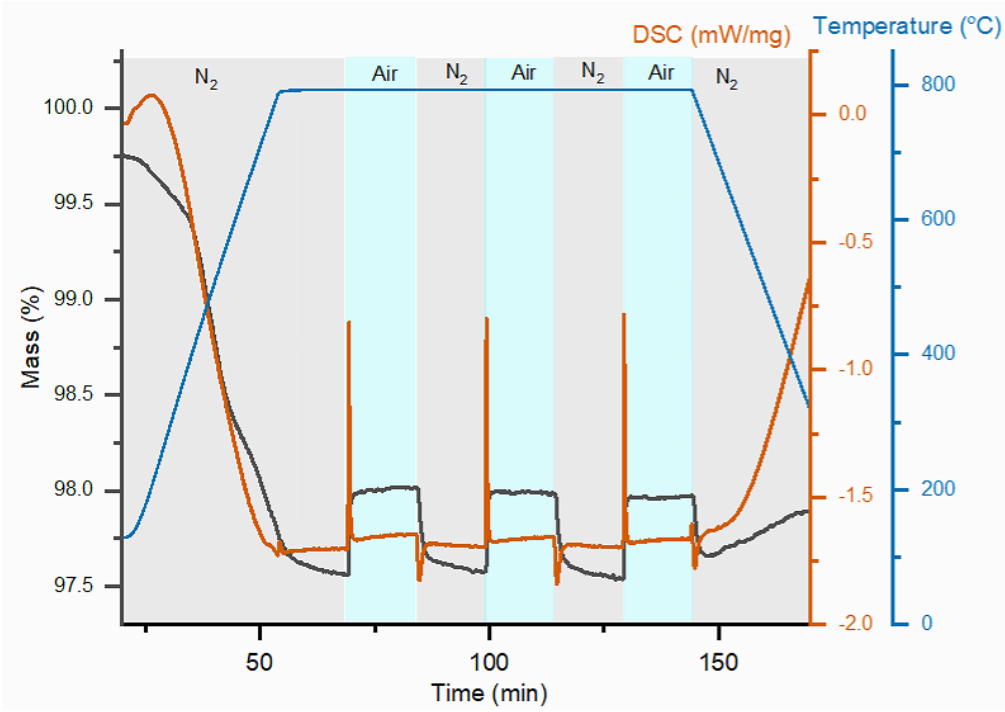

Figure B-3. Isothermal cycling data for $SrCo_{0.95}Sb_{0.05}O_{3-\delta}$ at a) 500 °C, b) 600 °C, c) 700 °C and d) 800 °C.

a)

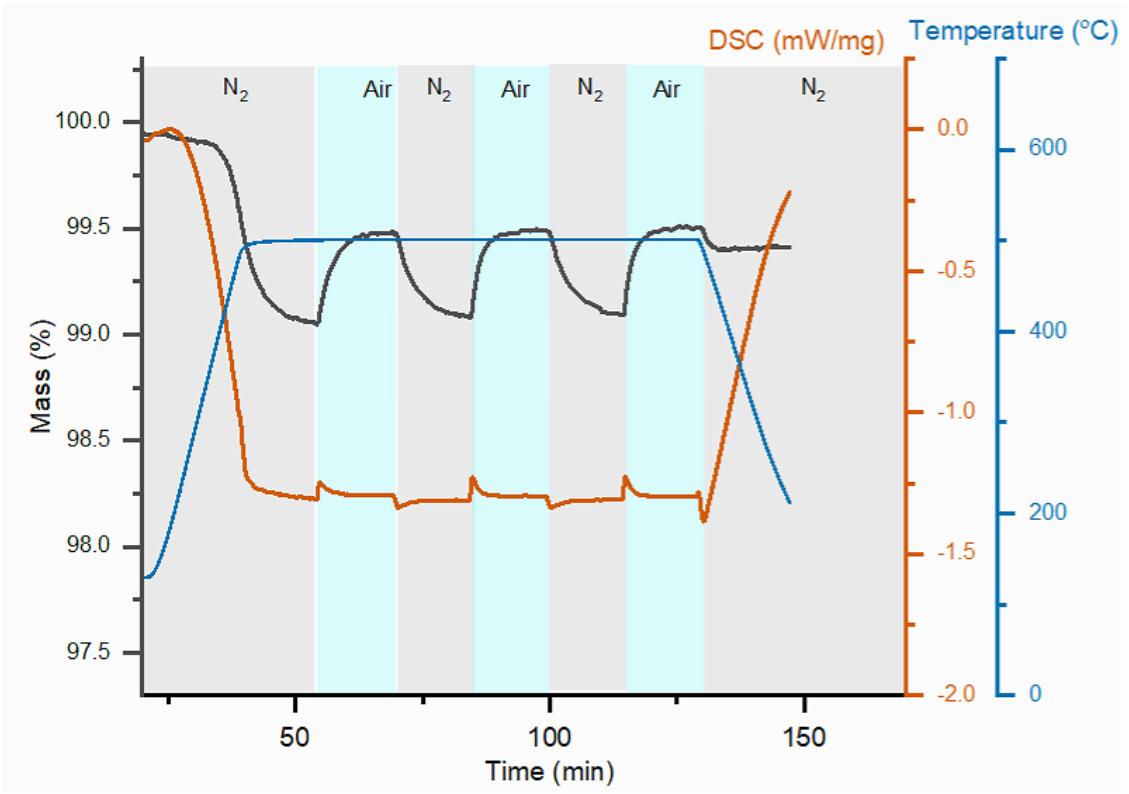
DSC (mW/mg)
Temperature (°C)
N2
Air
N2
Air
N2
Air
N2
100.0
99.5
99.0
98.5
98.0
97.5
Mass (%)
0.0
-0.5
-1.0
-1.5
-2.0
600
400
200
0
50
100
150
Time (min)

b)

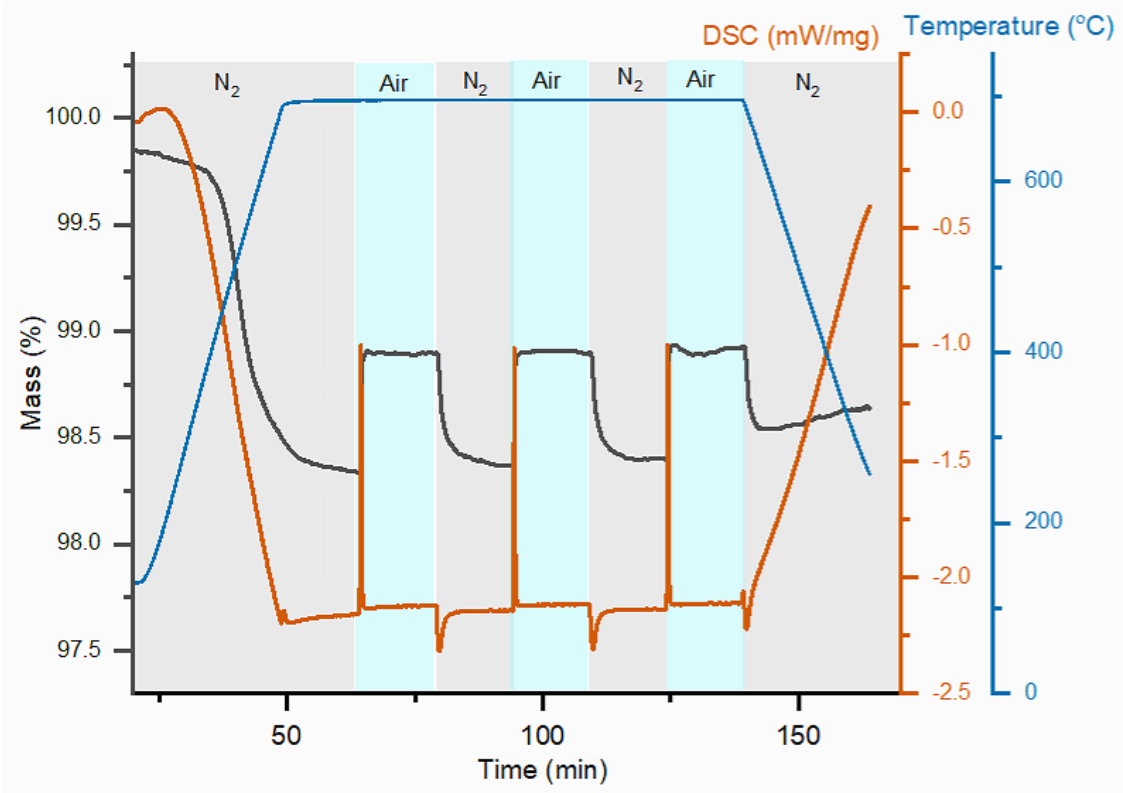
DSC (mW/mg)
Temperature (°C)
N2
Air
N2
Air
N2
Air
N2
100.0
99.5
99.0
98.5
98.0
97.5
Mass (%)
0.0
-0.5
-1.0
-1.5
-2.0
-2.5
600
400
200
0
50
100
150
Time (min)

c)

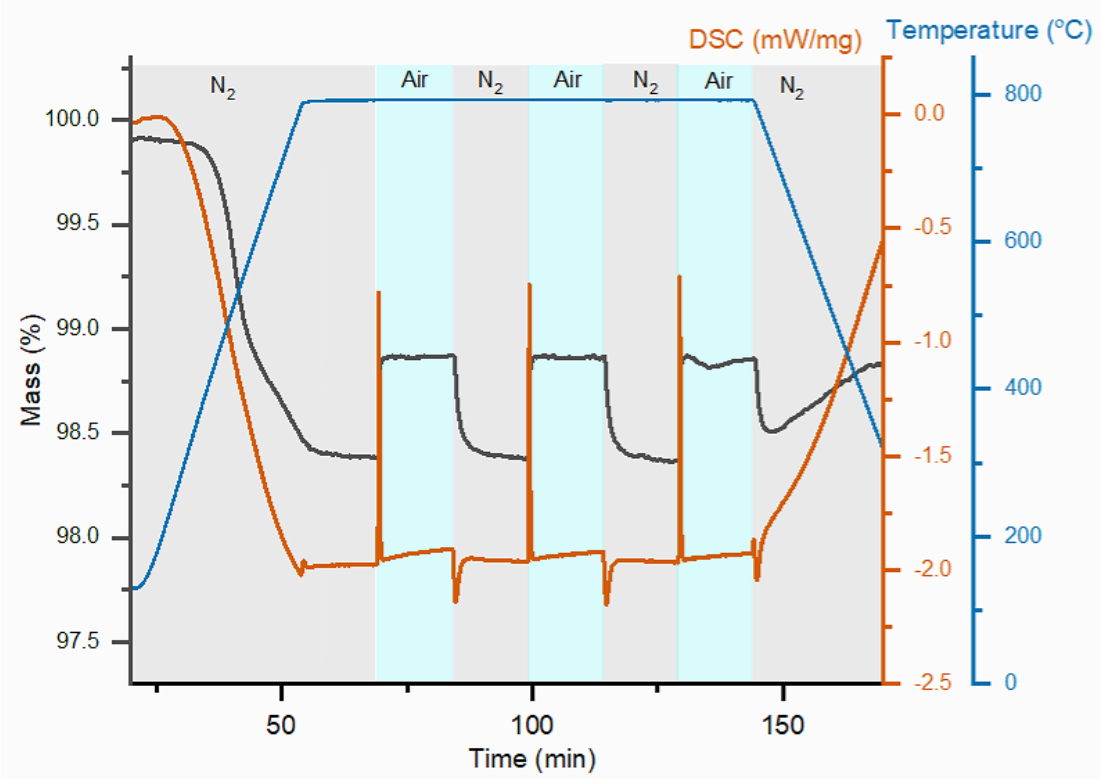

Figure B-4. Isothermal cycling data for $SrCo_{0.9}Sb_{0.1}O_{3-\delta}$ at a) 500 °C, b) 700 °C and c) 800 °C.

a)

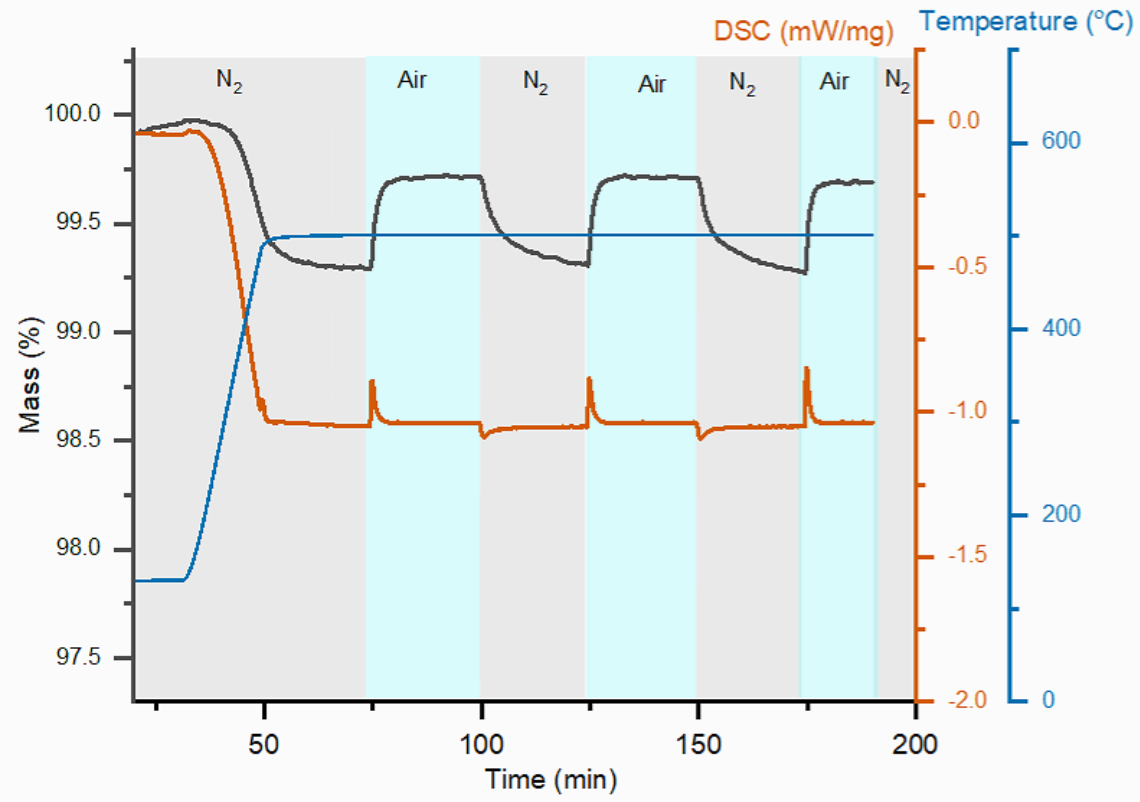
DSC (mW/mg)
Temperature (°C)
N2
Air
N2
Air
N2
Air
N2
100.0
99.5
99.0
98.5
98.0
97.5
Mass (%)
0.0
-0.5
-1.0
-1.5
-2.0
600
400
200
0
50
100
150
200
Time (min)

b)

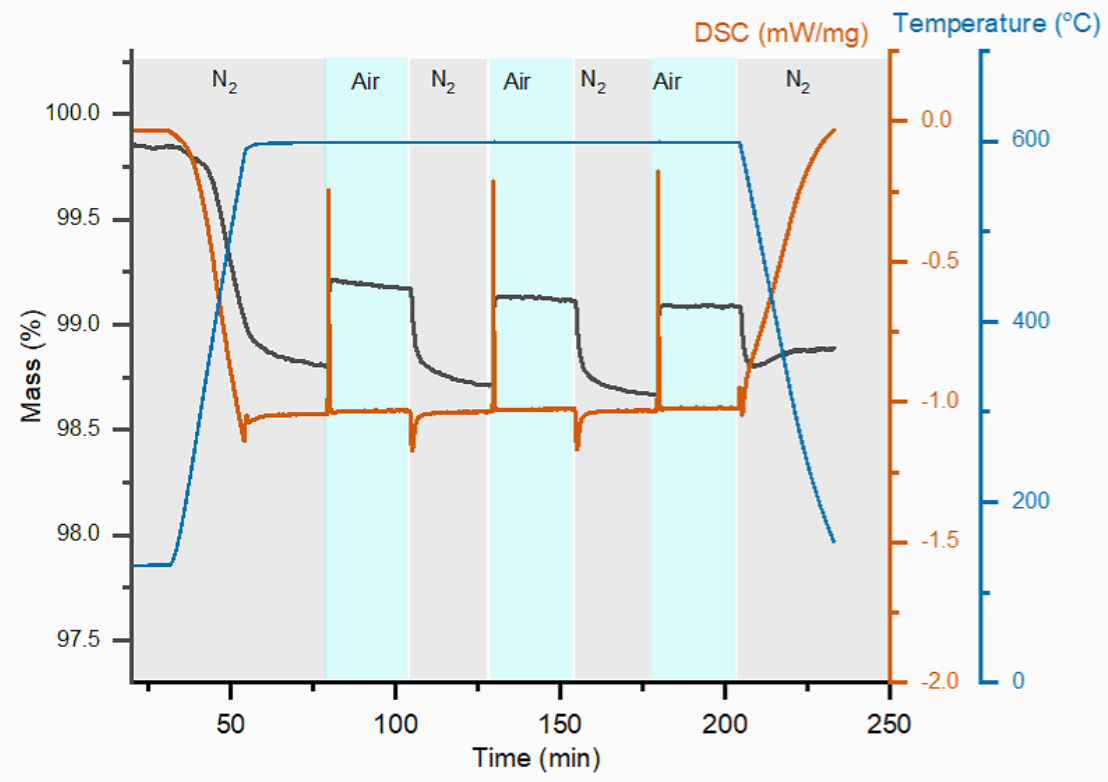
DSC (mW/mg)
Temperature (°C)
N2
Air
N2
Air
N2
Air
N2
100.0
99.5
99.0
98.5
98.0
97.5
Mass (%)
0.0
-0.5
-1.0
-1.5
-2.0
600
400
200
0
50
100
150
200
250
Time (min)

c)

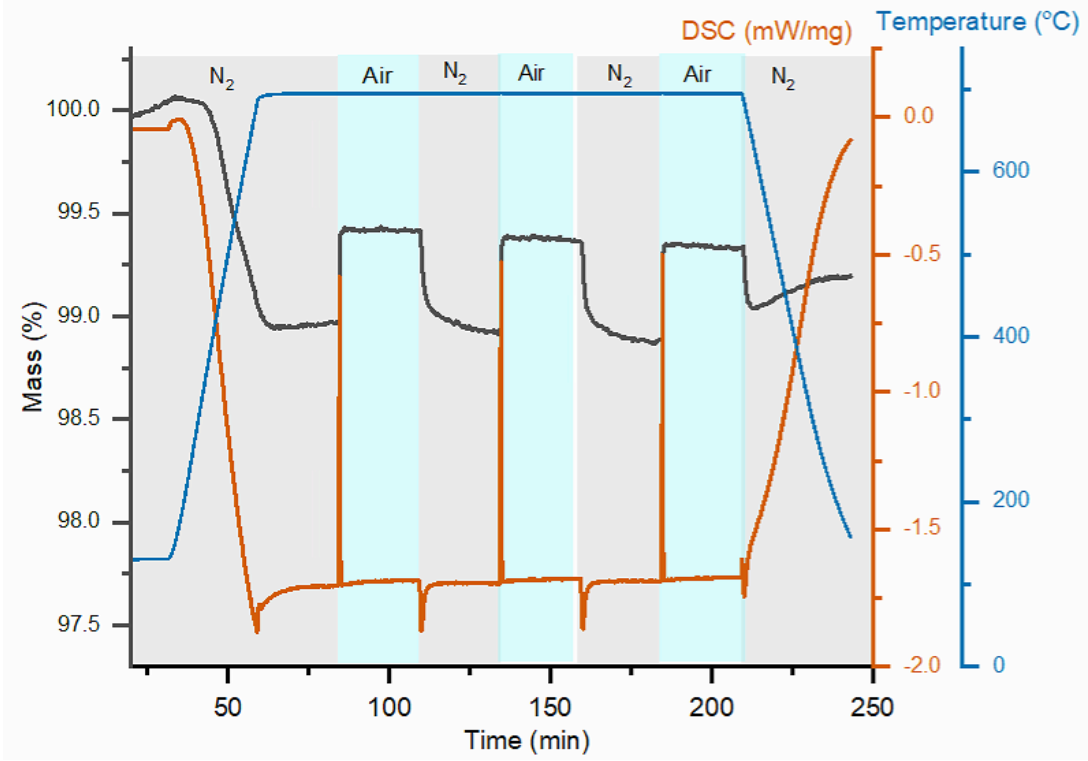

d)

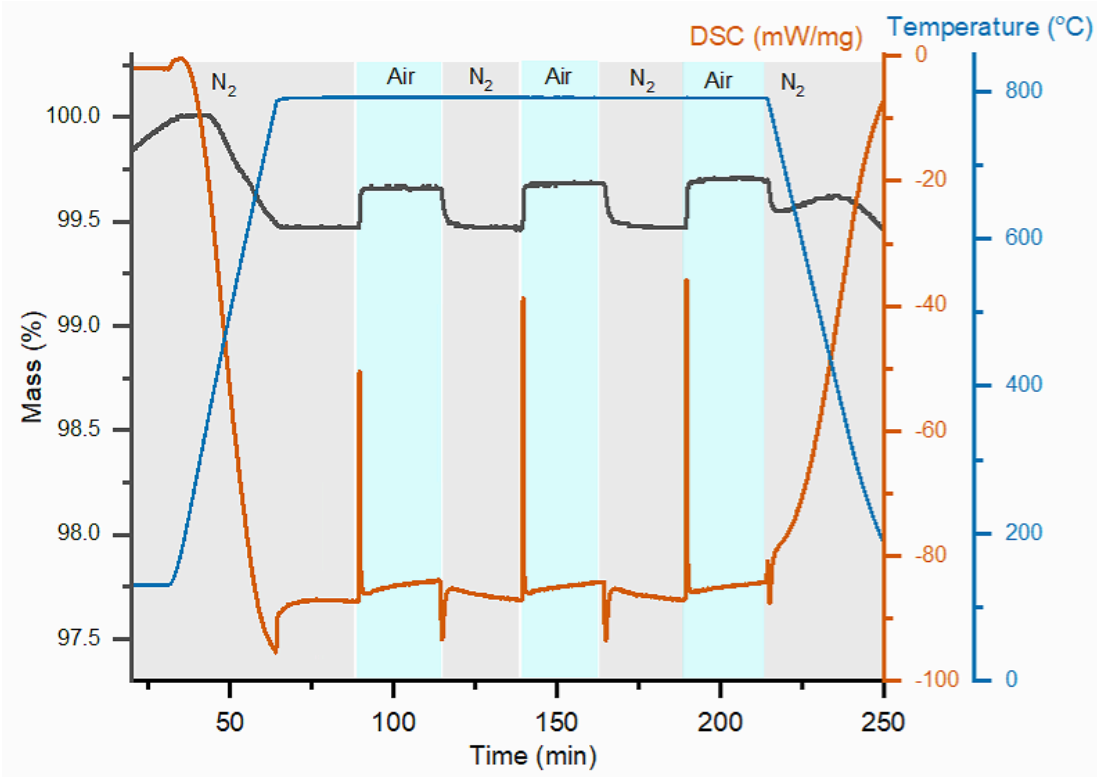

Figure B-5. Isothermal cycling data for $SrCo_{0.80}Sb_{0.20}O_{3-\delta}$ at a) 500 °C, b) 600 °C, c) 700 °C and d) 800 °C.

Appendix C – Supplementary information for Chapter 7

Convergence testing of DFT parameters

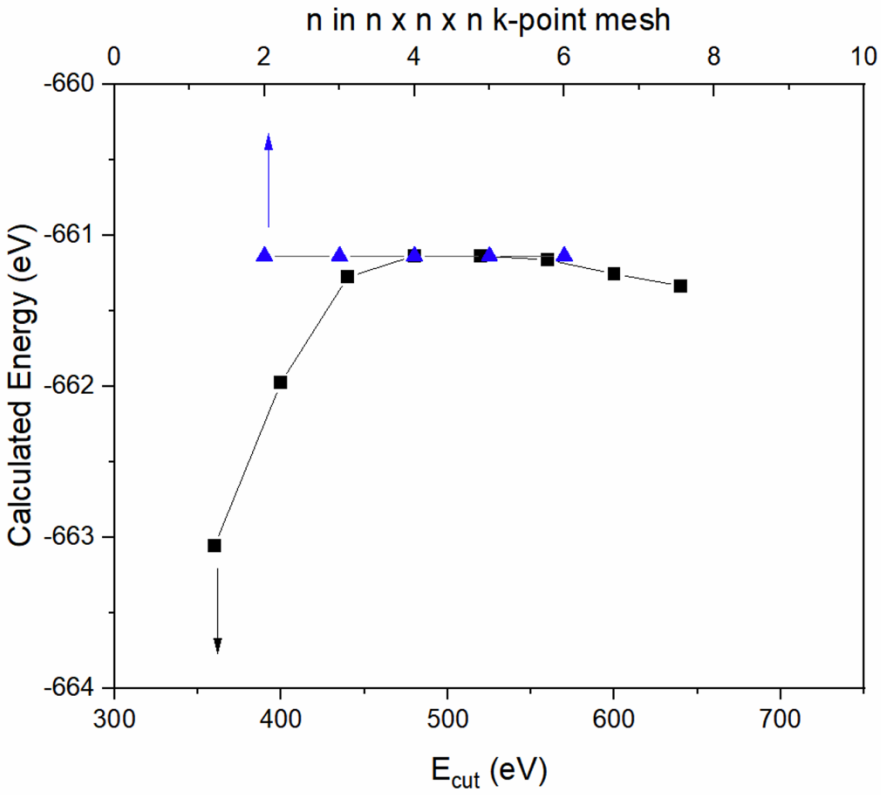

Figure C-1. Convergence testing results for the $LaCrO_3$ structure.

Appendix D – Supplementary information for Chapter 8

List of elements used for A and B sites for screening

Table D-1. Starting database of transition metal cations obtained from [393].

Element	Charge	Coordination	Spin State	Ionic Radius
Ac	3	VI		1.12
Ag	1	II		0.67
Ag	3	IVSQ		0.67
Ag	3	VI		0.75
Ag	2	IVSQ		0.79
Ag	2	VI		0.94
Ag	1	IV		1
Ag	1	IVSQ		1.02
Ag	1	V		1.09
Ag	1	VI		1.15
Ag	1	VII		1.22
Ag	1	VIII		1.28
Al	3	IV		0.39
Al	3	V		0.48
Al	3	VI		0.535
Am	4	VI		0.85
Am	4	VIII		0.95
Am	3	VI		0.975
Am	3	VIII		1.09
Am	2	VII		1.21
Am	2	VIII		1.26
Am	2	IX		1.31
Au	5	VI		0.57
Au	3	IVSQ		0.68
Au	3	VI		0.85
Au	1	VI		1.37
Ba	2	VI		1.35
Ba	2	VII		1.38
Ba	2	VIII		1.42
Ba	2	IX		1.47
Ba	2	X		1.52
Ba	2	XI		1.57

Ba	2	XII		1.61
Be	2	III		0.16
Be	2	IV		0.27
Be	2	VI		0.45
Bi	5	VI		0.76
Bi	3	V		0.96
Bi	3	VI		1.03
Bi	3	VIII		1.17
Bk	4	VI		0.83
Bk	4	VIII		0.93
Bk	3	VI		0.96
Ca	2	VI		1
Ca	2	VII		1.06
Ca	2	VIII		1.12
Ca	2	IX		1.18
Ca	2	X		1.23
Ca	2	XII		1.34
Cd	2	IV		0.78
Cd	2	V		0.87
Cd	2	VI		0.95
Cd	2	VII		1.03
Cd	2	VIII		1.1
Cd	2	XII		1.31
Ce	4	VI		0.87
Ce	4	VIII		0.97
Ce	3	VI		1.01
Ce	3	VII		1.07
Ce	4	X		1.07
Ce	4	XII		1.14
Ce	3	VIII		1.143
Ce	3	IX		1.196
Ce	3	X		1.25
Ce	3	XII		1.34
Cf	4	VI		0.821
Cf	4	VIII		0.92
Cf	3	VI		0.95
Cm	4	VI		0.85
Cm	4	VIII		0.95
Cm	3	VI		0.97
Co	4	IV		0.4
Co	4	VI	High Spin	0.53
Co	3	VI	Low Spin	0.545

Co	2	IV	High Spin	0.58
Co	3	VI	High Spin	0.61
Co	2	VI	Low Spin	0.65
Co	2	V		0.67
Co	2	VI	High Spin	0.745
Co	2	VIII		0.9
Cr	6	IV		0.26
Cr	5	IV		0.345
Cr	4	IV		0.41
Cr	6	VI		0.44
Cr	5	VI		0.49
Cr	4	VI		0.55
Cr	5	VIII		0.57
Cr	3	VI		0.615
Cr	2	VI	Low Spin	0.73
Cr	2	VI	High Spin	0.8
Cs	1	VI		1.67
Cs	1	VIII		1.74
Cs	1	IX		1.78
Cs	1	X		1.81
Cs	1	XI		1.85
Cs	1	XII		1.88
Cu	1	II		0.46
Cu	3	VI	Low Spin	0.54
Cu	2	IV		0.57
Cu	2	IVSQ		0.57
Cu	1	IV		0.6
Cu	2	V		0.65
Cu	2	VI		0.73
Cu	1	VI		0.77
Dy	3	VI		0.912
Dy	3	VII		0.97
Dy	3	VIII		1.027
Dy	2	VI		1.07
Dy	3	IX		1.083
Dy	2	VII		1.13
Dy	2	VIII		1.19
Er	3	VI		0.89
Er	3	VII		0.945
Er	3	VIII		1.004
Er	3	IX		1.062
Eu	3	VI		0.947

Eu	3	VII		1.01
Eu	3	VIII		1.066
Eu	3	IX		1.12
Eu	2	VI		1.17
Eu	2	VII		1.2
Eu	2	VIII		1.25
Eu	2	IX		1.3
Eu	2	X		1.35
Fe	6	IV		0.25
Fe	3	IV	High Spin	0.49
Fe	3	VI	Low Spin	0.55
Fe	3	V		0.58
Fe	4	VI		0.585
Fe	2	VI	Low Spin	0.61
Fe	2	IV	High Spin	0.63
Fe	2	IVSQ	High Spin	0.64
Fe	3	VI	High Spin	0.645
Fe	2	VI	High Spin	0.78
Fe	3	VIII	High Spin	0.78
Fe	2	VIII	High Spin	0.92
Fr	1	VI		1.8
Ga	3	IV		0.47
Ga	3	V		0.55
Ga	3	VI		0.62
Gd	3	VI		0.938
Gd	3	VII		1
Gd	3	VIII		1.053
Gd	3	IX		1.107
Hf	4	IV		0.58
Hf	4	VI		0.71
Hf	4	VII		0.76
Hf	4	VIII		0.83
Hg	2	II		0.69
Hg	2	IV		0.96
Hg	1	III		0.97
Hg	2	VI		1.02
Hg	2	VIII		1.14
Hg	1	VI		1.19
Ho	3	VI		0.901
Ho	3	VIII		1.015
Ho	3	IX		1.072
Ho	3	X		1.12

In	3	IV		0.62
In	3	VI		0.8
In	3	VIII		0.92
Ir	5	VI		0.57
Ir	4	VI		0.625
Ir	3	VI		0.68
K	1	IV		1.37
K	1	VI		1.38
K	1	VII		1.46
K	1	VIII		1.51
K	1	IX		1.55
K	1	X		1.59
K	1	XII		1.64
La	3	VI		1.032
La	3	VII		1.1
La	3	VIII		1.16
La	3	IX		1.216
La	3	X		1.27
La	3	XII		1.36
Li	1	IV		0.59
Li	1	VI		0.76
Li	1	VIII		0.92
Lu	3	VI		0.861
Lu	3	VIII		0.977
Lu	3	IX		1.032
Mg	2	IV		0.57
Mg	2	V		0.66
Mg	2	VI		0.72
Mg	2	VIII		0.89
Mn	7	IV		0.25
Mn	6	IV		0.255
Mn	5	IV		0.33
Mn	4	IV		0.39
Mn	7	VI		0.46
Mn	4	VI		0.53
Mn	3	V		0.58
Mn	3	VI	Low Spin	0.58
Mn	3	VI	High Spin	0.645
Mn	2	IV	High Spin	0.66
Mn	2	VI	Low Spin	0.67
Mn	2	V	High Spin	0.75
Mn	2	VI	High Spin	0.83

Mn	2	VII	High Spin	0.9
Mn	2	VIII		0.96
Mo	6	IV		0.41
Mo	5	IV		0.46
Mo	6	V		0.5
Mo	6	VI		0.59
Mo	5	VI		0.61
Mo	4	VI		0.65
Mo	3	VI		0.69
Mo	6	VII		0.73
Na	1	IV		0.99
Na	1	V		1
Na	1	VI		1.02
Na	1	VII		1.12
Na	1	VIII		1.18
Na	1	IX		1.24
Na	1	XII		1.39
Nb	5	IV		0.48
Nb	5	VI		0.64
Nb	4	VI		0.68
Nb	5	VII		0.69
Nb	3	VI		0.72
Nb	5	VIII		0.74
Nb	4	VIII		0.79
Nd	3	VI		0.983
Nd	3	VIII		1.109
Nd	3	IX		1.163
Nd	3	XII		1.27
Nd	2	VIII		1.29
Nd	2	IX		1.35
Ni	4	VI	Low Spin	0.48
Ni	2	IVSQ		0.49
Ni	2	IV		0.55
Ni	3	VI	Low Spin	0.56
Ni	3	VI	High Spin	0.6
Ni	2	V		0.63
Ni	2	VI		0.69
No	2	VI		1.1
Np	7	VI		0.71
Np	6	VI		0.72
Np	5	VI		0.75
Np	4	VI		0.87

Np	4	VIII	0.98
Np	3	VI	1.01
Np	2	VI	1.1
Os	8	IV	0.39
Os	6	V	0.49
Os	7	VI	0.525
Os	6	VI	0.545
Os	5	VI	0.575
Os	4	VI	0.63
Pa	5	VI	0.78
Pa	4	VI	0.9
Pa	5	VIII	0.91
Pa	5	IX	0.95
Pa	4	VIII	1.01
Pa	3	VI	1.04
Pb	4	IV	0.65
Pb	4	V	0.73
Pb	4	VI	0.775
Pb	4	VIII	0.94
Pb	2	IVPY	0.98
Pb	2	VI	1.19
Pb	2	VII	1.23
Pb	2	VIII	1.29
Pb	2	IX	1.35
Pb	2	X	1.4
Pb	2	XI	1.45
Pb	2	XII	1.49
Pd	1	II	0.59
Pd	4	VI	0.615
Pd	2	IVSQ	0.64
Pd	3	VI	0.76
Pd	2	VI	0.86
Pm	3	VI	0.97
Pm	3	VIII	1.093
Pm	3	IX	1.144
Pr	4	VI	0.85
Pr	4	VIII	0.96
Pr	3	VI	0.99
Pr	3	VIII	1.126
Pr	3	IX	1.179
Pt	5	VI	0.57
Pt	2	IVSQ	0.6

Pt	4	VI	0.625
Pt	2	VI	0.8
Pu	6	VI	0.71
Pu	5	VI	0.74
Pu	4	VI	0.86
Pu	4	VIII	0.96
Pu	3	VI	1
Ra	2	VIII	1.48
Ra	2	XII	1.7
Rb	1	VI	1.52
Rb	1	VII	1.56
Rb	1	VIII	1.61
Rb	1	IX	1.63
Rb	1	X	1.66
Rb	1	XI	1.69
Rb	1	XII	1.72
Rb	1	XIV	1.83
Re	7	IV	0.38
Re	7	VI	0.53
Re	6	VI	0.55
Re	5	VI	0.58
Re	4	VI	0.63
Rh	5	VI	0.55
Rh	4	VI	0.6
Rh	3	VI	0.665
Ru	8	IV	0.36
Ru	7	IV	0.38
Ru	5	VI	0.565
Ru	4	VI	0.62
Ru	3	VI	0.68
Sb	5	VI	0.6
Sb	3	IVPY	0.76
Sb	3	VI	0.76
Sb	3	V	0.8
Sc	3	VI	0.745
Sc	3	VIII	0.87
Se	6	IV	0.28
Se	6	VI	0.42
Se	4	VI	0.5
Sm	3	VI	0.958
Sm	3	VII	1.02
Sm	3	VIII	1.079

Sm	3	IX	1.132
Sm	2	VII	1.22
Sm	3	XII	1.24
Sm	2	VIII	1.27
Sm	2	IX	1.32
Sn	4	IV	0.55
Sn	4	V	0.62
Sn	4	VI	0.69
Sn	4	VII	0.75
Sn	4	VIII	0.81
Sr	2	VI	1.18
Sr	2	VII	1.21
Sr	2	VIII	1.26
Sr	2	IX	1.31
Sr	2	X	1.36
Sr	2	XII	1.44
Ta	5	VI	0.64
Ta	4	VI	0.68
Ta	5	VII	0.69
Ta	3	VI	0.72
Ta	5	VIII	0.74
Tb	4	VI	0.76
Tb	4	VIII	0.88
Tb	3	VI	0.923
Tb	3	VII	0.98
Tb	3	VIII	1.04
Tb	3	IX	1.095
Tc	7	IV	0.37
Tc	7	VI	0.56
Tc	5	VI	0.6
Tc	4	VI	0.645
Th	4	VI	0.94
Th	4	VIII	1.05
Th	4	IX	1.09
Th	4	X	1.13
Th	4	XI	1.18
Th	4	XII	1.21
Ti	4	IV	0.42
Ti	4	V	0.51
Ti	4	VI	0.605
Ti	3	VI	0.67
Ti	4	VIII	0.74

Ti	2	VI	0.86
Tl	3	IV	0.75
Tl	3	VI	0.885
Tl	3	VIII	0.98
Tl	1	VI	1.5
Tl	1	VIII	1.59
Tl	1	XII	1.7
Tm	3	VI	0.88
Tm	3	VIII	0.994
Tm	2	VI	1.03
Tm	3	IX	1.052
Tm	2	VII	1.09
U	6	II	0.45
U	6	IV	0.52
U	6	VI	0.73
U	5	VI	0.76
U	6	VII	0.81
U	5	VII	0.84
U	6	VIII	0.86
U	4	VI	0.89
U	4	VII	0.95
U	4	VIII	1
U	3	VI	1.025
U	4	IX	1.05
U	4	XII	1.17
V	5	IV	0.355
V	5	V	0.46
V	4	V	0.53
V	5	VI	0.54
V	4	VI	0.58
V	3	VI	0.64
V	4	VIII	0.72
V	2	VI	0.79
W	6	IV	0.42
W	6	V	0.51
W	6	VI	0.6
W	5	VI	0.62
W	4	VI	0.66
Y	3	VI	0.9
Y	3	VII	0.96
Y	3	VIII	1.019
Y	3	IX	1.075

Yb	3	VI	0.868
Yb	3	VII	0.925
Yb	3	VIII	0.985
Yb	2	VI	1.02
Yb	3	IX	1.042
Yb	2	VII	1.08
Yb	2	VIII	1.14
Zn	2	IV	0.6
Zn	2	V	0.68
Zn	2	VI	0.74
Zn	2	VIII	0.9
Zr	4	IV	0.59
Zr	4	V	0.66
Zr	4	VI	0.72
Zr	4	VII	0.78
Zr	4	VIII	0.84
Zr	4	IX	0.89

Appendix E – Supplementary information for Chapter 9

Convergence testing of DFT parameters

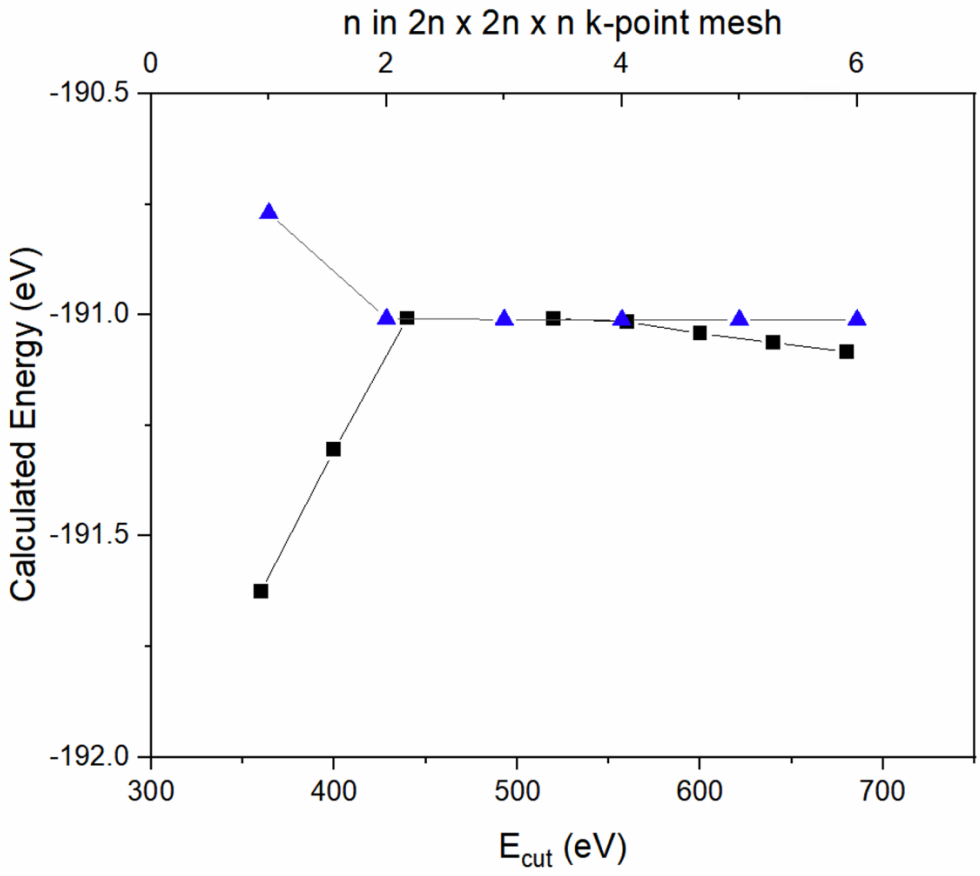

Figure E-1. Convergence testing results for the Ca_2MnO_4 structure.